

Advances in Meteorology

Hydrological Processes in Changing Climate, Land Use, and Cover Change

Guest Editors: Yongqiang Zhang, Fubao Sun, Ming Pan, Tom Van Niel, and Martin Wegehenkel





Hydrological Processes in Changing Climate, Land Use, and Cover Change

Advances in Meteorology

Hydrological Processes in Changing Climate, Land Use, and Cover Change

Guest Editors: Yongqiang Zhang, Fubao Sun, Ming Pan,
Tom Van Niel, and Martin Wegehenkel



Copyright © 2016 Hindawi Publishing Corporation. All rights reserved.

This is a special issue published in "Advances in Meteorology." All articles are open access articles distributed under the Creative Commons Attribution License, which permits unrestricted use, distribution, and reproduction in any medium, provided the original work is properly cited.

Editorial Board

José Antonio Adame, Spain
Cesar Azorin-Molina, Spain
Guillermo Baigorria, USA
Marina Baldi, Italy
Abderrahim Bentamy, France
Massimo A. Bollasina, UK
Stefania Bonafoni, Italy
Isabella Bordi, Italy
Alex Cannon, Canada
Claudio Carbone, Italy
Dominique Carrer, France
Charles Chemel, UK
Annalisa Cherchi, Italy
James Cleverly, Australia
Jill S. M. Coleman, USA
Gabriele Curci, Italy
Mladjen Ćurić, Serbia
Maher A. Dayeh, USA
Klaus Dethloff, Germany
Panuganti C. S. Devara, India
Julio Diaz, Spain
Arona Diedhiou, France
Stefano Dietrich, Italy
Eugenio Domínguez Vilches, Spain
Antonio Donateo, Italy
Igor Esau, Norway
Stefano Federico, Italy
Enrico Ferrero, Italy
Rossella Ferretti, Italy
Roberto Fraile, Spain
Charmaine Franklin, Australia
Jan Friesen, Germany

Maria Ángeles García, Spain
Herminia García Mozo, Spain
Eduardo García-Ortega, Spain
Luis Gimeno, Spain
Jorge E. Gonzalez, USA
Ismail Gultepe, Canada
Rafiq Hamdi, Belgium
Adel Hanna, USA
Hiroyuki Hashiguchi, Japan
Tareq Hussein, Jordan
Bradley G. Illston, USA
Ivar S A Isaksen, Norway
Yasunobu Iwasaka, Japan
Pedro Jiménez-Guerrero, Spain
Kuruvilla John, USA
Charles Jones, USA
Hann-Ming H. Juang, USA
George Kallos, Greece
Harry D. Kambezidis, Greece
Nir Y. Krakauer, USA
Simon O. Krichak, Israel
Hisayuki Kubota, Japan
Haim Kutiel, Israel
Richard Leaitch, Canada
Monique Leclerc, USA
Ilan Levy, Israel
Gwo-Fong Lin, Taiwan
Anthony R. Lupo, USA
Paolo Madonia, Italy
Andreas Matzarakis, Germany
Samantha Melani, Italy
Nicholas Meskhidze, USA

Christophe Messenger, France
Mario M. Miglietta, Italy
Takashi Mochizuki, Japan
Goro Mouri, Japan
Brian R. Nelson, USA
Efthymios I. Nikolopoulos, USA
Sandip Pal, USA
Giulia Panegrossi, Italy
Giulia Pavese, Italy
Kyaw T. Paw, USA
Olivier P. Prat, USA
Sara C. Pryor, USA
Philippe Ricaud, France
Tomeu Rigo, Spain
Filomena Romano, Italy
Jose Antonio Ruiz-Arias, Spain
Haydee Salmun, USA
Pedro Salvador, Spain
Arturo Sanchez-Lorenzo, Spain
Andres Schmidt, USA
Shraddhanand Shukla, USA
Fiona Smith, UK
Francisco J. Tapiador, Spain
Yoshihiro Tomikawa, Japan
Tomoo Ushio, Japan
Rogier Van Der Velde, Netherlands
Sergio M. Vicente-Serrano, Spain
Francesco Viola, Italy
Alastair Williams, Australia
Olga Zolina, France

Contents

Hydrological Processes in Changing Climate, Land Use, and Cover Change

Yongqiang Zhang, Fubao Sun, Ming Pan, Tom Van Niel, and Martin Wegehenkel
Volume 2016, Article ID 7273424, 2 pages

Interannual Variation of the Surface Temperature of Tropical Forests from Satellite Observations

Huilin Gao, Shuai Zhang, Rong Fu, Wenhong Li, and Robert E. Dickinson
Volume 2016, Article ID 4741390, 11 pages

Response of Extreme Hydrological Events to Climate Change in the Water Source Area for the Middle Route of South-to-North Water Diversion Project

Wei Yang, Liping Zhang, Lijie Shan, Xinchu Chen, and Shaodan Chen
Volume 2016, Article ID 2486928, 15 pages

Comparison of the Spatiotemporal Variability of Temperature, Precipitation, and Maximum Daily Spring Flows in Two Watersheds in Quebec Characterized by Different Land Use

Ali A. Assani, Raphaëlle Landry, Christophe Kinnard, Ouassila Azouaoui, Christine Demers, and Karine Lacasse
Volume 2016, Article ID 3746460, 8 pages

Predicting Surface Runoff from Catchment to Large Region

Hongxia Li, Yongqiang Zhang, and Xinyao Zhou
Volume 2015, Article ID 720967, 13 pages

Climate Change Impact on the Hydrology of a Typical Watershed in the Tianshan Mountains

Gonghuan Fang, Jing Yang, Yaning Chen, Shuhua Zhang, Haijun Deng, Haimeng Liu, and Philippe De Maeyer
Volume 2015, Article ID 960471, 10 pages

Hydrologic Responses to Land Use Change in the Loess Plateau: Case Study in the Upper Fenhe River Watershed

Zhixiang Lu, Songbing Zou, Zuodong Qin, Yonggang Yang, Honglang Xiao, Yongping Wei, Kai Zhang, and Jiali Xie
Volume 2015, Article ID 676030, 10 pages

Comparison of Stationary and Dynamic Conceptual Models in a Mountainous and Data-Sparse Catchment in the South-Central Chilean Andes

Camila Toledo, Enrique Muñoz, and Mauricio Zambrano-Bigiarini
Volume 2015, Article ID 526158, 14 pages

Groundwater—Surface Water Interactions in a Mountain-to-Coast Watershed: Effects of Climate Change and Human Stressors

S. B. Foster and D. M. Allen
Volume 2015, Article ID 861805, 22 pages

Modeling the Effects of Land-Cover Change on Rainfall-Runoff Relationships in a Semiarid, Eastern Mediterranean Watershed

Noa Ohana-Levi, Arnon Karnieli, Roey Egozi, Amir Givati, and Aviva Peeters
Volume 2015, Article ID 838070, 16 pages

The Elements of Water Balance in the Changing Climate in Poland

Małgorzata Szwed

Volume 2015, Article ID 149674, 13 pages

Hydrologic Variations and Stochastic Modeling of Runoff in Zoige Wetland in the Eastern Tibetan Plateau

Guanghua Qin, Hongxia Li, Zejiang Zhou, Kechao Song, and Li Zhang

Volume 2015, Article ID 529354, 6 pages

Serial Analysis of Ten Precipitation-Based Indices by Land Use in Semiarid Regions

Victor M. Rodríguez-Moreno, J. Ariel Ruíz-Corral, J. Saúl Padilla-Ramírez, Alfonso Peña-Ramos, and Thomas G. Kretzschmar

Volume 2015, Article ID 797434, 13 pages

Comparison of Two Approaches for Estimating Precipitation Elasticity of Streamflow in China's Main River Basins

Xinyao Zhou, Yongqiang Zhang, and Yonghui Yang

Volume 2015, Article ID 924572, 8 pages

Interpolation of Missing Precipitation Data Using Kernel Estimations for Hydrologic Modeling

Hyojin Lee and Kwangmin Kang

Volume 2015, Article ID 935868, 12 pages

Effects of Climate Change and Human Activities on Surface Runoff in the Luan River Basin

Sidong Zeng, Chesheng Zhan, Fubao Sun, Hong Du, and Feiyu Wang

Volume 2015, Article ID 740239, 12 pages

Web-Based Data Integration and Interoperability for a Massive Spatial-Temporal Dataset of the Heihe River Basin ESience Framework

Qingchun Guo, Yaonan Zhang, Zhenfang He, and Yufang Min

Volume 2015, Article ID 982062, 13 pages

An Evaluation of River Health for the Weihe River in Shaanxi Province, China

Jinxi Song, Dandong Cheng, Qi Li, Xingjun He, Yongqing Long, and Bo Zhang

Volume 2015, Article ID 476020, 13 pages

Identifying Vegetation Dynamics and Sensitivities in Response to Water Resources Management in the Heihe River Basin in China

Dongqin Yin, Xiang Li, Yuefei Huang, Yuan Si, and Rui Bai

Volume 2015, Article ID 861928, 12 pages

Research on Nonpoint Source Pollution Assessment Method in Data Sparse Regions: A Case Study of Xichong River Basin, China

Xing Liu, Donglong Li, Hongbo Zhang, Shixiang Cai, Xiaodong Li, and Tianqi Ao

Volume 2015, Article ID 519671, 10 pages

Analysis of Changes in Precipitation and Drought in Aksu River Basin, Northwest China

Yuhu Zhang, Wanyuan Cai, Qiuhua Chen, Yunjun Yao, and Kaili Liu

Volume 2015, Article ID 215840, 15 pages

Editorial

Hydrological Processes in Changing Climate, Land Use, and Cover Change

Yongqiang Zhang,¹ Fubao Sun,² Ming Pan,³ Tom Van Niel,⁴ and Martin Wegehenkel⁵

¹CSIRO Land and Water Flagship, P.O. Box 1666, Canberra, ACT 2601, Australia

²The Institute of Geographic Sciences and Natural Resources Research (IGSNRR), Chinese Academy of Sciences, Beijing 100101, China

³Department of Civil and Environmental Engineering, Princeton University, NJ 08544, USA

⁴CSIRO Land and Water, Private Bag No. 5, Wembley, WA 6913, Australia

⁵Institute of Landscape Systems Analysis, Leibniz Centre for Agricultural Landscape Research, Eberswalder Straße 84, 15374 Müncheberg, Germany

Correspondence should be addressed to Yongqiang Zhang; yongqiang.zhang@csiro.au

Received 20 August 2015; Accepted 27 August 2015

Copyright © 2016 Yongqiang Zhang et al. This is an open access article distributed under the Creative Commons Attribution License, which permits unrestricted use, distribution, and reproduction in any medium, provided the original work is properly cited.

Global environmental change, such as climate change, land use, and land cover change, is noticeably influencing hydrological processes from catchment to regional and to global scales, resulting in hydrologic nonstationarity. Therefore, it is urgent to improve our skills or methods to better understand mechanism of hydrological processes under global environmental change. This needs multidisciplinary studies that involve hydrology, meteorology, remote sensing, ecology, agriculture, and so forth.

We were invited by this journal to propose this special issue in June 2014. Researchers across globe were invited to contribute their original research articles to this special issue.

This special issue received high attention from hydrology, meteorology, remote sensing, agriculture, and ecology communities. The accepted papers cover wide ranges of topics, including (1) introducing physical/statistical methodologies and models to simulate hydrological processes in various spatial scales; (2) using various techniques/methods/models to separate climate change, land use, and cover change impact on hydrological processes; (3) detecting trends and variation of hydrological variables, such as runoff, actual evapotranspiration, and soil moisture.

There are papers studying predicting runoff, estimating runoff, and other water balance components' response to climate change and land cover changes. N. Ohana-Levi et al. (2015) modelled the effects of land cover change on rainfall-runoff relationships in a semiarid, eastern Mediterranean

watershed. Z. Lu et al. (2015) introduced a case study in the Loess Plateau investigating hydrologic responses to land use change. S. Zeng et al. (2015) studied effects of climate change and human activities on surface runoff in the Luan River Basin. G. Qin et al. (2015) simulated hydrologic variations and stochastic modeling of runoff in Zoige wetland in the Eastern Tibetan Plateau. H. Li et al. (2015) introduced a review paper summarizing state-of-the-art studies for predicting surface runoff from catchment to large region. W. Yang et al. (2015) explored the process of extreme floods by using multivariate analysis to characterize flood and precipitation event data in combination with historical data and simulated from global climate models for the water source area for the middle route of south-to-north water diversion project, China. G. Fang et al. (2015) investigated future climate change influencing runoff availability in Kaidu River Basin in the Tianshan Mountains. M. Szwed (2015) estimated changes in water balance components including precipitation, evaporation, and runoff between the historic period (1961–1990) and future period (2071–2100) in Poland.

There are papers investigating improving precipitation data accuracy, estimating drought and precipitation indices. H. Lee and K. Kang (2015) conducted interpolation of missing precipitation data using kernel estimations for hydrologic modeling. V. M. Rodríguez-Moreno et al. (2015) used serial analysis of ten precipitation-based indices by land use in the semiarid physiographic province of Mesa Central, Mexico.

X. Zhou et al. (2015) compared two approaches for estimating precipitation elasticity of streamflow in China's main river basins. Y. Zhang et al. (2015) estimated changes in precipitation and drought in Aksu River Basin, Northwest China.

There are papers addressing river and catchment environmental issues. X. Liu et al. (2015) conducted "Research on Nonpoint Source Pollution Assessment Method in Data Sparse Regions: A Case Study of Xichong River Basin, China." J. Song et al. (2015) evaluated river health for the Weihe River in Shaanxi Province, China.

The rest of the papers focus on various hydrological and ecohydrological topics from small catchments to large regions. S. B. Foster and D. M. Allen (2015) used a coupled numerical model to investigate groundwater and surface water interactions in a mountain-to-coast watershed in British Columbia, Canada. D. Yin et al. (2015) identified vegetation dynamics and sensitivities in response to water resources management in the Heihe River Basin in China. C. Toledo et al. (2015) compared stationary and dynamic conceptual models for estimating hydrological processes in a mountainous and data-sparse catchment in the south-central Chilean Andes. H. Gao et al. (2015) used remote sensing observations to detect interannual variation of the surface temperature of tropical forests over Amazon and Congo rainforests. A. A. Assani et al. (2015) compared spatiotemporal variability of temperature and precipitation with that of the magnitude and timing of maximum daily spring flow in L'Assomption River (agricultural) and Matawin River (forested) watersheds in Quebec, Canada. Q. Guo et al. (2015) proposed an approach for web-based data integration and interoperability for a massive spatial-temporal dataset of the Heihe River Basin framework.

Acknowledgments

We thank this journal for providing us with the opportunity to publish this special issue. We also thank all reviewers for their critical comments and constructive suggestions for selecting high-quality studies and improving quality of the papers published in this special issue.

*Yongqiang Zhang
Fubao Sun
Ming Pan
Tom Van Niel
Martin Wegehenkel*

Research Article

Interannual Variation of the Surface Temperature of Tropical Forests from Satellite Observations

Huilin Gao,¹ Shuai Zhang,¹ Rong Fu,² Wenhong Li,³ and Robert E. Dickinson²

¹Zachry Department of Civil Engineering, Texas A&M University, College Station, TX 77840, USA

²Department of Geological Sciences, Jackson School of Geosciences, University of Texas at Austin, Austin, TX 78712, USA

³Earth and Ocean Sciences, Nicholas School of the Environment, Duke University, Duke, NC 27708, USA

Correspondence should be addressed to Huilin Gao; hgao@civil.tamu.edu

Received 15 December 2014; Revised 8 May 2015; Accepted 17 May 2015

Academic Editor: Thomas Van Niel

Copyright © 2016 Huilin Gao et al. This is an open access article distributed under the Creative Commons Attribution License, which permits unrestricted use, distribution, and reproduction in any medium, provided the original work is properly cited.

Land surface temperatures (LSTs) within tropical forests contribute to climate variations. However, observational data are very limited in such regions. This study used passive microwave remote sensing data from the Special Sensor Microwave/Imager (SSM/I) and the Special Sensor Microwave Imager Sounder (SSMIS), providing observations under all weather conditions, to investigate the LST over the Amazon and Congo rainforests. The SSM/I and SSMIS data were collected from 1996 to 2012. The morning and afternoon observations from passive microwave remote sensing facilitate the investigation of the interannual changes of LST anomalies on a diurnal basis. As a result of the variability of cloud cover and the corresponding reduction of solar radiation, the afternoon LST anomalies tend to vary more than the morning LST anomalies. The dominant spatial and temporal patterns for interseasonal variations of the LST anomalies over the tropical rainforest were analyzed. The impacts of droughts and El Niños on this LST were also investigated. Differences between early morning and late afternoon LST anomalies were identified by the remote sensing product, with the morning LST anomalies controlled by humidity (according to comparisons with the National Centers for Environmental Prediction (NCEP) reanalysis data).

1. Introduction

Accurate and reliable observations are essential for characterizing and understanding climate variations and long term change. *In situ* observations in the tropics are sparse, and their uncertainty tends to be larger than that in the northern hemisphere mid-latitudes. Although several versions of gridded data have been interpolated from *in situ* meteorological measurements (e.g., [1]) and made available at a global scale, discrepancies arise amongst these datasets due to their different spatial averaging techniques, treatment of gaps in the data, and the number of stations used by different analyses [2]. Observations over tropical forests are extremely sparse, especially for the time period before the late 1970s [3]. Surface warming in these regions could substantially change the regional and global terrestrial exchange of carbon with the atmosphere [4–6]. *In situ* measurements, which represent the surface air temperature at 2 m above the surface, are mostly located over grass or bare ground and differ by as

much as 3 to 5 K from the land surface temperature (LST) of a tropical forest canopy [7]. Such large differences could confound accurate detection of changes in LST (which is also referred to as the canopy skin temperature, in the case of rainforests) and subsequently hinder evaluation of global climate models (GCMs) over tropical forests.

The most advanced (and now the most commonly used) LST measurements are those from the Moderate Resolution Imaging Spectroradiometer (MODIS), which resides on each of the NASA Earth Observation System (EOS) satellites—terra and aqua (since 1999 and 2002, resp.). However, MODIS measurements are limited to clear sky conditions and provide few samples over the tropical forests when skies are cloudy and/or rainy [7, 8]. To address this problem, Gao et al. [7] developed an empirical algorithm to provide the forest canopy skin temperature during all weather conditions using the Advanced Microwave Scanning Radiometer for the Earth Observing System (AMSR-E). In addition, about 30-year microwave data have been collected from passive radiometers

such as the Scanning Multichannel Microwave Radiometer (SSMR, 1978 to 1987), the Special Sensor Microwave/Imager (SSM/I, 1987 to present), and the Special Sensor Microwave Imager Sounder (SSMIS, 2003 to present). The LST based on these passive microwave retrievals from different radiometers, if calibrated against each other, could potentially allow us to examine changes of canopy skin temperature in the tropical forests since the late 1970s—the period when the global air temperature increase has become rapid and attributable to anthropogenic forcing [9, 10].

This work uses the microwave derived all weather LST product to investigate the interannual variability of the canopy skin temperature over tropical forests. The 19 GHz polarized brightness temperatures were collected by F13 SSM/I and F17 SSMIS. The F13 SSM/I was in service from May 1995 to November 2009, while F17 SSMIS has been collecting data from December 2006 to present. We focus on studying LST anomalies from January 1996 to December 2012 over both the Amazon and the Congo basin rainforests. An intersatellite calibration of the 19 GHz polarized brightness temperatures during the overlapping period between F13 SSM/I and F17 SSMIS was conducted to maintain consistency between the two data sources.

The objective of this study is to answer the following questions:

- (1) What are the dominant spatial and temporal patterns for interannual variations of canopy skin temperature over tropical rainforests?
- (2) How would droughts and El Niños affect the LST over these two regions?
- (3) How different are the interannual changes of early morning (6 a.m.) and late afternoon (6 p.m.) LST anomalies? Are these differences physically reasonable?

We concentrate on the Amazon and Congo basins. Section 2 introduces the satellite data and the intercalibration method, as well as the other data sources used in this study; Section 3 shows the results and analyses over the Amazon forest; Section 4 investigates the LST anomalies over the Congo basin forest; and Section 5 summarizes results and draws conclusions.

2. Data and Methodology

2.1. SSM/I and SSMIS Satellite Data. The first SSM/I sensor (F08) was launched in 1987 by the Defense Meteorological Satellites Program (DMSP). Since then, a series of SSM/I and SSMIS sensors (F11, F13, F15, F16, F17, and F18) have been launched consecutively to measure atmosphere, ocean, and terrain microwave brightness temperatures at near real time. Flying in a polar orbit, these sensors provide both vertically and horizontally polarized microwave data at 3 frequencies—19.35, 37.0, and 85.5 GHz—and horizontally polarized data at 22.2 GHz. The ascending and descending equatorial crossing times for the satellites used in this study (i.e., F13 and F17) are very near 6 p.m. and 6 a.m. This paper obtains the brightness temperatures from data

collected by the NOAA/NASA SSM/I Pathfinder Program made available from the National Snow and Ice Data Center (NSIDC). We used the level 3 Equal-Area Scalable Earth-Grid (EASE-Grid) brightness temperatures ([11], http://nsidc.org/data/docs/daac/nsidc0032.ssmi_ease_tbs.gd.html). The data are daily, separated by ascending and descending passes, and consist of gridded values at 25 km resolution. However, since the daily observations cannot cover the entire globe, there is typically one overpass on every other day for a given location. Consequently, the average number of observations per pixel per month is approximately 15. We further interpolated the EASE-Grid data into 0.25° resolution grids.

The input orbital brightness temperature data from NSIDC were ingested via the Remote Sensing Systems (RSS) software [12], with the mode for sensor intercalibrations turned off. We chose to study the 17-year period from January 1996 to December 2012, to cover significant climate variability—including events such as the 1997 to 1998 strong El Niño and the 2005 and 2010 droughts over the Amazon. The F17 observed horizontally and vertically polarized brightness temperatures ($T_{b,h}$ and $T_{b,v}$) were calibrated according to their counterpart F13 measurements. The process contains three steps: (1) averaging the ascending (and descending) brightness temperatures ($T_{b,h}$ and $T_{b,v}$) from daily to monthly for both the F13 and the F17 observations; (2) deriving a linear relationship between F13 and F17 for each pixel during the overlapping period of the two satellites (i.e., from 2007 to 2008); and (3) calibrating F17 observations from 2009 to 2012 based on the relationship established in step 2.

2.2. SSM/I LST over the Tropical Rainforest. A global land cover map derived from MODIS was used to select the tropical forests over the Amazon basin and Congo basin. The LST for these areas was retrieved using 19.35 GHz polarized brightness temperatures and an algorithm developed by Gao et al. [7]. The general concept of the LST microwave retrieval algorithm lies in the combined use of two equations, as outlined below. The first equation is based on the brightness temperature definition as follows:

$$T_s = \frac{T_{b,h}}{\varepsilon_h}, \quad (1)$$

where T_s is the LST, $T_{b,h}$ is the horizontal brightness temperature, and ε_h is the horizontal emissivity. The value for ε_h can be inferred from the Polarization Ratio (PR), which is defined as $PR = T_{b,h}/T_{b,v}$. To establish the empirical ε_h -PR relationship during a training period, ε_h was calculated as the ratio between MODIS LST and SSM/I $T_{b,h}$.

As described in Gao et al. [7], the quality controlled MODIS LST data during a dry month in July 2002 were selected as the training data. The training domain was the forested area within the entire Amazon basin, from 20°S to 13°N latitude and 82°W to 34°W longitude. Since the empirical relationship is independent of observation time, the same relationship was used for estimating LST both in the morning and in the afternoon. The empirical relationship is shown as

$$\varepsilon_h = 1.0038 \times PR \times PR - 0.1226 \times PR + 0.0799. \quad (2)$$

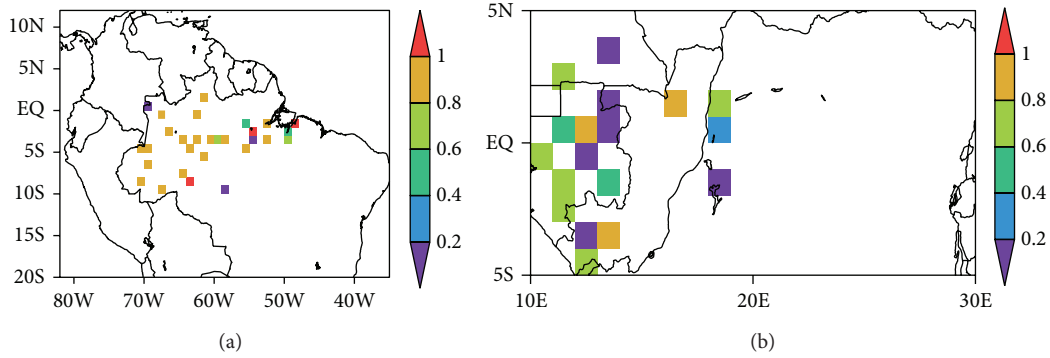


FIGURE 1: The temporal coverage of rain gauges within each $1^\circ \times 1^\circ$ pixel with the results represented as a fraction of the total time duration from 1996 to 2006 over (a) the Amazon rainforests and (b) the Congo rainforests.

Once the ε_h -PR relationship was established, passive microwave based LST could be estimated from $T_s = T_{b,h}/\varepsilon_h$.

In the study by Gao et al. [7], the passive microwave LST was validated using *in situ* temperature measurements (at the satellite overpass time) from 12 meteorological stations under all weather conditions over the Amazon forests. The correlation coefficient and Root Mean Square Error (RMSE) during the cloudy/rainy days were 0.68 and 1.7 K, respectively. The passive microwave LST during the cloudy/rainy days actually outperformed the remotely sensed LST during the clear days (both from the microwave sensor and from MODIS).

For each day from January 1, 1996, to December 31, 2012, LST values were calculated for the ascending and descending orbits, respectively. To eliminate the nonforested areas in this study, a $1^\circ \times 1^\circ$ mask which extracted the rainforests was applied to the SSM/I brightness temperature data. The mask was derived from the MODIS land cover classification map. The daily LSTs were then averaged for each month to smooth out random uncertainties from the daily data. We further calculated the temperature anomalies for each month for both the descending/morning and the ascending/afternoon orbits. In order to focus on variations at seasonal and inter-annual levels, the monthly anomalies were smoothed using a 3-month moving average.

2.3. Rainfall Data from the Global Precipitation Climatology Centre (GPCC). We used monthly precipitation from the Global Precipitation Climatology Centre (GPCC), at $1^\circ \times 1^\circ$ resolution, to assist the analysis. This precipitation data is derived from *in situ* measurements obtained from rain gauge networks [13]. Figure 1 shows the distribution of rain gauges and the temporal availability within each $1^\circ \times 1^\circ$ pixel, from 1996 to 2006 over the two rainforests studied. It appears that the Amazon has more evenly distributed stations than the Congo basin and that most of the gauges have collected data over the entire period studied. A comparison of rainfall datasets by Juarez et al. [14] suggests that GPCC data agree well with the Tropical Rainfall Measurement Mission (TRMM) product over tropical South America. The number of rain gauges over the Congo basin is very limited, and they tend to be concentrated at the edge of the forest. Additionally,

most of these instruments only collected data over a short period. Therefore, in the following sections, the comparison of rainfall with the LST anomalies is limited to the Amazon. The GPCC data is also used for calculating the Standard Precipitation Index (SPI [15]) to investigate the relationship between LST anomalies and drought in Section 3. Recommended by the World Meteorological Organization as a standard to characterize meteorological droughts [16], SPI is a probability index that has been used in many studies for abnormal wetness and dryness conditions [15, 17–20].

2.4. Data from the National Center for Environmental Prediction (NCEP) Reanalysis. Monthly surface air temperature and specific humidity data from the National Center for Environmental Prediction (NCEP) reanalysis [21] from 1996 to 2012 were employed for analyzing their linkage to the remotely sensed LST anomalies over the Amazon rainforests in the next section.

3. Results over the Amazon Tropical Rainforests

3.1. Time Series of the LST Anomalies Interannual Variations. Figure 2(a) indicates a good agreement between the remotely sensed morning LST anomalies and the NCEP surface air temperature, but this is not the case in the afternoon. This is because the LST anomalies from remote sensing physically represent the canopy skin temperature—which is more influenced by nighttime longwave radiation and thus has a stronger connection to the humidity and temperature of the overlying atmosphere and cloud base [22]. In contrast, the afternoon LST anomalies tend to be higher than the air temperature when it is warm and lower than the air temperature when it is cold.

Figure 2(b) shows that the LST anomalies have a negative correlation with SPI, with correlation coefficients of -0.73 and -0.36 , for the afternoon and morning data, respectively. The higher correlation of LST anomalies with SPI in the afternoon is as expected, because the daytime clouds associated with rainfall reduce surface solar flux and a larger fraction of solar heating goes into latent fluxes (e.g., [23]).

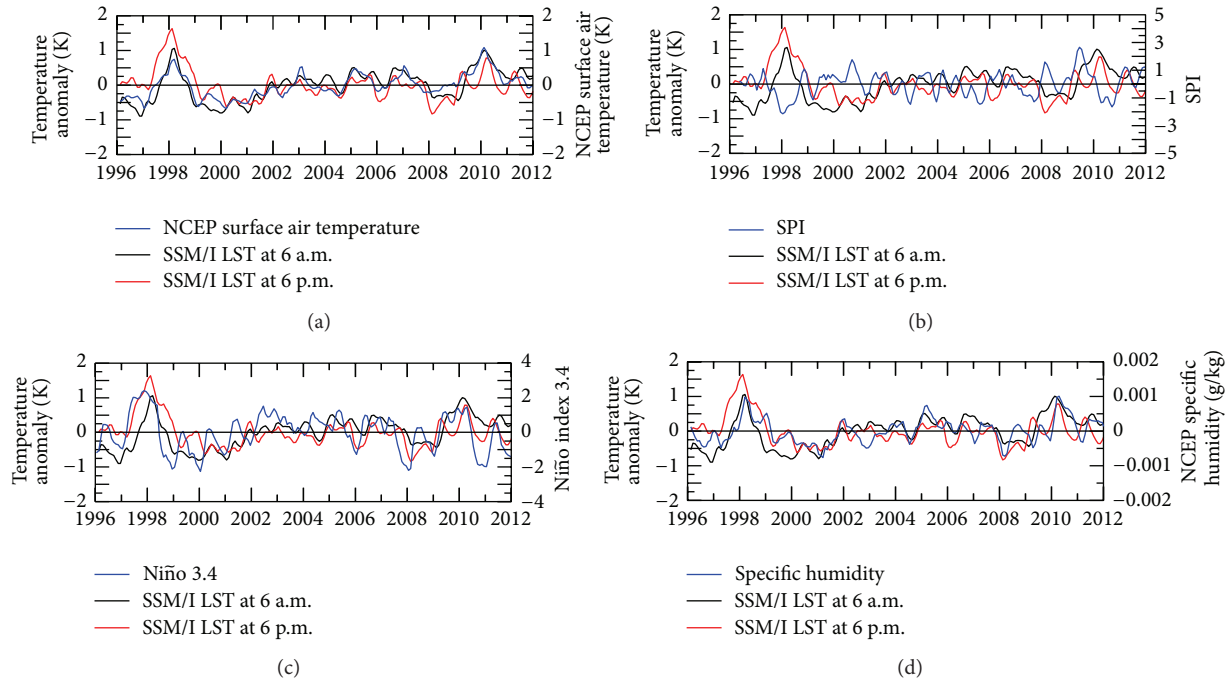


FIGURE 2: Comparison between time series of the domain averaged temperature anomalies of remotely sensed LST (at 6 a.m. and 6 p.m.) over Amazon rainforests with the following: (a) NCEP surface air temperature, (b) SPI, (c) Niño 3.4 index, and (d) NCEP specific humidity.

The interannual variation of climate over Amazon rainforests is mainly triggered by the El Niño Southern Oscillation (ENSO), an anomaly of sea-surface temperature (SST) and atmospheric pressure patterns over the equatorial Pacific that is commonly characterized by SST anomalies in the Niño 3.4 region (5°N - 5°S , 170°W - 120°W). Thus the Niño 3.4 index [24] is used to characterize ENSO. Figure 2(c) compares time series of both morning and afternoon LST anomalies with this Niño 3.4 index. They both strongly respond to the El Niño event of 1997-1998, but the 2002-2003 El Niño was too weak to impact the LST anomalies significantly. The 2010 drought shows a larger impact on the LST anomalies at 6 a.m. than at 6 p.m. The LST anomalies lag Niño 3.4 by 3-4 months (with lag correlations of 0.8 for morning LST anomalies and 0.7 for afternoon LST anomalies), consistent with the results reported by Trenberth et al. [25].

Figure 2(d) indicates a strong connection between the remotely sensed morning LST anomalies and the specific humidity from the NCEP reanalysis. The response of the canopies—as well as the response of their carbon flux—to droughts is related to canopy skin temperature. During the 17 years studied, three major drought events occurred over the Amazon: the 1998 drought triggered by a strong El Niño and the 2005 and 2010 droughts, each caused by an unusually long period of anomalously low rainfall. Figure 3 compares the spatial distributions of temperature anomalies for representative months of the three drought years, March 1998, March 2010 (peak of the 1997/98 and 2010 drought, resp.), and January 2005 (peak of the 2005 drought) in the morning and in the afternoon. The LST has strong positive anomalies in 1998 (especially in the afternoon), but little impact from the

drought in 2005 when the rainfall deficit was not particularly large (as shown in Figure 2(b)). This difference indicates—as expected—a dependence of LST anomalies on soil moisture. The greater shortage of soil moisture in 1998 is also confirmed by the SPI. The 2010 drought has shown a much larger impact on LST than does the 2005 drought, but its anomalies are slightly smaller than those in 1998. The spatial patterns from 1998 and 2010 are also very different.

3.2. Spatial Patterns of Interannual Variation by Season. It is difficult to obtain reliable spatial patterns of LST anomaly change with the sparse *in situ* measurements in the Amazon rainforests. In contrast, spaceborne remote sensing regularly provides spatially homogeneous measurements that are only limited by the length of their time series in determining the spatial patterns of the interannual changes of LST (and their relation to changes of rainfall). In this section, we examine the spatial patterns of interannual rainfall anomalies in the four different seasons (MAM, JJA, SON, and DJF) during the morning and afternoon separately.

The spatial patterns of the LST anomaly standard deviation are shown in Figures 4 and 5 for the morning and afternoon, respectively. In both morning and afternoon, variations of LST anomalies during the dry season (JJA) are smaller than those during the wet season (DJF). Furthermore, these variations are smallest at locations farthest from the equator, mainly because of the decreased variability of the rainfall. Variations are larger in the afternoon than in the morning, due to the greater variability of incident solar radiation.

The Empirical Orthogonal Function (EOF) is a statistical tool for identifying the dominant patterns of the correlated

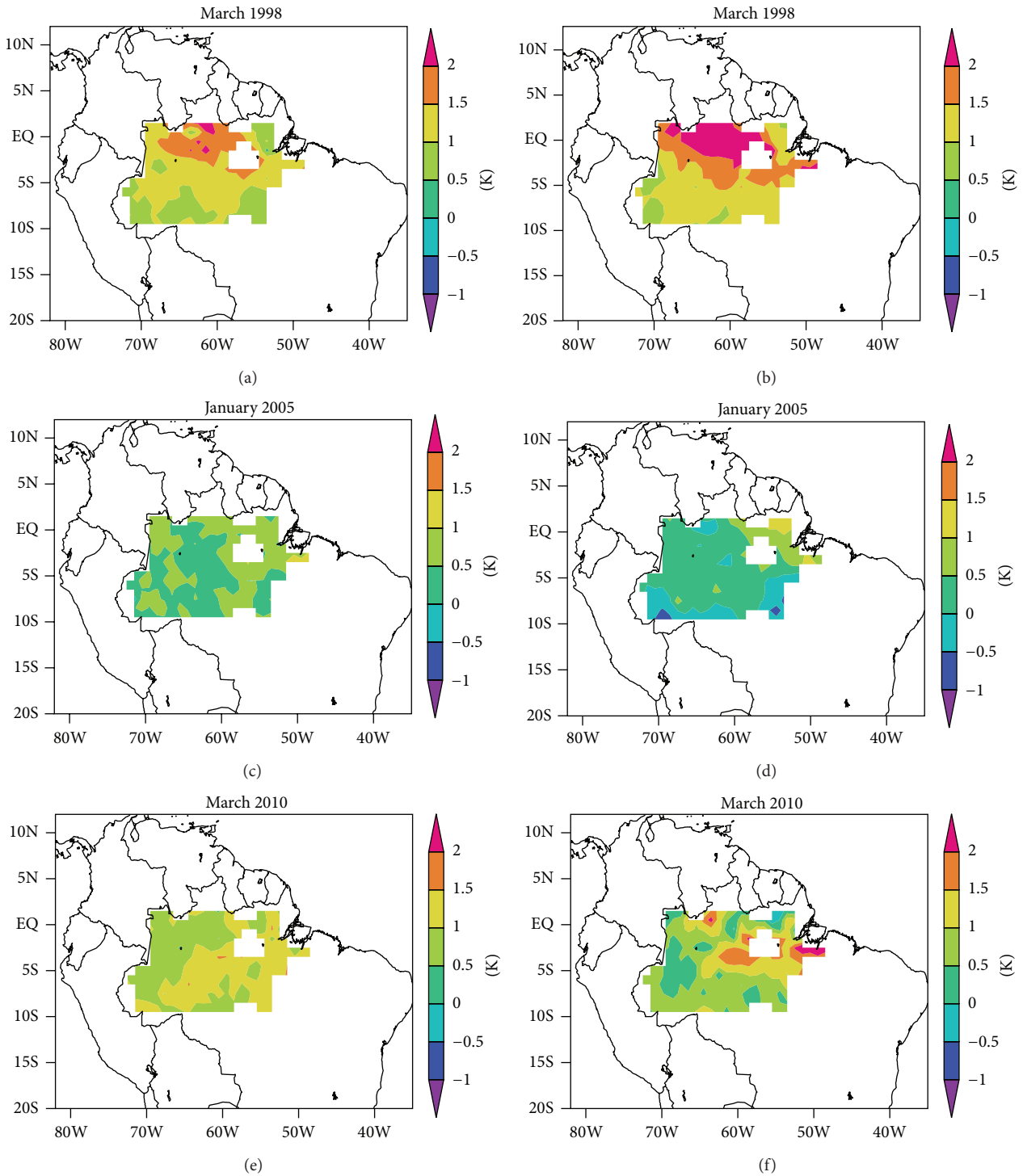


FIGURE 3: Spatial distribution of the remotely sensed LST anomalies over Amazon rainforests during three drought events in March 1998, January 2005, and March 2010. Left panels (a, c, and e) are for 6 a.m. and right panels (b, d, and f) are for 6 p.m.

structure in the data of interest. Thus, it is widely used to objectively characterize the dominant spatial and temporal patterns of climate variability [26]. Figure 6 shows the first EOF mode of LST anomalies in the morning by season. Its spatial pattern largely resembles that of the standard deviation and explains 72% (SON) to 86% (DJF) of the total

variance, suggesting that the variance of the LST anomalies is dominated by a large-scale coherent pattern. The temporal variation of the EOF1, the first principle component (PC1), resembles that of the ENSO. Thus, the anomalies of morning LST are dominated by El Niño (1997-1998)—more so during the MAM and DJF seasons than during the JJA and SON

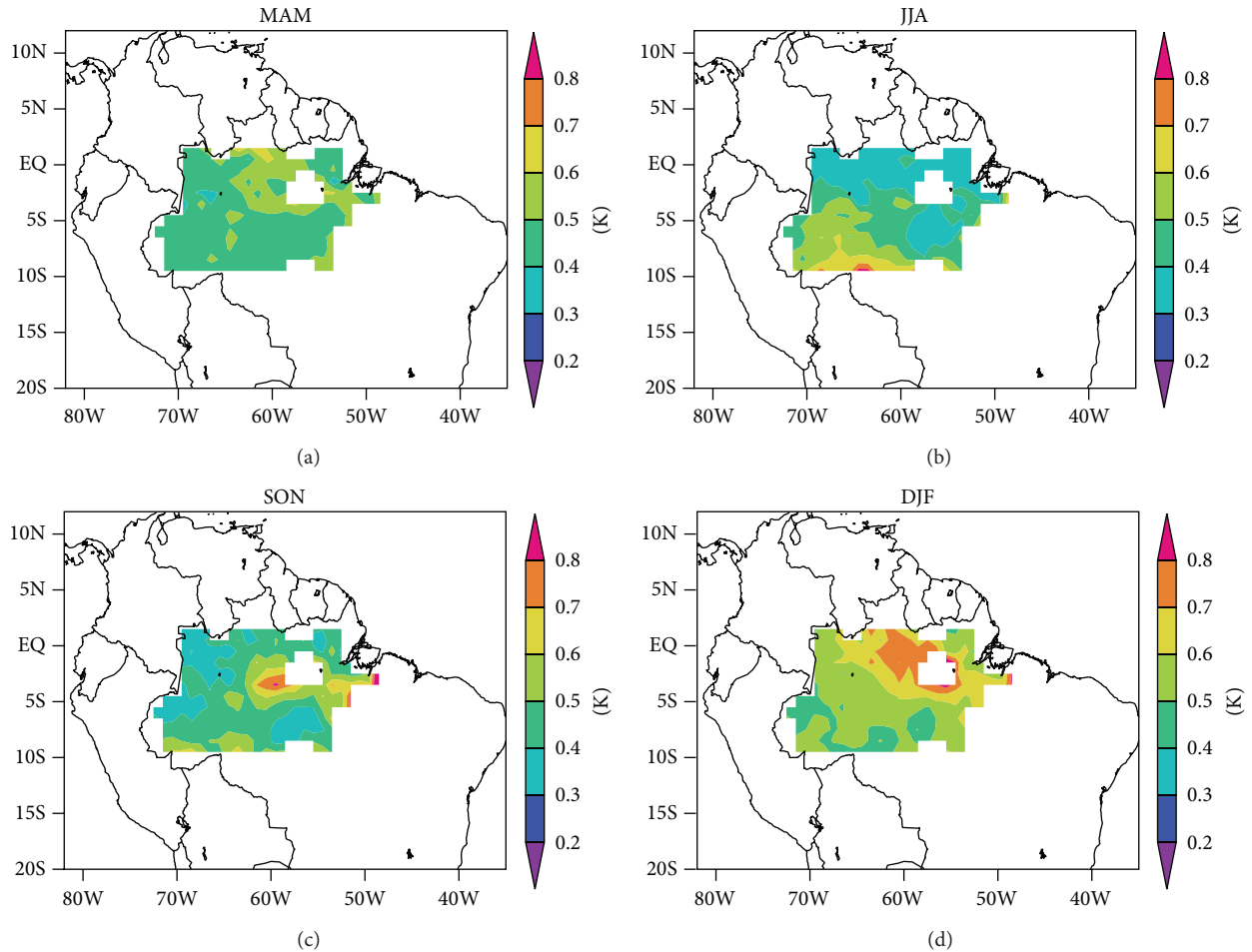


FIGURE 4: Standard deviation of the remotely sensed LST anomalies at 6:30 a.m. over Amazon rainforests for the following seasons: (a) MAM, (b) JJA, (c) SON, and (d) DJF.

TABLE 1: Correlation coefficient between EOF patterns (for the Amazon rainforests).

	MAM	JJA	SON	DJF
LST a.m. versus p.m.	0.7	0.68	-0.27	0.54
Rain versus LST a.m.	0.5	-0.04	0.25	-0.08
Rain versus LST p.m.	0.56	-0.05	-0.59	0.19

seasons. Such a seasonal dependence of LST variation is associated with a stronger influence of El Niño on rainfall and cloudiness (e.g., [8]).

The relationship between morning and afternoon LST anomalies can be used to infer their causes. For example, humid and rainy conditions would reduce longwave cooling and increase morning LST anomalies but will also increase evapotranspiration and thus reduce afternoon LST anomalies. Therefore, we would expect a negative correlation between the morning and afternoon LST anomalies. On the other hand, cold front incursions during the dry season could reduce both morning and afternoon LST [27, 28], leading to a positive correlation. Table 1 shows the correlations of

the EOF1 spatial patterns by season among three data sources: morning LST anomalies, afternoon LST anomalies, and rainfall anomalies.

4. Results over the Congo Basin Rainforest

The rainforests of Africa are mostly found in the Congo River basin on the Atlantic side of the continent. Thus we choose the domain of 10°E , -5°S to 30°E , 5°S for this study.

Figure 7 shows that there is a clear relationship between the domain averaged LST anomalies at 6:30 p.m. and the 6-month SPI over the Congo basin during the wet season. This negative correlation is reasonable because LST anomalies are more influenced by the cloud solar effect in daytime during the wet season.

The spatial patterns of the LST anomaly interannual variations for different seasons are shown in Figures 8 and 9. This variation is less during the rainy season (usually November to March) and larger during the dry season (usually April to October). This is presumably due to a greater sensitivity of the LST anomalies to changes of atmospheric humidity, cloudiness, and rainfall when the atmosphere and soil are less saturated. The variation is larger at sunset (afternoon) than

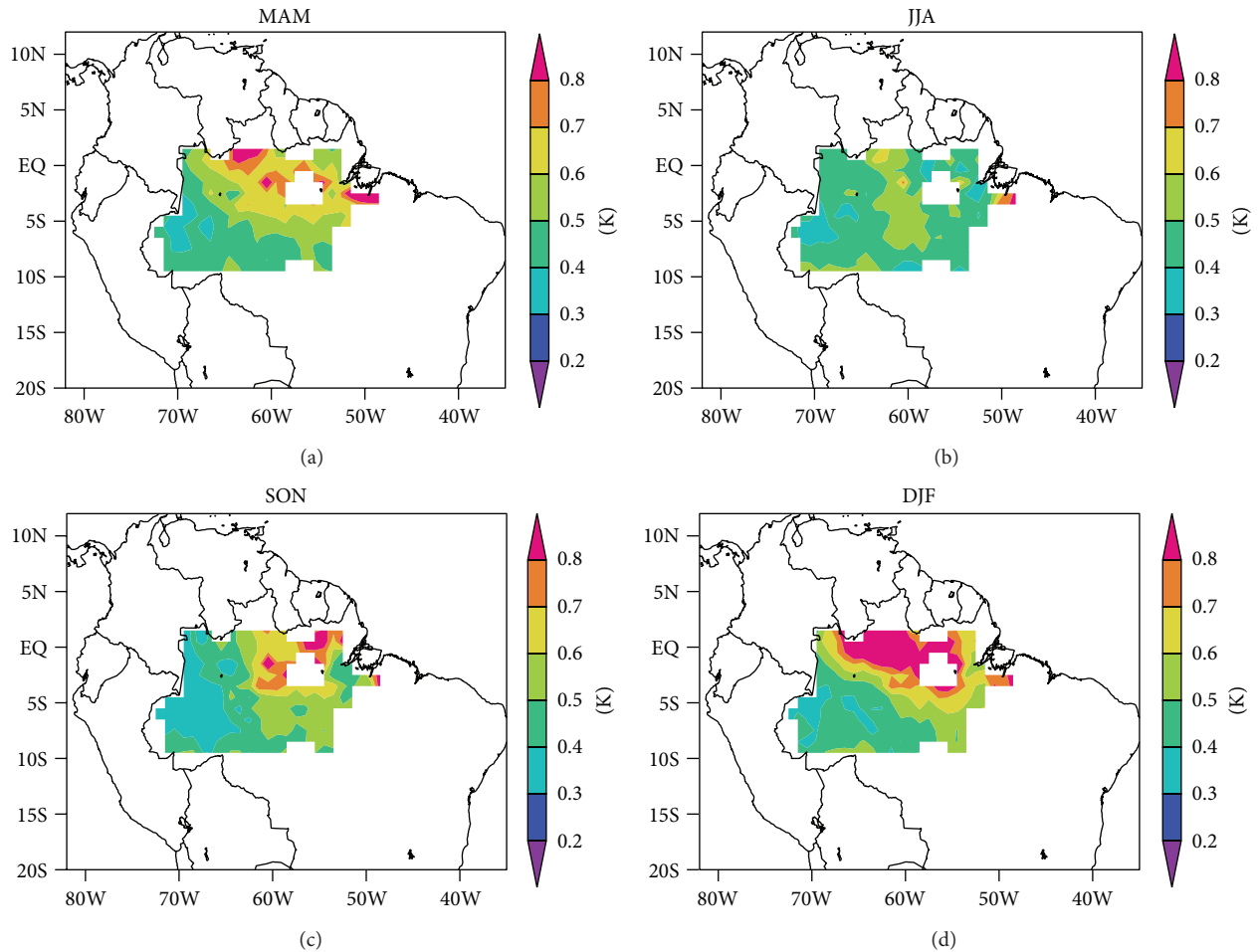


FIGURE 5: The same as Figure 4 but at 6:30 p.m.

at sunrise (morning), in agreement with observations of the diurnal cycle of temperature over the region [29].

Figure 10 shows the first EOF of SSM/I LST anomalies at 6:30 a.m. over the Congo basin. Its patterns are dominated by a north-south gradient in MAM and DJF. These patterns are directly related to the patterns of African monsoon rainfall variability. For instance, in JJA (boreal summer) the negative EOF values propagate from west to east with attenuation, which is consistent (in trend) with the extension of the precipitation zone from the east Atlantic. In DJF (austral summer), the EOF is clearly layered from north to south—with the precipitation zone occurring over the southern part of the continent, centered around 10°S latitude [30]. The JJA EOF pattern resembles the southwesterly gradient of the August rainfall in the domain of 10°E, -5°S to 20°E, 5°S [31]. The correlation coefficients between morning EOF and afternoon EOF are 0.29, 0.58, 0.15, and 0.49 for MAM, JJA, SON, and DJF, respectively (notice that they are better correlated when there is little rain (JJA) or near constant rain (DJF)). Low correlations are seen during the rainy seasons (MAM and SON) because of the higher soil moisture (and thus lower sensitivity of the afternoon LST anomalies to rainfall).

5. Summary and Conclusions

Interannual variations of LST anomalies over the tropical rainforests are correlated with variations of SST (e.g., El Niño), with the LST anomalies lag Niño 3.4 by 3-4 months. Of the two tropical forests considered, the Amazon forest is more sensitive to such SST variations than the Congo. Drought, as a consequence of soil moisture deficiency, causes an increase in LST anomalies by reducing the latent heat flux (i.e., evapotranspiration). The stronger drought in 1998 had a much greater impact on LST anomalies than the weaker one in 2005. This result is consistent with the greater drought stress and the increase in fire events seen in 1998 versus 2005 [32]. A previous study has suggested that a dry rainfall anomaly in the western Congo is associated with El Niño, although the influence of it is complicated by the effects of the tropical Atlantic and Indian Ocean SST anomaly [33].

The morning and afternoon observations from SSM/I and SSMIS facilitate the investigation of the interannual changes of LST anomalies on a diurnal basis. In general, the afternoon LST anomalies tend to vary more than the morning LST anomalies. A comparison with NCEP datasets indicates that

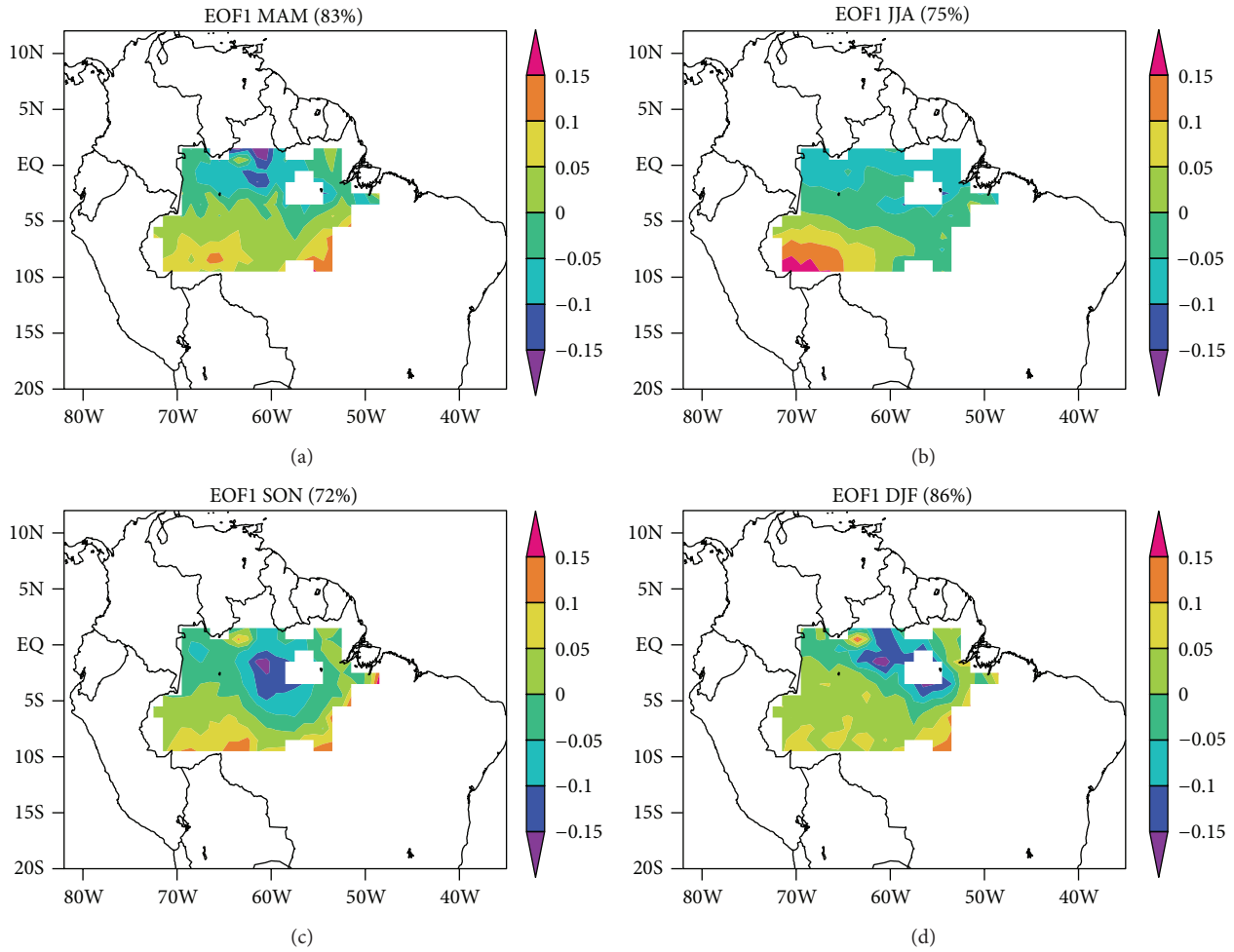


FIGURE 6: First EOF of the remotely sensed LST anomalies at 6:30 a.m. over Amazon rainforests for the following seasons: (a) MAM, (b) JJA, (c) SON, and (d) DJF.

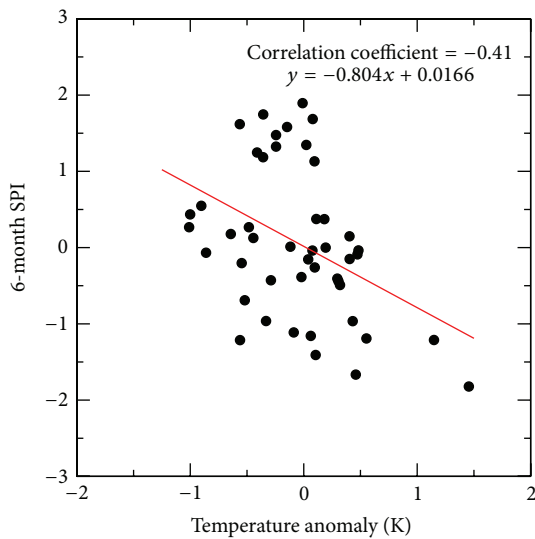


FIGURE 7: Scatterplot of domain averaged LST anomalies at 6:30 p.m. and 6-month SPI over Congo rainforests during the wet season. The linear trend is determined by a least-square fitting.

the differences between the morning and afternoon remotely sensed temperatures are physically reasonable. The morning LST seems to be controlled by humidity, and it is close to the surface air temperature from NCEP reanalysis.

For both tropical rainforests, the spatial patterns of the morning and afternoon LST anomalies were examined in terms of the standard deviations and EOFs. Change of LST anomalies in the Amazon shows a strong spatial variation, with the largest deltas (of LST anomalies) occurring in the central Amazon. In contrast, changes of LST anomalies in the Congo are more spatially uniform. Variability in both the Amazon and the Congo basins is most pronounced during the wet season—and in the afternoon. This is clearly a result of the variability of cloudiness and its reduction of solar radiation. The first EOF mode explains much of the variance in most of the cases. The LST anomaly spatial patterns during the transitional seasons tend to be less organized than those during the wet and dry seasons.

In conclusion, the SSM/I derived LST product over the tropical forests offers a unique data source for studying land atmosphere interactions. Its analysis shows the differences

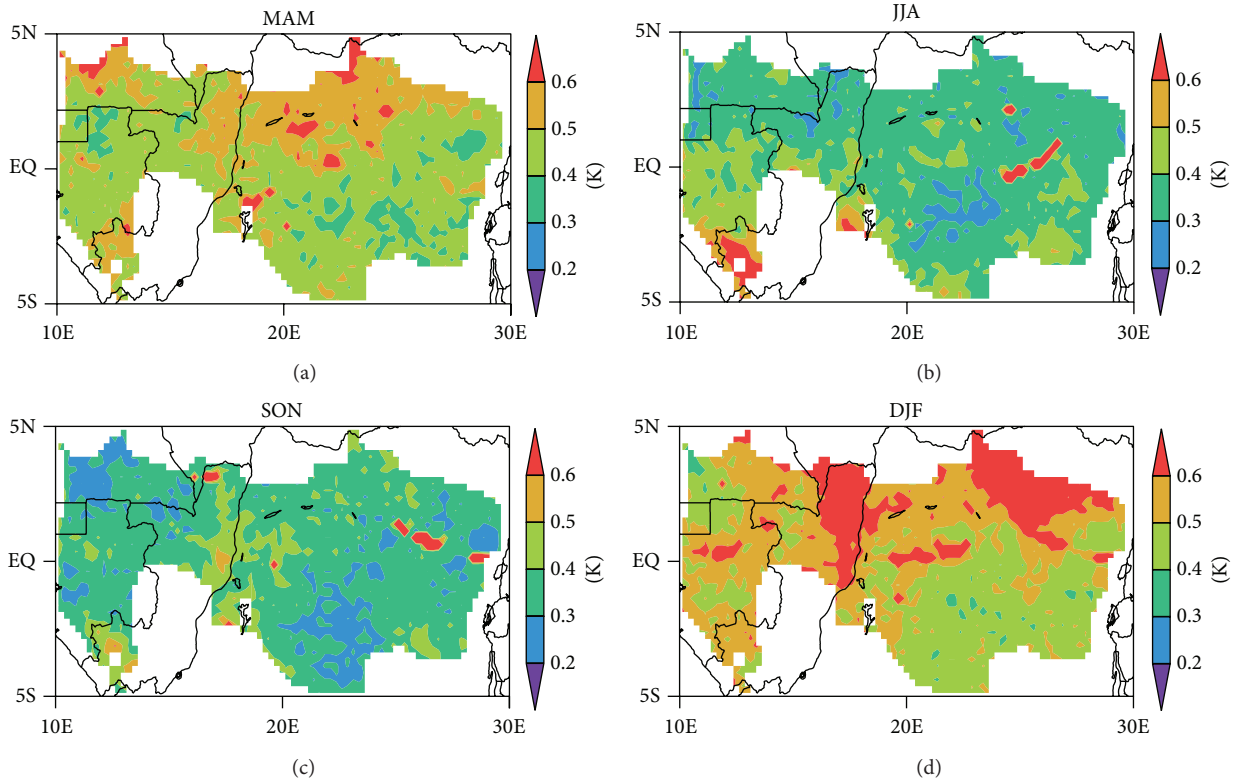


FIGURE 8: Standard deviation of the remotely sensed LST anomalies at 6:30 a.m. over Congo rainforests for the following seasons: (a) MAM, (b) JJA, (c) SON, and (d) DJF.

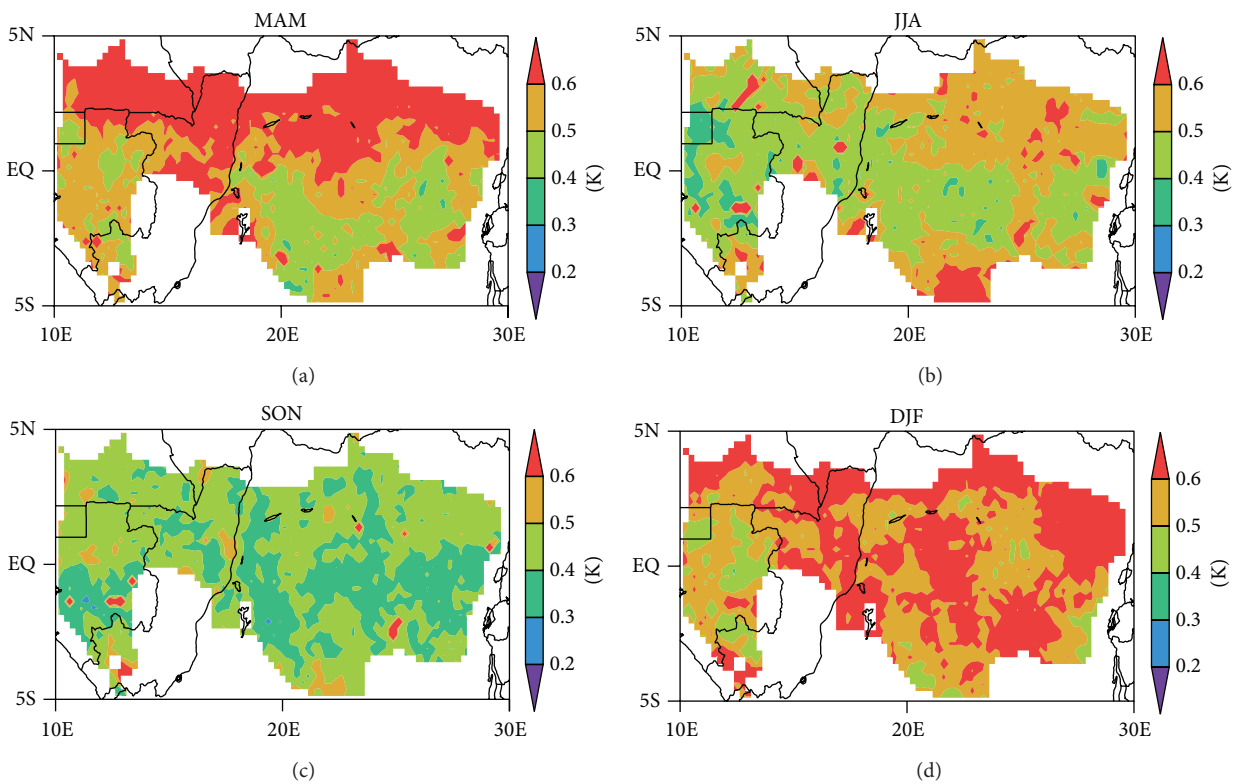


FIGURE 9: The same as Figure 8 but at 6:30 p.m.

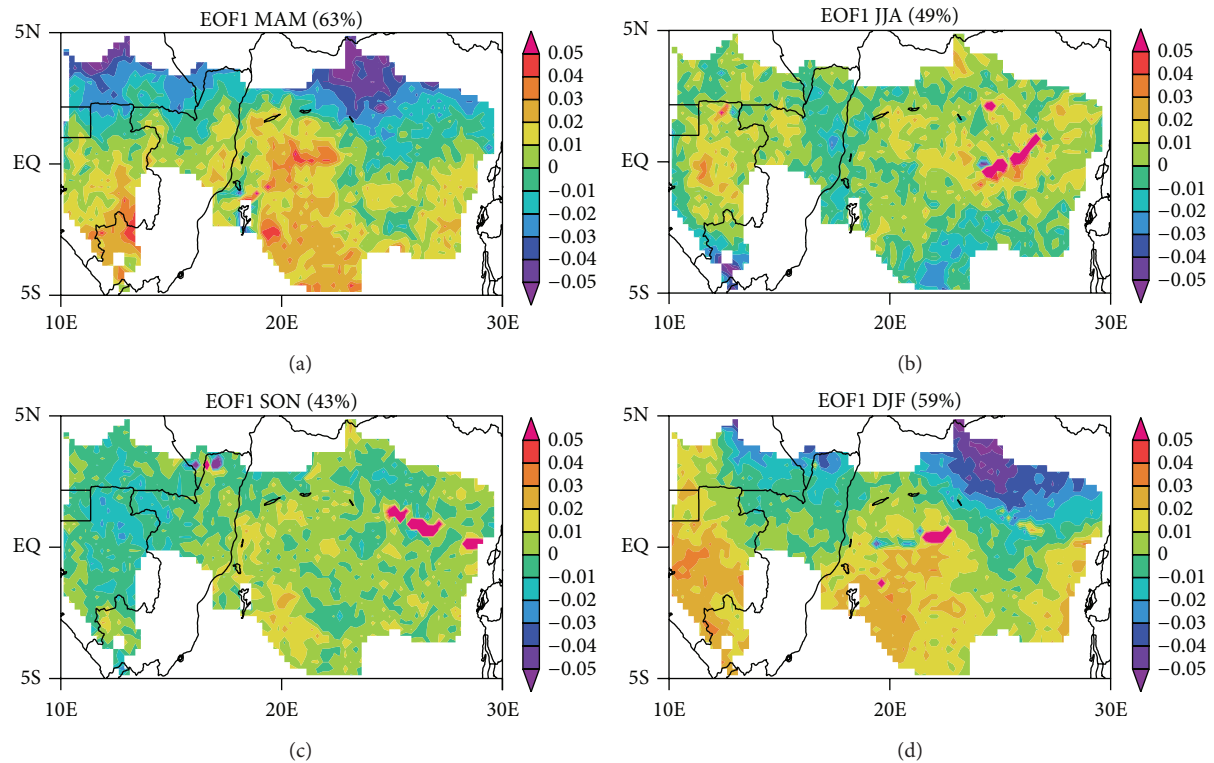


FIGURE 10: First EOF of the remotely sensed LST anomalies at 6:30 a.m. over Congo rainforests for the following seasons: (a) MAM, (b) JJA, (c) SON, and (d) DJF.

and similarities between morning and afternoon LST and reveals their physical linkages to SST, solar radiation, precipitation, and humidity.

This study contributes to our understanding of the linkage between climate extremes (e.g., drought) and canopy surface temperature. The comparisons between the morning and the afternoon LST anomalies offer a new perspective on land-atmospheric interactions. Since most tropical rainforests suffer from a lack of observational data, this passive microwave based LST dataset can be used for improving estimates from GCMs and hydrological models.

Conflict of Interests

The authors declare that there is no conflict of interests regarding the publication of this paper.

Acknowledgments

This work was supported by startup funds from the Texas A&M University College of Engineering and the Zachry Department of Civil Engineering, the National Science Foundation Grant (AGS-0937400), and DOE GoAmazon DE-SC0011117. It has benefitted from the use of the Texas A&M Supercomputing Facility (<http://sc.tamu.edu/>). The authors would also like to thank Dr. Chi-Fan Shih at the University Corporation for Atmospheric Research (UCAR) for his assistance with the NCEP data. The open access publishing fees for

this paper have been covered by the Texas A&M University Online Access to Knowledge (OAK) Fund, supported by the University Libraries and the Office of the Vice President for Research.

References

- [1] M. New, M. Hulme, and P. Jones, "Representing twentieth-century space-time climate variability. Part II: development of 1901-96 monthly grids of terrestrial surface climate," *Journal of Climate*, vol. 13, no. 13, pp. 2217–2238, 2000.
- [2] K. E. Trenberth, P. D. Jones, P. Ambenje et al., "Observations: surface and atmospheric climate change," in *Climate Change 2007: The Physical Science Basis*, S. Solomon, D. Qin, M. Manning et al., Eds., Contribution of Working Group I to the Fourth Assessment Report of the Intergovernmental Panel on Climate Change, Cambridge University Press, New York, NY, USA, 2007.
- [3] Y. Malhi and J. Wright, "Spatial patterns and recent trends in the climate of tropical rainforest regions," *Philosophical Transactions of the Royal Society B: Biological Sciences*, vol. 359, no. 1443, pp. 311–329, 2004.
- [4] A. White, M. G. R. Cannell, and A. D. Friend, "CO₂ stabilization, climate change and the terrestrial carbon sink," *Global Change Biology*, vol. 6, no. 7, pp. 817–833, 2000.
- [5] G. L. Vourlitis, N. P. Filho, M. M. S. Hayashi et al., "Effects of meteorological variations on the CO₂ exchange of a Brazilian transitional tropical forest," *Ecological Applications*, vol. 14, no. 4, pp. S89–S100, 2004.

- [6] W. Li, P. Zhang, J. Ye, L. Li, and P. A. Baker, "Impact of two different types of El Niño events on the Amazon climate and ecosystem productivity," *Journal of Plant Ecology*, vol. 4, pp. 91–99, 2011.
- [7] H. Gao, R. Fu, R. E. Dickinson, and R. I. N. Juárez, "A practical method for retrieving land surface temperature from AMSR-E over the Amazon forest," *IEEE Transactions on Geoscience and Remote Sensing*, vol. 46, no. 1, pp. 193–199, 2008.
- [8] P. A. Arias, R. Fu, C. D. Hoyos, W. H. Li, and L. M. Zhou, "Changes in cloudiness over the Amazon rainforests during the last two decades: diagnostic and potential causes," *Climate Dynamics*, vol. 37, no. 5, pp. 1151–1164, 2011.
- [9] J. Hansen, M. Sato, and R. Ruedy, "Radiative forcing and climate response," *Journal of Geophysical Research D: Atmospheres*, vol. 102, no. 6, pp. 6831–6864, 1997.
- [10] S. F. B. Tett, P. A. Stott, M. R. Allen, W. J. Ingram, and J. F. B. Mitchell, "Causes of twentieth-century temperature change near the Earth's surface," *Nature*, vol. 399, no. 6736, pp. 569–572, 1999.
- [11] R. L. Armstrong and M. J. Brodzik, "An earth-gridded SSM/I data set for cryospheric studies and global change monitoring," in *Satellite Monitoring of the Earth's Surface and Atmosphere*, pp. 155–163, Pergamon Press, Oxford, UK, 1995.
- [12] F. J. Wentz, "User's manual SSM/I antenna temperature tapes," RSS Technical Report 120191, Remote Sensing Systems, Inc., Santa Rosa, Calif, USA, 1993.
- [13] B. Rudolf and U. Schneider, "Calculation of gridded precipitation data for the global land-surface using in-situ gauge observations," in *Proceedings of the 2nd Workshop of the International Precipitation Working Group (IPWG '04)*, EUMETSAT, Monterey, Calif, USA, October 2004.
- [14] R. I. N. Juárez, M. L. Goulden, R. B. Myneni, R. Fu, S. Bernardes, and H. Gao, "An empirical approach to retrieving monthly evapotranspiration over Amazonia," *International Journal of Remote Sensing*, vol. 29, no. 24, pp. 7045–7063, 2008.
- [15] T. B. Mckee, N. J. Doesken, and J. Kleist, "The relationship of drought frequency and duration to times scales," in *Proceedings of the 8th Conference on Applied Climatology*, pp. 179–184, Anaheim, Calif, USA, January 1993.
- [16] World Meteorological Organization, "WMO: standardised verification system for long-range forecasts," in *Manual on the Global Data-Processing System*, WMO no. 485, World Meteorological Organization, Geneva, Switzerland, 2012.
- [17] D. S. Pai, L. Sridhar, P. Guhathakurta, and H. R. Hatwar, "District-wide drought climatology of the southwest monsoon season over India based on standardized precipitation index (SPI)," *Natural Hazards*, vol. 59, no. 3, pp. 1797–1813, 2011.
- [18] N. Subash and H. S. R. Mohan, "Trend detection in rainfall and evaluation of standardized precipitation index as a drought assessment index for rice-wheat productivity over IGR in India," *International Journal of Climatology*, vol. 31, no. 11, pp. 1694–1709, 2011.
- [19] S. M. Vicente-Serrano, S. Beguería, and J. I. López-Moreno, "A multiscalar drought index sensitive to global warming: the standardized precipitation evapotranspiration index," *Journal of Climate*, vol. 23, no. 7, pp. 1696–1718, 2010.
- [20] W. Li, R. Fu, R. I. N. Juárez, and K. Fernandes, "Observed change of the standardized precipitation index, its potential cause and implications to future climate change in the Amazon region," *Philosophical Transactions of the Royal Society B: Biological Sciences*, vol. 363, no. 1498, pp. 1767–1772, 2008.
- [21] E. Kalnay, M. Kanamitsu, R. Kistler et al., "The NCEP/NCAR 40-year reanalysis project," *Bulletin of the American Meteorological Society*, vol. 77, no. 3, pp. 437–471, 1996.
- [22] A. K. Betts, "Coupling of water vapor convergence, clouds, precipitation, and land-surface processes," *Journal of Geophysical Research D: Atmospheres*, vol. 112, no. 10, Article ID D10108, 2007.
- [23] H. J. I. Rinne, A. B. Guenther, J. P. Greenberg, and P. C. Harley, "Isoprene and monoterpene fluxes measured above Amazonian rainforest and their dependence on light and temperature," *Atmospheric Environment*, vol. 36, no. 14, pp. 2421–2426, 2002.
- [24] K. E. Trenberth, "The definition of El Niño," *Bulletin of the American Meteorological Society*, vol. 78, no. 12, pp. 2771–2777, 1997.
- [25] K. E. Trenberth, J. M. Caron, D. P. Stepaniak, and S. Worley, "Evolution of el niño-Southern Oscillation and global atmospheric surface temperatures," *Journal of Geophysical Research D: Atmospheres*, vol. 107, no. 8, pp. AAC 5-1–AAC 5-17, 2002.
- [26] E. N. Lorenz, "Empirical orthogonal functions and statistical weather prediction," Scientific Report 1, Statistical Forecasting Project, MIT, Department of Meteorology, Cambridge, Mass, USA, 1956.
- [27] W. Li and R. Fu, "Influence of cold air intrusions on the wet season onset over Amazonia," *Journal of Climate*, vol. 19, no. 1, pp. 257–275, 2006.
- [28] R. Fu, L. Yin, W. Li et al., "Increased dry-season length over southern Amazonia in recent decades and its implication for future climate projection," *Proceedings of the National Academy of Sciences of the United States of America*, vol. 110, no. 45, pp. 18110–18115, 2013.
- [29] C. B. Biona, A. Druilhet, B. Benech, and R. Lyra, "Diurnal cycle of temperature and wind fluctuations within an African equatorial rain forest," *Agricultural and Forest Meteorology*, vol. 109, no. 2, pp. 135–141, 2001.
- [30] S. Gadgil and S. Sajani, "Monsoon precipitation in the AMIP runs," *Climate Dynamics*, vol. 14, no. 9, pp. 659–689, 1998.
- [31] S. E. Nicholson, "The intensity, location and structure of the tropical rainbelt over west Africa as factors in interannual variability," *International Journal of Climatology*, vol. 28, no. 13, pp. 1775–1785, 2008.
- [32] L. E. O. C. Aragão, Y. Malhi, N. Barbier et al., "Interactions between rainfall, deforestation and fires during recent years in the Brazilian Amazonia," *Philosophical Transactions of the Royal Society B: Biological Sciences*, vol. 363, no. 1498, pp. 1779–1785, 2008.
- [33] S. E. Nicholson and A. K. Dezfuli, "The relationship of rainfall variability in western equatorial Africa to the tropical oceans and atmospheric circulation. Part I: the boreal spring," *Journal of Climate*, vol. 26, no. 1, pp. 45–65, 2013.

Research Article

Response of Extreme Hydrological Events to Climate Change in the Water Source Area for the Middle Route of South-to-North Water Diversion Project

Wei Yang,^{1,2} Liping Zhang,^{1,3} Lijie Shan,^{1,2} Xinchi Chen,^{1,2} and Shaodan Chen^{1,2}

¹State Key Laboratory of Water Resources and Hydropower Engineering Science, Wuhan University, Wuhan 430072, China

²Hubei Collaborative Innovation Center for Water Resources Security, Wuhan University, Wuhan 430072, China

³College of Tourism Culture and Geographical Science, Huanggang Normal University, Huanggang 438000, China

Correspondence should be addressed to Liping Zhang; zhanglp@whu.edu.cn

Received 20 February 2015; Revised 15 July 2015; Accepted 30 July 2015

Academic Editor: Yongqiang Zhang

Copyright © 2016 Wei Yang et al. This is an open access article distributed under the Creative Commons Attribution License, which permits unrestricted use, distribution, and reproduction in any medium, provided the original work is properly cited.

As the water source area for the middle route of China's South-to-North Water Diversion Project, the upper Hanjiang basin is of central concern for future management of the country's water resources. The upper Hanjiang is also one of the most flood-prone rivers in China. This paper explores the process of extreme floods by using multivariate analysis to characterize flood and precipitation event data in combination, for historical data and simulated data from global climate models. The results suggested that the generalized extreme value and Gamma models better simulated the extreme precipitation and flood volume sequence than the generalized Pareto model for the annual maximum series, while the generalized Pareto distribution model was the best-fit model for peaks over threshold series. For the two-dimensional joint distributions of precipitation and flood volume, the Frank Copula was preferred in simulation of the annual maximum flood series whereas the Gumbel Copula was the most appropriate function to simulate the points over threshold flood series. We concluded that, compared with the traditional univariate approach, multivariate statistical analysis produced flood estimates that were more physically based and statistically sound and carried lower risk for flood design purposes.

1. Introduction

The impact of climate change on water resources is a matter of worldwide concern [1–3]. Global warming accelerates processes of the hydrological cycle and leads to redistribution and change in the quantity of water resources in time and space. One important implication of this is predicted increases in the frequency and intensity of extreme hydrological events, namely, droughts and floods [4]. Droughts have become more serious in the Sahara, South Africa, and eastern Asia, and floods have generally increased in America and Europe in the last few decades [5, 6]. Similar observations have been made in China [7]. As well as risks to human safety, extreme hydrological events cause economic losses, and these costs are rising exponentially [8], threatening sustainable development. There is a need then to improve the scientific understanding of trends and patterns in extreme hydrological

events in the context of global climate change to inform planning for disaster protection and alleviation.

There is a large body of literature on the topic of characterizing the statistical distributions and likely future patterns of extreme hydrological events, with a few key papers highlighted below. Müller-Wohlfeil et al. [9] used a global climate model (GCM) downscaling and hydrological model to simulate extreme hydrological processes under current climate conditions and future scenarios. The impact and uncertainties of climate change on hydrology was assessed by Dessu and Melesse [10] by comparing and contrasting results across diverse GCMs, future climate scenarios, and two downscaling methods. A dramatic increase in the frequency of the heaviest precipitation events over Britain in the future was predicted by Jones and Reid [11]. Using a second-generation coupled global climate model under different emission scenarios and fitting a generalized extreme value

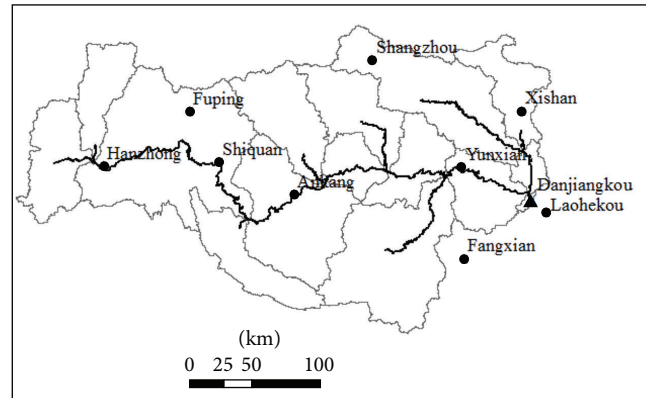
(GEV) distribution to the data, Kharin and Zwiers [12] concluded that the probability of extreme precipitation events would increase by a factor of about 2 by the end of the twenty-first century. For the Zhujiang basin, China, Fischer et al. [13] analyzed the precipitation extremes with four distribution functions and found GEV to be the most reliable and robust, while Wang et al. [14] applied the Gamma distribution and the Kolmogorov-Smirnov (KS) test to detect changes in extreme precipitation and extreme stream flow in southern China.

The South-to-North Water Diversion Project (SNWDP) is a major project to transfer water from the Yangtze River in the south of China to the drier northern areas suffering water deficit. The water source area for the middle route of SNWDP, the upper Hanjiang, is also known to be one of the most flood-prone rivers in China, so there are good reasons for seeking to characterize the hydrology of this basin in the context of future climate change. Zhang et al. [15] used the GEV and the generalized Pareto distribution (GPD) models to fit the extreme precipitation data in the upper reaches of the Hanjiang basin and evaluated the corresponding values for a number of return periods. The statistical relationship between the larger scale climate predictors and observed precipitation in the Hanjiang basin was investigated by Guo et al. [16]. They used a statistical downscaling method based on an artificial neural network (ANN) and predicted that precipitation in the basin would reduce in the 2020s and 2050s and increase in 2080s. Xu et al. [17] also applied statistical downscaling to establish a coupled relationship between GCM and the HBV precipitation-runoff model in order to predict runoff in the upper reaches of the Hanjiang basin under the A2 and B2 climate scenarios. They demonstrated that floods would likely be more frequent during the period 2011 to 2100. Most of the previous research on extreme hydrological events of the Hanjiang basin has taken a univariate approach to the analysis of flood and precipitation event data. As precipitation is the most important direct cause of flood events, we propose that new insight into the process of extreme floods can be gained by using multivariate analysis to characterize flood and precipitation event data in combination. We illustrate this approach using data from the Hanjiang but note that it has universal application.

This paper is organized as follows: Section 2 describes the study area and data used in the study; Section 3 introduces the regional frequency analysis methods and statistical probability models; Section 4 analyzes the statistical characteristics of extreme precipitation and extreme flood events based on the GEV, GPD and Gamma distribution models, and the Copula function; Section 5 predicts extreme precipitation and extreme flood events under future climate change scenarios; conclusions are presented in Section 6.

2. Study Area and Data

2.1. Study Area. Hanjiang, with a watershed area of 159,000 km² and a mainstream length of 1577 km, is the largest tributary of the Yangtze River. It originates in the south Qinling Mountains and flows through the five provinces of Shanxi, Gansu, Sichuan, Henan, and Hubei. The focus of this study



● Meteorological stations — Drainage network
▲ Reservoir □ Subbasins

FIGURE 1: Locations of meteorological stations and reservoir in the study area.

is the headwater area located upstream of the Danjiangkou Reservoir between 106–112°E and 31.4–34.1°N. This area serves as the water source area for the middle route of SNWDP, which draws water from Danjiangkou Reservoir. In this headwater area the mainstream has a length of 925 km and drains a watershed area of 95,200 km². The subtropical monsoon climate gives rise to mild and humid weather, with an annual average temperature of 14.6°C and mean annual precipitation of 819.5 mm. Rainfall is unevenly distributed in the basin, declining from south to north. The precipitation is strongly seasonal, with 70% occurring between May and September. The mean annual runoff is about 368.7 billion m³ and is also strongly seasonal, being dominantly sourced from storm event surface runoff.

2.2. Meteorological and Hydrological Data. The station-observed data used in the study included daily precipitation and daily runoff from 1969 to 2008. Daily precipitation data from 9 meteorological stations were obtained from the Shared Services Network of the China Meteorological Administration and China Hydrological Bureau. The daily inflow runoff data from Danjiangkou Reservoir were provided by the Changjiang Water Resources Commission (CWRC) (Figure 1). The areal mean precipitation was calculated with the Thiessen polygon method. Two extreme series were considered, the annual maximum (AM) series and peaks over threshold (POT) series. The AM series comprised the maximum daily precipitation in each year. The POT series comprised the daily precipitation exceeding the 98th percentile value of the data.

2.3. GCM Data. The Fourth Assessment Report of the Intergovernmental Panel on Climate Change (IPCC AR4) provides 23 GCMs which have the ability to simulate current climate over East Asia with a given degree of uncertainty [18]. In order to reduce the uncertainties of GCMs simulation of precipitation, it is common practice to adopt the coupled

TABLE 1: The Gumbel-Hougaard, Clayton, and Frank Copula functions and model parameters.

Copula function	2D distribution	3D distribution
Gumbel-Hougaard	$C(u, v) = \exp \left\{ - \left[(-\ln u)^\theta + (-\ln v)^\theta \right]^{1/\theta} \right\}$	$C(u, v, w) = \exp \left\{ - \left[(-\ln u)^\theta + (-\ln v)^\theta + (-\ln w)^\theta \right]^{1/\theta} \right\}$
Clayton	$C(u, v) = (u^{-\theta} + v^{-\theta} - 1)^{-1/\theta}$	$C(u, v, w) = (u^{-\theta} + v^{-\theta} + w^{-\theta} - 2)^{-1/\theta}$
Frank	$C(u, v) = -\frac{1}{\theta} \ln \left[1 + \frac{(e^{-\theta u} - 1)(e^{-\theta v} - 1)}{e^{-\theta} - 1} \right]$	$C(u, v, w) = -\frac{1}{\theta} \ln \left[1 + \frac{(e^{-\theta u} - 1)(e^{-\theta v} - 1)(e^{-\theta w} - 1)}{(e^{-\theta} - 1)^2} \right]$

climate model rather than the single model. The relative error of the simulation results for extreme precipitation indices with the coupled climate model is smaller than with the single model [19]. However, our research focuses on extreme events, and the homogenizing effect of the coupled climate model would dilute the extremes. Therefore, the single model dataset from the World Climate Research Programme (WCRP) Coupled Model Intercomparison Project Phase 3 (CMIP3) was applied in this study. The Special Report for Emission Scenarios (SRES) [20] developed four future greenhouse gas emission scenarios on the basis of possible long-term global and regional dynamics of the 21st century, and three of them, A2 (high emission), A1B (medium emission) and B1 (low emission) [18], were selected for use in this study. The daily precipitation series from CSIRO_MK3.5, INMCM3.0, and NCAR_PCM1 GCM models were adopted.

3. Methodology

3.1. Extreme Value Statistical Probability Models. The Gamma, GEV, and GPD models have been widely applied in simulations of extreme hydrological events. The GEV distribution integrates three extreme distributions [21–23], including the Weibull, Gumbel, and Fréchet. As the GEV distribution is independent of the probability distribution characteristics of the original data and only samples the extreme value, it is the most direct description of extreme climate information contained within climate observation data. The Gamma distribution is the most important skewed distribution in climatological statistics, it can be used to fit normal distributions, and it shows high stability in description of precipitation [24]. In application of the POT series, the GDP is often used to describe the probability distribution of all observation data beyond a certain threshold value [25]. The POT method increases the number of measurements included in the analysis and correspondingly reduces the statistical uncertainty of quantile variances and improves the fitting accuracy. The cumulative distribution functions (CDFs) of the GEV, GPD, and Gamma distribution are expressed as

$$F_{\text{GEV}}(x) = \exp \left\{ - \left[1 + \xi \left(\frac{x - \mu}{\sigma} \right) \right]^{-1/\xi} \right\}, \quad 1 + \xi \left(\frac{x - \mu}{\sigma} \right) > 0 \quad (1)$$

$$F_{\text{GPD}}(x) = 1 - \left[1 - \xi \left(\frac{x - \mu}{\sigma} \right) \right]^{1/\xi}$$

$$F_{\text{Gamma}}(x) = \frac{1}{\beta^\alpha \Gamma(\alpha)} \int_0^x x^{\alpha-1} e^{-x/\beta} dx,$$

where α and ξ are shape parameters, β and σ are scale parameters, and μ is a location parameter.

3.2. Copula Function. The Copula function plays an important role in the study of multivariate extreme theory [26–28]. The Copula function can connect joint distributions of several random variables with their marginal distributions [26]. In this study, three Copula functions, Gumbel-Hougaard, Clayton, and Frank, were used to build a joint distribution model of precipitation and flood discharge. These functions can be described by two-dimensional (2D) and three-dimensional (3D) distributions (Table 1). In this case, the joint CDF with two or three variables can expressed as

$$F(x_1, x_2) = C(F_{X_1}(x_1), F_{X_2}(x_2)) \quad (2)$$

$$F(x_1, x_2, x_3) = C(F_{X_1}(x_1), F_{X_2}(x_2), F_{X_3}(x_3)),$$

where $F_X(x)$ is the marginal CDF of each variable.

3.3. Selection of the Optimal Distribution. The Kolmogorov-Smirnov (KS) test was used to judge how well the presumed distributions fitted the sample data. The KS test compares the empirical cumulative distribution function of the observed series and the theoretical cumulative distribution function of the candidate distribution and then calculates the largest difference between them. Under the significance level $\alpha = 0.05$, if the KS test statistic (D) is greater than the critical value, the hypothesis on the distributional form is rejected. The smaller the value of D is, the better the assumed distribution fits the sample data.

Following common practice, the Root Mean Square Error (RMSE) criterion was used to measure the difference between values predicted by the model and the observed values. The RMSE value is defined as

$$\text{RMSE} = \sqrt{\frac{1}{n} \sum_{i=1}^n [P_c(i) - P_o(i)]^2}, \quad (3)$$

where $P_c(i)$ is actual frequency and $P_o(i)$ is theoretical frequency.

3.4. Return Periods. A return period is an estimate of the average time between rainfall or flood events of a given

magnitude. The return periods for variables greater than (or equal to) a specific value are usually determined as

$$T(x) = \frac{1}{1 - F_X(x)}. \quad (4)$$

For bivariate distributions, the probability that both x_1 and x_2 exceed certain thresholds can be derived in terms of Copulas:

$$P(X_1 \geq x_1, X_2 \geq x_2) = 1 - F_{X_1}(x_1) - F_{X_2}(x_2) + C(F_{X_1}(x_1), F_{X_2}(x_2)). \quad (5)$$

$$T(x_1, x_2, x_3) = \frac{1}{P(X_1 \geq x_1 \cap X_2 \geq x_2 \cap X_3 \geq x_3)} = \frac{1}{1 - F_{X_1} - F_{X_2} - F_{X_3} + C(F_{X_1}, F_{X_2}) + C(F_{X_1}, F_{X_3}) + C(F_{X_2}, F_{X_3}) - C(F_{X_1}, F_{X_2}, F_{X_3})}. \quad (7)$$

3.5. Mann-Kendall Tests for Trend and Change Point in Time Series. The Mann-Kendall (MK) test is a nonparametric method of detecting monotonic trend in a data series [29, 30]. As the MK method does not require the data to conform to any particular distribution and is less sensitive to outliers, it has been widely applied to hydrological data, which rarely follows a normal distribution. The data should not be serially correlated, so for this study the data were first prewhitened [31].

For a time series $\{x_i; i = 1, 2, \dots, n\}$, the test statistic S is defined as

$$S = \sum_{i=1}^{n-1} \sum_{j=i+1}^n \text{sgn}(x_j - x_i), \quad (8)$$

$$\text{sgn}(x_j - x_i) = \begin{cases} 1 & x_i < x_j \\ 0 & x_i = x_j \\ -1 & x_i > x_j \end{cases}$$

When $n \geq 10$, the distribution of S approaches a normal distribution, and the mean and variance of S are given as

$$E(S) = 0, \quad (9)$$

$$\text{Var}(S) = \frac{n(n-1)(2n+5)}{18}.$$

The normalized test statistic Z is calculated as

$$Z = \begin{cases} \frac{S-1}{\sqrt{\text{Var}(S)}} & S > 0 \\ 0 & S = 0 \\ \frac{S+1}{\sqrt{\text{Var}(S)}} & S < 0. \end{cases} \quad (10)$$

In a two-side trend test, the null hypothesis of no trend is rejected if $|Z| > Z_{1-\alpha/2}$ at the α level of significance ($\alpha =$

The joint return periods can be expressed as

$$T(x_1, x_2) = \frac{1}{P(X_1 \geq x_1 \cap X_2 \geq x_2)} = \frac{1}{1 - F_{X_1}(x_1) - F_{X_2}(x_2) + C(F_{X_1}(x_1), F_{X_2}(x_2))}. \quad (6)$$

For the 3D distribution, the joint return periods can be expressed as

5% in this study). A positive Z shows increasing trend and a negative Z shows decreasing trend.

The sequential version of Mann-Kendall test [32] is used to test assumptions about the start of a trend within a sample based on rank series of progressive and retrograde rows of the sample. The sequential MK test is therefore useful for detecting abrupt change points in a hydrological series [33, 34]. For a time series $\{x_i; i = 1, 2, \dots, n\}$, the rank series S_k is defined as

$$S_k = \sum_{i=1}^k r_i \quad (k = 2, 3, \dots, n), \quad (11)$$

$$r_i = \begin{cases} 1 & x_i > x_j \\ 0 & x_i \leq x_j \end{cases} \quad (j = 1, 2, \dots, i).$$

The mean and variance of S_k are given as

$$E(S_k) = \frac{n(n+1)}{4}, \quad (12)$$

$$\text{Var}(S_k) = \frac{n(n-1)(2n+5)}{72}.$$

Under the assumption that the time sequences are independent, the normalized test statistic UF_k is defined as

$$UF_k = \frac{S_k - E(S_k)}{\sqrt{\text{Var}(S_k)}} \quad (k = 1, 2, \dots, n) \quad (13)$$

which is the forward sequence, and the backward sequence UB_k is calculated using the same equation but in the reverse data series. $UF_1 = 0$, and the distribution of UF_k approaches a normal distribution. If $UF_k > 0$, the trend is increasing with time, and if $UF_k < 0$, the trend is decreasing with time. The calculated UF_k value is compared with the standard normal distribution table with two-tailed confidence levels. If

TABLE 2: The KS test statistic D value of marginal distribution models.

Variable	D for AM series			D for POT series		
	GEV	GPD	Gamma	GEV	GPD	Gamma
RX1day	0.0775	0.1251	0.0702	0.0850	0.0465	0.0894
RX3day	0.0840	0.0741	0.0737	0.0717	0.0649	0.0822
W1	0.0867	0.1138	0.0815	0.0626	0.0645	0.0984
W3	0.0965	0.0924	0.0975	0.1371	0.0635	0.0904

$|UF_k| > U_{\alpha/2}$, the trend is statistically significant; otherwise, the trend is not significant. The sequential MK test enables detection of the approximate beginning of a developing trend from the intersection point of the curves UF_k and UB_k of the test statistic. If the intersection point is significant at $\alpha = 0.05$, then the critical point of change is at that period [35, 36].

4. Statistical Characteristics of Extreme Hydrological Events

4.1. Univariate Frequency Analysis of Extreme Hydrological Events. The maximum 1-day precipitation (RX1day) series, maximum 3-day precipitation (RX3day) series, maximum 1-day flood discharge (W1) series, and maximum 3-days flood discharge (W3) series were established for the upper reaches of the Hanjiang basin by the AM and POT methods. The GEV, GPD, and Gamma models were selected for fitting of the series. The KS test statistic D was less than the critical value 0.21 ($\alpha < 0.05$) for the three models, suggesting that all were an adequate fit (Table 2). For the AM series, the Gamma model was the best-fit model for RX1day, RX3day, and W1 series, while GPD model was optimal for the W3 series. As a whole, the GEV and Gamma models better simulated the AM series than did the GPD model. For the POT series, the GPD model was the best fit for three of the four series (Table 2).

Estimated extreme precipitation and flood discharge associated with return periods of 10, 50, 100, 500, and 1000 years were calculated by these three distribution models for the AM and POT series (Table 3). The results indicated that, for AM series, for recurrence intervals ≥ 50 years, values of precipitation and flood discharge estimated by GPD model were noticeably lower than those by GEV and Gamma models. These lower values would translate to a higher risk for flood planning so GPD was regarded as unsuitable for the AM series. For the POT series, values estimated by GEV model were higher than those by GPD and Gamma models, and the values were distant from the observed data, indicating that GEV was unsuitable for the POT series (Table 3). For the AM series, the values calculated by Gamma distribution model indicated slightly higher values series than for the POT series. Adopting the more conservative estimates of the AM series would provide lower risk for flood planning.

4.2. Multivariate Frequency Analysis of Extreme Hydrological Events. The Kendall tau rank correlation coefficient and the Spearman's rank correlation coefficient were used to analyze the degree of bivariate correlation between pairs

of RX1day, RX3day, W1, and W3 for the AM and POT series (Table 4). There were significant positive correlations between extreme precipitation and extreme flood discharge, allowing the possibility of building a joint distribution model of precipitation and flood discharge using Copula functions.

Two-dimensional joint distributions were established based on the Gumbel-Hougaard, Clayton, and Frank Copula functions. The KS test and RMSE criterion suggested that the Frank Copula was superior for simulation of the AM series and the corresponding GEV distribution, while the Gumbel-Hougaard Copula was superior for simulation of the POT series and the corresponding GPD model (Table 5). All the values of the KS test statistic D of the optimal functions were smaller than the critical value of 0.21 under the significant level of $\alpha = 0.05$, demonstrating that the simulations passed the KS test.

The 2D Frank Copula (Figure 2) and Gumbel-Hougaard Copula (Figure 3) functions both displayed highly significant correlation between the empirical and theoretical frequencies. For the AM series, the correlation coefficient for RX1day-W1, RX1day-W3, RX3day-W1, and RX3day-W3 were 0.986, 0.989, 0.991, and 0.991, respectively, demonstrating that the Frank Copula function was a good fit to the AM samples. For the POT series, the correlation coefficient for RX1day-W1, RX1day-W3, RX3day-W1, and RX3day-W3 were 0.992, 0.995, 0.994, and 0.993, respectively, demonstrating that the Gumbel-Hougaard Copula function was a good fit to the POT samples and could be used to build the 2D joint distributions of precipitation and flood discharge.

Extreme precipitation and flood discharge under the return periods of 10, 20, 50, 100, 200, 500, and 1000 years were estimated using the 2D joint distributions (Figure 4). It was assumed that the frequency of precipitation and floods were the same. The notation used to describe the joint distributions was that, for example, "AM, RX1day-W1" represents that the variables of the ordinate were calculated via joint distributions of RX1day and W1 from the AM series, and so on (Figure 4).

Similar to the 2D joint distributions, 3D joint distributions were established based on the Gumbel, Clayton, and Frank Copula functions. The Frank Copula was the best-fit function for both the AM and POT series. Extreme precipitation and flood volume under the return periods of 10, 20, 50, 100, 200, 500, and 1000 years were estimated (Figure 5). The notation used to describe the joint distributions was that, for example, "AM, RX1day-W1-W3" represents that the variables of the ordinate were calculated by joint distributions of RX1day, W1, and W3 from the AM series, and so on (Figure 5).

The estimated extreme precipitation rates and flood discharges for the AM series were larger than those for the POT series under the same return period (Figures 4 and 5). Also, the estimated extreme value of the POT series did not increase with increasing return period to the same extent as the AM series. It appears that the Copula function and the corresponding GPD model for the POT series was unsuitable for estimating the extreme value under large return periods because of the limited extreme sample of the POT series. This result suggests that the AM series better described the

TABLE 3: Extreme precipitation and flood discharge estimated via marginal distribution models for a range of return periods.

Return periods (year)	AM series											
	RX1day (mm/d)			RX3day (mm/3 d)			W1 ($\times 10^9$ m ³ /d)			W3 ($\times 10^9$ m ³ /3 d)		
	Gamma	GEV	GPD	Gamma	GEV	GPD	Gamma	GEV	GPD	Gamma	GEV	GPD
10	55.6	55.2	59.9	96.4	95.9	100.2	2.000	1.964	2.107	4.323	4.270	4.533
50	72.3	70.9	71.6	123.0	127.9	117.1	2.796	2.693	2.500	6.001	5.866	5.233
100	78.9	76.8	74.3	133.4	141.5	120.9	3.117	2.982	2.581	6.677	6.505	5.364
500	93.3	89.2	77.8	156.0	173.1	125.9	3.834	3.610	2.678	8.183	7.906	5.508
1000	99.2	93.9	78.7	165.3	186.8	127.0	4.134	3.863	2.697	8.811	8.477	5.535

Return periods (year)	POT series											
	RX1day (mm/d)			RX3day (mm/3 d)			W1 ($\times 10^9$ m ³ /d)			W3 ($\times 10^9$ m ³ /3 d)		
	Gamma	GEV	GPD	Gamma	GEV	GPD	Gamma	GEV	GPD	Gamma	GEV	GPD
10	50.5	51.3	52.1	88.1	88.3	91.4	1.753	1.763	1.785	3.945	4.391	4.071
50	63.1	77.0	65.3	110.4	119.9	105.4	2.328	3.050	2.366	5.236	6.915	5.451
100	68.0	91.0	69.4	119.0	134.3	108.5	2.556	3.839	2.562	5.747	8.265	5.919
500	78.6	133.1	76.5	137.8	169.9	112.5	3.059	6.517	2.920	6.875	12.229	6.783
1000	83.0	156.3	78.8	145.5	186.3	113.3	3.267	8.176	3.041	7.342	14.377	7.077

TABLE 4: Correlation coefficient of the different extreme samples.

Variables	AM series		POT series	
	τ	ρ	τ	ρ
RX1day-W1	0.32	0.48	0.40	0.57
RX1day-W3	0.31	0.47	0.33	0.49
RX3day-W1	0.37	0.54	0.43	0.59
RX3day-W3	0.41	0.60	0.42	0.59

Note: τ is the Kendall coefficient; ρ is the Spearman's coefficient. RX1day-W1 represents the joint distribution of RX1day and W1.

TABLE 5: Optimal function and evaluation indicators of 2D joint distribution for AM and POT series.

Variables	AM series			POT series		
	Copula function	RMSE	D	Copula function	RMSE	D
RX1day-W1	Frank	0.0395	0.0893	Gumbel	0.0255	0.0815
RX1day-W3	Frank	0.0356	0.0999	Gumbel	0.0221	0.0659
RX3day-W1	Frank	0.0341	0.0996	Gumbel	0.0220	0.0582
RX3day-W3	Frank	0.0350	0.0938	Gumbel	0.0260	0.0652

extreme hydrological events for the purpose of lower risk flood planning.

The design floods of Danjiangkou Reservoir dam used in the preliminary design stage, calculated by a traditional single distribution hydrological method [37], were compared with the design value of W1 under a range of return periods calculated by 2D and 3D Copula functions for the AM series (Table 6). The design value calculated by the 3D Copula function was the highest of these for all return periods. The design values calculated by the 2D Copula function were slightly larger than the ones used in the preliminary dam design stage for 10-, 20-, and 1000-year return periods, while 2D Copula function estimates were slightly lower than preliminary dam design estimates for 50- and 100-year return periods. The joint distribution makes more use of available extreme information than a traditional single

distribution model, and the higher estimates of flood peaks given by the joint distribution are more conservative for application to flood planning. Overall, the results of the multivariate frequency analysis suggests that, in the case of the upper Hanjiang, this approach to describing extreme floods would lead to more conservative (lower risk) design than a traditional approach.

5. Prediction of Extreme Hydrological Events under Future Climate Change Scenarios

5.1. Simulation of Precipitation in the Baseline Period. Of the 23 GCMs of IPCC AR4, after excluding the models with incomplete daily precipitation series under A1B, A2, and B1 climate scenarios, the three models CSIRO_MK3.5,

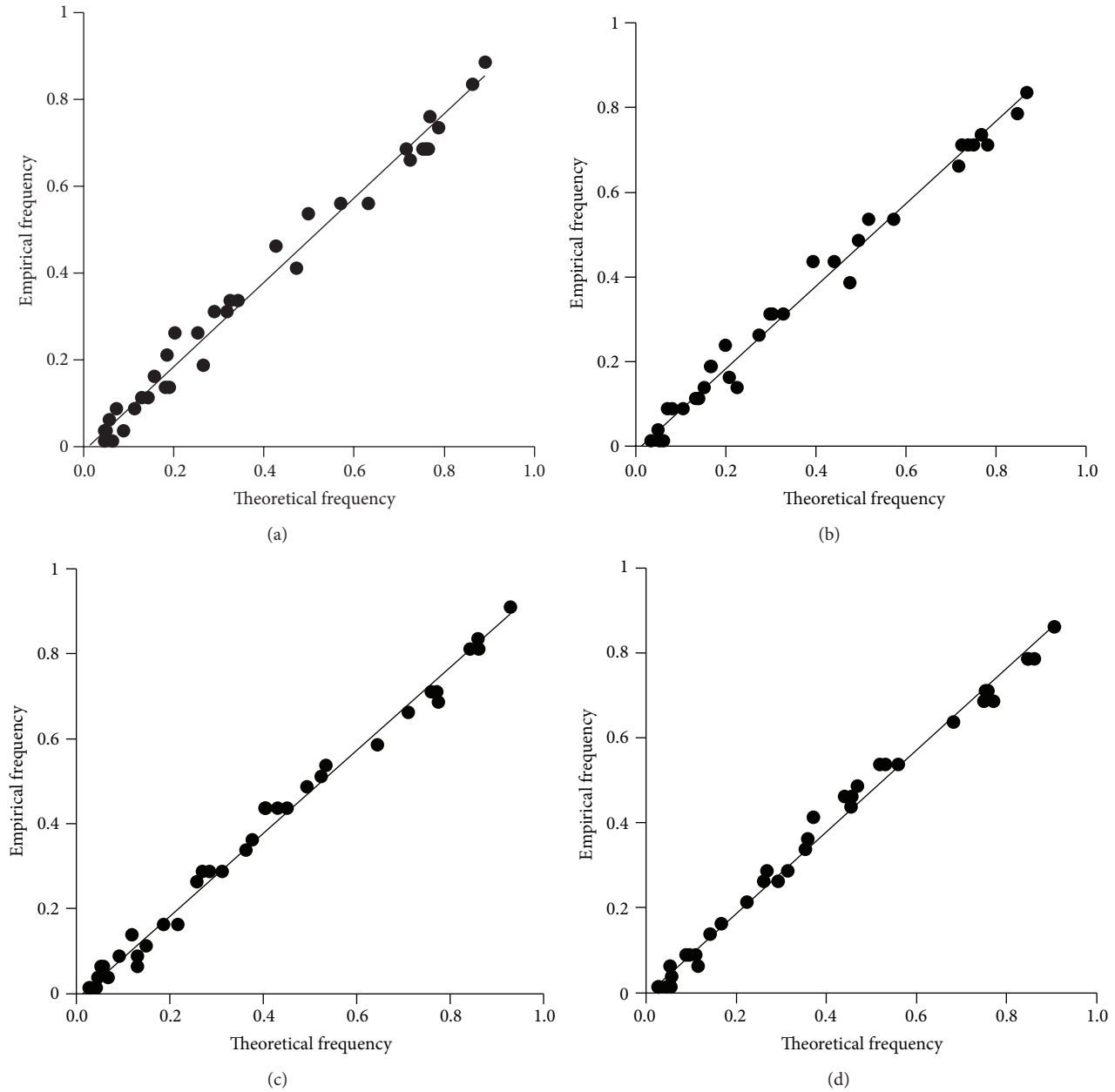


FIGURE 2: Empirical and theoretical frequency of 2D Frank Copula function joint distribution for different combination of the AM series: (a) X1day-W1, (b) RX1day-W3, (c) RX3day-W1, and (d) RX3day-W3.

INMCM3.0, and NCAR_PCM1, having complete daily outputs of precipitation data, were utilized for this study. Observed daily precipitation data in the baseline period (1961–2000) was used to assess the capability of these three GCMs in simulating the historical precipitation. Precipitation in the example years 1970, 1980, 1990, and 2000 and the total precipitation over the 40 years of the baseline period were used for comparison (Table 7). For the simulation of the total precipitation over 40 years, the errors of three models CSIRO_MK3.5, INMCM3.0, and NCAR_PCM1 were 3.65%, 88.69%, and 70.05%, respectively. As well as closely predicting the 40-year total precipitation, the CSIRO_MK3.5

model also closely predicted annual precipitation for the four example years, while the other two models were highly inferior (Table 7). This result is in agreement with previous work that has demonstrated the capacity of CSIRO_MK3.5 to simulate the contemporary climate of China [38, 39]. On this basis, the CSIRO_MK3.5 was chosen to simulate hydrological events in the study area under future climate change scenarios.

The annual precipitation series over the baseline period simulated by the CSIRO_MK3.5 model fitted the observed pattern of annual precipitation reasonably well, with both series having negative trend (Figure 6). However, the rate

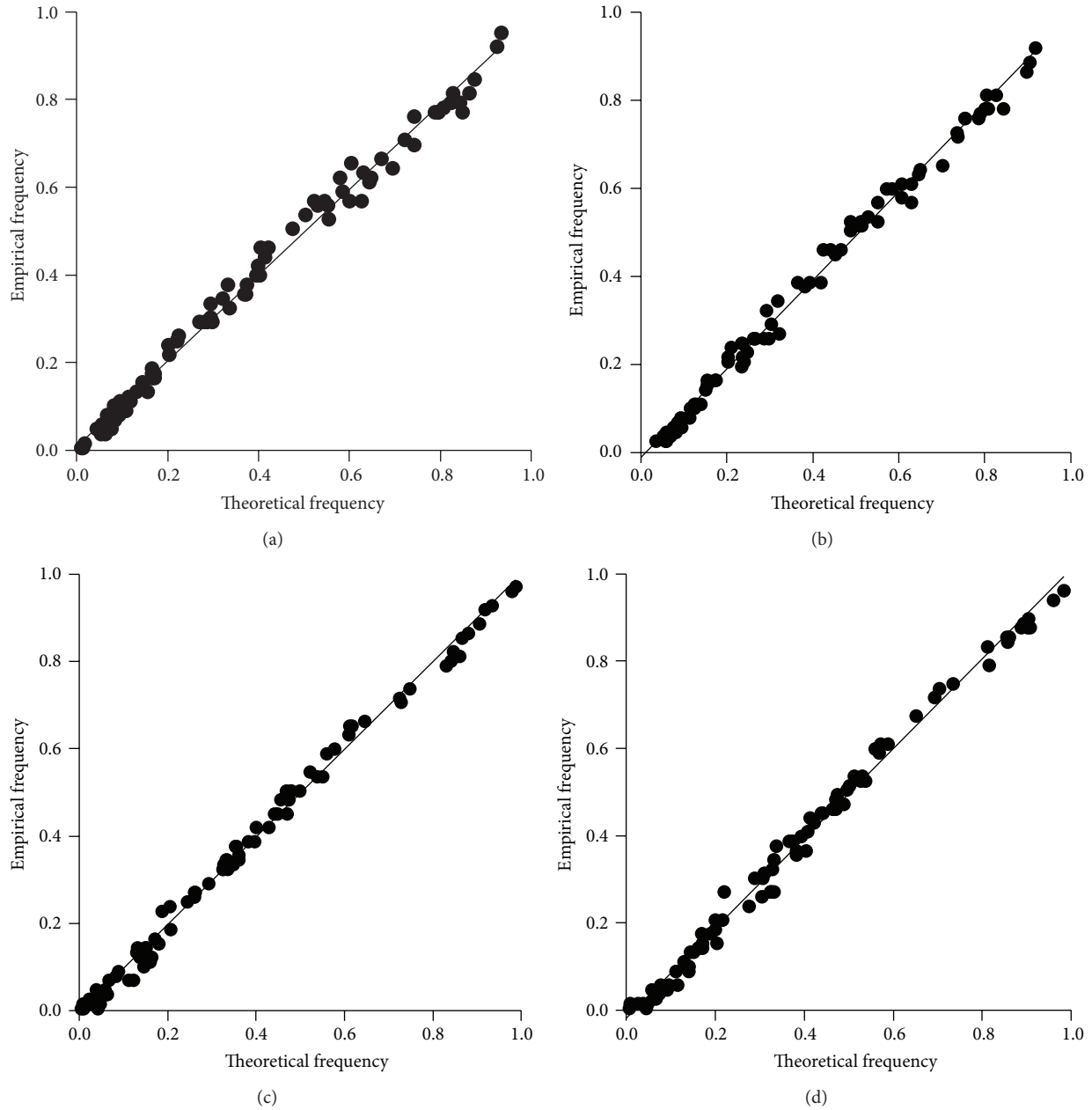


FIGURE 3: Empirical and theoretical frequency of 2D Gumbel Copula function joint distribution for different combination of the POT series: (a) RX1day-W1, (b) RX1day-W3, (c) RX3day-W1, and (d) RX3day-W3.

of decline in precipitation over time was greater for the simulated data, and there were years with large differences between observed and simulated precipitation, highlighting uncertainties in the CSIRO_MK3.5 simulation that transferred unavoidable uncertainty to our results.

5.2. Trends in Simulated Future Annual Precipitation. Simulated future precipitation over the period 2016 to 2100 (Figure 7) did not have significant trend under the A1B, A2, and B1 scenarios (the values of MK trend test statistic Z were -0.467 , -0.034 , and 0.793 , resp.). The results of sequential MK test statistic were shown in Figure 8. Under the A1B scenario, yearly plots of UF_k had no significant change, and the UF_k and

UB_k curves displayed several points of intersection, but all the change points were insignificant for this scenario. Under the A2 scenario, UF_k spots indicated a decreasing trend of precipitation over the considered periods, especially during the periods from 2045 to 2075, but no significant change points were found. The precipitation trend characteristics under the B1 scenario were similar to that under the A1B scenario; the UF_k and UB_k plots intersected each other for several times signifying no recognizable trend in the time series.

5.3. Trends in Simulated Future Extreme Precipitation. The AM series RX1day and RX3day (Figure 9) were selected to

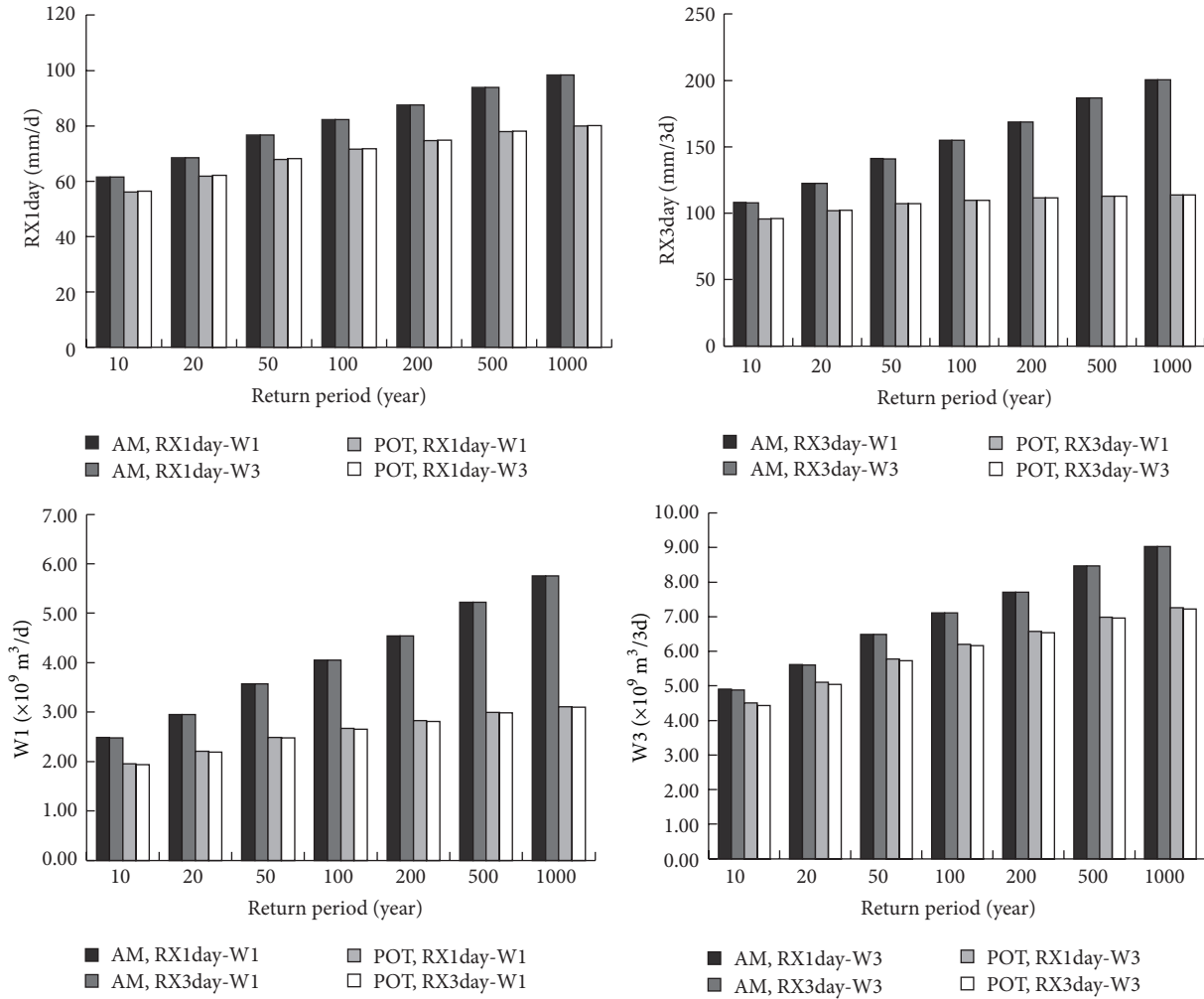


FIGURE 4: Extreme precipitation and flood discharge estimated via 2D joint distributions under a range of return periods.

test for trend in future extreme precipitation under the three climate change scenarios. The Z values of RX1day were 2.152, 2.167, and 1.454 for A1B, A2, and B1 scenarios, respectively, indicating an increasing trend of RX1day series under each scenario, and the trend was significant under A1B and A2 scenarios. The Z values of RX3day were 1.37, 1.438, and 0.452 for A1B, A2, and B1 scenarios, respectively, indicating increasing trend but the trend was not significant.

The results of sequential MK test statistic (Figure 10) indicated a similar pattern over time for the three climate change scenarios. The UF_k curves showed an increasing trend over the considered periods, and the UB_k curves indicated a decreasing trend. Under the A1B scenarios, the sequential version of MK test for RX1day series indicated a change point in 2053 (Figure 10(a)), and the UF_k also displayed that RX1day had shown an increasing trend since 2053. The UF_k and UB_k plots for RX3day series intersected each other several times (Figure 10(b)), but only 2046 can be recognized as a change point. Under the A2 scenarios, both RX1day and RX3day series had a change point in 2072, and the extreme precipitation showed a decreasing trend from 2016 till 2072

and afterward it had increased. Under the B1 scenarios, the UF_k and UB_k plots indicated that the change points of RX1day series were detected in 2025 and 2085, and the change points of RX3day series occurred in 2030 and 2075. Future precipitation had no significant trend under the three climate change scenarios (Figure 8), but the extreme precipitation had an increasing trend in most years (Figure 10), indicating that the proportion of the extreme precipitation in total precipitation increased constantly.

5.4. Change Trends of Future Extreme Flood. It was assumed that the frequencies of extreme precipitation and extreme flood are the same. Based on the Frank Copula function, the joint probability of precipitation and flood was calculated by the probability of future precipitation. This was used to represent the probability of floods in order to calculate the future 1-day (W1) and 3-day (W3) flood discharges via the marginal distribution function of flood volume. The future extreme flood discharge time series obtained for the AM series of RX1day and RX3day under the A1B, A2, and B1 scenarios indicated that future extreme flood volumes were

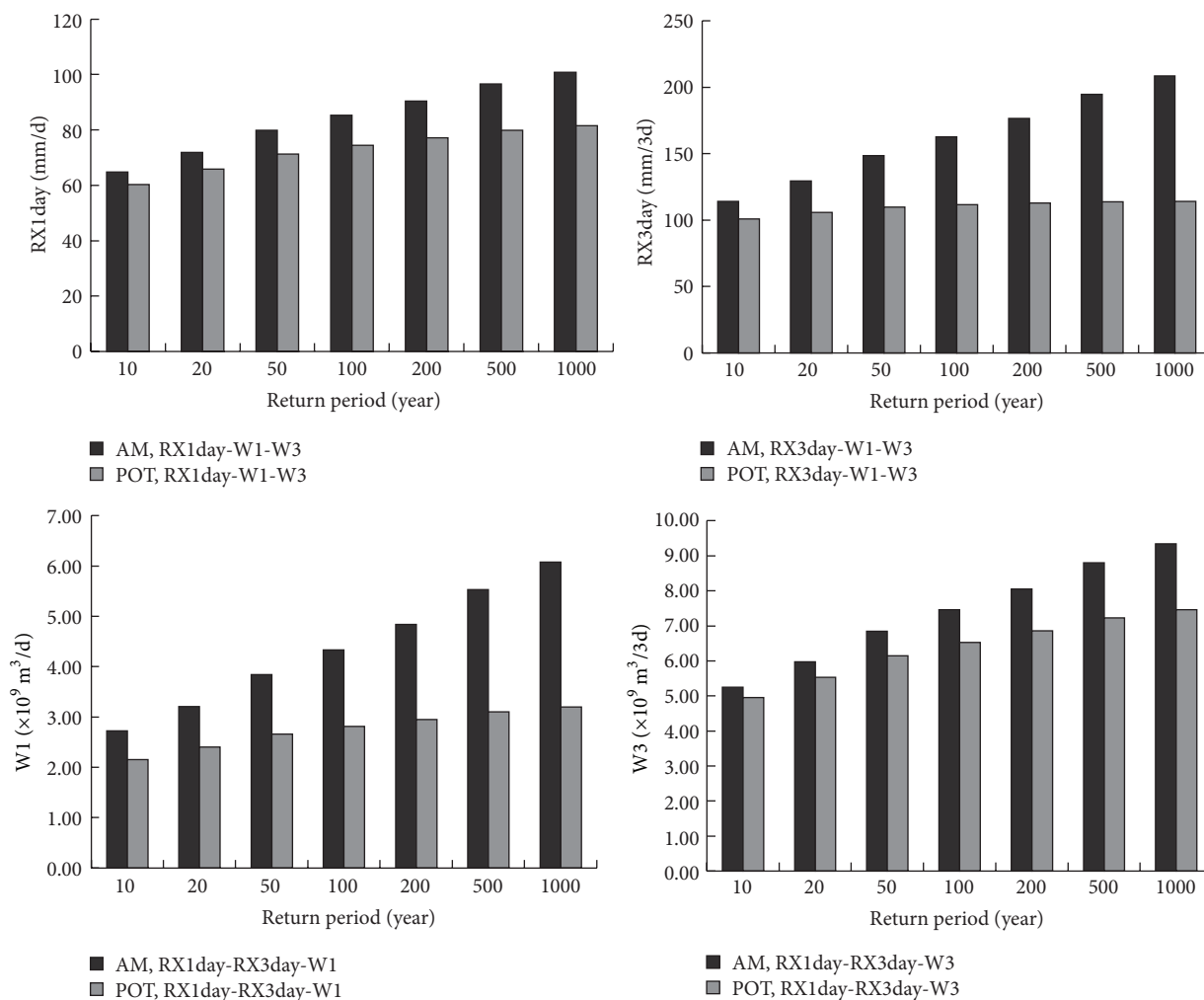


FIGURE 5: Extreme precipitation and flood discharge estimated via 3D joint distributions under a range of return periods.

TABLE 6: The design flood calculated by different methods under a range of return periods.

Method	Return period (year)				
	10	20	50	100	1000
The dam site design flood (x10 ⁹ m ³ /d)	2.445	2.946	3.577	4.069	5.616
2D Copula function (x10 ⁹ m ³ /d)	2.492	2.955	3.568	4.050	5.758
3D Copula function (x10 ⁹ m ³ /d)	2.697	3.191	3.835	4.329	6.079

TABLE 7: Comparison of simulated and observed annual precipitation in the study area.

Year	Observed precipitation (mm)	GCM simulated precipitation (mm)		
		CSIRO_MK3_5	INMCM3_0	NCAR_PCMI
1970	800	866	1892	1771
1980	972	1046	1600	1376
1990	810	592	1590	1244
2000	850	814	1727	1324
40 years	33248	34462	62736	56535

TABLE 8: Future and historical predicted extreme flood discharges for a range of return periods.

Return period (year)	5	10	20	30	40	50
Historical flood ($\times 10^9 \text{ m}^3/\text{d}$)						
W1	1.610	1.964	2.289	2.471	2.597	2.693
W3	3.504	4.270	4.980	5.379	5.655	5.866
Calculated by RX1day ($\times 10^9 \text{ m}^3/\text{d}$)						
W1	1.367	1.754	2.149	2.388	2.561	2.698
W3	2.926	3.651	4.343	4.739	5.017	5.230
Calculated by RX3day ($\times 10^9 \text{ m}^3/\text{d}$)						
W1	1.387	1.768	2.158	2.394	2.566	2.702
W3	2.989	3.692	4.368	4.756	5.030	5.240

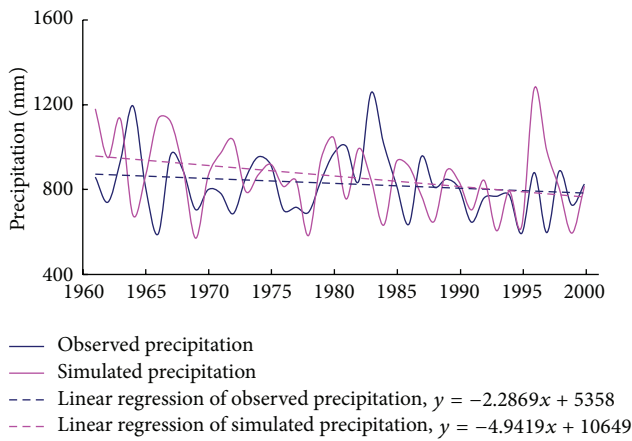


FIGURE 6: Comparison of simulated and observed annual precipitation in the study area.

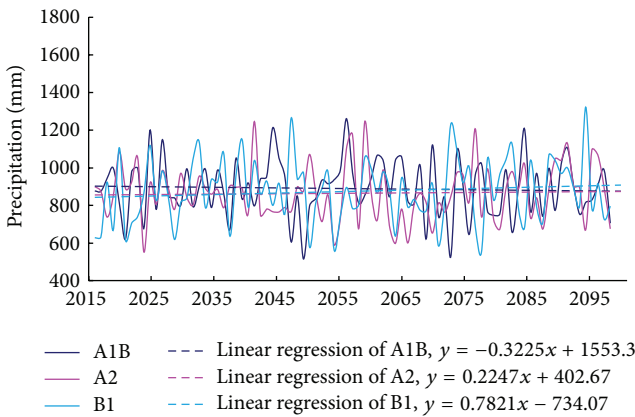


FIGURE 7: Annual precipitation changes from 2016 to 2100 under three climate change scenarios.

larger under the A2 scenarios than under the A1B and B1 scenarios (Figure 11).

The future extreme 1-day (W1) and 3-day (W3) flood discharges calculated from precipitation for a range of return periods were slightly smaller than the corresponding values calculated from the historical data (Table 8). This was consistent with the results of the previous research [40].

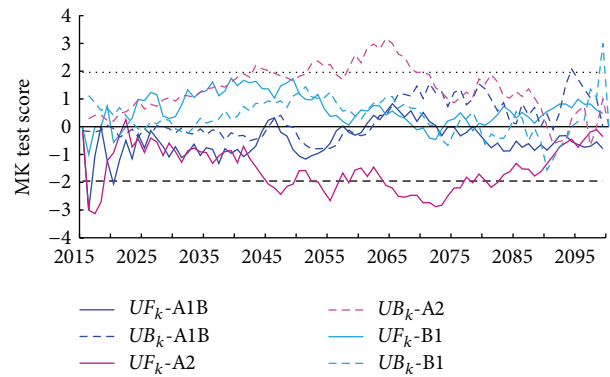


FIGURE 8: MK test score for annual precipitation from 2016 to 2100 under three climate change scenarios.

In China, the convention is to classify floods by size according to return period: (1) small, having a return period less than 5 years; (2) medium, having a return period between 5 and 20 years; (3) large, having a return period longer than 20 years. The frequencies of occurrence of floods of the three conventional size grades under the A1B, A2, and B1 scenarios (Figure 12) indicate that under the future scenarios small floods would occur less frequently than under historical conditions, while the frequency of occurrence of the medium floods and large floods under the future scenarios would be higher than the observed frequency of occurrence. Also, the frequency of occurrence of large floods under the A2 scenario was higher than that under the A1B and B1 scenarios, while the frequency of occurrence of small floods under the A2 scenario was less than that under the A1B and B1 scenarios.

6. Conclusions

In this study, the GEV, GPD, and Gamma distribution models and Copula functions were applied to estimate extreme hydrological events from 1969 to 2009 in the water source area of the middle route of South-to-North Water Diversion Project in China. Based on the simulated results of 23 GCMs from the World Climate Research Programme’s CMIP3 single-model dataset in the Intergovernmental Panel on Climate Change Fourth Assessment Report, the future extreme hydrological events from 2016 to 2100 were simulated

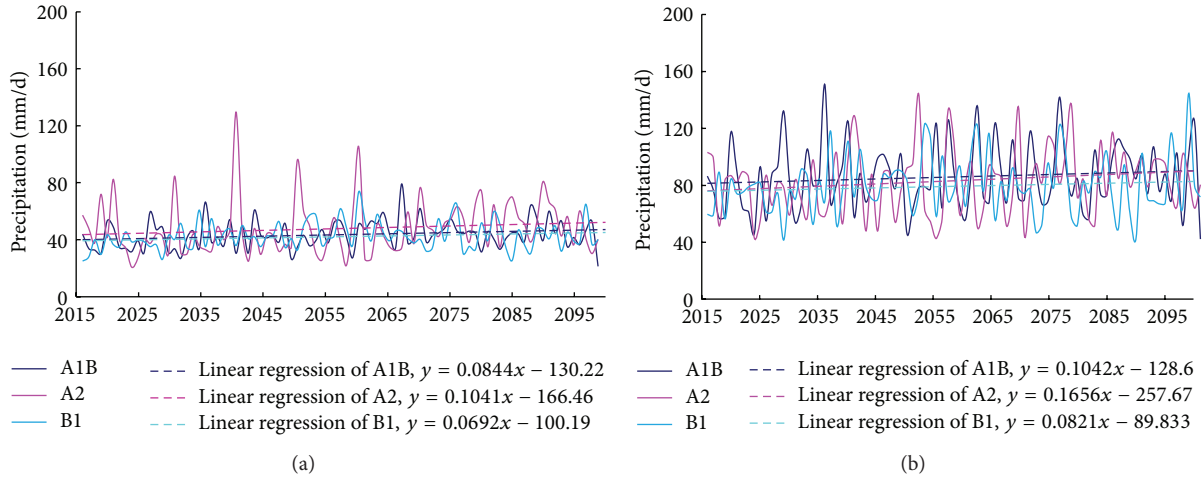


FIGURE 9: Extreme precipitation changes from 2016 to 2100 under three climate change scenarios: (a) RX1day and (b) RX3day.

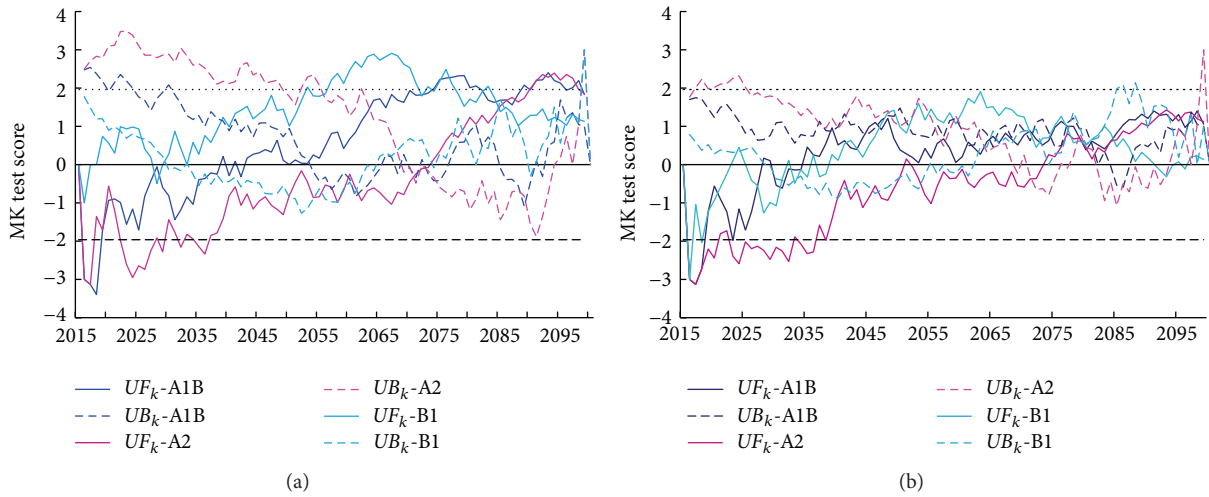


FIGURE 10: The MK test score of extreme precipitation from 2016 to 2100 under three climate change scenarios; (a) RX1day, (b) RX3day.

under the A1B, A2, and B1 scenarios. The main conclusions can be summarized as follows:

- (1) For the AM (annual maximum) series, the GEV and Gamma model better simulated the extreme precipitation and flood volume distributions than the GPD model, while the GPD model was the best fit for the POT (peaks over threshold) series.
- (2) For the 2D (two-dimensional) joint distributions of precipitation and flood volume, the Frank Copula performed better in simulation of the AM series and the corresponding GEV distribution, whereas the Gumbel Copula was the most appropriate function to simulate the POT series and the corresponding GPD distribution. The estimated extreme precipitation and flood discharges of the AM series were larger than those of the POT series for the same return period. Adopting the more conservative estimates of the AM series would provide lower risk for flood planning.

- (3) For the same return period, the magnitudes of the design floods calculated by the 2D and 3D (three-dimensional) Copula functions were larger than those used in the preliminary design stage of Danjiangkou Reservoir. The joint distributions utilize more of the available extreme information, and the higher estimated flood magnitudes carry lower risk for design purposes, suggesting that multivariate statistical analysis has benefits over a traditional univariate approach.
- (4) The outputs of CSIRO_MK3_5 global climate model were applied to simulate the future precipitation over the study area from 2016 to 2100. The results suggested that the future precipitation shows no significant trend under the three climate change scenarios, but the extreme precipitation showed a tendency that it will decrease in the first few years and increase in the last few years under these three scenarios, which indicated that the proportion of the extreme precipitation in total precipitation increases constantly.

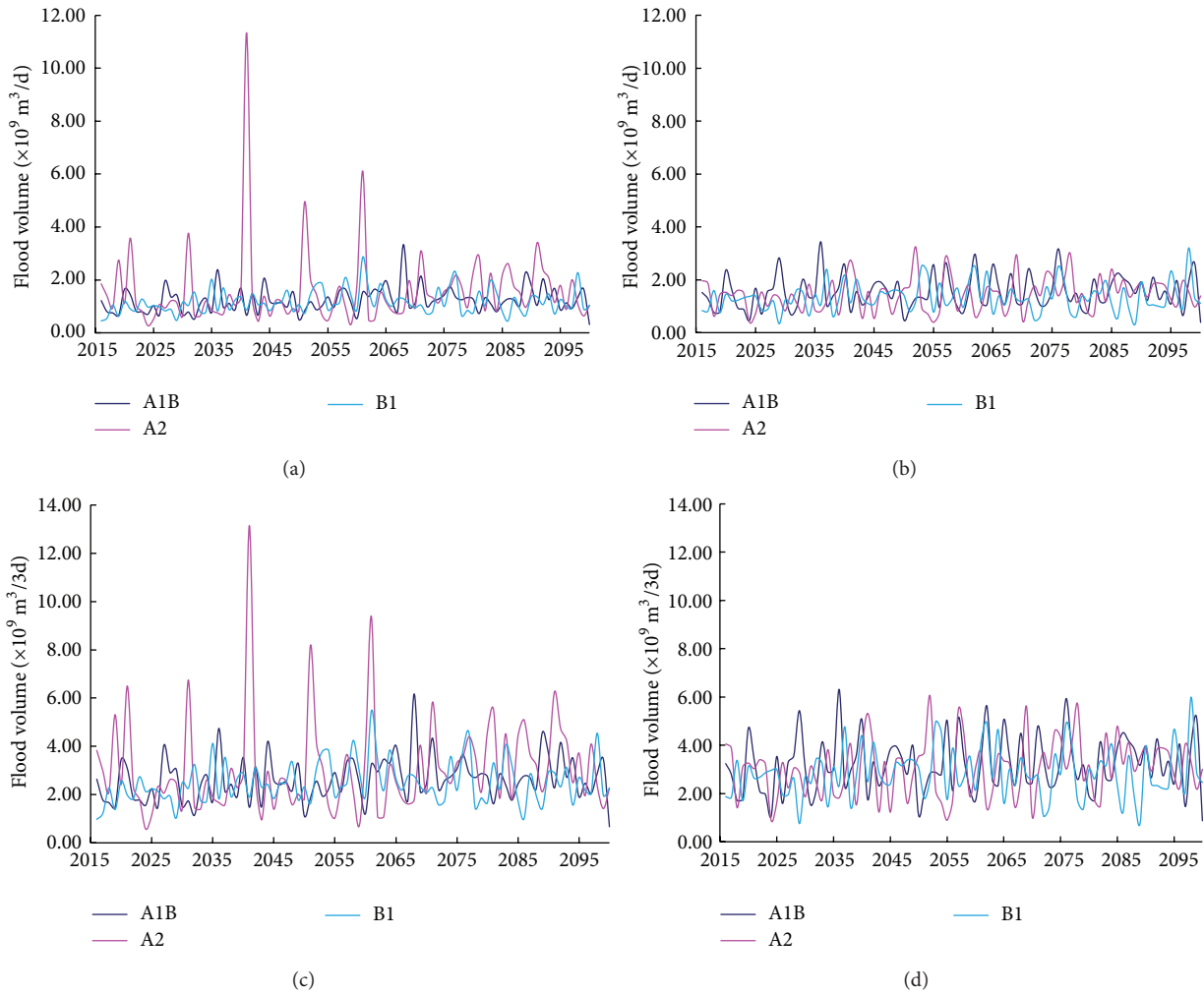


FIGURE 11: Extreme flood volume changes from 2016 to 2100 under three climate change scenarios. W1 calculated by (a) RX1day and (b) RX3day and W3 calculated by (c) RX1day and (d) RX3day.

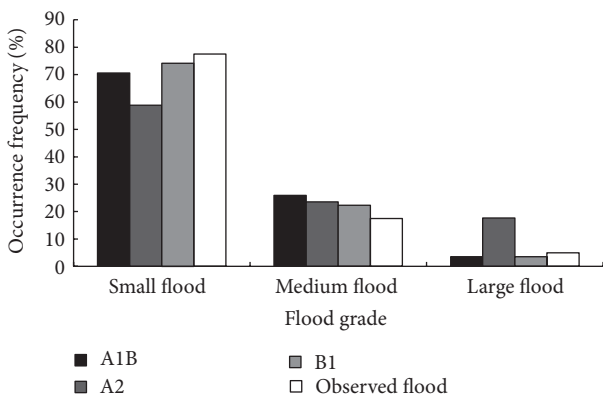


FIGURE 12: The frequency of occurrence of floods within standard size grades under three climate change scenarios and under historical conditions.

same return period, while the occurrence frequency of the medium and large floods under the future scenarios is higher than the observed occurrence frequency. The frequency of occurrence of the large flood under the A2 scenario is higher than that under the A1B and B1 scenarios, while the frequency of occurrence of the small flood under A2 scenario is less than that under the A1B and B1 scenarios.

Conflict of Interests

The authors declare that there is no conflict of interests regarding the publication of this paper.

Acknowledgments

This study was supported by the State Key Program of National Natural Science of China (no. 51339004), the National Natural Science Foundation of China (no. 51279139),

(5) The future extreme flood discharges were estimated to be slightly smaller than the historical values for the

and the Fundamental Research Funds for the Central Universities (no. 2015213020202). The authors appreciate the constructive comments of Christopher James Gippel as well as the excellent reviews of the coordinating editor and anonymous reviewers.

References

- [1] M. R. Allen and W. J. Ingram, "Constraints on future changes in climate and the hydrologic cycle," *Nature*, vol. 419, no. 6903, pp. 224–232, 2002.
- [2] M. D. Dettinger, D. R. Cayan, M. K. Meyer, and A. E. Jeton, "Simulated hydrologic responses to climate variations and change in the Merced, Carson, and American River basins, Sierra Nevada, California, 1900–2099," *Climatic Change*, vol. 62, no. 1–3, pp. 283–317, 2004.
- [3] T. Zhu, M. W. Jenkins, and J. R. Lund, "Estimated impacts of climate warming on California water availability under twelve future climate scenarios," *Journal of the American Water Resources Association*, vol. 41, no. 5, Article ID 03139, pp. 1027–1038, 2005.
- [4] T. G. Huntington, "Evidence for intensification of the global water cycle: review and synthesis," *Journal of Hydrology*, vol. 319, no. 1–4, pp. 83–95, 2006.
- [5] IPCC, *Climate Change 2001: The Science of Climate Change. Third Assessment Report of the Intergovernmental Panel on Climate Change*, Cambridge University Press, Cambridge, UK, 2001.
- [6] Z. Jiang, Y. Ding, and W. Chen, "Projection precipitation extremes for the 21st century over China," *Advances in Climate Change Research*, vol. 3, no. 4, pp. 202–207, 2007 (Chinese).
- [7] P. Zhai, X. Zhang, H. Wan, and X. Pan, "Trends in total precipitation and frequency of daily precipitation extremes over China," *Journal of Climate*, vol. 18, no. 7, pp. 1096–1108, 2005.
- [8] Y. Hong and R. F. Adler, "Predicting global landslide spatiotemporal distribution: integrating landslide susceptibility zoning techniques and real-time satellite rainfall estimates," *International Journal of Sediment Research*, vol. 23, no. 3, pp. 249–257, 2008.
- [9] D.-I. Müller-Wohlfeil, G. Bürger, and W. Lahmer, "Response of a river catchment to climatic change: application of expanded downscaling to Northern Germany," *Climatic Change*, vol. 47, no. 1–2, pp. 61–89, 2000.
- [10] S. B. Dessu and A. M. Melesse, "Impact and uncertainties of climate change on the hydrology of the Mara River basin, Kenya/Tanzania," *Hydrological Processes*, vol. 27, no. 20, pp. 2973–2986, 2013.
- [11] P. D. Jones and P. A. Reid, "Assessing future changes in extreme precipitation over Britain using regional climate model integrations," *International Journal of Climatology*, vol. 21, no. 11, pp. 1337–1356, 2001.
- [12] V. V. Kharin and F. W. Zwiers, "Estimating extremes in transient climate change simulations," *Journal of Climate*, vol. 18, no. 8, pp. 1156–1173, 2005.
- [13] T. Fischer, B. Su, Y. Luo, and T. Scholten, "Probability distribution of precipitation extremes for weather index-based insurance in the Zhujiang River Basin, South China," *American Meteorological Society*, vol. 13, no. 3, pp. 1023–1037, 2012.
- [14] W. Wang, X. Chen, P. Shi, and P. H. A. J. M. van Gelder, "Detecting changes in extreme precipitation and extreme streamflow in the Dongjiang River Basin in southern China," *Hydrology and Earth System Sciences*, vol. 12, no. 1, pp. 207–221, 2008.
- [15] L. Zhang, Y. Yang, L. Qin, Y. Duan, and Z. Yang, "Distribution of extreme precipitation events in water source area for the middle route project of south-to-north water transfer under A2, A1B, B1 scenarios," *Advances in Climate Change Research*, vol. 9, no. 1, pp. 29–34, 2013.
- [16] J. Guo, S. Guo, H. Chen, B. Yan, J. Zhang, and H. Zhang, "Prediction of changes of precipitation in Hanjiang River basin using statistical downscaling method based on ANN," *Engineering Journal of Wuhan University*, vol. 43, no. 2, pp. 148–152, 2010 (Chinese).
- [17] R. Xu, H. Chen, and J. Guo, "Impact of climate change on hydrological extreme events in upper reaches of the Hanjiang River basin," *Journal of Beijing Normal University (Natural Science)*, vol. 46, no. 3, pp. 383–386, 2010 (Chinese).
- [18] IPCC, *Climate Change 2007: The Science of Climate Change. Fourth Assessment Report of the Intergovernmental Panel on Climate Change*, Cambridge University Press, Cambridge, UK, 2007.
- [19] J. M. Murphy, D. M. H. Sexton, D. H. Barnett et al., "Quantification of modelling uncertainties in a large ensemble of climate change simulations," *Nature*, vol. 430, no. 7001, pp. 768–772, 2004.
- [20] N. Nakićenović, J. Alcamo, G. Davis et al., *Special Report on Emissions Scenarios: A Special Report of Working Group III of the Intergovernmental Panel on Climate Change*, Cambridge University Press, Cambridge, UK, 2000.
- [21] A. F. Jenkinson, "The frequency distribution of the annual maximum (or minimum) values of meteorological elements," *Quarterly Journal of the Royal Meteorological Society*, vol. 81, no. 348, pp. 158–171, 1955.
- [22] S. Coles and L. Pericchi, "Anticipating catastrophes through extreme value modelling," *Journal of the Royal Statistical Society. Series C. (Applied Statistics)*, vol. 52, no. 4, pp. 405–416, 2003.
- [23] S. Coles, *An Introduction to Statistical Modeling of Extreme Values*, Springer, Berlin, Germany, 2001.
- [24] J. Huang, "An index of precipitation probability for dryness/wetness analysis," *Meteorological Monthly*, vol. 16, no. 9, pp. 8–12, 1990.
- [25] B. B. Brabson and J. P. Palutikof, "Tests of the generalized Pareto distribution for predicting extreme wind speeds," *Journal of Applied Meteorology*, vol. 39, no. 9, pp. 1627–1640, 2000.
- [26] N. B. Roger, *An Introduction to Copula*, Springer, New York, NY, USA, 1999.
- [27] V. P. Singh and L. Zhang, "Bivariate flood frequency analysis using the Copula method," *Journal of Hydrologic Engineering*, vol. 11, no. 2, pp. 150–164, 2006.
- [28] B. Klein, M. Pahlow, Y. Hundedea, and A. Schumann, "Probability analysis of hydrological loads for the design of flood control systems using copulas," *Journal of Hydrologic Engineering*, vol. 15, no. 5, pp. 360–369, 2010.
- [29] H. B. Mann, "Nonparametric tests against trend," *Econometrica*, vol. 13, no. 3, pp. 245–259, 1945.
- [30] M. G. Kendall, *Rank Correlation Methods*, Griffin, 1970.
- [31] M. Bayazit and B. Önöz, "To prewhiten or not to prewhiten in trend analysis?" *Hydrological Sciences Journal*, vol. 52, no. 4, pp. 611–624, 2007.
- [32] R. Sneyers, "Climate chaotic instability: statistical determination and theoretical background," *Environmetrics*, vol. 8, no. 5, pp. 517–532, 1997.

- [33] Y. Yang and F. Tian, "Abrupt change of runoff and its major driving factors in Haihe River Catchment, China," *Journal of Hydrology*, vol. 374, no. 3-4, pp. 373-383, 2009.
- [34] D. Bisai, S. Chatterjee, A. Khan, and N. K. Barman, "Application of sequential Mann-Kendall test for detection of approximate significant change point in surface air temperature for Kolkata weather observatory, west Bengal, India," *International Journal of Current Research*, vol. 6, no. 2, pp. 5319-5324, 2014.
- [35] J. M. Moraes, G. Q. Pellegrino, M. V. Ballester, L. A. Martinelli, R. L. Victoria, and A. V. Krusche, "Trends in hydrological parameters of a southern Brazilian watershed and its relation to human induced changes," *Water Resources Management*, vol. 12, no. 4, pp. 295-311, 1998.
- [36] F.-W. Gerstengarbe and P. C. Werner, "Estimation of the beginning and end of recurrent events within a climate regime," *Climate Research*, vol. 11, no. 2, pp. 97-107, 1999.
- [37] T. Li, Y. Jiang, J. Yin et al., "Study on design flood of Danjiangkou Reservoir," *Yellow River*, vol. 32, no. 11, pp. 33-35, 2010.
- [38] X. Gao, Y. Ding, and Z. Zhao, "Climate change due to greenhouse effects in China as simulated by a regional climate model part I: evaluation of the model simulations," *Acta Meteorologica Sinica*, vol. 61, no. 1, pp. 20-28, 2003 (Chinese).
- [39] X. Shi, X. Xu, and Y. Xu, "Comparison of temperature between six hundreds stations in China and output of IPCC models," *Meteorological Monthly*, vol. 31, no. 7, pp. 49-53, 2005.
- [40] Z. Yang, L. Zhang, L. Qin, Y. Yang, and Y. Duan, "Flood characteristics and future response analysis under the climate change of the Danjiangkou reservoir," *Resources and Environment in the Yangtze Basin*, vol. 22, no. 5, pp. 588-594, 2013 (Chinese).

Research Article

Comparison of the Spatiotemporal Variability of Temperature, Precipitation, and Maximum Daily Spring Flows in Two Watersheds in Quebec Characterized by Different Land Use

Ali A. Assani, Raphaëlle Landry, Christophe Kinnard, Ouassila Azouaoui, Christine Demers, and Karine Lacasse

Department of Environmental Sciences, University of Quebec at Trois-Rivières, 3351 Boulevard of the Forges, Trois-Rivières, QC, Canada G9A 5H7

Correspondence should be addressed to Ali A. Assani; ali.assani@uqtr.ca

Received 26 February 2015; Revised 26 June 2015; Accepted 30 June 2015

Academic Editor: Fubao Sun

Copyright © 2016 Ali A. Assani et al. This is an open access article distributed under the Creative Commons Attribution License, which permits unrestricted use, distribution, and reproduction in any medium, provided the original work is properly cited.

We compared the spatiotemporal variability of temperatures and precipitation with that of the magnitude and timing of maximum daily spring flows in the geographically adjacent L'Assomption River (agricultural) and Matawin River (forested) watersheds during the period from 1932 to 2013. With regard to spatial variability, fall, winter, and spring temperatures as well as total precipitation are higher in the agricultural watershed than in the forested one. The magnitude of maximum daily spring flows is also higher in the first watershed as compared with the second, owing to substantial runoff, given that the amount of snow that gives rise to these flows is not significantly different in the two watersheds. These flows occur early in the season in the agricultural watershed because of the relatively high temperatures. With regard to temporal variability, minimum temperatures increased over time in both watersheds. Maximum temperatures in the fall only increased in the agricultural watershed. The amount of spring rain increased over time in both watersheds, whereas total precipitation increased significantly in the agricultural watershed only. However, the amount of snow decreased in the forested watershed. The magnitude of maximum daily spring flows increased over time in the forested watershed.

1. Introduction

Previous work on the hydrological impacts of land use changes (deforestation and agriculture) has revealed that they can vary widely from one region to another depending on numerous factors, such as climate, tree species and type of vegetation, forest management approach, and the physiographic features of watersheds (e.g., [1–3]). There is also controversy around the methods used to determine the effects of deforestation, in particular with regard to flood flows (see [4]).

In Quebec and in other neighbouring provinces in Canada, various studies have looked at the effects of land use changes on flood flows and low flows (e.g., [5–8]). This work has shown that deforestation and/or agriculture have led to an increase in minimum flows. However, they have had virtually no impact on flood flows, particularly spring flood flows from

snowmelt. In any event, a number of criticisms can be made regarding these studies.

- (i) The studies do not consider variability of temperatures, precipitation, and flows in conjunction with one another. As a result, it is not possible to determine the effects of land use changes on the spatial variability of climate variables (temperature and precipitation), on the one hand, or to accurately distinguish between the effects of land use changes and the effects of climate variability on flows, on the other. Hence, it is not always easy to interpret the hydrological changes that are observed, which can sometimes be attributed incorrectly to the effects of land use changes.
- (ii) Most of these studies look solely at the effects of land use changes on the magnitude of floods and low flows. They do not take into account the other elements

of flows, such as timing, duration, frequency or variability, despite their influence on the functioning of aquatic ecosystems [3].

- (iii) These studies do not look at the impact of land use changes on the temporal variability of climate variables or the characteristics of streamflow. They cannot distinguish between the effects of climate variability and those brought about by land use changes in watersheds for which hydrological data from before and after such changes are not available, even though there are many such watersheds in Quebec.

In light of the above, the three goals of this study are as follows:

- (1) To compare the spatial and temporal variability of spring peak flood flows in two watersheds that differ in terms of the area of forest cover and the presence of agricultural activity. Spring floods were chosen because previous studies did not highlight the impact of land use changes on maximum daily spring flows. In this study, we look at the impacts on the magnitude and timing of such flows from 1930 to 2013 along with the temporal variability of temperatures and precipitation measured in the two watersheds. The other characteristics (duration, frequency, and variability) of these flows will not be analyzed for the simple reason that they do not vary over time.
- (2) To compare the spatial and temporal variability of climate factors (temperature and precipitation) that influence these two characteristics (magnitude and timing) of maximum daily spring flows in the two types of watersheds.
- (3) To compare the relationship between these climate factors and the two characteristics of maximum daily spring flows in the two watersheds.

2. Data and Methodology

2.1. Choice and Description of Watersheds Analyzed. Two watersheds were selected because of their geographic proximity, the similarity of their physiographic (geographic area, length of watercourse, drainage density, and average slope) and climate properties, and the availability of existing temperature and precipitation data measured over a relatively long period, and their different land use distribution. The first watershed, that of the Matawin River, is fully contained within the Canadian Shield. It is covered entirely by forest and no farming takes place within it. This forested area, which also extends to the L'Assomption River watershed, comprises essentially sugar maple-yellow birch stands [9]. For the Matawin River, the watershed upstream from the Saint-Michel-des-Saints station covers 1390 km² (Figure 1). Flows have been measured continuously since 1931 and have not been affected by the dam built further downstream in 1930. With regard to the L'Assomption River watershed, two-thirds of it is located within the Canadian Shield and one-third in the Saint Lawrence Lowlands, where intensive

agriculture (mostly grains and fodder crops) is practiced. At the Joliette station, the geographic area of the L'Assomption River watershed is 1340 km². Flows have been measured there on an ongoing basis since 1925. For both watersheds, flow data as well as temperature and precipitation data were taken from the Environment Canada websites [10]. However, unlike for flow data, temperatures and precipitation were measured fairly regularly until 2008 for both watersheds and then only intermittently afterwards.

It is important to note that the magnitude of maximum daily spring flows in the two watersheds, both located on the north shore, is correlated with the Atlantic Multidecadal Oscillation [11], whereas their timing is correlated with the North Atlantic Oscillation [12], and, thus, the two watersheds are affected by the same climate forcing mechanisms.

2.2. Hydroclimatic Series. The following two streamflow series were assembled:

- (i) The magnitude of maximum daily spring flows (SMF) series, composed of the highest daily flows measured each spring (from April to June) from 1932 to 2013. Magnitude is expressed in L/s/km² to allow the comparison of magnitude values between the two watersheds, which are dissimilar (albeit very slightly) in size.
- (ii) The maximum daily spring flow timing series (STF), comprising the dates on which these flows were measured. Dates are expressed in Julian days.

With regard to climate variables, the following nine series have been assembled:

- (i) Three series of mean daily maximum temperatures measured in fall (TMAXf, October to December), winter (TMAXw, January to March), and spring (TMAXs, April to June). Mean values were calculated at the seasonal scale.
- (ii) Three series representing mean daily minimum temperatures measured in fall (Tminf, October to December), winter (Tminw, January to March), and spring (Tmins, April to June). Mean values were calculated at the seasonal scale.

We analyzed temperatures for the different seasons because of their influence on the amount of precipitation (snow and/or rain) that in turn affects SMF magnitude and timing. In the fall, temperatures influence the amount of snow. In winter, they affect the amounts of both snow and rain. Finally, in the spring, they affect the amount of snow and the timing of snowmelt. Summer temperatures have no impact on the amount of snow or rain that affects the two SMF characteristics and, for this reason, were not included in this study.

- (i) A series representing total snowfall (TSF) from October to May of each year, the time of the year when snowfall and snowmelt occur. However, snowmelt, which produces spring floods, occurs mainly in the spring (April and May).

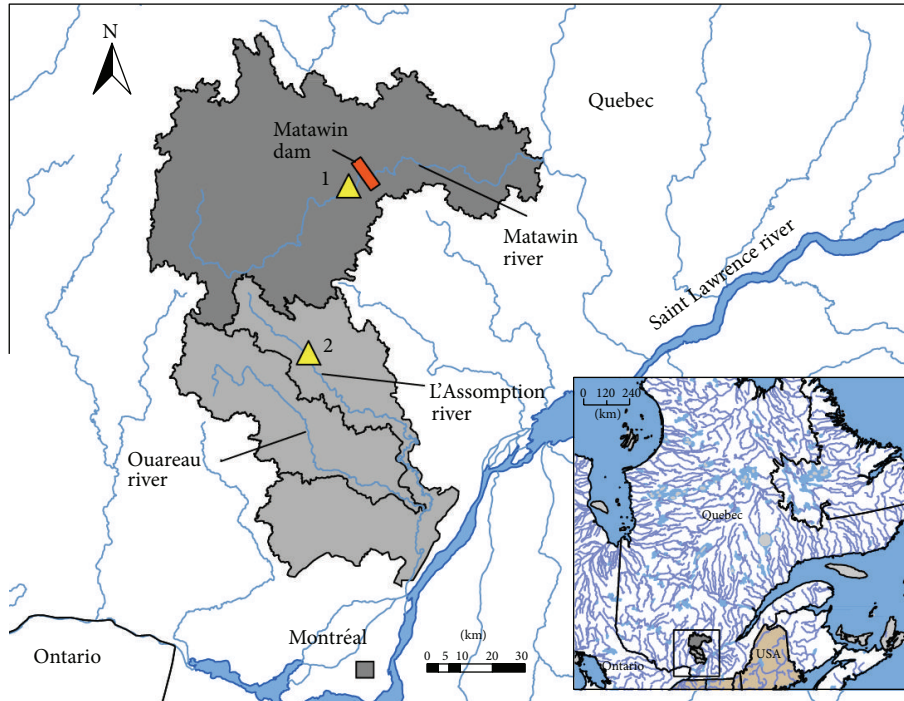


FIGURE 1: Location of two watersheds. 1: Saint-Michel-Des-Saints hydroclimatic station located in Matabwin River (forested basin); 2: Joliette hydroclimatic station located in L'Assomption River (agricultural basin).

- (ii) A series representing total precipitation (rain and snow) (TP) from October to May of each year.
- (iii) Lastly, a series of the total amount of spring rain (STR) measured each year from April to May.

These nine climate variables were selected because they have a direct or indirect impact on spring snowmelt from which spring flood flows arise.

2.3. *Statistical Analysis of Hydroclimatic Series.* Statistical analysis was performed in three steps.

- (i) For the first step, we compared the mean values of hydroclimate variable series measured in the two watersheds using Student's t -test and the paired t -test. The purpose of this step was to compare the spatial variability of hydroclimate variables in order to constrain the effect of differing land uses in the two watersheds. The same results were obtained from both tests.
- (ii) For the second step, we looked at the stationarity (changes in arithmetic means) of hydroclimate variables series using the Lombard method [13]. This method can be used to determine the nature and timing of changes (breaks) in mean and variance of a statistical series. The use of this method is justified by its general nature, which makes it possible to detect abrupt or gradual changes, unlike other methods commonly mentioned in the scientific literature (e.g., Pettitt's test). This general nature makes the Lombard method more sensitive than other methods

at detecting small breaks in mean or variance. In addition, missing data in a series do not affect the ability to determine the timing of changes in the mean or variance. It is therefore a powerful method [13]. Its mathematical development is presented in detail by [14]. This method was applied after removal of any autocorrelation present in the analyzed series. A change in the mean or variance of a statistical series is considered significant when the S_n value of the Lombard statistic is higher than the critical theoretical value ($S_n = 0.0403$) at the 5% level. The use of this method makes it possible to constrain the effect of differing land uses in the two watersheds on the stationarity (change in mean values) of hydroclimate series.

- (iii) For the final step, we correlated the two series of the characteristics (magnitude and timing) of maximum daily spring flows with the nine climate variables series. This correlation was calculated on standardized series in order to eliminate the influence of extreme values on correlation coefficient values. This analysis aims to constrain the effect of differing land uses in the two watersheds on the relationship between the climate variables and the two characteristics of maximum daily spring flows.

3. Results

3.1. *Comparison of Hydroclimatic Variables in the Two Watersheds to Analyze Their Spatial Variability.* Mean values of

TABLE 1: Comparison of mean values of hydroclimate variables in the L'Assomption River and Matawin River watersheds using Student's t -test.

Variables	L'Assomption River watershed	Matawin River watershed	p values
T_{Maxf} ($^{\circ}\text{C}$)	4.6 (1.50)	2.6 (1.46)	0.000
T_{Maxw} ($^{\circ}\text{C}$)	-3.1 (1.40)	-4.2 (1.50)	0.000
T_{Maxs} ($^{\circ}\text{C}$)	17.8 (1.25)	15.6 (1.22)	0.000
T_{minf} ($^{\circ}\text{C}$)	-4 (1.85)	-7 (1.74)	0.000
T_{minw} ($^{\circ}\text{C}$)	-13.4 (2.09)	-17.9 (2.44)	0.000
T_{mins} ($^{\circ}\text{C}$)	6.4 (0.94)	2.5 (1.01)	0.000
TSF (cm)	213 (76.1)	231 (58.3)	0.131
STR (mm)	225 (75.4)	213 (52.4)	0.524
TP (mm)	665 (139.5)	601 (85.8)	0.002
SMF (L/s/km^2)	133.6 (44.4)	102.7 (31.51)	0.000
STF (Julian/Days)	114 (10.8)	119 (11.7)	0.001

p values < 0.05 are statistically significant at the 5% level.

temperature, precipitation, and flow (magnitude and timing) measured in the two watersheds are recorded in Table 1. With regard to temperature, mean maximum and minimum temperatures during the three seasons are higher in the agricultural watershed (L'Assomption) than in the forested one (Matawin). The difference in minimum temperatures is higher than that in maximum temperatures. With regard to precipitation, the total amount of precipitation (rain and snow) is higher in the agricultural watershed than in the forested one. However, the amounts of snow and spring rains do not differ significantly between the two watersheds. With regard to the characteristics of maximum daily spring flows, magnitude is higher in the agricultural watershed than in the forested one. Moreover, this magnitude arises early in the season.

3.2. Comparison of Temporal Variability of Hydroclimate Variables in the Two Watersheds. Results of the analysis of the temporal variability of the hydroclimate variables are presented in Table 2. Maximum and minimum temperatures increased significantly in the fall in the agricultural watershed. Figure 2 shows the temporal variability of mean daily minimum temperature. This increase occurred after 1946 for maximum temperatures and after 1948 for minimum temperatures. In both watersheds, minimum spring temperatures increased significantly in the second half of the 1970s. A similar increase (after 1953) was also observed in winter in the forested watershed alone. The amount of snow decreased significantly in the forested watershed. This decrease occurred after 1976. However, the amount of rain in the spring increased significantly in both watersheds (Figure 3). This increase occurred during the same period, that is, after 1980, in the two watersheds. Lastly, the total amount of precipitation increased significantly in the agricultural watershed after 1992. With regard to flows, means values of the two characteristics (magnitude and timing) changed significantly in the forested watershed (Figures 4 and 5). This change resulted in an increase in the magnitude of maximum

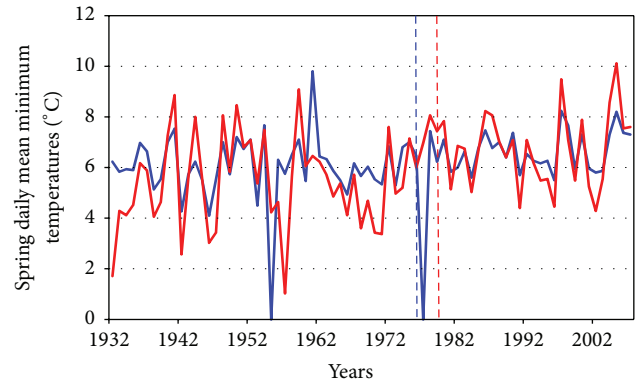


FIGURE 2: Comparison of the temporal variability of mean minimum daily spring temperatures at the Joliette (agricultural watershed, blue curve) and Saint-Michel-des-Saints (forested watershed, red curve) stations. The vertical bar indicates the year in which the significant change in the mean took place.

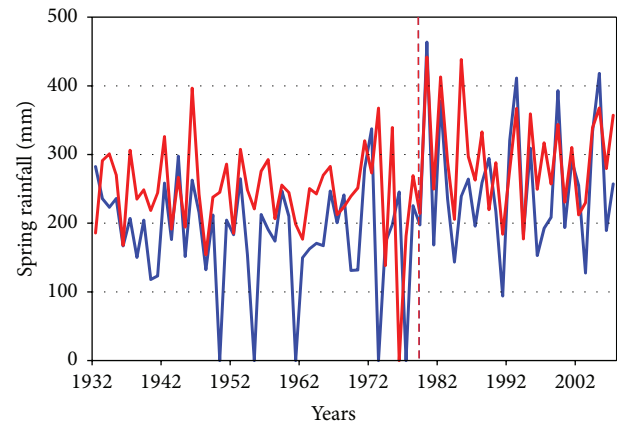


FIGURE 3: Comparison of temporal variability in the amount of spring rain at the Joliette (agricultural watershed, blue curve) and Saint-Michel-des-Saints (forested watershed, red curve) stations. The vertical bar indicates the year in which the significant change in the mean took place. Zero values actually reflect years for which data are missing.

daily spring flows after 1970, and their earlier occurrence after 1987. In contrast, no such changes in the stationarity of these two characteristics are observed in the agricultural watershed.

3.3. Relationship between Climate Variables and the Characteristics of Maximum Daily Spring Flows. Values of coefficients of correlation between hydroclimate variables of the two watersheds are presented in Table 3. With the exception of fall temperatures, there is a fairly strong correlation among the other variables. However, the lowest correlation is between the amounts of snow measured in the two watersheds and the strongest is for the magnitude of maximum daily spring flows. With regard to the link between the two characteristics (magnitude and timing) of streamflow and climate variables (temperature and precipitation), the magnitude of maximum

TABLE 2: Hydroclimate variables; results of the Lombard method analysis.

Variables	L'Assomption River watershed			Matawin River watershed		
	Sn	T1	T2	Sn	T1	T2
TMaxf (°C)	0.0434	1945	1946	0.0050	—	—
TMaxw (°C)	0.0385	—	—	0.0093	—	—
TMaxs (°C)	0.0229	—	—	0.0121	—	—
Tminf (°C)	0.0764	1945	1948	0.0050	—	—
Tminw (°C)	0.0385	—	—	0.0934	1952	1953
Tmins (°C)	0.0648	1978	1979	0.0675	1975	1976
TSF (mm)	0.0147	—	—	0.1182	1974	1976
STR (mm)	0.0550	1977	1980	0.0459	1979	1980
TP (mm)	0.0841	1991	1992	0.0016	—	—
SMF (L/s/km ²)	0.0195	—	—	0.0553	1967	1970
STF (L/s/km ²)	0.0199	—	—	0.0694	1986	1987

Lombard test Sn values > 0.0403 are statistically significant at the 5% level. T1 and T2 are the years of start and end, respectively, of significant changes in mean and variance values of a given series. f: fall; w: winter; s: spring.

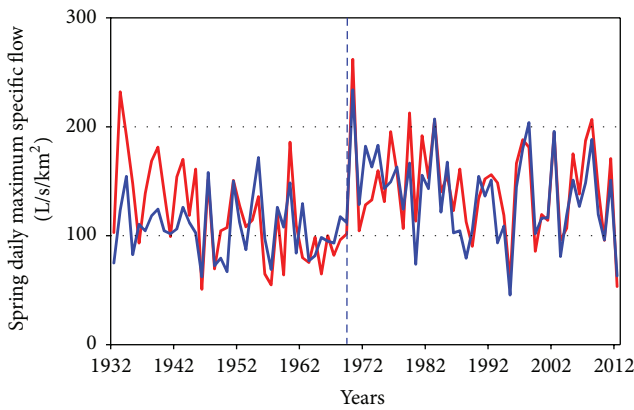


FIGURE 4: Comparison of temporal variability of the magnitude (specific discharge) of maximum daily spring flows at the Joliette (agricultural watershed, blue curve) and Saint-Michel-des-Saints (forested watershed, red curve) stations. The vertical bar indicates the year in which the significant change in the mean took place.

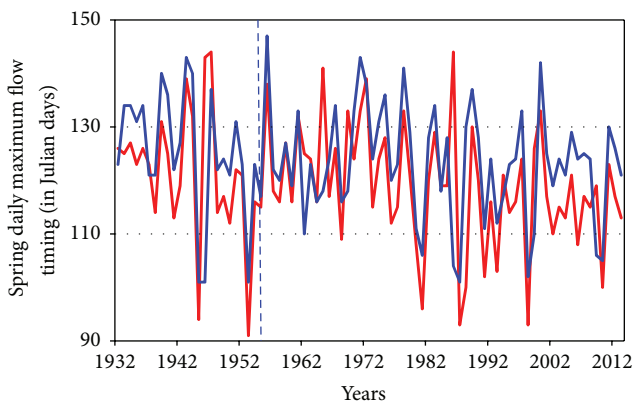


FIGURE 5: Comparison of temporal variability of the timing of maximum daily spring flows at the Joliette (agricultural watershed, blue curve) and Saint-Michel-des-Saints (forested watershed, red curve) stations. The vertical bar indicates the year in which the significant change in the mean took place.

TABLE 3: Correlation coefficients calculated between hydroclimate variables measured in the two watersheds.

Variables	Coefficients of correlation
TMaxf (°C)	-0.0507
TMaxw (°C)	0.7324
TMaxs (°C)	0.7782
Tminf (°C)	0.0690
Tminw (°C)	0.6836
Tmins (°C)	0.7635
TSF (mm)	0.2867
STR (mm)	0.6826
TP (mm)	0.3312
SMF (L/s/km ²)	0.7560
STF (L/s/km ²)	0.5919

Statistically significant coefficient of correlation values at the 5% level are shown in bold.

daily spring flows is positively correlated with precipitation in both watersheds (Table 4). Timing, for its part, is correlated negatively with winter and spring (maximum and minimum) temperatures in both watersheds. In contrast to precipitation, the correlation between timing and temperature is higher in the agricultural watershed than in the forested one. Table 4 reveals that the two characteristics of streamflow are correlated to the same climate variables. Thus, the difference in land use has no effect on the link between climate variables and the two characteristics of maximum daily spring flows.

4. Discussion

Comparison of the spatiotemporal variability of hydroclimate variables for a wholly forested watershed (Matawin River) and an agricultural watershed (L'Assomption River) revealed a number of significant facts. With regard to temperature, mean values of maximum and minimum daily temperatures are systematically higher in the agricultural watershed than in the forested watershed in fall, winter, and spring. The

TABLE 4: Correlation coefficients calculated between climate variables and characteristics (magnitude and timing) of maximum spring flows (1932–2008).

Climate variables	L'Assomption River watershed		Matawin River watershed	
	Magnitude	Timing	Magnitude	Timing
TMaxf	-0.1603	0.1225	-0.1119	0.0077
TMaxw	0.0702	-0.3564	0.0038	-0.2805
TMaxs	-0.0335	-0.5143	-0.0418	-0.4481
Tminf	-0.1808	0.0581	-0.0993	0.0234
Tminw	0.0195	-0.3387	-0.0212	-0.2436
Tmins	0.0884	-0.4575	0.0921	-0.5050
TSF	0.2439	0.1913	0.4150	0.1859
STR	0.2368	-0.0404	0.3019	0.0038
TP	0.3002	-0.0021	0.5008	-0.0103

Statistically significant coefficient of correlation values at the 5% level are shown in bold.

difference between the two watersheds is greater for minimum temperatures than for maximum temperatures. This temperature difference may be partly explained by the “shading” effect of forest cover, which reduces the amount of solar energy that reaches the ground surface. In addition, a portion of the solar energy is used by trees for evapotranspiration. With regard to precipitation, the two watersheds differ mainly in the total amount of precipitation, which is higher in the agricultural watershed than in the forested watershed. Given that the amount of snow and the amount of spring rainfall are not significantly different in the two watersheds, this increase in total precipitation in the agricultural watershed is apparently due to the increase in total rainfall during the fall given, since the amount of rain in winter is not significantly different in the two watersheds either. This means that the difference in land use does not affect the spatial variability of the amounts of snow and rain in winter and spring. It is in the fall that climate differences between the two watersheds are evident. This explains the lack of correlation observed between climate variables measured in the two watersheds.

With regard to the characteristics of flows, the magnitude of maximum daily flows was found to be higher in the agricultural watershed than in the forested watershed, despite a significant increase in magnitude over time (Table 2) in the latter watershed. All of the previous work carried out in Quebec has shown that land use has very little impact on flood flows in general, and on spring flood flows in particular [6, 7]. A number of different factors may account for the magnitude of maximum daily spring flows being higher in the agricultural watershed than in the forested watershed.

- (1) In the agricultural watershed, the total amount of precipitation measured from October to April is higher than in the forested watershed. This could cause spring flood flows to be higher in the first watershed than in the second. However, spring flood flows are generated mainly by snowmelt, sometimes in conjunction with spring rains. It has been established that there is no significant difference between the amounts of snow and rain in the two watersheds, with the exception of fall rain, which has no bearing whatsoever on spring floods.

- (2) Drainage density and the relatively high slope of the agricultural watershed could account for higher peak flows in the spring. However, these two factors do not come into play, as they are very similar in the two watersheds. In addition, in the agricultural watershed, slopes, and drainage density are much lower in the area in which agricultural land is concentrated.
- (3) Because of the decrease in forest cover (decrease in interception of precipitation) and because of farming activities, runoff is becoming more important in the agricultural watershed than in the forested watershed. Despite low slopes, the decrease in the infiltration capacity of the soil as a result of mechanized agriculture appears to result in much more substantial runoff, which in turn would account for higher peak floods. This phenomenon has been extensively documented in many parts of the world [3].
- (4) A significant decrease in total snowfall over time was observed in the forested watershed. However, as this decrease is incompatible with the increase in the magnitude of maximum daily spring flows, it is excluded as a possible explanation for the difference in magnitude between the two watersheds.

With regard to the timing of maximum daily spring flows, they occur earlier in the season in the agricultural watershed than in the forested watershed, despite the change over time in their mean values in the latter watershed. This relatively early onset could be explained by higher maximum and minimum spring temperatures in the first watershed as compared with the second.

Analysis of the temporal variability of temperatures using the Lombard method revealed that mean daily maximum temperatures in the agricultural watershed increased significantly over time in the fall. This increase, which did not occur in the forested watershed, took place during the second half of the 1940s. However, there is no reason to link this increase with the decrease in forest cover or the development of intensive agriculture that began after this decade. With regard to minimum temperatures, they increased significantly over time in spring in both watersheds,

in fall in the agricultural watershed and in winter in the forested watershed. This increase cannot be linked to the difference in land use. Rather, it reflects the changes that affect the temporal variability of temperatures throughout Quebec. Similar increases have been observed in numerous watersheds in Quebec. Minimum temperatures are more strongly affected than maximum temperatures [15, 16]. With regard to precipitation, the amount of spring rain increased significantly over time in the two watersheds after 1980, while the amount of precipitation did not increase in the agricultural watershed until after 1992. However, the amount of snow decreased significantly in the forested watershed after 1976. Such changes in precipitation have also been observed in other watersheds in Quebec. They therefore cannot be linked to land use changes. With regard to the amount of snow in particular, [17] has observed a significant decrease in snowpack since the 1980s in Quebec. According to [16], this decrease has had a particularly notable impact on the north shore of the St. Lawrence River (where the two watersheds are located), which is characterized by a continental-type climate.

The magnitude of maximum daily spring flows increased significantly over time in the forested watershed only after 1970. This increase could be linked to the increase in the amount of spring rain, since the amount of snow decreased significantly over time in the watershed. However, the changes in mean values of these variables are not synchronous. Thus, the increase in flow magnitude occurred approximately 10 years before the increase in the amount of spring rain. It seems that flows are much more sensitive to gradual changes in the amount of rain. The absence of change in magnitude of maximum daily spring flows in the agricultural watershed could partly be explained by a fairly high evaporation owing to relatively high temperatures that could mitigate the effects of the increase in spring rains. With regard to the timing of maximum daily spring flows, its temporal variability is reflected in their earlier timing in the forested watershed, likely because of the increase in minimum temperature in winter and spring. However, despite an increase in minimum temperature in spring, no change in the timing of these flows was observed in the agricultural watershed.

Analysis of the correlation between hydroclimate variables for the two watersheds revealed a strong link between these variables, with the exception of fall temperatures, which appear to be influenced by site-specific conditions. The correlation for total snowfall is very weak, albeit significant. The weakness of this correlation shows that the amount of snow is partly influenced by site conditions, particularly in the fall. Analysis of the relationship between climate variables and the two characteristics of streamflow in the two watersheds revealed that magnitude is positively correlated with precipitation (snow and rain). This correlation is higher in the forested watershed than in the agricultural watershed, probably because of the influence of relatively high temperatures, which promotes evapotranspiration and therefore affects the connection between precipitation and flow. With regard to the timing of maximum daily spring flows, it is negatively correlated with maximum and minimum winter and spring temperatures in both watersheds. When temperatures are

high, snowmelt giving rise to spring floods occurs early in the season. This correlation is higher in agricultural watershed than in the forested one due to the fact that temperatures are higher in the former than in the latter.

5. Conclusion

This study brought out the respective effects of land use on the spatiotemporal variability of temperature, precipitation, and streamflow characteristics in Quebec. As far as spatial variability is concerned, the difference in land use results in higher maximum and minimum seasonal temperatures and maximum daily spring flow magnitude in the agricultural watershed than in the forested watershed. As for the timing of maximum daily spring flows, they occur earlier in the agricultural watershed than in the forested watershed. With regard to the temporal variability of these hydroclimate variables, breaks in mean values that affect some of these variables occurred essentially at the same time as those observed in other watersheds in Quebec. Therefore, they cannot be linked to the difference in land use between the two watersheds. Finally, the difference in land use between the two watersheds has no effect on the link between climate variables (temperature and precipitation) and the two characteristics (magnitude and timing) of maximum daily spring flows. In both watersheds, flow magnitude is positively correlated with winter and spring temperatures, while timing is negatively correlated with these variables.

Conflict of Interests

The authors declare that there is no conflict of interests regarding the publication of this paper.

References

- [1] V. Andréassian, "Waters and forests: from historical controversy to scientific debate," *Journal of Hydrology*, vol. 291, no. 1-2, pp. 1-27, 2004.
- [2] C. Cosandey, V. Andréassian, C. Martin et al., "The hydrological impact of the mediterranean forest: a review of French research," *Journal of Hydrology*, vol. 301, no. 1-4, pp. 235-249, 2005.
- [3] N. L. Poff, B. P. Bledsoe, and C. O. Cuhacyan, "Hydrologic variation with land use across the contiguous United States: geomorphic and ecological consequences for stream ecosystems," *Geomorphology*, vol. 79, no. 3-4, pp. 264-285, 2006.
- [4] Y. Alila, P. K. Kuraś, M. Schnorbus, and R. Hudson, "Forests and floods: a new paradigm sheds light on age-old controversies," *Water Resources Research*, vol. 45, no. 8, 2009.
- [5] D. Caissie, S. Jolicoeur, M. Bouchard, and E. Poncet, "Comparison of streamflow between pre and post timber harvesting in Catamaran Brook (Canada)," *Journal of Hydrology*, vol. 258, no. 1-4, pp. 232-248, 2002.
- [6] M. Lavigne, A. N. Rousseau, R. Turcotte, A.-M. Laroche, J.-P. Fortin, and J.-P. Villeneuve, "Validation and use of a semidistributed hydrological modelling system to predict short-term effects of clear-cutting on a watershed hydrological regime," *Earth Interactions*, vol. 8, no. 3, pp. 1-19, 2004.

- [7] M. Muma, A. A. Assani, R. Landry, J. Quessy, and M. Mesfioui, "Effects of the change from forest to agriculture land use on the spatial variability of summer extreme daily flow characteristics in southern Quebec (Canada)," *Journal of Hydrology*, vol. 407, pp. 153–163, 2011.
- [8] R. Quilbé, A. N. Rousseau, J. Moquet, S. Savary, S. Ricard, and M. S. Garbouj, "Hydrological responses of a watershed to historical land use evolution and future land use scenarios under climate change conditions," *Hydrology and Earth System Sciences*, vol. 12, no. 1, pp. 101–110, 2008.
- [9] C. Fortier, A. A. Assani, M. Mesfioui, and A. G. Roy, "Comparison of the interannual and interdecadal variability of heavy flood characteristics upstream and downstream from dams in inverted hydrologic regime: case study of Matawin River (Québec, Canada)," *River Research and Applications*, vol. 27, no. 10, pp. 1277–1289, 2011.
- [10] Environment Canada Web Page, Données Hydrométriques, 2014, <http://climat.meteo.gc.ca/advanceSearch/searchHistoricData.f.html?>
- [11] A. A. Assani, S. Charron, M. Matteau, M. Mesfioui, and J.-F. Quessy, "Temporal variability modes of floods for catchments in the St. Lawrence watershed (Quebec, Canada)," *Journal of Hydrology*, vol. 385, no. 1–4, pp. 292–299, 2010.
- [12] R. Mazouz, A. A. Assani, J. Quessy, and G. Légaré, "Comparison of the interannual variability of spring heavy floods characteristics of tributaries of the St. Lawrence River in Quebec (Canada)," *Advances in Water Resources*, vol. 35, pp. 110–120, 2012.
- [13] F. Lombard, "Rank tests for changepoint problems," *Biometrika*, vol. 74, no. 3, pp. 615–624, 1987.
- [14] J.-F. Quessy, A.-C. Favre, M. Saïd, and M. Champagne, "Statistical inference in Lombard's smooth-change model," *Environmetrics*, vol. 22, no. 7, pp. 882–893, 2011.
- [15] A. Yagouti, G. Boulet, L. Vincent, L. Vescovi, and É. Mekis, "Observed changes in daily temperature and precipitation indices for southern Québec, 1960–2005," *Atmosphere-Ocean*, vol. 46, no. 2, pp. 243–256, 2008.
- [16] N. Guerfi, A. A. Assani, M. Mesfioui, and C. Kinnard, "Comparison of the temporal variability of winter daily extreme temperatures and precipitations in southern Quebec (Canada) using the Lombard and copula methods," *International Journal of Climatology*, 2015.
- [17] R. D. Brown, "Analysis of snow cover variability and change in Québec, 1948–2005," *Hydrological Processes*, vol. 28, pp. 4011–4022, 2010.

Review Article

Predicting Surface Runoff from Catchment to Large Region

Hongxia Li,¹ Yongqiang Zhang,² and Xinyao Zhou³

¹State Key Laboratory of Hydraulics and Mountain River Engineering, Sichuan University, Chengdu 610065, China

²CSIRO Land Water Flagship, Clunies Ross Street, Acton, Canberra, ACT 2601, Australia

³Key Laboratory of Agricultural Water Resources, Center for Agricultural Resources Research, Chinese Academy of Sciences, Shijiazhuang 050021, China

Correspondence should be addressed to Yongqiang Zhang; yongqiang.zhang@csiro.au

Received 5 January 2015; Accepted 7 June 2015

Academic Editor: Enrico Ferrero

Copyright © 2015 Hongxia Li et al. This is an open access article distributed under the Creative Commons Attribution License, which permits unrestricted use, distribution, and reproduction in any medium, provided the original work is properly cited.

Predicting surface runoff from catchment to large region is a fundamental and challenging task in hydrology. This paper presents a comprehensive review for various studies conducted for improving runoff predictions from catchment to large region in the last several decades. This review summarizes the well-established methods and discusses some promising approaches from the following four research fields: (1) modeling catchment, regional and global runoff using lumped conceptual rainfall-runoff models, distributed hydrological models, and land surface models, (2) parameterizing hydrological models in ungauged catchments, (3) improving hydrological model structure, and (4) using new remote sensing precipitation data.

1. Introduction

Runoff from land surface is the flow of water that comes from excess water from rain, meltwater, or other sources that flow over the Earth's surface. It is a major component in regional and global hydrological cycle. It has direct impacts on human lives since it is a key water resource for agriculture, industry, urban water use, and so forth. It is crucial to understand complex relationships between rainfall and runoff processes and then to accurately estimate surface runoff for efficient design, planning, and management of catchments. This can be achieved using hydrological modeling that not only estimates continuous surface runoff, but also helps in understanding catchment behaviors and modeling impacts of climate and land use changes on surface water balance [1, 2].

Model calibration is a necessary step for achieving good simulations and predictions of surface runoff. Hydrological models are usually calibrated against observed streamflow to tune their model parameters to account for the inputs and water fluxes in a catchment [3, 4]. With the development of remote sensing technology, more information is now available for hydrological modeling, for example, using

remote sensing precipitation and leaf area index as model inputs [5, 6], and incorporating more data (such as remote sensing soil moisture, evapotranspiration, groundwater, and snow cover area) for multiple objective model calibration [4, 7–9].

Local hydrological models have been largely used to predict runoff time series using a small number of catchments that covers a small region where climate conditions are similar [10, 11]. Recently, they were used to predict surface runoff in ungauged catchments in a large region, such as in southeastern Australia [12], the Tibetan Plateau [13], UK [14], and France [15]. This is important since lots of rivers and their reaches and tributaries in the world are ungauged or poorly gauged [14, 16, 17].

It is a hard task to have a credible prediction of surface runoff in ungauged catchments or regions where no runoff data are available or runoff data are available sparsely. Hydrologists have been attempting to develop strategies to estimate runoff on ungauged catchments since the 1970s, especially after the International Association of Hydrological Sciences (IAHS) launched an initiative Predictions in Ungauged Basins (PUB) in 2003, which aims at predicting or forecasting the hydrological responses in ungauged or poorly gauged

basins and their associated uncertainty [17]. Since then, many approaches have been developed for estimating surface runoff in ungauged basins [18], such as regionalization [15, 19, 20], and regional calibration against observations from multiple catchments [21, 22].

Predicting surface runoff using catchment, regional and global runoff models has achieved numerous outcomes, but there are still lots of issues that lead to unsatisfactory performances. This paper presents a comprehensive review of predicting surface runoff from catchments to large regions, which is a fundamental and challenging task in hydrology. This includes review and discussions in (1) hydrological models, (2) parameterization, (3) improvement of hydrological model structure, and (4) use of new forcing data.

2. Catchment, Regional and Global Runoff Models

There exist various models to simulate surface runoff in an empirical, semimechanistic or fully mechanistic way. Generally, surface runoff models are classified from deterministic to stochastic models, from physically based (white-box) to black-box or empirical and to conceptual models, from lumped to distributed models, and from global hydrological to land surface models (LSMs) [39, 73–75]. This paper separates the hydrological models into three categories according to complexity and application, including (1) lumped conceptual rainfall-runoff (RR) models, (2) distributed hydrological models, and (3) global hydrological/LSMs [73, 76]. The first two categories of the hydrological models are normally applied from catchments to regions and the third category of the hydrological models is generally applied from a large region to the global land surface. Table 1 summarizes the three categories of major hydrological models for runoff estimations/predictions across a wide range of climate and physiographic conditions.

2.1. Lumped Conceptual Rainfall-Runoff Models. Lumped conceptual RR models treat a catchment as a single homogeneous unit, and they are widely used since such models tend to be parametrically parsimonious while yielding good model performance after calibration using historical watershed input-output data [77].

Numerous RR models have been developed and documented [78, 79]. Crawford and Linsley’s Stanford Watershed Model was one of the notably successful efforts in introducing a complex RR model accounting for the dynamics of hydrologic processes governing in a watershed [32]. Other examples of conceptual RR models include Xinanjiang model developed in China in the 1980s [34] and Sacramento Soil Moisture Accounting Model (SAC-SMA) [30], widely used operational model in the US National Weather Service (NWS) for flood forecasting.

RR models have been used very successfully to estimate runoff at small and large catchments under different climate regimes. Usually, RR models use rainfall and other climate data (e.g., temperature and/or potential evaporation) to estimate runoff. Although the main emphasis of RR

TABLE 1: Major catchment, regional and global runoff models.

Model type	Model	Country	Reference
Lumped model	AWBM	Australia	[23]
	GR4J	Australia	[24]
	HBV	Sweden	[25]
	HEC	USA	[26]
	HSPF	USA	[27]
	HYDROLOG	Australia	[28]
	IHACRES	Australia	[29]
	Sacramento	USA	[30]
	SIMHYD	Australia	[31]
	SWM	USA	[32]
Tank	Japan	[33]	
Xinjiang	China	[34]	
SRM	Nordic	[35]	
Physical model	CEQUEAU	Canada	[36]
	HYDROTEL	USA	[37]
	IHDM	USA	[38]
	MIKE-SHE	Denmark	[39]
	SHE	Denmark	[40]
	SLURP	UK	[41]
	SWAT	USA	[42]
	SWMM	USA	[43]
	TOPMODEL	UK	[44]
	WATELOOD	Canada	[45]
Global hydrological/land surface model	BUCKET	Japan	[46]
	CABLE	Australia	[47]
	BATS	USA	[48]
	CLM	USA	[49]
	CLM TOP	USA	[50]
	COLASSIB	USA	[51]
	GWAVA	USA	[52]
	H08	USA	[53]
	HTESSEL	USA	[54]
	HYSSIB	USA	[55]
	ISBA	France	[56]
	JULES	UK	[57]
	LaD	USA	[58]
	LPJmL	USA	[59]
	MacPDM	USA	[60]
	MATSIRO	USA	[61]
	Mosaic	USA	[62]
	MOSES2	UK	[57]
	MPI-HM	USA	[63]
	Noah	USA	[64]
NSIPP	USA	[65]	
Orchidee	USA	[66]	
SiBUC	Japan	[67]	
SWAP	Russia	[68]	
SiB	USA	[69]	
VIC	USA	[70]	
VISA	USA	[71]	
WaterGAP	USA	[72]	

models is to estimate runoff, they are normally designed to simulate actual evapotranspiration to account for soil

water balance. However, they have no direct interest in quantifying surface energy fluxes [76]. The parameters in the RR models are usually optimized such that the runoff simulated matches as closely as possible the recorded runoff. A variety of model calibration techniques (including manual calibration and automatic calibration techniques) have been developed and implemented to ensure conformity between the model simulations of system behavior and observations [3, 80].

Compared to the distributed hydrological models, the RR models are simpler and need less input data, and the calibration cost is cheap, so they are quite easy to be used and are important tools for hydrologic analysis. More importantly, the RR models are comparable to the distributed hydrological models, in terms of model accuracy for predicting daily, monthly, and annual runoff time series. For instance, Vansteenkiste et al. [81] compared three RR models (NAM, PDM, and VHM) to two distributed models (WetSpa and MIKE-SHE) in a medium sized catchment in Belgium to assess the model accuracy. They found that all tested models perform well for estimating total runoff and their components, peak and low flow extremes. However, calibrating the RR models is much less time consuming and produced higher overall model performance in comparison to the two distributed models. Reed et al. [82] compared 12 distributed models with a lumped model, and the results show that the lumped model outperformed distributed models in more cases, while some calibrated distributed models can perform at a level comparable to or better than a calibrated lumped model. The limit of the RR models is that they cannot simulate the spatial pattern change in land cover and land use influencing surface water availability.

The RR models are normally applied at catchment scales. Hydrologic prediction of the RR models is highly influenced by the uncertainties in the forcing data (generally taken as deterministic), observed system response (due to errors in measuring the physical quantities), imperfection of the model structure, and the parameter values resulting from the model calibration which is profoundly affected by uncertainty sources [3].

In summary, the RR models are still very important tools in hydrological modeling, particularly for predicting runoff in ungauged catchments because of their simplicity and usability.

2.2. Distributed Hydrological Models. Distributed hydrological models make a series of hydrological processes interconnected, such as runoff generation, recharge to groundwater, snow accumulation and melt, soil moisture dynamics, evapotranspiration, and routing in lakes and rivers [10]. In addition, distributed hydrological models take account of the spatial variability of climate, terrain, soil, and vegetation. These elements are divided in smaller units that are more homogenous than the whole watershed. Therefore, this feature offers the potential to improve hydrologic predictions [83]. The distributed hydrological model can be directly used for estimating land use and land cover change impact on surface runoff and water availability [1, 2]. This is particularly

important for catchments with a wide range of climatic and land surface conditions.

The distributed hydrological models have been well developed since the 1970s because of the robust development of 3S (RS/GPS/GIS) technology. A representative semidistributed hydrological model is the topography-based hydrological model named as TOPMODEL that was developed in 1979. It describes runoff generation process including both saturation excess and infiltration excess runoff according to topographic index derived from digital elevation model (DEM) [44]. The spatial variability of precipitation, however, is not considered by TOPMODEL. After TOPMODEL, distributed hydrological models such as SHE (System Hydrologic European) [40] and SWAT (Soil and Water Assessment Tool) [42] are fully distributed and contain more complex hydrological processes.

Although the distributed hydrological models have more solid physical base compared to the lumped models, several model comparison studies [74, 75, 82, 84, 85] have shown that no single model performs consistently best but rather that individual model performances vary with the setting. So selecting models depends on objectives, application, and availability of data.

Despite their complexity, the distributed hydrological models are very useful for investigating changes in hydrological processes caused by anthropogenic activities, such as forestation, deforestation, and urbanization.

2.3. Global Hydrological and Land Surface Models. The hydrological models presented in Sections 2.1 and 2.2 are normally applied to a catchment to regional scale. At a larger scale from a large region to globe, global hydrological and LSMs (Table 1) are developed for simulating/predicting surface runoff. It is noted that global hydrological models are traditionally focused on water resources and lateral water fluxes while LSMs can be coupled to global climate models, to describe the vertical exchange of heat, water, carbon, or other elements. Based on the spatial application, this review paper does not separate the two kinds of models, naming them “global LSMs” on a whole.

Compared to the lumped RR and distributed hydrological models, the global LSMs are far more complicated since they can simulate not only hydrological processes, but also various material and energy transfer processes on land surface [86]. These processes include precipitation interception, snow accumulation and melt, runoff generation, water transfer amongst soil layers, shortwave radiation's reflection and transmission, longwave radiation's absorption and emission, separation of sensible heat and latent heat, plant growth and respiration, photosynthesis and gross primary production, microbe activities, and nutrient cycle.

The first-generation LSMs such as Bucket model [87] do not consider vegetation and include only one soil layer. The second-generation LSMs such as BATS [48] and SiB [69] contain “big-leaf” vegetation and 2-3 soil layers. The third-generation LSMs such as CLM [49] contain “two-leaf” vegetation and multilayer soil layer for hydrological

processes. Some widely used land surface models are listed in Table 1.

Surface runoff process is considered quite differently between distributed hydrological models and global land surface models. Surface runoff is a key output in lumped RR and distributed hydrological models, while it is taken as residue of water balance equation in global LSMs. Because of the accumulated errors built in land surface models, they perform generally more poorly than distributed hydrological models [88–90]. Gosling et al. [91] compared the projected impacts of climate change on river runoff from two types of distributed hydrological models, a global hydrological model (GHM) and catchment-scale hydrological models (CHMs). Results show that there are differences between GHMs and CHMs in mean annual runoff due to differences in potential evapotranspiration estimation methods, and the differences in projected changes of mean annual runoff between the two types of hydrological model can be substantial for a given GCM. Haddeland et al. [74] compared six land surface models and five global hydrological models and results show that significant simulation differences between models are found to be caused by the snow scheme employed, and differences between models are a major source of uncertainty.

The main strength of global hydrological and land surface models is that they can be used for answering the regional and global questions for water availability and changes in global hydrological cycles [74].

3. Parameterization of Hydrological Models in Ungauged Catchments

3.1. Regionalization. There are no observations or lack of observations in ungauged catchments. Therefore to predict surface runoff in the ungauged catchments depends on alternative prediction methods [17]. Regionalization is a commonly used method for runoff predictions [15, 92], in which model parameters calibrated from gauged catchments are transferred to ungauged catchments using various approaches. It is a challenge to get satisfactory regionalization results [15, 17, 93, 94] because of limit of dataset, a wide range of catchment attributes, poor quality of model inputs, unsatisfactory model calibrations, and so on [15, 17].

The regionalization is mainly conducted with hydrological models, although it can be achieved using model-independent methods (e.g., Artificial Neural Network) [20, 95]. The popular regionalization approaches that extrapolate hydrologic model parameters to estimate streamflow at ungauged catchments can be grouped into (a) arithmetic mean method (AM) [15, 19]; (b) spatial proximity approach (SP) (spatial distance) [96, 97]; (c) physical similarity approach (PS) [93, 98, 99]; (d) regression method (Reg) [14]; and (e) hydrological similarity approach (HS) [100].

All these regionalization methods have been applied in many catchments, and many attempts have been made to determine which regionalization approach was the most appropriate (Table 2). Merz and Blöschl [19] tried to regionalize an 11-parameter semidistributed conceptual RR model

based on more than 300 Austrian catchments. It shows that spatial proximity performs best, and using nested catchments as donors may significantly improve performance of spatial proximity. Young [14] tried to regionalize a six-parameter version of the PDM model on 260 UK catchments and found that regression approach yielded the best results, compared to other approaches. Oudin et al. [15] compared three regionalization schemes (SP, PS, and Reg) based on 913 French catchments using two lumped models and found that spatial proximity provides the best regionalization solution. Li et al. [101] proposed a new regionalization method (the index model), which establishes a nonparametric relationship between each parameter of predictive tools and a linear combination of predictors. The prediction results of 227 catchments in southeast Australia show that the index model produces the most accurate prediction compared to regional models based on the linear regression, nearest neighbor, and hydrological similarity. Shu and Ouarda [102] introduced a regression-based logarithmic interpolation method to estimate regional FDCs at ungauged sites, and the estimated FDC is combined with a spatial interpolation algorithm to obtain daily streamflow estimates. McIntyre et al. [103] and Oudin et al. [15] showed that output averaging (the target catchment is modeled using parameter values from many donor catchments) can reduce uncertainty in runoff predictions in ungauged catchments. Similarly, Reichl et al. [98] showed that flow prediction using an optimized model averaging method (based on physical similarities) is superior to regression and spatial proximity approaches.

In summary, the studies carried out in most countries, such as Austria, France, and Australia, found that SP is better than PS and Reg is the least satisfactory. This is also confirmed in the highest plateau, the Tibetan Plateau [105]. Only in UK did the studies find that Reg performs better than SP or PS.

There are various reasons explaining the different model performance between the abovementioned studies, including using different catchment sets, different catchment descriptors, and different hydrological models [14, 15]. This suggests that each regionalization approach does not always perform consistently. Razavi and Coulibaly [20] found that the performance of regionalization approaches is climate related, and overall spatial proximity and physical similarity have shown satisfactory performance in arid to warm temperate climates (e.g., Australia) and regression-based methods have been preferred in warm temperate regions (e.g., most European countries). To fully understand the performance of the various regionalization approaches, it is critical to have global comparison studies. However, such studies have not been reported yet.

3.2. Multiple Objective Model Calibration. It was recognized early [80, 107] that models calibrated only to observed hydrographs can be considered overparameterized if they consist of more than five parameters [29], because the predictive capability of hydrological models would be limited by high model complexity relative to the typically low number of model constraints used to calibrate the models

TABLE 2: Summary of regionalization approaches conducted using large datasets.

Method	Comparing	Model	Region/country	References
AM Reg	Average of nested neighbors is better than Reg (global or regional)	HBV	308 catchments in Austria	[19]
PS Reg	Output averaging based on PS is better than Reg	PDM	127 catchments in UK	[103]
AM SP PS Reg	SP (Kriging) and PS perform best; all regionalization methods perform similarly in simulating snow cover	HBV	320 catchments in Austria	[96]
PS Reg	For PDM, PS performs slightly better than the Reg, whereas for TATE Reg performs best	PDM TATE	119 catchments in the UK	[104]
Reg PS	The regression-based approach is better than the nearest neighbor based approach	PDM	260 catchments in UK	[14]
SP PS Reg	SP is the best, Reg is the least satisfactory, and PS is intermediary	GR4J, TOPMO	913 catchments in France	[15]
SP PS	SP is better than PS	Xinanjia	210 catchments in southeast Australia	[97]
SP PS Reg	An optimized averaging method (based on PS) is superior to Reg and SP approaches	SIMHYD	184 catchments in Australia	[98]
SP PS	SP performs slightly better than PS and the integrated similarity approach performs only very marginally better than SP	Xinanjia SIMHYD	210 catchments in southeast Australia	[12]
SP PS Reg HS	The index model that establishes relationships between hydrological signatures and catchment attributes is the best, followed by Reg, HS, and SP	Three- parameter FDC	227 catchments in southeast Australia	[101]
HS	HS based on FDC produces better runoff simulation compared to the others (drainage area and spatial proximity)	HBV	Karkheh river basin, western part of Iran	[100]
SP PS Reg	An approach coupling the SP (IDW) and the PS is better than SP, PS, and Reg	MAC-HBV	The main watersheds across the province of Ontario	[93]
SP PS	SP is better than PS	SIMHYD and GR4J	8 catchments in the southeastern Tibetan Plateau	[105]
SP Reg	An index model that establishes relationships between hydrological signatures and catchment attributes is better than SP for getting salient flow characteristics	An index model and GR4J	228 catchments in southeast Australia	[106]

AM: arithmetic mean method; SP: spatial proximity method; PS: physical similarity method; Reg: regression methods; HS: hydrological similarity method.

[108]. An important strategy to overcome this problem was the incorporation of more information (such as different aspects of the hydrograph, soil moisture, evapotranspiration, groundwater, and snow depth) for multiple objective model calibration.

Madsen [7] used a calibration scheme including optimization of multiple objectives that measure different aspects of the hydrograph (overall water balance, overall shape of the hydrograph, peak flows, and low flows). Seibert and McDonnell [109] reported that the inclusion of groundwater dynamics results in significantly improved and more consistent overall model performances. Nester et al. [110] demonstrated the value of remotely sensed snow cover patterns to constrain parameter uncertainty of catchment models.

Others used remotely sensed soil moisture and evaporation, respectively, to improve model parameterizations [111–113]. Zhang et al. [114] showed that the incorporation of remotely sensed leaf area index and surface soil moisture measurements into the calibration objective function marginally improves the daily runoff estimates but noticeably improves the leaf area index and soil moisture estimates in the validation catchments. Zhang et al. [4] used remotely sensed evapotranspiration estimates together with recorded streamflow to constrain rainfall-runoff model calibration and then used optimized parameter sets for runoff predictions. They found that the use of remotely sensed evapotranspiration data in calibration leads to improved daily or monthly runoff predictions in ungauged catchments. However, Willem Vervoort et

al. [9] show that satellite evapotranspiration did not improve the calibration results of the lumped conceptual model and confirm that the calibration of models using multiple environmental time series (such as MODIS evapotranspiration and streamflow) can be used to identify structural model issues.

3.3. Regional Calibration against Observations from Multiple Catchments. Regional model calibration is defined here as model calibration simultaneously against observations in multiple catchments (from dozens to hundreds) across a wide region to obtain a single parameter set for all catchments. In contrast, local model calibration is referred to as the calibration against observations in a single catchment.

The major advantage of the local model calibration is that an optimum parameter set can be obtained for each individual catchment and will match the local data most accurately. However, the locally optimized parameter values are not always suitable for runoff predictions because gauging stations can be few and far apart, resulting in that the underlying assumption that nearby catchments have similar responses can be problematic. Furthermore, observational errors (e.g., in streamflow gauging and rainfall inputs) can cause the local calibration to be biased, with biased model parameters being regionalized.

The main benefit of regional model calibration is that (1) use of one set of optimized parameter values (or perhaps several sets if different objective functions are considered or if a research region is divided into different subregions) can improve hydrological and vegetation estimates at the regional scale and (2) there is no noticeable degradation from model calibration to model validation. The disadvantage of regional calibration is that it requires lots of computation resources and it is normally conducted using super computer clusters.

Previous studies showed that regional calibration could improve the accuracy of simulated runoff in ungauged regions and has been used in runoff simulation and prediction [21, 115]. Regional calibration would be an important research field of large-scale hydrological simulation and predictions and will be strengthened with the computational development.

4. Improving Hydrological Model Structure

The model structure represents a formalized perception of how the catchment system is organized and how the various parts are interconnected [138]. Selection of a suitable model structure ideally depends on a number of factors as one strives to represent the runoff processes in a realistic way, so that the model can be safely used in a predictive mode. However, there is still some room for further improving model structures.

4.1. Modifying RR Model Structure. Usually, RR models use simply conceptual equations to simulate evapotranspiration based on soil wetness and potential evapotranspiration

(calculated from basic climate data) and seldom consider vegetation dynamics, which can play an important role in midlatitude catchments [11, 139, 140]. Because of lack of surface vegetation information in RR modeling inputs, calibrated RR models may not estimate water balance components, evapotranspiration, and water storage change accurately, which possibly limits their ability to estimate runoff.

Remotely sensed data can provide temporally dynamic and spatially explicit information on land surface characteristics such as vegetation cover types and leaf area index. Vegetation processes play an important role in evapotranspiration and runoff in midlatitude catchments [140, 141]. Yildiz and Barros [140] showed that vegetation properties such as fractional vegetation coverage and leaf area index (LAI) had significant effects on hydrological model results via control of evapotranspiration rates, and this control was especially critical during the spring-summer transition which coincided with the greening season in midlatitudes.

A suitable way to integrate vegetation process data into hydrological models is to use remote sensing vegetation data, such as LAI and fractional vegetation cover [142–144]. Recent studies have tried to include remote sensing vegetation information as inputs into RR models. Reference [97] used MODIS LAI data combined with the Penman-Monteith equation in the lumped Xinjiang model, and results showed that it can improve the prediction of runoff in ungauged basin. Oudin et al. [145] modified the water balance models to introduce the fractional coverage of land cover types and results showed that land cover information improves the overall model efficiency.

4.2. Improving Distributed Hydrological, Land Surface Model Structure. Appropriate land surface parameterization is based on comprehensive understanding to land surface processes and thus could improve performance of physically based models. For instance, Liang and Xie [146] used a new surface runoff parameterization which takes into account effects of soil heterogeneity on Horton and Dunne runoff to replace the old parameterization in VIC model. Results showed that the new parameterization plays a very important role in partitioning the water budget between surface runoff and soil moisture. Pitman et al. [147] compared the accuracy of estimated runoff in the region that ranged from 30 N to 90 N by BASE model with and without frozen soil parameterization. Results proved that frozen soil parameterization greatly influenced runoff generation with less runoff variability. Haverd and Cuntz [148] found that soil litter is important for simulation of soil moisture and evapotranspiration in forest region. When coupled with a soil litter model, the accuracy of CABLE has been greatly improved for estimating soil moisture and evapotranspiration in a forest flux site in Australia. Choi and Liang [149] detected several deficiencies in the existing formulations for terrestrial hydrologic processes in CLM and improved model performance for predicting runoff by five modifications of its parameterization. In summary, there is plenty of room

TABLE 3: Summary of precipitation datasets.

Name	Source	Domain	Period of record	Available timestep(s)	Available resolution	References
APHRODITE	U. of Tsukuba and JMA	Asia	1951–2007	Daily	$0.25 \times 0.25, 0.5 \times 0.5;$ 0.05×0.05 (Japan only)	[116]
CHOMPS	CICS	Global	1998–2007	Daily	0.25×0.25	[117]
GSWP-2	GEWEX	Global	1986–1995	Subdaily	1×1	[118]
WFD	EU-FP6	Global	1901–2001	Subdaily	0.5×0.5	[119]
WFDEI	EU-FP6	Global	1979–2012	Subdaily, daily	0.5×0.5	[120]
CMAP	NOAA CPC	Global	1979–2011	Monthly, pentad	2.5×2.5	[121]
CMORPH	CPC	Global	2002–2013	Subdaily, daily	0.25×0.25	[122]
CRU	CRU	Global	1901–2013	Monthly	0.5×0.5	[123]
Daymet	U. of Montana	North America	1980–2013	Daily	$1 \text{ km} \times 1 \text{ km}$	[124]
Global (land) precipitation and temperature	U. of Delaware	Global	1900–2010	Monthly	0.5×0.5	[125]
GPCC	DWD	Global	1900–2010	Monthly	$0.5 \times 0.5, 1 \times 1,$ 2.5×2.5	[126]
Princeton	Princeton University	Global	1948–2008	Subdaily	1×1	[127]
GPCP	GSFC (NASA)	Global	1979–2014	Monthly	2.5×2.5	[128]
HOAPS	CM SAF and Uni. of Hamburg	Global	1987–2008	Subdaily, monthly	0.5×0.5	[129]
COREV2	NCAR	Global	1949–2006	Subdaily, daily, monthly	1×1	[130]
NLDAS	NASA, NOAA, Princeton, U. of Washington	North America	1979–2014	Hourly	0.125×0.125	[131]
GLDAS	NASA, NOAA	Global	1948–2014	Subdaily, monthly	$0.25 \times 0.25, 1 \times 1$	[132]
PERSIANN	CHRS	Global	1979–2014	Subdaily, monthly	0.25×0.25	[133]
PREC/L	NOAA	Global	1948–2014	Monthly	$2.5 \times 2.5, 1 \times 1,$ 0.5×0.5	[134]
PRISM	Oregon State University	North America	1895–2014	Daily, monthly	$4 \text{ km}, 800 \text{ m}$	[135]
SSM/I, SSMIS	NASA	Global	1987–2012	Daily, monthly, weekly	0.25×0.25	[136]
TRMM	NASA and JAXA	Tropics	1998–2014	Subdaily, daily, monthly	0.25×0.25	[137]

APHRODITE: Asian Precipitation—Highly Resolved Observational Data Integration Towards Evaluation of Water Resources; JMA: Japan Meteorological Agency; CHOMPS: CICS High-Resolution Optimally Interpolated Microwave Precipitation from Satellites; CICS: Cooperative Institute for Climate Studies; GSWP: Global Soil Wetness Project; GEWEX: Global Energy and Water Cycle Experiment; NASA: National Aeronautics and Space Administration; NOAA: National Oceanic and Atmospheric Administration; WFD: WATCH Forcing Data; EU-FP6: European Union Sixth Framework Programme; WFDEI: WATCH Forcing Data methodology applied to ERA-Interim reanalysis data; CMAP: CPC Merged Analysis of Precipitation; CPC: Climate Prediction Center; CMORPH: CPC MORPHing technique high resolution precipitation ($60\text{S}-60\text{N}$); CRU: Climatic Research Unit; Daymet: Daily Surface Weather and Climatological Summaries; GPCC: Global Precipitation Climatology Centre; DWD: German Weather Service; GPCP: Global Precipitation Climatology Project; HOAPS: Hamburg Ocean Atmosphere Parameters and Fluxes from Satellite Data; CM SAF: Satellite Application Facility on Climate Monitoring; COREV2: Common Ocean Reference Experiment Version 2: Large-Yeager Air-Sea Surface Flux; NCAR: National Center for Atmospheric Research; NLDAS: North American Land Data Assimilation System; GLDAS: Global Land Data Assimilation System; PERSIANN: Precipitation Estimation from Remotely Sensed Information using Artificial Neural Networks; CHRS: Center for Hydrometeorology and Remote Sensing; PRISM: Parameter-Elevation Relationships on Independent Slopes Model; PREC/L: NOAA's Precipitation Reconstruction Land; SSM/I, SSMIS: Special Sensor Microwave/Imager and Sounder; TRMM: Tropical Rainfall Measuring Mission; JAXA: Japan Aerospace Exploration Agency.

to improve global land surface model structure for better estimation of runoff from large region to global land surface.

5. Improving Precipitation Inputs

High quality daily precipitation estimates are required for accurate hydrological modeling. There are two major sources to estimate precipitation fields: rain gauge stations and remote sensing devices (such as satellites and radar). The observations obtained from rain gauges are considered to be more accurate and reliable, but the spatial coverage is unsatisfactory. Hence, the areal precipitation estimates constructed solely by rain gauges exhibit a great deal of uncertainty especially in the areas of low rain gauge density. Remote sensing gridded precipitation estimates are presented in a good coverage in space/time and with less uncertainty [150, 151]. However, the coverage of weather radar network is currently limited to some areas in the world. So, with the advent of meteorological satellites in the 1970s, great efforts have been directed to estimating precipitation from satellite images (e.g., TRMM, TMPA, CMORPH, and GSMAP), which cover most of the globe (Table 3).

However, the accuracy of remote sensing satellites precipitation may not be desirable and the estimation of precipitation can be improved by blending rain gauge and satellite data [151]. Several statistical merging schemes have been developed for experimental or/and operational use, such as conditional merging [152], Bayesian merging [153], statistical objective analysis [154], data assimilation [137, 155], and double/single optimal estimation [156].

Gottschalck et al. [157] showed that the Climate Prediction Center (CPC) Merged Analysis of Precipitation (CMAP) has the closest agreement with a CPC rain gauge dataset for all seasons except winter, while TRMM overestimated summertime precipitation in the central United States (200–400 mm). Chappell et al. [158] evaluated geostatistical methods of blending satellite and gauge data to estimate near real-time daily rainfall for Australia and results showed that the blending considerably reduced the estimation variance. Mitra et al. [159] showed that TRMM merged with gauged station data can significantly improve the estimation of spatial distribution of precipitation of the Indian monsoon region. Ryo et al. [160] showed that the blended precipitation data can improve the hydrological modeling especially the flood modeling in Vietnam.

6. Summary

This paper provides a comprehensive review of catchment, regional and global runoff modeling. Continuous surface runoff modeling can be carried out through conceptual rainfall-runoff models, distributed models, and land surface models. Parameterization of hydrological models in ungauged catchments can be done by regionalization, multiple objective model calibration, and regional calibration against observations from multiple catchments. The models can be further improved by incorporating remote sensing vegetation data and remote sensing precipitation data.

There is still considerable room to improve surface runoff prediction from catchments to large regions. In a large region, improving regionalization performance can be attributed to improved catchment characteristics, ensemble of different regionalization approaches, multiple-donor output averaging, or model ensemble, and so forth. Special attention should be paid to use of remote sensing data for multiple objective model calibration and to improving hydrological model structure using remote sensing data since they have great advantages in ungauged catchments or data sparse regions. How to smartly parameterize global land surface models or smartly modify their structure for improving runoff predictions from large regions to globe will be a great challenge for hydrologists and meteorologists in the next couple of decades.

Conflict of Interests

The authors declare that there is no conflict of interests regarding the publication of this paper.

Acknowledgments

This research was supported by the National Natural Science Foundation of China (no. 51209152), the Open Fund (SKHL1406) supported by the State Key Laboratory of Hydraulics and Mountain River Engineering, and the CSIRO strategic project (R-7197-1) on global hydrology study.

References

- [1] H. Li, Y. Zhang, J. Vaze, and B. Wang, "Separating effects of vegetation change and climate variability using hydrological modelling and sensitivity-based approaches," *Journal of Hydrology*, vol. 420-421, pp. 403-418, 2012.
- [2] F. Zhao, F. H. S. Chiew, L. Zhang, J. Vaze, J. M. Perraud, and M. Li, "Application of a macroscale hydrologic model to estimate streamflow across Southeast Australia," *Journal of Hydrometeorology*, vol. 13, no. 4, pp. 1233-1250, 2012.
- [3] S. Sorooshian and V. Gupta, "Effective and efficient global optimization for conceptual rainfall-runoff models," *Water Resources Research*, vol. 28, no. 4, pp. 1015-1031, 1992.
- [4] Y. Zhang, F. H. S. Chiew, L. Zhang, and H. Li, "Use of remotely sensed actual evapotranspiration to improve rainfall-runoff modeling in Southeast Australia," *Journal of Hydrometeorology*, vol. 10, no. 4, pp. 969-980, 2009.
- [5] J. Andersen, G. Dybkjaer, K. H. Jensen, J. C. Refsgaard, and K. Rasmussen, "Use of remotely sensed precipitation and leaf area index in a distributed hydrological model," *Journal of Hydrology*, vol. 264, no. 1-4, pp. 34-50, 2002.
- [6] M. Li and Q. Shao, "An improved statistical approach to merge satellite rainfall estimates and raingauge data," *Journal of Hydrology*, vol. 385, no. 1-4, pp. 51-64, 2010.
- [7] H. Madsen, "Automatic calibration of a conceptual rainfall-runoff model using multiple objectives," *Journal of Hydrology*, vol. 235, no. 3-4, pp. 276-288, 2000.
- [8] J. A. Vrugt, H. V. Gupta, L. A. Bastidas, W. Bouten, and S. Sorooshian, "Effective and efficient algorithm for multiobjective optimization of hydrologic models," *Water Resources Research*, vol. 39, no. 8, p. 1214, 2003.

- [9] R. Willem Vervoort, S. F. Miechels, F. F. van Ogtrop, and J. H. Guillaume, "Remotely sensed evapotranspiration to calibrate a lumped conceptual model: pitfalls and opportunities," *Journal of Hydrology*, vol. 519, pp. 3223–3236, 2014.
- [10] A. Abu El-Nasr, J. G. Arnold, J. Feyen, and J. Berlamont, "Modelling the hydrology of a catchment using a distributed and a semi-distributed model," *Hydrological Processes*, vol. 19, no. 3, pp. 573–587, 2005.
- [11] M. Huang and L. Zhang, "Hydrological responses to conservation practices in a catchment of the Loess Plateau, China," *Hydrological Processes*, vol. 18, no. 10, pp. 1885–1898, 2004.
- [12] Y. Zhang and F. H. S. Chiew, "Relative merits of different methods for runoff predictions in ungauged catchments," *Water Resources Research*, vol. 45, no. 7, Article ID W07412, 2009.
- [13] F. Li, Y. Zhang, Z. Xu et al., "The impact of climate change on runoff in the southeastern Tibetan Plateau," *Journal of Hydrology*, vol. 505, pp. 188–201, 2013.
- [14] A. R. Young, "Stream flow simulation within UK ungauged catchments using a daily rainfall-runoff model," *Journal of Hydrology*, vol. 320, no. 1-2, pp. 155–172, 2006.
- [15] L. Oudin, V. Andréassian, C. Perrin, C. Michel, and N. Le Moine, "Spatial proximity, physical similarity, regression and ungauged catchments: a comparison of regionalization approaches based on 913 French catchments," *Water Resources Research*, vol. 44, no. 3, Article ID W03413, 2008.
- [16] A. K. Mishra and P. Coulibaly, "Developments in hydrometric network design: a review," *Reviews of Geophysics*, vol. 47, no. 2, Article ID RG2001, 2009.
- [17] M. Sivapalan, "Prediction in ungauged basins: a grand challenge for theoretical hydrology," *Hydrological Processes*, vol. 17, no. 15, pp. 3163–3170, 2003.
- [18] M. Hrachowitz, H. H. G. Savenije, G. Blöschl et al., "A decade of Predictions in Ungauged Basins (PUB)-a review," *Hydrological Sciences Journal*, vol. 58, no. 6, pp. 1198–1255, 2013.
- [19] R. Merz and G. Blöschl, "Regionalisation of catchment model parameters," *Journal of Hydrology*, vol. 287, no. 1–4, pp. 95–123, 2004.
- [20] T. Razavi and P. Coulibaly, "Streamflow prediction in ungauged basins: review of regionalization methods," *Journal of Hydrologic Engineering*, vol. 18, no. 8, pp. 958–975, 2013.
- [21] J. Parajka, G. Blöschl, and R. Merz, "Regional calibration of catchment models: potential for ungauged catchments," *Water Resources Research*, vol. 43, no. 6, Article ID W06406, 2007.
- [22] Y. Q. Zhang, N. R. Viney, F. H. S. Chiew, A. I. J. M. Van Dijk, and Y. Y. Liu, "Improving hydrological and vegetation modelling using regional model calibration schemes together with remote sensing data," in *Proceedings of the 19th International Congress on Modelling and Simulation (MODSIM '11)*, pp. 3448–3454, December 2011.
- [23] W. Boughton and F. Chiew, *Calibrations of the AWBM for Use on Ungauged Catchments*, 2004.
- [24] C. Perrin, C. Michel, and V. Andréassian, "Improvement of a parsimonious model for streamflow simulation," *Journal of Hydrology*, vol. 279, no. 1–4, pp. 275–289, 2003.
- [25] S. Bergstrom, "The HBV model," in *Computer Models of Watershed Hydrology*, V. P. Singh, Ed., 1995.
- [26] A. D. Feldman, "HEC models for water resources management simulation: theory and experience," *Advances in Hydroscience*, vol. 12, pp. 297–423, 1981.
- [27] N. H. Crawford and R. K. Linsley, *Digital Simulation in Hydrology: Stanford Watershed Model IV*, Stanford University, Stanford, Calif, USA, 1966.
- [28] J. W. Porter and T. A. McMahon, "A model for the simulation of streamflow data from climatic records," *Journal of Hydrology*, vol. 13, pp. 297–324, 1971.
- [29] A. J. Jakeman and G. M. Hornberger, "How much complexity is warranted in a rainfall-runoff model?" *Water Resources Research*, vol. 29, no. 8, pp. 2637–2649, 1993.
- [30] R. J. Burnash, C. Ferreal, R. A. McGuire, and R. L. McGuire, *A Generalized Streamflow Simulation System: Conceptual Modeling for Digital Computers*, U.S. Department of Commerce, National Weather Service, 1973.
- [31] F. H. S. Chiew, M. C. Peel, and A. W. Western, "Application and testing of the simple rainfall-runoff model SIMHYD," in *Mathematical Models of Small Watershed Hydrology and Applications*, V. P. Singh and D. K. Frevert, Eds., Water Resources Publications, Littleton, Colo, USA, 2002.
- [32] N. H. Crawford and R. K. Linsley, *The Synthesis of Continuous Streamflow Hydrographs on a Digital Computer*, Stanford University, 1962.
- [33] M. Sugawawa, I. Watanabe, E. Ozaki, and Y. Katsuyama, *Tank Model Programs for Personal Computer and the Way to Use*, National Research Center for Disaster Prevention, Tsukuba, Japan, 1961.
- [34] Z. Ren-Jun, "The Xinanjiang model applied in China," *Journal of Hydrology*, vol. 135, no. 1–4, pp. 371–381, 1992.
- [35] J. Martinec, "Snowmelt-Runoff Models for stream flow forecasts," *Nordic Hydrology*, vol. 6, no. 3, pp. 145–154, 1975.
- [36] G. Morin, CEQUEAU, INRS-ETE, 2002.
- [37] J.-P. Fortin, R. Turcotte, S. Massicotte, R. Moussa, J. Fitzback, and J. P. Villeneuve, "Distributed watershed model compatible with remote sensing and GIS data. I: description of model," *Journal of Hydrologic Engineering*, vol. 6, no. 2, pp. 91–99, 2001.
- [38] A. Calver and W. L. Wood, "The institute of hydrology distributed model," in *Computer Models of Watershed Hydrology*, V. P. Singh, Ed., pp. 595–626, Water Resources Publications, Highlands Ranch, Colo, USA, 1995.
- [39] J. C. Refsgaard and B. Storm, "MIKE SHE," in *Computer Models in Watershed Hydrology*, V. J. Singh, Ed., Water Resources Publications, Littleton, Colo, USA, 1995.
- [40] M. B. Abbott, J. C. Bathurst, J. A. Cunge, P. E. O'Connell, and J. Rasmussen, "An introduction to the European Hydrological System—Système Hydrologique Européen, 'SHE', 2: structure of a physically-based, distributed modelling system," *Journal of Hydrology*, vol. 87, no. 1-2, pp. 61–77, 1986.
- [41] G. W. Kite, "The SLURP model," in *Computer Models of Watershed Hydrology*, V. P. Singh, Ed., pp. 521–562, Water Resources Publications, 1995.
- [42] S. L. Neitsch, J. G. Arnold, J. R. Kiniry, J. R. Willams, and K. W. King, "Soil and Water Assessment Tool Theoretical Documentation," Version 2000, 2000, <http://swat.tamu.edu/documentation/>.
- [43] L. A. Rossman, *Storm Water Management Model User's Manual*, EPA/600/R-05/040, U.S. Environmental Protection Agency, Cincinnati, Ohio, 2007.
- [44] K. J. Beven and M. J. Kirkby, "A physically based, variable contributing area model of basin hydrology / Un modèle à base physique de zone d'appel variable de l'hydrologie du bassin versant," *Hydrological Sciences Bulletin*, vol. 24, no. 1, pp. 43–69, 1979.
- [45] N. Kouwen, *WATFLOOD/SPL9 Hydrological Model & Flood Forecasting System*, University of Waterloo, 2001.

- [46] N. Hanasaki, S. Kanae, and T. Oki, "Global energy and water balance simulation with bucket model for GSWP2," in *Proceedings of the 18th Conference on Hydrology and the 15th Symposium on Global Change and Climate Variations*, JP4.26, 2004.
- [47] E. A. Kowalczyk, Y. P. Wang, R. M. Law, H. L. Davies, J. L. McGregor, and G. Abramowitz, "CSIRO atmosphere biosphere land exchange (CABLE) model for use in climate models and as an offline model," CMAR Research Paper 013, 2006.
- [48] R. E. Dickinson, A. Henderson-Sellers, P. J. Kennedy, and M. F. Wilson, "Biosphere-atmosphere transfer scheme (BATS) for the NCAR community climate model," Technical Note TN-275+STR, National Center for Atmospheric Research, Boulder, Colo, USA, 1986.
- [49] K. W. Oleson, D. M. Lawrence, G. B. Bonan et al., "Technical description of version 4.5 of the Community Land Model (CLM)," NCAR Technical Note NCAR/TN-503+STR, 2013.
- [50] G. Y. Niu and Z. L. Yang, "The versatile integrator of surface and atmosphere processes (VISA). Part 2: evaluation of three topography-based runoff schemes," *Global and Planetary Change*, vol. 38, pp. 191–208, 2003.
- [51] P. A. Dirmeyer and F. J. Zeng, "An update to the distribution and treatment of vegetation and soil properties in SSiB," COLA Technical Report 78, 1999.
- [52] J. R. Meigh, A. A. McKenzie, and K. J. Sene, "A grid-based approach to water scarcity estimates for eastern and southern Africa," *Water Resources Management*, vol. 13, no. 2, pp. 85–115, 1999.
- [53] N. Hanasaki, S. Kanae, T. Oki et al., "An integrated model for the assessment of global water resources—part 1: model description and input meteorological forcing," *Hydrology and Earth System Sciences*, vol. 12, no. 4, pp. 1007–1025, 2008.
- [54] G. Balsamo, P. Viterbo, A. Beijaars et al., "A revised hydrology for the ECMWF model: verification from field site to terrestrial water storage and impact in the integrated forecast system," *Journal of Hydrometeorology*, vol. 10, no. 3, pp. 623–643, 2009.
- [55] D. M. Mocko and Y. C. Sud, "Refinements to SSiB with an emphasis on snowphysics: evaluation and validation using GSWP and valdai data," *Earth Interactions*, vol. 5, no. 1, pp. 1–31, 2001.
- [56] P. Etchevers, C. Golaz, and F. Habets, "Simulation of the water budget and the river flows of the Rhone basin from 1981 to 1994," *Journal of Hydrology*, vol. 244, no. 1-2, pp. 60–85, 2001.
- [57] P. M. Cox, R. A. Betts, C. B. Bunton, R. L. H. Essery, P. R. Rowntree, and J. Smith, "The impact of new land surface physics on the GCM simulation of climate and climate sensitivity," *Climate Dynamics*, vol. 15, no. 3, pp. 183–203, 1999.
- [58] P. C. D. Milly and A. B. Shmakin, "Global modeling of land water and energy balances. Part I: the land dynamics (LaD) model," *Journal of Hydrometeorology*, vol. 3, no. 3, pp. 283–299, 2002.
- [59] S. Rost, D. Gerten, A. Bondeau, W. Lucht, J. Rohwer, and S. Schaphoff, "Agricultural green and blue water consumption and its influence on the global water system," *Water Resources Research*, vol. 44, no. 9, Article ID W09405, 2008.
- [60] N. W. Arnell, "A simple water balance model for the simulation of streamflow over a large geographic domain," *Journal of Hydrology*, vol. 217, no. 3-4, pp. 314–335, 1999.
- [61] K. Takata, S. Emori, and T. Watanabe, "Development of the minimal advanced treatments of surface interaction and runoff," *Global and Planetary Change*, vol. 38, no. 1-2, pp. 209–222, 2003.
- [62] R. D. Koster and M. J. Suarez, "The influence of land surface moisture retention on precipitation statistics," *Journal of Climate*, vol. 9, no. 10, pp. 2551–2567, 1996.
- [63] S. Hagemann and L. D. Gates, "Improving a subgrid runoff parameterization scheme for climate models by the use of high resolution data derived from satellite observations," *Climate Dynamics*, vol. 21, no. 3-4, pp. 349–359, 2003.
- [64] F. Chen, K. Mitchell, J. Schaake et al., "Modeling of land surface evaporation by four schemes and comparison with FIFE observations," *Journal of Geophysical Research D: Atmospheres*, vol. 101, no. 3, pp. 7251–7268, 1996.
- [65] A. Ducharne, R. D. Koster, M. J. Suarez, M. Stieglitz, and P. Kumar, "A catchment-based approach to modeling land surface processes in a general circulation model 2. Parameter estimation and model demonstration," *Journal of Geophysical Research D: Atmospheres*, vol. 105, no. 20, pp. 24823–24838, 2000.
- [66] P. de Rosnay and J. Polcher, "Modelling root water uptake in a complex land surface scheme coupled to a GCM," *Hydrology and Earth System Sciences*, vol. 2, no. 2-3, pp. 239–255, 1998.
- [67] K. Tanaka, N. Tadanori, and I. Shuichi, "Land-surface parameterization in the Lake Biwa project," *Proceedings of Hydraulic Engineering*, vol. 42, pp. 79–84, 1998 (Japanese).
- [68] Y. M. Gusev and O. N. Nasonova, "An experience of modelling heat and water exchange at the land surface on a large river basin scale," *Journal of Hydrology*, vol. 233, no. 1-4, pp. 1–18, 2000.
- [69] P. J. Sellers, Y. Mintz, Y. C. Sud, and A. Dalcher, "A simple biosphere model (SiB) for use within general circulation models," *Journal of the Atmospheric Sciences*, vol. 43, no. 6, pp. 505–531, 1986.
- [70] D. P. Lettenmaier, E. F. Wood, and S. J. Burges, "A simple hydrologically based model of land surface water and energy fluxes for general circulation models," *Journal of Geophysical Research*, vol. 99, no. 7, pp. 14–428, 1994.
- [71] Z.-L. Yang and G.-Y. Niu, "The versatile integrator of surface and atmosphere processes part 1. Model description," *Global and Planetary Change*, vol. 38, no. 1-2, pp. 175–189, 2003.
- [72] J. Alcamo, P. Döll, T. Henrichs et al., "Development and testing of the WaterGAP 2 global model of water use and availability," *Hydrological Sciences Journal*, vol. 48, no. 3, pp. 317–338, 2003.
- [73] K. J. Beven, *Rainfall-Runoff Modeling—The Primer*, Wiley, Chichester, UK, 2001.
- [74] I. Haddeland, D. B. Clark, W. Franssen et al., "Multimodel estimate of the global terrestrial water balance: setup and first results," *Journal of Hydrometeorology*, vol. 12, no. 5, pp. 869–884, 2011.
- [75] T. Wagener, "Evaluation of catchment models," *Hydrological Processes*, vol. 17, no. 16, pp. 3375–3378, 2003.
- [76] F. H. S. Chiew, A. J. Pitman, and T. A. McMahon, "Conceptual catchment scale rainfall-runoff models and AGCM land-surface parameterisation schemes," *Journal of Hydrology*, vol. 179, no. 1-4, pp. 137–157, 1996.
- [77] H. Kling and H. Gupta, "On the development of regionalization relationships for lumped watershed models: the impact of ignoring sub-basin scale variability," *Journal of Hydrology*, vol. 373, no. 3-4, pp. 337–351, 2009.
- [78] G. Fleming, *Computer Simulation Techniques in Hydrology*, Elsevier, New York, NY, USA, 1975.
- [79] V. P. Singh, *Computer Models of Watershed Hydrology*, Water Resources Publications, 1995.

- [80] H. V. Gupta, S. Sorooshian, and P. O. Yapo, "Toward improved calibration of hydrologic models: multiple and noncommensurable measures of information," *Water Resources Research*, vol. 34, no. 4, pp. 751–763, 1998.
- [81] T. Vansteenkiste, M. Tavakoli, V. Ntegeka et al., "Intercomparison of hydrological model structures and calibration approaches in climate scenario impact projections," *Journal of Hydrology*, vol. 519, pp. 743–755, 2014.
- [82] S. Reed, V. Koren, M. Smith, Z. Zhang, F. Moreda, and D.-J. Seo, "Overall distributed model intercomparison project results," *Journal of Hydrology*, vol. 298, no. 1-4, pp. 27–60, 2004.
- [83] T. M. Carpenter and K. P. Georgakakos, "Intercomparison of lumped versus distributed hydrologic model ensemble simulations on operational forecast scales," *Journal of Hydrology*, vol. 329, no. 1-2, pp. 174–185, 2006.
- [84] D. J. Booker and R. A. Woods, "Comparing and combining physically-based and empirically-based approaches for estimating the hydrology of ungauged catchments," *Journal of Hydrology*, vol. 508, pp. 227–239, 2014.
- [85] C. Perrin, C. Michel, and V. Andréassian, "Does a large number of parameters enhance model performance? Comparative assessment of common catchment model structures on 429 catchments," *Journal of Hydrology*, vol. 242, no. 3-4, pp. 275–301, 2001.
- [86] G. B. Bonan, "A land surface model (LSM version 1.0) for ecological, hydrological, and atmospheric studies: technical description and user's guide," NCAR Technical Note NCAR/TN-417+STR, National Center for Atmospheric Research, 1996.
- [87] S. Manabe, "Climate and the ocean circulation I. The atmospheric circulation and the hydrology of the Earth's surface," *Monthly Weather Review*, vol. 97, no. 11, pp. 739–774, 1969.
- [88] R. D. Koster and P. C. D. Milly, "The interplay between transpiration and runoff formulations in land surface schemes used with atmospheric models," *Journal of Climate*, vol. 10, no. 7, pp. 1578–1591, 1997.
- [89] R. Stöckli, P. L. Vidale, A. Boone, and C. Schär, "Impact of scale and aggregation on the terrestrial water exchange: integrating land surface models and rhône catchment observations," *Journal of Hydrometeorology*, vol. 8, no. 5, pp. 1002–1015, 2007.
- [90] E. Widén-Nilsson, S. Halldin, and C.-Y. Xu, "Global water-balance modelling with WASMOD-M: parameter estimation and regionalisation," *Journal of Hydrology*, vol. 340, no. 1-2, pp. 105–118, 2007.
- [91] S. N. Gosling, R. G. Taylor, N. W. Arnell, and M. C. Todd, "A comparative analysis of projected impacts of climate change on river runoff from global and catchment-scale hydrological models," *Hydrology and Earth System Sciences*, vol. 15, no. 1, pp. 279–294, 2011.
- [92] G. Blöschl and M. Sivapalan, "Scale issues in hydrological modelling: a review," *Hydrological Processes*, vol. 9, no. 3-4, pp. 251–290, 1995.
- [93] J. Samuel, P. Coulibaly, and R. A. Metcalfe, "Estimation of continuous streamflow in ontario ungauged basins: comparison of regionalization methods," *Journal of Hydrologic Engineering*, vol. 16, no. 5, pp. 447–459, 2011.
- [94] S. Stoll and M. Weiler, "Explicit simulations of stream networks to guide hydrological modelling in ungauged basins," *Hydrology and Earth System Sciences*, vol. 14, no. 8, pp. 1435–1448, 2010.
- [95] L. M. Parada and X. Liang, "A novel approach to infer streamflow signals for ungauged basins," *Advances in Water Resources*, vol. 33, no. 4, pp. 372–386, 2010.
- [96] J. Parajka, R. Merz, and G. Blöschl, "A comparison of regionalisation methods for catchment model parameters," *Hydrology and Earth System Sciences*, vol. 9, no. 3, pp. 157–171, 2005.
- [97] H. Li, Y. Zhang, F. H. S. Chiew, and S. Xu, "Predicting runoff in ungauged catchments by using Xinanjiang model with MODIS leaf area index," *Journal of Hydrology*, vol. 370, no. 1-4, pp. 155–162, 2009.
- [98] J. P. C. Reichl, A. W. Western, N. R. McIntyre, and F. H. S. Chiew, "Optimization of a similarity measure for estimating ungauged streamflow," *Water Resources Research*, vol. 45, no. 10, Article ID W10423, 2009.
- [99] L. Samaniego, A. Bárdossy, and R. Kumar, "Streamflow prediction in ungauged catchments using copula-based dissimilarity measures," *Water Resources Research*, vol. 46, no. 2, Article ID W02506, 2010.
- [100] I. Masih, S. Uhlenbrook, S. Maskey, and M. D. Ahmad, "Regionalization of a conceptual rainfall-runoff model based on similarity of the flow duration curve: a case study from the semi-arid Karkheh basin, Iran," *Journal of Hydrology*, vol. 391, no. 1-2, pp. 188–201, 2010.
- [101] M. Li, Q. Shao, L. Zhang, and F. H. S. Chiew, "A new regionalization approach and its application to predict flow duration curve in ungauged basins," *Journal of Hydrology*, vol. 389, no. 1-2, pp. 137–145, 2010.
- [102] C. Shu and T. B. M. J. Ouarda, "Improved methods for daily streamflow estimates at ungauged sites," *Water Resources Research*, vol. 48, no. 2, Article ID W02523, 2012.
- [103] N. McIntyre, H. Lee, H. Wheeler, A. Young, and T. Wagener, "Ensemble predictions of runoff in ungauged catchments," *Water Resources Research*, vol. 41, no. 12, Article ID W12434, 2005.
- [104] A. L. Kay, D. A. Jones, S. M. Crooks, A. Calver, and N. S. Reynard, "A comparison of three approaches to spatial generalization of rainfall-runoff models," *Hydrological Processes*, vol. 20, no. 18, pp. 3953–3973, 2006.
- [105] F. Li, Y. Zhang, Z. Xu, C. Liu, Y. Zhou, and W. Liu, "Runoff predictions in ungauged catchments in southeast Tibetan Plateau," *Journal of Hydrology*, vol. 511, pp. 28–38, 2014.
- [106] Y. Zhang, J. Vaze, F. H. Chiew, J. Teng, and M. Li, "Predicting hydrological signatures in ungauged catchments using spatial interpolation, index model, and rainfall-runoff modelling," *Journal of Hydrology*, vol. 517, pp. 936–948, 2014.
- [107] K. J. Beven, "Changing ideas in hydrology—the case of physically-based models," *Journal of Hydrology*, vol. 105, no. 1-2, pp. 157–172, 1989.
- [108] H. V. Gupta, T. Wagener, and Y. Liu, "Reconciling theory with observations: elements of a diagnostic approach to model evaluation," *Hydrological Processes*, vol. 22, no. 18, pp. 3802–3813, 2008.
- [109] J. Seibert and J. J. McDonnell, "On the dialog between experimentalist and modeler in catchment hydrology: use of soft data for multicriteria model calibration," *Water Resources Research*, vol. 38, no. 11, pp. 231–2314, 2002.
- [110] T. Nester, R. Kirnbauer, J. Parajka, and G. Blöschl, "Evaluating the snow component of a flood forecasting model," *Hydrology Research*, vol. 43, no. 6, pp. 762–779, 2012.
- [111] Y. A. Mohamed, H. H. G. Savenije, W. G. M. Bastiaanssen, and B. J. J. M. van den Hurk, "New lessons on the Sudd hydrology learned from remote sensing and climate modeling," *Hydrology and Earth System Sciences*, vol. 10, no. 4, pp. 507–518, 2006.

- [112] J. Parajka and G. Blöschl, "Validation of MODIS snow cover images over Austria," *Hydrology and Earth System Sciences*, vol. 10, no. 5, pp. 679–689, 2006.
- [113] H. C. Winsemius, H. H. G. Savenije, and W. G. M. Bastiaanssen, "Constraining model parameters on remotely sensed evaporation: justification for distribution in ungauged basins?" *Hydrology and Earth System Sciences*, vol. 12, no. 6, pp. 1403–1413, 2008.
- [114] Y. Q. Zhang, F. H. S. Chiew, L. Zhang, R. Leuning, and H. A. Cleugh, "Estimating catchment evaporation and runoff using MODIS leaf area index and the Penman-Monteith equation," *Water Resources Research*, vol. 44, no. 10, Article ID W10420, 2008.
- [115] Y. Q. Zhang, N. R. Viney, F. H. S. Chiew, A. I. J. M. Dijk, and Y. Y. Liu, "Improving hydrological and vegetation modelling using regional model calibration schemes together with remote sensing data," in *Proceedings of the 19th International Congress on Modelling and Simulation (MODSIM '11)*, pp. 12–16, Perth, Australia, 2011.
- [116] A. Yatagai, K. Kamiguchi, O. Arakawa, A. Hamada, N. Yasutomi, and A. Kitoh, "APHRODITE: constructing a long-term daily gridded precipitation dataset for Asia based on a dense network of rain gauges," *Bulletin of the American Meteorological Society*, vol. 93, no. 9, pp. 1401–1415, 2012.
- [117] R. Joseph, T. M. Smith, M. R. P. Sapiano, and R. R. Ferraro, "A new high-resolution satellite-derived precipitation dataset for climate studies," *Journal of Hydrometeorology*, vol. 10, no. 4, pp. 935–952, 2009.
- [118] P. A. Dirmeyer, A. J. Dolman, and N. Sato, "The global soil wetness project: a pilot project for global land surface modeling and validation," *Bulletin of the American Meteorological Society*, vol. 80, pp. 851–878, 1999.
- [119] G. P. Weedon, S. Gomes, P. Viterbo et al., "Creation of the WATCH forcing data and its use to assess global and regional reference crop evaporation over land during the twentieth century," *Journal of Hydrometeorology*, vol. 12, no. 5, pp. 823–848, 2011.
- [120] G. P. Weedon, G. Balsamo, N. Bellouin, S. Gomes, M. J. Best, and P. Viterbo, "The WFDEI meteorological forcing data set: WATCH Forcing Data methodology applied to ERA-Interim reanalysis data," *Water Resources Research*, vol. 50, no. 9, pp. 7505–7514, 2014.
- [121] P. Xie and P. A. Arkin, "Global precipitation: a 17-year monthly analysis based on gauge observations, satellite estimates, and numerical model outputs," *Bulletin of the American Meteorological Society*, vol. 78, no. 11, pp. 2539–2558, 1997.
- [122] R. J. Joyce, J. E. Janowiak, P. A. Arkin, and P. Xie, "CMORPH: a method that produces global precipitation estimates from passive microwave and infrared data at high spatial and temporal resolution," *Journal of Hydrometeorology*, vol. 5, no. 3, pp. 487–503, 2004.
- [123] I. Harris, P. D. Jones, T. J. Osborn, and D. H. Lister, "Updated high-resolution grids of monthly climatic observations—the CRU TS3.10 Dataset," *International Journal of Climatology*, vol. 34, no. 3, pp. 623–642, 2014.
- [124] P. E. Thornton, M. M. Thornton, B. W. Mayer et al., *Daymet: Daily Surface Weather Data on a 1-km Grid for North America, Version 2. Data Set*, Oak Ridge National Laboratory Distributed Active Archive Center, Oak Ridge, Tenn, USA, 2014, <http://daac.ornl.gov/>.
- [125] D. R. Legates and C. J. Willmott, "Mean seasonal and spatial variability in global surface air temperature," *Theoretical and Applied Climatology*, vol. 41, no. 1–2, pp. 11–21, 1990.
- [126] U. Schneider, A. Becker, P. Finger, A. Meyer-Christoffer, M. Ziese, and B. Rudolf, "GPCC's new land surface precipitation climatology based on quality-controlled in situ data and its role in quantifying the global water cycle," *Theoretical and Applied Climatology*, vol. 115, no. 1–2, pp. 15–40, 2014.
- [127] J. Sheffield, G. Goteti, and E. F. Wood, "Development of a 50-year high-resolution global dataset of meteorological forcings for land surface modeling," *Journal of Climate*, vol. 19, no. 13, pp. 3088–3111, 2006.
- [128] R. F. Adler, G. J. Huffman, A. Chang et al., "The version-2 global precipitation climatology project (GPCP) monthly precipitation analysis (1979–present)," *Journal of Hydrometeorology*, vol. 4, no. 6, pp. 1147–1167, 2003.
- [129] A. Andersson, K. Fennig, C. Klepp, S. Bakan, H. Graßl, and J. Schulz, "The hamburg ocean atmosphere parameters and fluxes from satellite data—HOAPS-3," *Earth System Science Data*, vol. 2, no. 2, pp. 215–234, 2010.
- [130] W. G. Large and S. G. Yeager, "The global climatology of an interannually varying air—sea flux data set," *Climate Dynamics*, vol. 33, no. 2–3, pp. 341–364, 2009.
- [131] K. E. Mitchell, D. Lohmann, P. R. Houser et al., "The multi-institution North American Land Data Assimilation System (NLDAS): utilizing multiple GCIP products and partners in a continental distributed hydrological modeling system," *Journal of Geophysical Research*, vol. 109, Article ID D07S90, 2004.
- [132] M. Rodell, P. R. Houser, U. Jambor et al., "The global land data assimilation system," *Bulletin of the American Meteorological Society*, vol. 85, no. 3, pp. 381–394, 2004.
- [133] S. Sorooshian, K.-L. Hsu, X. Gao, H. V. Gupta, B. Imam, and D. Braithwaite, "Evaluation of PERSIANN system satellite-based estimates of tropical rainfall," *Bulletin of the American Meteorological Society*, vol. 81, no. 9, pp. 2035–2046, 2000.
- [134] M. Chen, P. Xie, J. E. Janowiak, and P. A. Arkin, "Global land precipitation: a 50-yr monthly analysis based on gauge observations," *Journal of Hydrometeorology*, vol. 3, no. 3, pp. 249–266, 2002.
- [135] C. Daly, M. Halbleib, J. I. Smith et al., "Physiographically sensitive mapping of climatological temperature and precipitation across the conterminous United States," *International Journal of Climatology*, vol. 28, no. 15, pp. 2031–2064, 2008.
- [136] R. R. Ferraro, F. Weng, N. C. Grody, and A. Basist, "An eight-year (1987–1994) time series of rainfall, clouds, water vapor, snow cover, and sea ice derived from SSM/I measurements," *Bulletin of the American Meteorological Society*, vol. 77, no. 5, pp. 891–905, 1996.
- [137] G. J. Huffman, R. F. Adler, D. T. Bolvin et al., "The TRMM multi-satellite precipitation analysis (TMPA): quasi-global, multiyear, combined-sensor precipitation estimates at fine scales," *Journal of Hydrometeorology*, vol. 8, no. 1, pp. 38–55, 2007.
- [138] G. Blöschl, C. Reszler, and J. Komma, "A spatially distributed flash flood forecasting model," *Environmental Modelling & Software*, vol. 23, no. 4, pp. 464–478, 2008.
- [139] N. K. Tuteja, J. Vaze, J. Teng, and M. Mutendeuzi, "Partitioning the effects of pine plantations and climate variability on runoff from a large catchment in southeastern Australia," *Water Resources Research*, vol. 43, no. 8, Article ID W08415, 2007.
- [140] O. Yildiz and A. P. Barros, "Elucidating vegetation controls on the hydroclimatology of a mid-latitude basin," *Journal of Hydrology*, vol. 333, no. 2–4, pp. 431–448, 2007.

- [141] N. K. Tuteja, J. Vaze, J. Teng, and M. Mutendeudzi, "Partitioning the effects of pine plantations and climate variability on runoff from a large catchment in southeastern Australia," *Water Resources Research*, vol. 43, no. 8, Article ID W08415, 2007.
- [142] M. Fang and W. Huang, "Tracking the Indonesian forest fire using NOAA/AVHRR images," *International Journal of Remote Sensing*, vol. 19, no. 3, pp. 387–390, 1998.
- [143] M. D. M. Islam and K. Sado, "Development of flood hazard maps of Bangladesh using NOAA-AVHRR images with GIS," *Hydrological Sciences Journal*, vol. 45, no. 3, pp. 337–355, 2000.
- [144] R. Ranzi, G. Grossi, and B. Bacchi, "Ten years of monitoring areal snowpack in the Southern Alps using NOAA-AVHRR imagery, ground measurements and hydrological data," *Hydrological Processes*, vol. 13, no. 12-13, pp. 2079–2095, 1999.
- [145] L. Oudin, V. Andréassian, J. Lerat, and C. Michel, "Has land cover a significant impact on mean annual streamflow? An international assessment using 1508 catchments," *Journal of Hydrology*, vol. 357, no. 3-4, pp. 303–316, 2008.
- [146] X. Liang and Z. Xie, "A new surface runoff parameterization with subgrid-scale soil heterogeneity for land surface models," *Advances in Water Resources*, vol. 24, no. 9-10, pp. 1173–1193, 2001.
- [147] A. J. Pitman, A. G. Slater, C. E. Desborough, and M. Zhao, "Uncertainty in the simulation of runoff due to the parameterization of frozen soil moisture using the Global Soil Wetness Project methodology," *Journal of Geophysical Research D: Atmospheres*, vol. 104, no. 14, pp. 16879–16888, 1999.
- [148] V. Haverd and M. Cuntz, "Soil-Litter-Iso: a one-dimensional model for coupled transport of heat, water and stable isotopes in soil with a litter layer and root extraction," *Journal of Hydrology*, vol. 388, no. 3-4, pp. 438–455, 2010.
- [149] H. I. Choi and X.-Z. Liang, "Improved terrestrial hydrologic representation in mesoscale land surface models," *Journal of Hydrometeorology*, vol. 11, no. 3, pp. 797–809, 2010.
- [150] W. F. Krajewski, G. Villarini, and J. A. Smith, "Radar-rainfall uncertainties: where are we after thirty years of effort," *Bulletin of the American Meteorological Society*, vol. 91, no. 1, pp. 87–94, 2010.
- [151] R. J. Moore, S. J. Cole, and A. J. Illingworth, *Weather Radar and Hydrology*, IAHS Publication 351, IAHS Press, Wallingford, Conn, USA, 2012.
- [152] U. Ehret, *Rainfall and flood nowcasting in small catchments using weather radar [Ph.D. thesis]*, University of Stuttgart, 2002.
- [153] E. Todini, "A Bayesian technique for conditioning radar precipitation estimates to rain-gauge measurements," *Hydrology and Earth System Sciences*, vol. 5, no. 2, pp. 187–199, 2001.
- [154] A. J. Pereira Filho, "Integrating gauge, radar and satellite rainfall," in *Proceedings of the 2nd International Precipitation Working Group Workshop*, 2004.
- [155] D. A. Vila, L. G. G. De Goncalves, D. L. Toll, and J. R. Rozante, "Statistical evaluation of combined daily gauge observations and rainfall satellite estimates over continental South America," *Journal of Hydrometeorology*, vol. 10, no. 2, pp. 533–543, 2009.
- [156] D.-J. Seo, "Real-time estimation of rainfall fields using rain gauge data under fractional coverage conditions," *Journal of Hydrology*, vol. 208, no. 1-2, pp. 25–36, 1998.
- [157] J. Gottschalck, J. Meng, M. Rodell, and P. Houser, "Analysis of multiple precipitation products and preliminary assessment of their impact on global land data assimilation system land surface states," *Journal of Hydrometeorology*, vol. 6, no. 5, pp. 573–598, 2005.
- [158] A. Chappell, L. H. Renzullo, T. J. Raupach, and M. Haylock, "Evaluating geostatistical methods of blending satellite and gauge data to estimate near real-time daily rainfall for Australia," *Journal of Hydrology*, vol. 493, pp. 105–114, 2013.
- [159] A. K. Mitra, I. M. Momin, E. N. Rajagopal, S. Basu, M. N. Rajeevan, and T. N. Krishnamurti, "Gridded daily Indian monsoon rainfall for 14 seasons: merged TRMM and IMD gauge analyzed values," *Journal of Earth System Science*, vol. 122, no. 5, pp. 1173–1182, 2013.
- [160] M. Ryo, O. C. S. Valeriano, S. Kanae, and T. D. Ngoc, "Temporal downscaling of daily gauged precipitation by application of a satellite product for flood simulation in a poorly gauged basin and its evaluation with multiple regression analysis," *Journal of Hydrometeorology*, vol. 15, no. 2, pp. 563–580, 2014.

Research Article

Climate Change Impact on the Hydrology of a Typical Watershed in the Tianshan Mountains

Gonghuan Fang,^{1,2,3} Jing Yang,^{1,4} Yaning Chen,¹ Shuhua Zhang,^{1,2} Haijun Deng,^{1,2} Haimeng Liu,^{2,5} and Philippe De Maeyer³

¹State Key Laboratory of Desert and Oasis Ecology, Xinjiang Institute of Ecology and Geography, Chinese Academy of Sciences, Urumqi 830011, China

²University of Chinese Academy of Sciences, Beijing 100049, China

³Department of Geography, Ghent University, 9000 Ghent, Belgium

⁴National Institute of Water and Atmospheric Research, Christchurch 8011, New Zealand

⁵Institute of Geographic Sciences and Natural Resources Research, Chinese Academy of Sciences, Beijing 100101, China

Correspondence should be addressed to Jing Yang; yangjing@ms.xjb.ac.cn

Received 28 November 2014; Revised 26 March 2015; Accepted 15 April 2015

Academic Editor: Ming Pan

Copyright © 2015 Gonghuan Fang et al. This is an open access article distributed under the Creative Commons Attribution License, which permits unrestricted use, distribution, and reproduction in any medium, provided the original work is properly cited.

To study the impact of future climatic changes on hydrology in the Kaidu River Basin in the Tianshan Mountains, two sets of future climatic data were used to force a well-calibrated hydrologic model: one is bias-corrected regional climate model (RCM) outputs for RCP4.5 and RCP8.5 future emission scenarios, and the other is simple climate change (SCC) with absolute temperature change of $-1\sim 6^{\circ}\text{C}$ and relative precipitation change of $-20\sim 60\%$. Results show the following: (1) temperature is likely to increase by 2.2°C and 4.6°C by the end of the 21st century under RCP4.5 and RCP8.5, respectively, while precipitation will increase by $2\sim 24\%$, with a significant rise in the dry season and small change in the wet season; (2) flow will change by $-1\sim 20\%$, while evapotranspiration will increase by $2\sim 24\%$; (3) flow increases almost linearly with precipitation, while its response to temperature depends on the magnitude of temperature change and flow decrease is significant when temperature increase is greater than 2°C ; (4) similar results were obtained for simulations with RCM outputs and with SCC for mild climate change conditions, while results were significantly different for intense climate change conditions.

1. Introduction

The Tianshan Mountains, regarded as the “water tower of Central Asia” [1], are located in the innermost center of the Eurasian continent. The long distance to the surrounding oceans causes a dry climate, especially for the surrounding basins. Rivers starting in the mountainous regions provide agricultural and domestic water for the surrounding basins and oases. With their distinctive topographic and landscape features, the Tianshan Mountains show a unique energy balance and hydrological cycle and are expected to be sensitive to climate change [2, 3].

Many reports show a widespread climatic and hydrologic change in the Tianshan Mountains during the past few decades [4]. For example, temperature demonstrated a significant rising trend (significant level is smaller than 0.001)

at a rate of $0.33\sim 0.34^{\circ}\text{C}/\text{decade}$ during 1960~2010, which is higher than China ($0.25^{\circ}\text{C}/\text{decade}$) and the entire globe ($0.13^{\circ}\text{C}/\text{decade}$) [5, 6]; precipitation increased substantially in most regions especially for the middle and high latitudes; glacier area decreased by 11.5% and the thickness of snowpack has also decreased [5, 7]. Pan evaporation and wind speed have also changed [3]. The annual runoff increased as well, for example, for the Urumqi River, the Kaidu River, and the Aksu River [8, 9].

Future changes in the streamflow and watershed hydrology have become increasingly important to water resource management in the Tianshan Mountains. However, only a limited number of studies currently focus on impact of future climate change on hydrology; for example, Sorg et al. [1] indicated that the total runoff is likely to remain stable or even increase slightly in the near future but it will decrease

at the end of the 21st century for Central Asia. There are also researches demonstrating that the annual runoff will decrease to some extent in the first half of the 21st century [2, 10]. Previous studies seldom address implications of climate change on the hydrological cycle and hydrological components (e.g., ET, surface flow, and groundwater). To complement these studies, this paper aims at understanding the future hydrological system and assessing the responses of the hydrologic system to climate change.

In the present study, two sets of climatic data, that is, RCM outputs and SCC data, are used to force SWAT [11] and are applied to the Kaidu River Basin, a typical watershed on the south slope of the Tianshan Mountains, to assess future changes of the hydrologic cycle and the hydrological effects of changes in climate variables. Questions that are addressed include the followings. (1) How will the future climate and hydrology change in this region? (2) What is the effect of climate change on the hydrologic cycling? (3) What is the difference between simulations with RCM outputs and SCC? Understanding these issues will enable assessing the future hydrological change and its unique hydrometeorological processes better. The remaining is constructed as follows: Section 2 introduces the study area and data; Section 3 describes the hydrological model, bias correction methods, and analysis procedures; Section 4 provides the results and discussion, followed by conclusions in Section 5.

2. Study Area and Data

The Kaidu River Basin, with a drainage area of 18,634 km² above the Dashankou hydrological station, is considered to be a very typical watershed in the Tianshan Mountains (Figure 1). Its altitude ranges from 1,342 m to 4,796 m above sea level (asl) with an average elevation of 2,995 m. The climate here is temperate continental with alpine climate characteristics and obvious seasonal variation. This river provides water resources for agricultural activity and the ecological environment of the oasis, with an area of over 70,000 km² and a population of over 1.15 million, which is mainly stressed by water scarcity [12]. Therefore, projecting the impact of future climate change on water resources is urgent for the sustainable development of this region and it also provides information on the implications of climate change on the water tower in Central Asia.

The daily observed meteorological data (including precipitation, maximum/minimum temperature, wind speed, and relative humidity) of two meteorological stations Bayanbulak and Baluntai from 1970 to 2005 are from the China Meteorological Data Sharing Service System (<http://www.cma.gov.cn/2011qx/fw/2011qsjgx/>). The annual mean temperature at the Bayanbulak meteorological station amounts to -4.1°C and the mean annual precipitation is 278 mm (Figure 1). Generally, precipitation falls as rain from May to September each year and as snow from October to April.

The observed streamflow data at the Dashankou hydrologic station are from the Xinjiang Tarim River Basin Management Bureau. The average flow at the Dashankou hydrologic station amounts to approximately 120 m³/s (equivalent to 202 mm runoff/year), ranging from 15 m³/s to 973 m³/s.

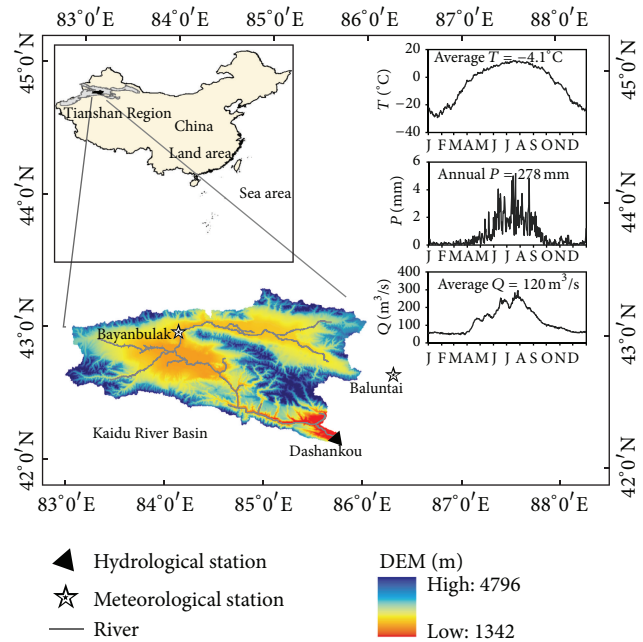


FIGURE 1: Location (top left), topography, and hydrometeorologic stations (bottom) of the Kaidu River Basin and the daily average temperature (T) and precipitation (P) at the Bayanbulak station and streamflow (Q) at the Dashankou station (top right).

3. Methodology

3.1. Regional Climate Model and RCP Scenarios. The outputs of a regional climate model (RegCM4.0) [13] forced by a global climate model (Beijing Climate Center Climate System Model, BCC_CSM1.1) [14, 15] at a horizontal resolution of 50 km are used as future climate data. Firstly, the RCM model was validated with the observational data set over China for the period from 1976 to 2005 and then it was used to predict the future climate change under the new emission scenarios of the Representative Concentration Pathways, RCP4.5 (lower emission scenario) and RCP8.5 (higher emission scenario). RCP4.5 is a stabilization scenario with the total radiative forcing rising until 2070 and then remaining at a stable centration of 4.5 W/m^2 . In contrast, RCP8.5 is a continuously rising radiative forcing pathway (at a target of 8.5 W/m^2 in 2100) with a further enhanced residual circulation and significant CH₄ increases [16, 17]. The RCM validation shows reasonable simulations of temperature and precipitation were obtained over China and, compared to the BCC_CSM1.1 model, marked improvement of the RCM was achieved in reproducing present day precipitation and temperature (for more details refer to [18]).

3.2. Bias Correction Methods. Five precipitation and three temperature correction methods were selected to bias-correct the raw RCM outputs. Precipitation correction methods include linear scaling, local intensity scaling, power transformation, distribution mapping, and quantile mapping. Temperature correction methods include linear scaling, variance scaling, and distribution mapping. They are combined into

15 schemes to evaluate their performances in simulating streamflow. It turns out that the precipitation correction methods have more significant influence than the temperature correction methods on streamflow simulation, and the power transformation and quantile mapping perform best in terms of frequency based statistics. Thereafter, the quantile mapping method (for precipitation) and the distribution mapping (for temperature) are selected to correct the raw RCM outputs for the future period (for more details see [19]).

3.3. Hydrologic Model and Uncertainty Analysis Method. SWAT has been extensively used for the comprehensive modeling of the impact of management practices and climate change. SWAT simulates the hydrologic and sedimentary processes, plant growth, river routing, and in-stream water quality process, among which the surface runoff is calculated from daily rainfall and snowmelt with a modified Soil Conservation Service (SCS) curve number method [20]; water routing is simulated using variable storage or the Muskingum river routing method [11].

The SWAT model input includes the digital elevation model (DEM), soil textural and physicochemical properties, and land use data. The meteorological variables including daily precipitation, max./min. temperature, relative humidity, solar radiation, and wind speed were used to force the SWAT model. SWAT uses elevation bands to represent the topographic effects on precipitation and temperature. Within each elevation band, the precipitation and temperature are estimated based on their lapse rates. For more details, refer to the SWAT manual (<http://www.brc.tamus.edu/>).

The SWAT model (forced by the observed meteorological data) was calibrated against the observed streamflow. The calibration period is from 1986 to 1989 and the validation period from 1990 to 2005 [21]. The calibrated optimal parameters are then kept fixed in the following simulations. The evaluation indices for the hydrological model include NS, PBIAS, and the determination coefficient R^2 . Consider

$$\text{NS} = 1 - \frac{\sum_{i=1}^n (Y_i^{\text{obs}} - Y_i^{\text{sim}})^2}{\sum_{i=1}^n (Y_i^{\text{obs}} - Y^{\text{mean}})^2}, \quad (1)$$

$$\text{PBIAS} = \frac{\sum_{i=1}^n (Y_i^{\text{obs}} - Y_i^{\text{sim}})}{\sum_{i=1}^n (Y_i^{\text{obs}})},$$

where Y_i^{obs} and Y_i^{sim} are the i th observed and simulated flows, Y^{mean} is the mean of the observed data, and n is the number of observations. Normally $\text{NS} > 0.50$, $|\text{PBIAS}| < 25\%$, and $R^2 > 0.6$ are taken as the criteria for satisfactory modeling of the river discharge and the model performance can be evaluated as excellent if $\text{NS} > 0.75$ and $|\text{PBIAS}| < 10\%$ [22].

GLUE (generalized likelihood uncertainty estimation) [23] is an uncertainty analysis technique, in which the parameter uncertainty accounts for all sources of uncertainty, such as input uncertainty, structure uncertainty, parameter uncertainty, and response uncertainty [24]. In GLUE, the parameter uncertainty is described as a set of discrete “behavioral” parameter sets with corresponding “likelihood weights.”

The procedure of a GLUE analysis consists of three steps. Firstly, after the definition of the “generalized likelihood measure,” $L(\theta)$, a large number of parameter sets are randomly sampled from the prior distribution and each parameter set is assessed as either “behavioral” or “nonbehavioral” by comparing its value of $L(\theta)$ to the threshold value. Secondly, each behavioral parameter set is given a “likelihood weight” and we gave them equal weights in this study. Finally, prediction uncertainty is represented by 5% and 95% quantiles of the cumulative distribution of the behavioral parameter sets.

Two indices are used to quantify the quality of the uncertainty performance. Those indices are the percentage of measurements bracketed by the 95% prediction uncertainty band (P -factor) and width of band (R -factor, calculated by the average width of the band divided by the standard deviation of the corresponding measured variable).

3.4. SCC Data Description and Analysis Procedures. In the following section, temperature and precipitation are denoted as T and P and the absolute and relative changes are represented by Δ and δ . For example, ΔT refers to an absolute temperature change and δP a relative precipitation change. The hydrological processes analyzed in this study include streamflow, surface runoff, subsurface runoff, and evapotranspiration, which are denoted as Q , R_s , R_g , and ET , and their relative changes are described as δQ , δR_s , δR_g , and δET , respectively.

The SCC was constructed to represent a wide range of changes in climatic variables and how these changes might translate in streamflow and other hydrological components and also to analyze the differences between simulations with RCM outputs and SCC. For SCC, perturbations of the corrected RCM simulated P and T from 1986~2005 (control period) are set; that is, for T , an additive change (Δ) is used: $\Delta T = -1, 0, 1, 2, 3, 4, 5$, and 6°C . For P , a relative change (δ) is used: $\delta P = -20\%, -10\%, 0, 10\%, 20\%, 30\%, 40\%, 50\%$, and 60% . They are put into 81 SCC scenarios, with $\Delta T = 0$ and $\delta P = 0\%$ being the climate for control period.

By investigating the transient evolution of climate change in the corrected RCM outputs on decadal scales, five periods (each spanning 20 years) are defined: 1986~2005 (control period) and 2020~2039, 2040~2059, 2060~2079, and 2080~2099. Due to the intra-annual characteristics of the hydrometeorology in the Kaidu River Basin (Figure 1), the wet season (from April to September) and dry season (from October to March next year) are defined based on the intra-annual distribution of P and Q ; for example, P and Q in the wet season account for 88% and 73% of their annual amounts. The climatic and hydrological changes are classified into three categories, that is, a significant change, small change, and insignificant change, to clearly demonstrate the changing magnitude according to the values of relative change for precipitation and hydrological components and absolute change of temperature. These categories are presented in Table 1.

TABLE 1: Classification of magnitude for climatic and hydrological changes. δ and Δ represent relative change and absolute change.

	Precipitation & hydrological components (%)	Temperature ($^{\circ}\text{C}$)
Significant change	$ \delta \geq 20$	$ \Delta \geq 2$
Small change	$10 \leq \delta < 20$	$1 \leq \Delta < 2$
Insignificant change	$ \delta < 10$	$ \Delta < 1$

4. Results and Discussion

4.1. Validation of the Hydrological Model and the Bias Correction Methods. Performance of the hydrological model forced by observed meteorological data and the 95% prediction uncertainty bands are shown in Figure 2. The simulated streamflow agrees quite well with the observation for both calibration period (1986~1989) and validation period (1990~2002). For the uncertainty analysis, NS is used as $L(\theta)$ and 0.70 as threshold value with 10,000 initial parameter sets; 288 sets were selected as behavioral points. The results show that most of the observations are bracketed by the 95% prediction uncertainty band (P -factor being 87% and 80% for calibration and validation periods and R -factor being 1.18 and 1.19, resp.). The lower P -factor for the validation period can be partly attributed to operation of hydropower station since 1991 (Figure 2) which leads to great fluctuation in winter streamflow. Statistics of model efficiency (Table 2) indicate excellent performances for both calibration and validation periods, with “NS”s and “ R^2 ”s over 0.80, which is highly acceptable according to Moriasi et al. [22]. Concerning the monthly streamflow, the “NS” is 0.89 during 1986~2005 and it indicates that the SWAT model captured the natural monthly streamflow variability adequately.

The performances of bias-corrected RCM outputs (compared to observed meteorological data) are listed in Table 2. The “NS”s are -0.57 (0.57) and 0.77 (0.95) for daily (monthly) precipitation and temperature for 1990~2005, respectively. And the statistics of the streamflow simulated with the bias-corrected RCM outputs shows acceptable results with “NS”s equal to 0.46 and 0.62 and PBIAS within 10% for daily and monthly streamflows.

4.2. RCM Projected Hydrometeorologic Changes

4.2.1. Changes in Temperature and Precipitation. Temperature is highly likely to increase in the future, with a basin warming of $1.0\sim 2.2^{\circ}\text{C}$ and $1.6\sim 4.6^{\circ}\text{C}$ under RCP4.5 and RCP8.5 in the 21st century (Table 3). Temperature increases continuously under both scenarios but the magnitude is larger under RCP8.5 (Figure 3).

Precipitation shows an overall increasing trend in the 21st century with an annual increase of $2\%\sim 16\%$ and $7\%\sim 24\%$ under RCP4.5 and RCP8.5, which confirms the previous arguments of Sorg et al. [1]. However, precipitation change varies substantially among seasons (Figure 3). Normally,

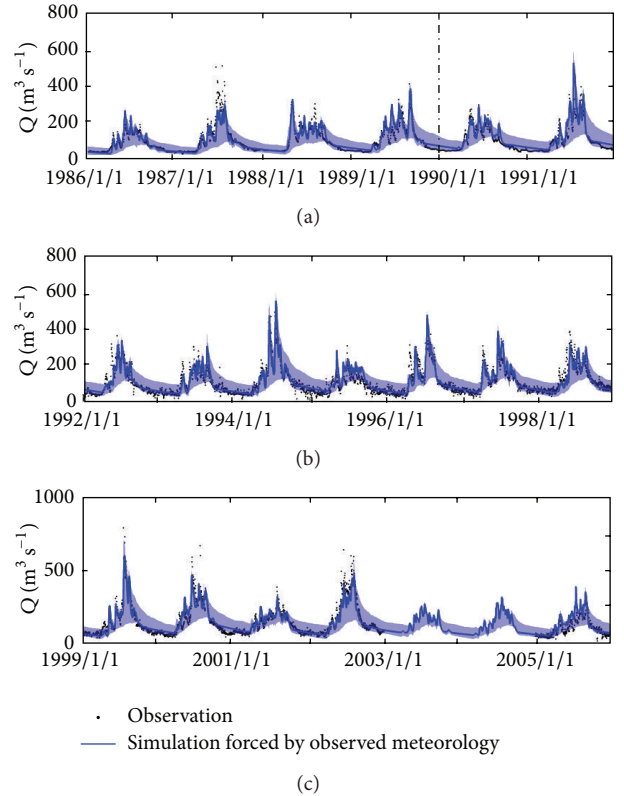


FIGURE 2: Time series of daily observed streamflows (dots) and simulated streamflows forced by observed meteorology (blue line) for calibration period (1986~1989) and validation period (1990~2005) with 95% prediction uncertainty bands (blue shaded area).

a small increase in the wet season ($-2\%\sim 16\%$) and a significant increase during dry season ($18\%\sim 78\%$) are projected. Note that the relative increase (not the absolute increment) of precipitation for the dry season is much bigger than for the wet season, which is in line with the climate changes in other regions, for example, the semiarid Colorado River Basin [25] and the wet Ganges-Brahmaputra-Meghna basin [26].

4.2.2. Changes in the Hydrological Cycle. The changes in precipitation and temperature cause changes in potential streamflow. The average annual streamflow rises by $-1\%\sim 18\%$ and $4\sim 20\%$ under the RCP4.5 and RCP8.5 in the 21st century, based on the average annual streamflow of 194 mm for the control period (1986~2005) (Table 3). Note that the streamflow stopped increasing in 2080~2099 (end of 21st century) under RCP8.5 despite the rise in precipitation, which confirms the finding of Sorg et al. [1] and may aggravate water scarcity in this region.

Figure 3 also shows the projected changes in surface runoff (R_s), subsurface runoff (R_g), and evapotranspiration (ET) under RCP4.5 and RCP8.5. Overall, changes of hydrologic components are bigger for RCP8.5 than for RCP4.5. The annual change of R_s is insignificant ($<5\%$) but with obvious seasonal variability; for example, changes of R_s range from -22% to 2% for the wet season and in $4\%\sim 78\%$ for the dry

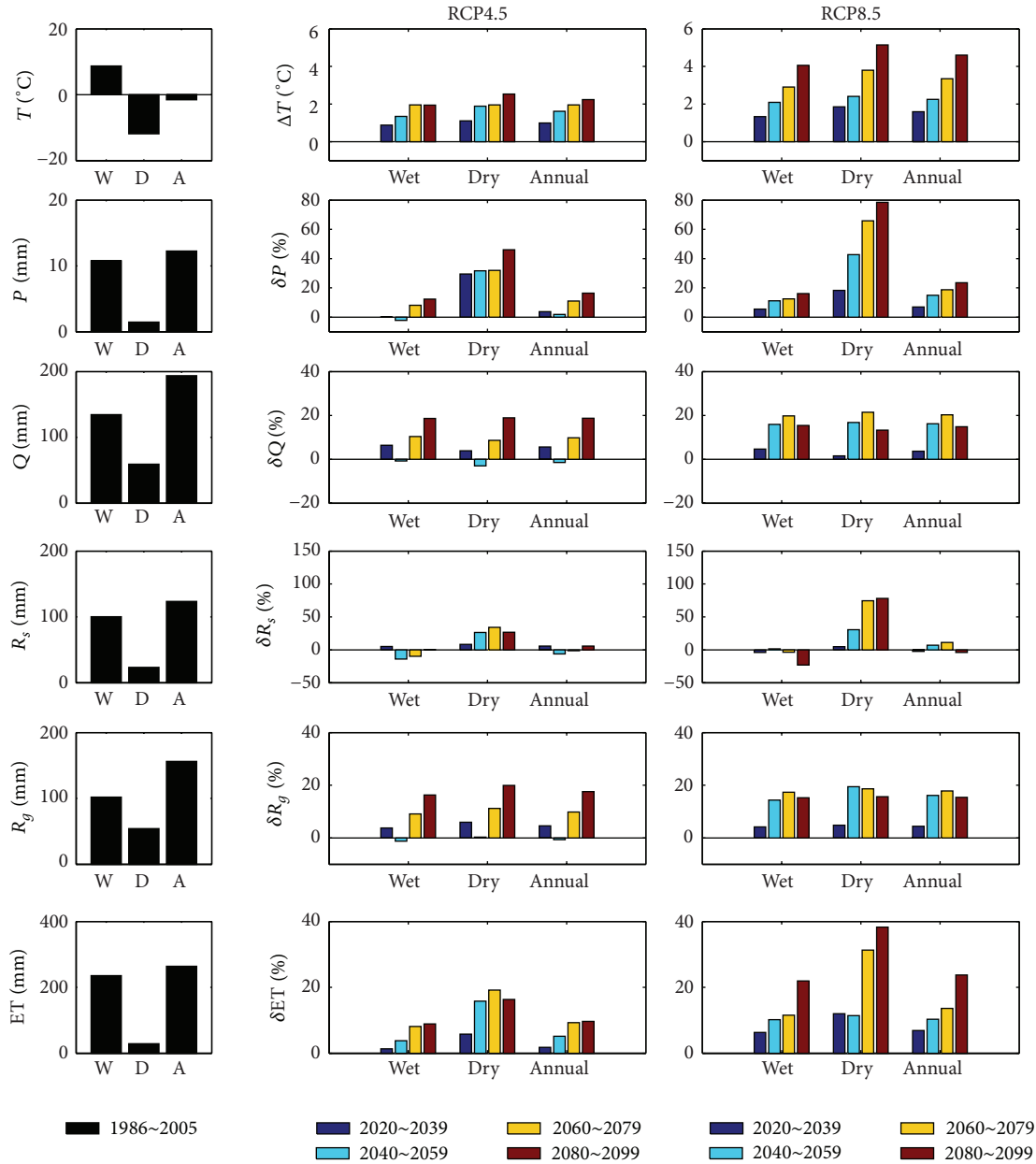


FIGURE 3: Summary of future climate inputs (P and T) and simulated hydrologic components (Q , R_s , R_g , and ET) under RCP4.5 and RCP8.5, compared to their values in the control period (1986~2005). All these hydrometeorologic factors are presented in terms of wet season, dry season, and annual values.

season under RCP8.5. The annual R_g changes by $-0.7\% \sim 17\%$ and $4\% \sim 18\%$ for RCP4.5 and RCP8.5, which is consistent with the changes of Q . ET increases continuously in the 21st century with average increases of $2\% \sim 10\%$ and $7\% \sim 24\%$ under RCP4.5 and RCP8.5.

4.3. Response of Hydrological Cycle to Climate Change. The response of the hydrological cycle to climate change is estimated by running the hydrological model forced by SCC. The responses of Q , R_s , R_g , and ET to climate change are demonstrated with response surfaces in Figure 4. Q is positively related to P and negatively related to T . The relationship

of δQ and δP is almost linear with the streamflow elasticity ($\delta Q/\delta P$) being about 1.0 when $\Delta T < 2^\circ\text{C}$; that is, a 1% change in the mean annual precipitation results in a 1% change in the mean annual streamflow. $\delta Q/\delta P$ is lower than that for other arid regions, for example, 2.0~3.5 for Australia [27]. The possible reasons are mentioned as follows: (1) the Kaidu River Basin, located in the south slope of the Tianshan Mountains with a high average altitude (2,995 m), is characterized by a cold climate (average annual temperature is -4.1°C for the Bayanbulak station) and accordingly there is a low amount of energy available for ET , which results in a relatively high runoff coefficient ($Q/P = 0.51$) and consequently a low

TABLE 2: Statistics of bias-corrected RCM outputs and SWAT simulated streamflows forced by the observed climate variables and bias-corrected RCM outputs.

Statistics	NS	PBIAS	R^2
"RCM simulated precipitation with bias correction" ^a			
Validation period 1990~2005 (daily) ^b	-0.57	-6.80%	0.00
Validation period 1990~2005 (monthly)	0.57	-6.80%	0.60
"RCM simulated maximum temperature with bias correction" ^a			
Validation period 1990~2005 (daily)	0.77	3.80%	0.80
Validation period 1990~2005 (monthly)	0.95	4.00%	0.90
"Streamflow simulated with observed meteorological data"			
Calibration period 1986~1989 (daily)	0.80	0.01%	0.80
First validation period 1990~2002 (daily)	0.81	2.94%	0.81
Second validation period 1986~2005 (monthly)	0.89	2.86%	0.90
"Streamflow simulated with bias-corrected RCM outputs"			
Validation period 1990~2002 (daily)	0.46	-6.98%	0.47
Validation period 1986~2005 (monthly)	0.62	-7.85%	0.63

^aBias correction methods used are quantile mapping for precipitation and distribution mapping for temperature [19].

^b"Daily" or "monthly" in the brackets means the time step used to calculate the statistics.

TABLE 3: RCM projected precipitation change (δP), temperature change (ΔT), and streamflow change (δQ) for the 21st century under RCP4.5 and RCP8.5 compared to the control period (1986~2005).

		2020~2039	2040~2059	2060~2079	2080~2099
RCP4.5	δP (%)	4.0	2.0	11.0	16.0
	ΔT ($^{\circ}\text{C}$)	1.0	1.6	2.0	2.2
	δQ (%)	6.0	-1.0	10.0	18.0
RCP8.5	δP (%)	7.0	15.0	19.0	24.0
	ΔT ($^{\circ}\text{C}$)	1.6	2.3	3.3	4.6
	δQ (%)	4.0	16.0	20.0	15.0

streamflow elasticity; (2) the streamflow is also influenced by temperature dominated snowmelt (snowfall accounts for about 17% of watershed precipitation), which reduces the dependence of streamflow on precipitation and therefore results in a low streamflow elasticity [27].

The response of Q to ΔT depends on the magnitude of ΔT . Q decreases slightly when $0 < \Delta T \leq 2.0^{\circ}\text{C}$ while it decreases dramatically when $\Delta T > 2.0^{\circ}\text{C}$ for both wet and dry seasons. For example, when $\Delta T = 2.0^{\circ}\text{C}$, a 40% precipitation increase results in an average value of Q being 240 mm (23% increase compared to the average streamflow of 194 mm) but when $\Delta T = 4.0^{\circ}\text{C}$, the same precipitation increase only generates an average Q of 180 mm (about 7% decrease) (Figure 4).

The responses of R_s , R_g , and ET to climate change are also demonstrated in Figure 4. For R_s , the responses of R_s to ΔT are quite different for the wet and dry seasons: the higher ΔT , the lower R_s for the wet season but the higher R_s for the dry season. Since R_s in the dry season only accounts for 13% of the annual R_s , the response of annual R_s is consistent with that of the wet season. For R_g , the responses of R_g to ΔT and δP are similar to the responses of Q due to the dominant role of groundwater recharge in water yield in the Kaidu River Basin. For ET, it is mainly influenced by ΔT with temperature sensitivity ($\delta\text{ET}/\Delta T$) being $7.3\%/^{\circ}\text{C}$. To verify this result, we firstly investigated basin-scale energy and water budget using

the Budyko method [28, 29]. It is shown that ET is mainly energy limited rather than water limited (average $\text{ET}/P = 0.67$ and $\text{PET}/P = 0.88$). Secondly, the high determinate coefficient $R^2 = 0.75$ (significant level is smaller than 0.01) between the mean annual T and ET also indicates that ET has a strong correlation with T . This is consistent with previous studies, which have shown that a significant variation in ET is expected to follow changes in air temperature [30, 31].

In addition, simulations with RCM outputs are shown in Figure 4 to analyze the differences between simulations of these two data sets. Two typical periods of RCM simulations are selected, that is, 2020~2039 under RCP4.5 and 2080~2099 under RCP8.5, to represent mild and intense climate change scenarios (shown as blue and red stars in Figure 4). It is indicated that the simulations of hydrological components with RCM outputs for 2020~2039 under RCP4.5 (mild climate change) are close to these of the nearby contour lines (simulations with SCC), which suggests that similar results of Q , R_s , R_g , and ET are obtained for RCM outputs and for SCC under mild climate change scenarios. However, for 2080~2099 under RCP8.5 with $\delta P = 24\%$ and $\Delta T = 4.6^{\circ}\text{C}$, the simulated values of Q , R_s , R_g , and ET deviate from the simulations of SCC. There are two possible reasons: (1) changes of other meteorological inputs, that is, solar radiation, wind speed, and humidity, are slightly smaller for

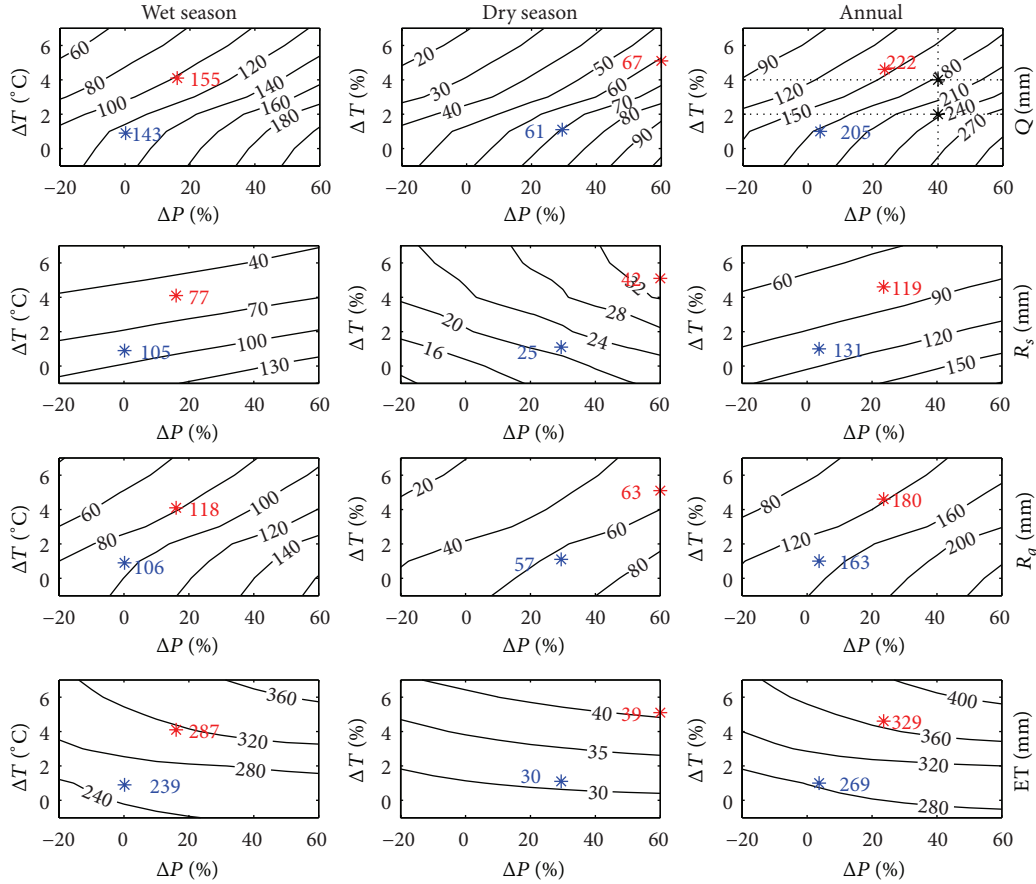


FIGURE 4: Response surfaces of streamflow (Q), surface runoff (R_s), subsurface runoff (R_g), and evapotranspiration (ET) to climate change. The simulations with RCM outputs for 2020~2039 under RCP4.5 and for 2080~2099 under RCP8.5 (their corresponding meteorological changes are listed in Table 3) are indicated using blue and red stars with labels.

2020~2039 under RCP4.5 than those for 2080~2099 under RCP8.5 (−0.8%, 2.6%, and 0.9% compared to −2.2%, 4.1%, and 1.4%); (2) for 2080~2099 under RCP8.5, precipitation increases by 24% with great seasonal variation, which may alter the hydrological regime; for example, precipitation increases by 139% for March, April, and May while it decreases by −0.1% for June, July, and August. Since changes of solar radiation, wind speed, and humidity are within $\pm 5\%$, the second reason, that is, the shift of the precipitation temporal distribution, contributes a lot to the deviation of simulations with RCM outputs from simulations with SCC.

Furthermore, the exceedance probability curves of the annual runoff in response to climate change are demonstrated in Figure 5. The exceedance probability curves are almost parallel when ΔT ranges in 0~6°C. However, the responses of Q to δP are not the same for each exceedance probability: high sensitivity of Q with probabilities less than 0.1 and low sensitivity of Q with probabilities larger than 0.9. A comparison of the simulations with RCM outputs (four future periods under RCP4.5 and RCP8.5) and with SCC (the same changes in T or P with the corresponding RCM outputs) indicates that differences between simulation with RCM outputs and SCC are becoming greater as climate change

gets more intense; for example, the simulation with RCM for 2080~2099 under RCP8.5 overestimates the corresponding simulations with SCC (Figure 5(h)), which collaborates the conclusion that under intense climate change scenarios the simulated hydrology with RCM deviates from that simulated with SCC.

The contributions of hydrologic components to water yield are displayed by the De Finetti diagram in Figure 6. For the control period, the averages of R_s , R_g , and ET are 0.22, 0.28, and 0.50. For SCC, as ΔT increases from 0 to 6°C, the contribution of ET increases rapidly from 0.49 to 0.73 and the contributions of R_s and R_g decrease from 0.22 to 0.11 and from 0.29 to 0.16. ΔT has a more significant influence on the proportion change than δP . As δP changes from −20% to 60%, ET decreases from 0.71 to 0.58 and R_s and R_g increase from 0.13 to 0.15 and from 0.16 to 0.27. For simulations with RCM outputs, proportions of hydrological components do not change significantly under RCP4.5, while the proportion of ET shows a significant increase under RCP8.5.

4.4. Sources of Uncertainty and Other Considerations. There are uncertainties in estimating climate change impact on hydrology. As indicated by previous studies [32], the sources

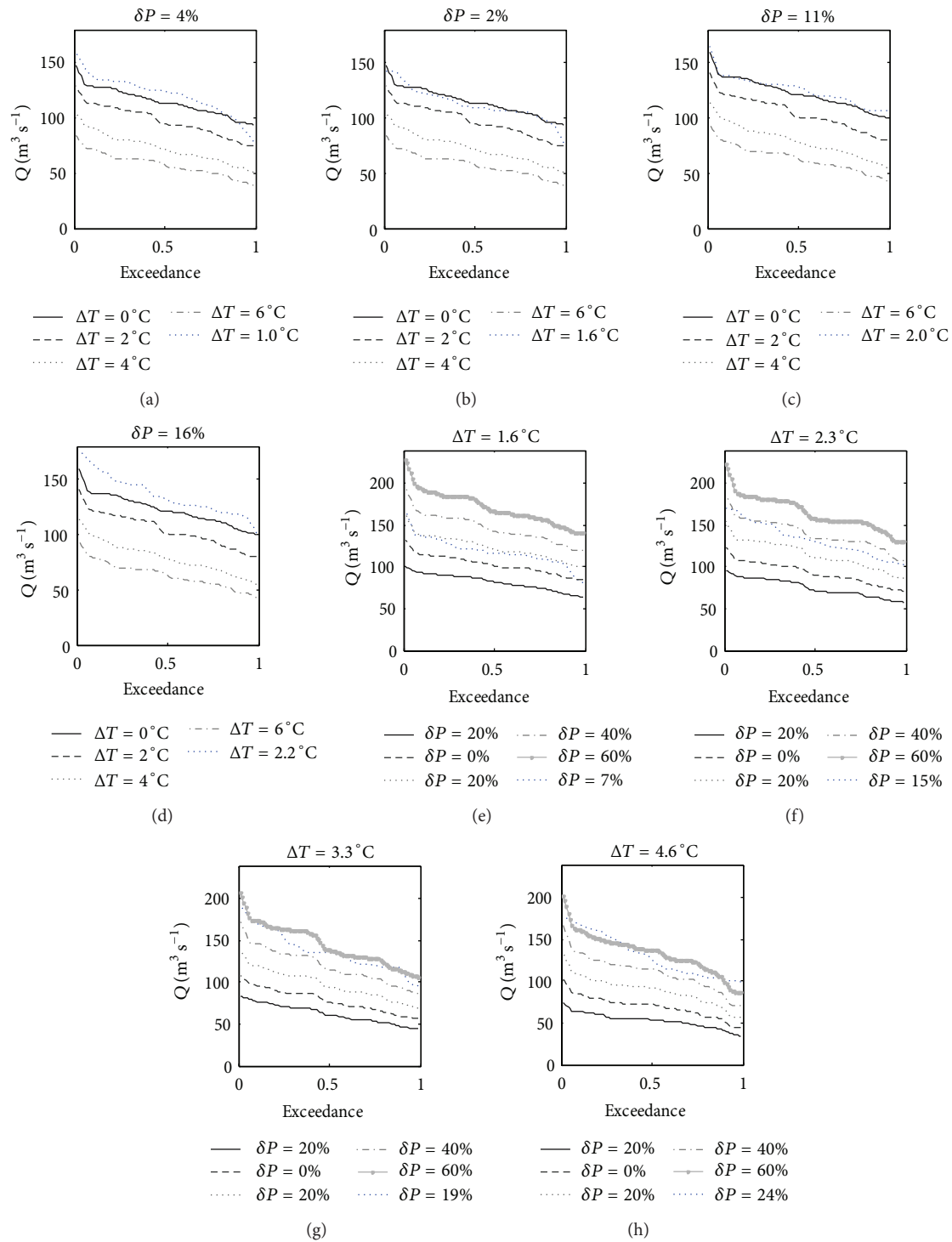


FIGURE 5: Exceedance probability curves of average annual streamflow (Q) in response to temperature change and precipitation change based on SCC with each plot either with fixed precipitation change (a~d) or with fixed temperature change (e~h). Dotted blue line in each plot denotes exceedance probability curves of average annual streamflow for the simulation with RCM outputs given fixed δP and ΔT as summarized in Table 3.

of uncertainty may rise from climate models, emission scenarios, downscaling, and the hydrological model.

For hydrological modeling itself, the effect of future climate in any specific catchment is difficult to project due to

the possibility that the hydrological system may not be stationary with complex feedbacks [33]. For example, the same land cover and soil data were used for both control period and future climate change period, which may not well represent

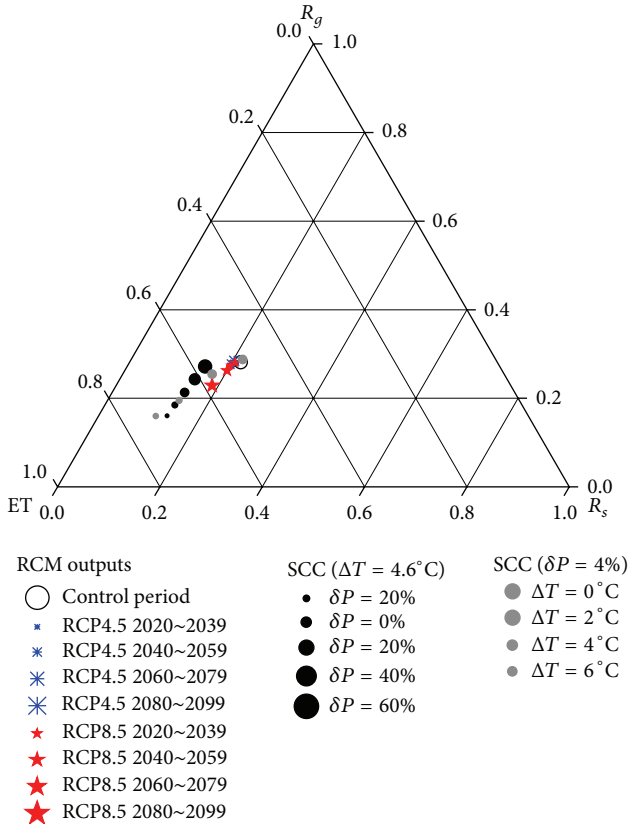


FIGURE 6: De Finetti diagram (ternary plot) of evapotranspiration (ET), surface runoff (R_s), and subsurface runoff (R_g) for SCC (shown as dots) and RCM outputs (shown as stars; for details of the projected changes in RCM outputs refer to Table 3).

the land surface under the future climate changes. Effects of land cover change on streamflows and other components of the hydrological cycle are not considered.

Though uncertainty in hydrologic modeling was quantified with the GLUE method, it only accounts for part of the total uncertainty in climate change impact studies [34]. Uncertainties associated with the climate model and downscaling were not considered here although two emission scenarios were included. Any uncertainty associated with them may cause the results to deviate from reality. However, we are dedicated to pursuing a thorough investigation of the response of the hydrological cycle to future climate change for this region and we believe this study is an important first step in achieving this goal.

5. Conclusions

This study assessed the implications of climate change on hydrology in a typical watershed in the Tianshan Mountains with two sets of climatic data, that is, RCM outputs and SCC, loosely coupled to a hydrological model (SWAT). Major conclusions can be summarized as follows:

- (1) The hydrological model shows excellent performance with “NS”s over 0.8 for the daily streamflow for both

calibration and validation periods. And the selected bias correction methods were effective in downscaling RCM outputs, with “NS”s being 0.57 and 0.95 regarding monthly precipitation and temperature.

- (2) T increases by $1.0^\circ\text{C}\sim 2.2^\circ\text{C}$ and by $1.6^\circ\text{C}\sim 4.6^\circ\text{C}$ under RCP4.5 and RCP8.5 in the 21st century. For P , it shows an overall increasing trend (2%~24%) with significant increase for the dry season (18%~78%) and relatively small change for the wet season (−2%~16%). The projected Q shows an overall increasing trend (−1%~18% and 4~20% for RCP4.5 and RCP8.5) in the 21st century.
- (3) Q increases almost linearly with P while the response of Q to T depends on the magnitude of ΔT and Q decreases significantly when ΔT is greater than 2°C .
- (4) Similar responses of Q , R_s , R_g , and ET to P and T are obtained for the RCM outputs and for SCC under mild climate change scenarios. However, for intense climate change scenarios, simulations of Q , R_s , R_g , and ET with RCM outputs (e.g., for 2080~2099 under RCP8.5) deviate from simulations with SCC.
- (5) ΔT has more significant influence on the proportion change of each hydrologic component than δP does. As ΔT increases from 0 to 6°C , the contribution of ET increases rapidly from 0.49 to 0.73 and R_s and R_g decrease by 0.11 and 0.13. As δP changes from −20% to 60%, ET , R_s , and R_g change by −0.13, 0.02, and 0.11 as a result.

It is valuable to quantify the future responses of hydrology to climate change in the Tianshan Mountains. This study will provide useful information for water resource management and will serve as a basis for further climate change impact studies.

Conflict of Interests

The authors declare that there is no conflict of interests regarding the publication of this paper.

Acknowledgments

Research was supported by the “Thousand Youth Talents Plan” (Xinjiang Project), the National Natural Science Foundation of China (41471030), and the Foundation of State Key Laboratory of Desert and Oasis Ecology (Y371163). The authors wish to thank Professor Xuejie Gao at the National Climate Center (China) for providing the outputs of the regional climate model used in this paper.

References

- [1] A. Sorg, T. Bolch, M. Stoffel, O. Solomina, and M. Beniston, “Climate change impacts on glaciers and runoff in Tien Shan (Central Asia),” *Nature Climate Change*, vol. 2, no. 10, pp. 725–731, 2012.
- [2] Z. Liu, Z. Xu, J. Huang, S. P. Charles, and G. Fu, “Impacts of climate change on hydrological processes in the headwater

- catchment of the Tarim River basin, China,” *Hydrological Processes*, vol. 24, no. 2, pp. 196–208, 2010.
- [3] Z. Li, Y. Chen, Y. Shen, Y. Liu, and S. Zhang, “Analysis of changing pan evaporation in the arid region of Northwest China,” *Water Resources Research*, vol. 49, no. 4, pp. 2205–2212, 2013.
 - [4] Y. Shi, Y. Shen, E. Kang et al., “Recent and future climate change in Northwest China,” *Climatic Change*, vol. 80, no. 3–4, pp. 379–393, 2007.
 - [5] S. Wang, M. Zhang, Z. Li et al., “Glacier area variation and climate change in the Chinese Tianshan Mountains since 1960,” *Journal of Geographical Sciences*, vol. 21, no. 2, pp. 263–273, 2011.
 - [6] B. Li, Y. Chen, and X. Shi, “Why does the temperature rise faster in the arid region of northwest China?” *Journal of Geophysical Research D: Atmospheres*, vol. 117, no. 16, Article ID D16115, 2012.
 - [7] V. B. Aizen, E. M. Aizen, J. M. Melack, and J. Dozier, “Climatic and hydrologic changes in the Tien Shan, central Asia,” *Journal of Climate*, vol. 10, no. 6, pp. 1393–1404, 1997.
 - [8] B. Ye, D. Yang, K. Jiao et al., “The Urumqi River source Glacier No. 1, Tianshan, China: changes over the past 45 years,” *Geophysical Research Letters*, vol. 32, no. 21, Article ID L21504, 2005.
 - [9] H. Wang, Y. Chen, W. Li, and H. Deng, “Runoff responses to climate change in arid region of northwestern China during 1960–2010,” *Chinese Geographical Science*, vol. 23, no. 3, pp. 286–300, 2013.
 - [10] T. Liu, P. Willems, X. L. Pan et al., “Climate change impact on water resource extremes in a headwater region of the Tarim basin in China,” *Hydrology and Earth System Sciences*, vol. 15, no. 11, pp. 3511–3527, 2011.
 - [11] J. G. Arnold, R. Srinivasan, R. S. Muttiah, and J. R. Williams, “Large area hydrologic modeling and assessment part I: model development,” *Journal of the American Water Resources Association*, vol. 34, no. 1, pp. 73–89, 1998.
 - [12] Y. Chen and Q. Du, *Sustainable Water Use in the Bosten Lake Basin*, Science Press, Beijing, China, 2013.
 - [13] F. Giorgi and L. O. Mearns, “Introduction to special section: regional climate modeling revisited,” *Journal of Geophysical Research*, vol. 104, no. D6, pp. 6335–6352, 1999.
 - [14] T. Wu, W. Li, J. Ji et al., “Global carbon budgets simulated by the Beijing climate center climate system model for the last century,” *Journal of Geophysical Research D: Atmospheres*, vol. 118, no. 10, pp. 4326–4347, 2013.
 - [15] X. Xin, T. Wu, J. Li et al., “How well does BCC_CSM1.1 reproduce the 20th Century climate change over China?” *Atmospheric and Oceanic Science Letters*, vol. 6, pp. 21–26, 2013.
 - [16] D. P. van Vuuren, J. Edmonds, M. Kainuma et al., “The representative concentration pathways: an overview,” *Climatic Change*, vol. 109, no. 1, pp. 5–31, 2011.
 - [17] H. Kawase, T. Nagashima, K. Sudo, and T. Nozawa, “Future changes in tropospheric ozone under Representative Concentration Pathways (RCPs),” *Geophysical Research Letters*, vol. 38, no. 5, 2011.
 - [18] X. Gao, M. Wang, and F. Giorgi, “Climate change over China in the 21st century as simulated by BCC_CSM1.1-RegCM4.0,” *Atmospheric and Oceanic Science Letters*, vol. 6, pp. 381–386, 2013.
 - [19] G. H. Fang, J. Yang, Y. N. Chen, and C. Zammit, “Comparing bias correction methods in downscaling meteorological variables for hydrologic impact study in an arid area in China,” *Hydrology and Earth System Sciences Discussions*, vol. 11, no. 11, pp. 12659–12696, 2014.
 - [20] Soil Conservation Service, “Urban hydrology for small watershed,” Technical Release 55, U.S. Department of Agriculture, 1968.
 - [21] G. Fang, J. Yang, Y. Chen, C. Xu, and P. de Maeyer, “Contribution of meteorological input in calibrating a distributed hydrologic model in a watershed in the Tianshan Mountains, China,” *Environmental Earth Sciences*, 2015.
 - [22] D. N. Moriasi, J. G. Arnold, M. W. van Liew, R. L. Bingner, R. D. Harmel, and T. L. Veith, “Model evaluation guidelines for systematic quantification of accuracy in watershed simulations,” *Transactions of the ASABE*, vol. 50, no. 3, pp. 885–900, 2007.
 - [23] K. Beven and A. Binley, “The future of distributed models: model calibration and uncertainty prediction,” *Hydrological Processes*, vol. 6, no. 3, pp. 279–298, 1992.
 - [24] J. Yang, P. Reichert, K. C. Abbaspour, J. Xia, and H. Yang, “Comparing uncertainty analysis techniques for a SWAT application to the Chaohe Basin in China,” *Journal of Hydrology*, vol. 358, no. 1–2, pp. 1–23, 2008.
 - [25] N. S. Christensen and D. P. Lettenmaier, “A multimodel ensemble approach to assessment of climate change impacts on the hydrology and water resources of the Colorado River Basin,” *Hydrology and Earth System Sciences*, vol. 11, no. 4, pp. 1417–1434, 2007.
 - [26] M. Masood, P. J. Yeh, N. Hanasaki, and K. Takeuchi, “Model study of the impacts of future climate change on the hydrology of Ganges–Brahmaputra–Meghna basin,” *Hydrology and Earth System Sciences*, vol. 19, no. 2, pp. 747–770, 2015.
 - [27] F. H. S. Chiew, “Estimation of rainfall elasticity of streamflow in Australia,” *Hydrological Sciences Journal*, vol. 51, no. 4, pp. 613–625, 2006.
 - [28] J. A. Jones, I. F. Creed, K. L. Hatcher et al., “Ecosystem processes and human influences regulate streamflow response to climate change at long-term ecological research sites,” *BioScience*, vol. 62, no. 4, pp. 390–404, 2012.
 - [29] M. I. Budyko, *Climate and Life*, Academic Press, New York, NY, USA, 1974.
 - [30] K. C. Abbaspour, M. Faramarzi, S. S. Ghasemi, and H. Yang, “Assessing the impact of climate change on water resources in Iran,” *Water Resources Research*, vol. 45, no. 10, 2009.
 - [31] S. G. Setegn, D. Rayner, A. M. Melesse, B. Dargahi, and R. Srinivasan, “Impact of climate change on the hydroclimatology of Lake Tana Basin, Ethiopia,” *Water Resources Research*, vol. 47, no. 4, Article ID W04511, 2011.
 - [32] S. Hagemann, C. Chen, D. B. Clark et al., “Climate change impact on available water resources obtained using multiple global climate and hydrology models,” *Earth System Dynamics*, vol. 4, no. 1, pp. 129–144, 2013.
 - [33] R. P. Silberstein, S. K. Aryal, J. Durrant et al., “Climate change and runoff in south-western Australia,” *Journal of Hydrology*, vol. 475, pp. 441–455, 2012.
 - [34] D. G. Kingston and R. G. Taylor, “Sources of uncertainty in climate change impacts on river discharge and groundwater in a headwater catchment of the Upper Nile Basin, Uganda,” *Hydrology and Earth System Sciences*, vol. 14, no. 7, pp. 1297–1308, 2010.

Research Article

Hydrologic Responses to Land Use Change in the Loess Plateau: Case Study in the Upper Fenhe River Watershed

Zhixiang Lu,^{1,2} Songbing Zou,¹ Zuodong Qin,³ Yonggang Yang,³
Honglang Xiao,¹ Yongping Wei,⁴ Kai Zhang,⁵ and Jiali Xie⁶

¹Key Laboratory of Ecohydrology of Inland River Basin, Cold and Arid Regions Environmental and Engineering Research Institute, Chinese Academy of Science, Lanzhou 730000, China

²University of the Chinese Academy of Science, Beijing 100049, China

³Institute of Loess Plateau, Shanxi University, Taiyuan 030006, China

⁴The Australia China Centre on Water Resources Research, University of Melbourne, Parkville, VIC 3010, Australia

⁵School of Soil and Water Conservation, Beijing Forestry University, Beijing 100083, China

⁶Key Laboratory of Desert and Desertification, Cold and Arid Regions Environmental and Engineering Research Institute, Chinese Academy of Science, Lanzhou 730000, China

Correspondence should be addressed to Songbing Zou; zousongbing@lzb.ac.cn

Received 20 November 2014; Revised 12 March 2015; Accepted 16 March 2015

Academic Editor: Yongqiang Zhang

Copyright © 2015 Zhixiang Lu et al. This is an open access article distributed under the Creative Commons Attribution License, which permits unrestricted use, distribution, and reproduction in any medium, provided the original work is properly cited.

We applied an integrated approach to investigate the impacts of land use and land cover (LULC) changes on hydrology at different scales in the Loess Plateau of China. Hydrological modeling was conducted for the LULC maps from remote sensing images at two times in the Upper Fenhe River watershed using the SWAT model. The main LULC changes in this watershed from 1995 to 2010 were the transformation of farmland into forests, grassland, and built-up land. The simulation results showed that forested land contributed more than any other LULC class to water yield, but built-up land had most impact due to small initial loss and infiltration. At basin scale, a comparison of the simulated hydrological components of two LULC maps showed that there were slight increases in average annual potential evapotranspiration, actual evapotranspiration, and water yield, but soil water decreased, between the two intervals. In subbasins, obvious LULC changes did not have clear impacts on hydrology, and the impacts may be affected by precipitation conditions. By linking a hydrological model to remote sensing image analysis, our approach of quantifying the impacts of LULC changes on hydrology at different scales provide quantitative information for stakeholders in making decisions for land and water resource management.

1. Introduction

Changing land use represents the greatest human impact on the surface of the earth, and between one-third and one-half has been altered over the last 300 years [1–3]. Land use directly impacts the hydrologic components of a watershed, such as evapotranspiration, surface runoff, groundwater recharge, and streamflow [4–7]. Many previous studies from around the world have demonstrated that land use significantly impacts hydrological processes [8–15]. For example, Ghaffari et al. (2010) found that a 34.5% decrease of grassland with increases of shrubland (13.9%) and rain-fed agriculture

(12.1%) led to a 33% increase in the amount of surface runoff and a 22% decrease in the groundwater recharge in northwest Iran [8]. Nie et al. (2011) revealed the effects of urbanization and agricultural development on the runoff in North America [9], and Wang et al. (2014), Li et al. (2015), and Yao et al. (2015) revealed the effects of urbanization, land use patterns, and changes on the runoff, temperature, evapotranspiration, and surface climate in Chinese landscapes [10–12]. López-Vicente et al. (2013) and Ohana-Levi et al. (2015) modeled the effects of land use change on the runoff and sediment yield in Europe's Pyrenees and rainfall-runoff relationships in an Eastern Mediterranean watershed, respectively [13, 14].

Wang et al. (2014) assessed the impacts of land use changes on evapotranspiration, quickflow, infiltration, and baseflow in the upstream regions of the Three Gorges reservoir in China [15]. Assessing impacts of land use and land cover (LULC) changes on hydrology is essential for watershed management and ecological restoration [7, 15, 16].

In general, regional impacts of land use change on hydrology vary from place to place and need to be considered for specific circumstances and environments [15, 16]. The Loess Plateau of western China is infamous for serious soil erosion and is the main source of sediment in the middle reaches of the Yellow River and has become the focus of world attention. As early as the 1950s, China started soil and water conservation works on the Loess Plateau in order to improve the local environment and mitigate sediment accessions to the middle reaches of the Yellow River, and works were expanded after the 1970s [17, 18]. As a consequence, land use in the Loess Plateau has undergone great changes. Likewise, in the past century, a range of management measures were carried out in the Fenhe River Basin on the eastern margin of the Loess Plateau. Some research has been done on the impacts of land use change on basin hydrology [19–22], but research on the contribution of individual LULC to the total runoff and the impacts of LULC changes on watershed hydrology is lacking. In particular, there is a lack of information for evaluating the benefits of soil and water conservation in the Fenhe River basin and the whole of the Loess Plateau, where it is difficult to distinguish the impacts of LULC changes on hydrology. Greater understanding of the contribution of individual LULC change to runoff and the impacts of LULC changes on the hydrology at different scales is needed to guide comprehensive natural resources management in this region.

Methods for assessing hydrological impacts of land use changes in watersheds include comparisons of paired catchments, statistical analysis, and hydrological modeling [5, 23, 24]. Among these approaches, hydrological modeling is the most suitable one for use in scenario studies at different scales. Widely used hydrological models in studies on the impacts on watershed hydrology include the Hydrologic Simulation Program, FORTRAN, the Soil and Water Assessment Tool (SWAT), and WaTEM/SEDEM [4, 5, 9, 15]. The SWAT model is widely used to assess hydrology and water quality in agricultural catchments around the world (https://www.card.iastate.edu/swat_articles/). It is readily available and user-friendly for data input [25].

The overall objectives of this study are to investigate the contributions of individual LULC change to runoff and to determine the impacts of LULC changes on the hydrology of the Upper Fenhe River watershed by an integrated approach that combines hydrological modeling and remotely sensed digital maps of LULC changes. To avoid the impacts of large-scale water resource development projects on hydrological processes, particularly the water diversion project from the Yellow River to Fenhe River at Wanjiazhai in the study area after 2002, the period from 1990 to 2000 was selected as the study period, during which sufficient data are available. The specific objectives are (1) to investigate the LULC changes of the watershed from 1995 to 2010 with LULC maps determined

by remote sensing images in 1995 and 2010; (2) to calibrate and validate the SWAT model in terms of monthly streamflow based on the DEM, soil map, land use in 1995, and climate data from 1990 to 2000; (3) to assess the hydrological effects of individual land uses, and (4) to simulate responses of hydrologic components to land use changes at basin and subbasin scales under the same climatic conditions. The results should assist decision-makers in target water resources planning and vegetation restoration on the Loess Plateau.

2. Study Area

The Fenhe River is located in the eastern part of the Loess Plateau, North China, and runs north to south through almost all of Shanxi Province [26]. The study area is the Upper Fenhe River watershed above the Hecha hydrological control station, which measures the amount of water and sediment entering Fenhe reservoir (Figure 1). The Upper Fenhe River watershed has an area of about 3242 km² and lies between latitudes 38°00' and 39°00' and longitudes 111°40' and 112°40'. Elevations in the basin range from 1,124 to 2,762 m and it has an arid to semiarid climate with a mean annual precipitation of 430 mm. The precipitation is concentrated between the months of June and September and accounts for approximately 70% of total annual precipitation, coming in the form of high-intensity storms that often cause extreme soil erosion. The average annual temperature is 9.0°C, with a minimum average temperature of −5°C in winter and a maximum average temperature of 20°C in summer. The land use classes of the watershed include farmland, forest, grassland, water or wetland, built-up land, and unused land; their percentages in 2010 were 30%, 28.3%, 39.57%, 1.39%, 0.73%, and 0.01%, respectively. The region is covered with highly erodible loess-derived soils. Major soil series include loess soil, cinnamon soil, brown soil, and calcium skeletal soil.

3. Methodology

A conceptual framework consisting of three stages was developed (Figure 2): (1) transition matrix analysis to describe the transformations of land use from 1995 to 2010; (2) hydrological modeling to simulate hydrological components for two LULC maps under the same climatic conditions; and (3) comparison of the contribution of each land use class to the watershed's water yield and their hydrological effects on subbasins.

3.1. Transition Matrix. The transition matrix of land use change was calculated as

$$B_{ij} = \begin{bmatrix} B_{11} & B_{12} & \cdots & B_{1n} \\ B_{21} & B_{22} & \cdots & B_{2n} \\ \vdots & \vdots & \cdots & \vdots \\ B_{n1} & B_{n2} & \cdots & B_{nn} \end{bmatrix}, \quad (1)$$

where B is the area of a certain kind of land use, n is the number of land use types in the study area, i and j ($i, j = 1, 2, \dots, n$) are the types of the land use before and after

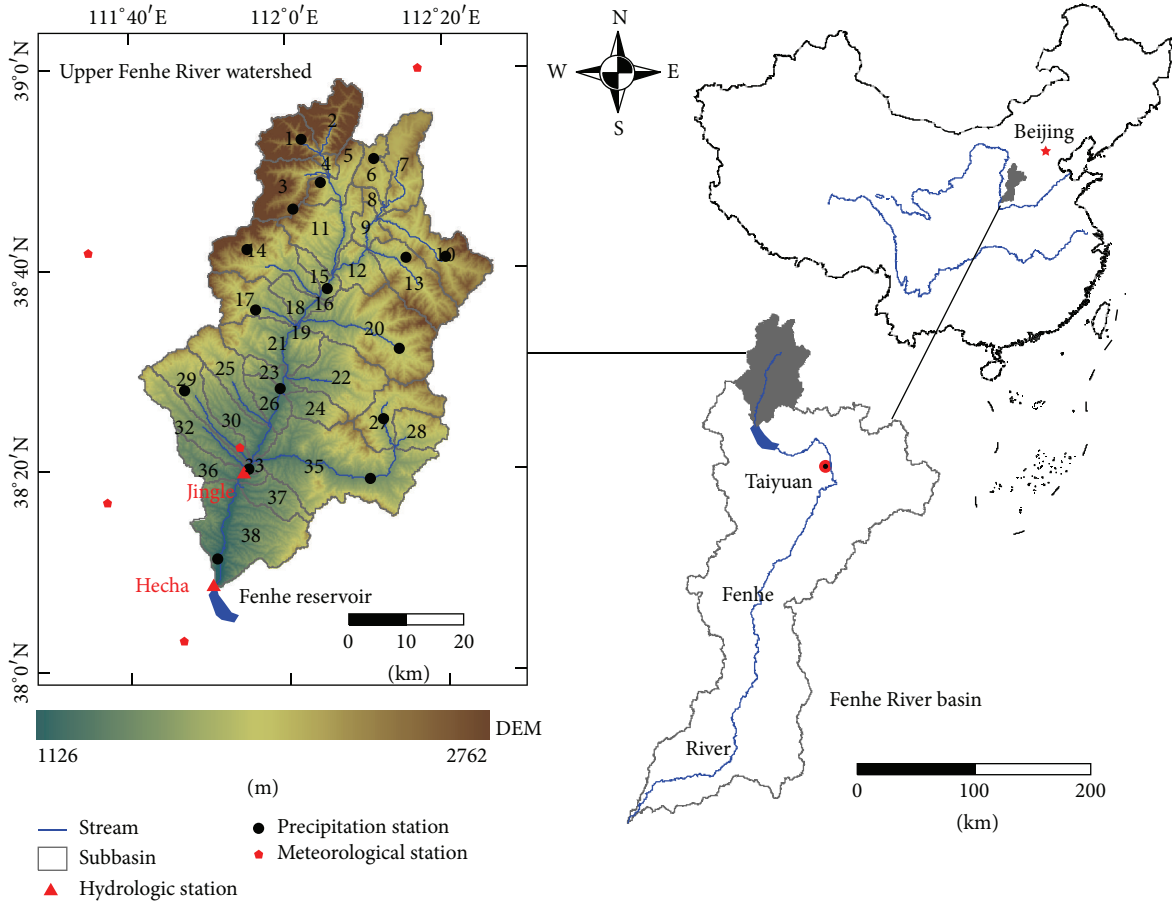


FIGURE 1: Locations of study area, hydrologic stations, and meteorological stations.

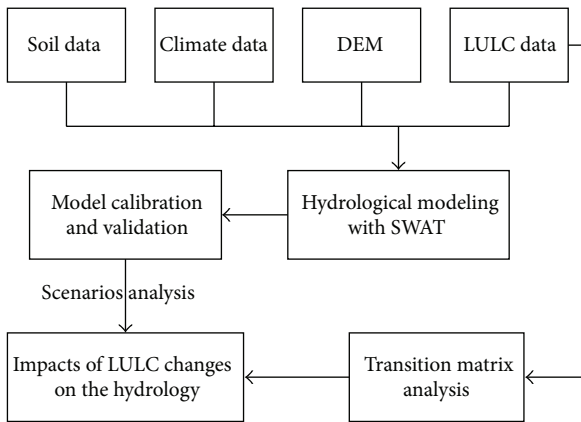


FIGURE 2: The conceptual framework for analyzing the impacts of LULC changes on the hydrology.

transition, respectively, and B_{ij} is area of the land use i turned into the land use j . The study period was defined as 1995 to 2010 because soil and water conservation practices were first implemented from 1988 to 1997, and a second ten-year conservation project was carried out from 1998 to 2007 [19, 20, 27]. The LULC maps in 1995 and 2010 represent the surface cover conditions in the latter part of the first

conservation project and after the projects, respectively. The LULC map for 1995 was used as input data to calibrate the model.

3.2. Hydrological Modeling

3.2.1. SWAT Model Description. The SWAT 2005 model [28] was applied to data of the Upper Fenhe River watershed to assess the impacts of LULC changes on hydrological components. The SWAT model is a continuous, long-term, physically based distributed model developed to assess impacts of climate and land management on hydrological components, sediment loading, and pollution transport in watersheds [25]. In the SWAT model, a watershed is divided into subbasins. Subbasins are further divided into a series of uniform hydrological response units (HRUs) based on slope, soil, and LULC changes. Hydrological components, sediment yield, and nutrient cycles are simulated for each HRU and then aggregated for the subbasins.

Hydrological components simulated by the SWAT model include evapotranspiration (ET), surface runoff, percolation, lateral flow, groundwater flow (return flow), and transmission losses [25]. Evaporation and transpiration are simulated using exponential functions of soil depth and water content and a linear function of potential evapotranspiration (PET) and

TABLE 1: Hydrometeorological stations in the study area.

Types of stations	Name	Factors	Data series
Hydrological stations	Jingle, Hecha	Monthly streamflow	1990–2000
Precipitation stations	Baergou, Haizibei, Dongzhai, Qianmalong, Gedongzi, Huaidao, Dongmafang, Ninghuabao, Xinbao, Tanger, Duanjiazhai, Ximafang, Suopo, Jingle, Kangjiahui, and Hecha	Daily precipitation	1990–2000
Meteorological stations	Ningwu, Kelan, and Jingle	Daily precipitation and maximum and minimum air temperature	1990–2000

leaf area index. Hargreaves method was used to estimate PET, which was originally derived from eight years of cool-season *Alta fescue* grass lysimeter data from Davis, California [29], and its reference crop is similar to grassland which is the dominant land use type in this watershed. The surface runoff is estimated using a modification of the SCS curve number method with daily rainfall amounts. Percolation is calculated using the combination of a storage routing technique and a crack flow model. The lateral flow is estimated simultaneously with percolation using a kinematic storage model. The groundwater flow (baseflow) into the channel is calculated from hydraulic conductivity of the shallow aquifer, distance from subbasin to main channel, and water table height.

3.2.2. SWAT Model Inputs and Outputs. The input data used in the SWAT model included a digital elevation model (DEM), soil data, digital LULC maps, and climate data. The DEM was derived from the USGS National Elevation Dataset with a resolution of about 90 m, and the soil data were obtained from the Resources and Environment Science Data Center, Chinese Academy of Sciences, with the scale of 1:1,000,000. The LULC data for two times (1995 and 2010) were used to assess the impacts of LULC change on hydrology and were derived from Landsat TM images with a spatial resolution of 30 m using an interpretation method. The climate data, including daily values of precipitation and minimum-maximum temperature from January 1st, 1990, to December 31, 2000, were derived from 3 meteorological stations and 16 precipitation stations located in and around the Upper Fenhe River watershed (Table 1).

The outputs of the SWAT model used in this study were hydrological components, including precipitation (P), PET, actual evapotranspiration (AET), water yield (WY), and soil water (SW).

3.2.3. SWAT Model Calibration and Validation. Simulations using the 1995 LULC map were used to calibrate monthly streamflows from January 1992 to December 1995 at two hydrological stations (Jingle and Hecha, Figure 1). After model calibration, simulations with the same model parameters and LULC map data were used to validate monthly streamflow from January 1996 to December 2000 (Table 2).

3.2.4. Performance Evaluation Criteria. The model was calibrated manually and three criteria were used to evaluate

TABLE 2: The warm-up, calibration, and validation period for the model.

Periods	Warm-up period	Calibration period	Validation period
Time series	1990-1991	1992–1995	1996–2000

performance of model calibration and validation. The Nash-Sutcliffe efficiency (NSE) is a normalized statistic that determines the relative magnitude of the residual variance compared to the measured data variance. NSE indicates how well the plot of observed versus simulated data fits the 1:1 line. Coefficient of determination (R^2) describes the degree of colinearity between simulated and measured data and the proportion of the variance in the measured data explained by the model. Percent bias (PBIAS) measures the average tendency of the simulated data to be larger or smaller than their observed counterparts [29]. The calibration and validation performance for the SWAT model were considered acceptable when R^2 and NSE were greater than 0.5. The SWAT model performance is satisfactory when NSE is larger than 0.5, adequate when NSE ranges from 0.54 to 0.65, and very good when NSE is larger than 0.65. The SWAT model is rated as satisfactory, when the absolute value of PBIAS ranges from 15 to 25, rated good when from 10 to 15, and very good when smaller than 10 [30].

3.3. Analyzing Hydrological Effects of Land Use Classes. The calibrated and validated hydrological model was run for each of the LULC maps (1995 and 2010) with constant DEM and soil data, from January 1990 to December 2000 (11 years), to quantify contributions of individual LULC classes to the total discharge and to evaluate impacts of LULC changes on hydrology at the basin and subbasin scales.

4. Results and Discussion

4.1. LULC Changes. The LULC maps of the Upper Fenhe River watershed in 1995 and 2010 are shown in Figure 3. Grassland, farmland, and forest were the main land use classes in the Upper Fenhe River watershed.

The results of the transition matrix of LULC changes between 1995 and 2010 are shown in Table 3. The transformations among farmland, forest, and grassland were the main

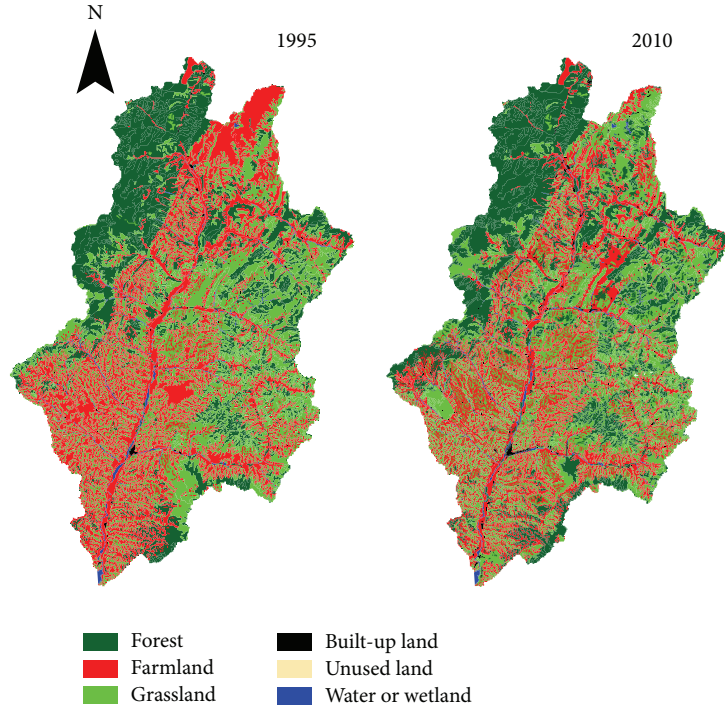


FIGURE 3: Maps for land uses and land cover in 1995 and 2010 in the Upper Fenhe River watershed.

TABLE 3: Transition matrix of land uses from 1995 to 2010 (km²).

Types	2010						Total
	Farmland	Forest	Grassland	Water or Wetland	Built-up land	Unused land	
1995 Farmland	908.26	17.74	79.66	1.13	6.99	0.29	1014.07
Forest	9.68	840.49	45.88	0.48	0.82	0.02	897.37
Grassland	54.04	59.11	1157.32	0.09	2.07	0.08	1272.71
Water or wetland	0.95	0.06	0.11	43.32	0.24	0.00	44.68
Built-up land	0.03	0.04	0.01	0.00	13.44	0.00	13.52
Unused land	0.00	0.00	0.00	0.00	0.00	0.00	0.00
Total	972.96	917.44	1282.98	45.02	23.56	0.39	3242.35

forms of land use changes in the Upper Fenhe watershed; the area of forest and grassland increased and the area of farmland decreased. Farmland showed the largest change. It was transformed into grassland in the northern part of the watershed due to the implementation of the “grain for green” government conservation program that compensated farmers for converting arable land to grassland. Meanwhile, due to the social development, the area of built-up land increased markedly at the expense of farmland. Finally, a tiny proportion of it was changed into water or wetland and unused land. In the southeast, a part of the watershed grassland was turned into farmland. Overall, the vegetation cover increased from 1995 to 2010, during periods of increased soil and water conservation measures.

4.2. *Model Calibration and Validation.* Parameter sensitivity analysis was carried out using the model parameters identified from the instructions for the calibration of the SWAT

model, as given in the user’s manual [29]. The model was calibrated with a comprehensive model calibration method [30]. The results of sensitivity analysis for the Upper Fenhe River watershed and the value of the parameters are shown in Table 4.

Comparisons between simulated and observed monthly streamflow values in the periods of calibration and validation are shown in Figure 4. Good matches were shown between simulated and observed values, except in 1997 and 2000. In these two years, the simulated runoff was overestimated for both Jingle and Hecha. For 1997, this may be because the water stored in the watershed in two consecutive wet years (1995 and 1996) was released in the subsequent year. For 2000, the overestimation may have happened because 1999 was an extremely dry year, and water bodies such as small swamps and lakes were dry, and the soil was also very dry. This was followed by heavy rain in 2000 that firstly wetted the soil, filled the dry water bodies, and did not form surface

TABLE 4: The results of parameter sensitivity analysis and calibration.

Parameter	Definition	Hydrologic process or variable affected	Rank	Value
Alpha_Bf	Baseflow recession constant	Baseflow	1	0.084
Cn2	Moisture condition curve number	Surface runoff	2	30~92
Ch_K2	Effective hydraulic conductivity in main channel alluvium (mm/h)	Concentration of channel	3	10
Esco	Soil evaporation compensation factor	Soil water and soil evaporation	4	0.6
Sol_K	Saturated hydraulic conductivity of first layer (mm/h)	Infiltration and soil water	5	0~2000
Sol_Z	Depth from soil surface to bottom of layer (mm)	Soil water	6	0~3500
Canmx	Maximum canopy storage (mm)	Interception	7	0~10
Sol_Awc	Available soil water capacity (mm/mm)	Soil water	8	0.0125~0.5

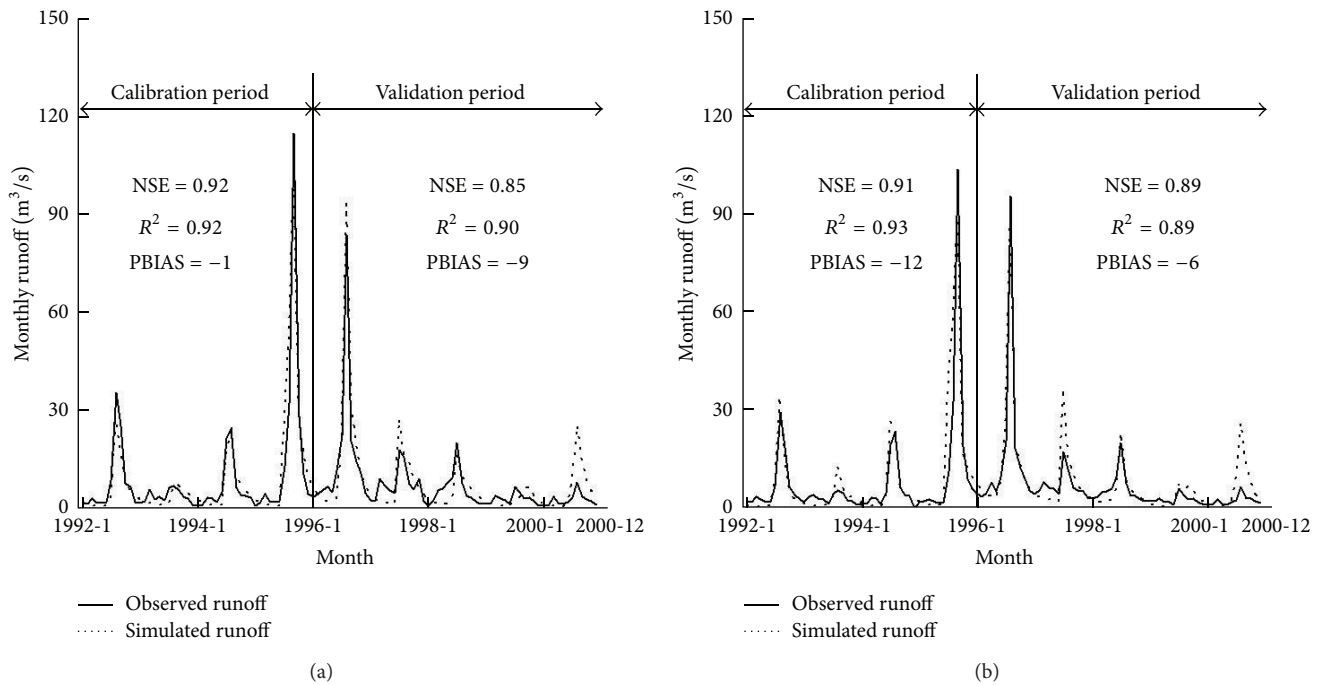


FIGURE 4: Monthly simulated and observed runoff in the Upper Fenhe River watershed. ((a) Hecha station; (b) Jingle station.)

runoff. This study did not take into account impounding of water in small water bodies which could have resulted in the overestimation of the actual runoff in 2000.

All NSE and R^2 values for the monthly calibration and validation were above 0.80, and PBIAS values were in the range of -15% to 0 (most PBIAS values were in the range of -10% to 0), suggesting very good model performance [30]. The overall performance of the model was very good as shown in Figure 4.

4.3. Contribution of Individual LULC Changes to Watershed Water Yield. The proportional contributions of five LULC changes (i.e., farmland, forest, grassland, water or wetland, and built-up land) and simulated water yield (WY) are shown in Figure 5. Grassland, farmland, and forest were the main LULC changes in the Upper Fenhe River watershed, and the sum of their areas accounted for 98% of the total area. Their contributions to water yield were up to about 98% but there was no obvious positive correlation between the area of individual LULC changes and their proportional

contributions to watershed WY. The grassland class includes mainly moderately dense and sparse grassland and very little dense grassland, so its water-yielding capacity was large. Although the area of forested land was much less than that of the grassland, its contribution to watershed WY was slightly more than the grassland's, because forests in this watershed are mainly shrubs and sparse trees. In addition, the rain mostly came in the form of high-intensity storms, which could reduce the amount of canopy interception compared with light rain. This is similar to the results obtained by Hao et al. (2004) in the upper Luohe River watershed and Song and Ma (2008) in the Nanhe River basin in the Longxi Loess Plateau [6, 7]. The area of farmland was between that for forests and grasslands, but its water-yielding capacity was much less. The farmland in the Upper Fenhe River watershed is terraced and used to grow close and straight row-seeded wheat and maize which greatly reduce the water yield.

By comparing the percentages of the area of each land use type and their contribution to water yield, it was found that an increase of built-up land was the main cause of increases

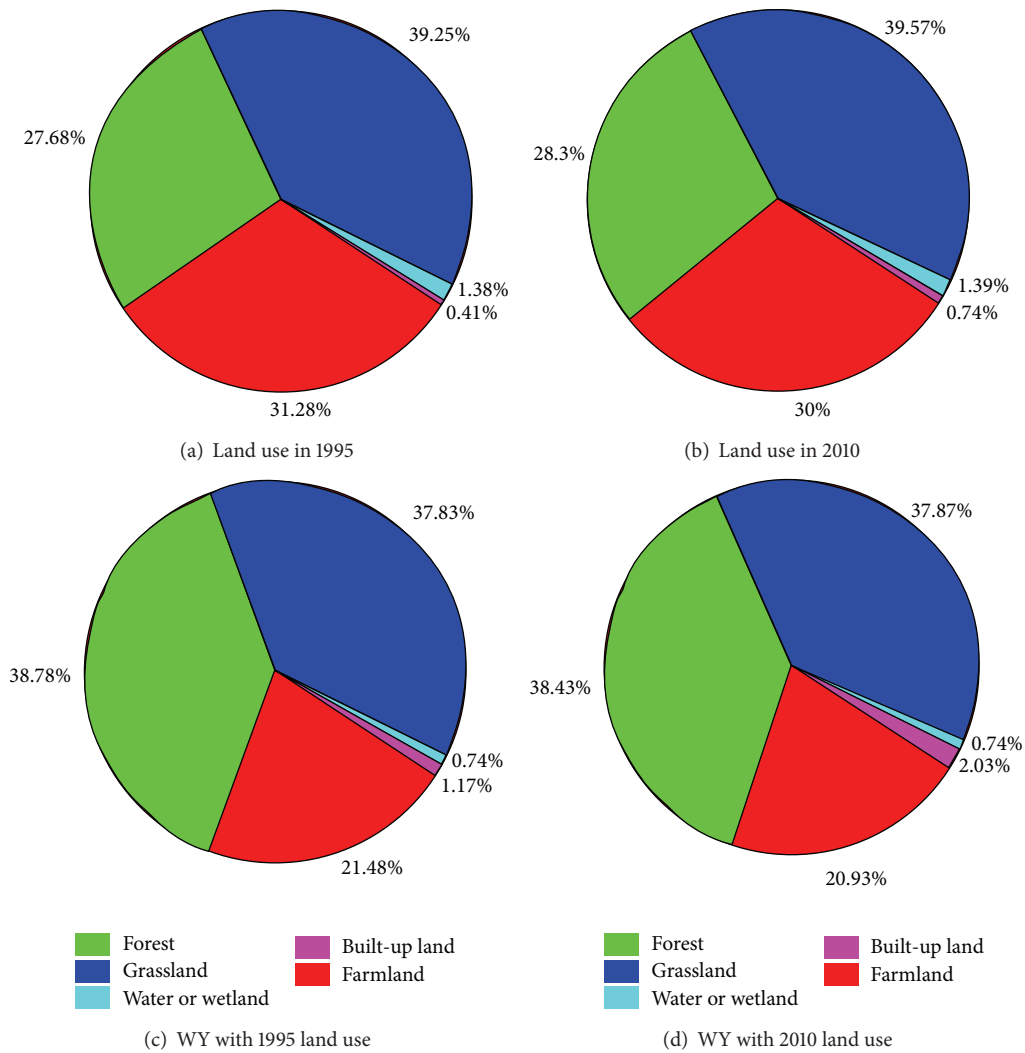


FIGURE 5: Percentage of each LULC change and its contribution to the total average annual water yields (WY) for the Upper Fenhe River watershed from 1992 to 2000.

of runoff, although the area of built-up land was very small. This is because its water-yielding capacity was the highest due to little initial loss and infiltration and rapid rainfall-runoff processes [9, 31].

As LULCs changed from 1995 to 2010, the contribution of individual LULC change to watershed WY changed too, but the change process was complex, because the WY is an integrated result of LULCs, soil, topography, and climate.

4.4. Impacts of LULC Changes on Hydrology at the Basin Scale. The average basin values of P, PET, AET, WY, and SW simulated from each LULC map in 1995 and 2010 are shown in Table 5. Compared to the LULC change baseline year of 1995, the average annual WY over the watershed was 0.13 mm higher in 2010. Similar to WY, average annual PET with LULC in 1995 was 1026 mm; it increased to 1028 mm by 2010. The AET increased from 391 mm for LULC in 1995 to 393 mm for LULC in 2010. On the contrary, the average annual SW for LULC in 2010 was 0.71 mm lower than that in 1995.

Furthermore, compared to the LULC baseline year 1995, the annual PET, AET, and SW for each year from 1992 to 2000 for LULC change in 2010 changed in a similar manner as the average annual PET, AET, and SW. But in contrast to the size of the average annual WY for LULC in 1995 and 2010, the annual WY for each year in this period did not increase consistently. For example, in years of abundant precipitation, such as 1995 and 1996, the annual WY for the LULC change in 1995 was higher than that in 2010. This indicated that the precipitation could affect the impacts of the LULC changes on the hydrology in this region, which was also found by Hao et al. (2004) in the upper Luohe River watershed [6].

The comparison of variations of PET and AET and changes in LULCs suggested that the increase of annual PET could be mainly attributed to returning cropland to forest and grassland and to urban expansion from 1995 to 2010. Further comparison between changes in WY and changes of LULCs indicated that an increase of WY was mainly due to increases of urbanization, which can increase the area of impervious surfaces, increase runoff, and decrease

TABLE 5: Annual basin values of hydrologic features for the Upper Fenhe River watershed on the different land use from 1992 to 2000 (mm).

Year	P	Scenario with land use in 1995				Scenario with land use in 2010			
		PET	ET	WY	SW	PET	ET	WY	SW
1992	540.96	987.47	423.23	66.42	41.10	989.30	426.06	66.40	40.37
1993	395.4	1017.43	359.38	34.74	36.10	1019.25	361.25	34.90	35.66
1994	493.39	1029.46	409.19	67.96	38.68	1031.40	412.00	68.04	37.63
1995	709.2	1000.44	418.90	215.99	54.46	1002.42	421.12	215.94	53.76
1996	618.65	966.47	427.45	166.85	53.57	968.45	430.58	166.51	52.48
1997	437.26	1048.62	359.69	76.13	49.58	1050.60	361.02	76.82	49.03
1998	448.72	1081.87	403.59	50.94	43.10	1083.77	405.50	51.27	42.78
1999	327.71	1086.06	294.28	33.34	45.65	1088.06	297.30	33.41	45.17
2000	501.18	1020.10	424.42	58.84	54.54	1021.87	426.83	59.09	53.52
Mean	496.94	1026.44	391.12	85.69	46.31	1028.35	393.52	85.82	45.60

Note: P: precipitation; PET: potential evapotranspiration; ET: actual evapotranspiration; WY: water yield; SW: soil water.

TABLE 6: LULC changes and average annual hydrologic features from 1992 to 2000 of three subbasins.

Subbasin	Number 7		Number 17		Number 35	
	1995	2010	1995	2010	1995	2010
Total area (km ²)	109.9	109.9	97.5	97.5	340	340
Farmland (%)	53.54	26.16	19.56	19.59	29.87	32.45
Forest (%)	9.31	17.42	49.6	46.51	15.57	16.78
Grassland (%)	36.98	55.35	28.1	31.18	52.75	48.23
Water or wetland (%)	0.01	0.72	2.29	2.29	1.25	1.24
Built-up land (%)	0.16	0.35	0.45	0.43	0.56	1.3
P (mm)	492.01	492.01	599.03	599.03	473.68	473.68
PET (mm)	918.93	926.55	1077.47	1077.5	1072.05	1072.18
ET (mm)	396.89	403.63	457.99	469.51	380.7	380.08
WY (mm)	64.74	66.57	124.43	116.62	71.17	72.17
SW (mm)	74.84	72.22	71.47	58.01	24.93	23.12

infiltration [9, 31]. An association between the decreases of SW and forest, grassland, and built-up land expansion from 1995 to 2010 could be indicated from the comparison between variations of average annual SW and changes in LULC from 1995 to 2010. Expansion of forest, grassland, and built-up land by replacing them with farmland could promote water infiltration and drainage because of well-developed root systems and prevention of infiltration due to increases in the areas of impervious surfaces.

4.5. Impacts of LULC Changes on Hydrology at the Subbasin Scale. Three subbasins (numbers 7, 17, and 35 in Figure 1) with obvious LULC changes were selected for analysis of the impacts of LULC changes on hydrology at the subbasin scale, and the results are shown in Table 6. In subbasin number 7, the area of farmland decreased sharply, and the areas of forest, grassland, water, and built-up land increased from 1995 to 2010. The PET, AET, and WY increased, and, in contrast, the SW decreased. In subbasin number 17 only the forested area decreased and grassland area increased a little, so the impacts on hydrology were that AET increased clearly and WY and SW decreased. In subbasin number 35, areas of farmland, forest, and built-up land increased and grassland decreased, and WY increased and SW decreased. By comparing the

LULC changes and the hydrological responses to them in these three sun-basins, obvious LULC changes may not show obvious impacts on hydrology, which means different combinations of LULCs may produce similar hydrological effects. Furthermore, the impacts of the same LULC changes on hydrology may be different under the conditions of different precipitation intensity and distribution.

5. Conclusions

In this study we aimed to investigate the impacts of LULC changes on hydrology in China's Loess Plateau. Major research findings and their implication on practices and future research are as follows.

From 1995 to 2010, the main land use changes were the transformations of farmland to forests and from farmland to grassland, and the area of built-up land increased at the expense of farmland. These changes were due to the implementation of watershed management measures and social and economic development. For the contribution of each LULC to the total WY of the watershed, the forest, grassland, and farmland areas were the largest contributors, with up to about 39%, 38%, and 21%, respectively. The land use that produced the greatest water yield was shown to be

built-up land, which was higher than any other land use, followed by forest, grassland, and farmland.

Accompanying the LULC changes in the Upper Fenhe River watershed, increases in PET, AET, and WY indicated soil and water conservation practices increased runoff, while the expansion of the forest and grassland increased the PET and AET. In addition, the consumption of SW was increased by vegetation combined with decreased infiltration because increases of the built-up land resulted in decreases in SW. Furthermore, the precipitation could affect the impacts of LULC changes on the hydrologic components in this arid and semiarid area.

The approach used in this study simply determined contributions of individual LULC classes to the total discharge, providing quantitative information for decision-makers to make better choices for land and water resource planning and management. This approach also provides a solid example of the potential of hydrologic modeling using remotely sensed digital LULCs in understanding the impacts of landscape change on water provisioning, a vital ecosystem service in the Loess Plateau of China. It can be widely applied to a variety of watersheds, where time-sequenced digital land cover data are available, and to predict hydrological consequences to LULC changes.

Conflict of Interests

The authors declare no conflict of interests.

Acknowledgments

This work was supported by the International Science & Technology Cooperation Program of China (2012DFA20770 and 2013DFG70990), the National Natural Science Foundation of China (41201043 and 91125007), the National Key Technology R&D Program (2011BAC07B05), and Shanxi Province Science Foundation for Youths (2012021026-3).

References

- [1] J. A. Foley, R. DeFries, G. P. Asner et al., "Global consequences of land use," *Science*, vol. 309, no. 5734, pp. 570–574, 2005.
- [2] E. F. Lambin, B. L. Turner, H. J. Geist et al., "The causes of land-use and land-cover change: moving beyond the myths," *Global Environmental Change*, vol. 11, no. 4, pp. 261–269, 2001.
- [3] N. Ramankutty and J. A. Foley, "Estimating historical changes in global land cover: croplands from 1700 to 1992," *Global Biogeochemical Cycles*, vol. 13, no. 4, pp. 997–1027, 1999.
- [4] L. M. Mango, A. M. Melesse, M. E. McClain, D. Gann, and S. G. Setegn, "Land use and climate change impacts on the hydrology of the upper Mara River Basin, Kenya: results of a modeling study to support better resource management," *Hydrology and Earth System Sciences*, vol. 15, no. 7, pp. 2245–2258, 2011.
- [5] D. N. Khoi and T. Suetsugi, "The responses of hydrological processes and sediment yield to land-use and climate change in the Be River Catchment, Vietnam," *Hydrological Processes*, vol. 28, no. 3, pp. 640–652, 2014.
- [6] F. Hao, L. Chen, C. Liu, and D. Dai, "Impact of land use change on runoff and sediment yield," *Journal of Soil and Water Conservation*, vol. 18, no. 3, pp. 5–8, 2004.
- [7] Y.-H. Song and J.-H. Ma, "SWAT-Aided research on hydrological responses to ecological restoration; a case study of the Nanhe River Basin in Huajialing of Longxi Loess Plateau," *Acta Ecologica Sinica*, vol. 28, no. 2, pp. 636–644, 2008.
- [8] G. Ghaffari, S. Keesstra, J. Ghodousi, and H. Ahmadi, "SWAT-simulated hydrological impact of land-use change in the Zanjanrood basin, Northwest Iran," *Hydrological Processes*, vol. 24, no. 7, pp. 892–903, 2010.
- [9] W. Nie, Y. Yuan, W. Kepner, M. S. Nash, M. Jackson, and C. Erickson, "Assessing impacts of Landuse and Landcover changes on hydrology for the upper San Pedro watershed," *Journal of Hydrology*, vol. 407, no. 1–4, pp. 105–114, 2011.
- [10] Y. Wang, W. Ji, X. Yu et al., "The impact of urbanization on the annual average temperature of the past 60 years in Beijing," *Advances in Meteorology*, vol. 2014, Article ID 374987, 9 pages, 2014.
- [11] Y. Li, J. Fan, Z. Hu, Q. Shao, L. Zhang, and H. Yu, "Influence of land use patterns on evapotranspiration and its components in a temperate grassland ecosystem," *Advances in Meteorology*. In press.
- [12] X. Yao, Z. Wang, and H. Wang, "Impact of urbanization and land-use change on surface climate in middle and lower reaches of the Yangtze River, 1988–2008," *Advances in Meteorology*. In press.
- [13] M. López-Vicente, J. Poesen, A. Navas, and L. Gaspar, "Predicting runoff and sediment connectivity and soil erosion by water for different land use scenarios in the Spanish Pre-Pyrenees," *Catena*, vol. 102, pp. 62–73, 2013.
- [14] N. Ohana-Levi, A. Karnieli, R. Egozi, A. Givati, and A. Peeters, "Modeling the effects of land-cover change on rainfall-runoff relationships in a semi-arid, Eastern Mediterranean watershed," *Advances in Meteorology*. In press.
- [15] G. Wang, H. Yang, L. Wang, Z. Xu, and B. Xue, "Using the SWAT model to assess impacts of land use changes on runoff generation in headwaters," *Hydrological Processes*, vol. 28, no. 3, pp. 1032–1042, 2014.
- [16] X. Li, "A review of the international researches on land use/land cover change," *Acta Geographica Sinica*, vol. 51, no. 6, pp. 553–558, 1996.
- [17] Q. F. Zhang, F. Q. Wu, L. Wang, L. Yuan, and L.-S. Zhao, "Application of PCA integrated with CA and GIS in eco-economic regionalization of Chinese Loess Plateau," *Ecological Economics*, vol. 70, no. 6, pp. 1051–1056, 2011.
- [18] C. Shi, Y. Zhou, X. Fan, and W. Shao, "A study on the annual runoff change and its relationship with water and soil conservation practices and climate change in the middle Yellow River basin," *Catena*, vol. 100, pp. 31–41, 2013.
- [19] J. Zhang, "Comprehensive treatment for large basin and harmonious development of upstream and downstream-survey on comprehensive harness engineering of soil and water conservation for upper Fenhe River," *Shanxi Water Resources*, vol. 21, no. 4, pp. 5–9, 2005.
- [20] X. Wang and X. Nie, "Analysis on the benefit of soil and water conservation in the upper-reach of Fenhe reservoir—a case study of comprehensive management to Fenhe during the second phase in Jingle county," *Journal of Shanxi Agricultural University (Social Science Edition)*, vol. 6, no. 3, pp. 237–240, 2007.
- [21] B. Yang, "Viewing the function of integrated treatment of soil and water conservation conducted in the upper Fenhe River from sediment discharge variations at Jingle hydrometric station," *Soil and Water Conservation in China*, no. 10, pp. 32–34, 2007.

- [22] W. Meng, S. Wang, and J. Niu, "Upstream Fenhe River the Basin humanity moves under the forest cover change," *Journal of Taiyuan Normal University (Natural Science Edition)*, vol. 6, no. 1, pp. 75–79, 2007.
- [23] Z. Li, W.-Z. Liu, X.-C. Zhang, and F.-L. Zheng, "Impacts of land use change and climate variability on hydrology in an agricultural catchment on the Loess Plateau of China," *Journal of Hydrology*, vol. 377, no. 1-2, pp. 35–42, 2009.
- [24] H. Li, Y. Zhang, J. Vaze, and B. Wang, "Separating effects of vegetation change and climate variability using hydrological modelling and sensitivity-based approaches," *Journal of Hydrology*, vol. 420-421, pp. 403–418, 2012.
- [25] J. G. Arnold, R. Srinivasan, R. S. Muttiah, and J. R. Williams, "Large area hydrologic modeling and assessment part I: model development," *Journal of the American Water Resources Association*, vol. 34, no. 1, pp. 73–89, 1998.
- [26] J. Sun, Y. Liu, Y. Wang, G. Bao, and B. Sun, "Tree-ring based runoff reconstruction of the upper Fenhe River basin, North China, since 1799 AD," *Quaternary International*, vol. 283, pp. 117–124, 2013.
- [27] X. Wang, "Studies on ecology and environment improvement of Fenhe reservoir and its upstream water sources," *China Water Resources*, vol. 16, pp. 44–47, 2008.
- [28] S. Neitsch, J. Arnold, J. Kiniry, J. Williams, and K. King, *Soil and Water Assessment Tool: Theoretical Documentation*, Version 2005, Texas A&M University, College Station, Tex, USA, 2005.
- [29] Z. Lu, S. Zou, Z. Yin, A. Long, and B. Xu, "A new suitable method for SWAT model calibration and its application in data-scarce basins," *Journal of Lanzhou University (Natural Sciences)*, vol. 48, no. 1, pp. 1–7, 2012.
- [30] D. N. Moriasi, J. G. Arnold, M. W. Van Liew, R. L. Bingner, R. D. Harmel, and T. L. Veith, "Model evaluation guidelines for systematic quantification of accuracy in watershed simulations," *Transactions of the ASABE*, vol. 50, no. 3, pp. 885–900, 2007.
- [31] J. Franczyk and H. Chang, "The effects of climate change and urbanization on the runoff of the Rock Creek basin in the Portland metropolitan area, Oregon, USA," *Hydrological Processes*, vol. 23, no. 6, pp. 805–815, 2009.

Research Article

Comparison of Stationary and Dynamic Conceptual Models in a Mountainous and Data-Sparse Catchment in the South-Central Chilean Andes

Camila Toledo,¹ Enrique Muñoz,² and Mauricio Zambrano-Bigiarini^{3,4}

¹Hydro-Environmental Institute IHA/UCSC, Universidad Católica de la Santísima Concepción, Alonso de Ribera 2850, Concepción, Chile

²Department of Civil Engineering, Universidad Católica de la Santísima Concepción, Alonso de Ribera 2850, Concepción, Chile

³Department of Environmental Engineering, Faculty of Environmental Sciences and EULA-Chile Centre, University of Concepción, Concepción, Chile

⁴Department of Civil Engineering, Faculty of Engineering and Sciences, Universidad de La Frontera, Temuco, Chile

Correspondence should be addressed to Enrique Muñoz; emunozo@ucsc.cl

Received 28 November 2014; Revised 5 March 2015; Accepted 6 March 2015

Academic Editor: Fubao Sun

Copyright © 2015 Camila Toledo et al. This is an open access article distributed under the Creative Commons Attribution License, which permits unrestricted use, distribution, and reproduction in any medium, provided the original work is properly cited.

In recent years, it has been documented that climatic variability influences hydrological processes; however, these influences, such as hydrologic dynamics, have not yet been incorporated into models, which have been assumed as stationary with regard to climatic conditions. In this study, the temporal variability of hydrological processes and their influence on the water balance of a mountainous and data-sparse catchment in Chile are observed and modeled through the comparison of a stationary (time-invariant parameters) and dynamic (time-variant parameters) model. Since conceptual models are the most adequate option for a data-scarce basin, a conceptual model integrated with the Monte Carlo Analysis Toolbox is used to perform the analyses. Simple analyses aimed at increasing the amount of information obtained from models were used. The General and Dynamic Identifiability Analyses were used to perform stationary and dynamic calibration strategies, respectively. As a result we concluded that the dynamic model is more robust than the stationary one. Additionally, DYNIA helped us to observe the temporal variability of hydrological processes. This analysis contributed to a better understanding of hydrological processes in a data-sparse Andean catchment and thus could potentially help reduce uncertainties in the outputs of hydrological models under scenarios of climate change and/or variability.

1. Introduction

Climate change has significant effects on the hydrological cycle; among some of the expected effects of climate change is an increase in the number (frequency) of floods and droughts on the planet [1]. This has a direct impact on the availability of water for agriculture, silviculture, and hydroelectricity, among other activities. Agriculture and hydroelectricity are the most important economic activities in south-central Chile, and they depend directly on the availability of water from Andean basins. Thus, it is necessary to improve the quality of and confidence in hydrological predictions and, at the same time, ascertain and better understand the behavior of hydrological processes in Andean basins. It is here that

hydrological modeling comes into play, since it is one of the most used tools for water resources management and planning [2].

Currently, there are many tools to support water resources planning and management. In particular, conceptual hydrological models have been widely used by the hydrological community [3, 4] to provide a better understanding of hydrological processes [5], to estimate long-term water availability [6], and to make projections of climate [7–9] and land use change [10, 11], among other uses. However, there is still a need not only to reproduce the past behavior of a basin, but also to evaluate the representativeness of the chosen model and its processes to assess the quality of the simulations for a given basin. This must be done not

only in terms of a given measurement or objective function, but also by incorporating a range of parameter values in which the model exhibits physically meaningful behavior. Recently, there has been an increasing concern for addressing equifinality, identifiability, and quantifying the uncertainty associated with model simulations [12].

The concept of equifinality [13] recognizes that several parameter sets might result in simulations with similar goodness of fit when compared to observations and therefore a single “best” parameter set cannot be identified [13]. However, under climate change conditions, there are several reasons to expect a change in model parameters as well [12]. Therefore, calibration parameters might change along different time periods or parts of the hydrograph [9].

Experience has shown that in rainfall-runoff modeling one set of calibrated parameters (i.e., a stationary model) may not yield equally good approximations of all events or for different parts of the observed hydrograph [14]. Moreover, for long-term simulations, the optimum parameter set may be different for separate periods and also must change concurrently with changes in boundary conditions and process characteristics. Most scientists now acknowledge that the traditional assumption of stationarity in a hydrological model may no longer be adequate [15–17]. Therefore, to properly consider the effects of hydrological variability (nonstationarity), different parameter sets are needed to represent the dynamic behavior of the catchment. In other words, dynamic calibration strategies are required for better confidence in model predictions.

Some initial studies attempting to address the aforementioned idea have been published [9, 18, 19]. They have shown through various methods why and how models must change in time and/or according to climatic and catchment properties.

Recently, the concept of hydrological dynamics has been much discussed in the hydrological literature to be further incorporated into the conceptual formulation of a model [12, 15, 20]. This means that changes in the response of a basin caused by, for example, climate variability and change, are taken into account in the modeling stage. It is therefore important to find and study ways of detecting this behavior in new models, in order to have more reliable simulations of these changes and increase the efficiency and confidence in the management of water resources and systems.

Traditionally, stationary model calibration (with fixed model parameters) is conducted through parameter optimization to maximize the agreement between observed and simulated streamflows. Usually, a single objective function or a combination of objective functions is used over the calibration period for better model representativeness and then for model validation the calibrated model is verified against the rest of the data. But is this method result adequate for long-term predictions? Is this method valid for a basin affected by climate variability such as the El Niño Southern Oscillation Phenomenon (ENSO)? Are these results reliable for predictions? As Luo et al. [21] mentioned, it is essential to carefully design model calibration procedures in order to ensure good performance of the hydrologic model for streamflow forecasting. Therefore, depending on the objective

of the study and the predictability expected for the model, different calibration strategies will be needed.

Most climate change impact studies run hydrological models calibrated against past observations with future climate inputs to predict future runoff characteristics. This approach is probably adequate for predicting changes in near-term runoff resulting from small changes in the climate inputs. However, these models cannot be extrapolated to predict changes in the future resulting from large changes in climate inputs and hydrological processes [17]. In other words, hydrological models calibrated using past observations may not adequately capture processes that may become more dominant in future and therefore a dynamic calibration strategy would probably be better in such cases.

This study aims to improve the representativeness and simulation ability of models by incorporating observed hydrological dynamics in a data-sparse Andean basin highly affected by climate variability. In addition, observation of the process dynamics of the basin will improve our understanding of hydrological processes and deepen our knowledge of the hydrology of an Andean basin. We thus expect to improve the conceptual design of a hydrological model by including dynamic calibrated parameters within the model formulation. The General Identifiability Analysis (GIA) and Dynamic Identifiability Analysis (DYNIA) [22] are carried out to perform a stationary and dynamic model calibration, respectively. Finally, the representativeness of the stationary model is compared against the model calibrated with the dynamic approach.

2. Study Area

The study area (Figure 1) corresponds to the upper Chillán catchment, measured at the *Chillán en Esperanza* streamflow station (latitudes 36.76° to 36.87°S and longitudes 71.4 to 71.6°W). The drainage area of this catchment is 210.4 km², with elevations ranging from 435 m a.s.l. at the gauging station up to 3200 m a.s.l. at the Nevados de Chillán volcano in the Andes mountain range. The catchment is located in the Chilean Andes in the piedmont area. It exhibits a complex topography and is a data-sparse area without rainfall and temperature stations in the catchment (Figure 1).

According to the rainfall rate described by Mardones et al. [23] at 36°45′ south, there exists a positive gradient of rainfall with the terrain altitude due to the so-called orographic effect (eastward, from the sea to the Andes mountains). Thus, rainfall increases at the western slopes of the Andean mountains, reaching the values of up to 3000 (mm) per year in the study area [24]. More than 70% of annual precipitation is concentrated in the rainy period (from May to September), and precipitation increases with elevation due to the orographic effect of the Andes mountain range [24, 25]. The annual rainfall is 2200 mm and the average seasonal temperature varies from 3.3°C in winter to 21.9°C in summer.

The river has a pluvial regime (see Figure 1), since more than 90% of the catchment is located below the annual average snow line of 2500 m a.s.l. [26]. Although the basin contains part of the western slope of the Chillán volcano, it does not present a marked snowmelt influence in spring

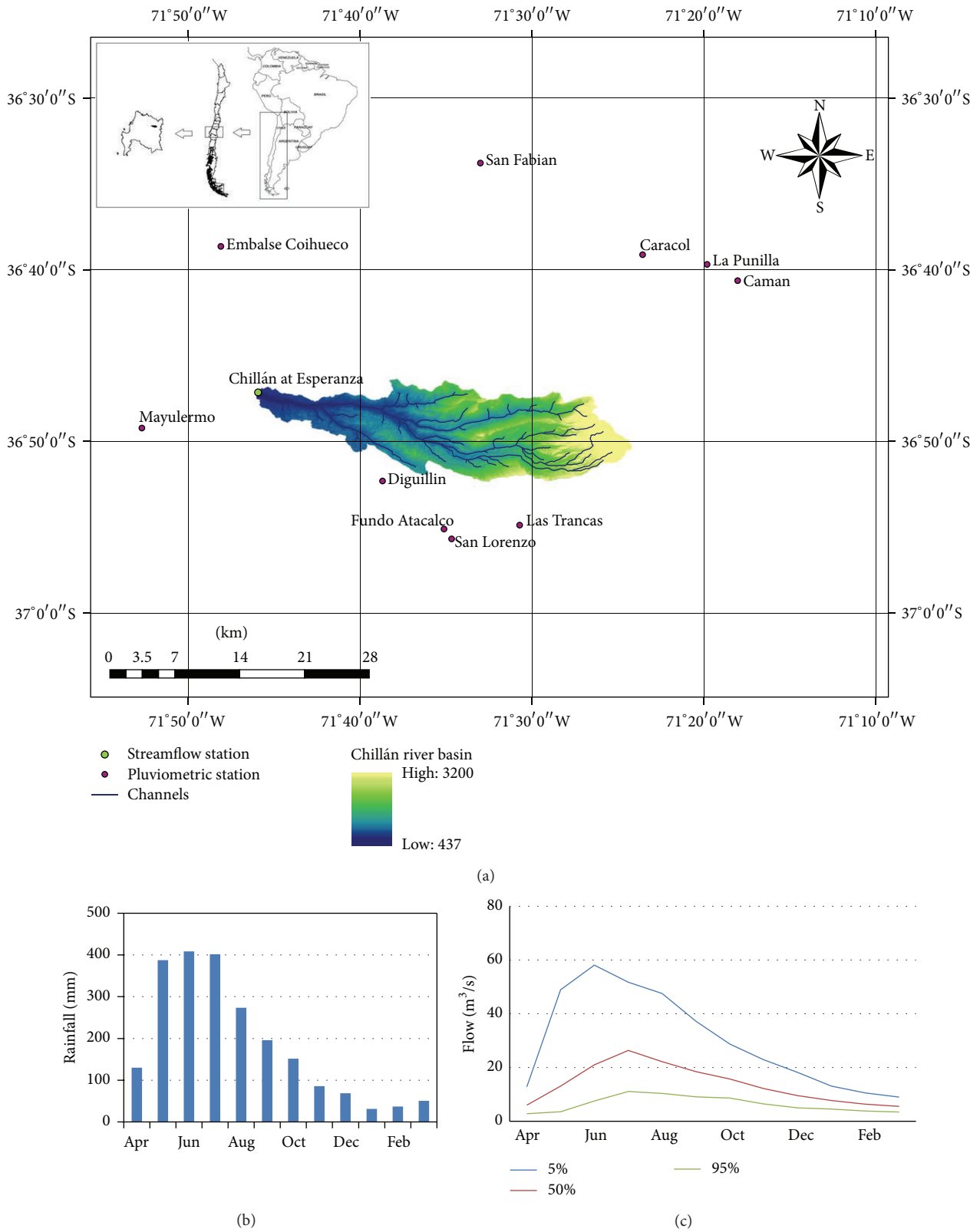


FIGURE 1: Digital elevation model and location of the *Chillán en Esperanza* basin (top), seasonal rainfall distribution (bottom left), and seasonal variation curves of 5, 50, and 95% exceedance probability of the *Chillán en Esperanza* river basin (bottom right).

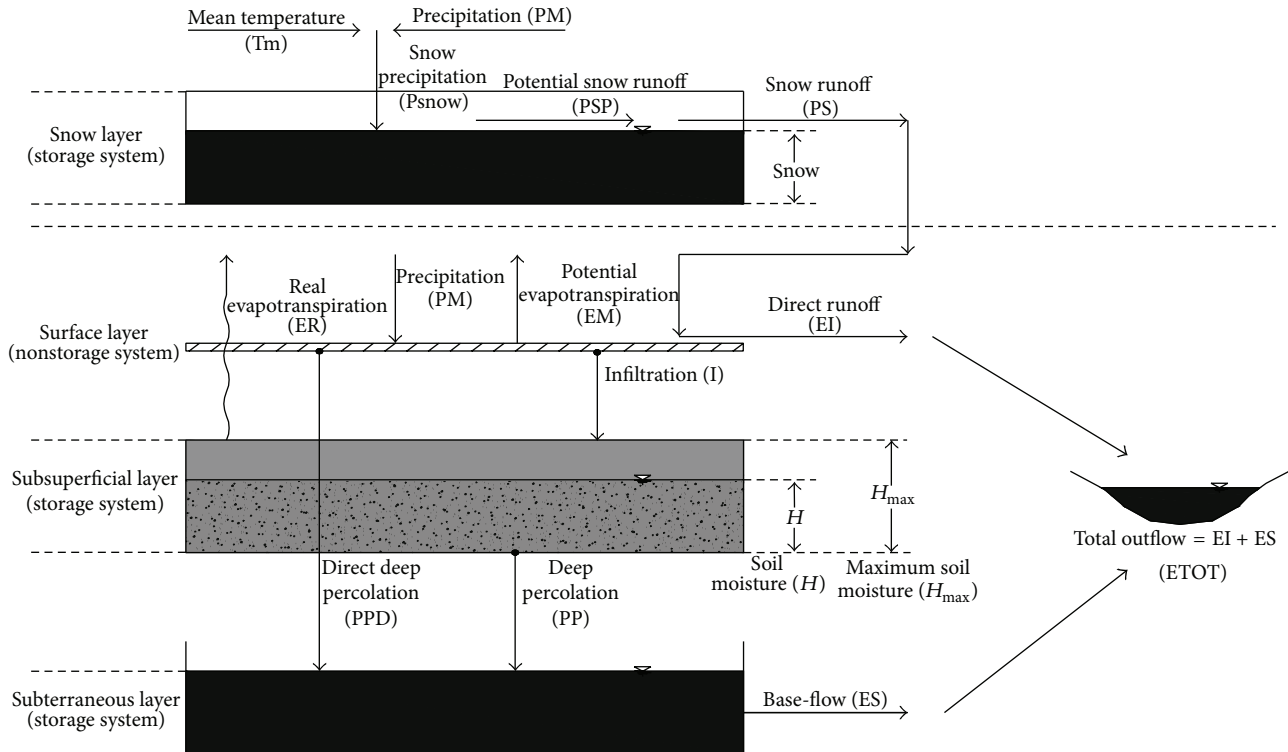


FIGURE 2: Conceptual model.

or early summer (see the seasonal variation curve of 5% of probability of exceedance in Figure 1 where a second peak between October and January is not observed).

Because the basin is located on the slope of a volcano, it presents high slopes and highly permeable soil layers. According to SERNAGEOMIN [27], most (over 80%) of the basin area is covered by a PPI3 substrate (from the Pliocene-Pleistocene period). This substrate is composed mainly of volcanic (extrusive) rocks formed when volcanic lava emerges, favoring a high degree of fracturing and permeable soil layers. Moreover, due to the old age of this substrate, weathering processes have started, increasing rock permeability. Therefore, the high slopes and permeable soil layers related to the volcano influence the hydrology of the Chillán basin with regard to rapid surface and groundwater runoff processes and permit a high amount of water to be stored in the basin each year. Moreover, these characteristics produce fast runoff responses in the basin (see Figure 1).

The *Chillán en Esperanza* river basin is covered mostly by native forest with scarce anthropogenic alterations [28], mainly because the basin is located at the slope of the Chillán volcano in a very difficult-to-access area. Therefore, negligible land use and cover change have occurred during recent decades.

3. Hydrological Model Description

Because the main characteristics in mountainous environments are the complexity and spatial variability of hydroclimatic patterns, one would be tempted to choose a detailed,

distributed, and physically based hydrological model to represent the hydrological behavior of a basin and the hydrological processes which occur in it [4]. But, in the case of a data-sparse basin, there will always be a need for more information (land use, soil map, vegetation map, etc.) than is available. Therefore, conceptual models are the simplest and most adequate option for data-sparse basins such as Andean basins. Thus, considering that conceptual pluvial models do not differ significantly in their conceptualization and capabilities [8], we chose the Muñoz model [29] to perform the analyses due to its simplicity and because it integrates the General and Dynamic Identifiability Analyses used in this study.

The model used in this paper is the conceptual water balance model presented in Muñoz [29] and Muñoz et al. [30] (Figure 2). This model simulates the rainfall-runoff and snowmelt-runoff processes separately. Because the pluvial regime predominates in the study area, only the rainfall-runoff module has been used, and it will be briefly described here.

The lumped model considers the watershed as a double storage system: subsurface (SS) and deep storage (US). SS represents the water stored in the unsaturated soil layer as soil moisture, while US is the water covering the saturated soil layer. The main input data for the model are rainfall (PM) and potential evapotranspiration (PET). The model output is the total runoff (ETOT) at the watershed outlet, which includes both base-flow (ES) and surface runoff (EI). For a further description of the model's characteristics, please refer to Muñoz [29] and Muñoz et al. [30].

4. Data

To estimate representative rainfall data of the catchment, 10 rain gauge stations located in the vicinity of the catchment were used as shown in Figure 1. It is important to point out that Andean catchments are usually difficult-to-access areas, and therefore most (even all in this case) meteorological stations are located outside of the catchment and far from the highest areas of the catchments under study. Therefore, in studies of these catchments, it becomes a challenge to adequately represent their meteorological characteristics.

Monthly data were provided by the National Water Agency (*Dirección General de Aguas*, or DGA) and were then interpolated using the inverse distance weighting method to obtain representative catchment values. This method was chosen due to its efficiency in interpolating rainfall from point measurements and due to the mountainous nature of the basin and its influence on the spatial variability of precipitation [31].

Due to the absence of long-term and reliable temperature data from DGA stations, temperature time-series were obtained from the Center for Climatic Research, University of Delaware [32]. To estimate distributed temperatures in the catchment, the Thiessen polygon method was used. Temperature data were then used to compute potential evapotranspiration using the Thornthwaite method.

The morphological characterization of the catchment and its area was defined using Advanced Spaceborne Thermal Emission and Reflection Radiometer (ASTER) images of 1 arc-second resolution (30 m approximately) (Figure 1).

5. Methodology

To compare a model which includes hydrological dynamics with one that does not, dynamic and stationary calibration strategies were used. Both calibration strategies were executed based on the regional sensitivity analysis (RSA) described by Hornberger and Spear [33]. For the stationary calibration, an RSA was performed over the whole period of analysis, while for the dynamic calibration the same analysis based on RSA was performed, but with a moving window.

To study the sensitivity and temporal variability of the model parameters the Monte Carlo Analysis Toolbox (MCAT) [22] was combined with the Muñoz et al. [30] hydrological model.

MCAT starts by running several simulations with different parameter sets sampled from physically meaningful ranges previously defined by the user. Then, it stores the parameter sets, the model outputs, and the values of the objective function(s) associated with each simulation, in order to evaluate model behavior afterwards [30]. The main analyses that were carried out in this study were (i) the General Identifiability Analysis (GIA) and (ii) Dynamic Identifiability Analysis (DYNIA) [22, 34]. Both analyses are based on the RSA and consist of a graphical consolidation of the results obtained from the MCAT simulations.

On one hand, GIA gives an overview of the probability distribution function (pdf) and the cumulative pdf (cdf) of individual model parameters for the best 10% of the

simulations based on the objective function (OF) computed over the whole simulation period. GIA relates the influence that each parameter has on the model outputs according to a predefined OF. This is achieved through a graphical analysis that compares the cumulative distribution curve of each parameter versus the value of each parameter for different intervals within the parameters' range. Thus, a greater slope in the cumulative distribution curve indicates that the analyzed parameter has a strong influence on the model outputs. In the same way a constant slope indicates that the model is not sensitive to the parameter.

On the other hand, DYNIA carries out a similar sensitivity analysis, but instead of using the entire simulation period, it considers a moving window of length n defined by the user. This window is moved through the available time-series in a stepwise fashion; that is, at time step t , it computes the residuals between $t - n$ and $t + n$. The size of n is selected depending on the time length in which each parameter is influential and on the period that is to be studied. The measure of model performance is then used to condition the marginal parameter distribution at that particular time step. A threshold is applied to consider only the best performing parameter sets (the best 10% in this study) according to an appropriate support measure.

In this study, windows of 3, 7, and 13 months were used, aiming at (i) obtaining the greatest variability associated with each parameter and objective function (3 months) and (ii) obtaining interannual variability in parameters (7 and 13 months).

It should be noted that DYNIA processes a great amount of information that varies with modeling time, objective function, and number of parameters. Thus, its graphical representation consists of a grayscale graphic where the darkest shading at any time step represents the steepest slope of the cumulative distribution curve, that is, greater identifiability. Similarly, lighter shading represents a gentler slope of the cumulative distribution curve and therefore lower identifiability (see Figure 3). A further description of GIA and DYNIA can be found in Wagener et al. [34, 35] and Wagener and Kollat [22].

In this study, GIA was used to constrain model parameters according to their identifiability and therefore to calibrate the model as stationary with time-invariant model parameters. DYNIA was used to identify the time variability of the most identifiable parameters and to calibrate a dynamic model. Then, further analyses were carried out based on the comparison of both calibration strategies.

5.1. Stationary Parameter Calibration. For the stationary parameter calibration, the method described by Muñoz et al. [30] was used as summarized below.

- (1) Estimation of the adequate number of simulations: because the MCAT is based on random trials, it normally requires a large number of simulations to cover the widest spectrum of possible simulations. The number of Monte Carlo simulations was estimated via trial and error, where the stop criterion was met when the correlation (according to the Pearson

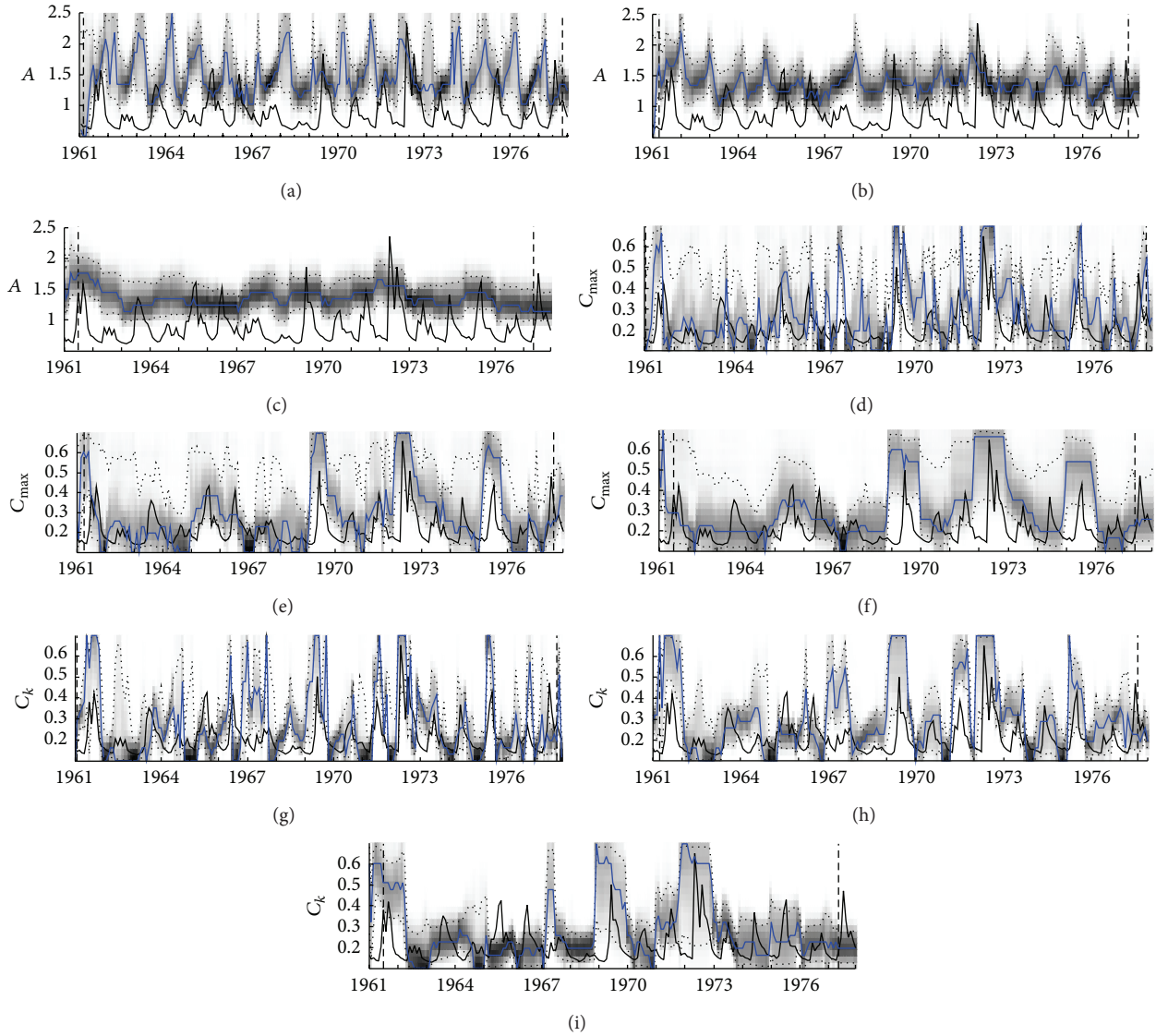


FIGURE 3: Dynamic Identifiability Analysis plots for the RMSE OF and for 3, 7, and 13 months and for parameters A (plots a, b, and c, resp.), C_{\max} (plots d, e, and f, resp.), and C_k (plots g, h, and I, resp.). The dashed lines show the 5 and 95% confidence limits, the black lines show the relative time-series of the streamflow data, and the blue lines show the time-series of highest identifiability for each time-window analyzed.

correlation coefficient) between uncertainty bands (calculated as a linear correlation between the time-series of the upper and lower limits of the bands of uncertainty) of two different trials, but with same number of simulations, was equal to or greater than 0.999. Under this criterion, it was determined that the adequate number of simulations for this study is 10,000.

- (2) Identifiability of the input modification factors: because it is possible for the inputs to not be representative of the hydrometeorological characteristics of the basin, the model considers the possibility of modifying them in terms of amounts in order to ensure the closure of the long-term mass balance. To do this, factors A and B serve the function of modifying the

precipitation and potential evapotranspiration series, respectively. Therefore, the identifiability analysis was first performed on A and B . These factors were constrained according to their positive identifiability and through an iterative process of constraining and then repeating the 10,000 Monte Carlo simulations. The stop criterion was met when A and B did not show further identifiability and then the mean value of the parameter range was used as a calibrated factor.

- (3) Identifiability of the model parameters: due to the parameter interactions, various Monte Carlo simulations were carried out, in which the ranges of each were constrained in accordance with its observed identifiability from GIA. If the parameter showed a range which has a positive influence on the model

outputs (i.e., positive identifiability), the parameter was constrained to that range. From this analysis the new range of an identifiable parameter was defined and then a new iteration (Monte Carlo simulations) was carried out.

A steeper slope in GIA indicates that the parameter is more observed (or repeated) in that range and therefore is identifiable in that range. Otherwise, a gentler slope indicates that the model parameter is not identifiable in such range and therefore was used to discard a nonidentifiable range of a model parameter. In this way, the range assigned to a particular parameter was constrained. The experiment was repeated in order to observe identifiability in the remaining parameters related to the aforementioned one. The exercise stopped when identifiability was not further observed within the range defined for each parameter.

5.2. Dynamic Parameter Calibration. An approach similar to the GIA calibration was used for the dynamic calibration, but instead of time-fixed, that is, stationary, parameter values, time-variant parameters were used, following the variability observed in the DYNIA. The calibration procedure is summarized below.

- (1) To define the adequate number of random trials for the Monte Carlo analysis, the same analysis as for the stationary calibration was used.
- (2) Dynamic identifiability of the input modification factors: as described above, factors *A* and *B* serve in modifying the precipitation and potential evapotranspiration series, respectively. Therefore, the Dynamic Identifiability Analysis was first performed on *A* and *B* starting with the one that showed the highest identifiability. The criterion to estimate the factor with higher identifiability was the highest slope in the cdf plot for the best 10% of the models (highest slope in the GIA plots).
Then, to obtain the time-varying factor identifiability, the same criterion as above was used but along a moving window. Therefore, the darkest shading for every time step was used to define the most identifiable value of the factor (or parameter) along time.
- (3) After ascertaining the time-series of the identifiable parameter, it was processed, and its seasonality (based on the mean monthly value of parameter) was recorded. Then, a seasonal parameter was incorporated into the model for model calibration instead of a fixed (stationary) parameter.
- (4) The same approach was then repeated for the remaining input modification factor, and then the same method was used for the dynamic calibration of the most identifiable model parameters.

It is important to point out that (i) the procedure consists of an iterative procedure where dynamic calibration is performed for each parameter one at

a time and (ii) the parameters that did not show seasonality after DYNIA were calibrated as fixed according to the GIA.

The analysis was performed using the full range of each parameter aimed at covering the full spectrum of variations that can present the different parameters along the moving window.

5.3. Objective Functions. For the analysis, three objective functions were used to analyze the influence of the hydrological processes in the different parts of the hydrograph used. The Root-Mean-Square Error (RMSE), transformed root-mean-square error (TRMSE), and runoff coefficient error (ROCE) were used (see (1)). These functions were selected because they are focused on the analysis of high flows, low flows, and the mass balance, respectively [36, 37]:

$$\begin{aligned} \text{RMSE} &= \sqrt{\frac{1}{n} \sum_{j=1}^n (S_j - O_j)^2}, \\ \text{TRMSE} &= \sqrt{\frac{1}{n} \sum_{j=1}^n \left(\frac{(1 + S_j)^\lambda - 1}{\lambda} - \frac{(1 + O_j)^\lambda - 1}{\lambda} \right)^2}, \quad (1) \\ \text{ROCE} &= \text{abs} \left(\frac{\bar{Q}_s}{\bar{P}} - \frac{\bar{Q}_o}{\bar{P}} \right), \end{aligned}$$

where O_j and S_j are the observed and simulated flows, respectively, λ is related to the Box-Cox transformation for the data series with a value of 0.3, and Q/P represents the mean annual runoff coefficient and is calculated by the rate between the mean annual flow \bar{Q} and the mean annual rainfall \bar{P} for the simulated (*s*) or observed (*o*) flows.

5.4. Model Implementation. The hydrological model was implemented on a monthly time step. Due to the data availability, 17 years of hydrometeorological records were used for calibration (1961–1977) and validation (1978–1994). Additionally 10,000 simulations by iteration were carried out, drawing random values from each parameter according to their initial or constrained range. The initial range considered is shown in Table 1.

Parameter values, simulated flows, and related OF values were stored for each iteration. Then, using this information, GIA and DYNIA were carried out.

It is important to point out that the streamflow station was destroyed by a flood in 1995 and thus from then on no new records are available at this location.

6. Results and Discussion

6.1. Hydrological Processes Representation. Results of the GIA (not shown here) revealed that for RMSE, TRMSE, and ROCE the most identifiable parameters were *A*, C_{\max} , and C_k . Therefore, the DYNIA was carried out only on these three parameters.

TABLE 1: Description of the model parameters and adjustment factors range for the rainfall-runoff module.

Parameter	Units	Description	Influence over	Parameter range	
C_{\max}	[—]	Maximum runoff coefficient when the subsurface layer is saturated	EI	0.1	0.7
P_{Lim}	[mm]	Limit of rainfall over which PPD exists	PPD	50	1000
D	[—]	Percentage of rainfall over P_{Lim} transformed into PPD	PPD	1	100
H_{\max}	[mm]	Maximum capacity of the soil layer to retain water	C_{\max} and ER	200	700
PORC	[—]	Fraction of H_{\max} that defines the soil water content restricting the evaporation processes	H_{crit} and ER	1	100
C_k	[—]	Subterranean runoff coefficient	ES	0.1	0.7
A	[—]	Adjustment factor of the precipitation data	PM	0.5	2.5
B	[—]	Adjustment factor of the potential evapotranspiration data	PET and ER	0.5	2.5

EI: direct runoff; PPD: direct deep percolation; ER: real evapotranspiration; ES: subterranean runoff; PM: precipitation; PET: potential evapotranspiration.

Figure 3 shows, for example, the dynamic identifiability plots according to the RMSE. It is observed that the shorter the time-window used for the DYNIA is, the more variability the time-series shows (e.g., Figures 3(a), 3(d), and 3(g)), and therefore wider areas are covered by the 90% confidence limits (area between the dashed lines) and the parameter is less identifiable. These results are probably related to uncertainties and noise in data (rainfall, evapotranspiration, and streamflow data), which are reduced and averaged out with larger time-windows. But also with larger time-windows, less variability can be observed in parameter series and aggregated responses are observed mainly because with a larger time-window the DYNIA tends to approximate a GIA. Figures 4, 5, and 6 summarize the information from the DYNIA plots for A , C_{\max} , and C_k and according to RMSE, TRMSE, and ROCE OFs, respectively. The boxes show the 25th and 75th percentiles (bottom and top blue lines) for each parameter, while the monthly average is shown by a red plus sign. Figures 5 and 6 do not show the boxes for the ROCE, because C_{\max} and C_k did not show identifiability on this OF.

Figure 3 shows that parameter A achieves values greater than 1 for the three OFs studied. A fulfills the function of correcting for orographic precipitation amounts. This parameter allows the long-term mass balance to be closed. In the cordillera and precordillera in south-central Chile, it is necessary to carry out this correction due to the absence of meteorological stations in the high zones of the Andes, due to which the increase in orographic precipitation is not well measured by the available instruments [25]. Similar analyses have been carried out by Muñoz et al. [30, 38, 39], and Zúñiga et al. [40].

Figure 3(a) shows that parameter A exhibits greater identifiability during high-flow periods (darker shaded areas and narrower ranges in high-flow periods). Figure 4 shows the seasonal variation of each parameter using boxes with the 25th and 75th percentiles (bottom and top blue lines) and the average (red plus sign) of the monthly time-series of each parameter. The range between the 25th and 75th percentiles is narrower for the rainy season (May–October), indicating that

A is more identifiable in winter than in summer (December–March) (wider box) and suggesting that A is highly related to orography. Moreover, these results suggest that, for better representativeness of the rainfall amounts in the basin, the measured and interpolated data need to be amplified about 1.25 to 1.45 times in the rainy period.

Parameter A is not identifiable (wider box) in summer because there is no rainfall that needs to be corrected. Similar results were obtained by Muñoz [4] in the Polcura River basin, close to the basin under study, in south-central Chile. These results suggest that the documented phenomenon of orography described by previous studies (e.g., [23, 25]) must be considered as part of the main hydrometeorological processes of the basin.

Parameter C_{\max} represents the maximum runoff coefficient that is reached when the subsurface storage system becomes saturated, and it is related to the surface runoff processes.

C_{\max} exhibits seasonal variability for RMSE (time-window of 3 and 7 months) and TRMSE (time-window of 3 months) (Figure 5). Comparing the dry and wet season, low parameter values are observed during summer (an average of about 0.2), which are related to less surface runoff, while the highest parameter values are observed during the rainy season (May–October), mostly with mean values between 0.3 and 0.4. However, the results suggest not only an influence of rainfall variability, but also the fact that geomorphology has a strong influence on surface runoff values and variability. More than 80% of the study area presents rocky and fractured formations [41]. This type of geology along with steep hillslopes influences the maximum runoff coefficient, which reaches only 0.2 during the dry period and up to 0.4–0.5 in rainy periods. Despite the high rainfall amounts that can occur in the Chillán basin throughout the year and its high slopes, the maximum runoff coefficient is not as high as would be expected. This is probably related to the volcanic nature of the basin and the high permeability of the soil layers [27]. Therefore, these results suggest that surface runoff tends to be reduced by infiltration and percolation processes.

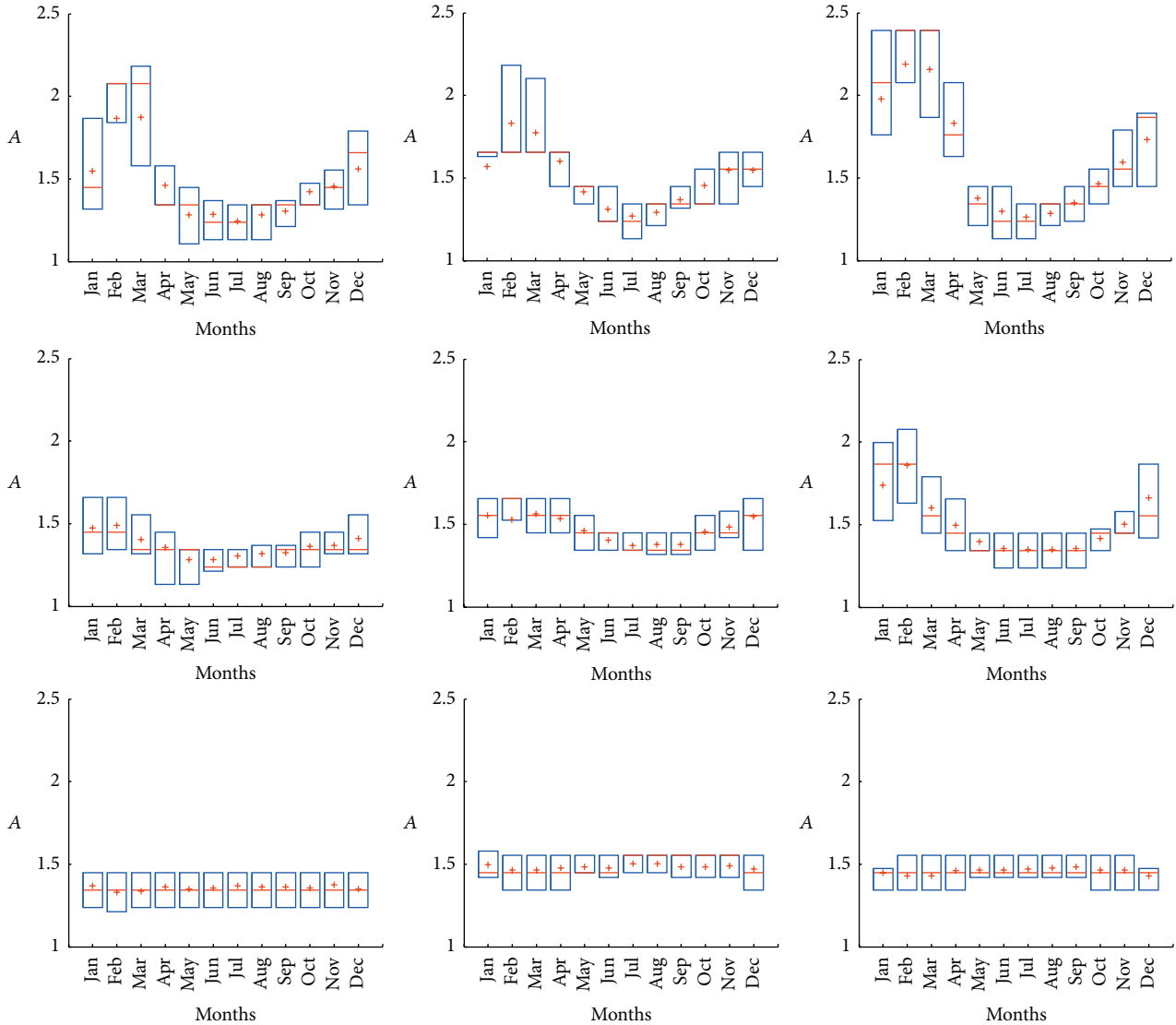


FIGURE 4: Seasonal variation of parameter A based on the DYNIA for the RMSE (left column), TRMSE (central column), and ROCE (right column) OFs and for 3 (top), 7 (middle), and 13 (bottom) months.

In addition, the observed seasonality has a direct connection to the rainfall patterns of the zone, in which there are greater C_{max} values in periods with increased precipitation and therefore a greater degree of saturation in the surface layers of the basin.

Regarding variability of C_{max} observed with the OF ROCE, a clear trend is not observed. Lower identifiability was observed in the dynamic identifiability plots (summarized by Figure 5) than in the RMSE and TRMSE, probably because ROCE is focused on the mass balance, and thus the runoff rates will be, relative to the other functions, much less identifiable than, for example, rainfall adjustment factor A. This suggests that the OF ROCE is only adequate to study the mass balance of the basin; after achieving it with the model, no further processes can be clearly identified.

Figure 6 shows the seasonal variation of parameter C_k , which represents the proportion of the subterranean storage

system that becomes the base-flow. It is observed that C_k shows higher identifiability during low-flow periods (darker shadings in Figure 3(g)), indicating that it is more influential on model outputs during summer, where the only observed discharge is the base-flow. Similar results can be found in Figure 6 where the boxes become narrower during summer.

Additionally, C_k tends to be larger during winter periods than during summer. This behavior is probably due to the type of geology described in the study area by SERNA-GEOMIN [27] (fractured volcanic rocks), which favors the rapid movement of groundwater. Thus, as the basin recharges, the proportion of the deep storage that is discharged as base-flow also increases (in winter and early spring) increasing the C_k values, and then when the catchment starts to get dry the deep storage contribution decreases and therefore the proportion of groundwater storage that becomes the base-flow, that is, C_k , decreases.

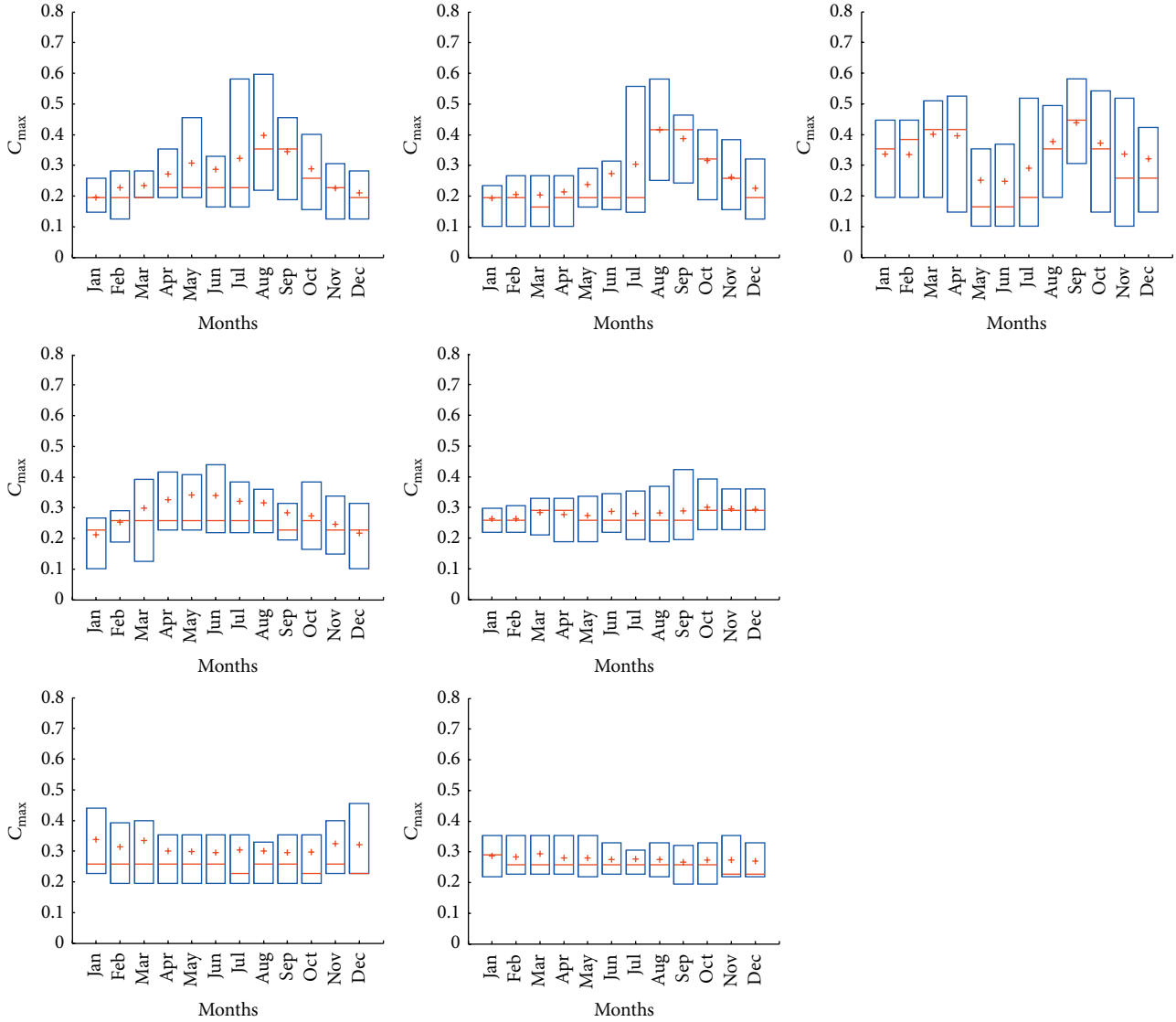


FIGURE 5: Seasonal variation of parameter C_{max} based on the DYNIA for the RMSE (left column), TRMSE (central column), and ROCE (right column) OFs and for 3 (top), 7 (middle), and 13 (bottom) months.

For the TRMSE, it is observed that C_k values tend to be more bounded than the rest of the analyzed OFs, suggesting that the TRMSE is adequate for studying base-flow dynamics.

These results are in line with the expected conceptual behavior of a volcanic basin with high slopes and highly permeable and fractured soil layers. The DYNIA is an adequate method to observe the main hydrological process dynamics and to perform a dynamic calibration strategy because it recovers the natural variability of identifiable processes.

6.2. Stationary against Dynamic Calibration. To compare both strategies of calibration, OF values were compared (Table 2). Also the Nash–Sutcliffe efficiency index (NSE) related to each calibration strategy (stationary or dynamic) and related to each OF was included to better discuss the model results.

Table 2 shows the OF values for the stationary and dynamic calibration of 3, 7, and 13 months. For the RMSE and TRMSE, the stationary calibration shows slightly better values than the dynamic approach, which is counterintuitive. However, for the 13-month time-window, the dynamic calibration shows a better RMSE value during the validation period and also shows a slightly smaller value than that for calibration. Something similar is observed for the TRMSE. The calibration-validation varies from 0.483 to 0.606 with a stationary calibration while it varies from 0.503 to 0.605 for a time-window of 7 months and from 0.489 to 0.585 for a time-window of 13 months. This indicates that although with dynamic calibration better values are not achieved, the validation tends to be better (smaller). In other words, the difference between calibration and validation values tends to be smaller in a dynamic than in a stationary calibration.

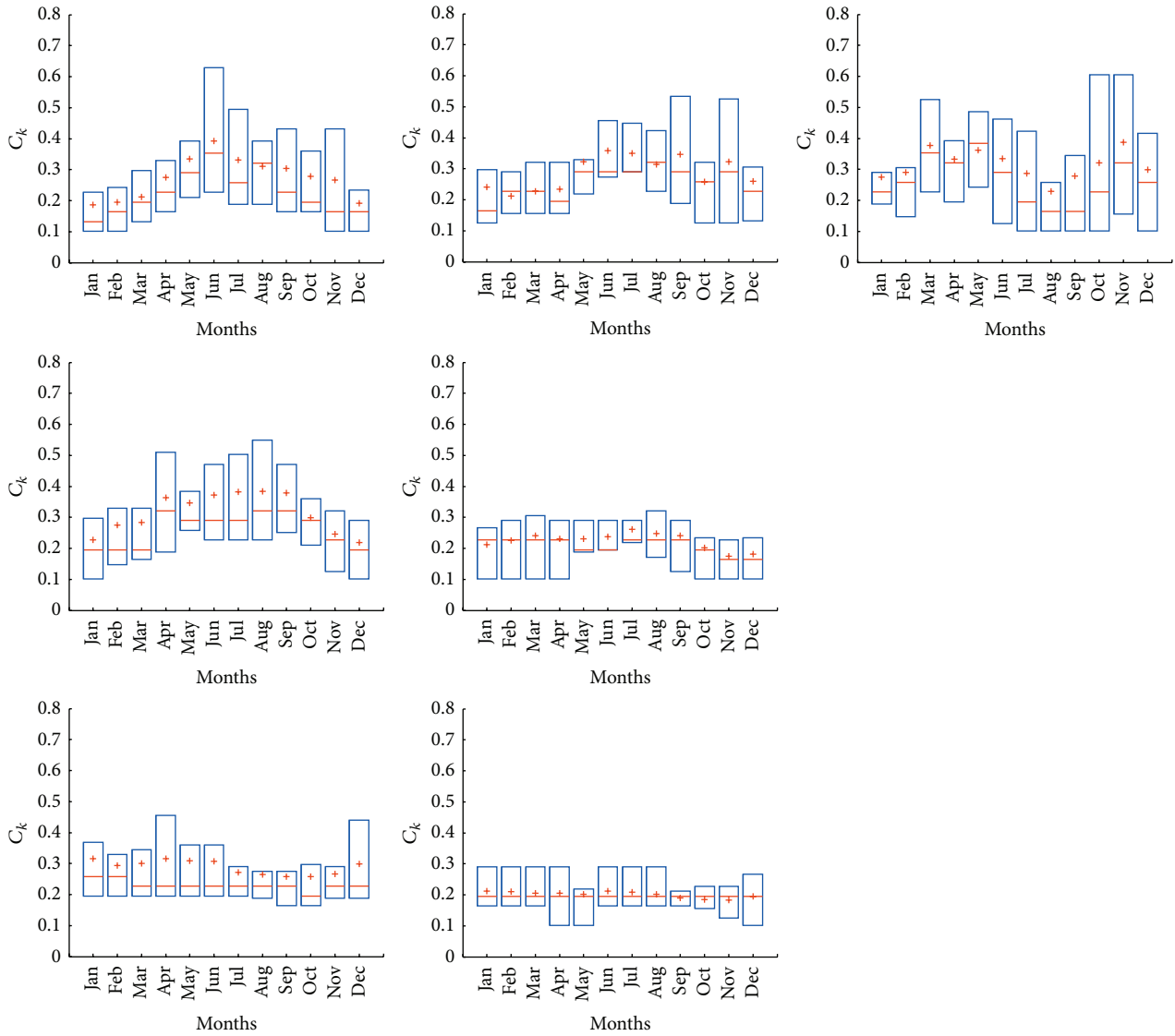


FIGURE 6: Seasonal variation of parameter C_k based on the DYNIA for the RMSE (left column), TRMSE (central column), and ROCE (right column) OFs and for 3 (top), 7 (middle), and 13 (bottom) months.

TABLE 2: OF and NSE-related values for the stationary and dynamic strategies of calibration.

	Stationary		Dynamic					
	Calibration 1961–1977	Validation 1978–1994	Calibration (1961–1977)			Validation (1978–1994)		
			3 months	7 months	13 months	3 months	7 months	13 months
RMSE	4.327	4.694	5.343	4.464	4.475	6.173	4.754	4.455
TRMSE	0.483	0.606	0.571	0.503	0.489	0.676	0.605	0.585
ROCE	0.001	0.006	0.002	0.000	0.000	0.010	0.007	0.008
			NSE-related					
RMSE	0.840	0.860	0.774	0.841	0.843	0.785	0.867	0.872
TRMSE	0.840	0.860	0.740	0.827	0.843	0.779	0.867	0.869
ROCE	0.840	0.850	0.728	0.770	0.749	0.734	0.757	0.758

A stationary model calibration seeks to maximize the agreement between observed and simulated streamflows in the evaluation period; therefore, all parameter values are defined to maximize a measure of evaluation (i.e., an objective function). On the other hand, dynamic calibration is performed to maximize the measure of evaluation as well as hydrological process representativeness. These processes (represented by parameters) have exhibited interannual variability and seasonality. The observed seasonality was realistic for processes such as orography, surface runoff, and groundwater runoff in a mountainous Chillán river basin.

As many authors have discussed (e.g., [12, 17, 18]), hydrological processes vary in time, and therefore a dynamic model should better simulate basin behavior and its processes. The narrower range observed for the calibration-validation analysis suggests that a dynamic model tends to be better (more robust) than a stationary model and tends to better approximate realistic basin behavior. Moreover, the dynamic calibration also contributed to a better understanding of the system under study and was a very useful option in poorly understood basins such as Chilean Andean basins.

When we compare the ROCE no benefits are observed in the dynamic calibration. This is probably due to the OF which is only focused on the mass balance and therefore does not take into account the hydrological processes of the basin and the exact shape of the hydrograph while a good water balance is achieved. Further studies using ROCE for studying the mass balance combined with a secondary OF for comparing the shape of the hydrograph can be recommended for the future.

The NSE-related values show the same behavior as discussed above. Validation NSE values tend to be slightly better with the dynamic calibration (7 and 13 months), suggesting that the model representativeness is improved by including the dynamic variation of parameters in the model conceptualization and its equations.

This study has shown for an Andean basin that, using a time-varying approach for model conceptualization, a better (more robust and representative) model can be obtained, which is in full agreement with the results of Oudin et al. [18].

7. Conclusions

Stationary (with fixed model parameters) and dynamic (time-varying parameters) calibration strategies were performed based on the General and Dynamic Identifiability Analyses, respectively.

The General Identifiability Analysis was performed to maximize the agreement between simulated and observed streamflows, while the Dynamic Identifiability Analysis also aimed to better represent the variability of basin processes.

The DYNIA proved to be a very useful option for studying data-sparse basins such as the *Chillán en Esperanza* river basin. DYNIA, combined with a conceptual model, was an adequate option for obtaining realistic information about hydrological process variability in the basin. Therefore, DYNIA contributed to a better understanding of a data-sparse mountainous basin.

Time variability of processes such as the orography, surface runoff, and base-flow was observed and moreover modeled.

Dynamic calibration proved to be better than stationary. Although stationary calibration resulted in better OFs in calibration, the dynamic model presented better validation values. Additionally, the differences between calibration and validation were lower with the dynamic calibration strategy, suggesting that the dynamic conceptualization and formulation of a hydrological model are better (more robust) and more realistic than in a stationary model.

The results shown in the present study suggest that the incorporation of hydrological dynamics in models must be considered in the modeling stage, not only for a better measurement of the OFs but also because it is the most adequate option for representing the hydrological processes that predominate in the basin and the variability that they could have in time.

This study helped to improve our understanding of the hydrological processes related to groundwater runoff, surface runoff, and the orographic effect produced in a data-sparse Andean catchment. Regarding the seasonality of these processes, it was observed that they could be directly related to fluctuations in model inputs and are probably related to climate variability and change.

Further studies which include larger scales variability such as climate change trends and variability, caused by, for example, the El Niño Southern Oscillation phenomenon, are recommended.

It is expected that including these dynamics in modeling will help make forecasts and predictions less uncertain and more representative of the hydrological processes in the study area.

Conflict of Interests

The authors declare that there is no conflict of interests in this paper.

Acknowledgments

The authors thank the *Dirección General de Aguas* for providing the rain gauge and fluviometric data and the FONDECYT 11121287 Project “Hydrological Process Dynamics in Andean Basins. Identifying the Driving Forces, and Implications in Model Predictability and Climate Change Impact Studies” which has supported this research.

References

- [1] T. F. Stocker, D. Qin, G.-K. Plattner et al., Eds., *Climate Change 2013: The Physical Science Basis. Contribution of Working Group I to the Fifth Assessment Report of the Intergovernmental Panel on Climate Change*, Cambridge University Press, Cambridge, UK, IPCC, New York, NY, USA, 2013.
- [2] X. Jin, C.-Y. Xu, Q. Zhang, and V. P. Singh, “Parameter and modeling uncertainty simulated by GLUE and a formal Bayesian method for a conceptual hydrological model,” *Journal of Hydrology*, vol. 383, no. 3-4, pp. 147–155, 2010.

- [3] S. Uhlenbrook, J. Seibert, C. Leibundgut, and A. Rodhe, "Prediction uncertainty of conceptual rainfall-runoff models caused by problems in identifying model parameters and structure," *Hydrological Sciences Journal*, vol. 44, no. 5, pp. 779–797, 1999.
- [4] E. Muñoz, *Perfeccionamiento de un modelo hidrológico: aplicación de análisis de identificabilidad dinámico y uso de datos grillados [Ph.D. thesis]*, Departamento de Recursos Hídricos, Universidad de Concepción, Chillán, Chile, 2011.
- [5] F. Fenicia, J. J. McDonnell, and H. H. G. Savenije, "Learning from model improvement: on the contribution of complementary data to process understanding," *Water Resources Research*, vol. 44, no. 6, 2008.
- [6] J. Schuol, K. C. Abbaspour, R. Srinivasan, and H. Yang, "Estimation of freshwater availability in the West African sub-continent using the SWAT hydrologic model," *Journal of Hydrology*, vol. 352, no. 1-2, pp. 30–49, 2008.
- [7] J. Alcamo, P. Döll, T. Henrichs et al., "Development and testing of the WaterGAP 2 global model of water use and availability," *Hydrological Sciences Journal*, vol. 48, no. 3, pp. 317–338, 2003.
- [8] T. Jiang, Y. D. Chen, C.-Y. Xu, X. Chen, X. Chen, and V. P. Singh, "Comparison of hydrological impacts of climate change simulated by six hydrological models in the Dongjiang Basin, South China," *Journal of Hydrology*, vol. 336, no. 3-4, pp. 316–333, 2007.
- [9] R. Merz, J. Parajka, and G. Blöschl, "Time stability of catchment model parameters: implications for climate impact analyses," *Water Resources Research*, vol. 47, no. 2, 2011.
- [10] D. Legesse, C. Vallet-Coulomb, and F. Gasse, "Hydrological response of a catchment to climate and land use changes in Tropical Africa: case study south central Ethiopia," *Journal of Hydrology*, vol. 275, no. 1-2, pp. 67–85, 2003.
- [11] Y.-P. Lin, N.-M. Hong, P.-J. Wu, C.-F. Wu, and P. H. Verburg, "Impacts of land use change scenarios on hydrology and land use patterns in the Wu-Tu watershed in Northern Taiwan," *Landscape and Urban Planning*, vol. 80, no. 1-2, pp. 111–126, 2007.
- [12] E. Muñoz, J. L. Arumí, and D. Rivera, "Watersheds are not static: implications of climate variability and hydrologic dynamics in modeling," *Bosque*, vol. 34, no. 1, pp. 7–11, 2013.
- [13] K. Beven, "A manifesto for the equifinality thesis," *Journal of Hydrology*, vol. 320, no. 1-2, pp. 18–36, 2006.
- [14] G. Wriedt and M. Rode, "Investigation of parameter uncertainty and identifiability of the hydrological model WaSiM-ETH," *Advances in Geosciences*, vol. 9, pp. 145–150, 2006.
- [15] P. C. D. Milly, J. Betancourt, M. Falkenmark et al., "Stationarity is dead: whither water management?" *Science*, vol. 319, no. 5863, pp. 573–574, 2008.
- [16] M. C. Peel and G. Blöschl, "Hydrological modelling in a changing world," *Progress in Physical Geography*, vol. 35, no. 2, pp. 249–261, 2011.
- [17] F. H. S. Chiew, N. J. Potter, J. Vaze et al., "Observed hydrologic non-stationarity in far south-eastern Australia: implications for modelling and prediction," *Stochastic Environmental Research and Risk Assessment*, vol. 28, no. 1, pp. 3–15, 2014.
- [18] L. Oudin, V. Andréassian, T. Mathevet, C. Perrin, and C. Michel, "Dynamic averaging of rainfall-runoff model simulations from complementary model parameterizations," *Water Resources Research*, vol. 42, no. 7, 2006.
- [19] M. L. Roderick and G. D. Farquhar, "A simple framework for relating variations in runoff to variations in climatic conditions and catchment properties," *Water Resources Research*, vol. 47, no. 6, pp. 1–11, 2011.
- [20] D. Koutsoyiannis, "Hurst-Kolmogorov dynamics and uncertainty," *Journal of the American Water Resources Association*, vol. 47, no. 3, pp. 481–495, 2011.
- [21] J. Luo, E. Wang, S. Shen, H. Zheng, and Y. Zhang, "Effects of conditional parameterization on performance of rainfall-runoff model regarding hydrologic non-stationarity," *Hydrological Processes*, vol. 26, no. 26, pp. 3953–3961, 2012.
- [22] T. Wagener and J. Kollat, "Numerical and visual evaluation of hydrological and environmental models using the Monte Carlo analysis toolbox," *Environmental Modelling & Software*, vol. 22, no. 7, pp. 1021–1033, 2007.
- [23] M. Mardones, H. Hernández, O. Cristi et al., *Geografía VIII Región del BíoBío*, Instituto Geográfico Militar (IGM), Santiago, Chile, 2001.
- [24] C. Henríquez, "El proceso de urbanización en la cuenca del río Chillán y su capacidad adaptativa ante precipitaciones extremas," *Instituto de Geografía, Pontificia Universidad Católica de Chile. Estudios Geográficos*, vol. 80, pp. 155–179, 2009.
- [25] R. D. Garreaud, "The Andes climate and weather," *Advances in Geosciences*, vol. 22, pp. 3–11, 2009.
- [26] G. Casassa, "Glacier inventory in Chile: current status and recent glacier variations," *Annals of Glaciology*, vol. 21, pp. 317–322, 1995.
- [27] Servicio Nacional de Geología y Minería (SERNAGEOMIN), *Mapa Geológico de Chile: Versión Digital. Servicio Nacional de Geología y Minería*, no. 4, Publicación Geológica Digital, Santiago, Chile, 2003.
- [28] R. Figueroa, A. Palma, V. Ruiz, and X. Niell, "Análisis comparativo de índices bióticos utilizados en la evaluación de las aguas en un río mediterráneo de Chile: río Chillán, VIII Región," *Revista Chilena de Historia Natural*, vol. 80, no. 2, pp. 225–242, 2007.
- [29] E. Muñoz, *Desarrollo de un modelo hidrológico como herramienta de apoyo para la gestión del agua. Aplicación a la cuenca del Río Laja, Chile [Master thesis]*, Universidad de Cantabria, Santander, Spain, 2010.
- [30] E. Muñoz, R. Rivera, F. Vergara, P. Tume, and J. L. Arumí, "Identifiability analysis: towards constrained equifinality and reduced uncertainty in a conceptual model," *Hydrological Sciences Journal*, vol. 59, no. 9, pp. 1690–1703, 2014.
- [31] D. Ruelland, S. Ardoin-Bardin, G. Billen, and E. Servat, "Sensitivity of a lumped and semi-distributed hydrological model to several methods of rainfall interpolation on a large basin in West Africa," *Journal of Hydrology*, vol. 361, no. 1-2, pp. 96–117, 2008.
- [32] C. Willmott and K. Matsuura, *Terrestrial Air Temperature and Precipitation: Monthly and Annual Time Series (1900–2010) (Version 3.01)*, Center for Climatic Research, University of Delaware, Newark, Del, USA, 2012, <http://climate.geog.udel.edu/~climate/>.
- [33] G. M. Hornberger and R. C. Spear, "An approach to the preliminary analysis of environmental systems," *Journal of Environmental Management*, vol. 12, no. 1, pp. 7–18, 1981.
- [34] T. Wagener, D. P. Boyle, M. J. Lees, H. S. Wheater, H. V. Gupta, and S. Sorooshian, "A framework for development and application of hydrological models," *Hydrology and Earth System Sciences*, vol. 5, no. 1, pp. 13–26, 2001.
- [35] T. Wagener, N. McIntyre, M. J. Lees, H. S. Wheater, and H. V. Gupta, "Towards reduced uncertainty in conceptual rainfall-runoff modelling: dynamic identifiability analysis," *Hydrological Processes*, vol. 17, no. 2, pp. 455–476, 2003.

- [36] T. Wagener, K. van Werkhoven, P. Reed, and Y. Tang, “Multiobjective sensitivity analysis to understand the information content in streamflow observations for distributed watershed modeling,” *Water Resources Research*, vol. 45, no. 2, 2009.
- [37] K. van Werkhoven, T. Wagener, P. Reed, and Y. Tang, “Sensitivity-guided reduction of parametric dimensionality for multi-objective calibration of watershed models,” *Advances in Water Resources*, vol. 32, no. 8, pp. 1154–1169, 2009.
- [38] E. Muñoz, C. Álvarez, M. Billib, J. L. Arumí, and D. Rivera, “Comparison of gridded and measured rainfall data for basin-scale hydrological studies,” *Chilean Journal of Agricultural Research*, vol. 71, no. 3, pp. 459–468, 2011.
- [39] E. Muñoz, J. L. Arumí, D. Rivera, A. Montecinos, M. Billib, and C. Álvarez, “Gridded data for a hydrological model in a scarce-data basin,” *Proceedings of the ICE—Water Management*, vol. 167, no. 5, pp. 249–258, 2014.
- [40] R. Zúñiga, E. Muñoz, and J. L. Arumí, “Estudio de los procesos hidrológicos de la cuenca del Río Diguillín,” *Obras y proyectos*, no. 11, pp. 69–78, 2012.
- [41] J. A. Naranjo, J. Gilbert, and R. S. Sparks, “Geología del complejo volcánico Nevados de Chillán, Región del Biobío. Servicio Nacional de Geología y Minería,” in *Carta Geológica de Chile*, Serie Geología Básica 114, 1 map scale 1:50.000, p. 28, 2008.

Research Article

Groundwater—Surface Water Interactions in a Mountain-to-Coast Watershed: Effects of Climate Change and Human Stressors

S. B. Foster and D. M. Allen

Department of Earth Sciences, Simon Fraser University, Burnaby, BC, Canada V5A 1S6

Correspondence should be addressed to D. M. Allen; dallen@sfu.ca

Received 11 November 2014; Accepted 13 February 2015

Academic Editor: Yongqiang Zhang

Copyright © 2015 S. B. Foster and D. M. Allen. This is an open access article distributed under the Creative Commons Attribution License, which permits unrestricted use, distribution, and reproduction in any medium, provided the original work is properly cited.

Watersheds located within a mountain to coast physiographic setting have been described as having a highly interconnected surface water and groundwater environment. The quantification of groundwater—surface water interactions at the watershed scale requires upscaling. This study uses MIKE SHE, a coupled numerical model, to explore the seasonally and spatially dynamic nature of these interactions in the Cowichan Watershed on Vancouver Island, British Columbia, Canada. The calibrated model simulates a transition of the Cowichan River from mostly gaining within the valley, to losing stream near the coast where groundwater extraction is focused. Losing and gaining sections correlate with geological substrate. Recharge across the watershed accounts for 17% of precipitation. Climate change is projected to lessen snowpack accumulation in the high alpine and alter timing of snowmelt, resulting in higher spring and winter river discharge and lower summer flows.

1. Introduction

Watersheds located within a mountain-to-coast physiographic setting are unique in that they have been described as having a highly connected surface water and groundwater environment [1]. The high degree of coarse alluvial material, coupled with a steep topographic setting, creates conditions whereby the surface water and groundwater systems strongly interact. In regions where the climate is seasonally dry, the principal source of water within a stream is often from the discharge of groundwater [1–3]. Streams, however, may also recharge the aquifer, particularly during the freshet (e.g., [4]). These relationships are often poorly understood aspects of the hydrology within a mountainous watershed. Water balances, including estimates of recharge and discharge, are also highly variable within this type of setting, especially since the climate gradient (heavy precipitation in the mountains to relatively low precipitation near the ocean) is both seasonally and spatially variable. Also, there is a high degree of geological variability (shallow or exposed bedrock near the crest of the valley, and alluvium of variable thickness and composition

within the valley). Management of water in such watersheds thus requires sound understanding of a range of hydrologic processes and particularly those factors that influence the interaction of groundwater and surface water at a range of spatial and temporal scales [1, 2, 5].

Coupled groundwater–surface water models are being increasingly used to examine a variety of environmental interactions, including interactions in small mountainous catchments [6]; solute transport [7, 8], flood wave modeling [9], catchment water resource management and understanding [10–17], the role of aquifer heterogeneity [18, 19], and wetland alterations and aquaculture [20, 21].

This study aims to contribute to the knowledge of surface water and groundwater interactions within a mountain-to-coast watershed, specifically through investigating how these interactions may be influenced by different stressors within the watershed. The study area is the Cowichan Watershed, situated on Vancouver Island in British Columbia, Canada (Figure 1). The steep topographical setting and geological conditions create conditions whereby the groundwater and

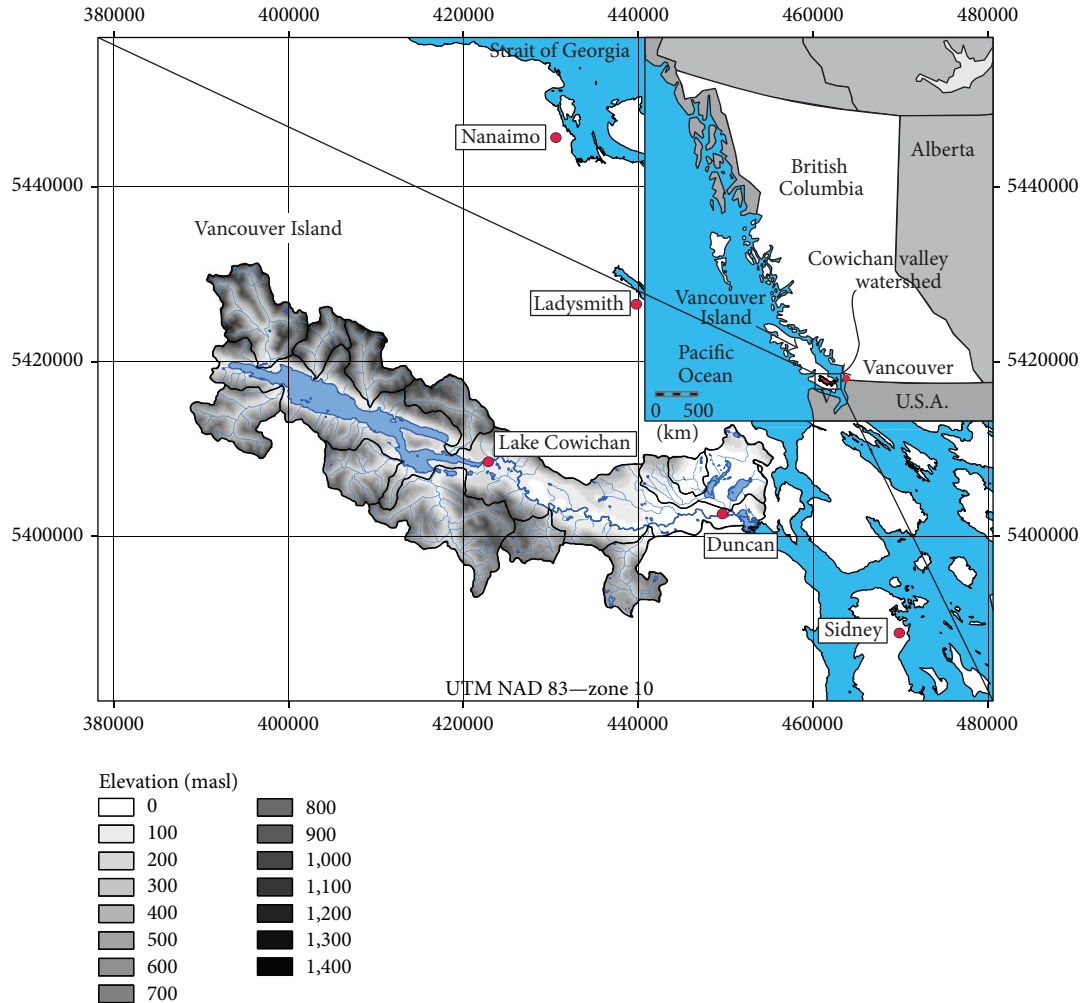


FIGURE 1: Location of the Cowichan Watershed, British Columbia, Canada.

surface water systems are dynamically coupled. The watershed is comprised of several catchments, covers an area of approximately 930 km², attains a maximum elevation of approximately 1483 metres above mean sea level (masl) in the headwater region to the west, and terminates at sea elevation near its eastern extent. Cowichan Lake has a surface area of 62 km² and stretches nearly 31 km from west to east. The Cowichan River flows from the headwaters at Cowichan Lake eastward for nearly 45 km to the estuary in Cowichan Bay near Duncan.

The watershed itself is a vast valley with a large accumulation of valley fill sediments, flanked by valley walls with thin veneers of soil. The climate is temperate with cool and wet fall and winter seasons, while the spring and summer months are warm and typically much drier. There is a strong precipitation gradient (decreasing to the east) due to a rain shadow effect. The lower coastal section of the watershed receives half the amount of precipitation (~1000 mm/year) than that received at Lake Cowichan (~2000 mm/year). It is estimated that the mountainous regions at the western boundary of this watershed can receive up to 4500 mm of precipitation annually [22]. Most precipitation occurs during

the winter months, while very low amounts are measured in the summer months. At most, snow accounts for ~5–15% of the total precipitation.

The watershed provides fresh water to over 43,000 people, as well as agriculture and several forms of industry (fish farms, paper mills, etc.). More than 530 surface water licenses have been issued to divert water from streams and lakes in the watershed, and more than 1,300 wells have been drilled to pump water from the aquifers [23]. Water users within the watershed include agriculture, industry, and urban and rural water supply. There are several large water users within the watershed including, the pulp and paper industry (Catalyst Paper), fish hatcheries, and municipal water supply (Figure 2).

Recently, seasonal fluctuations, and changes in the timing of rainfall events have created challenges for managing water in the watershed. The variability in seasonal rainfall is extremely large; flooding conditions can occur in the winter, while drought conditions can prevail in the summer. Water demand puts added stress onto the hydrologic system, as peak demands for water occur during the summer low flow season. In 2012, the seriousness of the problem

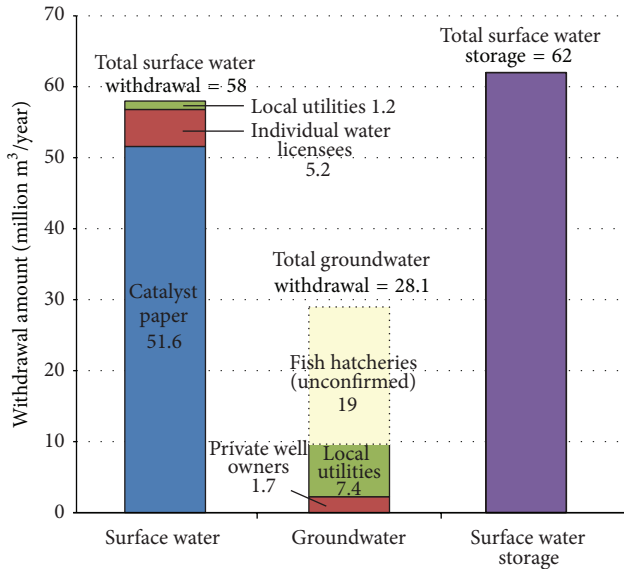


FIGURE 2: Water use according to user group within the Cowichan Watershed.

became obvious as returning salmon struggled to reach their spawning locations; this gained attention from the press. To address these issues and gain insight on the hydrologic conditions, a coupled groundwater-surface water model was developed using MIKE SHE [24]. The calibrated model is used to assess groundwater recharge and discharge, estimate the contributions of groundwater to the surface water system, identify key gaining portions of the Cowichan River, and evaluate the impact of localized pumping on the system. Lastly, the model is used to project how future climate may affect the dynamics of the hydrogeological system (over the next 40 and 70 years).

2. Materials and Methods

2.1. The MIKE SHE Modeling Interface. MIKE SHE is a deterministic and distributed modeling system that uses finite difference representations in mass and energy and measured empirical relationships to simulate aspects of the hydrologic cycle [24]. At its core is a framework of modules that are used to simulate the following processes: interception and evaporation, overland flow, unsaturated zone flow, saturated zone flows, and water quality. Rivers, lakes, and other channels are operated in the one-dimensional model, MIKE 11, which is coupled directly to the MIKE SHE model. The interception and evaporation module computes the actual evaporation (AET) from an area using user-defined potential evaporation (PET), using the Kristensen and Jensen [25] model. This model requires vegetation dependent parameters such as leaf area index (LAI), root characteristics, and an interception parameter. Unsaturated flow is calculated in 1D, vertically. A soil moisture retention curve along with the saturated hydraulic conductivity are defined for each soil class spatially, and the vertical layer. Richards' equation is solved, and water flows from the unsaturated zone to the saturated

zone, or vice versa. The overland flow component simulates runoff when the infiltration capacity of the soil is exceeded, when groundwater discharges to the surface, or when streams flood their banks. In this study, the flow solution utilized the diffusive wave approximation of the Saint-Venant equation, whereby topography, and the Manning's M coefficient control the direction and rate of runoff, respectively. The saturated zone flow component in MIKE SHE is 3D and is based on Darcy's equation. Boundary conditions such as fixed head, zero flux, gradient, and specified flux are options which control the flow of groundwater within the model. Subsurface conditions are modelled as layers and lenses, with representative hydraulic properties assigned.

As mentioned, MIKE 11 controls the routing of water in rivers and lakes. The rivers module comprises four main components: the river network, river cross-sections, boundary conditions, and hydrodynamic parameters. MIKE 11 solves channel flow through the use of a 1D St. Venant equation based on the complete dynamic wave formulation [26]. MIKE SHE and MIKE 11 are coupled through the use of river links (h -points). During a simulation, the amount of water entering or exiting the linking cells is calculated based on Darcy's equation. Lateral inflows and outflow from overland flow as well as river-aquifer exchanges are completed for each computational time step [24].

2.2. Model Setup. The simulation period spanned January 1, 1998, to December 31, 2012 (the most recent date of available data). It was important to capture the year 2012, as the motivation for this study was the anomalously low river discharge of the Cowichan River during the salmon spawning season and the timing of late summer rains in that year. The initial groundwater levels were assigned at ground surface, as discussed below; therefore, the model had to spin up to achieve a dynamically stable state in which the deep groundwater levels no longer decline over time. It was found that starting the model in 1998 was adequate for both spin up and providing a suitable time frame (12 years) for analysis. All data output time steps were set to 24 hours with the exception of groundwater, which was set to 48 hours.

The model grid size was 200 m by 200 m. Topography was assigned using a 200 m digital elevation model (DEM). The model boundary conditions consist of a zero flux boundary to represent the topographical boundary of the watershed, and a specified head (sea level) within the alluvial layer where the model meets the ocean and Cowichan Bay. Underneath the alluvial layer, the bedrock layer is set to a zero flux boundary. These boundary conditions attempt to mimic groundwater discharge in a coastal environment, whereby deep groundwater is directed upward when it intersects the freshwater-saltwater interface. Thus, any discharge from the bedrock will be directed upward to the surficial sediments and subsequently out of the model. Overall, the assigned boundary conditions route whatever precipitation falls onto the model domain out of the model along three potential pathways: evaporation, surface water termination at the ocean, and groundwater discharge upward along the coast and directly into the ocean.

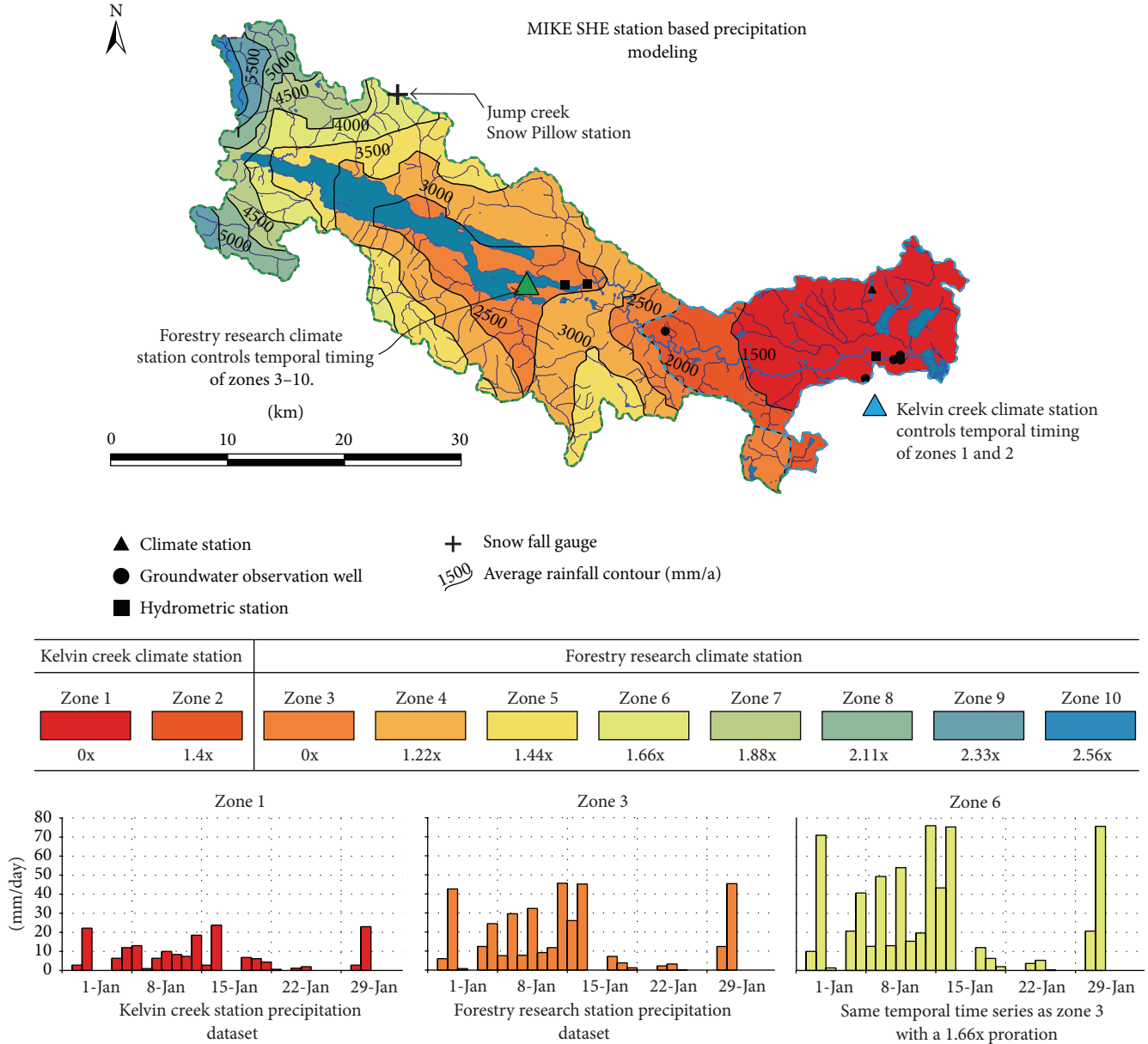
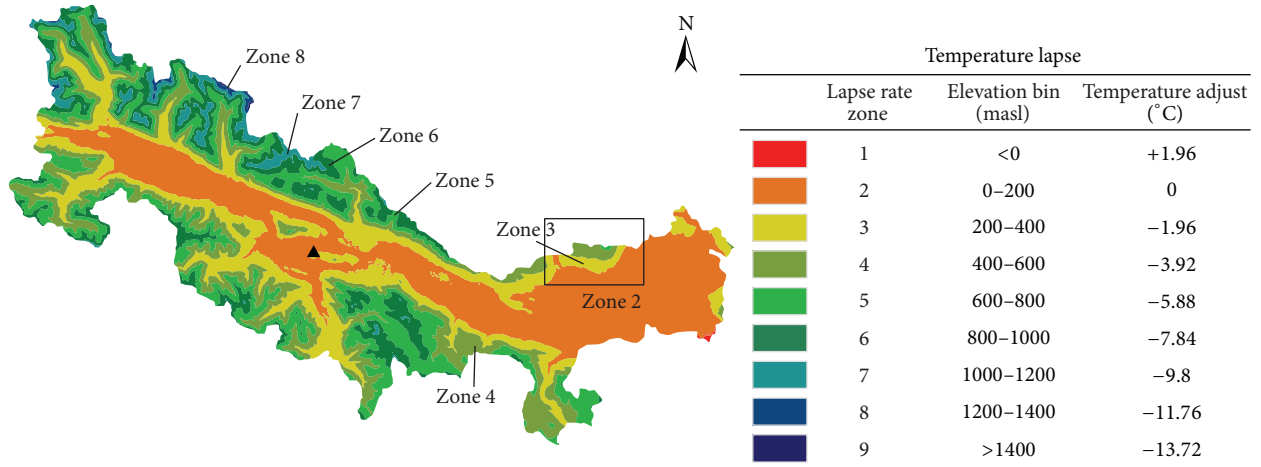


FIGURE 3: Method of applying meteorological data across the watershed to the MIKE SHE model.

2.3. *Meteorological Data.* Precipitation was imported into MIKE SHE using a “station based” time varying format. Throughout the watershed, annual precipitation ranged from approximately 1000 to 5600 mm/yr and was used as a basis to divide the watershed into 10 zones based on an increase of 500 mm/yr per zone (Figure 3). Zones 1 and 2 were represented by the precipitation recorded at the Kelvin Creek climate station, while Zones 3 through 10 were represented by the Forestry Research Station (Figure 3). To model the increase in precipitation due to orographic and rain shadow effects, a proration was applied to each zone, based on the median amount of precipitation observed within that zone as illustrated on Figure 3.

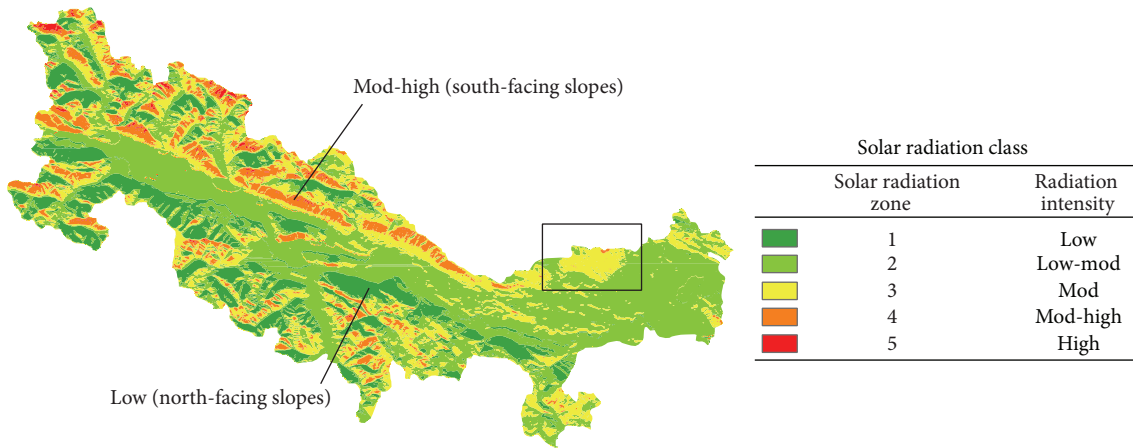
Air temperature was defined using the dataset from the Forestry Research Station as there were negligible differences between this station and the Kelvin Creek Station. The spatial variation in temperature was modified from the station data according to a fixed temperature lapse rate (Figure 4(a)). The temperature recorded at the Jump Creek Snow Pillow Station was used as a calibration for the temperature lapse rate parameter.

Potential evapotranspiration (PET) was calculated using the Penman-Monteith method, carried out using a software package AWSET [27]. Daily climate data consisted of mean air temperature, humidity, solar radiation, and wind speed. Due to the variability of these climate parameters at

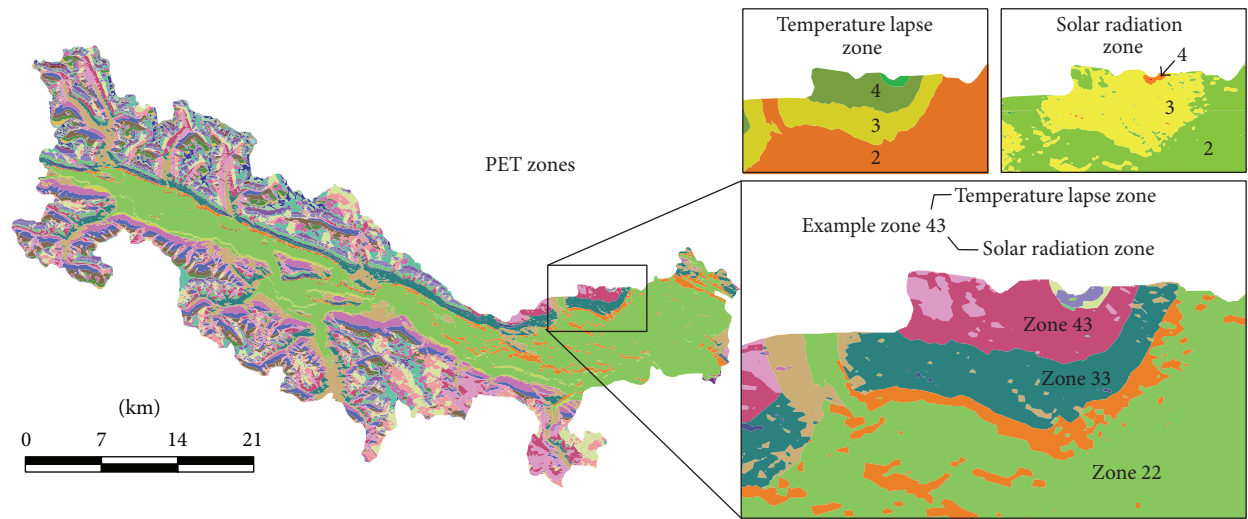


▲ Climate station

(a)



(b)



(c)

FIGURE 4: PET zone estimation methodology for mountainous terrain. (a) Temperature distribution estimated from the lapse rate (-9.8°C per 1000 m increase in elevation); (b) solar radiation classes (range of zones: Zone 1—consisting of steep north-facing slopes with reduced radiation from mountain shadow, to Zone 5—high altitude, south facing slopes not impeded by mountain shadows); (c) merged PET zones (42 PET permutations across the watershed).

Class	Est. LAI range	Represents	Coverage of watershed (%)	Est. seasonal range	Est. rooting depth (mm)
1	0-1	Open water bodies and urban areas	14	0	0
2	1-5	Highways and clear-cut areas	19	1-3	400
3	5-10	Previously logged	31	1-7.5	400
4	10-15	Pristine	32	10-12.5	400
5	>15	Exceptionally densely vegetated	4	10-17.5	400

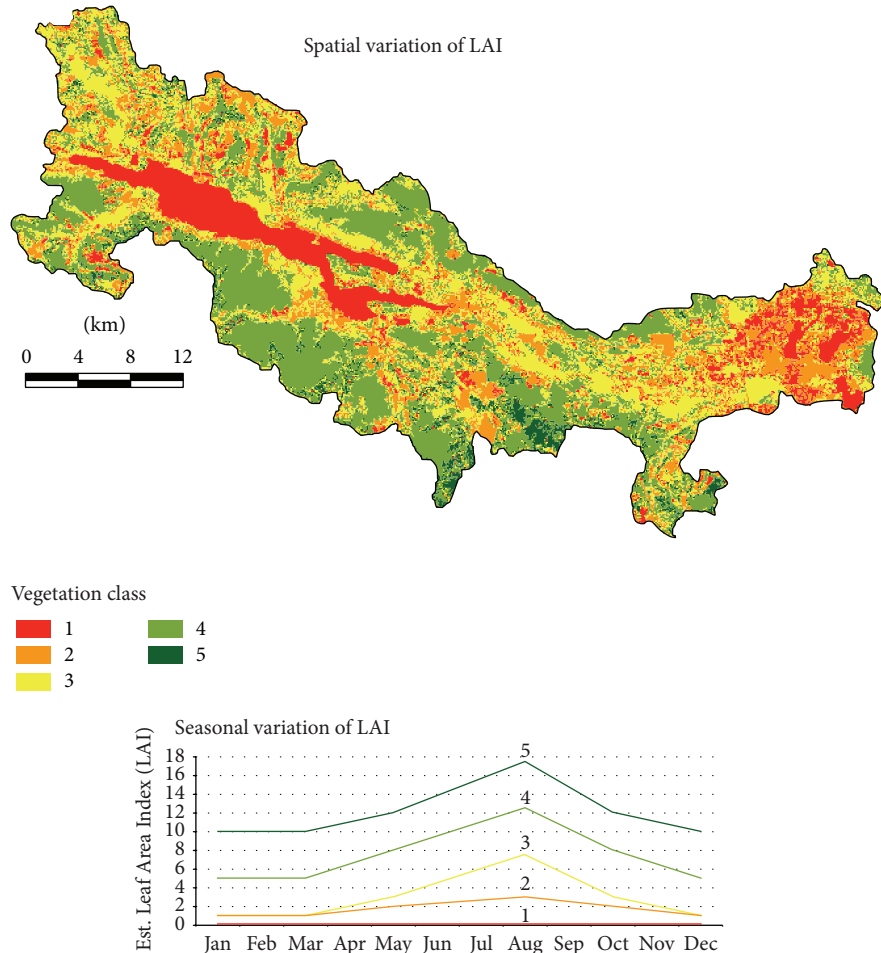


FIGURE 5: Spatial and seasonal variations of leaf area index (LAI) within the Cowichan Watershed.

the watershed scale, PET was estimated by recording the variability of daily mean temperature as it relates to altitude and location (Figure 4(a)), and then mapping the spatial variability of solar radiation (slope and aspect) within the region using the solar radiation analysis tool in ArcGIS [28] (Figure 4(b)). These two spatial datasets were then merged to create a PET zone map consisting of 42 zones (Figure 4(c)). The PET values were adjusted to an appropriate range based on values in an area with similar climate [29, 30]. All 42 permutations were added to MIKE SHE as time series.

Precipitation, PET, and temperature were set input parameters not subject to calibration, while parameters such as temperature lapse rate and snowmelt parameters were adjusted, through calibration, to match observed snowmelt

data recorded at the alpine Jump Creek Snow Pillow Station. Table 1 shows the final snowmelt parameters.

2.4. Land Surface Data. The Cowichan region is classified into two main biogeoclimatic zones: Coastal Douglas-Fir and Coastal Western Hemlock (BC Biogeoclimatic Ecosystem Classification (BEC) system). Leaf area index (LAI) was estimated using satellite reflection imagery and calibrated to a published statistical relationship [31]. Observed data were grouped into five land use classes (Figure 5). For example, LAI values between 0 and 1 were grouped into Class 1 and assigned a LAI value of 0, which spatially represents open bodies of water, and urban areas. LAI values ranging from 5 to

TABLE 1: Final parameters used for the snowmelt module.

Snowmelt parameter	Value
Temperature lapse rate ($^{\circ}\text{C}/100\text{ m}$)	-0.495
Melting coefficient for thermal energy in rain ($^{\circ}\text{C}^{-1}$)	0.3
Degree-day melting coefficient ($\text{mm}/^{\circ}\text{C}/\text{d}$)	1
Max wet snow fraction (Fraction)	0.3

10 were grouped into Class 3 and assigned a LAI value of 7.5 to represent a moderate LAI and distinguish previously logged areas. Classes 4 and 5 represent old growth and biologically dense areas, respectively.

These classes were also defined in terms of phenology to represent seasonal variations in vegetation density. Due to the fact that the Landsat satellite image used in the calculation of LAI was recorded in August of the year 2002, it likely represented a maximum LAI value. The BEC system suggests that most of the mature trees within the study area are coniferous (Western Hemlock, Redcedar, Douglas-Fir, lesser Arbutus, and Garry Oak); however, the understory is made up of ferns and shrubs. Therefore, some variation in LAI is expected [32]. Accordingly, Class 3 was assigned the highest seasonal variation as it represents a deforested system and, therefore, would largely comprise quickly inhabiting deciduous trees (Cottonwood, Aspen, Alder, and various shrubs). The seasonal variation for Classes 4 and 5 was set lower, based on the assumption that the forest cover is likely more mature and reflects the descriptions in the BEC. Within MIKE SHE, a consistent rooting depth of 400 mm was applied. Rooting depths are typically dependent on soil fertility and structure; however, Curt [33] suggests that majority of root mass is concentrated within the top 400 mm of soil, regardless of soil quality.

Along with the spatially and time varying LAI dataset, the vegetation module also contains ET parameters, which can be altered based on site specific data. The parameters include canopy interception (value of 0.05 mm), which needs to be met before stem flow and ground infiltration can occur, and empirical coefficients labelled C1, C2, and C3, which relate to the Kristensen and Jensen equation used to calculate actual transpiration and soil evaporation. Coefficients C1 and C2 are plant dependent and influence the distribution between soil evaporation and transpiration. These parameters were set to 0.3 and 0.2 mm/d, respectively. The coefficient C3 is soil dependent and controls the release of water at certain matrix potentials and root densities; this parameter set to 20 mm/day. Finally, AROOT controls the fraction of ET extracted as a function of depth, as larger values have a greater range of ET and approach uniformity as the value nears 0. A value of 0.25 m^{-1} was used.

Overland flow is defined as the portion of runoff that occurs as sheet flow. If rainfall exceeds the infiltration capacity of the soil, water will move horizontally across the surface, being routed by surface topography at a rate that is calculated using the diffusive wave approximation. The resistance to flow overland is controlled by the “roughness” of the land surface, which can be inferred from land use/cover

maps. Each land classification or surface then needs to be transformed directly into a number that assigns hydraulic “roughness.” Within MIKE SHE, the Manning’s M coefficient (reciprocal of Manning’s n), which is equivalent to the Strickler roughness coefficient, controls the amount of friction and the velocity at which water can move horizontally. The value of n is typically in the range of 0.01 (smooth channels) to 0.10 (thickly vegetated channels). There are several literature sources for estimating Manning’s n coefficients over a variety of surfaces (e.g., [34–36]), although most values tend to be modified through the calibration process. The initial settings of Manning’s M were obtained from Engman [35] as described below.

To represent the land surface within the Cowichan region, a present land use/cover dataset was used (Figure 6(a)) [37]. To represent mountainous streams, which are often very steep and rocky, all streams within the model were converted to points, assigned a high Manning’s M coefficient ($100\text{ m}^{1/3}/\text{s}$) and merged with the land use dataset. Accordingly, urban, forested, recently forested, agricultural, streams, and so forth, are represented in terms of a Manning’s M within the MIKE SHE overland flow module (Figure 6(b)).

2.5. Unsaturated Zone Data. The surficial soils dataset was obtained from Liggett and Gilchrist [38], which is a simplified form of the soil type classifications of Jungen [39], based on the soil’s drainage ability (very poorly to well drained). Surficial geology maps [40, 41] illustrate a thin coverage, or veneer, of soil towards the valley side walls. To capture this morphology, the soil map was further defined to include additional underlying strata. Within ArcGIS, the watershed was divided into two main zones, alluvium and bedrock. The soil classification map was imposed on top of the geology layer and a “merge analysis” was performed, adding the underlying geological contact to the soil layer. Therefore, each of the soil classes contains either an “A” (alluvium) or “B” (bedrock) to signify the underlying material. The unsaturated zone geology was then defined vertically within the model. All soil classes, with the exception of “10A and 10B,” were assigned a base of 2 m below ground surface. Below 2 m depth, the underlying material (alluvium or bedrock) was assigned. Classes 10A and 10B were described as thin soil, and therefore, the unsaturated soil depth is 1 m. Within MIKE SHE, each unsaturated zone requires a “to and from” depth, which must be defined for the full range of the unsaturated zone. Therefore, the depths of the underlying units (alluvium and bedrock) were extended to a range deeper than the maximum simulated thickness of the unsaturated zone (up to 60 m). Figure 7 illustrates the spatial pattern of unsaturated soils, as well as an example of the vertical representation along a cross-section.

The soil class properties were initially defined based on the UNSODA unsaturated soil hydraulic database [42]. Texture class was assigned to each soil class (drainage ability) according to values of saturated conductivity (K_s) in the literature. Table 2 shows the van Genuchten soil parameters. As mentioned previously, to represent the deep unsaturated

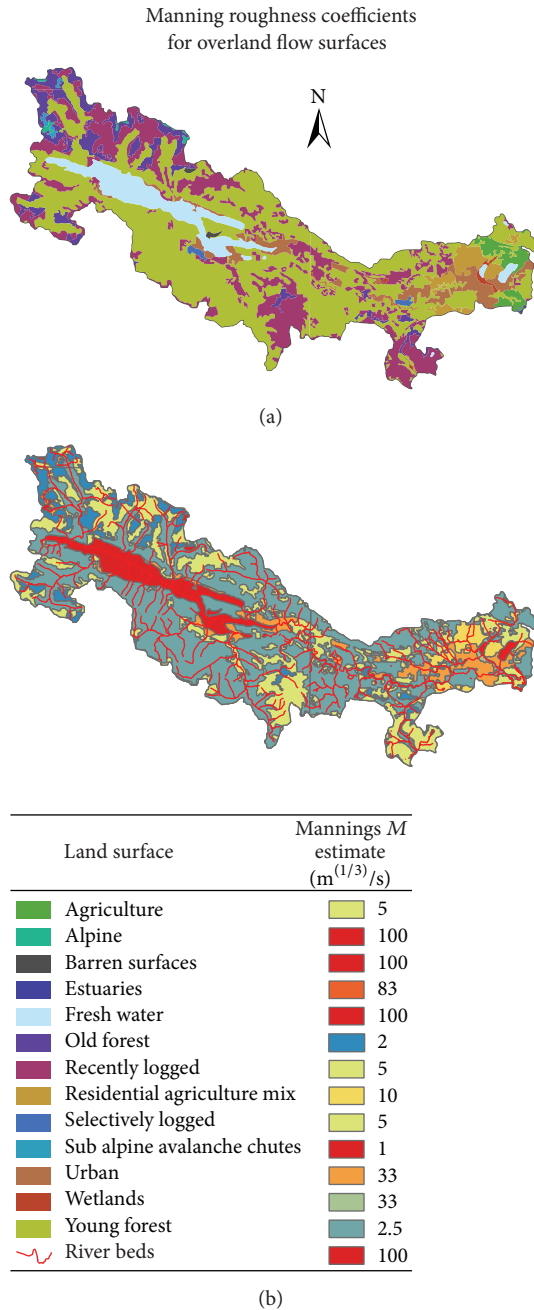


FIGURE 6: (a) Land surface distinctions within the Cowichan Watershed and (b) the assigned Manning's M estimates for controlling overland flow.

zone, additional unsaturated zone materials and properties were included for alluvium and bedrock.

2.6. Saturated Zone Data. The saturated zone is based on a conceptual model of an alluvial valley and bedrock, whereby a deeply incised valley has been infilled with alluvial sediments, while the mountainous upland areas are covered with a thin veneer of unconsolidated material. Therefore, the saturated zone consisted of two geological layers, "Alluvium" and "Bedrock." The layers' setup requires both geological

layers to be present throughout the model domain and a measurement to the bottom of the unit specified. To represent the "thinning" of the alluvium material outside of the valley (up the mountain sides), the thickness was set to near zero, while the thickness of the alluvium within the valley ranged from 0.1 to 125 m. The underlying bedrock extended to 500 m so that the "active flow zone," considered to be in the upper 200 m, was fully captured [45–47].

To represent each mapped aquifer in the valley, geological lenses were added to the model. Each lens represents a hydrogeological unit (HGU), which contains a top and bottom elevation and a spatial extent to represent the unit's limits. The hydraulic properties for each of the designated aquifer HGUs were obtained from a summary of all available pumping and recovery test data [44]. Not all identified aquifers contained a well that had a pumping test completed and, conversely, pumping tests were completed within areas that did not contain a classified aquifer. Where pumping test data were not available, estimates from the literature were used according to material type [48]. The geomeans of hydraulic conductivity and specific storage provided the initial estimates of parameter values for the model. Throughout the calibration process, several of these values were altered based on model performance. Table 3 shows the final parameter values and Figure 8 shows the hydraulic conductivity distribution throughout the watershed.

2.7. MIKE 11 Stream Network and Hydrometric Flow Data. MIKE 11 models lake and river interactions using cross-sections and assigned elevations. The lake and river network was obtained from the BC Watershed Atlas [49]. Lake and rivers were represented in 1D as single line segments, with the extent of the feature defined by the width of the cross-section. Once MIKE 11 is coupled with MIKE SHE, bed topography and the extent of Cowichan Lake are specified in detail (3D).

Cowichan Lake has a major influence on the hydrology of this region; therefore, special care was taken to represent the lake as accurately as possible. The bathymetry of Cowichan Lake was defined by digitizing published bathymetry maps [50]. Cowichan Lake has a surface area of 62 km², a shoreline distance of approximately 106.78 km, an estimated average volume of 2.5 billion m³, an average depth of approximately 50 m, and a maximum depth of approximately 160 m.

The Cowichan River network was converted to river nodes (h -points) and river branches. Discharge and stage levels are calculated at "Q" and "h" points, respectively. The discharge measurements at Q-points (positioned half way between each h -point) are extrapolated from points in between input cross-sections. Stage measurements are calculated at all h -points and are determined by the dynamics of flow within the cross-sections. The coupling of between MIKE 11 and MIKE SHE takes place at the h -points.

Conductance values that control the flow of water between the river and the groundwater system were estimated solely from the subsurface geology hydraulic conductivity values as shown previously in Figure 8. These values were adjusted during model calibration.

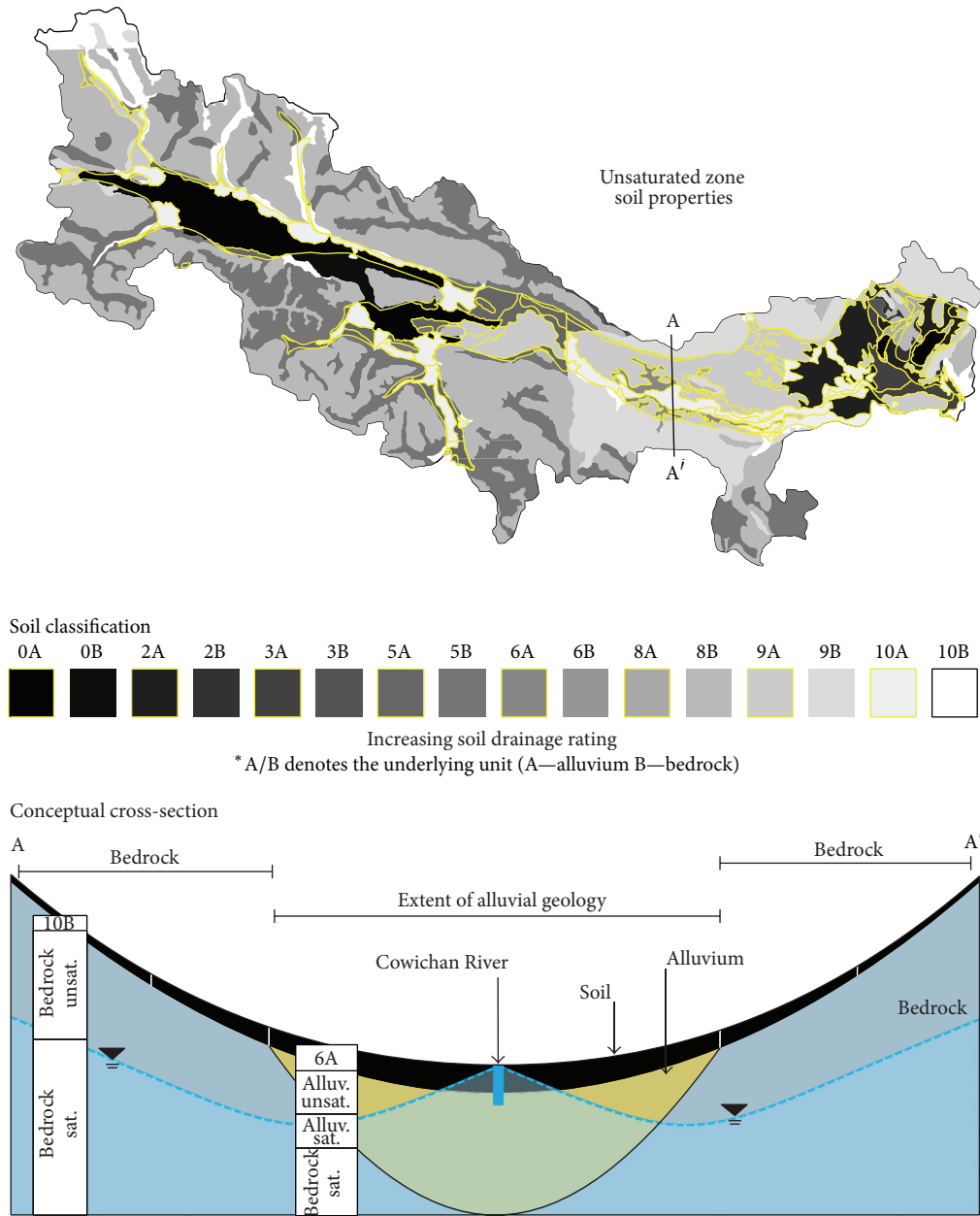


FIGURE 7: Conceptual representation of the variation of unsaturated zone soils within the MIKE SHE model, spatially and with depth.

Boundary conditions were assigned to the MIKE 11 river network. A closed boundary was assigned to the upstream end of the network, while an open boundary was assigned to the mouth of the Cowichan River at Cowichan Bay. This coastal open boundary consists of a water level condition, whereby the tide variations observed at Patricia Bay were used as input. The tide varies from 1.79 to 3.02 m over the simulation period.

The lake stage was initially specified at elevation of 160 masl, with a global bed resistance Manning number of 30. All other parameters (wind factor, computation scheme, and computation parameters) were set to MIKE 11 default values.

2.8. Groundwater and Surface Water Extraction. To model the influence that large water users have on the groundwater and surface water levels within the Cowichan, the estimated extraction rates were added to the model. Six large groundwater users and one large surface water user were included (see Figure 2). The majority of the pumping occurs near the City of Duncan (see Figure 1) clustered around the lower reaches of the Cowichan River. Most groundwater extraction values were provided as monthly totals and, therefore, were modified to be a constant pumping rate in cubic metres per second (m^3/s). The groundwater extraction rates for the municipal wells peak during the summer season, nearly doubling relative to the other seasons. The hatcheries generally

TABLE 2: van Genuchten parameters for unsaturated zone materials.

Model classification (drainage ability)	Residual saturation (θ_r)	Saturated moisture content (θ_s)	α (cm ⁻¹)	n	K_s (cm/d)	Bulk ¹ density (kg/m ³)	Texture class
(1) V. poor	0.1	0.38	0.027	1.23	2.88	1280	Sandy clay
(2) Poor to v. poor	0.095	0.41	0.019	1.31	6.24	1280	Clay loam
(3) Imperfect	0.034	0.46	0.016	1.37	6	1280	Silt
(4) Mod. well to imperfect	0.067	0.45	0.02	1.41	10.8	1280	Silt loam
(5) Mod. well	0.078	0.43	0.036	1.56	24.96	1360	Loam
(6) Well to mod. well	0.1	0.39	0.059	1.48	31.44	1280	Sandy clay loam
(7) Well	0.065	0.41	0.075	1.89	106.08	1440	Sandy loam
(8) Rapid to well	0.045	0.43	0.145	2.68	712.8	1520	Sand
(9) Rapid	0.045	0.43	0.145	2.68	712.8	1520	Sand
Alluvial ²	0.034	0.46	0.016	1.37	6	1280	—
Bedrock ²	0.068	0.38	0.008	1.09	4.8	2400	—

¹Bulk density from Linsley et al. [43], ²initial estimates.

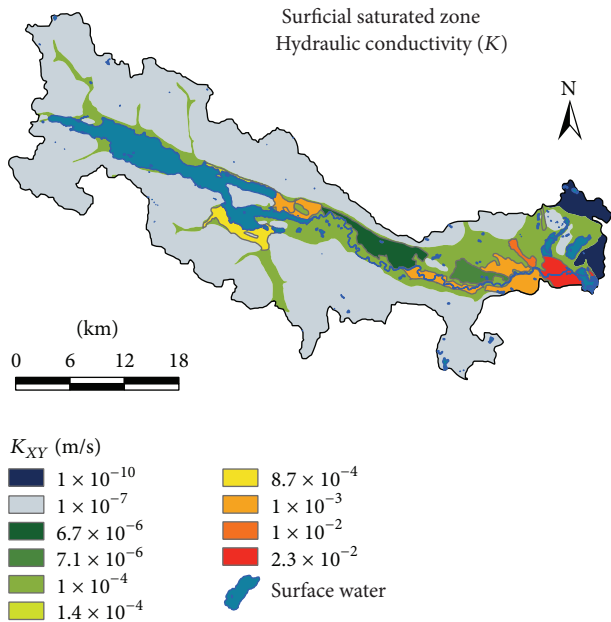


FIGURE 8: Spatial representation of the initial hydraulic conductivity values.

have an opposite withdrawal schedule, with extraction rates doubling in the winter season compared to the summer season. The identified small and medium water groundwater users were not included in the model as most represent single domestic wells. These small domestic users of groundwater also likely have a septic system on the property (which recycles a large portion of the groundwater back to the subsurface), and therefore, the amount of water lost to the system is thought to be minimal.

Only one large user of surface water was included in the model. Catalyst Paper has an intake on the lower reach of the Cowichan River near Duncan and withdraws water directly from the river. The water leaves the watershed. An annual

withdrawal of approximately 50 to 60 million m³ is extracted annually from this location. To model this abstraction, a point-source inflow boundary condition, at the location of the intake, was defined in MIKE 11. The inflow boundary condition was set to a maximum withdraw of -2 m³/s for the entirety of the model simulation. This rate equates to the 63 million m³ of water extracted annually.

2.9. Model Calibration and Validation. The model was setup to run for a simulation period of 14 years (1998–2012). The calibration period for this model was 2002–2010 (8 years). The validation period was from 2010 to 2012. The degree of model fit or calibration was determined by correlation statistics including the mean error (ME), residual mean square error (RMSE), correlation (R), and the Nash-Sutcliffe efficiency.

Model calibration first focused on the climatic conditions (snowmelt modeling). Snowmelt calibration consisted of adjusting model parameters including degree day coefficient, temperature lapse rate, and the max wet snow fraction. Each parameter affected the simulated timing (onset and release of snow) and the amount of snow accumulation. Mean daily temperatures measured at the Jump Creek Snow Pillow Station were used to calibrate the temperature lapse. The snow water equivalent (SWE) recorded at the climate station was used to calibrate the amount of water held in snow storage in the alpine regions. The second phase of calibration focused on the hydrometric characteristics. The calibration consisted of adjusting the physical conditions of the MIKE 11 stream system, Manning's M for overland flow and channel flow, and the streambed leakage coefficients. The next phase of calibration included comparing the measured stage and discharge from MIKE 11 to observed lake level and hydrometric data. The Water Survey of Canada (WSC) maintains three stations within watershed, measuring Cowichan Lake levels (08HA009), Cowichan River stage/discharge near the junction of Cowichan Lake to Cowichan River (08HA002), and the stage/discharge of the Cowichan River near Duncan

TABLE 3: Saturated zone initial hydraulic properties.

HSU ¹	Material	Unit type	Horizontal extent (km ²)	Initial K_{XY} (m/s)	Initial K_Z (m/s)	Specific yield	Specific storage (m ⁻¹)
178	Sand and gravel	Surficial confined	19.0	6.37E-04	6.37E-05	0.2	9.33E-05
179	Gravel and sand	Surficial unconfined	7.6	1.00E-03	1.00E-04	0.2	2.00E-01
180	Sand and gravel	Surficial confined	8.4	7.06E-06	7.06E-07	0.2	1.00E-04
182	Shale	Bedrock	31.6	1.97E-06	1.97E-07	0.2	1.40E-03
183	Sand and gravel	Surficial confined	6.3	1.00E-03	1.00E-04	0.2	5.00E-04
185	Sand and gravel	Surficial confined	14.9	1.00E-03	1.00E-04	0.2	5.00E-04
186	Sand and gravel	Surficial unconfined	17.0	2.27E-02	2.27E-03	0.2	7.10E-04
189	Gravel and sand	Surficial unconfined	10.5	8.68E-04	8.68E-05	0.2	4.46E-03
190	Sand and gravel	Surficial unconfined	1.9	1.39E-04	1.39E-05	0.2	3.89E-04
191	Sand and gravel	Surficial unconfined	3.2	1.00E-03	1.00E-04	0.2	2.00E-01
Alluvial	Alluvium	Unmapped aquifer	287.0	1.00E-05	1.00E-06	0.3	1.00E-04
Bedrock	Bedrock	Base unit	980.0	1.00E-07	1.00E-08	0.05	1.00E-06
Aquitard	Clay Till	Confining unit	46.2	3.17E-10	3.17E-11	0.02	1.00E-03

¹HGUs numbered using the BC Aquifer Classification System numbering. Values in bold represent the geometric mean from pumping test data [44].

(08HA011). The final phase of calibration focused on the groundwater flow within the region, while still evaluating the hydrometric characteristics. Calibration of groundwater levels within the saturated zone involved adjusting the horizontal and vertical hydraulic conductivity and specific storage. Calibration for groundwater level used the hourly data from the Ministry of Environment (MOE) observation well #204 within Aquifer 186, which has the longest period of record. Historical static groundwater levels measured at the end of drilling of domestic wells (both in alluvium and bedrock) were used to verify the calibration. All other modules (evaporation, soil hydraulic parameters) remained constant during the model simulations due to the limited availability of calibration data.

2.10. Climate Change Simulations. The general consensus from the results of climate modeling in British Columbia indicates that temperatures will generally rise, with the largest increases occurring in the summer [51]. Precipitation is projected to increase in the winter months and decrease in the summer months. These trends are expected to increase atmospheric evaporative demand, decrease snow accumulation, accelerate snowmelt, alter groundwater storage and recharge, alter timing and magnitude of streamflow, and result in a variety of ecological changes [51].

In order to assess how vulnerable the Cowichan Watershed is to the potential impacts of climate change, future climate change data were used to force the MIKE SHE model. Two MIKE SHE simulations were run (one representing the 2050s and one the 2080s). The projected climate change impacts were assessed using the BC Regional Analysis Tool [52]. Specifically, the climate projections from the “TreeGen ensemble” were used [53–55]. The TreeGen downscaling tool was applied to an ensemble of global climate models (GCMs) and SRES AR4 emissions scenarios, with the results compiled for the Province of BC. The results from Canadian Global

Coupled Model 3 (CGCM3)-A2 (five model runs) and the Max-Planck Institute for Meteorology (MPI) ECHAM5-A2 (one model run) were used in this study. The A2 emissions scenario was selected because it represents a “worst case” scenario in terms of emissions, CO₂ concentrations, and the resulting temperature increase [56].

Several datasets were extracted for the Cowichan area: absolute temperature change (max, min, mean, and medium) and percent change for precipitation and relative humidity for the time periods 2050s (2039–2069) and 2080s (2070–2099). Figure 9 illustrates the absolute change in mean monthly temperature and relative change (as a percent) in monthly precipitation averaged across the study area. Temperature is expected to increase between 1 and 3°C during the period 2050, and by as much as 2–5°C for the 2080s time period (Figure 9, left). The largest temperature differences are expected from July to August and from December to January. (Figure 9, right) indicates that by the 2050s an increase in precipitation of 10–20% is expected for the winter months and a reduction by up to 20% in the summer months. This trend continues throughout the 2080s, increasing by up to 30% in the winter months, and decreasing by 40% in the summer months.

The mean monthly climate shift factors (from the selected models in the ensemble) for each future time period were applied to historical data (1998–2012) from the Cowichan Lake Forestry Research Climate Station and the Kelvin Creek Climate Station. Specifically, the mean monthly climate shifts were applied directly (subtraction or addition to the mean daily temperatures or % increase/decrease to the precipitation rates) to the temporal climate datasets in MIKE SHE. The model was rerun for two 14 years’ period (representing a shift in the 1998–2012 climate data to each of the 2050s and 2080s climate). The baseline climate data and future climate data are discussed in the section on results of the climate change models (see Results and Discussion).

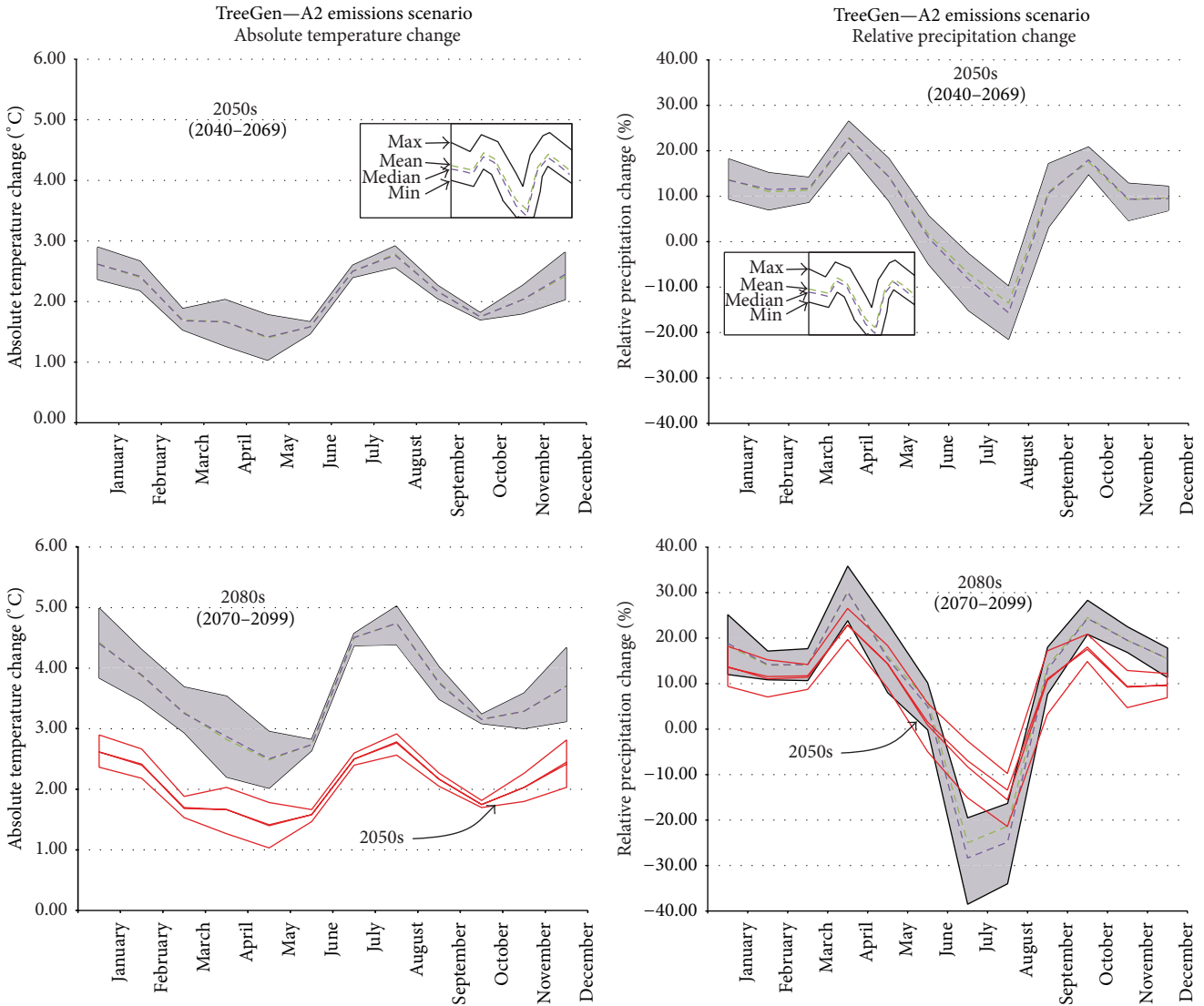


FIGURE 9: Projected climate shifts for the 2050s and 2080s for the Cowichan Region (TreeGen ensemble—A2 emissions scenario). Data from Pacific Climate Impacts Consortium [52].

PET was also adjusted for the climate change simulations. The projected minimum, maximum, and mean temperatures, as well as the projected changes in relative humidity were used to calculate new PET values to reflect the projected climate. Again, the AWSET program was utilized to generate daily PET using the Penman-Monteith equation. The shifts to the temperature and humidity were added to the AWSET program by subtracting or adding the absolute temperature change to the min, max, and mean historical daily values, as well as the relative percent change to the historical relative humidity daily values. Modeled solar insolation and wind speed remained the same. By the 2050s, PET is expected to increase by 6.4 to 12.1% and by the 2080s by 11.9 to 21.2% for climate zone 22 (dominant zone in the watershed). The relative shifts in PET closely reflect the projected shifts in temperature. The same relative change in PET (% change)

obtained for zone 22 was applied to the daily PET estimations for the other 41 PET permutations.

3. Results and Discussion

3.1. Model Calibration and Validation. The calibration fit statistics are given in Table 4. Figure 10 shows the fit for the two hydrometric stations, and Figure 11 shows the fit for groundwater level. In addition, measurements of groundwater levels made following drilling and reported in the BC WELLS database were compared to the simulated groundwater levels for wells completed in alluvium and bedrock. For the wells completed in alluvium, the R^2 was 0.97 and the root mean squared error (RMSE) was 10.78 ($n = 327$). For the bedrock wells, the R^2 was 0.70 and the RMSE

TABLE 4: Calibration results for snowmelt, lake level, stream discharge, and groundwater level (1998–2010).

Calibration station	Data type	ME	MAE	RMSE	STDEV residuals	R-correlation	Nash-Sutcliffe
Jump Creek Snow Pillow Station	Snow water equivalent (mm)	112.27	162.60	297.45	275.49	0.92	0.80
Alpine Temperature at Jump Creek	Air temperature (°C)	-0.66	2.25	2.93	2.85	0.91	0.81
08HA009 Cowichan Lake	Water level (Stage masl)	0.061	0.57	0.64	0.63	0.83	-0.63
08HA002 Cowichan River	Discharge (m ³ /s)	8.59	11.93	20.55	18.67	0.91	0.79
08HA011 Cowichan River	Discharge (m ³ /s)	15.95	19.56	32.59	28.42	0.89	0.72
Observation Well #204-Aquifer 186	Shallow GW water level (masl)	0.0025	0.24	0.31	0.31	0.86	0.74

* ME = mean error; MAE = mean absolute error; RMSE = root mean squared error; STDEV = standard deviation.

was 21.5 ($n = 189$) with observed groundwater levels being slightly overestimated, likely due to the fact that water levels measured in bedrock wells following drilling have not fully recovered and so would tend to be too low.

3.2. Water Balance. A water balance extraction was performed following calibration. Of interest to this study are the overall exchanges of water between different parts of the model (e.g., between the river and groundwater), the amount of recharge to the saturation zone, and the effect of pumping on the hydrologic system. The total input of water to the model occurs solely as precipitation (100% in input). Water is then partitioned (runoff or overland flow, infiltration or recharge to saturated zone, evaporation) and leaves the model through evaporation, boundary flow from the saturated zone into the ocean, river boundary flow to ocean, surface water extraction, or groundwater extraction, with some water in various stores at any one time (e.g., snow storage, canopy storage overland storage, subsurface storage, etc.).

Table 5 reports the total water balance for the Cowichan Region including error (mm/year). Values are reported for the water year (October 1 to September 30). Recharge is shown in the last column as a separate item. Recharge is computed from the exchange between the unsaturated zone and the saturated zone, and therefore, does not appear in the overall water balance for the watershed.

The water balance results must be examined carefully because there are numerous exchanges that take place. Therefore, the annual percentages do not add up. Overland flow to river (Cowichan River) and ET are the dominant fluxes of water within the Cowichan, constituting 55 and 43% of the annual budget water budget. ET is lost from the watershed; however, overland flow to river may, at other points in the watershed, contribute to groundwater (through the river to baseflow component) and perhaps return to the river downstream (baseflow to river). Thus, these terms are linked and likely elevate the overland flow to river component. The baseflow (groundwater) to river and river to baseflow (groundwater) represent exchange flows between the MIKE

SHE and MIKE 11 models. These exchanges take place at the h -points.

The water balance results suggest that the Cowichan River is approximately equal in the amount of water the river loses and gains along its length. This relationship is very consistent throughout each water year. The spatial representation of this relationship is explained in detail later. Small negative and positive values are reported for changes in overland flow and snow storage, while 3% of the average annual budget is accounted for by storage changes in the saturated zone. Over the long term, unless the saturated zone is being depleted, this should be zero. The amount of water pumped from the major groundwater users in the lower valley accounts for less than 1% of the total water balance. The average error associated with the convergence of processes in the model was approximately 1% over the calibration and validation periods of the model.

Based on the detailed saturated zone water balance (not shown), annual recharge (determined as the amount of water exchanged from the unsaturated to the saturated zone) is 438 mm/yr, or 17% of the annual precipitation (last column in Table 5). This amount is determined from a yearly average over the calibration and validation period (2002–2012). During this period, the amount of recharge to groundwater varies (253–630 mm/yr) accordingly with yearly variations in precipitation. Taking into account the total variation in precipitation, recharge to groundwater ranges from 14 to 21% of the total annual (WY) precipitation. Hydrogeological studies in close proximity [57–59] have estimated recharge rates to be from 23 to 45% of annual precipitation. However, these recharge rates reflect recharge to individual unconsolidated sand and gravel aquifers, rather than the net recharge across the entire watershed (including low conductivity bedrock).

At a monthly time scale (results not shown), the temporal variation in exchanges with surface water and groundwater mimic closely precipitation variations. Groundwater entering the Cowichan River dominantly occurs from December to May (6–7 mm/month) and is slightly lower from June to November. The exchange from surface water to groundwater follows a similar trend; as one might expect, a higher

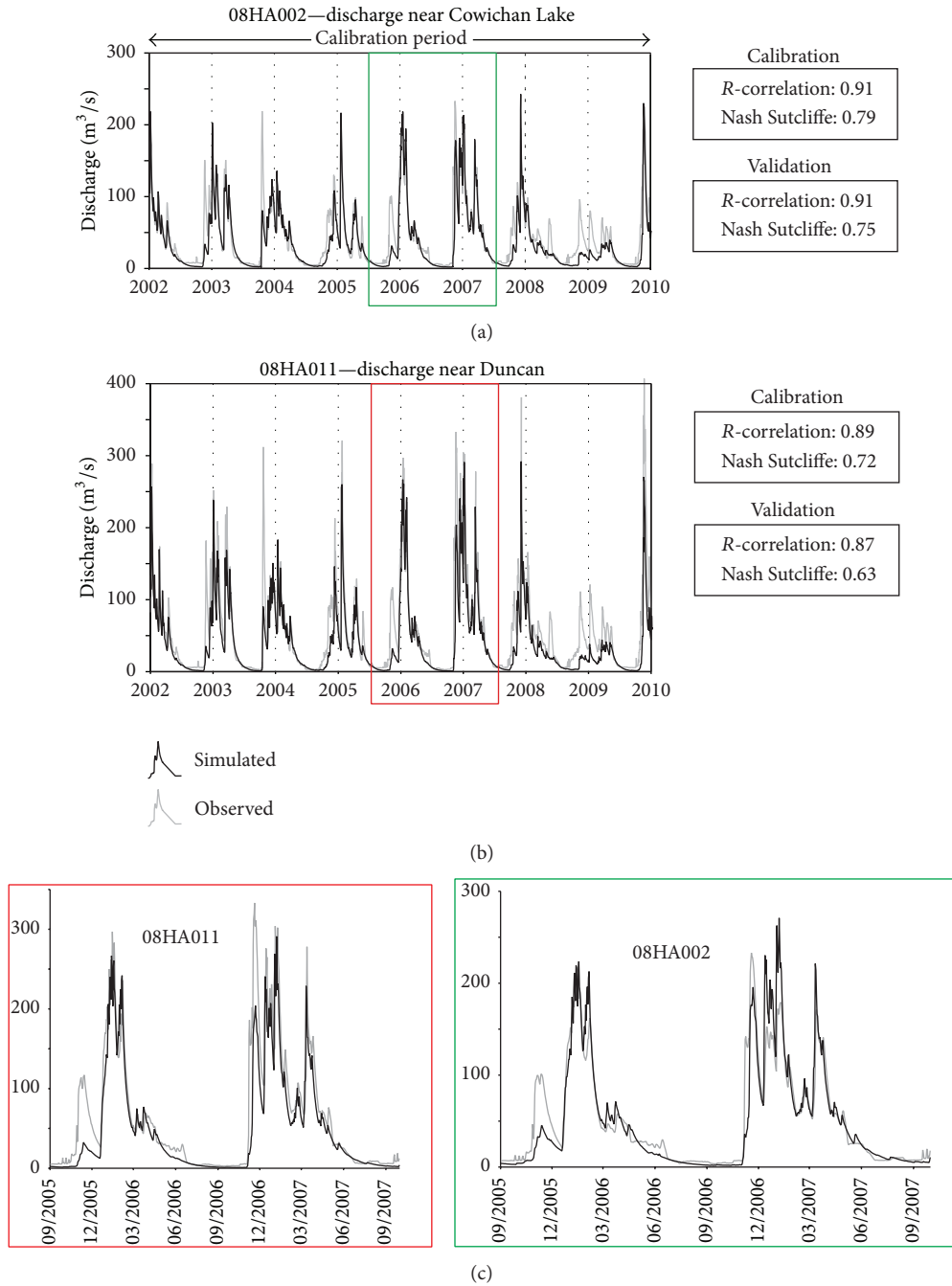


FIGURE 10: Cowichan River discharge calibration results at (a) hydrometric station 08HA002 and (b) at hydrometric station 08HA011 and (c) at higher resolution for both stations. The calibration statistics are also shown for the calibration period (2002–2010) and the validation period (2010–2012).

exchange occurs during the summer when the groundwater table is depressed. Recharge also varies significantly throughout the year. The highest recharge occurs in October and November (>100 mm/month), while a recharge deficit (P-ET) is indicated in the months of June, July and August, with peak deficits at -28 mm/month (loss of water from the saturated zone to the unsaturated zone). This deficit is not only evident in recharge, but also when comparing ET to precipitation

over that same time period. May also experiences negative moisture conditions (ET being greater than incoming precipitation); however, recharge is still positive. These results likely reflect the effect of the melting snowpack in the alpine. As the snow melts, it infiltrates the unsaturated zone and eventually reaches the saturated zone.

The year 2012 was particularly bad in terms of sustained discharge within the Cowichan River. Discharge was

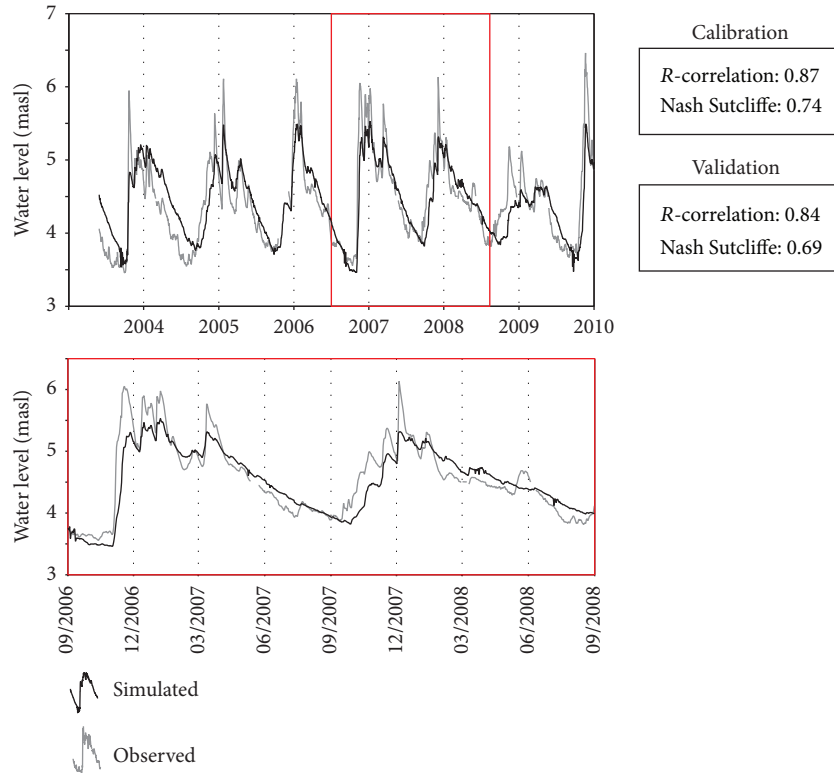


FIGURE 11: Calibration of groundwater levels within Aquifer 186 using Obs. well #204.

TABLE 5: Simulated total water balance for each water year (WY) and yearly averages (mm/yr).

Year	P	ET	OL-flow to river	OL storage change	OL-BF	Baseflow to river	River to baseflow	SZ-storage change	SZ-BF	Pump	Total error	Recharge
WY-02-03	2563	-1061	-1458	-1	-71	-57	59	113	0	-24	62	371
WY-03-04	2804	-1187	-1465	-6	-71	-60	59	-58	0	-24	-10	582
WY-04-05	2484	-1207	-1355	-1	-66	-56	59	129	0	-24	-37	417
WY-05-06	2594	-1151	-1487	0	-73	-56	60	124	0	-24	-14	411
WY-06-07	3490	-1167	-2071	-16	-100	-69	64	-77	0	-24	31	630
WY-07-08	2393	-1161	-1336	10	-66	-62	60	153	0	-24	-32	385
WY-08-09	1504	-1081	-546	3	-34	-46	49	134	0	-24	-42	253
WY-09-10	2950	-1142	-1608	-7	-83	-67	58	-55	0	-24	20	539
WY-10-11	2794	-1100	-1631	2	-83	-68	59	61	0	-24	9	431
WY-11-12	2349	-1009	-1424	2	-72	-63	59	188	0	-24	6	357
Yearly Avg.	2593	-1127	-1438	-1	-72	-61	59	71	0	-24	-1	438
Water (%)	100	-43	-55	0	-3	-2	2	3	0	-1	0	17

P = precipitation; ET = evapotranspiration; OL = overland flow; UZ = unsaturated zone; BF = boundary flow; SZ = saturated zone.

extremely low, and there was very little precipitation in the later summer months. August and September of 2012 differed the greatest from the average conditions in the Cowichan Watershed. August 2012 had unseasonably low precipitation, resulting in a very large moisture deficit (-102 mm/month) compared to the average of -73 mm/month. This also resulted in greater than 100% reduction in recharge during that month. September was much the same; the moisture deficit

in September was -57 mm/month compared to the +21 mm/month average. The climatic variations also caused a recharge deficit in September (-26 mm/month) as compared to the average groundwater recharge of 13 mm/month.

3.3. *Recharge and Discharge Areas.* Recharge is highly variable across the watershed (Figure 12), which reflects the range of parameters that influence recharge: the rate and

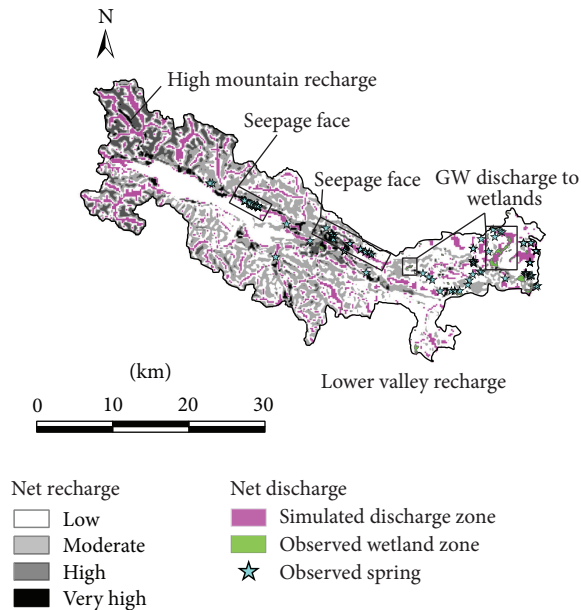


FIGURE 12: Averaged (2002–2012) and classified spatial distribution of recharge and discharge throughout the Cowichan Watershed.

annual amount of precipitation, the rate of evapotranspiration, topography and surface roughness coefficients, the hydraulic properties of the unsaturated soil, and, likely most importantly, the depth to the water table from ground surface (unsaturated zone thickness). Areas with a thin soil cover, high amounts of precipitation, and a permeable subsurface material with a groundwater table close to surface will have recharge that is orders of magnitude greater than areas with less precipitation, a low permeability substrate and a deep groundwater table. Figure 12 shows a gradient of recharge from west to east. This gradient results primarily from the precipitation patterns within the valley, as yearly precipitation values in the west are several times larger than the east. There are several relatively small circular areas of highly focused recharge. These anomalous areas likely represent topographic depressions in the DEM, where water ponds and infiltrates throughout the simulation.

To assess the accuracy of the discharge features simulated by the model, the location of observed groundwater discharge features, such as springs and wetlands, were superimposed over the simulation results (Figure 12). The simulated linear seepage faces along the northern valley slopes correspond well to observed locations of springs. As well, observed wetland features tend to correspond with low topographic depressions within the lower valley where groundwater discharge occurs. Most discharge features throughout the watershed are situated in the valleys flanked by steep ridges. The discharge occurs as saturated zone to overland exchange.

3.4. Groundwater/Surface Water Interactions. Exchanges at the watershed scale are largely controlled by variations in subsurface lithology, including depth to bedrock and aquifer properties [60, 61]. For example, exchanges that occur in

reaches of the Cowichan River where surface water overlies bedrock directly are controlled largely by the hydraulic conductivity of the bedrock, whereas, in other locations, the Cowichan River passes through zones of permeable alluvial deposits where the river channel is deeply incised into the alluvium. Valley width may also affect exchanges [60, 61].

To illustrate the influence of geology on exchanges, the Cowichan River itself (A-A') was used as a cross-section (Figure 13(a)). This cross-section illustrates the material in contact with the river bed, the depth to bedrock or where bedrock is exposed in the river bed, and the thickness of the alluvial sediments. Also imposed on the figure are the relative positions (at y -metres away from the river) of the surface water diversion and groundwater extraction wells to the nearest point of the river. All of the groundwater extraction wells are within unconfined sand and gravel Aquifer 186. Figure 13(b) shows the gaining and losing portions of the river, alongside the geology based on the annual exchanges simulated in 2008. For the majority of the up-river reaches, the Cowichan River is a gaining system (with the exception of a reach from 19500 to 21000 m, near Stoltz Pool). However, further down valley where the relief is lower, the river becomes predominantly losing. Large volumes of water are lost where the river crosses Aquifer 186. Right at the coast, the Cowichan River gains water, as would be expected in a coastal setting due to the presence of the saltwater-freshwater interface at depth, which directs fresh groundwater discharge upwards along a seepage face. As this was a freshwater model, the actual interface was simulated by placing zero flux boundaries in the bedrock and forcing discharge to exit the model domain through the alluvium.

Groundwater discharge into the river is highest during the spring season (when groundwater levels are highest) and lowest during the fall (when groundwater levels are low) (Figure 14). Losing conditions are the greatest (most negative) during the winter months when the stage of the river is high and the groundwater table may still be low (due to lag time), resulting in a higher hydraulic gradient. At 44000 m, the exchange conditions shift from predominantly losing to predominantly gaining, but the magnitude of the exchange varies seasonally. When groundwater levels are greater than the river stage (evident in March of 2008), the river is gaining, which illustrates how important groundwater levels are to conditions in the river.

As shown in Figure 15, the river is dominantly losing in the area where a number of wells are concentrated. To assess whether the pumping conditions within the lower reaches of the river are the cause of losing conditions, the model was rerun with the groundwater extraction rates set to zero. Figure 15 shows the results of the simulation with and without pumping for 2008. While the overall shapes of the curves are consistent, there are differences in the magnitudes of exchanges (highlighted within the ovals). With no pumping, the losing condition that is evident at 43000 and 44000 m during pumping becomes dominantly a gaining condition. Within the losing segments, the large negative peaks are lessened with no pumping, nearby, and at a fairly large distance (kms) from the wells. This result suggests that the

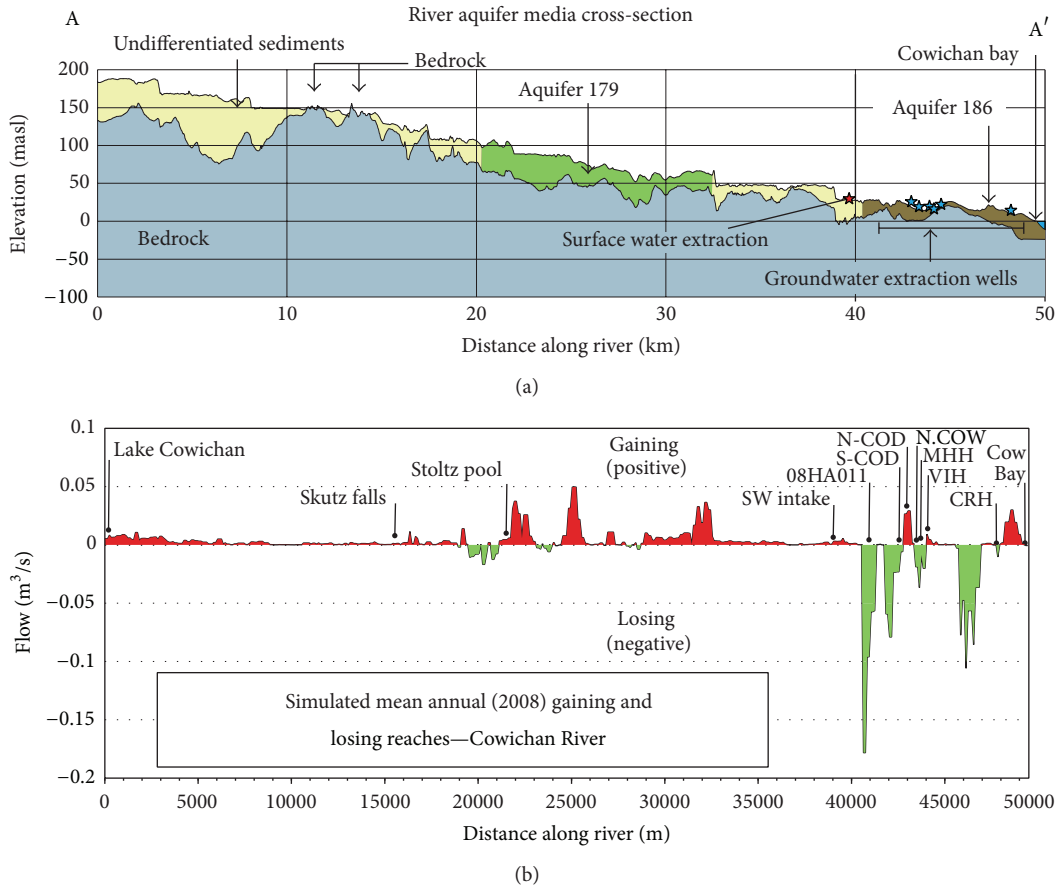


FIGURE 13: (a): the subsurface geology underlying the Cowichan River. Blue stars show groundwater wells and the red star shows the surface water diversion (pumping wells: S-COD/N-COD—City of Duncan wells, MHH—Marine Harvest Hatchery, N.Cow—North Cowichan well, VIH—Vancouver Island Hatchery, and CRH—Cowichan River Hatchery). (b): simulated annual exchanges between the Cowichan River and the aquifer.

pumping wells can lower the water table such that the effects are manifested at large distances.

3.5. Comparison of Simulated GW-SW Exchanges with Field Data. In-stream data throughout the Cowichan Region are limited due to data collection challenges including: the bedrock and gravel river substrate makes installing piezometers difficult; river discharge is high throughout much of the year rendering it unsafe to make in-stream measurements; and the perceived dangers of using of chemical tracers (e.g., solute and fluorescence tracers) on a Canadian Heritage River. However, some data were collected during the summer low flow season in 2013 at a few in-stream locations (S. Barroso, BC Ministry of Forests, Lands and Natural Resources Operations personal communication). The data include a series of in-stream mini-piezometer measurements of hydraulic head differences between the river stage and shallow groundwater levels within the river bed (using a pressure manometer board), as well as seepage rates between the shallow aquifer and the riverbed (using the same piezometer apparatus as a seepage meter). The seepage measurements (volumetric flow) and the modeled MIKE SHE exchange flow values were converted to a flux (m/s), by dividing the

measured flow by the surface area. An additional source data came from snorkel surveys (fish count and habitat) that have been historically conducted within the Cowichan River (Mike McCulloch, BC Ministry of Forests, Lands and Natural Resource Operations, personal communication). Fish count numbers, as well as descriptions of the habitat, were made. Indications of groundwater welling (gaining reaches of the river) often coincide with areas where fish counts are large and decrease in the temperature of the water.

Figure 16 shows the geographic positions of the gaining portions observed from snorkel surveys (blue markers), the locations of losing portions from seepage measurements (red markers), alongside the model results. The model is accurate overall in representing the gaining and losing conditions along the Cowichan River. Groundwater welling indicated by the snorkel surveys correlate well with the gaining conditions in the majority of the upper Cowichan River, although the gaining conditions from the model are not strong due to the low hydraulic conductivity of the sediments and bedrock within that portion of the river. Overall, the first 40,000 m (40 km) of the river is dominantly gaining (small magnitude), while the bottom 10,000 m (10 km) is losing (large magnitude).

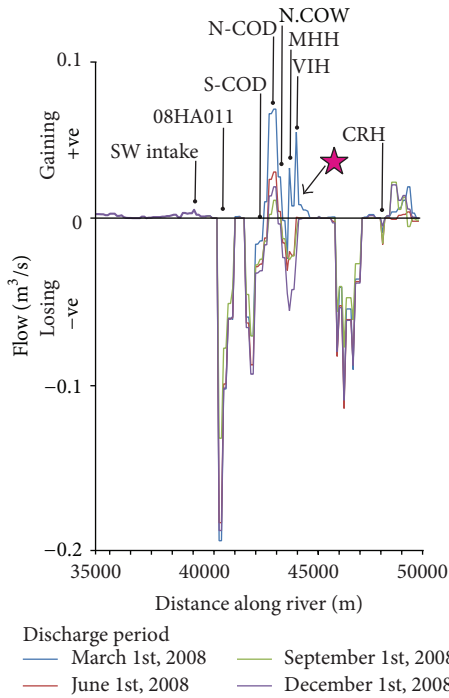


FIGURE 14: Seasonal variations in GW-SW interactions for the lower reaches of the Cowichan River. Note: the red star shows the location of seasonal variation of exchange conditions.

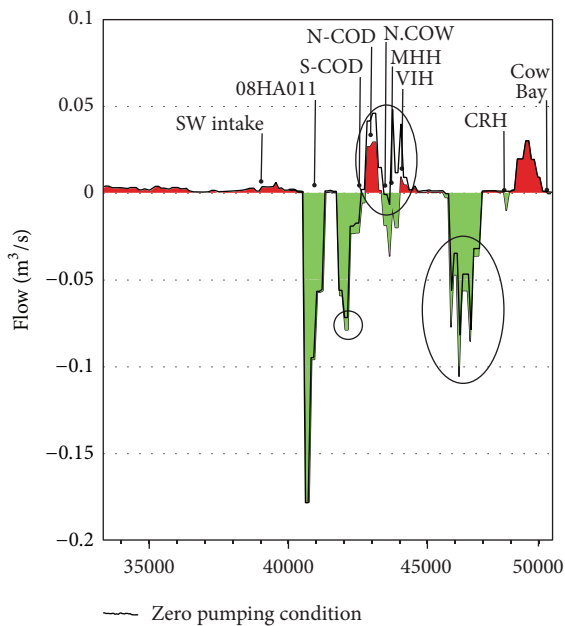


FIGURE 15: Comparison of pumping versus nonpumping conditions on GW/SW interactions.

3.6. *Climate Change Simulation Results.* The climate change results were analyzed over the last 10 years of the full 14-year simulation period to avoid the model spin-up time. The results represent a ten year time span during each of the 2050s and 2080s. Compared to the annual water balance values for

the baseline model, the following trends are observed over time (baseline to 2050s to 2080s):

- (i) precipitation increases, with subsequent increases in runoff (overland flow) to the Cowichan River;
- (ii) evapotranspiration increases;
- (iii) all other aspects of the water balance remain fairly constant, including recharge, which is shown to increase only slightly; the estimated changes in recharge are within the uncertainty (error) range in the model.

Table 6 summarizes the changes to precipitation, ET, and recharge on a monthly basis for the baseline model and the 2080s (as amounts and percent changes). Key observations are as follows:

- (i) precipitation rates increase (relative to baseline) from September through to June, with the greatest increases in April, October, and November;
- (ii) ET rates increase (relative to baseline) throughout the entirety of the year, with the greatest increases from December to January;
- (iii) recharge rates increase (relative to baseline) for all months except June and August; the greatest increases (63%) occur in September.

The most noticeable effects of climate change within the Cowichan Watershed are related to snow. The continued increases in temperature consistently decrease the amount of snow accumulation (water storage) and alter the melt timing (earlier melt) as projected for other regions of BC and the Pacific Northwest [62–64]. Snow accumulation within the Cowichan is especially sensitive to climate change due to the dependency of altitude for snow accumulation (currently simulated at above the 200 masl snow line). A warmer climate means that rain, as opposed to snow, will fall at progressively higher elevations during the winter months and elevations where snow accumulation is currently limited may have less winter snowpack and that snowpack will melt rapidly. Figure 17 illustrates the simulated spatial snowpack for the Cowichan region under the current climate condition, the 2050s, and the 2080s. A drastic decrease in snow accumulation is projected for the 2050s and 2080s. The snowpack becomes increasingly restricted to higher elevations, controlled largely by the temperature lapse rates, as temperatures within the valley are largely above 0°C. Both the spatial extent of the snowpack and the amount of accumulation within snowpack areas are greatly reduced. The timing of peak snowmelt also shifts from May-June to early January (results not shown).

As larger portions of winter precipitation fall as rain in future, the amount of water stored as snowpack decreases significantly, which greatly alters river flow dynamics throughout the year [51]. In general, in the Cowichan, the freshet will occur approximately 44 days earlier by the 2050s, and >100 days earlier by the 2080s. The simulated earlier freshet season results in increased peak flows during the winter months and lower flows during the summer and fall. Figure 18 shows

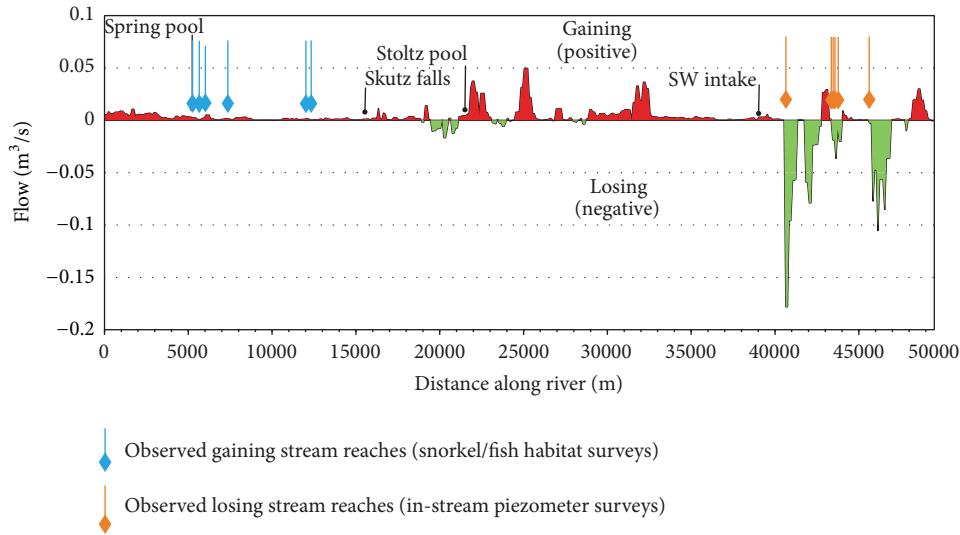


FIGURE 16: Comparison between simulated exchange conditions and observed springs (GW inflow) and in-stream losing piezometric survey locations.

TABLE 6: Comparison of mean monthly water balance results for the baseline and 2080s (mm/month and percent change).

Parameter Scenario	Precipitation			ET			Recharge		
	Baseline	2080s	% change	Baseline	2080s	% change	Baseline	2080s	% change
Jan	464	549	18%	-60	-74	23%	60	61	2%
Feb	221	252	14%	-70	-85	21%	25	29	16%
Mar	309	352	14%	-86	-100	16%	53	57	8%
Apr	154	200	30%	-110	-124	13%	20	27	35%
May	98	114	16%	-138	-154	12%	18	26	44%
Jun	55	59	7%	-146	-161	10%	-7	-4	43%
Jul	35	27	-23%	-138	-152	10%	-26	-31	-19%
Aug	43	34	-21%	-108	-113	5%	-20	-19	+5%
Sep	92	104	13%	-81	-87	7%	8	13	63%
Oct	253	315	25%	-66	-75	14%	103	124	20%
Nov	456	545	20%	-54	-63	17%	126	136	8%
Dec	418	481	15%	-53	-64	21%	65	68	5%

the Cowichan River discharge (at the 08HA011 hydrometric station) near Duncan throughout the simulation for the baseline and climate change simulations. The higher resolution time series (bottom) shows that the peak flows in the winter increase by as much as 100 m³/s, while snowmelt-driven flows are no longer observed and summer flows are more than 50% less. These trends are fairly consistent for all model years. The hydrologic results are consistent with results of studies for other areas of BC [65, 66]. The simulation results suggest that the decreased summer flows may put additional stress on already sensitive aquatic habitat.

4. Conclusions

The MIKE SHE model was developed for the Cowichan Watershed with the intent to simulate the regional hydrology. Simplifications and assumptions were necessary to represent the unsaturated zone, the saturated zone, and the surface

hydrology at a large scale. The following points summarize the key findings of the study:

- (i) the Cowichan River is dominantly gaining in the upper reaches except at a few isolated locations. At lower elevation, the river becomes dominantly losing;
- (ii) the aquifer hydraulic properties appear to be the main control on the magnitude of exchange that occurs, as most exchange occurs through the aquifers with the higher hydraulic conductivities;
- (iii) groundwater recharge over the extent of the watershed is spatially variable and ranged from approximately 253 to 630 mm/yr, with a mean of 438 mm/yr (17% of the annual precipitation);
- (iv) recharge varies significantly throughout the year. The highest recharge occurs in October and November (>100 mm/month), while a recharge deficit (P-ET) is

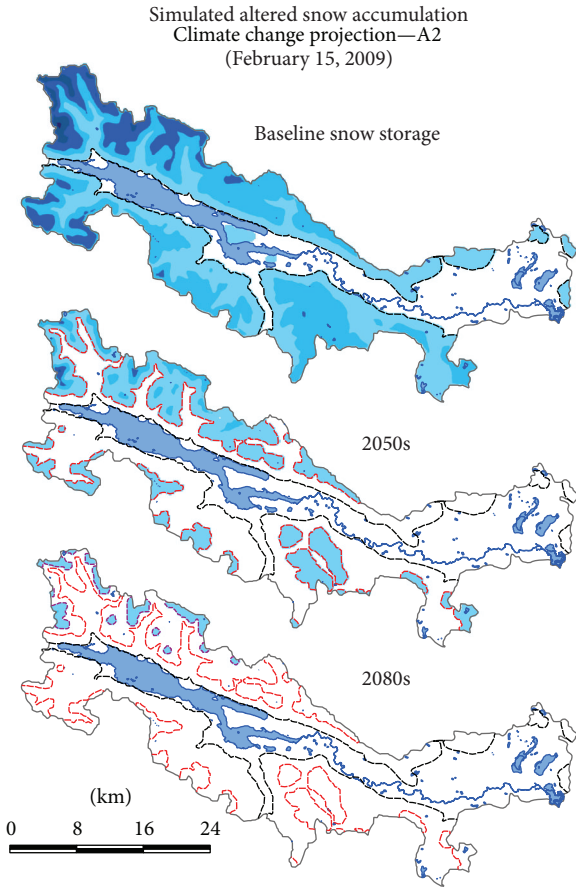


FIGURE 17: Simulated spatial snowpack SWE (mm) for baseline, 2050s, and 2080s.

- indicated in the months of June, July, and August, largely reflecting precipitation patterns;
- (v) simulated groundwater discharge locations coincide with mapped springs and wetland areas;
- (vi) evapotranspiration ranges from 0.5 to 10 mm daily and is estimated at 1126 mm annually (44% of the annual precipitation);
- (vii) the water balance for year 2012 (extreme low flow conditions in the Cowichan River) shows significantly lower amounts of recharge and precipitation, with increased evapotranspiration, when compared to average conditions;
- (viii) groundwater pumping noticeably affects exchanges between the Cowichan River and the aquifer within the lower valley (near Duncan). Exchange conditions at this location change from gaining (no pumping included in the model) to losing (pumping included).

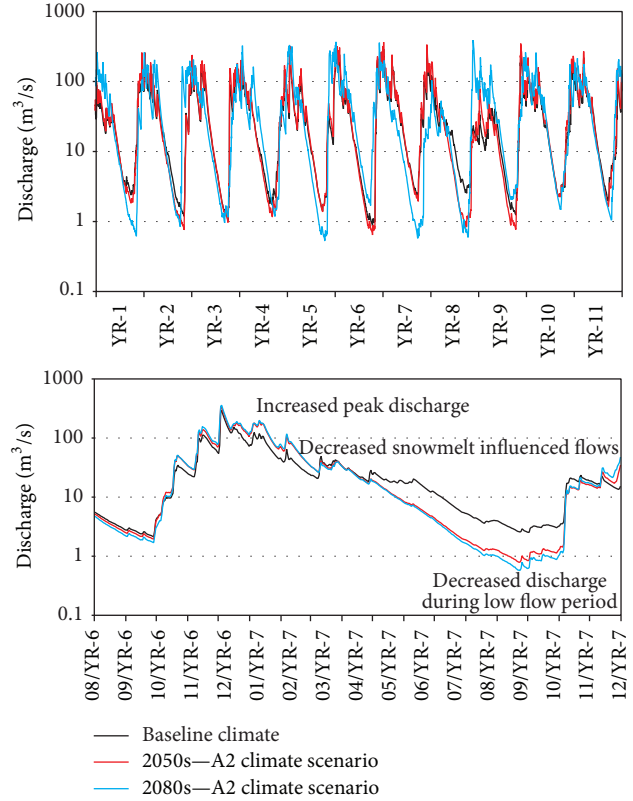


FIGURE 18: Simulated Cowichan River flows under baseline and climate change conditions.

Within the losing segments of the river, the large negative peaks in losses are lessened with no pumping;

- (ix) climate change is expected to influence the Cowichan Watershed in the following ways: precipitation and subsequent runoff increases; evapotranspiration increases; while all other aspects of the water balance remain fairly constant, including recharge, which is shown to increase only slightly;
- (x) climate change simulations show significant alteration to the accumulation of snow within alpine regions, as the snowpack in the 2080s simulation become increasingly limited to higher elevations.

Conflict of Interests

The authors declare that there is no conflict of interests regarding the publication of this paper.

Acknowledgments

This research was funded primarily through a research grant to Diana Allen by the Cowichan Valley Regional District. The authors also acknowledge the feedback provided by Pat Lapcevic and Sylvia Barosso at the BC Ministry of Forests, Lands and Natural Resource Operations.

References

- [1] T. C. Winter, J. W. Harvey, O. L. Franke, and W. M. Alley, "Groundwater and surface water—a single resource," US Geological Survey Circa 1139, US Geological Survey, 1998.
- [2] M. Sophocleous, "Interactions between groundwater and surface water: the state of the science," *Hydrogeology Journal*, vol. 10, no. 1, pp. 52–67, 2002.
- [3] D. A. Sear, P. D. Armitage, and F. H. Dawson, "Groundwater dominated rivers," *Hydrological Processes*, vol. 13, no. 3, pp. 255–276, 1999.
- [4] J. Scibek, D. M. Allen, A. J. Cannon, and P. H. Whitfield, "Groundwater-surface water interaction under scenarios of climate change using a high-resolution transient groundwater model," *Journal of Hydrology*, vol. 333, no. 2–4, pp. 165–181, 2007.
- [5] W. W. Woessner, "Stream and fluvial plain ground water interactions: rescaling hydrogeologic thought," *Ground Water*, vol. 38, no. 3, pp. 423–429, 2000.
- [6] H. M. Voekler, D. M. Allen, and Y. Alila, "Modeling coupled surface water—groundwater processes in a small mountainous headwater catchment," *Journal of Hydrology*, vol. 517, pp. 1089–1106, 2014.
- [7] M. Hussein and F. W. Schwartz, "Modeling of flow and contaminant transport in coupled stream–aquifer systems," *Journal of Contaminant Hydrology*, vol. 65, no. 1–2, pp. 41–64, 2003.
- [8] J. S. Christiansen, M. Thorsen, T. Clausen, S. Hansen, and J. C. Refsgaard, "Modelling of macropore flow and transport processes at catchment scale," *Journal of Hydrology*, vol. 299, no. 1–2, pp. 136–158, 2004.
- [9] D. Liang, R. A. Falconer, and B. Lin, "Coupling surface and subsurface flows in a depth averaged flood wave model," *Journal of Hydrology*, vol. 337, no. 1–2, pp. 147–158, 2007.
- [10] J. Andersen, J. C. Refsgaard, and K. H. Jensen, "Distributed hydrological modelling of the Senegal River Basin—model construction and validation," *Journal of Hydrology*, vol. 247, no. 3–4, pp. 200–214, 2001.
- [11] H. J. Henriksen, L. Troldborg, A. L. Højberg, and J. C. Refsgaard, "Assessment of exploitable groundwater resources of Denmark by use of ensemble resource indicators and a numerical groundwater-surface water model," *Journal of Hydrology*, vol. 348, no. 1–2, pp. 224–240, 2008.
- [12] Q. Li, A. J. A. Unger, E. A. Sudicky, D. Kassenaar, E. J. Wexler, and S. Shikaze, "Simulating the multi-seasonal response of a large-scale watershed with a 3D physically-based hydrologic model," *Journal of Hydrology*, vol. 357, no. 3–4, pp. 317–336, 2008.
- [13] E. A. Sudicky, J. P. Jones, Y.-J. Park, A. E. Brookfield, and D. Colautti, "Simulating complex flow and transport dynamics in an integrated surface-subsurface modeling framework," *Geosciences Journal*, vol. 12, no. 2, pp. 107–122, 2008.
- [14] P. Goderniaux, S. Brouyère, H. J. Fowler et al., "Large scale surface–subsurface hydrological model to assess climate change impacts on groundwater reserves," *Journal of Hydrology*, vol. 373, no. 1–2, pp. 122–138, 2009.
- [15] L.-T. Hu, Z.-J. Wang, W. Tian, and J.-S. Zhao, "Coupled surface water-groundwater model and its application in the arid Shiyang River Basin, China," *Hydrological Processes*, vol. 23, no. 14, pp. 2033–2044, 2009.
- [16] R. Carroll, G. Pohl, D. McGraw et al., "Mason valley groundwater model: linking surface water and groundwater in the walker river Basin, Nevada," *Journal of the American Water Resources Association*, vol. 46, no. 3, pp. 554–573, 2010.
- [17] Z. Sultana and P. Coulibaly, "Distributed modelling of future changes in hydrological processes of Spencer Creek watershed," *Hydrological Processes*, vol. 25, no. 8, pp. 1254–1270, 2011.
- [18] S. Frei, J. H. Fleckenstein, S. J. Kollet, and R. M. Maxwell, "Patterns and dynamics of river-aquifer exchange with variably-saturated flow using a fully-coupled model," *Journal of Hydrology*, vol. 375, no. 3–4, pp. 383–393, 2009.
- [19] J. H. Fleckenstein, S. Krause, D. M. Hannah, and F. Boano, "Groundwater-surface water interactions: new methods and models to improve understanding of processes and dynamics," *Advances in Water Resources*, vol. 33, no. 11, pp. 1291–1295, 2010.
- [20] K. Werner, P. Collinder, S. Berglund, and E. Mårtensson, "Ecohydrological responses to diversion of groundwater: case study of a deep-rock repository for spent nuclear fuel in Sweden," *Ambio*, vol. 42, no. 4, pp. 517–526, 2013.
- [21] I. Zacharias, E. Dimitriou, and T. Koussouris, "Quantifying land-use alterations and associated hydrologic impacts at a wetland area by using remote sensing and modeling techniques," *Environmental Modeling and Assessment*, vol. 9, no. 1, pp. 23–32, 2004.
- [22] T. Wang, A. Hamann, D. L. Spittlehouse, and T. Q. Murdock, "ClimateWNA-high-resolution spatial climate data for western North America," *Journal of Applied Meteorology and Climatology*, vol. 51, no. 1, pp. 16–29, 2012.
- [23] Kerr Wood Leidal Associates (KWL), "Cowichan River watershed climate change impact assessment," Technical Memorandum, Kerr Wood Leidal Associates, BC Conservation Foundation, 2011.
- [24] DHI, *MIKE SHE User Manual, Volume 2: Reference Guide*, Danish Hydraulic Institute, Horsholm, Denmark, 2007.
- [25] K. J. Kristensen and S. E. Jensen, "A model for estimating actual evapotranspiration from potential evapotranspiration," *Nordic Hydrology*, vol. 6, no. 3, pp. 170–188, 1975.
- [26] J. R. Thompson, H. R. Sørensen, H. Gavin, and A. Refsgaard, "Application of the coupled MIKE SHE/MIKE 11 modelling system to a lowland wet grassland in southeast England," *Journal of Hydrology*, vol. 293, no. 1–4, pp. 151–179, 2004.
- [27] AWSET, Version 3.0, Cranfield University Silsoe, 2002.
- [28] Environmental Systems Research Institute (ESRI), *ArcGIS Desktop*, Release 10, Environmental Systems Research Institute (ESRI), Redlands, Calif, USA, 2011.
- [29] R. G. Allen, L. S. Pereira, D. Raes, and M. Smith, "Crop evapotranspiration: guidelines for computing crop water requirements," FAO Irrigation and Drainage Paper 56, FAO, Rome, Italy, 1998.
- [30] S. Cohen, D. Nielsen, and R. Welbourn, Eds., *Expanding the Dialogue on Climate Change & Water Management in the Okanagan Basin, British Columbia. Final Report*, Environment Canada, Agriculture and Agri-food Canada and University of British Columbia. Project A463/433 submitted to the Adaptation Liaison Office, Climate Change Impacts and Adaptation Directorate, Natural Resources Canada, Ottawa, Canada, 2004.
- [31] R. Fernandes, C. Butson, S. Leblanc, and R. Latifovic, "Landsat-5 TM and landsat-7 ETM+ based accuracy assessment of leaf area index products for Canada derived from SPOT-4 VEGETATION data," *Canadian Journal of Remote Sensing*, vol. 29, no. 2, pp. 241–258, 2003.
- [32] M. Rautiainen, J. Heiskanen, and L. Korhonen, "Seasonal changes in canopy leaf area index and MODIS vegetation products for a boreal forest site in central Finland," *Boreal Environment Research*, vol. 17, no. 1, pp. 72–84, 2012.

- [33] T. Curt, E. Lucot, and M. Bouchaud, "Douglas-fir root biomass and rooting profile in relation to soils in a mid-elevation area (Beaujolais Mounts, France)," *Plant and Soil*, vol. 233, no. 1, pp. 109–125, 2001.
- [34] Hydrologic Engineering Center (HEC), *HEC-1 Flood Hydrograph Package: Users Manual*, Fort Belvoir; U.S. Army Corps of Engineers. Water Resources Support Center, Davis, Calif, USA, 1985.
- [35] E. T. Engman, "Roughness coefficients for routing surface runoff," *Journal of Irrigation & Drainage Engineering*, vol. 112, no. 1, pp. 39–53, 1986.
- [36] S. U. S. Senarath, F. L. Ogden, C. W. Downer, and H. O. Sharif, "On the calibration and verification of two-dimensional, distributed, Hortonian, continuous watershed models," *Water Resources Research*, vol. 36, no. 6, pp. 1495–1510, 2000.
- [37] DataBC, Baseline thematic mapping present land use version 1 spatial layer, 2013, <https://apps.gov.bc.ca/pub/geometadata/metadataDetail.do?recordUID=43171&recordSet=ISO19115>.
- [38] J. Liggett and A. Gilchrist, *Technical Summary of Intrinsic Vulnerability Mapping Methods in the Regional Districts of Nanaimo and Cowichan Valley*, Open File 6168, Geological Survey of Canada, 2010.
- [39] J. R. Jungen, "Soils of southern Vancouver Island. Report no. 44, British Columbia soil survey," MoE Technical Report 17, British Columbia Ministry of Environment, Victoria, Canada, 1985.
- [40] E. C. Halstead, Surficial geology, Shawinigan, British Columbia (15-1965) Geological Survey of Canada, 1966.
- [41] E. C. Halstead, "The Cowichan ice tongue, Vancouver Island," *Canadian Journal of Earth Sciences*, vol. 5, no. 6, pp. 1409–1415, 1968.
- [42] F. J. Leij, *The UNSODA Unsaturated Soil Hydraulic Database: User's Manual*, National Risk Management Research Laboratory, Office of Research and Development, US Environmental Protection Agency, Cincinnati, Ohio, USA, 1996.
- [43] R. K. Linsley, M. A. Kohler, and J. L. H. Paulhus, *Hydrology for Engineers*, McGraw-Hill, New York, NY, USA, 1982.
- [44] BC Ministry of Environment, Compendium of re-evaluated pumping tests in the Cowichan valley regional district, Vancouver Island, British Columbia (unpublished) Ministry of Environment, Environmental Sustainability Division, V. Carmichael, 2014.
- [45] D. T. Snow, "Mountain groundwater supplies," *Mountain Geology*, vol. 10, no. 1, pp. 19–24, 1973.
- [46] I. Stober and K. Bucher, "Hydraulic properties of the crystalline basement," *Hydrogeology Journal*, vol. 15, no. 2, pp. 213–224, 2006.
- [47] D. Blessent, "Stochastic fractured rock facies for groundwater flow modeling," *Dyna-Colombia*, vol. 80, no. 182, pp. 88–94, 2013.
- [48] R. A. Freeze and J. A. Cherry, *Groundwater*, Prentice-Hall, Englewood Cliffs, NJ, USA, 1979.
- [49] DataBC, BC Watershed Atlas, 2005, <https://apps.gov.bc.ca/pub/geometadata/metadataDetail.do?recordUID=4434&recordSet=ISO19115>.
- [50] BC Ministry of Environment Recreation Fishers Branch, "Cowichan Lake bathymetry (2-sheets)," Tech. Rep. 92C/16, 1990.
- [51] R. G. Pike, T. E. Redding, R. D. Moore, R. D. Winkler, and H. D. Bladon, *Compendium of Forest Hydrology and Geomorphology in British Columbia*, British Columbia Forest Science Program, FORREX, BC Ministry of Forests and Range, Victoria, Canada, 2010.
- [52] Pacific Climate Impacts Consortium (PCIC), Regional Analysis Tool, 2014, <http://www.pacificclimate.org/analysis-tools/regional-analysis-tool>.
- [53] A. J. Cannon, "Probabilistic multisite precipitation downscaling by an expanded Bernoulli-Gamma density network," *Journal of Hydrometeorology*, vol. 9, no. 6, pp. 1284–1300, 2008.
- [54] K. Stahl, R. D. Moore, J. M. Shea, D. Hutchinson, and A. J. Cannon, "Coupled modelling of glacier and streamflow response to future climate scenarios," *Water Resources Research*, vol. 44, no. 2, Article ID W02422, 2008.
- [55] D. M. Allen, A. J. Cannon, M. W. Toews, and J. Scibek, "Variability in simulated recharge using different GCMs," *Water Resources Research*, vol. 46, no. 10, 2010.
- [56] N. Nakicenovic, Ed., *Special Report on Emissions Scenarios: A Special Report of Working Group III of the Intergovernmental Panel on Climate Change*, Cambridge University Press, Cambridge, UK, 2000.
- [57] D. A. Lowen, *Mill Bay Subdivision Impacts of Water Supply and Wastewater Disposal*, Alpex development Corporation, SEACOR Environmental Engineering, Victoria, Canada, 1994.
- [58] R. Kreye, M. Wei, and D. Reksten, *Defining the Source Area of Water Supply Springs*, Hydrology Branch, Ministry of Environment, Lands and Parks, 1996.
- [59] EBA Engineering Consultants (EBA), "Cobble Hill area well protection plan," Tech. Rep. 0802-2840349, Braithwaite Estates Improvement District Board, Millar's Water Supply Society and Cobble Hill Improvement District, 2006.
- [60] J. A. Stanford and J. V. Ward, "An ecosystem perspective of alluvial rivers: connectivity and the hyporheic corridor," *Journal of the North American Benthological Society*, vol. 12, no. 1, pp. 48–60, 1993.
- [61] S. Buss, Z. Cai, B. Cardenas et al., *The Hyporheic Handbook: A Handbook on the Groundwater-Surfacewater Interface and Hyporheic Zone for Environmental Managers*, Environment Agency, Bristol, UK, 2009.
- [62] D. R. Rodenhuis, K. E. Bennet, A. T. Werner, T. Q. Murdock, and D. Bronaugh, "Hydro-climatology and future climate impacts in British Columbia," Pacific Climate Impacts Consortium Report, 2007.
- [63] J. H. Casola, L. Cuo, B. Livneh et al., "Assessing the impacts of global warming on snowpack in the Washington cascades," *Journal of Climate*, vol. 22, no. 10, pp. 2758–2772, 2009.
- [64] P. W. Mote, R. Slaughter, A. K. Snover et al., "Preparing for climatic change: the water, salmon, and forests of the Pacific Northwest," *Climatic Change*, vol. 61, no. 1-2, pp. 45–88, 2003.
- [65] A. Loukas, L. Vasiliades, and N. R. Dalezios, "Climatic impacts on the runoff generation processes in British Columbia, Canada," *Hydrology and Earth System Sciences*, vol. 6, no. 2, pp. 211–227, 2002.
- [66] W. S. Merritt, Y. Alila, M. Barton, B. Taylor, S. Cohen, and D. Neilsen, "Hydrologic response to scenarios of climate change in sub watersheds of the Okanagan basin, British Columbia," *Journal of Hydrology*, vol. 326, no. 1-4, pp. 79–108, 2006.

Research Article

Modeling the Effects of Land-Cover Change on Rainfall-Runoff Relationships in a Semiarid, Eastern Mediterranean Watershed

Noa Ohana-Levi,¹ Arnon Karnieli,¹ Roey Egozi,² Amir Givati,³ and Aviva Peeters¹

¹The Remote Sensing Laboratory, The Jacob Blaustein Institutes for Desert Research, Ben-Gurion University of the Negev, Sede Boqer Campus, 84990 Midreshet Ben-Gurion, Israel

²Soil Erosion Research Station, Ministry of Agriculture, Emek-Hefer, 40250 Rupin, Israel

³Surface Water and Hydrometeorology, Israeli Hydrological Service, Water Authority, Israel

Correspondence should be addressed to Arnon Karnieli; karnieli@bgu.ac.il

Received 9 August 2014; Revised 12 January 2015; Accepted 14 January 2015

Academic Editor: Martin Wegehenkel

Copyright © 2015 Noa Ohana-Levi et al. This is an open access article distributed under the Creative Commons Attribution License, which permits unrestricted use, distribution, and reproduction in any medium, provided the original work is properly cited.

Temporal changes and spatial patterns are often studied by analyzing land-cover changes (LCCs) using spaceborne images. LCC is an important factor, affecting runoff within watersheds. The objective was to estimate the effects of 20 years of LCCs on rainfall-runoff relations in an extreme rainfall event. A 1989 Landsat TM-derived classification map was used as input for a Kinematic Runoff and Erosion (KINEROS) hydrological model along with the precipitation data of an extreme rainfall event. Model calibration was performed using measured runoff volume data. Validation of the model performance was conducted by comparing the model results to measured data. A similar procedure was used with a 2009 land-cover classification map as an input to the KINEROS model, along with similar precipitation data and calibration parameters, in order to understand the possible outcomes of a rainfall event of such a magnitude and duration after 20 years of LCCs. The results show an increase in runoff volume and peak discharge between the time periods as a result of LCCs. A strong relationship was detected between vegetation cover and the runoff volume. The LCCs with most pronounced effects on runoff volumes were related to urbanization and vegetation removal.

1. Introduction

Land-cover mapping and monitoring can serve as important indicators of landscape and environmental status, distributions, and patterns. A common and effective way to better understand temporal changes, as well as the spatial variability of an area, is through the study of land-cover change (LCC) and its analysis [1–3]. LCCs are caused by human activities and in many cases have local and regional impacts on populations [4]. There is a growing awareness of LCCs importance and their impacts in order to gain a better understanding of their effects on hydrologic, ecologic, climatic, and biologic processes over space and time [5–8]. One of these processes is the effect of LCC on runoff regime within a watershed. The LCCs are often related to urbanization, a shift to agriculture, afforestation, and vegetation removal [1, 9–12].

The impact of LCCs on the landscape features of watersheds greatly affects slopes and channel flows [13]. One of

the most influential changes is urbanization, as urban areas increase runoff rates and peak discharges due to increased imperviousness and reduced infiltration of precipitation [14–17]. Moreover, vegetation removal, which usually accompanies the process of urbanization, is responsible for the reduction of rainfall interception and storage and, in arid/semiarid regions, the creation of physical crusts [18]. Other LCCs can be attributed to the use of land resources for agricultural activities, leading to the replacement of grasslands and forested areas with croplands [9]. The spatial distribution and patterns of land-cover dynamics are crucial factors in estimating imperviousness along the slopes and quantifying the areas that contribute runoff to the channels that drain the watershed area [19]. Understanding the spatial variability and patterns in LCCs can greatly improve the process of determining the most influential LCCs and other environmental factors on rainfall-runoff relationship [20].

Expected worldwide climate-change trends are likely to introduce shifts in the frequency and intensity of extreme climatic events, including increase in mean annual temperatures and increase/decrease in mean annual rainfall, depending on the region in question [21, 22], and will have a strong impact on hydrologic regime in the watershed scale. Future global trends predict an increase in heavy precipitation events [21]. This projection and its probable effects on the hydrologic regime in the watershed scale led to the decision to focus on one storm event, with a return period of 50 years. The problem at issue is dealing with the extensive urbanization processes occurring worldwide, which are most likely to increase runoff and consequently endanger the urban areas along stream channels during future extreme storm events [23]. These expected climate-change trends highlight the importance of quantifying the shifts in land-cover through time since the last extreme storm, in order to predict the outcome of a similar hazardous event in the future and the effects it may have on the well-being of the population within the watershed.

Several means for observing LCCs have been developed and documented. Satellite images have a great potential for monitoring and analyzing LCCs both temporally and spatially [24]. In this study, remote-sensing data was integrated with geographic information system (GIS) techniques. In the scope of this work, LCCs as well as patterns and distribution were monitored and analyzed using remote sensing and GIS techniques and then implemented into a hydrological model in order to estimate their effects on the hydrologic patterns caused by a severe rainstorm in a watershed scale [17, 25].

The hydrological model that was chosen for this study was KINEROS2, for two main reasons: (1) it was originally designed for arid and semiarid regions and is appropriate for the research area; (2) it is an even-based model and suits the study scope of modelling a single hydrological event [26, 27]. Moreover, this research implements statistical and spatial analyses for studying spatial and temporal LCCs and hydrological trends. In order to quantify temporal LCCs, a statistical ordination approach was used, after which the LCC effects on runoff volume were analyzed using GIS spatial analysis tools. Land-cover patterns effects of runoff volume were also analyzed spatially, using spatial statistics GIS tools. The aim of this work was to estimate the temporal effects of LCCs on rainfall-runoff relations within the Yarkon-Ayalon watershed, Israel, on a subbasin scale. The specific objectives were twofold: (1) to extract and characterize land-cover classes, for each subbasin, using satellite imagery for assessing LCCs between two time periods, 20 years apart; (2) to use the LCCs findings, together with the data of an extreme rainfall event scenario, in order to simulate runoff variables for past and present land-cover status.

2. Methodology

2.1. Study Area. The research was conducted within the Yarkon-Ayalon watershed, located in central Israel (Figure 1(a)), due to its hydrologic vulnerability. This watershed contains the most densely populated region of the country: Tel Aviv and some of its satellite cities [28]. The

watershed is divided by the border between Israel and the West Bank, Palestinian Authority (PA), hence the limitations on conducting extensive field research and the inevitable need for a remote sensing tool and LCC monitoring methods. This area has experienced an extensive urbanization process during the past decades, at the expense of agricultural and natural areas [14, 29].

The Yarkon-Ayalon watershed has a total drainage area of 1,805 km², originating in the Samaria Mountains, located in the PA in the east and draining west towards the Mediterranean Sea. There is a large variability in elevation along this watershed, with its headwaters defined as mountainous and reaching altitudes of about 800–900 meters above sea level (Figure 1(b)) [30, 31]. The watershed area is located in a semiarid climate zone with a mean annual precipitation of about 550 mm and a mean annual discharge of 43 million cubic meters (MCM) [23].

The Yarkon-Ayalon watershed consists of several soil types, as a factor of slopes and geological characteristics. Soft rocks (chalk and marl) and harder rocks (limestone and dolomite) are both abundant. The soils in this region are mostly terra rossa and brown rendzina along the eastern region of the watershed, while the plains along the central area are characterized by gromosols [32]. Most of the vegetation in the watershed area is composed of Mediterranean forests, woodlands, and shrubs, such as Palestine oaks, mastic shrubs, carob trees, terebinths, *Poteriums*.

The research area contains a wide array of land-cover and land-use types, some of which are still natural while most are controlled and managed. These include forests, different types of residential land-uses (high/low density, built/unbuilt areas, large cities, and villages), industrial areas, commercial areas, roads, grasslands, agricultural lands (row crops, orchards), and quarries. All of these differ in magnitude, size, quality, and shape between Israel and the PA.

The research was conducted on a subbasin scale. Therefore, the Yarkon-Ayalon watershed was partitioned into six subbasins according to the locations of the Israeli Hydrological Service hydrometric stations: Yarkon, Beit Dagan, Shilo, Natuf, Kana, and Lod (Figure 2). Each subbasin was chosen according to hydrometric data availability and was studied independently. As demonstrated in Figure 2, the Yarkon subbasin contains both the Kana and Shilo subbasins, and the Beit Dagan subbasin comprises the Natuf and Lod subbasins. In 1957 a reservoir named Mishmar Ayalon was built at the eastern part of Lod subbasin, in order to minimize the peak discharges during severe flooding events, and was never breached. This means that the outflow volume runoff and discharge values that were measured at the hydrometric station represented only the runoff generated downstream from the reservoir. Therefore, the Mishmar Ayalon drainage area was excluded from the Lod and Beit Dagan subbasin areas (Figure 2).

2.2. Hydrological Model and Tools. The model used in the course of this research for simulating runoff within the Yarkon-Ayalon watershed was KINEROS2 [26, 27]. This model is designed for assessing runoff rates and volumes in ungauged watersheds in arid and semiarid regions. It is

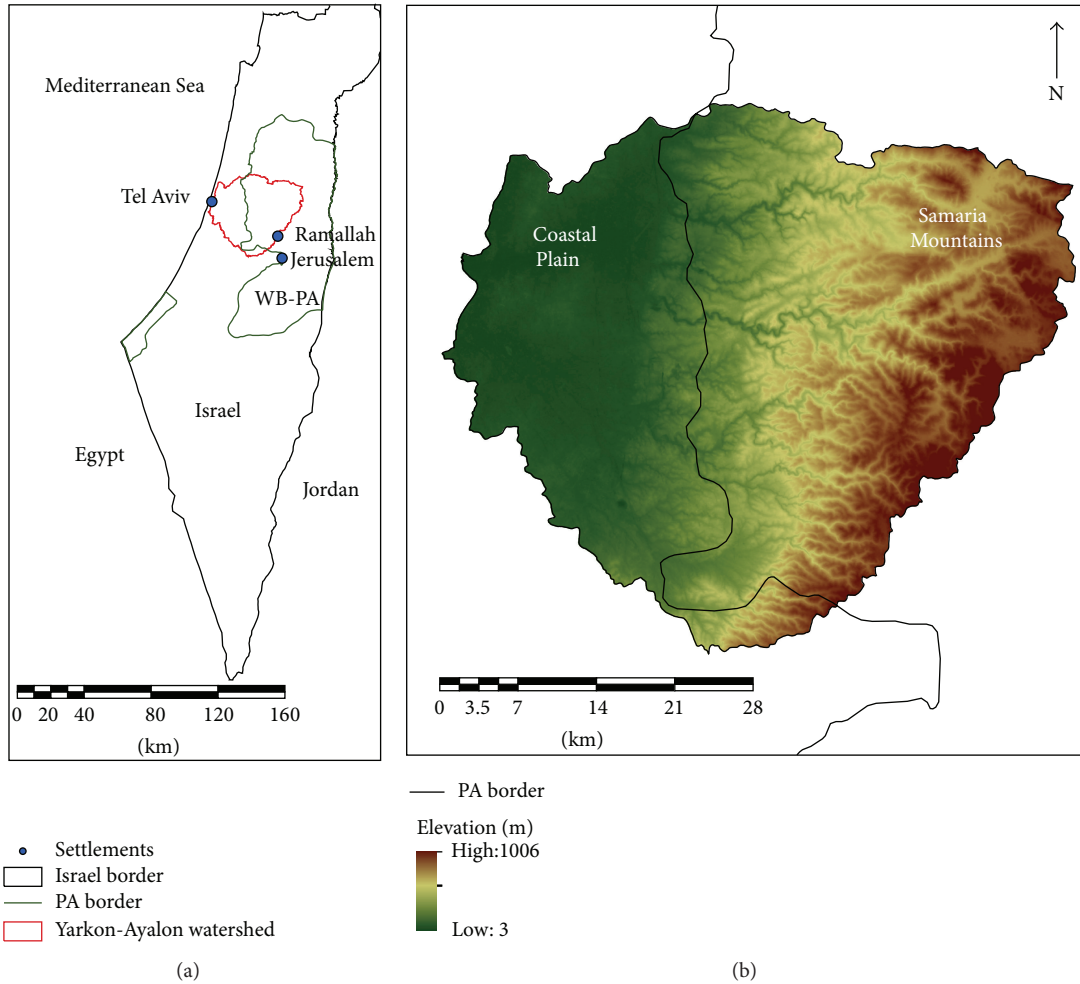


FIGURE 1: Yarkon-Ayalon watershed: (a) watershed location within Israel and the West Bank (WB), Palestinian Authority (PA); (b) watershed elevation map.

a physically based, distributed, event-oriented, and rainfall-runoff model, which simulates runoff response over the watershed. The watershed is divided into two types of spatially distributed model elements with a specified connectivity: (1) overland flow elements or planes (polygons) and (2) channel elements (lines). These elements can be oriented so that a one-dimensional flow can be assumed. Surface flow is simulated for all planes and channels using a finite difference solution of the one-dimensional kinematic wave equations [26, 33–35].

KINEROS2 describes a Hortonian overland flow from complex watersheds and accounts for the spatial and temporal variability of rainfall input. It deals with processes of rainfall, interception, infiltration, overland flow, open channel flow, erosion, sediment transport, reservoir routing, and sedimentation [33, 34, 36]. The current research focuses on the rainfall-runoff process only. A detailed and thorough description of the model, its processes, and mechanisms can be found in Woolhiser et al. (1990) and Semmens et al. (2008).

The choice of KINEROS2 was based on its capability to simulate runoff in semiarid regions, which is appropriate for the climate regime along the Yarkon-Ayalon watershed. Moreover, this study aimed to examine the spatial behavior

and characteristics of one storm event. KINEROS2, being an event-based model that deals with specific storms, was suitable for the purpose of this study.

The model is operated using a GIS interface named the Automated Geospatial Watershed Assessment (AGWA2) tool [27, 37, 38]. It was developed in order to implement two models: KINEROS2 and the Soil and Water Assessment Tool (SWAT) via a GIS interface. The data requirements for running the AGWA2 tool include elevation, classified land-cover map, soil map, and precipitation data. The model input variables are derived from these data using look-up tables (LUTs), provided by the tool. The model requires first generating the watershed outline followed by dividing it into model elements. The desired model is then chosen (KINEROS2 in this case), after which the soils and land-cover maps, along with LUT data, are entered into the system, and the storm event precipitation data is generated in order to complete the input dataset. The model can then be calibrated and run, and the simulation results can be displayed. The model output includes runoff, sediment yield, infiltration, peak runoff rate, and peak sediment discharge [27, 38]. The current study focused only on runoff simulations since

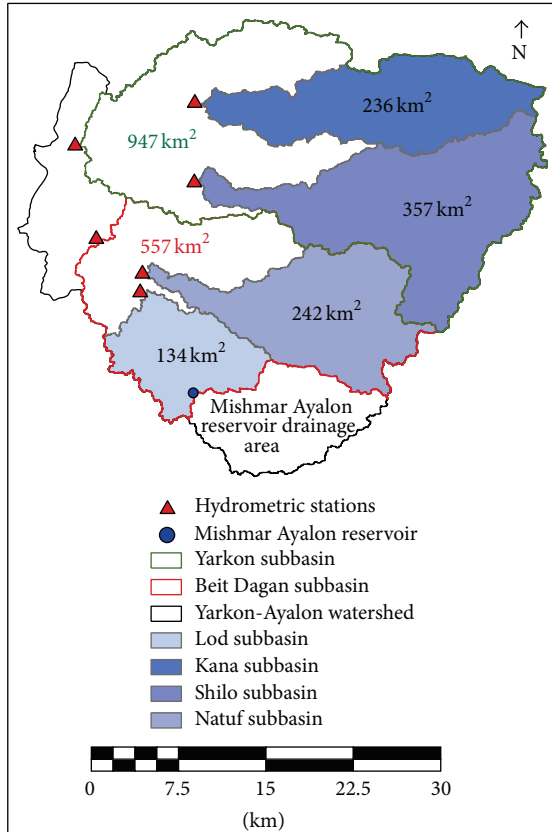


FIGURE 2: Yarkon-Ayalon watershed partitioned into six subbasins according to hydrometric stations. The number within each subbasin polygon represents its area.

gauged validation data for the other output variables were not available.

2.3. Model Input Data. In order to meet the model's requirements, the Yarkon-Ayalon watershed was initially divided into six different subbasins according to available hydrometric data for validation of the predicted results (Figure 2). Each of these subbasins was modeled separately, and model results were analyzed. Figure 3 shows the model's flowchart that is specified hereinafter.

A digital elevation model (DEM) was essential for providing elevation data. The DEM for this research was produced from optical stereo data acquired by the Advanced Spaceborne Thermal Emission and Reflection Radiometer (ASTER) that operates on the NASA Terra platform and has a spatial resolution of 30 m [39].

Soil data was represented through a digital soil map of the world provided by the Food and Agriculture Organization (FAO) of the United Nations (UN) and the UN Educational, Scientific and Cultural Organization (UNESCO). It was last updated in 2003 and has a spatial resolution of 1:5 million [40].

The model used a specific extreme rainfall storm that occurred between December 29, 1991, and January 3, 1992, and had an average rainfall depth of 165 mm over

the study watershed. Raw precipitation data from 24 stations, within and in vicinity of the watershed, were extracted from the Israeli Meteorological Service. The Thiessen polygon interpolation method [41] was conducted in order to receive estimations of precipitation values for each subbasin. Based on a Generalized Pareto Distribution method [42], this storm event is known to have had a precipitation return period of 50 years and led to the loss of 12 lives nationwide, damaged agricultural yields, and direct damage to buildings and infrastructure. Several main cities along the shoreline in central Israel were flooded, and the storm events during this winter were officially classified as a "natural disaster" [23]. Within the Yarkon-Ayalon watershed, some 153 million cubic meters (MCM) was discharged (compared to a mean annual discharge of 43 MCM) with a maximum discharge of 491 m³/s [23, 43]. Finally, a saturation index between 0.14 and 0.93 was entered into the model, representing the initial relative soil saturation [44].

Land-cover data was extracted using satellite imagery. In order to understand the temporal effect of LCCs on rainfall-runoff relationships, a model simulation of the same storm event, given the land-cover data status of a time period 20 years later, was implemented. This required using two images, both from the Landsat Thematic Mapper (TM), with a 30 m spatial resolution; the earlier image, representing the land-cover status during the time of the selected storm event, was acquired on December 17, 1989, and the second image was acquired about 19 years later, on January 3, 2009. The two images underwent radiometric and atmospheric corrections, as well as a topographic correction, due to the steep topography of the research area. All of these processes were carried out using Atmospheric/Topographic Correction (ATCOR) software that is specifically detailed in Richter (1998, 2010) [45, 46].

Six different land-cover classes were then decided upon in order to examine LCC through the years: (1) residential areas; (2) agricultural land; (3) orchards; (4) natural areas; (5) forests; and (6) bare exposed rocks, mines, and quarries. In order to extract land-cover patterns and distribution, a supervised maximum likelihood classification technique was conducted for both images [47], followed by an accuracy assessment procedure against high resolution orthophoto data, using 600 validation points. The methods chosen for classification accuracy assessment and evaluation were Kappa coefficient and overall accuracy as calculated from an error (confusion) matrix [48, 49].

Since each of the land-cover classes has its own characteristics, they were expressed and linked to the land-cover classes through the LUT; each of the six land-cover classes received representative values for the following variables: estimated canopy cover, interception, Manning's roughness coefficient, and imperviousness (percent paved area), specifically detailed by Miller et al. (2007) and Semmens et al. (2008). The LUTs are provided by the AGWA2 tool and can be modified by the user.

2.4. Model Calibration, Validation, and Output. The AGWA2 tool provides a number of output variables. In this work, the focus was on outflow runoff volume (m³) and maximum

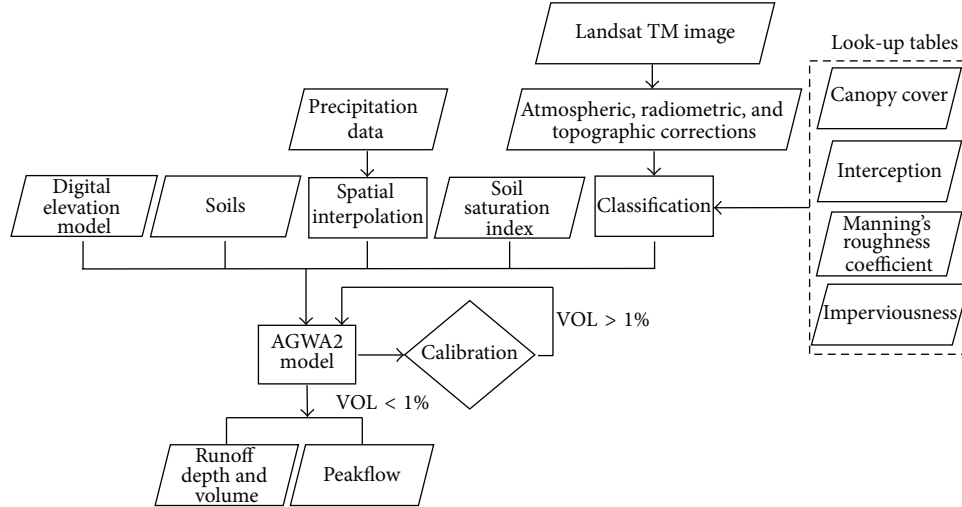


FIGURE 3: The study flowchart. AGWA2 is the Automated Geospatial Watershed Assessment tool. VOL is the objective function used for calibration that calculates the total runoff volume ratio between predicted and observed measurements.

TABLE 1: Calibration and validation objective functions (OFs). V_{obs} and V_{sim} are the observed and simulated runoff volume values, respectively; Q_{MXobs} and Q_{MXsim} are the observed and simulated peak discharge values, respectively; Q_{pred} and Q_{sim} are the simulated and observed discharge values, respectively. i denotes time increment.

Function	Description
$VOL = \left(\frac{V_{obs} * 100}{V_{sim}} \right) - 100$	Total runoff volume ratio between simulated and observed measurements, VOL, in %.
$PQR = \left(\frac{Q_{MXobs} * 100}{Q_{MXsim}} \right) - 100$	Peak discharge ratio between simulated and observed measurements, PQR, in %.
$ADPQ = Q_{MXpred} - Q_{MXsim} $	Absolute deviation between peak discharges of simulated and observed measurements, ADPQ, in m^3/s .
$MAQD = \frac{1}{n} \sum Q_{pred}(i) - Q_{sim}(i) $	Mean absolute discharge deviation between simulated and observed measurements, MAQD, in m^3/s .
$RMS = \sqrt{\frac{1}{n} \sum Q_{pred}(i) - Q_{sim}(i) ^2}$	Root mean square discharge deviation between simulated and observed measurements, RMS, in m^3/s .
$MXAQ = \max Q_{pred}(i) - Q_{sim}(i) $	Maximum absolute discharge deviation between simulated and observed measurements, MXAQ, in m^3/s .

peak discharge (m^3/s) (Figure 3). For each subbasin, these model output variables were simulated and examined. The *in situ* measured data for these variables enabled validation of the model results. The output map given by the model is discretized and represented by a collection of plane elements (polygons) and channel elements (polylines). Each element has its own value of the variable being examined.

The evaluation process was carried out using objective functions (OFs) as measures of the ratios and differences between the simulated values derived by the model, using the 1989 classification image as an input representing land-cover status during the storm, and the observed data measured during the actual rainstorm. In order to avoid bias, a number of OFs, rather than a single one, were chosen to evaluate the model accuracy [50, 51]. The calibration and validation OFs are summarized in Table 1. The objective was to keep the deviation between observed and simulated volume runoff values (VOL) as low as possible and in all cases under 1%, so that there was a minimum of 99% accuracy between measured and predicted total runoff volumes.

The calibration process included changing the model's parameter multipliers, which are values used to adjust plane and channel parameters (e.g., percent cover, interception, roughness for planes, and width, depth, and field effective saturated hydraulic conductivity) [27]. This was conducted up to the point where VOL is under 1%.

All of the OFs were calculated separately for the six subbasins. Each of the validation OF results was plotted against the subbasins' sizes (in km^2). A regression model, along with its significance level, was fitted in order to determine the relationship between the model accuracy and the subbasin size.

Initially, the model was simulated using the 1989 classification map, representing land-cover status during the rainfall event of winter 1991-1992. In order to determine the changes in rainfall-runoff relations caused by LCCs during a period of 19 years, the 2009 land-cover map was entered into the model instead of the 1989 map, while all other input variables remained static (e.g., calibration parameters, soil saturation index, precipitation data, soil map, and DEM). This was

performed in order to examine a scenario in which a rainfall event, with a fifty-year return period, occurs after 19 years of LCCs and to evaluate any changes and trends in future runoff volumes and peak discharges.

2.5. Analyses. Two major trends were analyzed from the model's simulated results. The first was a temporal trend, determining whether LCCs throughout 19 years affected runoff volumes and peak discharges in each of the six Yarkon-Ayalon subbasins and to what extent. The second was a spatial trend evaluating the factors that best-explain the spatial variability of the runoff volume across the different subbasins.

In order to conduct the temporal analysis, two factors were examined: (1) LCC between 1989 and 2009, using the land-cover maps; and (2) comparison of model results of the two time periods and how they were affected by LCCs. The first factor was analyzed by summing the total number of pixels for each land-cover in each subbasin, for both land-cover maps. The total number of pixels for each of the six land-cover classes was compared between the two images (1989 versus 2009) in order to analyze shifts. Then, the two land-cover maps were overlaid and a transition map was extracted, followed by summing up all of the transitions for every subbasin. For example, if a pixel with an agriculture land-cover type in the 1989 map was classified as a residential type in the 2009 map, it was defined as an agriculture-to-residential transition. For every subbasin, all of the pixels having this transition type were summed. This led to a total of 31 different transition phases (with "no-change" transition being the same for all types of land-cover undergoing no transition). The different transition phases for all subbasins were converted into a transition matrix and normalized to the area of each subbasin. Then, the transitions were analyzed using principal component analysis (PCA) ordination in order to determine which transitions were more pronounced in each subbasin.

The second factor of the temporal analysis initially involved conducting, for every subbasin, a comparison between total simulated runoff volume and peak discharge values, between the real rainfall event and the 2009 rainfall event scenario, and between their land-cover representations (1989 and 2009) in order to examine the runoff trends. This step included spatially examining the LCCs. It was performed by zooming into every plane element (polygon) in the subbasin and exploring the changes within the subbasin's elements, by calculating the percentage change between the two simulated runoff volume values (1989 and 2009) of every plane element. Only the most pronounced changes in runoff volumes were of interest, so only plane elements that had a value of above or below 1 standard deviation (SD) percent change were considered. The third step was to determine how LCCs affected the runoff changes in these plane elements. To do so, a zonal statistic tool for majority calculation of land-cover classes was used [52] for each plane element that was extracted in step 2. This means that each plane element (lower or higher than 1 SD of percent change) received one value of the land-cover class that had the largest representation within it. This was done for both time period images so that a qualitative comparison could be performed for each plane

element that exhibited runoff changes satisfying the threshold of ± 1 SD.

The spatial analysis process was performed in order to gain a better understanding regarding the environmental factors spatially affecting the runoff trends and was conducted only for the 2009 land-cover map. For every subbasin, the simulated runoff volume values were considered as the dependent variable. Three explanatory variables were examined as predictors of the runoff volume: land-cover, represented by the land-cover classification map, elevation, represented by DEM, and vegetation cover, represented by a normalized difference vegetation index (NDVI) map [53], extracted from the 2009 image. In order to determine the relationship characteristics between these explanatory variables and the runoff volume, a geographically weighted regression (GWR) was conducted. This method is designed to consider spatial data and nonstationarity, where the variable estimates vary locally, and spatially varying relationships can be explored [54, 55]. The results were expected to point out the relations between the runoff volume and the three explanatory variables, represented by regression coefficient R^2 , for each subbasin. The main goal was to understand which variable, or combination of variables, affects runoff volume variability the most for each subbasin.

Seven GWR tests were built and considered for each subbasin. They were conducted for the runoff volume variable against each independent variable separately, followed by modeling paired independent variables against runoff volume and finally by running all three independent variables. The model with the highest R^2 for each subbasin implies which variable, or combination of variables, had the strongest effect on runoff.

3. Results and Discussion

3.1. Model Input Data. Figures 4(a) and 4(b) show the Yarkon-Ayalon watershed after the classification process for the two time periods investigated. The overall classification accuracy and Kappa statistics for the two classification maps are 81.3% and 0.75 for the 1989 map and 82.97% and 0.78 for the 2009 map, respectively. Using the Thiessen polygons method, followed by weighting each interpolated polygon relative to its portion within each subbasin, six rainfall depth (mm) values were extracted, one for every subbasin. The totals of these values range between 155.3 mm and 172.1 mm for the five-day event (December 29, 1991–January 3, 1992).

3.2. Model Calibration, Validation, and Output. The 1989 model results are presented in Table 2, describing the simulated and predicted runoff volume values. The 1989 model output values were introduced into the OF equations, along with *in situ* measurements, in order to validate the model's accuracy.

The OF results are shown in Table 3, each calculated for all six subbasins. The relationships between the OF results and the subbasin sizes were studied using a regression model, supported by significance levels (P value). Figures 5(a)–5(e) display these relations, along with the supporting statistics. Mean absolute discharge deviation (MAQD), root mean

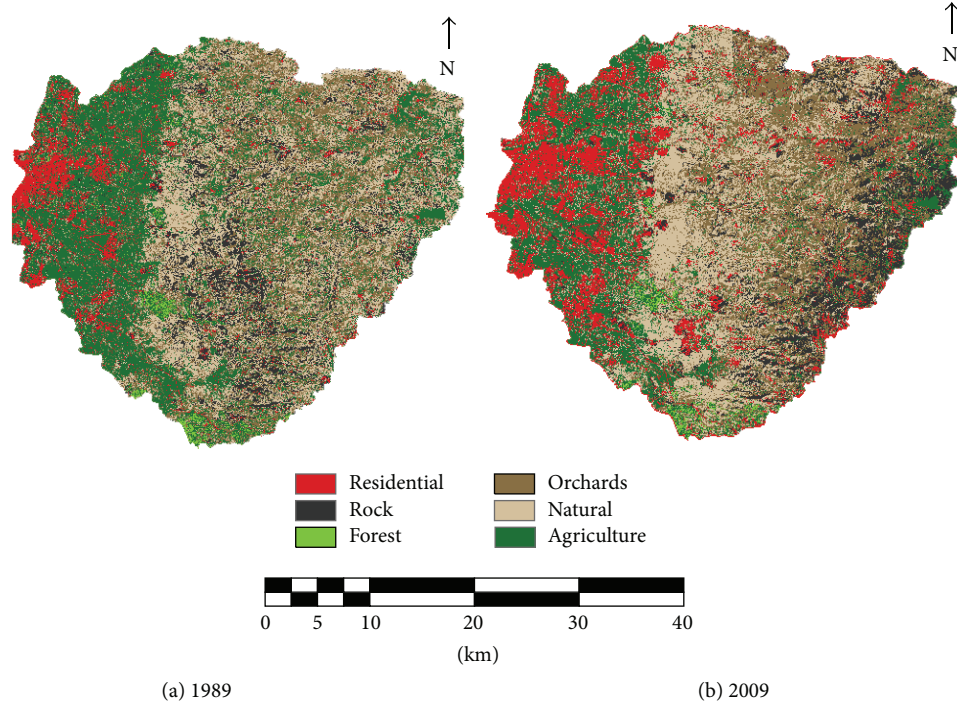


FIGURE 4: Land-cover classification maps of (a) 1989 and (b) 2009.

TABLE 2: Observed total runoff volume (million cubic meters (MCM)) for the storm event that was used for model calibration. The right column shows the simulated runoff values from the 1989 model after calibration.

Subbasin	1991-1992 observed values (MCM)	1989 values (MCM) after calibration
Yarkon	42.93	42.77
Beit Dagan	30.63	30.35
Shilo	10.72	10.77
Natuf	16.74	16.65
Kana	8.37	8.39
Lod	8.81	8.88

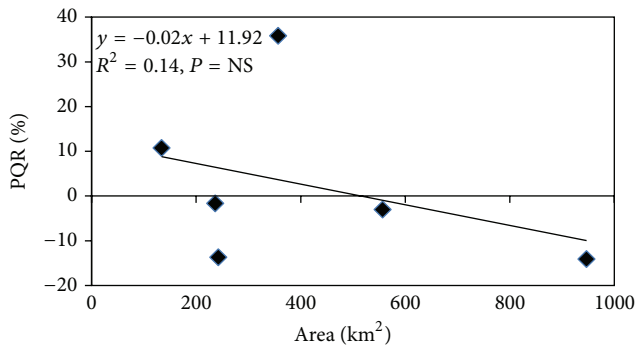
square discharge deviation (RMS), and maximum absolute discharge deviation (MXAQ) all show linear, significant relationships to subbasin size, with R^2 values of 0.9, 0.9, and 0.95, respectively. The peak discharge ratio (PQR) and absolute peak deviation (ADPQ) OFs are both measures of peak discharges and exhibit a nonsignificant relationship to subbasin size. It can be concluded, from the OF relationships to the subbasin areas, that as the latter increases, so does the deviation between the model simulations and *in situ* measurements concerning discharge throughout the event (Figures 5(a)–5(c)). When dealing with peak discharge deviation (Figures 5(d) and 5(e)), however, there is no significance to the subbasin size, and the modeled results show large inaccuracies.

The validation results demonstrate that a smaller subbasin is preferable to use with this model [56], as its simulations are most likely to perform more accurately.

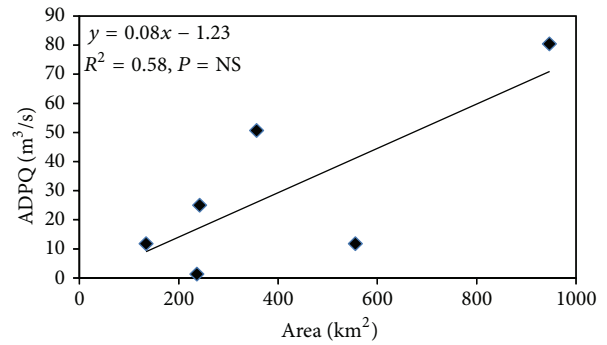
3.3. Temporal LCC Analysis. The first factor of the temporal analysis includes examination of LCCs. Comparison results of the land-cover trends between 1989 and 2009 for each subbasin are shown in Table 4. For all of the subbasins, the residential class went through the largest change. The number of pixels classified as residential was more than doubled during the 19 years examined. Lod shows the highest increase in the number of residential pixels by 2009, more than tripling the number of pixels in 1989. However, when considering the percent change relative to the entire subbasin area, a different trend emerges. The agriculture land-cover class in three of the subbasins went through the largest change, showing a decreasing trend between -6% and -13% . The other large trend belongs to the residential land-cover class, implying a shift from agricultural lands to residential areas. Shilo shows a quite different behavior, with a relatively large decrease in natural area (-15%) and an increase of bare rock (13.1%), due to urbanization processes that involve vegetation removal. Next, the transition phases for each pixel were derived by overlaying the land-cover classification maps. Figure 6 shows a biplot of PCA results. Components 1 and 2 explain a total of 85.2% of the data variance. The direction of each transition phase vector points at the subbasin it characterizes the most, while the length of the vectors expresses the portion of the transition occurrence relative to the other vectors. All of the subbasins are mostly characterized by no change at all, while Lod and Yarkon experienced the slightest change. The Yarkon subbasin experienced transitions from agricultural land, natural area, and orchards to residential area. The Shilo subbasin had greater transitions from natural areas, agricultural land, and orchards to bare rock than any other subbasin, along with transitions from natural area to

TABLE 3: The results of the objective functions (OFs).

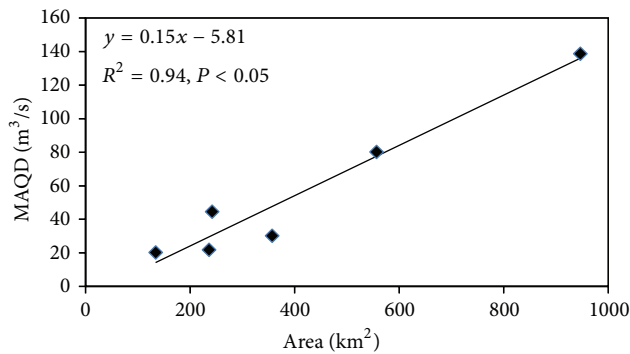
Subbasin	Size (km ²)	Total runoff ratio (VOL)	Peak discharge ratio (PQR)	Absolute peak deviation (ADPQ)	Mean absolute discharge deviation (MAQD)	Root mean square discharge deviation (RMS)	Maximum absolute discharge deviation (MXAQ)
Yarkon	947	0.36	-14.08	80.48	138.71	182.73	356
Beit Dagan	557	0.93	-2.96	11.48	80.16	104.77	224.37
Shilo	357	-0.45	35.85	50.66	30.19	43.67	126.4
Natuf	242	0.53	-13.64	25.01	44.56	57.03	125.46
Kana	236	-0.22	-1.632	1.7	22	35.12	94.25
Lod	134	-0.77	10.81	11.77	20.24	29.28	83.62



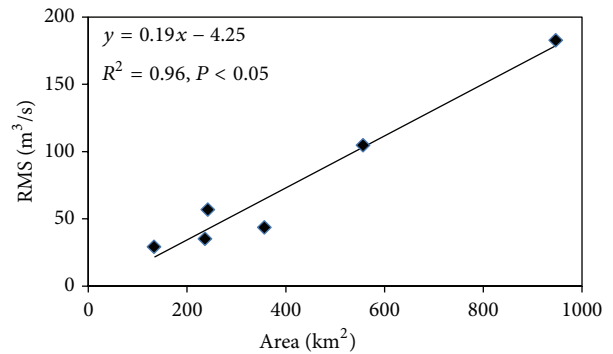
(a)



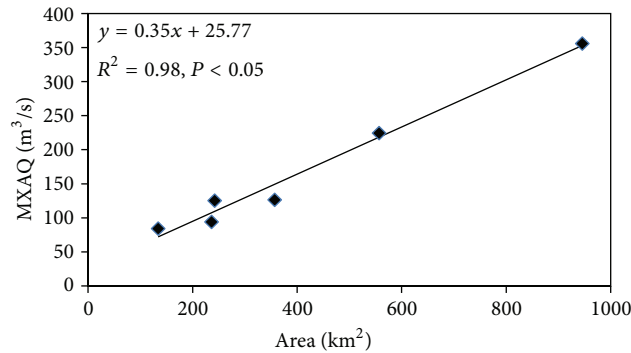
(b)



(c)



(d)



(e)

FIGURE 5: Evaluation of (a) peak discharge ratio (PQR); (b) absolute deviation between peak discharges (ADPQ); (c) mean absolute discharge deviation (MAQD); (d) root mean square discharge deviation (RMS); and (e) maximum absolute discharge deviation (MXAQ) as functions of the subbasin area by means of objective functions.

TABLE 4: Changes in land-cover classes between 1989 and 2009. Values in bold mark the largest changes.

Land-cover	Number of pixels in 1989	Number of pixels in 2009	Change of specific land-cover between years (%)	Change out of total subbasin (%)	Number of pixels in 1989	Number of pixels in 2009	Change of specific land-cover between years (%)	Change out of total subbasin (%)
Yarkon								
Residential	45830	116316	153.80	6.97	30496	79637	161.14	8.27
Bare rock	92196	145011	57.29	5.23	88798	63719	-28.24	-4.22
Forest	5022	3106	-38.15	-0.19	7302	8132	11.37	0.14
Orchards	283741	315179	11.08	3.11	123224	121657	-1.27	-0.26
Natural area	290190	259873	-10.45	-3.00	159854	182431	14.12	3.80
Agricultural land	293927	171308	-41.72	-12.13	184744	138838	-24.85	-7.72
Shilo								
Residential	9208	19917	116.30	2.81	6955	18969	172.74	4.65
Bare rock	41795	91806	119.66	13.12	55905	49271	-11.87	-2.57
Forest	765	434	-43.27	-0.09	1343	3015	124.50	0.65
Orchards	115226	146357	27.02	8.17	72206	82477	14.22	3.97
Natural area	132613	75376	-43.16	-15.02	81506	80775	-0.90	-0.28
Agricultural land	81483	47199	-42.08	-9.00	40662	24070	-40.80	-6.42
Kana								
Residential	6620	18149	174.15	4.57	7664	25545	233.31	12.50
Bare rock	22029	35127	59.46	5.19	10374	6229	-39.96	-2.90
Forest	839	760	-9.42	-0.03	4581	4048	-11.64	-0.37
Orchards	92137	103379	12.20	4.46	25067	12789	-48.98	-8.58
Natural area	80675	77806	-3.56	-1.14	33743	42701	26.55	6.26
Agricultural land	49997	16994	-66.01	-13.09	61650	51764	-16.04	-6.91

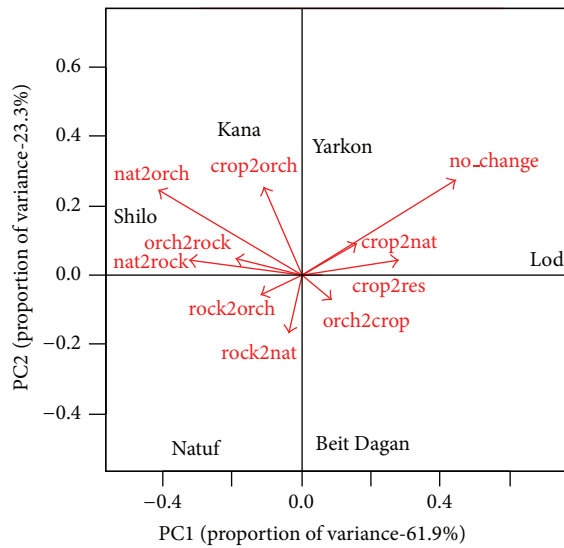


FIGURE 6: Principal component analysis (PCA) biplot of the transition phases' data. The land-cover classes represented are residential areas (res), agricultural land (crop), orchards (orch), natural areas (nat), and bare exposed rocks (rock).

orchards. The Natuf subbasin shows the highest transition portions from bare rock to orchards and natural areas. The main transition in the Kana subbasin was from agricultural

land to orchards. The Lod and Beit Dagan subbasins did not experience any major transition, apart from agricultural land transformation to residential areas, as did the Yarkon subbasin.

It is worth mentioning that the decrease in orchard land-cover occurred mostly in the Israeli side of the watershed, while increase in orchards was observed mainly along the PA part of the watershed. This can be explained by the extensive urbanization process in the western part of the watershed that led to a reduction in orchards in favor of urban development. Along the West Bank, however, orchards are an effective mean for Palestinian farmers to establish facts on the ground, thus the increase in this land-cover type along the Palestinian side of the watershed.

3.4. Temporal Runoff Change. The second factor of temporal analysis, the comparison between simulated runoff volume and peak discharge values for the two examined time periods, is presented in Table 5, along with the percent change between the simulated values. All of the subbasins show a moderate increase in both runoff volumes and peak discharge, aside from the Natuf subbasin that presents an opposite trend. This trend corresponds to the findings of the Israeli Hydrological Service reports during the past 40 years [57].

The percent changes in runoff volume above or below 1 SD within the planes are shown in Table 6. It exhibits the portion of the area that had experienced a change of ± 1 SD from the whole subbasin size. Figure 7 presents this data graphically.

TABLE 5: Simulated runoff volume (million cubic meters (MCM)) and peak discharge values (m^3/s) extracted from the 1989 and 2009 models.

Subbasin		1989 simulated value	2009 simulated value	Percent change between simulated values
Yarkon	Runoff volume (MCM)	42.77	43.74	2.26
	Peak discharge (m^3/s)	571.48	582	1.84
Beit Dagan	Runoff volume (MCM)	30.35	31.96	5.3
	Peak discharge (m^3/s)	388.48	405.99	4.51
Shilo	Runoff volume (MCM)	10.77	11.39	5.79
	Peak discharge (m^3/s)	141.34	147.245	4.18
Natuf	Runoff volume (MCM)	16.65	16.56	-0.57
	Peak discharge (m^3/s)	183.66	182.71	-0.52
Kana	Runoff volume (MCM)	8.39	8.78	4.64
	Peak discharge (m^3/s)	104.1	108.55	4.28
Lod	Runoff volume (MCM)	8.88	9.47	6.69
	Peak discharge (m^3/s)	108.93	114.68	5.28

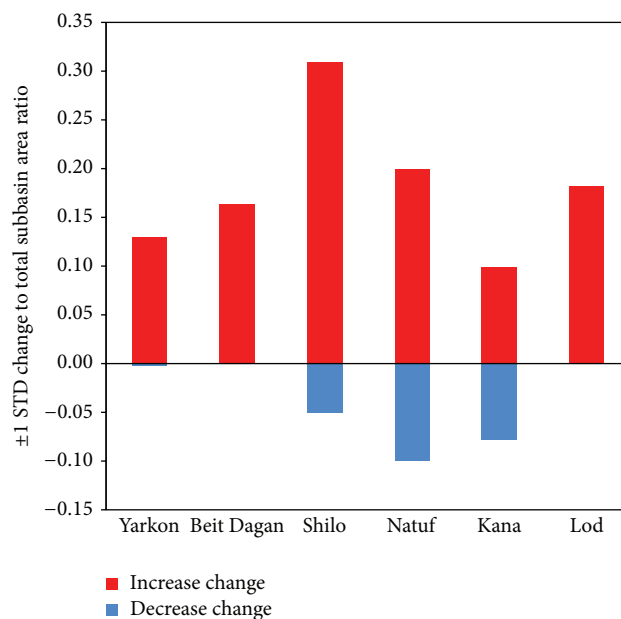
TABLE 6: Area size and percent change of ± 1 SD increase, decrease, and total change in runoff volume values.

Subbasin	1 SD of % runoff change area	Subbasin area (km^2)	Increase change area (km^2)	Increase change portion	Decrease change area (km^2)	Decrease change portion	Total change area (km^2)	Total change
Yarkon	3.45	946.7	123.0	0.13	2.1	0.00	125.1	0.13
Beit Dagan	66.87	556.7	80.9	0.15	0.0	0.00	80.9	0.15
Shilo	7.5	356.9	110.4	0.31	18.0	0.05	128.4	0.36
Natuf	2.95	242.1	48.4	0.20	24.2	0.10	72.6	0.30
Kana	16.4	236.3	23.4	0.10	18.4	0.08	41.8	0.18
Lod	16.1	134	24.4	0.18	0.1	0.00	24.5	0.18

The Shilo subbasin went through the largest total change of ± 1 SD, with 30% and 5% increase and decrease changes, respectively, followed by the Natuf subbasin, in which 20% of its total area experienced an increase in runoff values larger than 1 SD, as opposed to only a 10% decrease of those below 1 SD. At the same time, the Natuf subbasin had the largest decrease change value, compared to the other subbasins. The other cases show similar trends, with about a 9–18% increase change and a 5–8% decrease change of runoff volume above or below 1 SD.

Examples of the temporal analysis results, for the two of the six subbasins examined, are presented in Figures 8 and 9. Maps in Figures 8(a) and 9(a) present the positive and negative changes in runoff volume of ± 1 SD. It should be noted that while Natuf exhibits a trend toward increasing runoff where these values are limited to ± 1 SD, the general trend of runoff change (total increase and decrease percent change) is 47.3% increase and 52.7% decrease. This is complementary with Table 5 that implies a decreasing trend in runoff volume for this subbasin.

A land-cover comparison is shown in Figures 8(b), 8(c), 9(b) and 9(c) through majority zonal statistics calculations (each polygon receives the value of the most common land-cover class within it) for the land-cover status of the polygons

FIGURE 7: Increase, decrease, and total runoff volume change of ± 1 standard deviation (SD) out of the total subbasin area, within the planes.

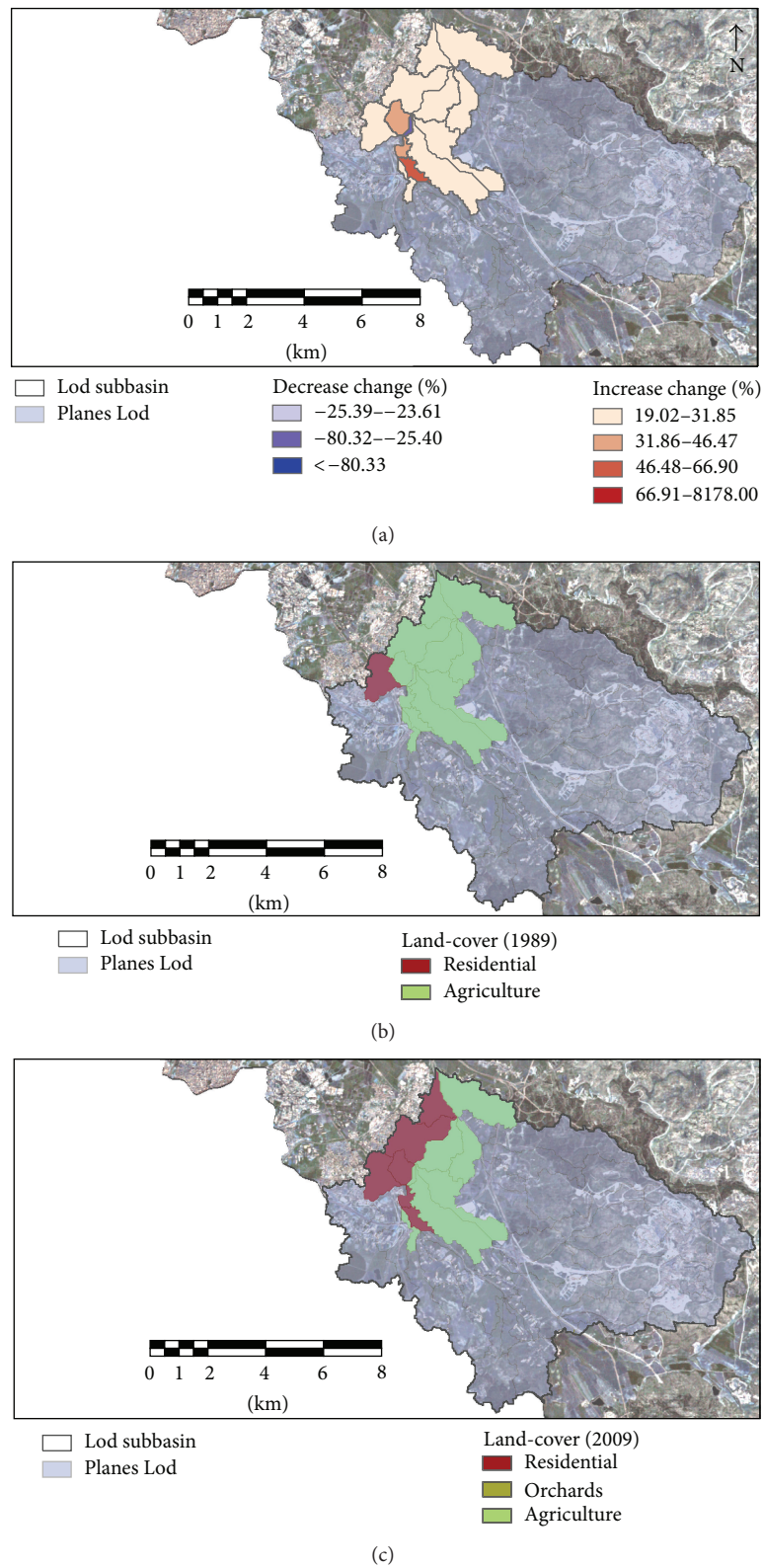
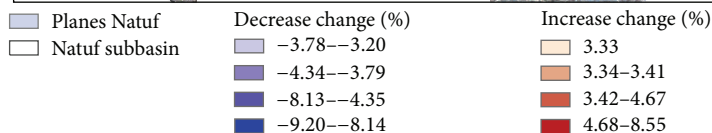
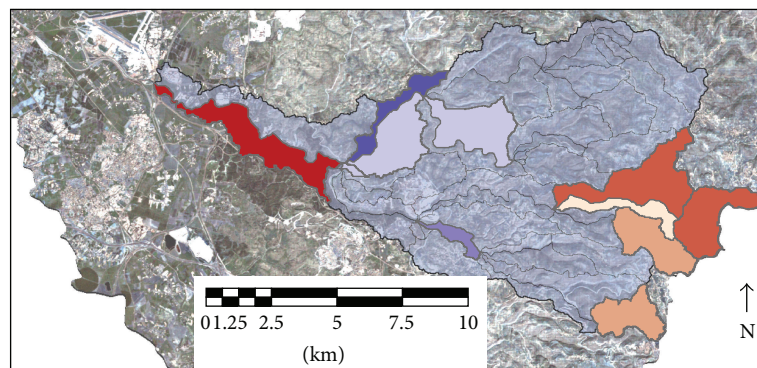
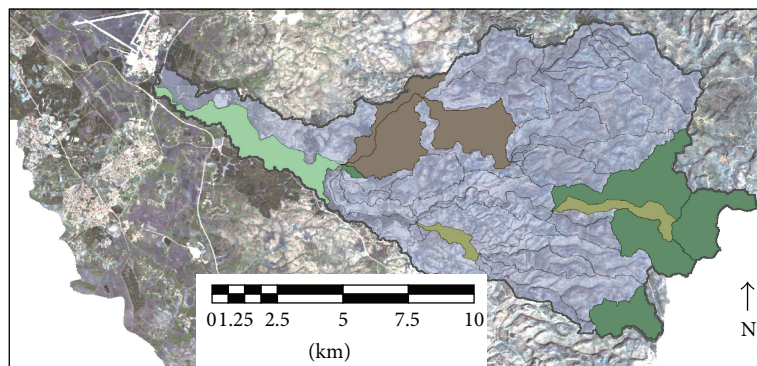


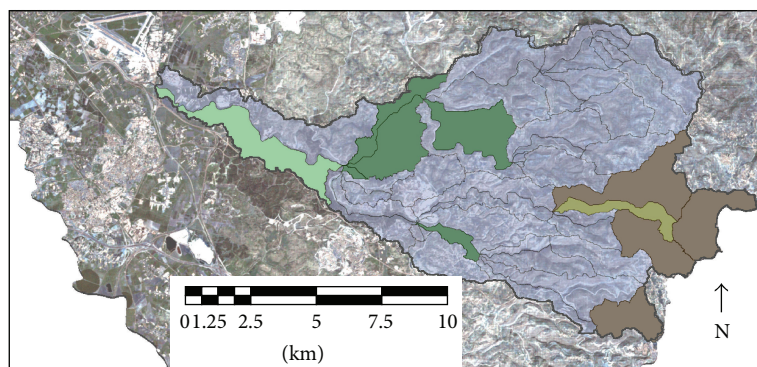
FIGURE 8: Temporal land-cover changes (LCCs) in the Lod subbasin between the years 1989 and 2009: (a) change in simulated runoff volume of ± 1 SD; (b) land-cover status in 1989, based on majority zonal statistics calculations; (c) land-cover status in 2009, based on majority zonal statistics calculations.



(a)



(b)



(c)

FIGURE 9: Temporal land-cover changes (LCCs) in the Natuf subbasin between the years 1989 and 2009: (a) change in simulated runoff volume of ± 1 SD; (b) land-cover status in 1989, based on majority zonal statistics calculations; (c) land-cover status in 2009, based on majority zonal statistics calculations.

TABLE 7: Geographically weighted regression (GWR) results for runoff volume as the dependent variable and the digital elevation model (DEM), land-cover classes, and the normalized difference vegetation index (NDVI) as explanatory variables. The bold highlighted values are the highest R^2 results for each subbasin.

Spatial statistics and explanatory variables	Yarkon	Beit Dagan	Shilo	Natuf	Kana	Lod
GWR-classification	0.9	0.86	0.82	0.78	0.91	0.82
GWR-DEM	0.65	0.66	0.77	0.43	0.67	0.59
GWR-NDVI	0.93	0.92	0.94	0.89	0.92	0.93
GWR-DEM + classification	0.57	0.63	0.96	0.39	0.72	0.92
GWR-NDVI + classification	0.88	0.84	0.73	0.77	0.89	0.79
GWR-NDVI + DEM	0.59	0.63	0.96	0.37	0.72	0.92
GWR-all	0.5	0.60	0.97	0.87	0.66	0.93

undergoing ± 1 SD of runoff volume change (%), where maps in Figures 8(b) and 9(b) are the 1989 status and maps in Figures 8(c) and 9(c) represent 2009. This analysis was conducted for all six subbasins (Table 6), providing the following outcomes.

- (i) Yarkon: most of the area that changed ± 1 SD of the total percent runoff change has experienced a positive change in runoff volumes; this trend is owing to an increase in residential areas, mostly downstream towards the coastline. The shifts are usually from agricultural areas to built-up landscapes.
- (ii) Beit Dagan: there was no decrease in percent runoff change below 1 SD; rather, all of the changes are larger than 1 SD due to alterations from agricultural activities to residential land-cover.
- (iii) Shilo: most of the large changes are positive, located upstream along the headwaters. The land-cover shifts are of different characteristics. Some natural areas changed into orchards or bare exposed rock and so did the agricultural land. This greatly implies that the growing built-up trend along the headwaters is due to the activities of Palestinian villages and cities. The rocky nature of the shift is due to quarries, road paving, preparation of the area for urban development, and a general exposure of the ground.
- (iv) Lod (Figure 8): this subbasin experienced mostly increase of larger than 1 SD runoff change, with an insignificant portion of the area going through decrease in lower than 1 SD runoff change (0.1 km^2). This is a result of a transformation of an agricultural landscape to an urbanized landscape.
- (v) Natuf (Figure 9): similar to the Shilo subbasin, this area also experienced an increase in runoff change along the headwaters, shifting from natural and orchard land-cover to bare exposed rocks. However, the lower areas show a decrease in runoff change below 1 SD, due to a shift from bare exposed rock to natural covered area. The lowest, western part of this subbasin expresses a strong increase in runoff, mostly due to urbanization development at the expense of agricultural activities.
- (vi) Kana: in this subbasin, similar portions of the area went through both an increase and a decrease in

the amounts of runoff (10% and 8%, resp.). The increase was mostly due to urbanization where some natural cover or agricultural activities used to take place, while the decreasing trend is a result of orchard-covered areas' transformation to natural covered landscape.

Most increase changes are explicitly due to a transformation from agricultural activities or natural land-cover to residential uses or bare rocks, mostly occurring along the rural-urban fringe and known as "urban-sprawl," on the Israeli side of the watershed. This might be due to several reasons, including immigration and increase in population, natural growth, economic processes, and planning policies [58]. The Palestinian part of the watershed has also experienced a constant and rapid urban growth. The Ramallah governorate, which is mostly contained within the Yarkon-Ayalon watershed and affects the Natuf and Shilo subbasins, has a population size that constitutes about 12% of the total population in the West Bank, with an urban expansion reaching its limits in all directions of the municipal boundary. Between 1989 and 1994 the built-up area of Ramallah expanded by 16.1% and, between 1994 and 2000, it added another 24.5% to its area [29]. The inevitable outcome, in most cases of increased urban areas, is increases in runoff volumes, peak discharges, and flash floods [14, 59].

3.5. Geographically Weighted Regression (GWR) Statistical Tests. The spatial analysis results for the GWR statistical tests are shown in Table 7, where the final adjusted R^2 values for each of the statistical models that were performed are presented. The GWR results indicate that, in all of the subbasins aside from Shilo, the vegetation cover variable (represented by NDVI values) alone was the best explanatory variable for the runoff variation along these subbasins (in Lod subbasin the coefficient of determination (R^2) value for NDVI was slightly higher than the value received from all of the explanatory variables combined). The NDVI variable was able to explain 89 to 93% of the runoff volume spatial variance. This corresponds to a large number of studies in this field, concluding that vegetation cover decrease has a great effect on runoff volumes, runoff peak discharge [10, 60], and the lag time between the rainfall event and runoff generation as well as on soil erosion and nutrient loss [61, 62]. For the Shilo subbasin, all of the explanatory variables put together

produced the highest regression coefficient; while vegetation cover is the main contributor, the elevation variable provides an additional explanation to the runoff volume variance, owing to the steep topography along the headwaters of this subbasin.

4. Conclusions

Between the years 1989 and 2009, some changes in land-cover occurred along the Yarkon-Ayalon watershed. Although most of the considered area experienced no change at all, the major trends that were observed at locations where change took place included a decrease in agricultural lands and an increase in residential cover or residential-related processes. Changes in land-cover, through this period of 19 years, were spotted via remote-sensing tools and coupled with hydrological simulation tools in order to find the relationship between LCC and rainfall-runoff relationships. LCCs were found to have some effect on the runoff volumes and peak discharges. In locations in which land-cover shifts towards natural covered areas occurred, a minor decrease in runoff was observed, thus pointing once more to the strong relationship between vegetative cover and runoff volumes and peak discharge values. The LCCs that had the largest impact on the runoff regime were those related to urbanization and vegetation removal.

Spatially, this research demonstrates high correlations between vegetation cover and runoff volume values within the study area, implying that a continuing trend of vegetation removal will result in higher runoff volumes across the watershed during extreme rainfall events. Soil erosion trends were not examined due to a lack of validation data, although it can be expected that they would correspond to the runoff findings.

An extreme rainfall event was used to examine the outcomes of LCCs on runoff volumes and peak discharges. While this might highlight different phenomena across the watershed, it would be interesting and important to examine the effects of frequent rainfall events on the runoff trends throughout periods of changing land-covers, since these events are far more frequent and have a greater impact on the watershed area.

Conflict of Interests

The authors declare that there is no conflict of interests regarding the publication of this paper.

Acknowledgments

This study was conducted with partial financial support from the Ministry of Agriculture and the Jewish National Fund (JNF). The authors would like to thank The Israeli Water Authority for providing data, Shea Burns and David Goodrich (of the USDA/ARS) for their invaluable assistance, and the Jacob Blaustein Institutes for Desert Research Remote Sensing Laboratory staff and students for their most appreciated support and knowledge sharing.

References

- [1] P. P. N. Raj and P. A. Azeez, "Land use and land cover changes in a tropical river basin: a case from Bharathapuzha River Basin, Southern India," *Journal of Geographic Information System*, vol. 2, no. 4, pp. 185–193, 2010.
- [2] P. H. Verburg, K. Neumann, and L. Nol, "Challenges in using land use and land cover data for global change studies," *Global Change Biology*, vol. 17, no. 2, pp. 974–989, 2011.
- [3] J. R. Anderson, E. E. Hardy, J. T. Roach, and R. E. Witmer, "A land use and land cover classification system for use with remote sensing data," US Geological Survey Professional Paper no. 964, United States Geological Survey, Reston, Va, USA, 1976.
- [4] F. Wu, J. Zhan, Q. Xu, Y. Xiong, and Z. Sun, "A comparison of two land use simulation models under the RCP4.5 Scenario in China," *Advances in Meteorology*, vol. 2013, Article ID 578350, 7 pages, 2013.
- [5] O. Rozenstein and A. Karnieli, "Comparison of methods for land-use classification incorporating remote sensing and GIS inputs," *Applied Geography*, vol. 31, no. 2, pp. 533–544, 2011.
- [6] G. Blöchl, S. Ardoin-Bardin, M. Bonell et al., "At what scales do climate variability and land cover change impact on flooding and low flows?" *Hydrological Processes*, vol. 21, no. 9, pp. 1241–1247, 2007.
- [7] Y. Kidane, R. Stahlmann, and C. Beierkuhnlein, "Vegetation dynamics, and land use and land cover change in the Bale Mountains, Ethiopia," *Environmental Monitoring and Assessment*, vol. 184, no. 12, pp. 7473–7489, 2012.
- [8] E. Fredj, M. Silver, and A. Givati, "An integrated simulation and distribution system for early flood warning," *Water Resources Management*. In press.
- [9] D. Mao and K. A. Cherkauer, "Impacts of land-use change on hydrologic responses in the Great Lakes region," *Journal of Hydrology*, vol. 374, no. 1–2, pp. 71–82, 2009.
- [10] M. H. Costa, A. Botta, and J. A. Cardille, "Effects of large-scale changes in land cover on the discharge of the Tocantins River, Southeastern Amazonia," *Journal of Hydrology*, vol. 283, no. 1–4, pp. 206–217, 2003.
- [11] J. Delgado, P. Llorens, G. Nord, I. R. Calder, and F. Gallart, "Modelling the hydrological response of a Mediterranean medium-sized headwater basin subject to land cover change: the Cardener River basin (NE Spain)," *Journal of Hydrology*, vol. 383, no. 1–2, pp. 125–134, 2010.
- [12] C. Deasy, A. Titman, and J. N. Quinton, "Measurement of flood peak effects as a result of soil and land management, with focus on experimental issues and scale," *Journal of Environmental Management*, vol. 132, pp. 304–312, 2014.
- [13] M. D. White and K. A. Greer, "The effects of watershed urbanization on the stream hydrology and riparian vegetation of Los Peñasquitos Creek, California," *Landscape and Urban Planning*, vol. 74, no. 2, pp. 125–138, 2006.
- [14] N. Kliot, "Man's impact on river basins: an Israeli case study," *Applied Geography*, vol. 6, no. 2, pp. 163–178, 1986.
- [15] B. Verbeiren, T. van de Voorde, F. Canters, M. Binard, Y. Cornet, and O. Batelaan, "Assessing urbanisation effects on rainfall-runoff using a remote sensing supported modelling strategy," *International Journal of Applied Earth Observation and Geoinformation*, vol. 21, no. 1, pp. 92–102, 2012.
- [16] B. Hong, K. E. Limburg, M. H. Hall et al., "An integrated monitoring/modeling framework for assessing human-nature interactions in urbanizing watersheds: wappinger and Onondaga

- Creek watersheds, New York, USA," *Environmental Modelling & Software*, vol. 32, pp. 1–15, 2012.
- [17] W. Choi and B. M. Deal, "Assessing hydrological impact of potential land use change through hydrological and land use change modeling for the Kishwaukee River basin (USA)," *Journal of Environmental Management*, vol. 88, no. 4, pp. 1119–1130, 2008.
- [18] O. M. Issa, C. Valentin, J. L. Rajot, O. Cerdan, J.-F. Desprats, and T. Bouchet, "Runoff generation fostered by physical and biological crusts in semi-arid sandy soils," *Geoderma*, vol. 167–168, pp. 22–29, 2011.
- [19] Y. Zhang and W. Shuster, "Impacts of spatial distribution of impervious areas on runoff response of hillslope catchments: simulation study," *Journal of Hydrologic Engineering*, vol. 19, no. 6, pp. 1089–1100, 2014.
- [20] I.-Y. Yeo, S. I. Gordon, and J.-M. Guldmann, "Optimizing patterns of land use to reduce peak runoff flow and nonpoint source pollution with an integrated hydrological and land-use model," *Earth Interactions*, vol. 8, no. 6, pp. 1–20, 2004.
- [21] IPCC, "Summary for policymakers," in *Climate Change 2007: The Physical Science Basis, in Contribution of Working Group I to the Fourth Assessment Report of the Intergovernmental Panel on Climate Change*, S. Solomon, D. Qin, M. Manning et al., Eds., Intergovernmental Panel on Climate Change, Cambridge, UK, 2007.
- [22] B. C. Bates, Z. W. Kundzewicz, S. Wu, and J. P. Palutikof, "Climate change and water," Technical Paper of the Intergovernmental Panel on Climate Change, IPCC Secretariat, Geneva, Switzerland, 2008.
- [23] H. Gvirtzman, *Israel Water Resources, Chapters in Hydrology and Environmental Sciences*, Yad Ben-Zvi Press, Jerusalem, Israel, 2002.
- [24] F. Yuan, K. E. Sawaya, B. C. Loeffelholz, and M. E. Bauer, "Land cover classification and change analysis of the Twin Cities (Minnesota) Metropolitan Area by multitemporal Landsat remote sensing," *Remote Sensing of Environment*, vol. 98, no. 2–3, pp. 317–328, 2005.
- [25] C. He, "Integration of geographic information systems and simulation model for watershed management," *Environmental Modelling & Software*, vol. 18, no. 8–9, pp. 809–813, 2003.
- [26] D. J. Semmens, D. Goodrich, C. L. Unkrich, R. E. Smith, D. A. Woolhiser, and S. N. Miller, *KINEROS, A Kinematic Runoff and Erosion Model, Documentation and User Manual*, ARS-77, Department of Agriculture, Agricultural Research Service, Washington, DC, USA, 1990.
- [27] D. J. Semmens, D. C. Goodrich, C. L. Unkrich, R. E. Smith, D. A. Woolhiser, and S. N. Miller, "KINEROS2 and the AGWA modeling framework," in *Hydrological Modelling in Arid and Semi-Arid Areas*, pp. 49–68, Cambridge University Press, 2008.
- [28] A. Rahamimoff, *Master Plan for the Yarqon River—Summary of the Master Plan*, Y. R. Authority, Ramat Gan, Israel, 2005.
- [29] J. AbuSada and S. Thawaba, "Multi criteria analysis for locating sustainable suburban centers: a case study from Ramallah Governorate, Palestine," *Cities*, vol. 28, no. 5, pp. 381–393, 2011.
- [30] S. Ben-Yosef, *The New Israel Guide*, Keter Publishing House, The Israel MOD Publishing House, Miskal-Yedioth Aharonoth Books and Chemed Books, 2001.
- [31] A. Givati, E. Fredj, T. Rumlmer et al., "Using the fully coupled WRF-Hydro model for extreme events flood at Mediterranean basins," *Journal of Hydrology*, Under review.
- [32] S. Rabikovich, "Classification of the soils of Israel," in *Soils of Israel*, pp. 269–276, The Hebrew University of Jerusalem, Faculty of Agriculture, Rehovot, Israel, 1960.
- [33] M. Schaffner, C. L. Unkrich, and D. C. Goodrich, "Application of the KINEROS2 site specific Model to South-Central NY and Northeast PA: forecasting Gaged and Ungaged Fast Responding Watersheds," NWS Eastern Region Technical Attachment 2010-01, 2010.
- [34] A. Al-Qurashi, N. McIntyre, H. Wheeler, and C. Unkrich, "Application of the Kineros2 rainfall-runoff model to an arid catchment in Oman," *Journal of Hydrology*, vol. 355, no. 1–4, pp. 91–105, 2008.
- [35] L. M. Norman, M. L. Villarreal, C. S. A. Wallace et al., "A high-resolution land-use map—Nogales, Sonora, Mexico," U.S. Geological Survey Open-File Report 2010-1156, USGS National Center, Reston, Va, USA, 2010.
- [36] D. A. Woolhiser, R. E. Smith, and D. Goodrich, *KINEROS, A Kinematic Runoff and Erosion Model: Documentation and User Manual*, US Department of Agriculture, Agricultural Research Service, ARS-77, 1990.
- [37] D. J. Semmens, W. G. Kepner, D. C. Goodrich, D. P. Guertin, M. Hernez, and S. N. Miller, "From research to management: a suite of GIS-based watershed modeling, assessment and planning tools," in *Environmental Modeling Software*, International Environmental Modelling and Software Society, Burlington, Vt, USA, 2006.
- [38] A. J. Cate, *AGWA Design Document: Migrating to ArcGIS and the Internet*, US Environmental Protection Agency, Office of Research and Development, Washington, DC, USA, 2005.
- [39] ASTER-GDEM-Validation-Team, *ASTER Global DEM Validation Summary Report*, 2009.
- [40] FAO, IIASA, ISRIC, ISSCAS, and JRC, *Harmonized World Soil Database (version 1.2)*, International Institute for Applied Systems Analysis, Rome, Italy, Food and Agriculture Organization, Laxenburg, Austria, 2012.
- [41] G. Q. Tabios and J. D. Salas, "A comparative analysis of techniques for spatial interpolation of precipitation," *Journal of the American Water Resources Association*, vol. 21, no. 3, pp. 365–380, 1985.
- [42] J. Xia, D. She, Y. Zhang, and H. Du, "Spatio-temporal trend and statistical distribution of extreme precipitation events in Huaihe River Basin during 1960–2009," *Journal of Geographical Sciences*, vol. 22, no. 2, pp. 195–208, 2012.
- [43] Israel-Water-Authority, *Hydrological Multi-Yearbook for Israel, Hydro-Report 2013*, Israel Water Authority, Jerusalem, Israel, 2013.
- [44] M. Hernandez, D. J. Semmens, S. N. Miller, D. Goodrich, and W. G. Kepner, "Development and applications of the automated geospatial watershed assessment tool," in *Modeling and Remote Sensing Applied to Agriculture (U.S. and Mexico)*, C. W. Richardson, A. S. Baez-Gonzalez, and M. Tiscareno-Lopez, Eds., chapter 9, USDA-INIFAP, Aguascalientes, Mexico, 2006.
- [45] R. Richter, "Correction of satellite imagery over mountainous terrain," *Applied Optics*, vol. 37, no. 18, pp. 4004–4015, 1998.
- [46] R. Richter, *Atmospheric/Topographic Correction for Satellite Imagery, ATCOR-2/3 User Guide*, Version 1.7, DLR, German Aerospace Center, Remote Sensing Data Center, Weßling, Germany, 2010.
- [47] G. Arbia, R. Benedetti, and G. Espa, "Contextual classification in image analysis: an assessment of accuracy of ICM," *Computational Statistics & Data Analysis*, vol. 30, no. 4, pp. 443–455, 1999.

- [48] R. G. Congalton, "A review of assessing the accuracy of classifications of remotely sensed data," *Remote Sensing of Environment*, vol. 37, no. 1, pp. 35–46, 1991.
- [49] G. M. Foody, "Status of land cover classification accuracy assessment," *Remote Sensing of Environment*, vol. 80, no. 1, pp. 185–201, 2002.
- [50] M. H. Diskin and E. Simon, "A procedure for the selection of objective functions for hydrologic simulation models," *Journal of Hydrology*, vol. 34, no. 1-2, pp. 129–149, 1977.
- [51] A. M. Karnieli, M. H. Diskin, and L. J. Lane, "CELMOD5—a semi-distributed cell model for conversion of rainfall into runoff in semi-arid watersheds," *Journal of Hydrology*, vol. 157, no. 1–4, pp. 61–85, 1994.
- [52] M. Sonwalkar, L. Fang, and D. Sun, "Use of NDVI dataset for a GIS based analysis: a sample study of TAR Creek superfund site," *Ecological Informatics*, vol. 5, no. 6, pp. 484–491, 2010.
- [53] N. Bakr, D. C. Weindorf, M. H. Bahnassy, S. M. Marei, and M. M. El-Badawi, "Monitoring land cover changes in a newly reclaimed area of Egypt using multi-temporal Landsat data," *Applied Geography*, vol. 30, no. 4, pp. 592–605, 2010.
- [54] G. M. Foody, "Geographical weighting as a further refinement to regression modelling: an example focused on the NDVI-rainfall relationship," *Remote Sensing of Environment*, vol. 88, no. 3, pp. 283–293, 2003.
- [55] J. Tu, "Spatially varying relationships between land use and water quality across an urbanization gradient explored by geographically weighted regression," *Applied Geography*, vol. 31, no. 1, pp. 376–392, 2011.
- [56] S. N. Miller, D. J. Semmens, D. C. Goodrich et al., "The automated geospatial watershed assessment tool," *Environmental Modelling & Software*, vol. 22, no. 3, pp. 365–377, 2007.
- [57] A. Givati, *Natuf Subbasin*, 2012.
- [58] M. Shoshany and N. Goldshleger, "Land-use and population density changes in Israel-1950 to 1990: analysis of regional and local trends," *Land Use Policy*, vol. 19, no. 2, pp. 123–133, 2002.
- [59] S. Rozalis, E. Morin, Y. Yair, and C. Price, "Flash flood prediction using an uncalibrated hydrological model and radar rainfall data in a Mediterranean watershed under changing hydrological conditions," *Journal of Hydrology*, vol. 394, no. 1-2, pp. 245–255, 2010.
- [60] M. Hernandez, S. N. Miller, D. C. Goodrich et al., "Modeling runoff response to land cover and rainfall spatial variability in semi-arid watersheds," *Environmental Monitoring and Assessment*, vol. 64, no. 1, pp. 285–298, 2000.
- [61] E. Wahlstrom, K. Loague, and P. C. Kyriakidis, "Hydrologic response: Kahoʻolawe, Hawaii," *Journal of Environmental Quality*, vol. 28, no. 2, pp. 481–492, 1999.
- [62] T. Lasanta, J. M. García-Ruiz, C. Pérez-Rontomé, and C. Sancho-Marcén, "Runoff and sediment yield in a semi-arid environment: the effect of land management after farmland abandonment," *Catena*, vol. 38, no. 4, pp. 265–278, 2000.

Research Article

The Elements of Water Balance in the Changing Climate in Poland

Małgorzata Szwed

Institute for Agricultural and Forest Environment of Polish Academy of Sciences, Bukowska 19, 60-809 Poznań, Poland

Correspondence should be addressed to Małgorzata Szwed; mszwed@man.poznan.pl

Received 7 November 2014; Revised 9 February 2015; Accepted 10 February 2015

Academic Editor: Yongqiang Zhang

Copyright © 2015 Małgorzata Szwed. This is an open access article distributed under the Creative Commons Attribution License, which permits unrestricted use, distribution, and reproduction in any medium, provided the original work is properly cited.

Strong global warming has been observed in the last three decades. Central Europe, including Poland, is not an exception. Moreover, climate projections for Poland foresee further warming as well as changes in the spatial and seasonal distribution and quantity of precipitation. However, climate models do not agree on the sign of change of precipitation. In Poland precipitation is projected to decrease in summer (this finding is not robust, being model-dependent) and to increase in winter. Therefore, there is still considerable uncertainty regarding likely climate change impacts on water resources in Poland. However, there is no doubt that changes in the thermal characteristics as well as in precipitation will influence changes in the water balance of the country. In this study, the components of climatic water balance, that is, precipitation, evaporation, and runoff, are calculated for the average conditions in the control period of 1961–1990 and in the future (2071–2100) in Poland. The changes of the water balance components for the present and for the future are compared and analysed. Due to insufficient consistency between climate models a possible range of changes should be presented; hence the multimodel projections from ENSEMBLES Project of the European Union are used in this study.

1. Background

There is persuading evidence (cf. [1]) that significant global warming has been observed over more than a century and a particularly strong warming—over the last three decades. Central Europe, including Poland, is not an exception. Moreover, climate projections for Poland foresee further warming in all seasons, as well as changes in the distribution and quantity of precipitation.

Observations and climate model simulations indicate an acceleration of the water cycle, with possible consequences to extremes [2, 3]. A warmer climate is likely to increase risks of both floods and droughts in many areas [1, 4].

In the present climate, many regions of Poland (and predominantly the Wielkopolska region) suffer frequent shortages of water, especially in the growing season. Water problems in the Wielkopolska region are particularly critical due to the agricultural character of this region. On the other hand, increase in intense precipitation in a warming Europe (also in Poland) is observed and projected [5] and

may increase flood hazard. In the last two decades Poland experienced many extreme events connected with heavy precipitations, for example, floods in 1997 and 2010.

Climate changes noticeable today are projected to intensify in the future. Therefore, water shortages/surpluses may be even more common and more severe in the future. Changes in the thermal characteristics as well as in precipitation are projected to influence changes in the climatic water balance in the country. What will they be like? In what way will they influence the water conditions in Poland? Will they be spatially differentiated or perhaps have similar character in the entire country? Unfortunately, climate projections for the future foresee detrimental changes in water availability caused mainly by higher temperature accompanied by simultaneous changes in the distribution and quantity of precipitations. For the northern part of Europe, the average precipitation is projected to increase while for the southern part considerable decreases are projected in brief—dry areas are likely to be much drier and wetter—to become wetter. Effects of future climate change on precipitation and water

resources in Poland are particularly uncertain due to location of Poland in the zone between northern Europe getting wetter and the south of Europe getting drier.

In the present paper, changes in the water balance in Poland are evaluated, based on multimodel ensemble climate projections, obtained within the ENSEMBLES Project of the 6th Framework Programme of the European Union.

2. Data

In this study, based on results from different climate models, time series of ten-day values of the climatic water balance components, that is, precipitation, evaporation, and runoff, are examined for the average conditions in two time horizons, that is, 1961–1990 (control period) and 2061–2090, for selected stations over Poland.

For climate simulation, the model is expected to approximately reproduce the observed distribution of mean temperature and of mean daily and seasonal cycles of temperature since these are forced deterministic components. The remaining variability is an internally generated nonlinear natural random component. Its modelled and observed values are not expected to be correlated either. Thus, as characteristic for intercomparison results, different climate variables are simulated with various levels of success by different models and no single model is the “best” for all variables or for all areas. Different studies on climate change suggest that, due to insufficient consistency between climate models, the broadest possible range of changes should be presented, which represent uncertainty. Therefore, the multimodel projections from the ENSEMBLES EU Project are used in this study.

The main calculations are based on the simulation results of daily temperature, precipitation, relative humidity, and wind speed from five ENSEMBLES regional climate models for 16 grid-cells around Poland. In selected grid-cells, 16 Polish towns and cities are situated entirely or partly, that is, Białystok, Chojnice, Gorzów Wielkopolski, Hel, Katowice, Kielce, Łódź, Olsztyn, Poznań, Rzeszów, Suwałki, Swinoujście, Warszawa, Włodawa, Wrocław, and Zielona Góra (Figure 1). In this research chosen grid-cells are called conventionally after the name of the city which is located there.

The regional models from the ENSEMBLES Project used in this study are C4IRCA3 from Rossby Centre (Norrköping, Sweden); CLM from ETH (Zurich, Switzerland); KNMI-RACMO2 from the Royal National Meteorological Institute (de Bilt, the Netherlands); METO-HC from the Met Office’s Hadley Centre (Exeter, UK); and MPI-M-REMO from the Max Planck Institute (Hamburg, Germany). Chosen regional climatic models were generated based on two different global circulation models (GCMs). Regional models C4IRCA3, ETHZ-CLM, and METO-HC are based on the global model METO-HC Standard, while models MPI-M-REMO and KNMI-RACMO2 are calibrated based on the global circulation model ECHAM of fifth generation.

All of the used ENSEMBLES regional climate models cover Europe with a spatial resolution of about 25 by 25 km and draw just one possible future, corresponding to a specific SRES emission scenario, A1B [6].

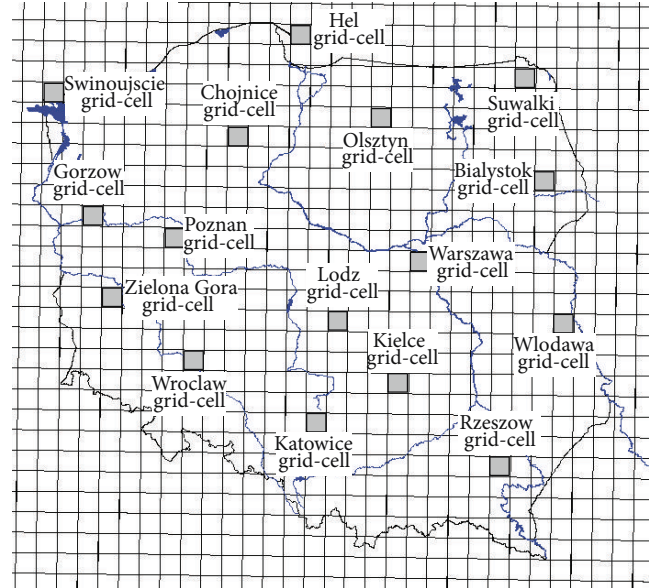


FIGURE 1: The studied grid-cells (grid-cell containing the towns/cities over Poland).

In order to verify model simulations and to assess the usefulness of the ENSEMBLES RCM models for this research, the control period data (1961–1990) from the models were compared to observation data for selected stations in Poland for the same period.

3. Verification of the Models

The models were validated for the territory of Poland based on monthly observational data of temperature and precipitation for the reference period of 1961–1990 and values simulated by five ENSEMBLES models for the same period. The validation was significantly simplified as observational data represented individual points in space derived from the observation station and the model data were averaged for the surface (usually a square 25 km × 25 km). So in fact, values of the meteorological variables for the points were compared with the values of the same variables for the grid-cell where these points (stations in towns) are located. Validation was carried out for 16 stations in case of the temperature and for 19 stations in case of precipitation and for 16 and 19 grid-cells, respectively. Unfortunately, it was not possible to carry out detailed areal validation due to lack of data.

There are many ways to measure the skill of model simulations. In a study by Szwed et al. [7] the models were validated based on such characteristics as sum of absolute differences between real and predicted values, standard deviations, and variances and correlation between real and predicted values of the monthly data. These second-order measures were analysed in the annual and seasonal context, for the warm and cold thermal seasons.

For every point in space (observational station) the models were ranked from 1 (best) to 5 (worst) according to following rules: (i) correlation level (the higher positive the better); (ii) sum of squared differences (the lower the better);

TABLE 1: Comparison of modelled and observed temperature for the city of Poznan referring to second-order statistics: sums of squared differences, ratios of variances, and correlation coefficients (corresponding rank in brackets) and the final ranks for the models based on the temperature.

Model	Sum of squared differences (model – real) in °C	Ratio of variance of the model to observational variance	Correlation	Final rank
C4IRCA	18.61 (4)	1.047 (1)	0.9967 (3)	3
ETHZ	21.46 (5)	1.282 (5)	0.9947 (5)	5
KNMI	10.23 (2)	0.823 (3)	0.9974 (1)	2
METO-HC	16.35 (3)	1.218 (4)	0.9955 (4)	4
MPI-M-REMO	6.48 (1)	0.867 (2)	0.9973 (2)	1

TABLE 2: Verification of models for temperature. The final ranks of models for all the stations and the mean ranks for Poland.

Model	Bielsko Biala	Chojnice	Hel	Jelenia Gora	Kalisz	Katowice	Legnica	Lodz	Poznan	Suwalki	Swinoujscie	Szczecin	Torun	Warszawa	Wlodawa	Wroclaw	Zakopane	Average		
C4IRCA	3	3	1	3	3	3	3	3	3	3	1	1	3	3	3	3	3	3	3	
ETHZ	5	5	3	5	5	5	5	5	5	5	5	5	5	5	5	5	5	5	5	5
KNMI	2	2	4	1	2	2	2	2	2	1	3	2	2	2	2	2	2	2	2	2
METO-HC	4	4	2	4	4	4	4	4	4	4	2	4	4	4	4	4	4	4	4	4
MPI-M-REMO	1	1	5	2	1	1	1	1	1	2	4	3	1	1	1	1	1	1	1	1

(iii) variances for the model (the better fit to observational variances the better). The ultimate rank for each model was established by multiplication of all previously calculated ranks. This procedure was applied separately to the values of temperature and precipitation. Finally, for every model its “average value for Poland” was calculated as an average range from all the station data.

3.1. Validation for Temperature. The models are reasonably successful in reproducing/simulating the observed distribution of mean temperature and of seasonal cycles of temperature. Table 1 presents the comparison of two data sets (modelled and observed) referring to second-order statistics, such as square differences, variances, and the associated correlation for the city of Poznan.

The average value of correlation for Poland between the observed and the modelled temperature (mean value for all the station data) is 0.99 or more for every model. There is no one “best” model for the whole area of Poland. The degree of consistency between modelled and observed values varies between models and is location-specific. Yet, in all the studied models, mapping of the average temperature is by far the worst for the coastal areas, while being the best for some central parts, depending on the model.

It seems, based on range values, that the MPI-M-REMO and KNMI models simulate the temperature in the reference period 1961–1990 a little better than the other models (Table 2). Applications using modelled temperature data for Poland should be based on an ensemble of models, so that the range of uncertainty, resulting from model disagreement, is adequately illustrated.

3.2. Validation for Precipitation. As for precipitation, in most cases the agreement between climate models and real data for the control period is not satisfactory. There are very high monthly and seasonal differences of modelled precipitation values from the climatological mean. In some cases unrealistic distributions of annual precipitation seem to negate the usefulness of certain models. Table 3 presents the comparison of two data sets referring to second-order statistics, such as square differences, variances, and the associated correlation for the city of Poznan, for precipitation.

“Average correlations for Poland” (mean value for all the station data) between observed and predicted values for every model are rather low and vary from 0.014 to 0.864. There are even negative correlations for some stations for 3 of models (C4IRCA, for 9 stations, ETHZ, for 5 stations, and METO-HC, for 2 stations). The degree of consistency between modelled and observed values varies between models and is location-specific. It seems, based on range values, that, for Poland, the MPI-M-REMO model (from the ENSEMBLES set) simulates the precipitation in the reference period 1961–1990 better than other models (Table 4).

To recapitulate, Figure 2 (according to the concept of diagram from [8]) gives the standard deviation and correlation with observations of the total spatial and temporal variability of temperature and precipitation in the validated models (mean value for 16 stations for temperature and 19 stations for precipitation, resp.). The standard deviation is normalized to its observed value and the correlation ranges from zero along an upward vertical line (y -axis) to unity and along a line pointing to the right (x -axis). Consequently, the observed behaviour of the climate is represented by a point on the horizontal axis which is a unit distance from the origin.

TABLE 3: Comparison of modelled and observed precipitation for the city of Poznan referring to second-order statistics: sums of squared differences, ratios of variances, and correlation coefficients (corresponding rank in brackets) and the final ranks for the models based on the precipitation.

Model	Sum of squared differences (model – real) in mm	Ratio of variance of the model to observational variance	Correlation	Final rank
C4IRCA	5583.10 (5)	0.284 (4)	0.123 (5)	5
ETHZ	4971.38 (3)	0.255 (5)	0.362 (4)	4
KNMI	4172.73 (2)	0.503 (3)	0.709 (2)	2
METO-HC	5543.56 (4)	1.096 (2)	0.563 (3)	3
MPI-M-REMO	3619.26 (1)	1.028 (1)	0.846 (1)	1

TABLE 4: Verification of models for precipitation. The final ranks of models for all the stations and the mean ranks for Poland.

Model	Bielsko Biala	Chojnice	Hel	Jelenia Gora	Kalisz	Katowice	Legnica	Lesko	Lodz	Poznan	Rzeszow	Slubice	Suwalki	Swinoujscie	Szczecin	Torun	Warszawa	Wlodawa	Wroclaw	Zakopane	Average
C4IRCA	5	5	3	5	5	5	5	5	5	5	5	5	5	1	5	4	5	5	4	4	5
ETHZ	4	3	4	2	4	4	4	4	4	4	4	4	4	5	3	5	4	4	4	2	4
KNMI	3	3	2	4	2	3	3	3	3	2	3	2	3	2	2	3	2	3	3	1	3
METO-HC	2	2	5	3	2	2	1	2	2	3	2	3	2	3	1	2	1	2	2	3	2
MPI-M-REMO	1	1	1	1	1	1	2	1	1	1	1	1	1	4	4	1	2	1	1	5	1

In this coordinate system, the linear distance between each model's point and the "observed" point is proportional to the r.m.s. model error [8]. Based on this figure, it can be concluded that the temperature is particularly well simulated, with nearly all models closely matching the observed magnitude of variance and exhibiting a correlation more than 0.99 with the observations. Precipitation is simulated rather poorly, but for the MPI-M-REMO model the simulated variance is still within 20% of observed one and the correlation with observations is noticeably positive (0.78).

Thus, the outcome of the verification of models for the territory of Poland indicates that MPI-M-REMO model provides the best fit for both temperature and precipitation conditions. That is why the results of this model are presented in this paper in more detail. Nevertheless, as it was mentioned before, due to insufficient consistency between climate models, the full possible ranges of changes are presented.

4. Methods

The climatic water balance equation is the starting-point for all the calculations in this study. It is usually written as $P = H + E + \Delta R$, where P is the precipitation, H is the climatic runoff, E is the evaporation, and ΔR is the change of retention (storage). If the assumption of no changes in retention is made (for appropriately long time horizon), the equation of water balance becomes $P = H + E$. So the climatic runoff is calculated as the difference between precipitation and evaporation. Water balance components are expressed in millimetres of water layer.

From the variables of water balance which should be examined in this research only precipitation, input of water, is "directly" available from models. However "output of water," that is, climatic runoff and evaporation, is an essence of the problem. It is very important to know whether precipitation "is enough" and what part of water remains "at disposal." Output elements of the water balance have to be estimated for further analyses.

In this research, the values of evaporation for the different land-use units for the growing season (March–October) are estimated based on the heat balance method developed in the Department of Agrometeorology of the Poznan University of Life Sciences [9]. This method was developed for the purpose of estimating heat balance components based on standard meteorological data, plant development stage, and land-use conditions. Estimates of latent heat flux components allowed obtaining values of areal evaporation and surface runoff.

The energy balance equation is $R_n + LE + A + G = 0$, where R_n is the net radiation, LE is the latent heat flux, A is the sensible heat flux, and G is the soil heat flux. In the remaining part of the year (November–February), the values of evaporation were calculated based on the Ivanov equation; that is, $LE = 0.0018 \cdot (T + 25)^2 \cdot (100 - Rh)$, where T is the air temperature and Rh is the relative humidity [10]. The latent heat flux is used for calculating the actual evaporation because a simple relationship exists between evaporation expressed in mm (E) and latent heat expressed in $\text{MJ} \cdot \text{m}^{-2}$ (LE); that is, $E = LE/2.83$.

The method allows estimating heat balance components based on standard meteorological data, plant development stage, and land-use conditions. The heat balance components are expressed in mega joules per square meter and given

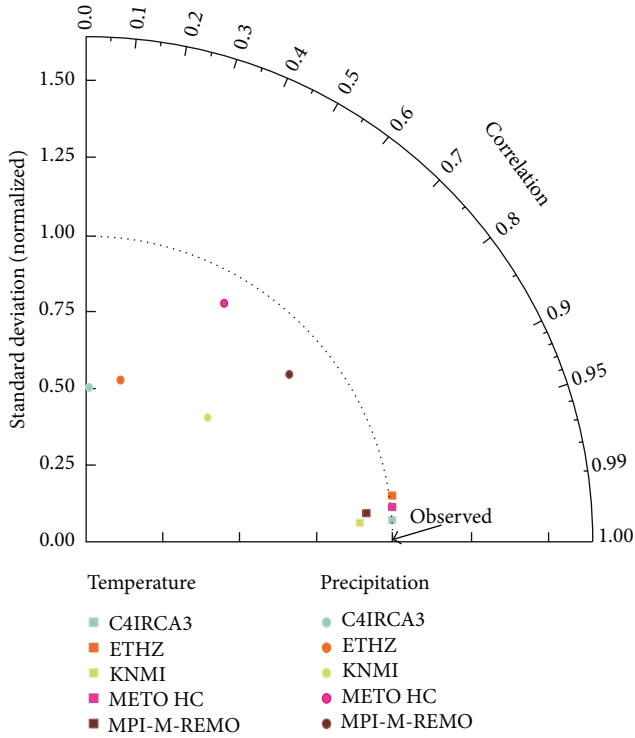


FIGURE 2: Taylor diagram—the standard deviation and correlation of the validated models with observations for temperature and precipitation (mean value for all the stations around Poland).

period [MJ·m⁻²·period⁻¹] or in Watts per square meter [W·m⁻¹]. All fluxes towards the active surface are taken as positive while the outgoing fluxes are assumed negative.

In the applied method, time series of ten-day values of precipitation, air temperature, relative humidity, and wind speed stemming from regional climate models are used. Ten-day values of sunshine duration are calculated based on the sunshine duration model for Poland according to Górski and Górska [11], whereas values of plant development stages are assumed according to Leśny [12].

The heat and water balance structure depends not only on meteorological conditions but also on many environmental factors as well as plant characteristics. In this study, for all analysed grid-cells the land-use structure is assessed based on the Corine Land Cover 2000 as well as on additional data from the Statistical Yearbooks for Poland (e.g., Figures 3 and 4). In this paper eight types of physiographical units are taken into account, namely, coniferous and deciduous forests, arable lands (including cereal and root crops), meadows, wastelands, water bodies, and urban areas. The heat balance components are calculated for all these land-use units.

All estimations are made for two time horizons, that is, the control period 1961–1990 and the future interval of 2061–2090. In spite of the fact that the author has real meteorological observation data (even if pertaining to points rather than providing satisfactory areal coverage) in this study the model-based values of meteorological variables are used also for the present (control period). Hence for estimation of changes of the water balance components in

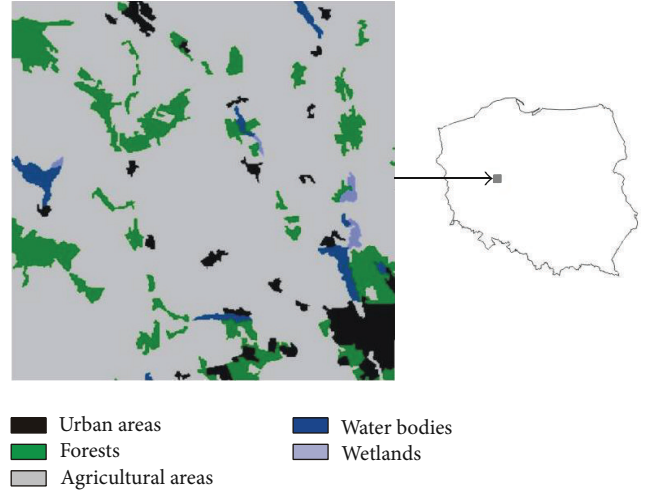


FIGURE 3: Land-use units near the city of Poznan based on the Corine Land Cover 2000.

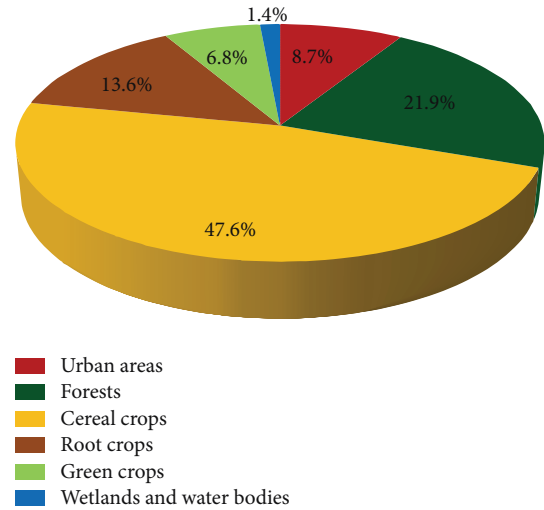


FIGURE 4: Land-use units in the Poznan province based on the Statistical Yearbooks for Poland.

the future it seems more sensible to compare model-based simulations for two time horizons of interest than to compare of observations (or reanalyses) from 1961 to 1990 and model-based projections for 2061–2090.

5. Results

Results are presented for two 30-year periods of 1961–1990 and 2061–2090, that is, the control and the projection period, respectively. The 1961–1990 values are based on model simulations and not on observations. In this study the land-use changes in the future are not taken into consideration.

5.1. Changes in Precipitation. The present value of annual precipitation based on models is slightly overestimated (by about 25–35%), but the distribution and values of the monthly precipitation differ significantly between modelled

TABLE 5: The changes of the annual precipitation [in mm] in the future (2061–2090) compared to the control period 1961–1990, based on the MPI-M-REMO model.

Grid-cell	Jan	Feb	Mar	Apr	May	Jun	Jul	Aug	Sep	Oct	Nov	Dec	Year
Bialystok	8	3	10	12	14	−10	−3	2	12	−6	9	10	60
Chojnice	11	4	2	3	4	−8	6	−1	10	5	6	9	51
Gorzow	8	−3	−3	6	−2	−2	−5	−12	0	6	7	7	8
Hel	12	13	9	12	7	−2	3	4	6	2	15	24	104
Katowice	8	3	5	16	1	−18	−14	−5	15	0	7	5	22
Kielce	9	3	2	10	4	−20	−21	−4	12	−2	12	10	15
Lodz	7	6	0	6	5	−13	−2	−4	16	−6	9	9	32
Olsztyn	14	5	6	5	9	2	10	13	6	−12	7	7	74
Poznan	6	0	0	5	−8	−1	6	−13	4	1	11	8	18
Rzeszow	10	2	1	12	−3	−31	−22	−14	8	−6	8	7	−29
Suwalki	10	6	10	12	9	−7	9	11	6	−8	9	7	74
Swinoujscie	5	9	4	6	4	5	12	−11	14	7	9	21	85
Warszawa	7	3	7	8	6	−13	10	−5	11	−14	15	8	44
Wlodawa	5	0	2	16	5	−20	7	−9	7	−3	6	9	24
Wroclaw	8	1	4	12	10	−7	−5	−12	2	4	7	9	32
Zielona G.	6	−1	−3	7	1	1	3	−8	4	3	9	6	28

and observed data. The winter precipitation is too high, while the summer precipitation is too low. All the models overestimate the values of winter precipitation with surpluses varying from 40 to 140%. On the contrary, precipitation for June and July is often underestimated, even by 30%, while in fact July is the most rainy month. The MPI-M-REMO model overestimates precipitation during all the year.

Mostly the projections for the future foresee increases of annual sum of precipitation. According to MPI-M-REMO model (which correlates best with the current climatic conditions), the annual precipitation is projected to rise in all, but one, considered grid-cells in Poland, while the increases range from 8 mm (in Gorzow grid-cell) to 104 mm (in Hel grid-cell). In general, the smallest increases are projected in the west (Wielkopolska region) while being the highest in the northern part of the country (Baltic Sea coast and Pomerania and Masuria Lake District). The only exception is the southeast of Poland (grid-cell Rzeszow), where a decrease of precipitation (28 mm in an average year) is projected (see Table 5). The general pattern of precipitation changes after five climate models is similar to the one described by MPI-M-REMO model. As for seasonal distribution, mostly increases are projected in the winter season and decreases in the summer. Summer increases of precipitation are projected for Baltic coast and the Masurian Lake District. The highest decreases of precipitation in summer are projected for the south of Poland (Figure 5).

On average, simulation of precipitation changes by five climate models is similar to the general pattern of changes described by MPI-M-REMO model. Increases of annual sums of precipitation around Poland are projected, with the higher increases in winter season and decreases in summer (except for areas in the northern part of Poland). The details of changes of the monthly and annual precipitation are included in Table 6 (annual values) and in Figure 6 (seasonal values).

5.2. Changes in Evaporation. The evaporation was calculated for eight land-use units, namely, coniferous and deciduous forests, arable lands (including cereal and root crops), meadows, wastelands, water bodies, and urban areas. MPI-M-REMO model estimates that in average year the evaporation from water bodies (i.e., maximum potential evaporation) in Poland varies from 716 mm (in Suwalki grid-cell) to 837 mm (in Wlodawa grid-cell). The highest monthly values—about or above 140 mm—are recorded in June and July.

Due to a large percentage of the cultivated area (60.3% of the total area of Poland) and forested areas (30.7%) [13] it seems interesting to describe the evaporation from agricultural lands (e.g., of cereal and root crops) as well as from forested areas in more detail. The evaporation from agricultural lands (based on MPI-M-REMO model) in Poland differs annually from 508 mm (in Suwalki grid-cell) to 598 mm (in Wlodawa grid-cell). The highest monthly values, above 100 mm, are recorded also in June and July. For the root crops these values are, respectively, from 498 mm (in grid-cell Suwalki) to 593 mm (in Wlodawa and Hel grid-cells), while being above 105 mm in July. Coniferous forests occupy over 60 percent of the area of Polish forests. The MPI-M-REMO model estimates the average annual evaporation from a coniferous forest in Poland from 652 mm (in Suwalki grid-cell) to 768 mm (in Wlodawa grid-cell). The forest evaporates a lot of water during the growing season, with the highest amounts—more than 100 mm—each month from May to August (Table 7).

Projections for the future foresee mostly increases of the evaporation, among other due to increases of air temperature. The evaporation from water bodies (according to MPI-M-REMO model) is projected to rise throughout Poland. The smallest changes (about 40 mm) are projected for the Masurian Lake District, while being the highest for the southern part of Poland (with maximum value in Rzeszow grid-cell—71 mm). The increases on the arable ground will

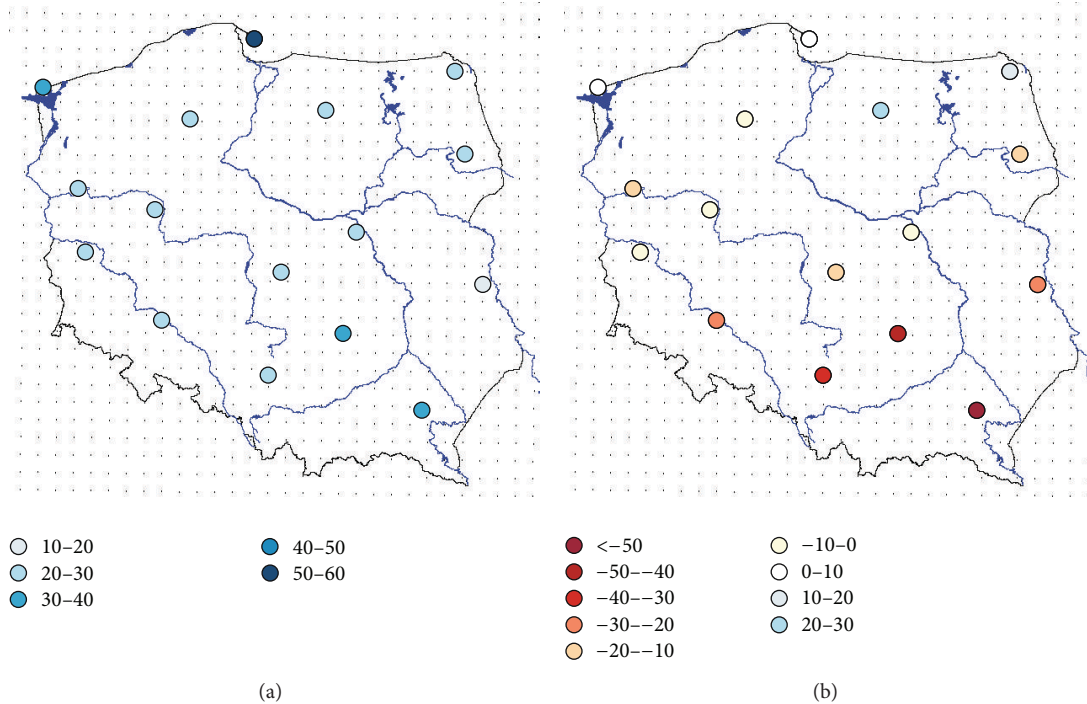


FIGURE 5: The changes of winter (a) and summer (b) precipitation [in mm] in the future (2061–2090) compared to the control period 1961–1990, based on the MPI-M-REMO model.

TABLE 6: The changes of the monthly and annual precipitation [in mm] in the future (2061–2090) compared to the control period 1961–1990—average value from five models.

Grid-cell	Jan	Feb	Mar	Apr	May	Jun	Jul	Aug	Sep	Oct	Nov	Dec	Year
Bialystok	17	13	10	10	15	-8	6	-6	3	-4	9	16	81
Chojnice	17	13	7	2	6	1	9	-7	2	2	7	13	74
Gorzow	16	9	7	6	10	1	0	-11	-1	3	10	14	61
Hel	18	17	9	7	7	6	7	-2	3	3	10	19	104
Katowice	18	11	8	7	16	-8	-8	-6	1	-3	9	11	57
Kielce	15	11	8	4	13	-14	-6	-5	4	-3	12	14	53
Lodz	16	11	6	7	16	-5	1	-6	3	-4	10	15	69
Olsztyn	19	13	11	6	8	3	8	-1	-2	-2	9	15	89
Poznan	16	10	4	3	6	-2	4	-9	0	-2	9	14	52
Rzeszow	15	14	6	8	11	-20	-11	-12	3	-3	10	12	34
Suwalki	19	15	13	8	9	-3	4	-4	1	-1	8	15	83
Swinoujscie	15	14	10	4	8	6	7	-3	5	3	11	19	98
Warszawa	15	11	7	8	14	-5	4	-2	2	-5	12	15	76
Wlodawa	14	12	7	6	13	-17	1	-11	5	-3	10	16	53
Wroclaw	14	11	5	5	17	-2	-6	-7	-2	0	8	15	57
Zielona G.	15	10	2	5	13	0	3	-3	-1	3	10	12	69

probably vary from about 30 mm in the Baltic Sea coast and the Masurian Lake District to more than 60 mm in the south of Poland. The increases of evaporation from forested areas will be even higher. They are projected at about 40 mm in Masurian Lake District to even 70 mm in the south of the country (see Figure 7(a) and Table 8). The MPI-M-REMO model projects the largest changes of evaporation at the end of the growing season (particularly in August).

Other models, similarly to the MPI-M-REMO model, project the same direction of changes of the evaporation values—that is, increases of evaporation from different land-use units (see Figure 7(b), Table 9). Differences, sometimes significant ones, concern these surpluses/values, as well as distribution within one year. Thus, relatively a great unanimity of 3 models (C4IRCA3, ETHZ, and KNMI) is prevailing as for the annual values. For these 3 models the increases

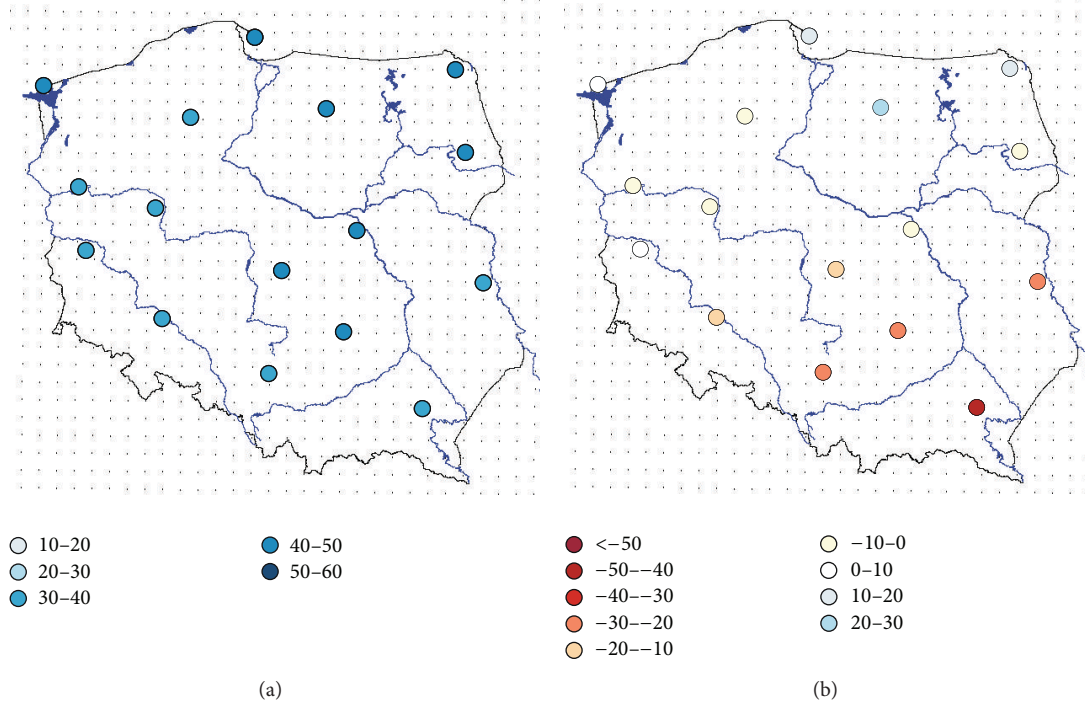


FIGURE 6: The changes of winter (a) and summer (b) precipitation [in mm] in the future (2061–2090) compared to the control period 1961–1990, based on five models.

TABLE 7: The annual values of evaporation [in mm] for different land-use units for the control period 1961–1990 compared to the control period 1961–1990, based on the MPI-M-REMO model.

Grid-cell	Deciduous forest	Coniferous forest	Urban areas	Water bodies	Wastelands	Meadows	Cereal crops	Root crops
Bialystok	596	654	307	718	381	466	510	500
Chojnice	617	678	321	744	393	485	528	517
Gorzow	644	706	340	772	411	508	552	541
Hel	678	736	400	803	477	552	588	593
Katowice	640	699	348	763	419	510	552	543
Kielce	649	711	344	778	418	513	557	547
Lodz	644	706	337	773	410	506	551	541
Olsztyn	609	667	321	731	394	480	522	513
Poznan	644	707	335	774	407	506	551	540
Rzeszow	663	725	355	790	426	524	568	561
Suwalki	594	652	307	716	382	465	508	498
Swinoujscie	663	721	372	788	448	529	567	575
Warszawa	641	702	334	768	406	502	548	538
Wlodawa	703	768	370	837	440	551	598	593
Wroclaw	654	715	355	779	425	520	563	555
Zielona G.	657	719	353	784	422	521	564	555

of evaporation from the free surface water in Poland in the future amount to about 30–40 mm. For the METO-HC model, much differing from the other models, changes are twice higher, of 60–80 mm. There is an agreement between these 4 models as regards when, in which months of the year, those changes will take place. C4IRCA3, ETHZ, KNMI,

and METO-HC models similarly project the highest changes in summer months (June–July–August), but in case of the METO-HC model summer increases of evaporation are the third part of all annual increases while in C4IRCA3 and ETHZ models over half of the annual changes are projected in summer. The changes of the evaporation values from water

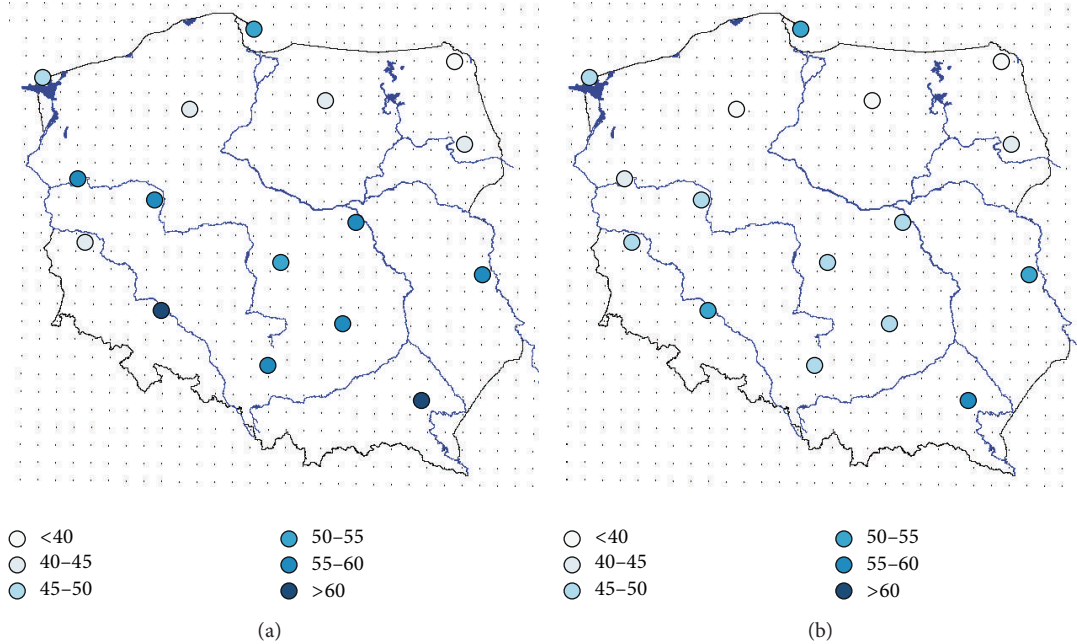


FIGURE 7: The increases of the annual evaporation from the water bodies [in mm] in the future (2061–2090) compared to the control period 1961–1990, based on MPI-M-REMO model (a) and average value from five models (b).

TABLE 8: The increases of the annual evaporation [in mm] for different land-use units in the future (2061–2090) compared to the control period 1961–1990, based on the MPI-M-REMO model.

Grid-cell	Deciduous forest	Coniferous forest	Urban areas	Water bodies	Wastelands	Meadows	Cereal crops	Root crops
Bialystok	37	40	19	42	13	29	29	31
Chojnice	40	42	21	44	17	31	31	34
Gorzow	52	54	33	55	29	42	43	46
Hel	47	50	24	52	17	37	39	38
Katowice	55	57	36	58	31	45	45	50
Kielce	55	57	35	59	30	44	45	50
Lodz	50	52	30	53	25	40	40	44
Olsztyn	39	41	20	43	15	30	31	32
Poznan	52	54	32	55	28	42	43	46
Rzeszow	68	70	46	71	41	56	57	62
Suwalki	32	35	13	37	8	24	24	25
Swinoujscie	42	45	22	46	16	32	34	34
Warszawa	52	55	32	56	28	42	43	46
Wlodawa	55	57	34	59	29	44	45	48
Wroclaw	63	64	43	66	39	52	53	57
Zielona G.	40	42	21	43	17	30	31	35

bodies projected by five models for the future of 2061–2090 are presented in Table 10 for the example of the grid-cell of Poznan.

5.3. *Changes in Runoff.* For every grid-cell analysed in this paper (usually a square of 25 km × 25 km) a total evaporation from the grid-cell area (taking into consideration the share of individual land-use units) is estimated. The values of the total evaporation from the area as well as the values of precipitation (directly available from the model) were the basis for

the runoff estimations. The values of a runoff coefficient from every grid-cell are used for detailed analyses.

The estimated values of the runoff coefficient based on modelled data are somewhat higher than the real ones. In principle, they are similar to the values typical for the observations from a wet year. This is probably caused first of all by the overestimation of precipitation and inaccuracies in the distribution of monthly sums of precipitation. Secondly, one should expect overestimated values of the runoff coefficient due to quite substantial percentage of urbanized areas in

TABLE 9: The increases of the annual evaporation [in mm] from different land-use units in the future (2061–2090) compared to the control period 1961–1990, based on five models (average values).

Grid-cell	Deciduous forest	Coniferous forest	Urban areas	Water bodies	Wastelands	Meadows	Cereal crops	Root crops
Bialystok	36	39	11	41	5	24	25	29
Chojnice	33	36	10	38	5	22	23	25
Gorzow	41	43	16	45	11	28	29	34
Hel	47	51	18	52	10	33	36	36
Katowice	44	47	18	48	12	30	32	37
Kielce	44	47	17	48	11	29	31	37
Lodz	43	46	17	47	11	29	31	36
Olsztyn	34	37	10	38	4	22	23	26
Poznan	44	46	18	48	12	30	32	36
Rzeszow	54	57	25	58	18	38	40	46
Suwalki	32	35	8	37	1	21	21	24
Swinoujscie	43	47	16	48	9	29	32	34
Warszawa	45	47	18	49	12	31	32	37
Wlodawa	48	51	20	53	13	33	34	40
Wroclaw	49	52	24	53	19	35	37	43
Zielona G.	42	45	18	46	12	29	30	35

TABLE 10: The increases of the monthly evaporation from water bodies [in mm] in the future (2061–2090) compared to the control period 1961–1990, based on five models—example of the grid-cell of Poznan.

	Models				
	C4IRCA	ETHZ	KNMI	METO-HC	MPI-M-REMO
Jan	3.7	1.1	4.1	5.6	7.3
Feb	0.1	0.8	3.9	6.8	8.4
Mar	-0.8	1.4	2.7	9.3	7.5
Apr	1.0	-0.2	1.0	0.3	0.6
May	2.7	2.1	2.6	3.8	2.0
Jun	4.8	4.4	4.7	6.8	3.7
Jul	7.4	6.1	4.9	9.2	4.0
Aug	7.4	8.7	4.5	12.1	4.6
Sep	5.0	3.6	3.1	5.0	3.4
Oct	2.7	2.4	2.3	2.7	2.4
Nov	0.3	2.6	2.2	9.1	6.8
Dec	3.6	0.4	0.5	5.5	4.5
Year	37.7	33.5	36.6	76.2	55.3

selected grid-cells (with the maximum value for Warszawa grid-cell about 0.52% of the area). The runoff coefficients based on the five RCMs for the control period and for the future are presented in Table II. The spatial variability of the runoff coefficient for Poland in the control period 1961–1990 is presented in Figure 8. Figure 8 presents two variants of the runoff coefficient values: first one based on MPI-M-REMO model and the second one as an average value from five models.

According to RCMs, in an average year at present no area in Poland experiences a dramatic problem with water scarcity or surpluses, though some water scarcity appears during summer. Furthermore, regional climate models foresee slight

changes of the annual runoff coefficient in a normal year (if the land-use changes in the future are not taken into consideration). In Figure 9 estimated values of the runoff coefficient in the future 2061–2090 are presented. Figure 9, presented similarly to the convention applied to Figure 8, illustrates two variants of the foreseen changes: (a) based on MPI-M-REMO model and (b) as an average value from five models.

Two models—METO-HC and MPI-M-REMO—point at slight decreasing, while three—C4IRCA3, ETHZ, and KNMI—point at slight increasing of the runoff coefficient around Poland. In different models, the most severe scarcity of water could appear during several seasons, for example, summer and autumn, ETHZ, autumn and winter, C4IRCA3, or summer and winter, KNMI, and so forth.

These differences result from different preconditions and different projections of changes in some meteorological variables, most notably precipitation. In any case, while all the models are compatible with respect to the mean temperature increase, not all of them are compatible as to the changes in precipitation. All the studied ENSEMBLES RCMs indicate an increase in winter precipitation (with different magnitudes), but models disagree on projections for the summer precipitation. Thus, for example, ETHZ model foresees small decreases in precipitation from June to October (on the level of 10–20%), while C4IRCA3 projects large increases in precipitation from May to July and in May alone even 50% higher.

6. Conclusions

In the present climate, many regions of Poland (and predominantly the Wielkopolska region) suffer frequent shortages of water, especially in the growing season. On the other hand, increase in intense precipitation is observed. In the last decades Poland experienced many extreme events connected with heavy precipitations, for example, floods in 1997 and

TABLE 11: The annual runoff coefficient for the control period 1961–1990 and for the future 2061–2090 based on five models.

Control period (1961–1990)					Future (2061–2090)					
C4IRCA	ETHZ	KNMI	METO	MPI		C4IRCA	ETKZ	KNMI	METO	MPI
0.24	0.25	0.24	0.24	0.32	Bialystok	0.33	0.31	0.33	0.24	0.33
0.25	0.19	0.30	0.27	0.18	Chojnice	0.35	0.23	0.33	0.26	0.20
0.15	0.14	0.23	0.19	0.23	Gorzow	0.28	0.18	0.24	0.16	0.18
-0.13	-0.05	0.00	-0.12	-0.01	Hel	0.01	0.05	0.05	-0.09	0.06
0.26	0.30	0.34	0.42	0.26	Katowice	0.33	0.31	0.37	0.38	0.22
0.25	0.25	0.30	0.33	0.16	Kielce	0.30	0.24	0.32	0.28	0.11
0.28	0.23	0.27	0.41	0.20	Lodz	0.34	0.30	0.29	0.38	0.18
0.27	0.19	0.33	0.21	0.27	Olsztyn	0.36	0.27	0.36	0.21	0.29
0.16	0.24	0.20	0.26	0.21	Poznan	0.26	0.23	0.23	0.22	0.17
0.11	0.27	0.23	0.49	0.30	Rzeszow	0.18	0.29	0.23	0.44	0.21
0.37	0.19	0.36	0.27	0.23	Suwalki	0.44	0.26	0.39	0.26	0.27
0.06	0.14	0.15	0.01	0.22	Swinoujscie	0.16	0.21	0.18	0.07	0.25
0.23	0.34	0.33	0.33	0.41	Warszawa	0.36	0.40	0.35	0.30	0.39
0.05	0.11	0.12	0.12	0.13	Wlodawa	0.14	0.15	0.11	0.07	0.09
0.11	0.34	0.21	0.40	0.19	Wroclaw	0.21	0.35	0.25	0.35	0.15
0.09	0.16	0.12	0.27	0.13	Zielona G.	0.20	0.18	0.20	0.22	0.11
0.17	0.21	0.23	0.26	0.21	Average	0.27	0.25	0.26	0.24	0.20

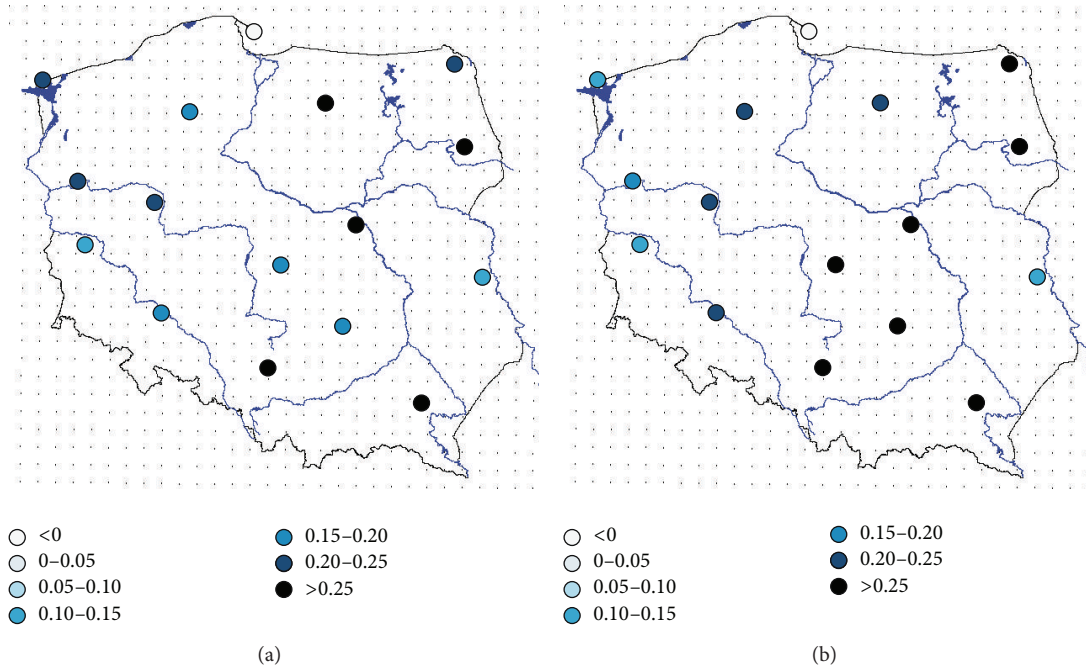


FIGURE 8: The annual runoff coefficient for the control period 1961–1990: (a) based on MPI-M-REMO model and (b) an average value from five models.

2010. Climate changes noticeable today are projected to intensify in the future. Therefore, water shortages/surpluses may be even more common and more severe in the future. There is still a great deal of uncertainty regarding likely climate change impacts on water resources. However, there is no doubt that changes in thermal characteristics as well as

in precipitation will influence changes in the water balance of the country.

Due to insufficient consistency between climate models a possible range of changes should be presented; hence the multimodel projections from ENSEMBLES Project of the European Union are used in this study. According to

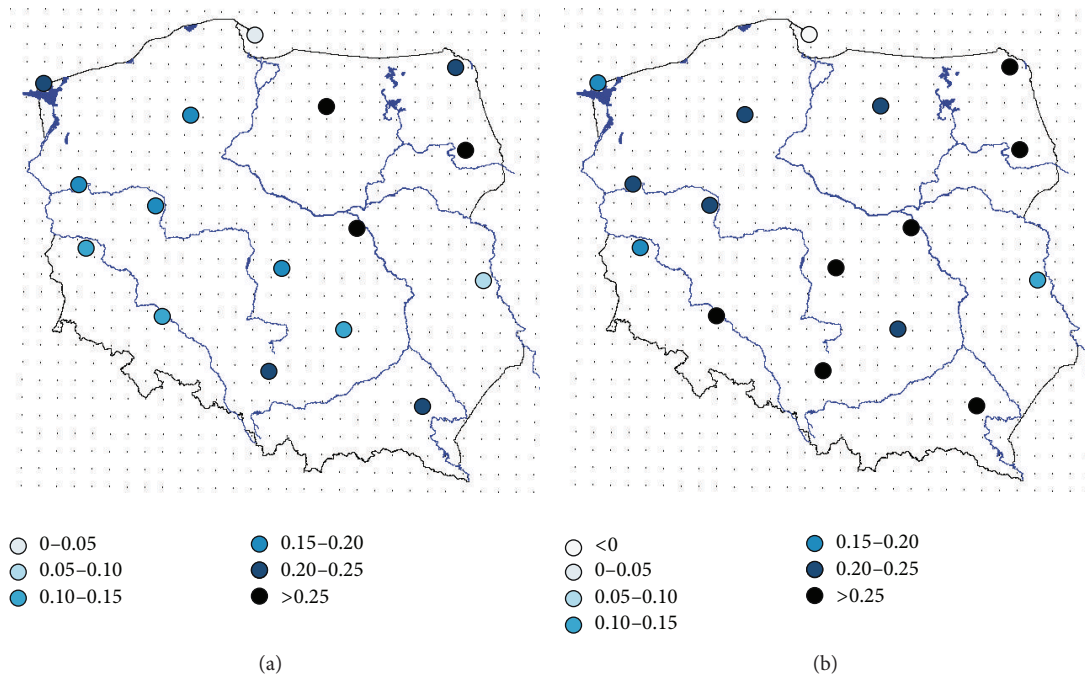


FIGURE 9: The annual runoff coefficient for the future 2061–2090: (a) based on MPI-M-REMO model and (b) an average value from five models.

applied RCMs, at present in an average year no area in Poland experiences a dramatic problem with water scarcity or surplus, though some water scarcity appears during summer.

Climate models project changes in the water availability in Poland in the future caused mainly by a rise of temperature, as well as changes of values and distribution of precipitation. The average value from five climate models points at increases of annual sums of precipitation around Poland, with the higher increases in winter season and decreases in summer. Simultaneously, increases of evaporation from different land-use units are projected. As a result, regional climate models foresee slight changes of the annual runoff coefficient in a normal year (if the land-use changes in the future are not taken into consideration). However, there is a strong uncertainty in future projections. Two models, METO-HC and MPI-M-REMO, point at slight worsening, while three, C4IRCA3, ETHZ, and KNMI, point at slight improvement of the water conditions in Poland.

To conclude, projections for the future indicate continuing water problems in Poland. Even though projected changes in water balance are not strong enough to force changes in the land-use structure, the values of the water balance components at present and in the future support the necessity to modify the landscape in such a way as to improve the water balance in many regions of Poland. In any case, essential system solutions capturing water outflow from the area of Poland in early spring and optimal water management in the agriculture could be put into practice. Probably, so-called small water retention will need to be increased and/or building of water reservoirs will be required. Better adaptation of the kind of cultivation plants/species to climatic conditions and to the accessible water quality could also be necessary.

Conflict of Interests

The author declares that there is no conflict of interests regarding the publication of this paper.

Acknowledgment

Support of the Research Project CHASE-PL (Climate Change Impact Assessment for Selected Sectors in Poland) of the Polish-Norwegian Research Programme is gratefully acknowledged.

References

- [1] IPCC, *Climate Change 2013: The Physical Science Basis. Contribution of Working Group I to the Fifth Assessment Report of the Intergovernmental Panel on Climate Change*, Cambridge University Press, Cambridge, UK, 2013, edited by: T. F. Stocker, D. Qin, G.-K. Plattner, M. Tignor, S. K. Allen, J. Boschung, A. Nauels, Y. Xia, V. Bex, P. M. Midgley.
- [2] T. G. Huntington, "Evidence for intensification of the global water cycle: review and synthesis," *Journal of Hydrology*, vol. 319, no. 1–4, pp. 83–95, 2006.
- [3] R. T. Wetherald and S. Manabe, "Simulation of hydrologic changes associated with global warming," *Journal of Geophysical Research*, vol. 107, no. D19, pp. ACL 7-1–ACL 7-15, 2002.
- [4] Z. W. Kundzewicz, L. J. Mata, N. W. Arnell et al., "The implications of projected climate change for freshwater resources and their management," *Hydrological Sciences Journal*, vol. 53, no. 1, pp. 3–10, 2008.
- [5] S. I. Seneviratne, N. Nicholls, D. Easterling et al., "Changes in climate extremes and their impacts on the natural physical environment," in *Managing the Risks of Extreme Events and*

- Disasters to Advance Climate Change Adaptation*, C. B. Field, V. Barros, T. F. Stocker et al., Eds., A Special Report of Working Groups I and II of the Intergovernmental Panel on Climate Change (IPCC), pp. 109–230, Cambridge University Press, Cambridge, UK, 2012.
- [6] IPCC SRES, N. Nakićenović, and R. Swart, Eds., *Special Report on Emissions Scenarios: A Special Report of Working Group III of the Intergovernmental Panel on Climate Change*, Cambridge University Press, 2000.
- [7] M. Szwed, G. Karg, I. Pińskwar et al., “Applying agricultural, hydrological, and human health indices to evaluate the changing risk of weather extremes in Poland, based on multi-model ensemble climate projections,” *Natural Hazards and Earth System Sciences*, vol. 10, pp. 1725–1737, 2010.
- [8] K. E. Taylor, “Summarizing multiple aspects of model performance in a single diagram,” PCMDI Report 65, Program for Climate Model Diagnosis and Intercomparison, Lawrence Livermore National Laboratory, University of California, Livermore, Calif, USA, 2000.
- [9] J. Olejnik and A. Kędziora, “A model for heat and water balance estimation and its application to land use and climate variation,” *Earth Surface Processes and Landforms*, vol. 16, no. 7, pp. 601–617, 1991.
- [10] A. Kędziora, *Podstawy Agroklimatologii*, PWRiL, Warsaw, Poland, 1999.
- [11] T. Górski and K. Górka, “An algorithm for evaluating the cycle of sunshine duration in Poland,” in *Book of Proceedings: EuroSun 98, The Second ISES Europe Solar Congress : [Portorož, Slovenia, September 14–17, 1998]*, vol. 1, pp. 1–6, 1998.
- [12] J. Leśny, *Bilans cieplny powierzchni czynnej wybranych upraw w Wielkopolsce*, vol. 429 of *Rozprawy Naukowe*, Wydawnictwo Uniwersytetu Przyrodniczego, 2011.
- [13] Statistical Yearbook of Agriculture, GUS, 2013, http://stat.gov.pl/cps/rde/xbcr/gus/rs_rocznik_rolnic-twa_2012.pdf.

Research Article

Hydrologic Variations and Stochastic Modeling of Runoff in Zoige Wetland in the Eastern Tibetan Plateau

Guanghua Qin,¹ Hongxia Li,¹ Zejiang Zhou,² Kechao Song,¹ and Li Zhang³

¹State Key Laboratory of Hydraulics and Mountain River Engineering, Sichuan University, Chengdu 610065, China

²Guangxi Water and Power Design Institute, Nanning 53000, China

³Everglades Wetland Research Park, Florida Gulf Coast University, Naples, FL 34112, USA

Correspondence should be addressed to Hongxia Li; hx_li406@126.com

Received 18 December 2014; Accepted 10 February 2015

Academic Editor: Yongqiang Zhang

Copyright © 2015 Guanghua Qin et al. This is an open access article distributed under the Creative Commons Attribution License, which permits unrestricted use, distribution, and reproduction in any medium, provided the original work is properly cited.

Hydrological time series data (1988–2008) of the Hei River, the main water source to Zoige wetland in the Eastern Tibetan Plateau, were investigated. Results showed that the runoff distribution of Hei River varies with the relative change in amplitude ($C_m = 15.9$) and the absolute change in amplitude ($\Delta Q = 37.1 \text{ m}^3/\text{s}$) during the year. There was a significant decreasing trend since 1988 with annual runoff of $20.0 \text{ m}^3/\text{s}$ (1988–1994), $19.0 \text{ m}^3/\text{s}$ (1995–2000), and $15.2 \text{ m}^3/\text{s}$ (2001–2008). There were double peaks in runoff during the water year: the highest peak in the period of 1988–2000 occurred in July while in the period of 2001–2008 it occurred in October. Shifting peak flow means less water quantity in wetland during growing season. Nearest neighbor bootstrapping regressive method was used to predict daily runoff of the Hei River. Model results show that it was fitted with 94.23% of R^2 for daily time series, which can provide a basis for the development and utilization of regional water resources.

1. Introduction

The Zoige wetland contains the largest high altitude wetland ecosystem in the world, which is over $5,000 \text{ km}^2$ and $\sim 3500 \text{ m}$ above sea level [1]. The Zoige wetland ecosystem provides at least 30% of the water flowing into the upper reaches of the Yellow River (e.g., [2, 3]). However, the area of the wetland has been recently lost by desertification which is increasing at a rate of more than 10% per year [4–6]. The recent degradation of Zoige Peatland was often attributed to both the ditching drainage and climate change [3]. With the global warming becoming stronger, it will therefore become increasingly necessary to understand hydrologic processes to prevent further degradation (e.g., [7, 8]).

Hydrologic processes such as hydroperiod, flow duration and variability, and flood recession significantly impact the dynamics of wetland ecosystems [9, 10]. Times series approach to model hydrologic process and dynamics in river and stream has been well documented (e.g., [11–14]), since Thomas and Fiering [15] and Yevjevich [16] revealed that the hydrological phenomenon shows objective dependency

on time domain and was described by the Markov model. Shinohara et al. [17] used a stochastic approach to explore the impact of climate change on runoff from a midlatitude mountainous catchment in central Japan. Verma et al. [13] explore the seasonal changes of soil moisture influenced by daily rainfall in New South Wales Australia using a stochastic model.

More recently, a couple of studies with stochastic model approaches have been published such as spatial and temporal distribution stochastic model in Raoli River basin in Sanjiang Plain and the hydrologic trend stochastic model in Wuyuer River in Zhalong wetland, Northeast China [18]. However, the stochastic models with hydrological time series used in alpine region are probably different from low elevation areas. So it is necessary to develop a stochastic model for runoff prediction in Zoige wetland in the Eastern Tibetan Plateau.

The objective of this study is to explore the Hei River runoff variations annually, monthly, and daily for a long term (1988–2008) and to understand hydrologic process during the wet and dry seasons and how the changes impact ecosystem of Zoige wetland in the Eastern Tibetan Plateau with climate

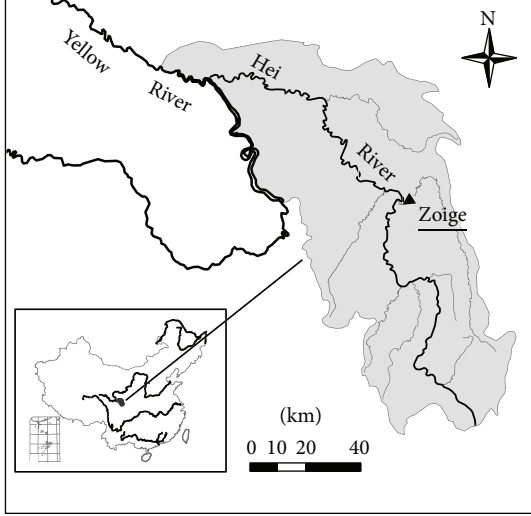


FIGURE 1: Location of the study area.

changes. Nearest neighbor bootstrapping regressive method was used to model the variations of daily runoff in order to provide a basis for the development and utilization of regional water resources.

2. Data and Methods

2.1. Data. Hei River is located in the Eastern Tibetan Plateau where wetlands are distributed widely. As the largest river in Zoige wetland, Hei River is the major tributary of the upstream of the Yellow River (Figure 1) and it flows from the south to the north and turns to the northwest at Zoige county town and flows finally to the Yellow River [19]. The length of the Hei River is 455.9 km, with an average gradient of 0.2% and the drainage area of 7608 km² [20]. There are many small lakes, which mostly are small swamps and oxbow lakes in the watershed.

We collected daily runoff, temperature, and precipitation during 1988 to 2008 at the Zoige hydrologic station in the Hei River middle reaches. The moving average method, Mann-Kendall testing method [21], and self-correlation diagram were used to analyze the trend and the dependency of the annual runoff, and homogeneous degree and variation and self-correlation diagram were used to analyze the distribution of the monthly runoff.

2.2. Nearest Neighbor Bootstrapping Regressive Model. Nearest neighbor bootstrapping regressive model (NNBR) is data driven and nonparametric, with potential priority, and needs no assumption in the form of dependence and probability distribution, as well as no estimate of many parameters [22–24].

Generally, there exists correlation between hydrology phenomena along timescale. Thus, to an extent, X_t depends on the historical daily runoff $Q_{t-1}, Q_{t-2}, \dots, Q_{t-p}$. Given $D_t = (Q_{t-1}, Q_{t-2}, \dots, Q_{t-p})$, it is named as eigenvector of the daily

runoff series. Then, $X_t = (Q_t, Q_{t+1}, \dots, Q_{t+m-1})$ ($t = P+1, P+2, \dots, n-m+1$) can be defined as the succeeding value of D_t .

Among D_t ($t = P+1, P+2, \dots, n$) which are constituted by $\{Q_t\}_n$, there must be some nearest neighbor eigenvectors to current eigenvector D_i . Suppose the number of nearest neighbor eigenvectors is K , and it is represented by $D_{1(i)}, D_{2(i)}, \dots, D_{K(i)}$. $X_{1(i)}, X_{2(i)}, \dots, X_{K(i)}$ must be the succeeding values of each corresponding eigenvector. The nearest neighbor is judged by the difference between D_i and D_t , which is defined as

$$r_{t(i)} = \left(\sum_{j=1}^P (d_{ij} - d_{tj})^2 \right)^{1/2}, \quad (1)$$

where $r_{t(i)}$ represents the difference between D_i and D_t , d_{ij} and d_{tj} are number j variable of D_i and D_t , respectively, and P is the dimension of eigenvector. Then, $r_{j(i)}$ ($j = 1, 2, \dots, K$) is denoted by the difference between $D_{j(i)}$ and D_i , and it should be mentioned that $r_{1(i)} < r_{2(i)} < \dots < r_{K(i)}$ (the number j is ordered according to the value of $r_{j(i)}$). The less $r_{j(i)}$ is, the nearer D_i and $D_{j(i)}$ will be, and X_i is more similar to $X_{j(i)}$. Let $G_{j(i)}$ be the nearest neighbor bootstrapping weight of $X_{j(i)}$, which shows similarity between X_i and $X_{j(i)}$. Obviously, $G_{j(i)}$ is related to $r_{j(i)}$.

As discussed above, the relative value of number i variable of number j nearest neighbor succeeding vector $X_{j(i)}$ is known. The succeeding vector X_i can be obtained through multiplying predicted daily runoff $G_{j(i)}$. Thus, the ultimate formula of NNBR model can be given as

$$X_i = \sum_{j=1}^K G_{j(i)} X_{j(i)}. \quad (2)$$

NNBR model is confirmed when the number of nearest neighbor K , the dimension of eigenvector P , and the nearest neighbor bootstrapping weight $G_{j(i)}$ are estimated.

Generally, $K = \text{int} \sqrt{n-P}$ is given. If $P \geq 2$, the dimension of eigenvector P can be estimated by runoff autocorrelation graph or partial-correlation graph.

There are a number of methods to estimate bootstrapping weight $G_{j(i)}$. When estimating, first of all, its restraint condition must be satisfied, and then bootstrapping weight $G_{j(i)}$ should be related to $r_{j(i)}$, and the bootstrapping weight function should equal one (3). As the number j is ordered according to the value of $r_{j(i)}$, in this paper, the following formula is adopted:

$$\sum_{j=1}^K G_{j(i)} = 1, \quad (3)$$

$$G_{j(i)} = \frac{(1/j)}{\sum_{L=1}^K 1/L} \quad (j = 1, 2, \dots, K). \quad (4)$$

When K is confirmed, we can only calculate $G_{j(i)}$ once.

We used the following qualification rate (QR) and coefficient of determination R^2 to estimate model fits for the calibration and validation. In this study, if the prediction of

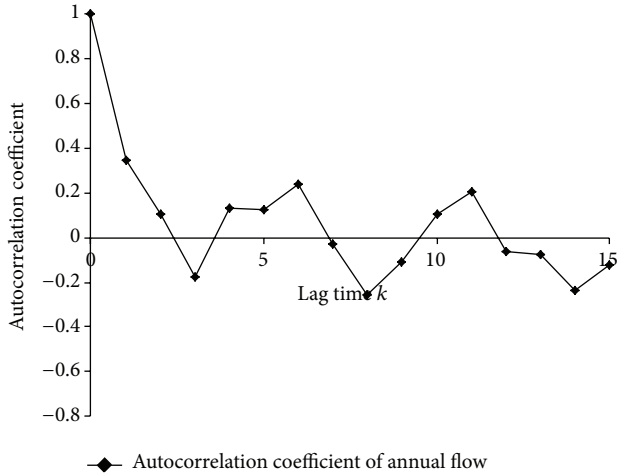


FIGURE 2: Autocorrelation coefficient and lag time of the annual runoff.

relative error was less than 20%, thus the model was assumed to be qualified:

$$QR = \frac{n}{m} \times 100\%, \quad (5)$$

where n is the number of qualified predictions and m represents the totality.

3. Results and Discussions

According to the runoff observation data from 1988 to 2008 (except 1998) at Zoige hydrologic station, the average annual runoff is $20.40 \pm 1.70 \text{ m}^3/\text{s}$, the average annual runoff depth is $161.0 \pm 13.37 \text{ mm}$, and the average annual discharge is $(6.44 \pm 0.53) \times 10^8 \text{ m}^3$, respectively.

The degree of dispersion of annual runoff time series is too large with the variation coefficient $C_v = 0.37$ and skewness coefficient $C_s = 0.2$. It is because Hei River belongs to the river with the rain-snow and ice fusion. Discharge of runoff depends largely on the precipitation variation and snowmelt [25]. However, because average annual runoff of the area itself is small, interannual variation of runoff is relatively small, which led to weak dependence of the annual runoff series (Figure 2).

During the period of 1988~2008, the largest annual flow occurred in 1999 (up to $32.6 \text{ m}^3/\text{s}$), while the lowest annual runoff occurred in 2002, only $8.3 \text{ m}^3/\text{s}$, respectively. Hei River runoff decreasing trend is remarkable since 1988 (Table 1 and Figure 3). The higher temperature and less precipitation led to the decreasing trend of runoff (Figures 4 and 5). From 1988 to 1999 is the abundant water period; from 2000 to date is the drier period. According to the observation data, the average annual flow from 1988 to 1994 is $27.0 \pm 0.75 \text{ m}^3/\text{s}$ and the average annual flow has decreased to $19.0 \pm 1.24 \text{ m}^3/\text{s}$ during 1995~2000 and $15.2 \pm 0.74 \text{ m}^3/\text{s}$ during 2001~2008, respectively (Figure 3). The trend of decreased annual runoff impacted ecosystems of Zoige wetland and partly contributed to wetland degradation with habitats loss.

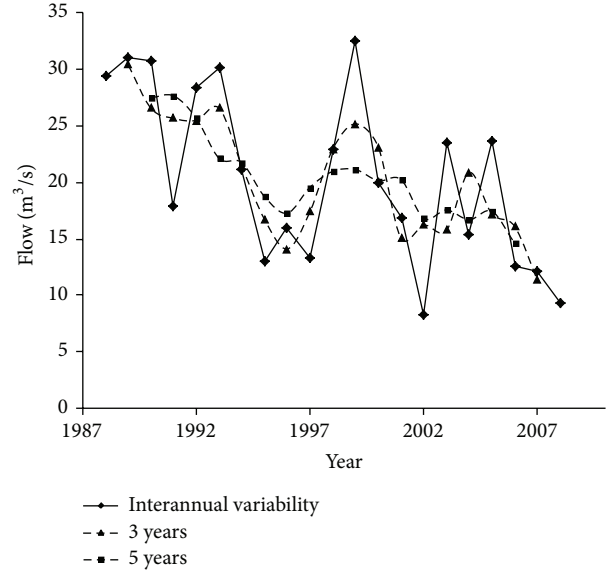


FIGURE 3: Trend of the variation of annual runoff.

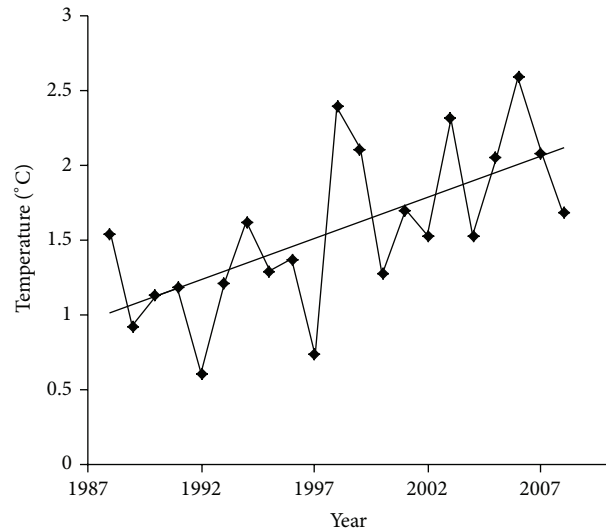


FIGURE 4: Trend of the variation of annual temperature.

TABLE 1: Tendency of the runoff series of years by Mann-Kendall statistical test.

Test statistic U	Significance α	Critical value $U_{\alpha/2}$	Judge result	Tendency
-2.92	0.05	1.96	$ U > U_{\alpha/2}$	Significant decrease

The results of this study are consistent with previous findings of degradation of the wetland (-13.08% for swamp, -6.31% for river, and -20.24% for lake) from 1987 to 2004 that associated significantly with changes in hydrological processes [3]. Due to decreasing annual runoff, it resulted in the fact that overflow of water could not reach adjacent wetlands and led to wetland function loss [3].

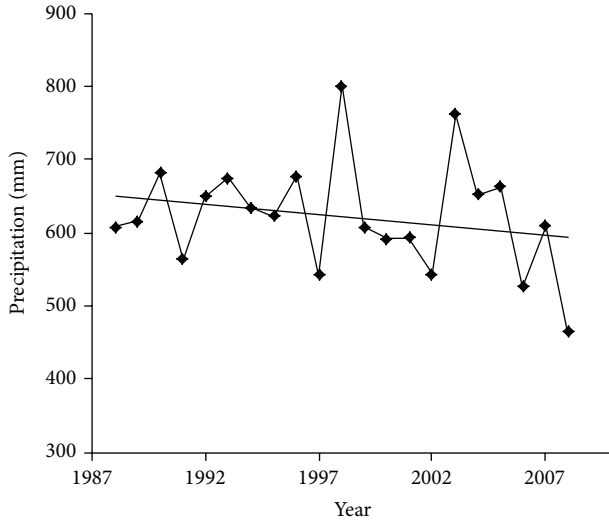


FIGURE 5: Trend of the variation of annual precipitation.

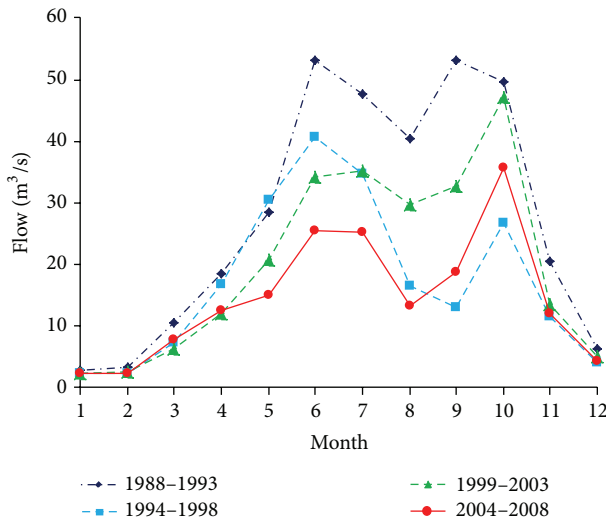


FIGURE 6: Monthly runoff distribution during 1988 to 2008 with a 4-year increment.

The monthly runoff distribution during the year is uneven (Figure 6), and the relative change amplitude C_m is 15.9 and absolute change amplitude is $37.1 \pm 4.04 \text{ m}^3/\text{s}$. Peak runoff mainly concentrated in the months 5–10. This river is supplied at the same time by two ways: precipitation and snow and ice ablation. In winter, the runoff is very small because the low temperature makes the surface frozen. With the spring coming, it becomes swarm, but the temperature is still very low, and the wetland is covered by ice and snow, while in summer when the temperature is higher, peak flow occurred by precipitation, snowmelt, and the runoff of the river in summer. Pulsing flooding water during growing season made high net primary production from wetland plant communities [10, 26].

Dry season (December to February) contributes only 4.4% of discharges for all the year, while wet season

TABLE 2: Daily runoff prediction for 2008 of Hei River using NNBR model.

NNBR model	Mean of relative error (%)	QR (%)	R^2
	5.61	97.50	0.98

(May to October) contributes 82.8% of discharges for all the year, respectively. The nonflood season (November to next April) contributes 17.2% of discharge for all the year (Figures 5 and 6). It may be because the precipitation's rapid decrease after July leads to the runoff's decrease, and the air temperature is still higher; it has led higher evaporation in August and September and lower in October. The highest peak in the period of 1988–1994 and 1995–2000 occurred in July while in the period of 2001–2008 the highest peak occurred in October (Figure 6). Shifting peak flow means less water quantity in wetland during growing season, which significantly impacts plant communities and also biogeochemical process [27]. The restoration approach used in Zoige wetland resulted in one peat-mining site being filled with water and aquatic vegetation with increased water levels up to 26–50 cm higher than previously recorded in canals and shallow water canal, respectively. Pioneering vegetation including *Eleocharis* Horsetail (*Equisetum*, *Eleocharis*) and *Halerpestes* (*Halerpestes tricuspis*) colonized in the restored sites [3]. The similar hydrologic function study was presented from peat wetlands in Canada where the impact of a change in hydrological function from transmitting to contributing on aquatic chemistry may depend on the residence time of water in the wetland. Shifting peak flow also contributed a short residence time in the wetland to not fully develop characteristic chemical traits of wetland ground water [28]. In general, natural- and human-induced factors may produce gradual and instantaneous trends and shifts (jumps) in hydroclimatic series. For example, the historical shifts in snowmelts suggested that an increase in global and regional temperature affected the discharge from a midlatitude mountain area of central Japan by using a simplified hydrological model and associated stochastic treatments [17, 29]. The occurrence of trends and shifts in hydrologic time series and the ensuing effects on water resources, the environment, and society still are concerned (e.g., [17]).

Through primary selection of the model parameters, trial and error, it determines that $P = 2$, nearest neighbor number $K = 33$. Then daily runoff of 1988~2007 is used to constitute the feature vector D_t , which is used to predict daily runoff of the year 2008. The QR is 97.50% and the R^2 is 0.98 (Table 2 and Figure 7) in validation phase owing to NNBR model's superiority.

Because NNBR model is data driven and nonparametric, it avoids the uncertainty of parameter and the problem of model choice which is different from other models based on the traditional prediction patterns of "assume-calibration-validation." So it was widely used to predict the hydrological series, such as the annual runoff of the Yangtze River in the upper reaches [30]. However, NNBR, the same as other models, would make no sense when the future motion trail of the series is out of the law obtained by its historical data.

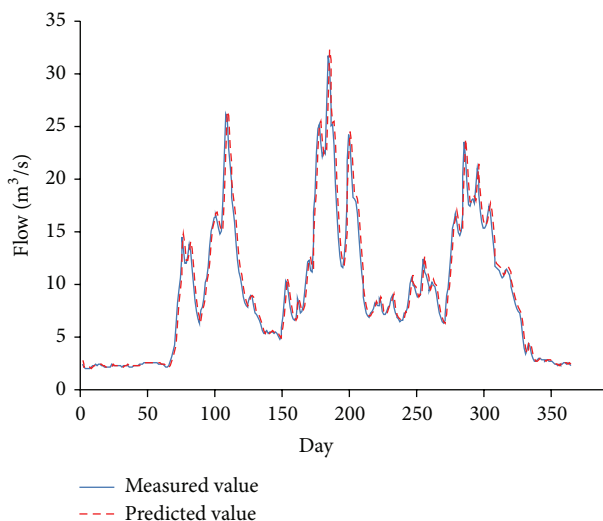


FIGURE 7: Daily runoff prediction for 2008 of Hei River using NNBR mode.

4. Conclusions

The annual runoff of Hei River decreased from $27.0 \text{ m}^3/\text{s}$ (1988~1994) to $15.2 \text{ m}^3/\text{s}$ (2001~2008). The monthly runoff distribution during the year is uneven, and the relative change amplitude C_m is 15.9; absolute change amplitude is $37.1 \text{ m}^3/\text{s}$. The maximum value of runoff appeared in July in 1988 to 2000 and shifted to October after 2000, which may be because of the precipitation's rapid decrease after July leading to the runoff's decrease, and the temperature is still high; evaporation force is strong in August and September while October evaporation is reduced, so the maximum appears.

A stochastic model and modeling schemes were developed for simulation of hydrologic processes of Hei River. Daily runoff modeling with NNBR model during 2008 has good fits with 97.5% which is probably more suitable than liner regressive model especially when the time series has no obviously short-dependency.

Conflict of Interests

The authors declare that there is no conflict of interests regarding the publication of this paper.

Acknowledgments

This present research is supported by the National Key Basic Research Program of China (973 Program, no. 2013CB036401) and National Natural Science Foundation of China (no. 51209152).

References

- [1] X. Chai and S. Jin, "The types of Zoige Alpine Marsh and its development," *Acta Geographica Sinica*, vol. 29, pp. 219–240, 1963.
- [2] G. Y. Sun, W. F. Zheng, J. Luo, and F. M. Yang, "A study of ecological environment and rational exploration of mires in the Zoige Plateau," *Journal of National Resources*, vol. 2, no. 4, pp. 359–368, 1987.
- [3] X. Zhang, H. Liu, and Z. Xing, "Challenges and solutions for sustainable land use in ruoergai-the highest altitude peatland in Qinhai-Tibetan Plateau, China," *Energy Procedia*, vol. 5, pp. 1019–1025, 2011.
- [4] B. Junhong, O. Hua, C. Baoshan, W. Qinggai, and C. Hui, "Changes in landscape pattern of alpine wetlands on the Zoige Plateau in the past four decades," *Acta Ecologica Sinica*, vol. 28, no. 5, pp. 2245–2252, 2008.
- [5] H. Chen, N. Wu, Y. Gao, Y. Wang, P. Luo, and J. Tian, "Spatial variations on methane emissions from Zoige alpine wetlands of Southwest China," *Science of the Total Environment*, vol. 407, no. 3, pp. 1097–1104, 2009.
- [6] S. Xiang, R. Guo, N. Wu, and S. Sun, "Current status and future prospects of Zoige Marsh in Eastern Qinghai-Tibet Plateau," *Ecological Engineering*, vol. 35, no. 4, pp. 553–562, 2009.
- [7] M. Schumann, N. Thevs, and H. Joosten, "Extent and degradation of peatlands on the Ruoergai Plateau (Tibet, China) assessed by remote sensing," in *After Wise Use—The Future of Peatlands, Proceedings of the 13th International Peat Congress: Pristine Mire Landscape*, pp. 77–80, International Peat Society, 2008.
- [8] X. Zhang, H. Liu, C. Baker, and S. Graham, "Restoration approaches used for degraded peatlands in Ruoergai (Zoige), Tibetan Plateau, China, for sustainable land management," *Ecological Engineering*, vol. 38, no. 1, pp. 86–92, 2012.
- [9] W. J. Junk and K. M. Wantzen, "The flood pulse concept: new aspects, approaches and applications—an update," in *Proceedings of the 2nd International Symposium on the Management of Large Rivers for Fisheries*, R. L. Welcomme and T. Petr, Eds., vol. 2 of *RAP Publication 2004/17*, pp. 117–140, Food and Agriculture Organization of the United Nations & Mekong River Commission, FAO Regional Office for Asia and the Pacific, Bangkok, Thailand, 2004.
- [10] W. J. Mitsch and J. G. Gosselink, *Wetlands*, John Wiley & Sons, New York, NY, USA, 4th edition, 2007.
- [11] D. Machiwal and M. K. Jha, *Hydrologic Time Series Analysis: Theory and Practice*, Capital Publishing, 2012.
- [12] T. A. Ula and A. A. Smadi, "Periodic stationarity conditions for periodic autoregressive moving average processes as eigenvalue problems," *Water Resources Research*, vol. 33, no. 8, pp. 1929–1934, 1997.
- [13] P. Verma, J. Yeates, and E. Daly, "A stochastic model describing the impact of daily rainfall depth distribution on the soil water balance," *Advances in Water Resources*, vol. 34, no. 8, pp. 1039–1048, 2011.
- [14] F. Worrall and T. P. Burt, "A univariate model of river water nitrate time series," *Journal of Hydrology*, vol. 214, no. 1–4, pp. 74–90, 1999.
- [15] H. A. Thomas and M. B. Fiering, "Mathematical synthesis of stream-flow sequences for the analysis of river basin by simulation," in *Design of Water Resources Systems*, P. J. Purcell, Ed., pp. 459–493, Harvard University Press, Cambridge, Mass, USA, 1962.
- [16] V. Yevjevich, *Fluctuations of Wet and Dry Years (Hydrology Paper1)*, Colorado State University, Fort Collins, Colo, USA, 1963.

- [17] Y. Shinohara, T. Kumagai, K. Otsuki, A. Kume, and N. Wada, "Impact of climate change on runoff from a mid-latitude mountainous catchment in central Japan," *Hydrological Processes*, vol. 23, no. 10, pp. 1418–1429, 2009.
- [18] X. X. Luo, *Study on the wetland water system in the Naoli River watershed in the Sanjiang plain [Ph.D. thesis]*, Northeast Institute of Geography and Agroecology, Chinese Academy of Sciences, 2002.
- [19] S. F. Zhang, S. F. Jia, C. M. Liu et al., "Water cycle change law of the headwater of the yellow river and its impact," *Science in China E*, vol. 34, pp. 117–125, 2004.
- [20] S. Jiang, *The study of hydrologic characteristic of the alpine wetland rivers in northwest of Sichuan [Ph.D. thesis]*, Sichuan University, 2006.
- [21] K. H. Hamed, "Trend detection in hydrologic data: the Mann-Kendall trend test under the scaling hypothesis," *Journal of Hydrology*, vol. 349, no. 3-4, pp. 350–363, 2008.
- [22] U. Lall and A. Sharma, "A nearest neighbor bootstrap for resampling hydrologic time series," *Water Resources Research*, vol. 32, no. 3, pp. 679–693, 1996.
- [23] W. Wang, P. Yuan, and J. Ding, "Application of nearest neighbor bootstrap regressive model in prediction of water environment," *China Environmental Science*, vol. 21, no. 4, pp. 367–370, 2001.
- [24] P. Yuan, W. Wang, and J. Ding, "Nonparametric perturbing nearest neighbor bootstrapping model for simulation of flood time series," *Journal of Sichuan University (Engineering Science Edition)*, vol. 32, no. 1, pp. 82–86, 2000.
- [25] Q. Tang, Y. Qu, and Y. Zhou, *The Utilization of Hydrology and Water Resources in Arid Areas of China*, Science Press, Beijing, China, 1992.
- [26] W. J. Junk, P. B. Bayley, and R. E. Sparks, "The flood pulse concept in river-floodplain systems," in *Proceedings of the International Large Rivers Symposium*, D. P. Dodge, Ed., vol. 106, pp. 110–127, Canadian Special Publication of Fisheries and Aquatic Sciences, 1989.
- [27] K. R. Reddy and R. D. DeLaune, *Biogeochemistry of Wetlands: Science and Applications*, CRC Press, 2008.
- [28] C. Spence, X. J. Guan, and R. Phillips, "The hydrological functions of a boreal wetland," *Wetlands*, vol. 31, no. 1, pp. 75–85, 2011.
- [29] N. Wada, K. Kawada, R. Kawamura, K. Aoki, and A. Kume, "Increasing winter runoff in a middle-latitude mountain area of central Japan," *Journal of the Meteorological Society of Japan*, vol. 82, no. 6, pp. 1589–1597, 2004.
- [30] W. Wang, H. Xiang, and J. Ding, "Predication of hydrology and water resources with nearest neighbor bootstrapping regressive model," *International Journal Hydroelectric Energy*, vol. 19, no. 2, pp. 8–10, 2001.

Research Article

Serial Analysis of Ten Precipitation-Based Indices by Land Use in Semiarid Regions

Victor M. Rodríguez-Moreno,¹ J. Ariel Ruíz-Corral,² J. Saúl Padilla-Ramírez,¹ Alfonso Peña-Ramos,¹ and Thomas G. Kretzschmar³

¹*Instituto Nacional de Investigaciones Forestales, Agrícolas y Pecuarias (INIFAP), Experimental Field Station “Pabellón”, km 32.5, Highway Ags-Zac, 20660 Pabellón de Arteaga, AGS, Mexico*

²*INIFAP, Experimental Field Station “Centro Altos de Jalisco”, km 8, Highway Tepatitlán-Lagos de Moreno, 47600 Tepatitlán de Morelos, JAL, Mexico*

³*Earth Sciences Division, Department of Geology, Centro de Investigación Científica y de Educación Superior de Ensenada (CICESE), Highway Tijuana-Ensenada, 22860 Ensenada, BC, Mexico*

Correspondence should be addressed to Victor M. Rodríguez-Moreno; rodriguez.victor@inifap.gob.mx

Received 5 November 2014; Revised 13 January 2015; Accepted 8 February 2015

Academic Editor: Fubao Sun

Copyright © 2015 Victor M. Rodríguez-Moreno et al. This is an open access article distributed under the Creative Commons Attribution License, which permits unrestricted use, distribution, and reproduction in any medium, provided the original work is properly cited.

Open ecosystems in Mexico are under increasing pressure, due particularly to the expansion of cities and agricultural activities. These developments occur without integrating biodiversity concerns in land use planning and result in extensive fragmentation and transformation of the landscapes. The semiarid region of Mesa Central was characterized using ten precipitation-based indices. Using multivariate statistical and geostatistical spatial analysis techniques, the influence of those indices on five land use strata was explored. Land use analysis indicated that the maximum values of the five significant precipitation-based indices were found in Grasslands, Agricultural Use, and Shrubs; minimum values were characteristic of substrates Secondary Desert Vegetation and Other Use. Our results suggest that the greatest number of extreme precipitation events is likely to occur in open ecosystems and consequently will have a strong influence on landscaping and land use. The semivariogram analysis and geostatistical layers demand attention from research institutions, policy makers, researchers, and food producers to take the appropriate and coordinated actions to propose scenarios to deal with climate change. Perhaps this study can stimulate thought concerning research endeavours aimed at promoting initiatives for biodiversity conservation and planning programs for climate change mitigation.

1. Introduction

Climate results from a combination of atmospheric factors and environmental conditions that operate at different levels [1]. Indices for climate variability and extremes have been used for a long time, often by assessing days with precipitation observations above or below specifically based thresholds [2]. Because vegetation covers most of the global land surface, it strongly affects the land-atmosphere exchanges of energy, momentum, and materials [3] through the distinctive combination of interacting elements that are repeated in similar form through the landscape; it also impacts runoff and erosion rates along with soil stability. Most semiarid regions suffer severe rainfall erosion [4]; since water has a high erosive

capacity, more damage is likely to occur in these areas because of reduced vegetative protection.

Climate system warming is unequivocal, and since the 1950s many of the observed changes are unprecedented when seen over decades, even millennia [5]. According to Zeng et al. [3], arid and semiarid regions are dominated by shrub communities with many subtypes. In addition, within the spatial limits of these regions, an exceptional richness of biodiversity and an astonishing variety of biomes are found; exceptionally high species diversity and endemism occur. Plant community spatial distribution is strongly influenced by rainfall distribution, soil water retention rate, and the soil itself as substrate. Additionally, temperature and geomorphic factors influence plant community distribution in the

landscape by influencing evaporation rate and the amount of sun insolation. According to Kuyler [6], the origin and development of landscapes are influenced by a combination of natural processes and human influences. Land use, particularly its intensity, is considered one of the determining factors of the abundance and richness in populations of soil organisms [7]. The diversity and heterogeneity of land use processes require detailed analysis because of their differential effects on the environment. Land use degradation occurs when the ecosystem is not able to regenerate its structures and ecological processes (resilience) in order to recover its stability. Most semiarid regions are characterized by a hot summer and extremely limited and spatially erratic annual precipitation (less than 300 mm). Changes in temperature and rain events have received extensive attention from researchers, since many regions worldwide have experienced significant variations in climate extremes during the past few decades [8, 9]. The number and frequency of rainfall events along with extended droughts raise the question as to whether extreme climate events are truly increasing and also whether they are associated with climate change. Knapp et al. [10] documented growing evidence at global, regional, and local levels that intra-annual precipitation regimes have become more extreme; global precipitation records during the 20th century show an average increase of only 9 mm over land areas, excluding Antarctica. Therefore, according to Pearson et al. [11], climate data are essential input variables for ecological modelling and play a significant role in flora and fauna distributions.

Climate change impacts add further complication to the already demanding water management challenges in arid and semiarid regions. Its effect on hydrological processes such as infiltration, percolation, runoff, and soil water storage is highly complex [12]. In Mexico an issue demanding attention is limited and often lack of serial climate data records on open ecosystems because of the absence of meteorological devices. Along with the high cost of maintenance, the spatial representation of ground-weather monitoring stations is a function of regional climatic variability, measurement site characteristics, observational practices [13], and frequency of instrument calibration to standards. Some stations may be strongly influenced by an unusual or changing microclimate within their immediate surroundings and therefore have less utility representing climatic dynamism over large spatial scales. The scientific community has extensively documented the robust influence of geomorphic factors (elevation, slope [north, south, east, west facing, or level]), and topographic setting (ridge top, valley, etc.) as biased sources for recorded data and trend analysis. A station near hills or hollows, in or out of nocturnal drainage channels, or influenced by other subtle features may result in errors in climate data records. Concerning this issue, the World Meteorological Organization (WMO) contends that for developing high quality datasets the database must consider these potential limitations: general measurement and sampling errors; lack of homogeneity (where external factors can influence the record, e.g., new trees or buildings near the observation site); and the practice of having to make statistical averages over large geographical regions when limited data are available to

represent those areas. According to Jamaludin and Suhaimi [14], dealing with these issues implies a high cost and an overwhelming number of procedures, in fact way too many. Scientists, accordingly, have developed a number of interpolating methods to keep inherent data uncertainty at a minimum to ensure enough accuracy for its use in climate analyses.

Ordinary Kriging is an interpolator that works well on any scale because of its accuracy in improving the calculation of model error. In a geographic information system (GIS) environment it uses statistical models that allow a variety of thematic output maps that include predictions, standard errors of predictions, probability, and quantile (ArcGIS). With the use of interpolation, the idea is to have an estimate of the distance one would need to travel before data points separated by that distance are uncorrelated [15]. This information is usually presented in the form of the variogram, which is a function of the semivariance *versus* the distance lag. The basic difference between variance and semivariance data is that the first category is represented by a number (scalar) and the second one by a curve (vector).

The use of indices instead of data is a better way to make the influence of climate change on the landscape more evident. An index represents information derived from the data itself and is useful for supporting a variety of climate change analyses. The RclimDex is an R based package designed to provide a user-friendly interface to compute indices of climate extremes [16].

This study endeavours to provide new information which integrates a serial dataset of direct measurements of daily precipitation in order to derive precipitation-based climate indices, their spatial mapping interpretation, and trend analysis. The study area is the Mesa Central, a semiarid physiographic province of Mexico. This region has highly fragmented land use and a landscape of contrasting elevation and landforms. Daily precipitation data of a sufficient number of ground-weather stations were used to derive climate indices datasets as well as the slope of the estimated trend line equation. All datasets were fully incorporated into a GIS project to extend the analysis to regional scale, taking into consideration the land use categories. The goal is to improve the knowledge of how precipitation-based indices may help to clarify the way regional land use may be affected by climate change.

2. Materials and Methods

2.1. Description of the Study Area. The Mesa Central is a physiographic province that is part of the northern high plateau region in Mexico and covers two-thirds of the country's arid and semiarid regions. It is located in central Mexico (Figure 1) and embodies ~8.6 Mha. Its spatial limits were originally delineated based on morphologic and geologic characteristics contrasting with those of neighbouring physiographic provinces [17]. It is a large area of folds and separated mountain failures with vast flood plains that become part of large and extended flat basins. Two physiographic features characterize this region: a semiarid area of volcanic cones separated by high alluvial basins adjacent to Sierra Madre Oriental (SMOr) and, secondly, desert lands and semiarid areas along

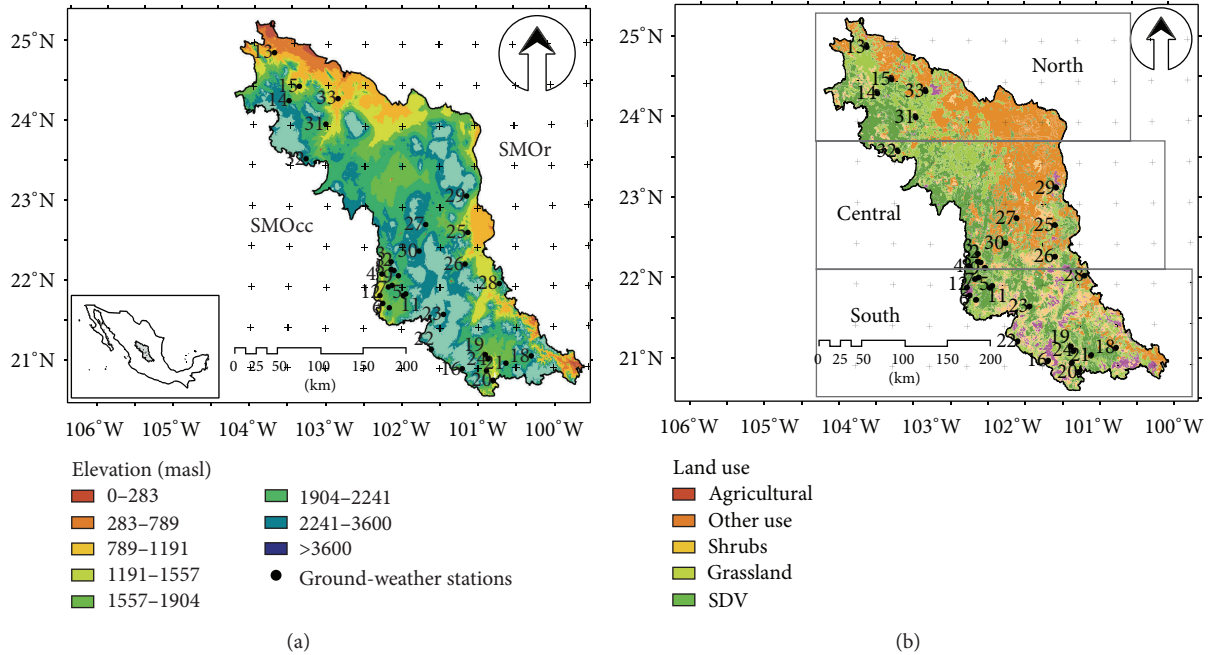


FIGURE 1: Digital elevation model (DEM (a)) and land use (b), along with the location of ground-weather stations. The scale is 1 : 250,000.

with inner basins, located in the lower central zone and eastern region of the plateau [18]. The province combines rough topographic relief and flat areas. Over half of its surface is above 1,900 masl (Figure 1(a)) and the inside topographic elevations are moderate, generally forming ramps at 600 m or less. On the north and east it is bordered by the SMOr, on the west by the Sierra Madre Occidental (SMOcc), and on the south by the depression known as El Bajío. The spatial limits are in accord with the Instituto Nacional de Estadística y Geografía (INEGI) of Mexico. Regional land use incorporates five gross classes: the Agricultural Class, covering ~2.65 Mha (30.81% of the area); Shrubs (chaparral), comprising ~2.76 Mha (32.09%); Secondary Desert Vegetation (SDV), embodying ~1.89 Mha (22.98%); Grassland, totalling ~0.86 Mha (10.00%); and Other Use, accounting for the rest of the study area ~0.44 Mha (5.12%). Agricultural activity is under both irrigation and precipitation-dependent regimes; the shrub class includes crassicaule, rosetophyll, microphyll, and submountainous species; the SDV stratum has holm oaks, pine, mesquite, and their associations; the Grassland category incorporates halophytic, along with introduced and native species (Figure 1(b)); the Other Use stratum includes water bodies, human settlements, and bare soil.

Because of its considerable latitudinal size, the province was subdivided into three virtual regions, each corresponding to ~175 km of latitude distance. The Agricultural Class is regional and widely distributed. In the northern region the horizontal spatial distribution is dominated by a transition of the Shrubs, SDV, and Agricultural Classes. This region also displays an outstanding contrast in elevation with a transition from flat areas (northern) to peaks (east, central, and west). The southern region is a blend of all land use strata where the transition among classes is not specifically dominated by

any particular class; there is, however, a distinct transition in elevation. Most of the Other Use class is located in this region, along with significant areas of the other land use strata. The central region exhibits a pattern of land use distribution comparable to the north region.

2.2. Data Description and Quality. Daily precipitation data of 32 ground-weather stations (Figure 1 and Table 1) were used to derive precipitation-based indices (Table 2).

The “X” and “Y” columns refer to coordinate data: North American Lambert Conformal Conic Projection, Datum ITRF92. Bold numbers denote a simple consecutive list corresponding to the station numbers in Figure 1. The CNT column designates the number of years with data. Columns Yr STRT and Yr END indicate initial and final years of recorded data. Elevation data are provided in the ELEV column; data was acquired by point extraction from a digital elevation model (DEM) with ~30 m spatial resolution. The serial dataset range was 41 > years < 86. Elevation ranged from 1,594 to 2,310 masl.

Data quality was a priority because the indices are sensitive to changes in station location, sun exposure, equipment precision, and observer’s practice [19]. Before calculating the indices, the dataset preparation and processing instructions of the RClimDex user’s manual were followed, as proposed by Zhang and Yang [20] to insure data quality. Two phases are involved: the Quality Control (QC) and the Homogeneity Test (HT). The goal of QC is to identify errors in daily datasets that may potentially interfere with the correct assessment of the extremes; that is, all missing values (currently coded as -99.9) are replaced with an internal code that the software recognizes (i.e., NA: not available); and all allegedly aberrant data are substituted with the NA code. The quality test also

TABLE 1: Metadata of 32 ground-weather stations.

ID	X	Y	CNT	Yr STRT	Yr END	ELEV (masl)
1	2479653	1109989	41	1970	2010	1910
2	2486208	1131433	52	1959	2010	2310
3	2482803	1143829	48	1963	2010	1990
4	2470043	1127050	70	1937	2006	1900
5	2503141	1099876	44	1967	2010	2020
6	2481042	1080332	62	1949	2010	1970
7	2483763	1110871	42	1969	2010	2030
8	2482620	1133640	49	1962	2010	2100
9	2493072	1124451	62	1949	2010	2015
10	2468155	1097585	64	1947	2010	1870
11	2500000	1097918	40	1971	2010	2005
12	2471762	1087203	62	1949	2010	1890
13	2329266	1426223	62	1948	2009	1594
14	2344222	1362695	65	1942	2006	2000
15	2363559	1381750	47	1963	2009	1800
16	2579963	997979	62	1949	2010	2280
17	2612885	994396	49	1962	2010	1909
18	2673414	1015524	62	1949	2010	2114
19	2610387	1017095	61	1951	2011	1937
20	2621930	982281	50	1961	2010	1850
21	2640491	1004184	49	1962	2010	2000
22	2537885	1024753	65	1947	2011	2100
23	2553592	1070379	86	1924	2009	2250
24	2616265	1010894	50	1961	2010	1915
25	2588990	1183040	41	1969	2009	1800
26	2589705	1140237	68	1942	2009	2062
27	2536066	1192513	45	1965	2009	2030
28	2630237	1113825	50	1961	2010	1970
29	2590633	1233933	69	1941	2009	2210
30	2521958	1157819	43	1967	2009	2122
31	2396833	1329940	68	1942	2009	1913
32	2371687	1283722	68	1942	2009	2071

identifies outliers in daily precipitation data. An outlier is an observation that falls outside the statistical limits of probability or else is negative. Currently these limits are defined as n times standard deviation (stdev) of the value for the day; that is, $(\bar{x} - n \times \text{stdev}, \bar{x} + n \times \text{stdev})$, where stdev stands for the day and n is an input from the user. Here we assigned a threshold value of four stdev's. According to Vincent et al. [21], HT consists in the detection of shifts in climate time series, which are often due to station relocation, changes in instruments observation practices, and automation.

The RCLimDex User's Manual is the best source for a more detailed and extensive description of these indices; it is available for online consultation and downloading.

2.3. Statistical Analysis. All descriptive statistics were processed according to Chebyshev's theorem; it formally states

that "the proportion of observations falling within k standard deviations of those numbers of the mean of those numbers is at least $1 - 1/k^2$ " [22]. The advantage of this theorem is that it applies to any dataset regardless of the distribution shape of the data. For calculation, the serial maximum datum was indicated as the "upper limit" (1); then, k datum was further added to (2):

$$k = \frac{[\text{"upper limit"} - \bar{x}]}{\text{stdev}} \quad (1)$$

$$\text{Chebyshev's theorem} = \left[1 - \left(\frac{1}{k^2} \right) \right] * 100. \quad (2)$$

In (1), the calculated k is the number of standard deviations that the serial maximum datum amounts to by dividing it by the standard deviation. Stated simply, the theorem gives the *minimum* proportion of data which must lie within a given number of standard deviations of the mean; true proportions found within the indicated regions could be greater than what the theorem guarantees. The correct interpretation is that at least Chebyshev's value (percent) of each index is in the interval of $\bar{x} \pm k$ and the rest of the proportion is outside this interval.

The geostatistical layers of surface map predictions were obtained by applying the Ordinary Kriging interpolation technique. It is considered superior to other commonly used interpolation techniques for precipitation estimation [23]. This technique provides an unbiased interpolation with minimum square mean estimation error and it is used for its ability to incorporate regional data and data indicating local trends. It has also been used frequently in soil science [24, 25], hydrology [26], and more recently in forestry [27], ecology, and climatology [28–30]. Its calculation is based on a semivariogram, a geostatistical tool that analyses the spatial variability of one variable within the spatial limits of a specific area. A semivariogram is commonly used to model spatial structure in a single variable by measuring the strength of statistical correlation as a function of distance. According to Gringarten and Deutsch [31], the expected squared difference between two data values separated by a distance vector, \mathbf{h} , is the variogram. The semivariogram $\gamma(\mathbf{h})$ is one half of the variogram $2\gamma(\mathbf{h})$. The variogram is a measure of variability; it increases as samples become more dissimilar. According to Webster and Oliver [32], the parameters that define the variogram are (1) the sill, which is the total variance and represents the variability in the absence of spatial correlation; (2) the range, which is the distance at which the variogram approaches the sill; and (3) the nugget effect, which is a combination of spatially unstructured variance (e.g., attribute error) and spatially structured variance at distances shorter than the minimum measurement separation. The sill minus nugget is known as partial sill or structural variance.

Because of the lack of the specific data for calibrating the semivariogram runs, we used fixed parameters for all runs; the primary variable was the precipitation-based index and the covariable was the elevation grid. Run-parameters were the model, ordinary co-Kriging; lag, 2,318.92; nugget, 0, 0; range, 204,168.71; and sill, 1.5631. According to Schabenberger and Pierce [33], the decision about whether or not to include

TABLE 2: Acronyms and short descriptions of the ten precipitation-based indices.

ID	Short name. Description	Output time units
CWD	Consecutive wet days. Maximum number of consecutive days with RR ≥ 1 mm	Days
PRCPTOT	Annual total wet-day precipitation. Annual total PRCP in wet days (RR ≥ 1 mm)	Annual
R10mm	Number of heavy precipitation days. Annual count of days when PRCP ≥ 10 mm	Annual
R20mm	Number of very heavy precipitation days. Annual count of days when PRCP ≥ 20 mm	Annual
R95p	Very wet days. Annual total PRCP when RR >95th percentile	Annual
R99p	Extremely wet days. Annual total PRCP when RR >99th percentile	Annual
R25mm	Number of days above 25 mm. Annual count of days when PRCP ≥ 25 mm	Annual
R1day	Max 1-day precipitation amount. Monthly maximum 1-day precipitation	Monthly
R5day	Max 5-day precipitation amount. Monthly maximum consecutive 5-day precipitation	Monthly
SDII	Simple daily intensity index. Annual total precipitation divided by the number of wet days (defined as PRCP ≥ 1.0 mm) in the year	Annual

a nugget effect is difficult. Its inclusion probably results in a better-fitting model [34], but considering that the geomorphology of the study area varies considerably and also that land use is disparate and delineated on a 1:250,000 scale, the decision to set the nugget value at 0, 0 seemed appropriate. This decision follows the recommendation of Schabenberger and Pierce [33] that nugget inclusion is not necessary.

There are several models of semivariance to choose from. According to Glover [15], the linear model seems to provide the best results because the data do not support evidence for a sill or a range; rather, they appear to have increasing semivariance as the lag increases. Gallardo [35] proposed a rule of thumb about the number of pairs to represent a point in the semivariogram; it must be greater than 30. This general rule means that the number of data on the space object would not be less than 50. The same author mentions that this rule serves as a guide and does not have to be followed absolutely. In this study the number of ground-weather stations is 32, which seems adequate to support the research.

For statistical analyses, the multivariate analysis of variance (MANOVA) along with the *post hoc* Bonferroni test for homogeneous groups was applied. To make the database for analysis suitable for the general MANOVA model, one which accepts categorical variables, the dataset was augmented with two categorical predictors: the three virtual regions (North, Central, and South) and the five land use classes. Resampling the geostatistical surface map layer with a randomly distributed dataset of 3,569 coordinate pairs provided the land use analysis. Each data point is an n -dimensional vector whose coordinates are $x_1(t), x_2(t) \dots x_i(t)$, at a time (t) [36]. The required number of points, along with their distribution, was determined by applying a random distribution function and a restriction distance of 200 m between points. Because land use was originally delineated at a 1:250,000 scale and also divided into five appreciable strata for this study, it seemed imperative to select a minimum number of points by class. Calculating an appropriate sample size relies on the subjective choice of certain factors and sometimes crude estimates of others; as a result, this outcome may seem rather artificial. However, at worst it is a well educated guess, and it is

considerably more useful than a completely arbitrary choice [37].

3. Results and Discussion

3.1. *R*Climdex. A variation in statistical significance of trend lines was evident. Of the ten precipitation-based indices, five were seen as significant ($P < 0.05$): PRCPTOT, R10 mm, R20 mm, R25 mm, and SDII. Hence, the discussion of the results and analysis will be limited to these indices.

To choose indices for mapping purposes and statistical analysis, along with a consideration of significance, we separated indices by applying two additional criteria: a minimum of 5 ground-weather stations had to result as significant for the index and their spatial distribution could not be concentrated in reduced areas. Of the calculated 320 trend lines (32 ground-weather stations \times 10 indices), a positive trend was observed for 38 (~12%), whereas a negative trend was perceived for ~5% (15); the remaining trend line equations, 267 (~83%), were seen as nonsignificant ($P > 0.05$). These results appear to accentuate a regional spatial distribution for precipitation events which lacks homogeneity in frequency and intensity; they also seem to indicate that certain areas may be more susceptible than others to a strong influence of topography. Those regions may provide a good target for focusing research on the effects of land use and climate change for integrating plant communities and how this may influence spatial landscaping. As observed in Table 3, indices that met the proposed criteria and resulted in a positive trend were those related to heavy rain (R10 mm), total precipitation (PRCPTOT), days with rain ≥ 25 mm (R25 mm), and SDII; the only index displaying a negative trend was R20 mm. Hereafter the results and discussion will be limited to these five indices.

3.2. *Surface Analysis.* The variations and trend of climate indices as well as the observed semivariogram must be understood for reliable interpretation and modelling. The surface prediction maps on Figure 2 represent the individual spatial variability of each index along with the positive/negative trend of each ground-weather station. The legend (classes)

TABLE 3: Significant trend line equations of precipitation-based indices by ground-weather stations; table includes only all the stations with significant $P < 0.05$ for at least one index. Bold numbers indicate a positive trend and normal text a negative trend; empty cells were nonsignificant ($P > 0.05$).

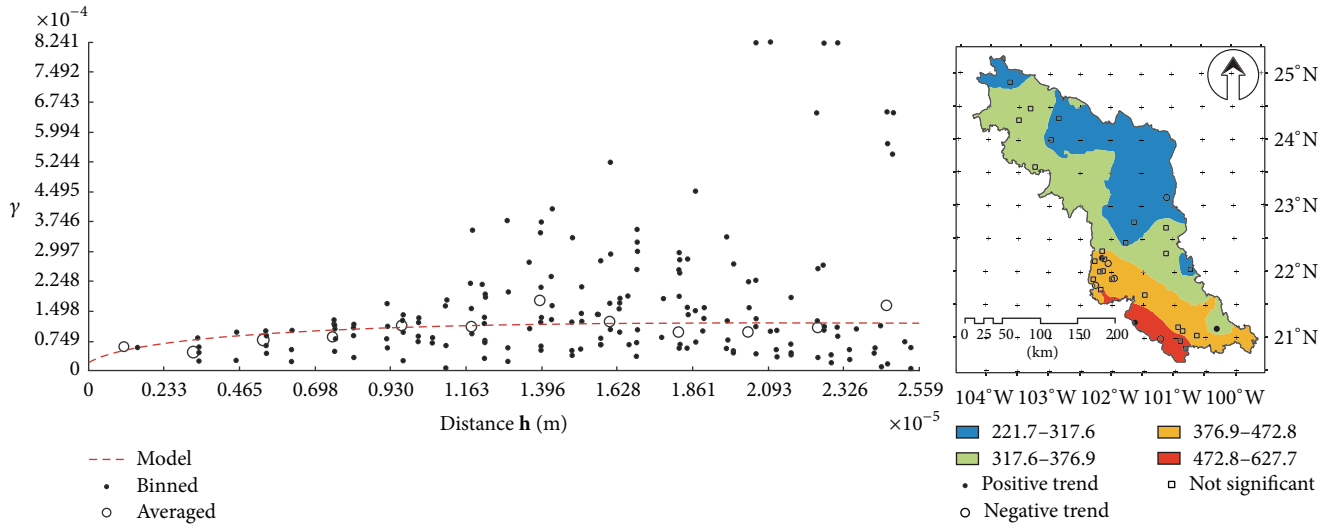
ID	PRCPTOT	R10mm	R20mm	R25mm	SDII
2				y = 0.08 * +0.03	
5	y = 4.33 * +1.64			y = 0.07 * +0.03	
6					y = 0.06 * +0.02
7		<i>y = -0.15 * +0.07</i>			
8	<i>y = -3.06 * +1.45</i>	<i>y = -0.14 * +0.06</i>			
9	y = 2.045 * +0.97	y = 0.09 * +0.04			y = 0.06 * +0.02
11	y = 3.24 * +1.51				
12		y = 0.15 * +0.06			
13					y = 0.09 * +0.02
14		y = 0.11 * +0.04			y = 0.04 * +0.01
15	y = 4.39 * +1.66				
16		y = 0.16 * +0.07		y = 0.09 * +0.03	
17	<i>y = -3.41 * +1.54</i>				
18		<i>y = -0.14 * +0.06</i>	<i>y = -0.09 * +0.03</i>	<i>y = -0.05 * +0.02</i>	
19					<i>y = -0.04 * +0.02</i>
21	<i>y = -5.51 * +1.99</i>				
22		<i>y = -0.16 * +0.07</i>	<i>y = -0.09 * +0.04</i>	<i>y = -0.07 * +0.03</i>	
28	y = 3.52 * +0.95				y = 0.09 * +0.04
29		y = 0.10 * +0.04	y = 0.07 * +0.02	y = 0.06 * +0.02	
31			y = 0.07 * +0.02	y = 0.06 * +0.02	
32			y = 0.04 * +0.02	y = 0.04 * +0.01	y = 0.02 * +0.01

for geostatistical surface layers is in accord with regional land use spatial distribution. Di Gregorio and Jansen [38] define land use spatial distribution as the spatial arrangement of life forms (e.g., trees, Shrubs, Grasslands, etc.) in a given region. Land use spatial distribution reflects an ecological or an evolutionary aspect of vegetation (e.g., scattered vegetation in arid areas, agricultural encroachment inside forest areas, and degradation due to overgrazing). In defining a particular classification design in a particular area two concepts is considered: the Minimum Mappable Area (MMA) and the Mixed Mapping Units (MMU). Di Gregorio and Jansen [38] mention that MMA is applied by cartographers when addressing the smallest area that can be shown on a map; it is scale-dependant and not related to classification. The same authors mention that the MMA is cartography related. The classifier is free to decide if land use implies an intricate mixture of classes where no one class is clearly dominant. Our study region was considered a spatially separate entity (e.g., patches of each stratum of land use inside all) in an intricate mixture (crops, Shrubs, and Grasslands). In the case of spatially separated entities of two or more classes, we followed the general criteria proposed by Di Gregorio and Jansen [38] that the cover of each class considered must be more than 20 percent (and consequently less than 80 percent) of the mapping unit. Based on these criteria, we defined four major classes for all significant indices.

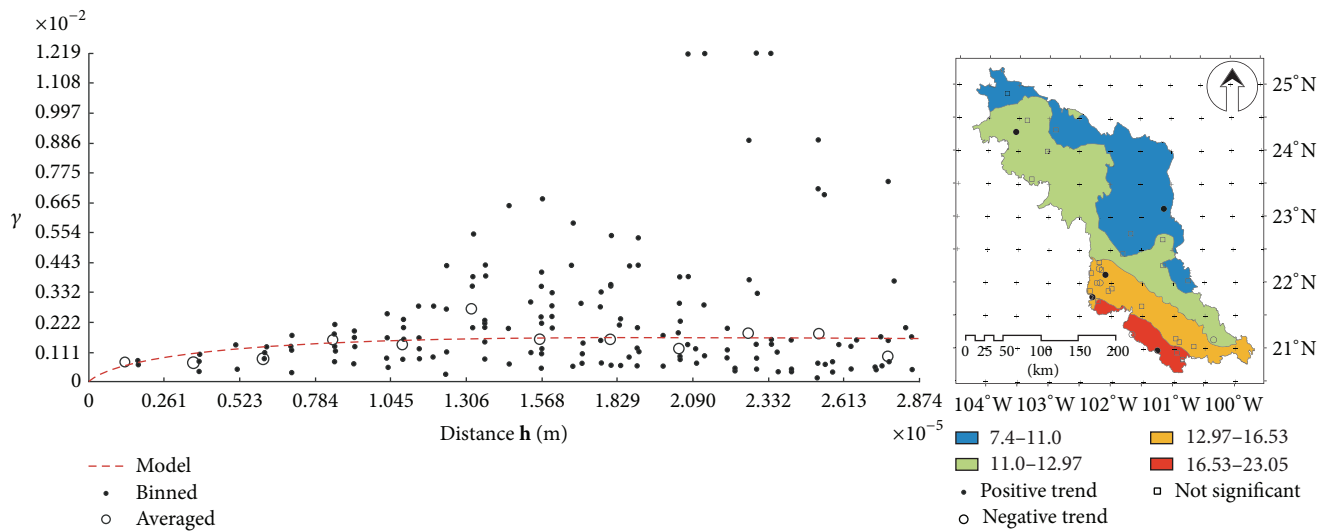
The PRCPTOT index showed a pronounced effect on model performance because of the strong influence of the spatial autocorrelation range. Despite its designation as zero,

a slight nugget effect was observed in two locations (Table 4). The nugget effect and the origin of slope are the most important features for fitting the semivariogram [39] and the nugget effect is also the most unpredictable because of the lack of closer samples in the dataset.

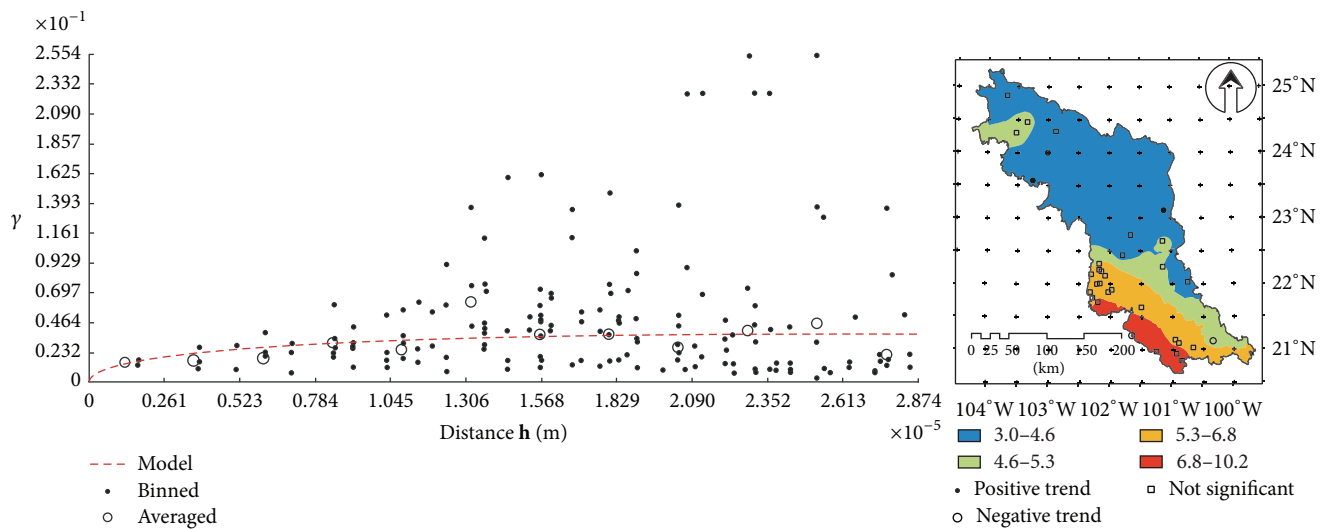
The discontinuity in the semivariogram's origin can be viewed as a nonsense situation since landscape realities [40] and environmental conditions may be considered a continuous surface. According to Clark and Harper [41], the discontinuity of semivariogram origin should not occur in most spatial environmental processes because space is generally continuous; however, some individual processes in nature, such as gold mineralization, are exceptions to this pattern. Nevertheless, the semivariogram should be continuous at the origin. "One of our basic assumptions is physical continuity of the phenomena being measured" [41]. As evident in the PRCPTOT index, the nugget effect indicates erratic behaviour over very short distances along with considerable variability over distances less than specified lag spacing or sampling interval. This would imply that "perfect" sampling would eliminate the nugget effect entirely, but the methodology and the applied analysis techniques of this study are limited and circumscribed by the number of ground-weather stations; this limitation prompts us to consider the resulting value of the nugget effect as inconclusive. In addition, a key issue is the interpolation approach for a given set of input data [42]. This is especially true for areas such as those with contrasting topography (mountainous regions), where data collection is sparse and measurements for given variables



(a)



(b)



(c)

FIGURE 2: Continued.

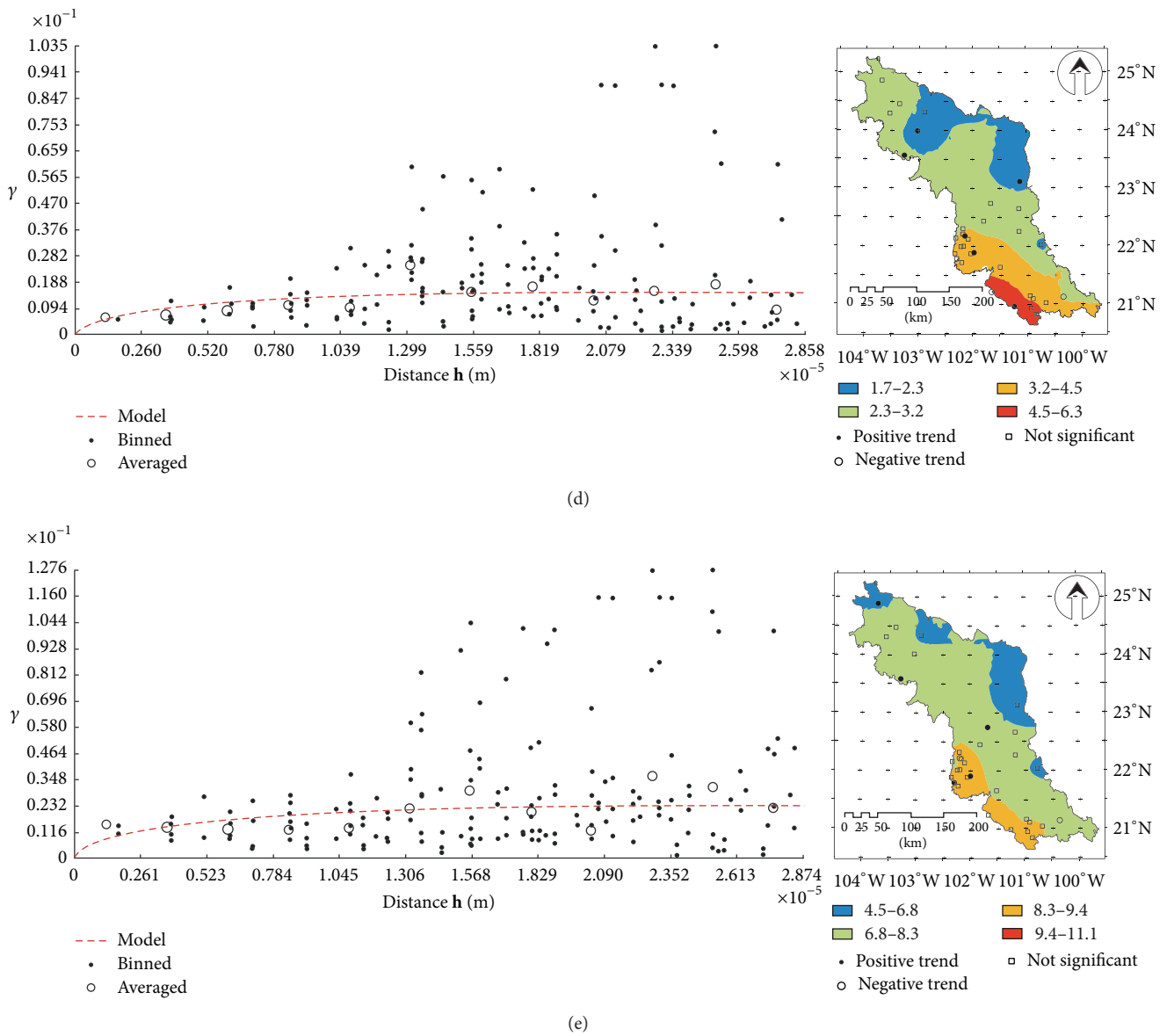


FIGURE 2: Semivariograms and geostatistical surface map layers of significant indices. (a) = PRCPTOT; (b) = R10 mm; (c) = R20 mm; (d) = R25 mm; and (e) = SDII.

TABLE 4: Semivariogram parameters for significant indices by location.

Index	Range	Partial sill 0,0	Partial sill 0,1	Partial sill 1,1	Nugget 0,0	Nugget 1,1
PRCPTOT	176,010.1	10,109.4	7,782.7	43,723.2	1,825.20	1,427.4
SDII	205,120.5	2.4	115.1	46,597.4	0.00	0.0
R25mm	204,168.7	1.6	112.7	46,574.8	0.00	0.0
R20mm	205,120.5	3.7	164.3	46,597.4	0.00	0.0
R10mm	205,120.5	16.7	285.9	46,597.4	0.00	0.0

may differ significantly even at relatively reduced spatial scales [43]. Burrough and McDonnell [42] state that when data are abundant most interpolation techniques give similar results. When data are sparse, the underlying assumptions about the variation among sampled points may differ and the choice of interpolation method and parameters may become critical. Results of spatial interpolation contain a certain degree of error, and this error is sometimes measurable [44]. As apparent in this study, land use in this semiarid region is highly fragmented and the number of stations seems to be locally adequate; this is notable in central region. According to Ahrens [45], the geographical representativeness of the stations diverges, but this is not systematically dependent on station elevation. Since this is not addressed by geographical distance weighting and by the knowledge that precipitation increases with elevation, it is expected that interpolated precipitation will be tendentially overestimated in those areas with rough terrain. One limitation that has been reported when using geostatistical spatial analysis is that the underlying stochastic concept relies on the distribution and on the stationarity of mean and spatial covariance [46]. Some studies have used prescribed data transformation: for example, Schuurmans et al. [47] use a square root transformation in application with situations of abundant daily rainfall; Verworn and Haberlandt [48] use a log transformation for selected flood cases. Nevertheless, in our study region precipitation events are erratic and even absent; to our knowledge the application of transformation is not a common practice, and the effect of transformation as well as the role of transformation choice has not been systematically examined so far. Nonetheless, this feature recommends further exploration for future research studies and may suggest incorporating additional datasets for remotely sensed net shortwave and longwave radiation, latent and sensible heat flux, and surface and subsurface runoff.

These results seem to support those reported by Wagner et al. [49] where they indicate that in an interpolation scheme the choice of a covariate had a significant impact on estimated precipitation and runoff amounts. Our results demonstrate that the incorporation of an elevation grid as a covariate should improve and enhance the spatial representativeness of ground-weather station datasets. Naimi et al. [50] mention that the value of the covariate of an interpolated location would be similar to that of an actual location. According to Gringarten and Deutsch [31] at some scales the processes are highly nonlinear and chaotic, leading to variations that have no spatial correlation structure. Typically, only a small amount of variability is explained by random behaviour. The results here seem to validate the erratic distribution and randomness of precipitation events in this semiarid region.

All semivariograms showed that spatial correlation to elevation decreases with separation distance. For all indices the size of the range of correlation scale depends on direction; that is, the vertical range of correlation is much less than the horizontal range due to the greater lateral distance between stations.

The interpretation of the geostatistical layers resulted in mean differences in all indices. Surfaces A and B resulted in an almost comparable spatial distribution with an evident latitude gradient that starts with the lowest area of the north

region and extends to the highest area in the south region. In Figure 2(c), all of the north region and most of central region fundamentally had the lowest number of heavy precipitation days. For geostatistical layer D, the maximum number of days in a year with precipitation ≥ 25 mm is limited to a small area in the south region where the most of the Other Use class is present. For layer E, results indicated that the mean precipitation in wet days (6.8–8.3) was essentially homogeneous along the central north/south length of the study area.

3.3. Land Use. Based on the Chebyshev's theorem it appears evident that the north region had the greatest dispersion among land use strata and significant indices indicating the proportion of observations from the mean ($>41\%$ proportion $<82\%$). This was especially notable for the Other Use and Shrubs classes, but this was in contrast to the k value which regionally showed the closest approach to the mean, as observed on the k graphic with a >1.2 stdev <2.4 (Figure 3). Consistently, the central region resulted in the highest proportion around the mean (72–91%), but in contrast with the highest range of k (1.6–3.4); south region was influenced by the values of the SDII index resulting in a smaller proportion around the mean (47–66%), but the closest range from the mean (>1.4 k <1.7) (Figure 3). These results emphasize the variation among strata by the latitude gradient and land use.

Among significant indices the PRCPTOT indicated the lowest value for the Other Use stratum. This result may suggest evidence that anthropogenic activity is influencing the hydrologic cycle by affecting the total amount of precipitation within the region. Jacobson and Kaufman [51] reported a reduction in precipitation in California due to emissions of anthropogenic aerosol particles and precursor gases; that is, anthropogenic SO_x , NO_x , NH_3 , and speciated organic gases, but not CO_2 , CH_4 , or N_2O . This feature deserves further research and extended study, but it is beyond the scope of this project.

According to Gringarten and Deutsch [31], the extent of spatial correlation decreases with separation distance until reaching a distant point where no spatial correlation exists. Virtually all climatic relationships impart trends which affect land use. By way of examples, water distribution upland or a systematic decrease in reservoir quality from proximal to distal locations may have an impact on an ecosystem's integration processes, gas exchange, and functionality; likewise, geomorphology exerts a significant influence on the amount of solar radiation incident on a surface, since radiation varies with slope and aspect as a function of slope angle; elevation influences spatial distribution of wetness on soil, biotic composition of plant communities, pedogenic process, and runoff. This is especially important for terrain with highly complex geomorphology, where topography shading generally has important effects on energy balance. The cause for night time warming and variations in energy balance has been attributed to changes in atmospheric water vapour, cloud cover, jet contrails, and changes in surface characteristics such as land cover and land use [52–54]. Local effects such as urban growth, irrigation, desertification, and variations in local land use can affect the wetness distribution, particularly in urban areas. Large-scale climatic effects on regional

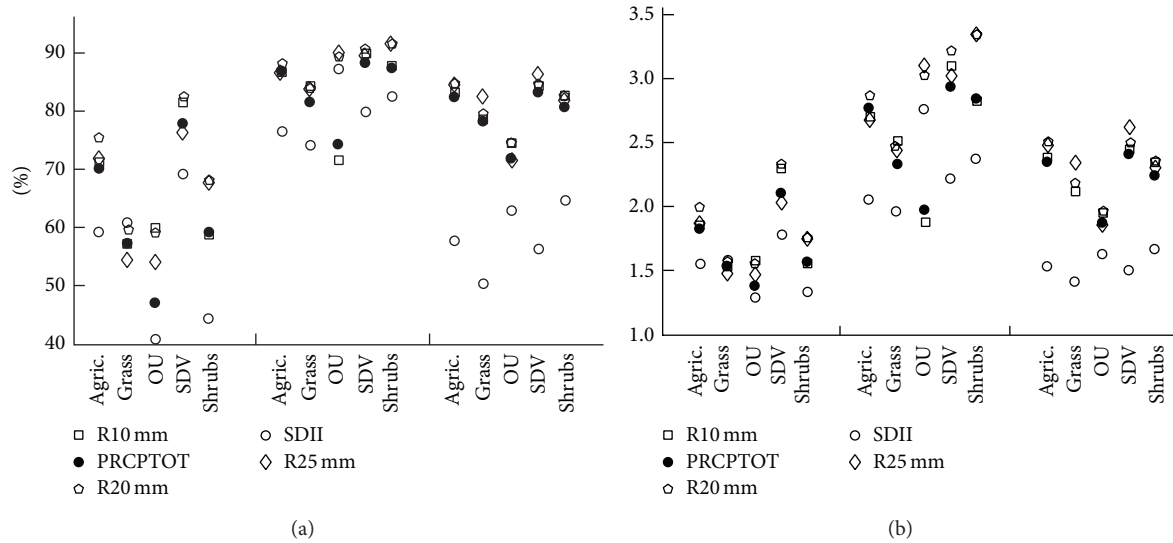


FIGURE 3: Chebyshev's theorem (a) and k value (unitless) (b) for the significant indices by land use by virtual region. From left to right: north, central, and south regions.

TABLE 5: The Bonferroni test for homogeneous groups ($\alpha = 0.05$) by region and by land use.

	PRCPTOT	R10mm	R20mm	R25mm	SDII
Region					
North	312.04 ^a	10.77 ^b	4.11 ^b	2.48 ^b	7.26 ^b
Central	311.26 ^a	10.57 ^a	3.89 ^a	2.25 ^a	6.92 ^a
South	408.48 ^b	14.06 ^c	5.82 ^c	3.68 ^c	8.10 ^c
Land use					
SDV	333.17 ^b	11.35 ^b	4.45 ^b	2.70 ^b	7.32 ^b
Other Use	337.56 ^{ab}	11.60 ^{ab}	4.48 ^{ab}	2.72 ^{ab}	7.36 ^{ab}
Shrubs	341.62 ^a	11.72 ^a	4.57 ^a	2.78 ^b	7.40 ^a
Agricultural	343.28 ^a	11.80 ^a	4.58 ^a	2.77 ^b	7.43 ^a
Grasslands	344.58 ^a	11.85 ^a	4.61 ^a	2.78 ^{ab}	7.44 ^a

Each letter separates the significant differences between pairs of classes. The comparison is based on the calculated value of statistic F .

wetness distribution may include increases in cloud cover, surface evaporative cooling from precipitation, greenhouse gases, tropospheric aerosols [52], and extreme meteorological events, along with hydric and energy imbalance. This in turn may have consequences for runoff rate, sediment transport, groundwater recharge, and of course land use conformation.

3.4. Statistical Analysis. Data analysis was performed on the sample dataset points with added categorical variables for land use and regions. The MANOVA model provided significant outcomes ($P < 0.05$) for both categorical predictors. As expected, most of the variation was observed in land use (Wilk's lambda = 0.18, $F = 951.8$, $P = 0.00$) and less by regions (Wilk's lambda = 0.96, $F = 6.8$, $P = 0.00$). The *post hoc* Bonferroni test showed significant differences ($P < 0.05$) for regions and indices, except for PRCPTOT where no significance ($P > 0.05$) was observed between the central and north regions (Table 5). The most outstanding results were found in land use.

The PRCPTOT index indicated significantly different results ($P < 0.05$) when pairing the Shrubs, Grasslands and Agricultural Classes with the SDV stratum for all indices. For the remaining paired associations, no significance ($P > 0.05$) was observed (Table 5). For the R10 mm, R20 mm, and SDII indices, results for a number of pairs were similar to PRCPTOT index; a notable exception was in the R25 mm index, which indicated two well defined groups. The first group included the SDV, Shrubs, and Agricultural strata; the second one encompassed the Other Use and Grasslands strata.

Regional variation is apparent by observing the latitude gradient. The south region consistently received the highest annual precipitation, the greatest number of extreme precipitation events, and the largest number of wet days per year (SDII index). Land use analysis indicated two well defined groups for all indices, except the most extreme index (R25 mm). Regionally the Shrubs, Agricultural Use, and Grasslands strata ranked highest in all indices, showing yearly more total precipitation, the greatest number of heavy

precipitation days, and the greatest number of wet days. By contrast the SDV stratum ranked lowest in all indices.

In general, documentation showed that in the Mesa Central region precipitation-based indices indicated a definite influence on land use integration and the latitude gradient. Mahmood et al. [55] showed that land cover changes exert an important role in variations of atmospheric temperature, humidity, cloud cover, circulation, and precipitation. These changes have an impact ranging from local and regional scale to subcontinental and even global scales; they affect agriculture, deforestation/afforestation, desertification, and urbanization. From this perspective Betts et al. [56] have shown that land cover change can influence climate by modifying the physical properties of land surface.

4. Conclusions

This study, using multivariate statistical and geostatistical spatial analysis techniques, explored how different land use strata in the semiarid region of Mesa Central respond to ten precipitation-based indices. The very first conclusion of this study is that spatial autocorrelation, as observed through the analysis of the indices' interpolated geostatistical layers, reduced the positional uncertainty in semivariograms and decreased with distance. The nugget value appearing in the PRCPTOT prompts the incorporation of other datasets, especially those that indirectly register sun insolation, soil humidity, and runoff. These datasets would help to measure the response of soil cover to precipitation and humid conditions.

The second conclusion is about the role of elevation as a dispersion factor affecting the proportion of observations from the mean; the dispersion was greater in the north region than in the central and south regions of the Mesa Central; but this dispersion is in contrast to the number of observations closest to the mean (>1.2 stdev <2.4) and suggests further research initiatives.

The last conclusion is based on an interpretation of the semivariograms and predicted surface, along with the trend in indices. The spatial interpretation of resulted geostatistical layers deserves consideration as an important step in defining programs for biodiversity conservation and land use planning, in designing climate change mitigation programs, and in pursuing carbon sequestration and biomass production studies. This study, therefore, provides a foundation that can be confidently used in future research for exploring these important issues.

Conflict of Interests

The authors declare that there is no conflict of interests regarding the publication of this paper.

Acknowledgments

The authors wish to express their gratitude to the Instituto Nacional de Investigaciones Forestales, Agrícolas y Pecuarias (INIFAP) and Centro de Investigación Científica y de Educación Superior de Ensenada (CICESE) for their financial and

technical support. This gratitude is extended to Mario Salazar, Jaime Luévano, and Eulogio López for their assistance and technical comments. Special recognition goes to Wally Werts for advising on grammar and English structure.

References

- [1] V. M. Rodríguez-Moreno and S. H. Bullock, "Vegetation response to rainfall pulses in the Sonoran Desert as modelled through remotely sensed imageries," *International Journal of Climatology*, vol. 34, no. 15, pp. 3967–3976, 2014.
- [2] X. Zhang, L. Alexander, G. C. Hegerl et al., "Indices for monitoring changes in extremes based on daily temperature and precipitation data," *Climate Change*, vol. 2, no. 6, pp. 851–870, 2011.
- [3] X. D. Zeng, X. Zeng, and M. Barlage, "Growing temperate shrubs over arid and semiarid regions in the Community Land model- Dynamic global vegetation model," *Global Biogeochemical Cycles*, vol. 22, no. 3, Article ID GB3003, 2008.
- [4] FAO, *Soil and Water Conservation in Semi-Arid Areas*, Natural Resources Management and Environment Department, 2014, <http://www.fao.org/docrep/t0321e/t0321e-08.htm>.
- [5] Intergovernmental Panel on Climate Change (IPCC), "Climate change 2013: the physical science basis," in *Contribution of Working Group I to the Fifth Assessment Report of the Intergovernmental Panel on Climate Change*, T. F. Stocker, D. Qin, G. K. Plattner et al., Eds., p. 1535, Cambridge University Press, New York, NY, USA, 2013.
- [6] P. Kuyler, "Application of multi-criteria analysis in land use decisions," 2006, <http://etd.uovs.ac.za/ETD-db/theses/available/etd-11032006-110741/unrestricted/KuylerP.pdf>.
- [7] K. E. Giller, D. E. Bignell, P. Lavelle et al., "Soil biodiversity in rapidly changing tropical landscapes: scaling down and scaling up," in *Biological Diversity and Function in Soils*, M. B. Usher, R. Bardgett, and D. W. Hopkins, Eds., Cambridge University Press, Cambridge, UK, 2005.
- [8] D. R. Easterling, J. L. Evans, P. Y. Groisman, T. R. Karl, K. E. Kunkel, and P. Ambenje, "Observed variability and trends in extreme climate events: a brief review," *Bulletin of the American Meteorological Society*, vol. 81, no. 3, pp. 417–425, 2000.
- [9] J. Wang and X. Zhang, "Downscaling and projection of winter extreme daily precipitation over North America," *Journal of Climate*, vol. 21, no. 5, pp. 923–937, 2008.
- [10] A. K. Knapp, C. Beier, D. D. Briske et al., "Consequences of more extreme precipitation regimes for terrestrial ecosystems," *BioScience*, vol. 58, no. 9, pp. 811–821, 2008.
- [11] R. G. Pearson, T. P. Dawson, P. M. Berry, and P. A. Harrison, "SPECIES: a spatial evaluation of climate impact on the envelope of species," *Ecological Modelling*, vol. 154, no. 3, pp. 289–300, 2002.
- [12] T. Svoray and A. Karnieli, "Rainfall, topography and primary production relationships in a semiarid ecosystem," *Ecohydrology*, vol. 4, no. 1, pp. 56–66, 2011.
- [13] M. J. Janis and S. M. Robeson, "Determining the spatial representativeness of air-temperature records using variogram-nugget time series," *Physical Geography*, vol. 25, no. 6, pp. 513–530, 2004.
- [14] S. Jamaludin and H. Suhaimi, "Spatial interpolation on rainfall data over peninsular Malaysia using ordinary kriging," *Jurnal Teknologi*, vol. 63, no. 2, pp. 51–58, 2013.
- [15] D. Glover, "Objective mapping and kriging," 2014, <http://w3eos.who.edu/12.747/notes/lect05/lectno05.html>.

- [16] W. Dos Santos-Araujo and J. I. Barbosa-de Brito, "Indices of trends of climatic changes for the states of the Bahia and Sergipe by means of daily precipitation indices and its relation with SST's of the Pacific and Atlantic," *Revista Brasileira de Meteorologia*, vol. 26, no. 4, pp. 541–554, 2011.
- [17] A. F. Nieto-Samaniego, S. A. Alaníz-Alvarez, and A. Camprubí-Cano, "La Mesa Central de México: estratigrafía, estructura y evolución tectónica cenozoica," *Boletín de la Sociedad Geológica Mexicana*, vol. 3, no. 62, pp. 285–318, 2005.
- [18] R. C. West, "Surface configuration and associated geology of Middle America," in *Handbook of Middle American Indians*, R. Wanhope and R. C. West, Eds., pp. 33–82, University of Texas Press, Austin, Tex, USA, 1964.
- [19] M. R. Haylock, T. C. Peterson, L. M. Alves et al., "Trends in total and extreme South American rainfall 1960–2000 and links with sea surface temperature," *Journal of Climate*, vol. 19, no. 8, pp. 1490–1512, 2006.
- [20] X. Zhang and F. Yang, *RCLimDex (1.0) User Guide*, Climate Research Branch Environment Canada, Downsview, Canada, 2004.
- [21] L. A. Vincent, E. Aguilar, M. Saindou et al., "Observed trends in indices of daily and extreme temperature and precipitation for the countries of the western Indian Ocean, 1961–2008," *Journal of Geophysical Research D: Atmospheres*, vol. 116, no. 10, Article ID D10108, 2011.
- [22] L. L. Lapin, *Statistics: Meaning and Method*, Harcourt Brace Jovanovich, New York, NY, USA, 1975.
- [23] G. Q. Tabios and J. D. Salas, "A comparative analysis of techniques for spatial interpolation of precipitation," *Journal of the American Water Resources Association*, vol. 21, no. 3, pp. 365–380, 1985.
- [24] T. M. Burgess and R. Webster, "Optimal interpolation and isarithmic mapping of soil properties. I. The semi-variogram and punctual kriging," *Journal of Soil & Science*, vol. 31, no. 2, pp. 315–331, 1980.
- [25] R. Webster and T. M. Burgess, "Spatial variation in soil and the role of kriging," *Agricultural Water Management*, vol. 6, no. 2–3, pp. 111–122, 1983.
- [26] J. P. Delhomme, "Kriging in the hydrosociences," *Advances in Water Resources*, vol. 1, no. 5, pp. 251–266, 1978.
- [27] J. S. Samra, H. S. Gill, and V. K. Bhatia, "Spatial stochastic modeling of growth and forest resource evaluation," *Forest Science*, vol. 35, no. 3, pp. 663–676, 1989.
- [28] S. K. Seilkop and P. L. Finkelstein, "Acid precipitation patterns and trends in eastern North America, 1980–84," *Journal of Climate and Applied Meteorology*, vol. 26, no. 8, pp. 980–994, 1987.
- [29] A. S. Lefohn, H. P. Knudsen, and L. R. McEvoy Jr., "The use of kriging to estimate monthly ozone exposure parameters for the Southeastern United States," *Environmental Pollution*, vol. 53, no. 1–4, pp. 27–42, 1988.
- [30] M.-J. Fortin, P. Drapeau, and P. Legendre, "Spatial autocorrelation and sampling design in plant ecology," *Vegetatio*, vol. 83, no. 1–2, pp. 209–222, 1989.
- [31] E. Gringarten and C. V. Deutsch, "Teacher's aide: variogram interpretation and modeling," *Mathematical Geology*, vol. 33, no. 4, pp. 507–534, 2001.
- [32] R. Webster and M. A. Oliver, *Geostatistics for Environmental Scientists*, John Wiley and Sons, Chichester, UK, 2nd edition, 2007.
- [33] O. Schabenberger and F. J. Pierce, *Contemporary Statistical Models for the Plant and Soil Sciences*, CRC press, Boca Raton, Fla, USA, 2002.
- [34] L. A. Waller and C. A. Gotway, *Applied Spatial Statistics for Public Health*, John Wiley & Sons, 2004.
- [35] A. Gallardo, "Geoestadística," *Ecosistemas. Revista Científica y Técnica de Ecología y Medio Ambiente*, vol. 3, pp. 1–11, 2006.
- [36] A. T. Karunanithi, H. Cabezas, B. R. Frieden, and C. W. Pawlowski, "Detection and assessment of ecosystem regime shifts from fisher information," *Ecology and Society*, vol. 13, no. 1, article 22, 2008.
- [37] E. Whitley and J. Ball, "Statistics review 4: sample size calculations," *Critical Care*, vol. 6, no. 4, pp. 335–341, 2002.
- [38] A. Di Gregorio and L. J. M. Jansen, *Land Cover Classification System (LCCS): Classification Concepts and User Manual: For Software Version 1.0*, Environment and Natural Resources Service, GCP/RAF/287/ITA Africover-East Africa Project and Soil Resources, Management and Conservation Service, FAO, Rome, Italy, 1998.
- [39] M. Armstrong, *Basic Linear Geostatistics*, Springer, Berlin, Germany, 1998.
- [40] J. Negreiros, A. C. Costa, P. Cabral, and T. Oliveira, "The nugget-effect approaches of SAKWeb for environmental modelling," in *Geo-Environment and Landscape Evolution III*, vol. 100 of *WIT Transactions on the Built Environment*, pp. 47–56, WIT Press, 2008.
- [41] I. Clark and W. Harper, *Practical Geostatistics 2000*, (CD-ROM), chapter 9, Ecosse North America, 2000.
- [42] P. A. Burrough and R. A. McDonnell, *Principles of Geographical Information Systems*, Oxford University Press, New York, NY, USA, 1998.
- [43] F. C. Collins and P. V. Bolstad, "A comparison of spatial interpolation techniques in temperature estimation," in *Proceedings of the 3rd International Conference/Workshop on Integrating GIS and Environmental Modeling*, National Center for Geographic Information Analysis (NCGIA), Santa Fe, New Mexico, January 1996.
- [44] A. D. Hartkamp, K. De Beurs, A. Stein, and J. W. White, *Interpolation Techniques for Climate Variables*, NRS-GIS Series 99-01, CIMMYT, Mexico City, Mexico, 1999.
- [45] B. Ahrens, "Distance in spatial interpolation of daily rain gauge data," *Hydrology and Earth System Sciences*, vol. 10, no. 2, pp. 197–208, 2006.
- [46] R. Erdin, C. Frei, and H. R. Künsch, "Data transformation and uncertainty in geostatistical combination of radar and rain gauges," *Journal of Hydrometeorology*, vol. 13, no. 4, pp. 1332–1346, 2012.
- [47] J. M. Schuurmans, M. F. P. Bierkens, E. J. Pebesma, and R. Uijlenhoet, "Automatic prediction of high-resolution daily rainfall fields for multiple extents: the potential of operational radar," *Journal of Hydrometeorology*, vol. 8, no. 6, pp. 1204–1224, 2007.
- [48] A. Verworn and U. Haberlandt, "Spatial interpolation of hourly rainfall—effect of additional information, variogram inference and storm properties," *Hydrology and Earth System Sciences*, vol. 15, no. 2, pp. 569–584, 2011.
- [49] P. D. Wagner, P. Fiener, F. Wilken, S. Kumar, and K. Schneider, "Comparison and evaluation of spatial interpolation schemes for daily rainfall in data scarce regions," *Journal of Hydrology*, vol. 464–465, pp. 388–400, 2012.
- [50] B. Naimi, A. K. Skidmore, T. A. Groen, and N. A. S. Hamm, "Spatial autocorrelation in predictors reduces the impact of positional uncertainty in occurrence data on species distribution modelling," *Journal of Biogeography*, vol. 38, no. 8, pp. 1497–1509, 2011.

- [51] M. Z. Jacobson and Y. J. Kaufman, "Wind reduction by aerosol particles," *Geophysical Research Letters*, vol. 33, no. 24, Article ID L24814, 2006.
- [52] D. R. Easterling, B. Horton, P. D. Jones et al., "Maximum and minimum temperature trends for the globe," *Science*, vol. 277, no. 5324, pp. 364–367, 1997.
- [53] A. Dai, K. E. Trenberth, and T. R. Karl, "Effects of clouds, soil moisture, precipitation, and water vapor on diurnal temperature range," *Journal of Climate*, vol. 12, no. 8, pp. 2451–2473, 1999.
- [54] I. Durre and J. M. Wallace, "Factors influencing the cold-season diurnal temperature range in the United States," *Journal of Climate*, vol. 14, no. 15, pp. 3263–3278, 2001.
- [55] R. Mahmood, R. A. Pielke, K. G. Hubbard et al., "Land cover changes and their biogeophysical effects on climate," *International Journal of Climatology*, vol. 34, no. 4, pp. 929–953, 2014.
- [56] R. A. Betts, P. D. Falloon, K. K. Goldewijk, and N. Ramankutty, "Biogeophysical effects of land use on climate: model simulations of radiative forcing and large-scale temperature change," *Agricultural and Forest Meteorology*, vol. 142, no. 2–4, pp. 216–233, 2007.

Research Article

Comparison of Two Approaches for Estimating Precipitation Elasticity of Streamflow in China's Main River Basins

Xinyao Zhou,¹ Yongqiang Zhang,² and Yonghui Yang¹

¹Key Laboratory of Agricultural Water Resources, Key Laboratory of Agricultural Water Saving, Center for Agricultural Resources Research, Institute of Genetics and Developmental Biology, Chinese Academy of Sciences, 286 Huaizhong Road, Shijiazhuang 050021, China

²CSIRO Land and Water Flagship, P.O. Box 1666, Canberra, ACT 2601, Australia

Correspondence should be addressed to Yonghui Yang; yonghui.yang@sjziam.ac.cn

Received 14 October 2014; Revised 5 February 2015; Accepted 8 February 2015

Academic Editor: Gwo-Fong Lin

Copyright © 2015 Xinyao Zhou et al. This is an open access article distributed under the Creative Commons Attribution License, which permits unrestricted use, distribution, and reproduction in any medium, provided the original work is properly cited.

Two widely used approaches, nonparametric approach and Budyko framework approach, were used to calculate precipitation elasticity of streamflow (ϵ) in China's main river basins. While the Budyko framework illustrates only the effect of climate on ϵ , the nonparametric approach illustrates the effects of both climate and human activity on ϵ . Both approaches showed similar spatial pattern of ϵ , with high values for northern arid catchments and low values for southern humid catchments, suggesting high sensitivity of streamflow to climate in the arid catchments in China's north. Inland catchments had low ϵ values, probably because most of the annual streamflow was driven by glacial and snowmelt. While strong anthropologic activities reduce the sensitivity of streamflow to precipitation in some northern arid catchments, which was indicated by lower ϵ values produced by nonparametric approach, the combined use of the two approaches underscored the significance in identifying the effects of anthropologic factors on streamflow.

1. Introduction

As precipitation is a major factor of streamflow, it is important that water resources scientists and managers understand the sensitivity of streamflow to precipitation. Most studies involving streamflow sensitivity are based on conceptual catchment modeling by varying atmospheric inputs to estimate changes in streamflow [1, 2]. However, conceptual model is limited by high uncertainties in the structures and parameterization [3, 4].

Sankarasubramanian et al. [2] developed a nonparametric model for estimating precipitation elasticity of streamflow (ϵ), which is the proportional change in streamflow resulting from changes in precipitation. While $\epsilon = 2.0$ indicates that 1% change in precipitation results in 2% change in streamflow, higher ϵ suggests higher streamflow sensitivity to precipitation. Several studies suggest that ϵ is highly related to catchment climate attributes, denoted as aridity index (AI), which is the ratio of mean annual potential evapotranspiration (PET) to precipitation. Using nonparametric analysis

of 219 Australian catchments for a 25-year period, Chiew [5] noted that ϵ generally increases with increasing climate dryness (i.e., increasing AI). Zheng et al. [6] also observed a positive correlation between ϵ and AI in a long term (1960–2000) of the headwater regions of Yellow River basin. Sankarasubramanian and Vogel [7] noted that watershed aridity index together with watershed soil water holding capacity is more related to ϵ .

A major advantage of the nonparametric method is that it provides a simple estimate of the sensitivity of streamflow to changes in long-term precipitation [5]. Its main limitation is that it neglects the effects of precipitation frequency, changes in vegetation, and feedback between the atmosphere and land surface. To deal with this limitation, algorithms considering more climatic factors were developed [6, 8, 9]. Amongst them, Budyko framework estimator (driven by AI) is widely used to quantify climate elasticity of streamflow. Studies showed a strong similarity between the nonparametric estimator and the other estimators in unregulated catchments [5, 6].

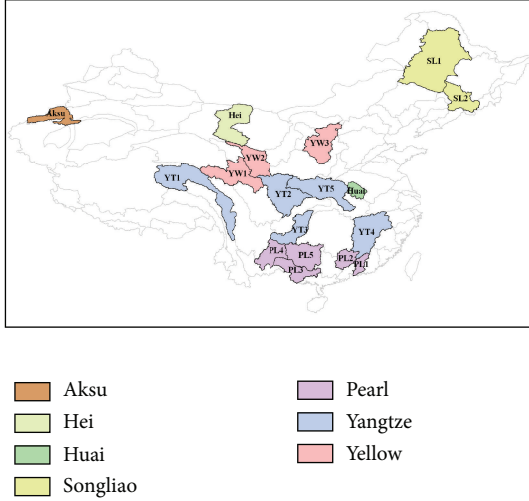


FIGURE 1: Location of 18 investigated catchments including 5 subcatchments in the Yangtze River basin (YT1, YT2, YT3, YT4, and YT5), 5 subcatchments in the Pearl River Basin (PL1, PL2, PL3, PL4, and PL5), 1 subcatchment in the Huai River Basin, 3 subcatchments in the Yellow River Basin (YW1, YW2, and YW3), 2 subcatchments in Songliao Basin (SL1 and SL2), Aksu River Basin, and Hei River Basin (Hei).

China stretches across various climatic regions, ranging from humid tropical climate in the south to arid/frigid temperate climate in the north and from the plains in the east to the “earth’s third pole” mountains of the Tibetan Plateau in the west. Thus the water resources in the south of China are rich while those in the north are poor. The increasing water shortage in North China is driven by the rapid expansion of population, agriculture, and industry. Despite this, the response of streamflow to climate regimes and anthropogenic activities in China’s main catchments remains largely unclear.

This study compares precipitation elasticity of streamflow from the nonparametric estimator with that from the Budyko framework estimator for seven main river basins in China—Yangtze, Pearl, Yellow, Songliao, Huai, Aksu, and Hei (Figure 1). The specific objectives of this study are to (1) investigate the spatial patterns of ε in the seven main river basins; (2) determine any (in)consistency between the two approaches and the related causes; and (3) compare ε between catchments in China and catchments in other regions. This is critical for water scientists and managers in taking informed decisions for sustainable and environmentally friendly water resources management and for the benefits it brings to water users and society at large.

2. Materials and Methods

2.1. Study Area. A total of 18 of catchments with 55 years (1955–2009) of annual streamflow data were used to analyze precipitation elasticity of streamflow. The catchments belong to seven large basins (Songliao, Yellow, Huai, Yangtze, Pearl, Aksu, and Hei) stretching across different climatic zones in China. The catchment boundaries were derived from “Data Sharing Infrastructure of Earth System Science” at

TABLE 1: Surface coefficients used to convert pan evapotranspiration into potential evapotranspiration in the six investigated main basins in China.

Basin	Coefficient	Reference
Yangtze	0.69	Wang et al., 2007 [20]
Pearl	0.65	Liu et al., 2012 [21]
Yellow	0.53	Liu et al., 2004 [22]
Songliao	0.62	Liu et al., 2004 [22]
Huai	0.55	Liu et al., 2004 [22]
Inland (Hei and Aksu)	0.64	Liu et al., 2004 [22]

<http://www.geodata.cn/Portal/metadata/viewMetadata.jsp?id=210008-10081>.

Songliao basin is chilly subhumid, Yellow basin is temperate with subhumid upstream and subarid downstream, Huai basin is warm subhumid, Yangtze basin is warm with subhumid upstream and humid downstream, Pearl basin is hot humid, and Aksu and Hei basins are arid temperate. Figure 1 shows the distribution of the 18 catchments, with each catchment denoted by a unique acronym. Except for Hei, Huai, and Aksu, two letters are used to symbolize the catchments as SL for Songliao, YW for Yellow, YT for Yangtze, and PL for Pearl.

2.2. Data Types and Sources. Annual streamflow data for the catchments were obtained from China river sediment Bulletin (2000–2009) and other sources with catchment outlet hydrological station data [10, 11]. Annual precipitation and pan evapotranspiration data from meteorological stations in the catchments were downloaded from China Meteorological Data Sharing Service System at <http://cdc.cma.gov.cn/home.do>. The pan evapotranspiration was measured using 20 cm diameter and 10 cm high metal pan installed at 70 cm above the land surface [12]. A surface coefficient factor (Table 1) was used to convert the pan evapotranspiration into PET. Simple arithmetic averages of the station-based annual precipitation and PET within the catchments were used to derive catchment-average values. And AI (aridity index) is derived from the ratio of mean annual potential evapotranspiration (PET) to precipitation.

2.3. Elasticity Estimation. Two approaches, nonparametric estimator and Budyko framework estimator, were used to calculate precipitation elasticity of streamflow. The nonparametric estimator can be expressed as [2]

$$\varepsilon_P = \text{median} \left(\frac{(Q_i - \bar{Q}) \bar{P}}{(P_i - \bar{P}) \bar{Q}} \right), \quad (1)$$

where ε_P is precipitation elasticity of streamflow in a catchment; \bar{P} and \bar{Q} are mean annual precipitation and streamflow for the period of study; and P_i and Q_i are annual precipitation and streamflow for the i th year. Observed annual streamflow used in calculating ε_P reflects the impacts of natural factors and anthropogenic activities since the catchments are heavily regulated via processes such as water diversions or

TABLE 2: Details of the six commonly used forms of Budyko framework estimator and the related derivatives.

Function	$f(\text{AI})$	$f'(\text{AI})$
Schreiber, 1904 [23]	$1 - e^{-\text{AI}}$	$e^{-\text{AI}}$
Ol'dekop, 1911 [24]	$\text{AI} \tanh(1/\text{AI})$	$\tanh(1/\text{AI}) - 4/[\text{AI}(e^{-1/\text{AI}} + e^{1/\text{AI}})^2]$
Budyko, 1958 [25]	$\text{AI} \tanh(1/\text{AI})(1 - e^{-\text{AI}})^{0.5}$	$0.5[\text{AI} \tanh(1/\text{AI})(1 - e^{-\text{AI}})]^{-0.5} [\tanh(1/\text{AI}) - 1/\text{AI} \operatorname{sech}^2(1/\text{AI})(1 - e^{-\text{AI}}) + \text{AI} \tanh(1/\text{AI})e^{-\text{AI}}]$
Pike, 1964 [26]	$1/\sqrt{1 + \text{AI}^{-2}}$	$1/[\text{AI}^3(1 + (1/\text{AI})^2)^{1.5}]$
Fu, 1981 [27]	$1 + \text{AI} - (1 + \text{AI}^\alpha)^{1/\alpha}, \alpha = 2.5$	$1 - (1 + \text{AI}^{2.5})^{-0.6} \text{AI}^{1.5}$
Zhang et al., 2001 [28]	$(1 + w\text{AI})/(1 + w\text{AI} + 1/\text{AI}), w = 1$	$(2/\text{AI} + 1/\text{AI}^2)/(1 + \text{AI} + 1/\text{AI})^2$

control dams. Therefore ε_p calculated using the nonparametric method is the combined effects of both climatic and anthropologic factors.

The second approach is the Budyko framework estimator, expressed as [9]

$$\varepsilon_p = 1 + \frac{\text{AI} f'(\text{AI})}{1 - f'(\text{AI})}, \quad (2)$$

where $f'(\text{AI})$ is the Budyko equation derivative which is a function of AI, where $\text{AI} = \overline{\text{PET}}/\overline{P}$. Here, long-term (>5 years) mean annual streamflow is the difference between mean annual precipitation and actual evapotranspiration (AET) in unregulated catchment ($\overline{Q} = \overline{P} - \overline{E}$). In the Budyko framework, AET is a function of AI. Thus the elasticity of the Budyko framework represents only natural or climatic effect on streamflow. Table 2 shows the six commonly used Budyko frameworks and the related derivatives. In the table, elasticity is the average of the six estimators from the six Budyko frameworks.

2.4. Cluster Analyses. Using hierarchical cluster analysis based on Euclidean distance (the shortest distance method) and at a maximum of 3 clusters, precipitation elasticity of streamflow was grouped into three clusters. Analysis in MATLAB showed that elasticity within each group (cluster) was much closer than between the different groups (clusters). This was used to determine the similarity between every two catchments in terms of the sensitivity of streamflow to precipitation.

3. Results and Discussions

3.1. Nonparametric and Budyko Framework Approaches. Figure 2 plotted precipitation elasticity of streamflow estimated for the 18 catchments using the nonparametric and Budyko framework approaches. Although some of the catchments such as the subcatchments of the Yangtze (YT1) and Yellow (YW2 and YW3) River basins showed large deviations, the spatial distributions of streamflow elasticity were similar for most of the investigated catchments. Elasticity for relatively

arid basins (e.g., Songliao and Yellow River basins) was higher than that for relatively humid basins (e.g., Yangtze and Pearl River basins) and was lowest for inland basins. Compared with Budyko framework (hereafter denoted as PE2), estimated elasticity by nonparametric approach (hereafter denoted as PE1) was much lower for catchments with large deviations.

The large deviations in estimated elasticity between the two approaches in three catchments (YW2, YW3, and YT1) could largely result from the difference in ε calculation. While nonparametric approach relies on actual streamflow and precipitation for calculation of ε , Budyko framework approaches, on the other hand, use purely climate variables for estimating ε . Thus, the comparison of the two approaches becomes very meaningful in identifying the intensity of anthropologic activities.

Catchment YW2 is in the upstream region of Yellow River basin, receiving inflows from two tributaries—Huang River and Tao River. Due to intense agricultural activities, water use in Huang River is over 50% of the total streamflow [13]. Moreover, water-diversion projects take some 20% of flow in Datong River (the main tributary of Huang River) and deliver it to Qinwangchuan River in another province [14].

Catchment YW3 is the middle reach of Yellow River basin, receiving flows from 17 tributaries. The section of the Loess Plateau in the middle reach of Yellow River basin produces large volumes of sediments, the major driver of flooding in the downstream regions of the river. This calls for more water/soil conservation efforts such as reservoir construction and loss sediment control in the region [15]. There are some 2184 reservoirs in this section of the river [16]. Such large amount of reservoirs heavily regulates the streamflow in the middle reach and results in low streamflow sensitivity to precipitation.

Catchment YT1 is the upstream region of Jinsha River, an upstream tributary of Yangtze River. Previous studies showed that precipitation in the headwater regions of the three rivers greatly influences change in streamflow in the upstream region of Jinsha River [10]. The weak correlation between streamflow and precipitation in YT1 was because the average precipitation was only for the local catchments.

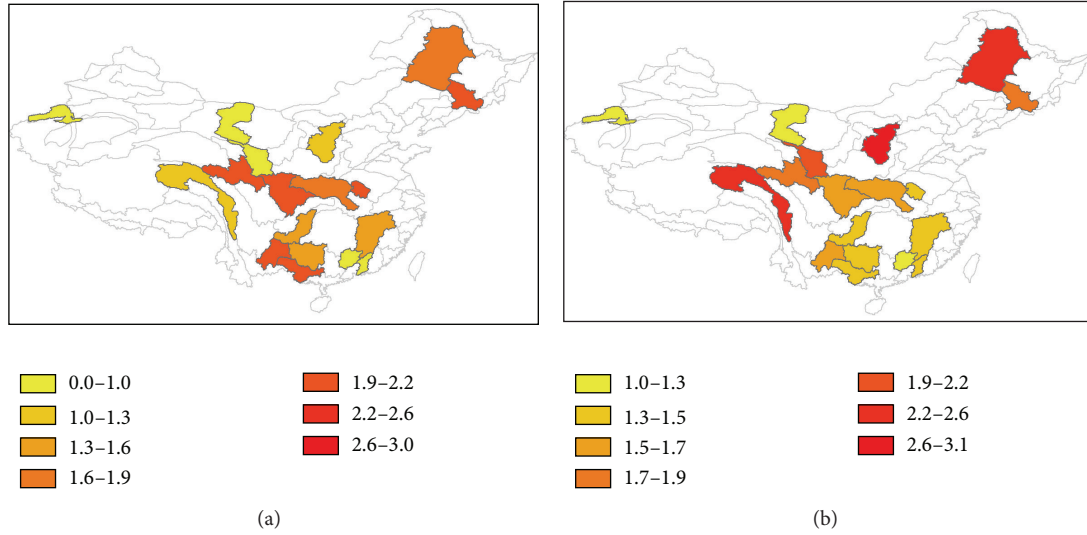


FIGURE 2: Comparison of precipitation elasticity of streamflow between nonparametric approach (a) and Budyko framework approach (b).

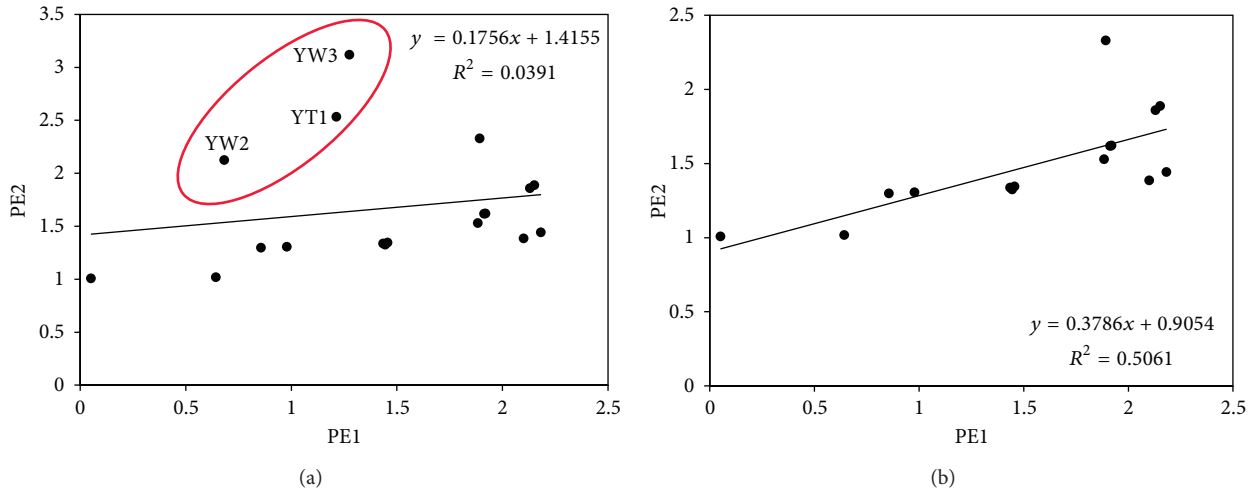


FIGURE 3: Comparison of precipitation elasticity of streamflow between nonparametric approach (PE1) with Budyko framework approach (PE2). The plot on the left is for all the catchments and the one on the right excludes three catchments in the red circle in the left plate.

There was virtually no correlation between PE1 and PE2 (Figure 3), probably due to the large deviations for YW2, YW3, and YT1 catchments. After removing these three catchments, the coefficient of determination improved to 0.5. Because PE1 includes the combined effects of anthropogenic and climatic factors, the attribution analysis was limited to this approach.

3.2. Nonparametric Estimated Elasticity. Figure 4 showed how PE1 corresponds with AI, with that for the two inland catchments depicted in the inset plot of the figure. Interestingly, PE1 increased with increasing AI for humid catchments ($AI < 1.5$) while it largely decreased with increasing AI for arid catchments ($AI > 1.5$). It was assumed that PE1 for arid catchments differed from that for humid catchments. However, hierarchical cluster analysis showed strong similarity in arid and humid catchments in terms of streamflow sensitivity to precipitation.

Compared with natural conditions, the study suggested that streamflow in arid catchments was lower and less sensitive to precipitation. This was attributed to intensive water use due mainly to rapid expansion in population, industry, and agriculture in the country. For instance, there is intensive surface water and groundwater use in Yellow River basin (YW1, YW2, and YW3) and Songliao River basin (SL1 and SL2), limiting streamflow and worsening water shortage in the basins. The generally limited water resources in the arid north of China are not conducive for the rapidly expanding population, industry, and agriculture.

PE1 was lowest for Hei and Aksu inland catchments, probably due to low sensitivity of flow to precipitation in the catchments. According to Wang et al. [17], precipitation counts for 55%, groundwater 35%, and snowmelt 10% of streamflow in Hei catchment. This study suggested limited annual streamflow variation in Hei catchment, driven largely by groundwater and snowmelt. Like in Hei catchment,

TABLE 3: Comparison of estimated elasticity in the literature with estimated elasticity in this study by the nonparametric approach.

Catchment	Country	Period	Elasticity	Reference
MDB	Australia	1950–2006	2.14	Fu et al., 2011 [29]
Spokane	USA	1940–2000	1.38–1.65	Fu et al., 2011 [29]
Yellow River	China	1960–2000	1.76	Fu et al., 2011 [29]
1337 catchments	USA	1951–1988	1.5–2.5	Sankarasubramanian and Vogel, 2003 [7]
219 catchments	Australia	25–93 years	2.0–3.5	Chiew, 2006 [5]
521 catchments	Globe	23–64 years	0.4–3.1	Chiew et al., 2006 [19]
Yellow River (headwater)	China	1960–2000	2.1	Zheng et al., 2009 [6]
Han River	Korea	1973–2006	1.5–2.0	Kim et al., 2013 [30]
Nakdong River	Korea	1973–2006	0.7–1.5	Kim et al., 2013 [30]
Geum River	Korea	1973–2006	1.0–2.0	Kim et al., 2013 [30]
Seomjin River	Korea	1973–2006	1.2–1.5	Kim et al., 2013 [30]
Yeongsan River	Korea	1973–2006	1.6–1.7	Kim et al., 2013 [30]
Yangtze River	China	1955–2009	1.2–1.9	This study
Yellow River	China	1955–2009	0.7–2.1	This study
Pearl River	China	1955–2009	0.8–2.1	This study
Huai River	China	1955–2009	2.2	This study
Songliao	China	1955–2009	1.9–2.2	This study
Hei River	China	1955–2009	0.6	This study
Aksu	China	1955–2009	0.05	This study

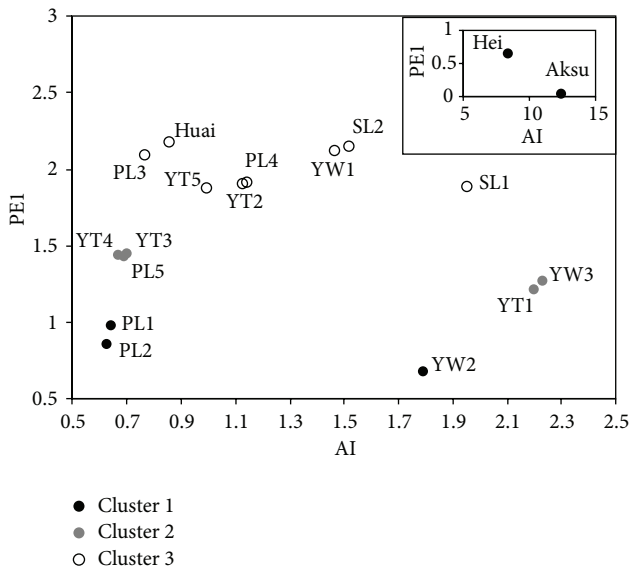


FIGURE 4: Correspondence of elasticity estimated by nonparametric approach (PEI) with aridity index. The hierarchical cluster analysis yielded three derivatives of precipitation streamflow elasticity—cluster 1 denoted by shaded black circle, cluster 2 denoted by shaded grey circle, and cluster 3 denoted by unshaded circle. The inset plate is the precipitation elasticity of streamflow for Hei and Aksu inland catchments in China.

snowmelt in Aksu catchment accounts for over 40% of the total streamflow [18]. Figure 5 further clarifies this point, depicting a weak correlation between precipitation and streamflow in both Hei and Aksu catchments.

Boxplots showed the variations (by way of 7 basins) in PEI, precipitation, streamflow, and PET for the 18 catchments (Figure 6). While there was large PEI for Yellow River basin, the variations in meteorological factors and streamflow were small. This further explained the wide discrepancies in the intensity of anthropologic activities in the basin. While variations in meteorological factors and streamflow were high in Yangtze River basin, those in PEI were minimal. This suggested that water resources in Yangtze River basin were generally sufficient for anthropologic needs. Variations in all the estimated variables were relatively minimal for Pearl River basin, also suggesting rich water resources conditions in the basin. The lower precipitation, higher PET, and similar PEI for Songliao River basin suggested stronger anthropologic activities in that basin than in Huai River basin. The lowest PEI was for the two inland catchments—Songliao and Huai River basins.

3.3. *Elasticity for China and Other Countries.* Using the nonparametric precipitation elasticity of streamflow, the hydroclimatic characteristics of the main catchments in the world were summarized in Table 3. The comparison in Table 3 further deepens our understanding of the characteristics of the hydrologic cycle, precipitation elasticity of streamflow, and water available in the world’s major catchments.

For 1337 catchments in USA, ϵ range is 1.5–2.5 [7] and that for 219 catchments in Australia is 2.0–3.5 [5]. Also ϵ is notably higher for arid than for humid catchments. The global range of ϵ is estimated at 0.4–3.1, with high values for southeastern Australia and southern/western Africa and low values for mid-/high-latitude Northern Hemisphere [19].

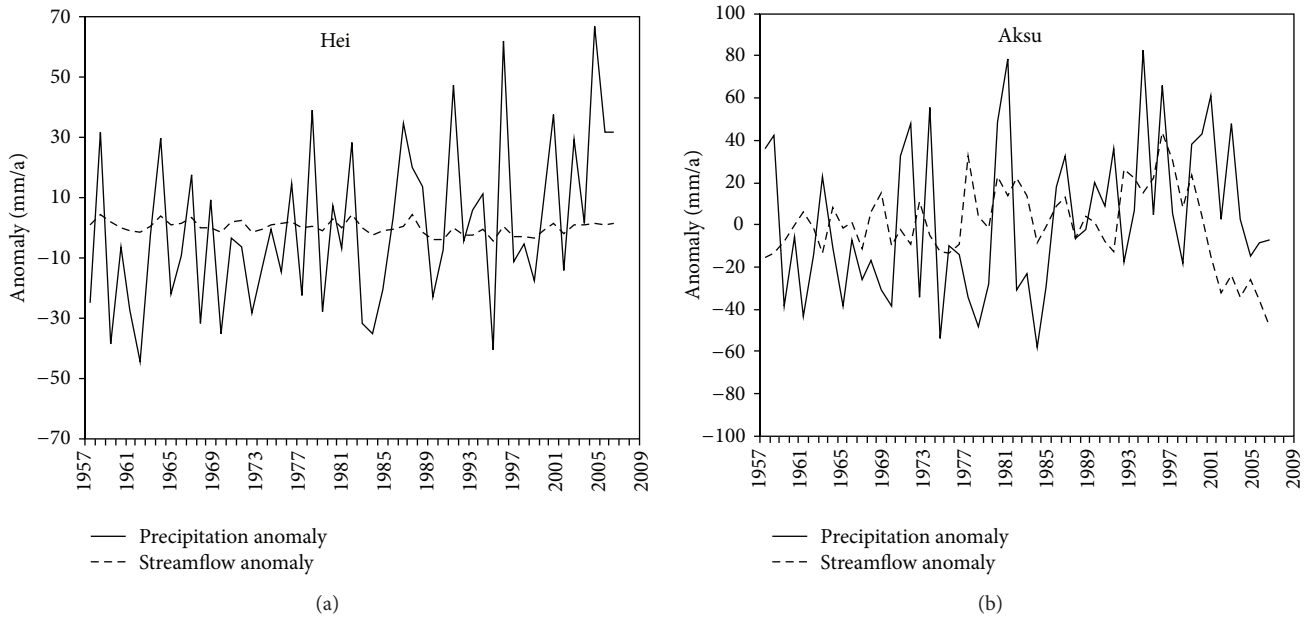


FIGURE 5: Precipitation and streamflow anomalies (1957–2009) for Hei and Aksu inland catchments in China.

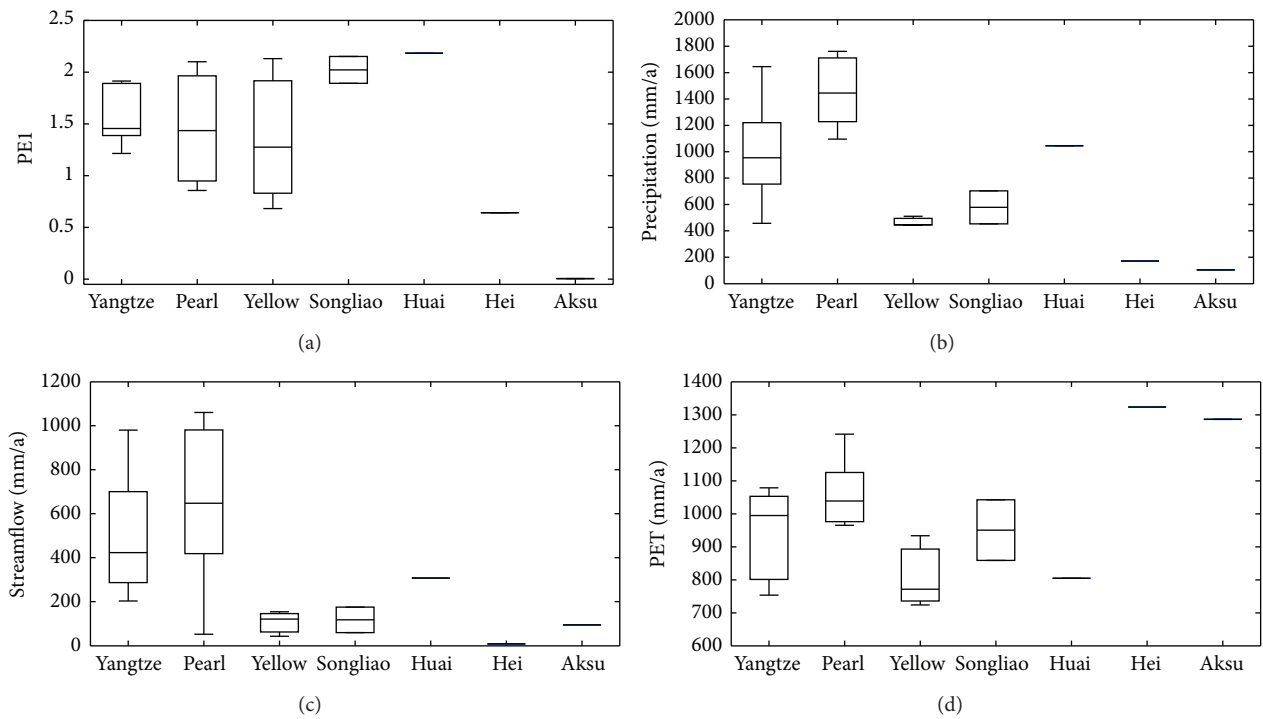


FIGURE 6: Boxplots of elasticity estimated by the nonparametric approach (PEI) for precipitation, streamflow, and potential evapotranspiration (PET) for seven main basins in China.

4. Conclusions

This study used two different approaches (nonparametric and Budyko framework) to estimate precipitation elasticity of streamflow in seven main basins in China. Both the two approaches were driven by long-term (1955–2009) meteorological and streamflow data from 18 large catchments in China.

The results showed that the two approaches were generally consistent, both showing higher elasticity for dry than for wet catchments. The disparities between the two approaches were explained as the differences in the effects of anthropologic activities on streamflow in the investigated catchments. While the nonparametric estimator was positively correlated with AI for wet catchments ($AI < 1.5$), it was negatively correlated with AI for wet catchments ($AI > 1.5$). There were large variations in elasticity for Yellow River catchments along with minimal variations in meteorological and streamflow characteristics, suggesting varying intensities of anthropologic activities.

The study suggested that the Budyko-framework was particularly good for quantifying the effects of natural factors on precipitation elasticity of streamflow. Then the nonparametric approach was particularly fit for quantifying the effects of both anthropologic and natural factors on precipitation elasticity of streamflow. Generally, the discrepancies between the two approaches identified the effects of anthropologic activities on precipitation elasticity of streamflow. Compared with precipitation elasticity of streamflow in catchments in similar latitude zones, rivers in China were less sensitive to precipitation due to heavy anthropologic activities.

Conflict of Interests

The authors declare that there is no conflict of interests regarding the publication of this paper.

References

- [1] G. H. Leavesley, "Modeling the effects of climate change on water resources—a review," *Climatic Change*, vol. 28, no. 1-2, pp. 159–177, 1994.
- [2] A. Sankarasubramanian, R. M. Vogel, and J. F. Limbrunner, "Climate elasticity of streamflow in the United States," *Water Resources Research*, vol. 37, no. 6, pp. 1771–1781, 2001.
- [3] L. L. Nash and P. H. Gleick, "Sensitivity of streamflow in the Colorado Basin to climatic changes," *Journal of Hydrology*, vol. 125, no. 3-4, pp. 221–241, 1991.
- [4] J. C. Schaake, "From climate to flow," in *Climate Change and U.S. Water Resources*, P. E. Waggoner, Ed., chapter 8, pp. 177–206, John Wiley & Sons, New York, NY, USA, 1990.
- [5] F. H. S. Chiew, "Estimation of rainfall elasticity of streamflow in Australia," *Hydrological Sciences Journal*, vol. 51, no. 4, pp. 613–625, 2006.
- [6] H. Zheng, L. Zhang, R. Zhu, C. Liu, Y. Sato, and Y. Fukushima, "Responses of streamflow to climate and land surface change in the headwaters of the Yellow River Basin," *Water Resources Research*, vol. 45, no. 7, Article ID W00A19, 2009.
- [7] A. Sankarasubramanian and R. M. Vogel, "Hydroclimatology of the continental United States," *Geophysical Research Letters*, vol. 30, no. 7, article 1363, 2003.
- [8] G. Fu, S. P. Charles, and F. H. S. Chiew, "A two-parameter climate elasticity of streamflow index to assess climate change effects on annual streamflow," *Water Resources Research*, vol. 43, no. 11, Article ID W11419, 2007.
- [9] H. Li, Y. Zhang, J. Vaze, and B. Wang, "Separating effects of vegetation change and climate variability using hydrological modelling and sensitivity-based approaches," *Journal of Hydrology*, vol. 420-421, pp. 403–418, 2012.
- [10] Q. Zhang, C.-Y. Xu, S. Becker, and T. Jiang, "Sediment and runoff changes in the Yangtze River basin during past 50 years," *Journal of Hydrology*, vol. 331, no. 3-4, pp. 511–523, 2006.
- [11] G. Zhao, X. Mu, A. Strehmel, and P. Tian, "Temporal variation of streamflow, sediment load and their relationship in the Yellow River Basin, China," *PLoS ONE*, vol. 9, no. 3, Article ID e91048, 2014.
- [12] Y. Zhang, C. Liu, Y. Tang, and Y. Yang, "Trends in pan evaporation and reference and actual evapotranspiration across the Tibetan Plateau," *Journal of Geophysical Research D: Atmospheres*, vol. 112, no. 12, Article ID D12110, 2007.
- [13] L. Bing, Q. Shao, and J. Liu, "Runoff characteristics in flood and dry seasons based on wavelet analysis in the source regions of the Yangtze and Yellow rivers," *Journal of Geographical Sciences*, vol. 22, no. 2, pp. 261–272, 2012.
- [14] S. Zhang, D. Hua, X. Meng, and Y. Zhang, "Climate change and its driving effect on the runoff in the 'Three-River Headwaters' region," *Journal of Geographical Sciences*, vol. 21, no. 6, pp. 963–978, 2011.
- [15] Z.-B. Xin and X.-X. Yu, "Impact of vegetation restoration on hydrological processes in the middle reaches of the Yellow River, China," *Forestry Studies in China*, vol. 11, no. 4, pp. 209–218, 2009.
- [16] The Ministry of Water Resources of the People's Republic of China, *China Water Statistical Yearbook: Completed Reservoirs by Grade-I Water Resources Regions*, The Ministry of Water Resources of the People's Republic of China, Beijing, China, 1989.
- [17] J. Wang, H. Li, and X. Hao, "Responses of snowmelt runoff to climatic change in an inland river basin, Northwestern China, over the past 50 years," *Hydrology and Earth System Sciences*, vol. 14, no. 10, pp. 1979–1987, 2010.
- [18] X. Gao, B. S. Ye, S. Q. Zhang, C. J. Qiao, and X. W. Zhang, "Glacier runoff variation and its influence on river runoff during 1961–2006 in the Tarim River Basin, China," *Science China Earth Sciences*, vol. 53, no. 6, pp. 880–891, 2010.
- [19] F. H. S. Chiew, M. C. Peel, T. A. McMahon, and L. W. Siriwardena, "Precipitation elasticity of streamflow in catchments across the world," in *Climate Variability and Change—Hydrological Impacts*, Publication Number 308, pp. 256–262, International Association of Hydrological Sciences, IAHS Press, Wallingford, UK, 2006.
- [20] Y. Wang, T. Jiang, O. Bothe, and K. Fraedrich, "Changes of pan evaporation and reference evapotranspiration in the Yangtze River basin," *Theoretical and Applied Climatology*, vol. 90, no. 1-2, pp. 13–23, 2007.
- [21] C. Liu, D. Zhang, X. Liu, and C. Zhao, "Spatial and temporal change in the potential evapotranspiration sensitivity to meteorological factors in China (1960–2007)," *Journal of Geographical Sciences*, vol. 22, no. 1, pp. 3–14, 2012.

- [22] B. Liu, M. Xu, M. Henderson, and W. Gong, "A spatial analysis of pan evaporation trends in China, 1955–2000," *Journal of Geophysical Research D: Atmospheres*, vol. 109, no. 15, Article ID D15102, 2004.
- [23] P. Schreiber, "Über die Beziehungen zwischen dem Niederschlag und der Wasserführung der Flüsse in Mitteleuropa," *Zeitschrift für Meteorologie*, vol. 21, no. 10, pp. 441–452, 1904.
- [24] E. M. Oldekop, "On evaporation from the surface of river basins," *Transactions on Meteorological Observations*, vol. 4, 1911.
- [25] M. I. Budyko, *The Heat Balance of the Earth's Surface*, U.S. Department of Commerce, Washington, DC, USA, 1958, Translated from Russian by N. A. Stepanova.
- [26] J. G. Pike, "The estimation of annual run-off from meteorological data in a tropical climate," *Journal of Hydrology*, vol. 2, no. 2, pp. 116–123, 1964.
- [27] B. P. Fu, "On the calculation of the evaporation from land surface," *Scientia Meteorologica Sinica*, vol. 5, pp. 23–31, 1981 (Chinese).
- [28] L. Zhang, W. R. Dawes, and G. R. Walker, "Response of mean annual evapotranspiration to vegetation changes at catchment scale," *Water Resources Research*, vol. 37, no. 3, pp. 701–708, 2001.
- [29] G. Fu, F. H. S. Chiew, S. P. Charles, and F. Mpelasoka, "Assessing precipitation elasticity of streamflow based on the strength of the precipitation-streamflow relationship," in *Proceedings of the 19th International Congress on Modelling and Simulation*, pp. 3567–3572, Perth, Australia, December 2011.
- [30] B. S. Kim, S. J. Hong, and H. D. Lee, "The potential effects of climate change on streamflow in rivers basin of Korea using rainfall elasticity," *Environmental Engineering Research*, vol. 18, no. 1, pp. 9–20, 2013.

Research Article

Interpolation of Missing Precipitation Data Using Kernel Estimations for Hydrologic Modeling

Hyojin Lee¹ and Kwangmin Kang²

¹APEC Climate Center, 12 Centum 7-ro, Haeundae-gu, Busan 612-020, Republic of Korea

²School of Agriculture and Natural Science, University of Maryland, College Park, MD 20742, USA

Correspondence should be addressed to Kwangmin Kang; hbkangkm@gmail.com

Received 17 October 2014; Revised 15 January 2015; Accepted 5 February 2015

Academic Editor: Fubao Sun

Copyright © 2015 H. Lee and K. Kang. This is an open access article distributed under the Creative Commons Attribution License, which permits unrestricted use, distribution, and reproduction in any medium, provided the original work is properly cited.

Precipitation is the main factor that drives hydrologic modeling; therefore, missing precipitation data can cause malfunctions in hydrologic modeling. Although interpolation of missing precipitation data is recognized as an important research topic, only a few methods follow a regression approach. In this study, daily precipitation data were interpolated using five different kernel functions, namely, Epanechnikov, Quartic, Triweight, Tricube, and Cosine, to estimate missing precipitation data. This study also presents an assessment that compares estimation of missing precipitation data through K th nearest neighborhood (KNN) regression to the five different kernel estimations and their performance in simulating streamflow using the Soil Water Assessment Tool (SWAT) hydrologic model. The results show that the kernel approaches provide higher quality interpolation of precipitation data compared with the KNN regression approach, in terms of both statistical data assessment and hydrologic modeling performance.

1. Introduction

Precipitation data are key factors in hydrologic modeling for estimating rainfall-runoff mechanism [1]. Malfunctions in running hydrologic modeling can occur due to non-continuous time series precipitation inputs. In light of this important issue, estimation of missing precipitation data is a challenging task for hydrologic modeling. Many hydrologic modeling require interpolation of missing precipitation data [2], meteorological data series completion [3], or imputation of meteorological data [4]. To estimate missing precipitation, researchers should consider spatiotemporal variations in precipitation (rainfall and snowfall) values and the related physical processes. However, accounting for spatial-temporal variation and physical processes can be difficult if there is a lack of equipment for measuring precipitation. Thus, statistical approaches have emerged as widely used methods for filling in missing precipitation data [5].

Many studies have investigated supplanting missing streamflow data with several statistical approaches [5], but there are limited studies on the interpolation of incomplete precipitation and temperature data [6–10]. Recently,

the investigation of artificial neural networks (ANNs: [11]), a more advanced statistical approach, to estimate missing precipitation data, has been proposed [12]. ANNs can learn from training data to reconstruct a nonlinear relationship and obtain values for missing data. Pisoni et al. [13] investigated the interpolation of missing data for sea surface temperature (SST) satellite images using the ANN method; they found that the results from the ANN approach show better accuracy than the results from an interpolation system, as suggested by Seze and Desbois (1987). Nevertheless, ANNs are still under dispute because their neuron systems cannot provide clear relationships between data [14].

The American Society of Civil Engineers (ASCE) Task Committee [15] discussed that although the performance of ANNs for estimating missing precipitation data has already been verified, an alternate solution should be suggested for cases in which the available data are insufficient due to the reliance of ANNs on high data quality and quantity. Additionally, ANNs have other limitations, such as a lack of physical concepts and relations, based on the experience and preferences of those using, studying, and training the networks [15–17]. Since ANNs are regarded as black-box

model [18], it is difficult to use this method for realizing more linear relationships, even though ANNs can achieve convergence for almost any problem [17]. Thus, for real mechanisms in hydrologic models, in which linear relationships exist between series of weather inputs, the solution is less explicit [19].

Generally, a regression or a distance weighted method is most commonly used for estimating missing precipitation for hydrologic modeling [20]. Daly et al. [21] also propose a variety of regression models to incorporate spatial variation in weather data. However, Creutin et al. [22] found that even though simple linear regression of interpolation approaches show satisfactory serial correlation of daily or monthly streamflow; precipitation patterns do not show proper correlation when simple linear regression or interpolation approaches are used. Furthermore, if a regression method is used for estimating missing precipitation to make refined precipitation time series, a small data sample would not follow the normal distribution based on basic theory of linear regression.

Another approach for estimating missing precipitation data to use neighboring data is based on distance weight. Xia et al. [23] used the closest station to reconstruct missing precipitation data through geometrical distance weight; Willmott et al. [24] used arithmetic data averaging from neighboring data to filling missing precipitation; and Teegavarapu and Chandramouli [25] used an inverse distance weight method from neighboring data to estimate missing precipitation data. Smith [26], Simanton and Osborn [27], and Salas [28] suggest that traditional weighting and data-driven methods, namely, distance based weighting methods, are interpolated for estimating missing precipitation data. Distance weight approaches for estimating missing precipitation data are combined with linear regression and median distribution of regression [29, 30]. Young [31] and Filippini et al. [32] suggested spatially interpolating the correlation to define weight in terms of each station.

Estimation of missing precipitation data is possible when data are available for the same location. Linacre (1992) investigated the interpolation of missing precipitation data by using the mean value of a data series at the same location and Lowry [33] suggested simple interpolation between available data series. Acock and Pachepsky [34] used data from several days before and after missing precipitation data points for estimating the incomplete precipitation data. *K*-nearest neighborhood (*knn*) regression is a basic method for estimating missing precipitation data that considers vicinity. However, the method has some weaknesses when the data have outliers or a nonlinear trend exists around the missing data. While *knn* regression has a fundamental assumption to follow a normal distribution which is statistically unsound, the kernel method uses a mean value, which can overcome *knn* regression's weakness through the kernel weighting method. By using neighbor data in a kernel function, even though the data show a nonlinear trend, it can overcome *knn* regression weakness.

The objective of this study was to reconstruct daily precipitation data by using five different kernel functions (Epanechnikov, Quartic, Triweight, Tricube, and Cosine) to

estimate missing precipitation data. This study also presents an assessment that compares estimation of missing precipitation data through *knn* regression to the five different kernel estimations and their performance in simulating streamflow using the Soil Water Assessment Tool (SWAT) hydrologic model. The remainder of this paper is organized as follows. Section 2 provides a description of the study area and the hydrologic model. In Section 3, the methodology of the five different kernel methods is presented. Section 4 presents the results of the interpolation of the missing daily precipitation data and the hydrologic model simulation. Finally, conclusions are in Section 5.

2. Study Area and Hydrologic Model

The Imha (Figure 1) watershed was selected as the test bed for this study. The Imha watershed is a tributary of the Nakdong River basin and is located in the upper side of the Nakdong River basin in South Korea. It is characterized by a mountainous area; approximately 79.8% of the total area of 1,361 km² is mountainous. The slope in the Imha watershed is 40% to 60%, that is, 655 km² as 33% of total watershed area. The elevation of the Imha watershed ranges from 80 to 1215 m. The average annual precipitation, minimum temperature, maximum temperature, humidity, and wind speed for the Imha watershed are 1,050 mm, 7°C, 18.8°C, 65%, and 1.6 m/s, respectively (Water Management Information System (WAMIS), <http://www.wamis.go.kr/>). Since the climate conditions in this area are defined by warm temperatures, there is no precipitation in the form of snow; all precipitation consists of rainfall. For this evaluation of interpolation of precipitation data and hydrologic model performance, precipitation and streamflow gauges were selected as shown in Figure 1 and precipitation and streamflow data were sourced from the Water Management Information System (<http://www.wamis.go.kr/>).

This study selected the SWAT model for analysis. SWAT has a GIS extension, ArcSWAT, which allows the use of various GIS based datasets to model the geomorphology of a given basin. The SWAT model was developed through research by the USDA (United States Department of Agriculture), Agricultural Research Service (ARS). Major data inputs for SWAT include temperature (maximum and minimum), daily precipitation, solar radiation, relative humidity, wind speed, and geospatial data representing soil types, land cover, and elevation. A watershed is divided into smaller subbasins, which must be broken up into smaller units known as hydrologic response units (HRU). Each of these HRUs is characterized by uniform land use and soil type. SWAT can be used to accurately predict hydrologic patterns for extended periods of time [35]. Canopy interception is implicit in the curve number (CN) method and is explicit for the Green-Ampt method. Infiltration is most accurately accounted for using the CN method in SWAT. An alternative method may be used to account for infiltration is the Green-Ampt method. However, the Green-Ampt method has not been shown to increase accuracy over the CN method, thus the CN method was used in this study.

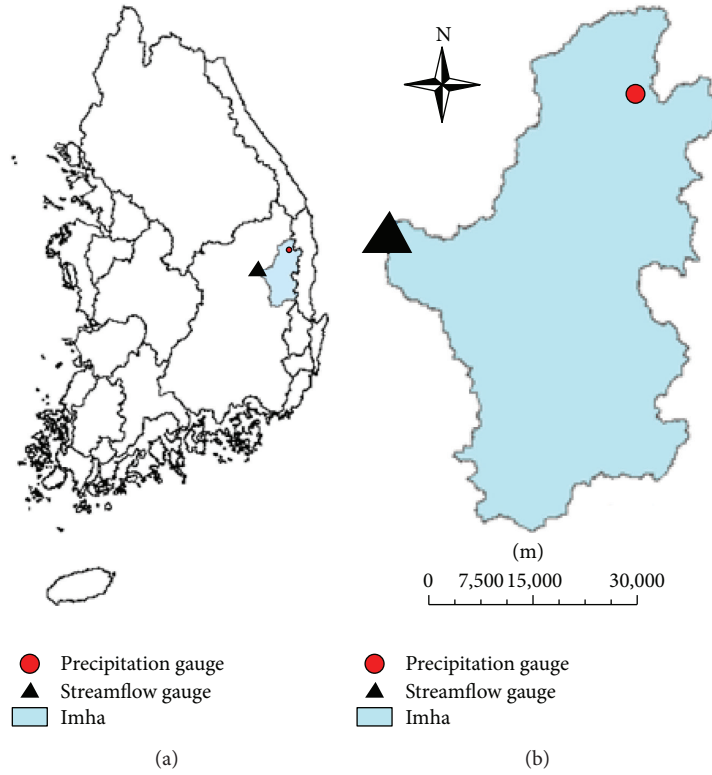


FIGURE 1: Study basin locations including rain and stream gauges (left figure: map of South Korea; right figure: Imha watershed).

3. Methodology

This study used the five kernel functions, Epanechnikov, Quartic, Triweight, Tricube, and Cosine, as a weight to predict missing values. Tricube method has large weight around target point. Even though Tricube weight is similar to Triweight, the decreasing acceleration of weight as far away from target point is less than Triweight. Next higher weight around target point is Quartic, which speed in decreasing weight is similar to Triweight. Both Epanechnikov and Cosine have small effect on neighboring values. A brief description of the five kernel functions and their application for reconstructing the missing values is presented in the following and specific kernel functions are described in Appendix A.

3.1. Epanechnikov. The Epanechnikov kernel is the most often used kernel function. The Epanechnikov kernel assigns zero weight to observations that are a distance of four, six, and eight away from the reference point. These values correspond to the choice of the interval width. This is often called the choice of smoothing parameter or band width selection. The main character of the Epanechnikov kernel is that even though the distance is far away from target value, namely, the missing value in this research, its estimation is smooth. A brief description is given by the following:

$$K(x) = \frac{3}{4}(1 - x^2), \quad (1)$$

where $K(x)$ is the kernel function and x is surrounding the nearest value as an independent in data.

3.2. Quartic. The second kernel function used in this research was the Quartic kernel which has more weight sensitivity based on distance from the missing value. Since the applied weight is largely different between near and far data points, it is more influenced by surrounding data. It consists of a fourth-order equation which has more sensitivity in terms of distance than second-order equation. It is described by the following:

$$K(x) = \frac{15}{16}(1 - x^2)^2. \quad (2)$$

3.3. Triweight. The third kernel function used in this research was the Triweight kernel which consists of a sixth-order equation. It has the most sensitivity in terms of distance because a sixth-order equation estimates the missing value based on the difference in distance with a weighted function as shown by the following:

$$K(x) = \frac{35}{32}(1 - x^2)^3. \quad (3)$$

3.4. Tricube. The fourth kernel function used in this research was the Tricube kernel, which uses absolute values. Since it uses absolute values, it presents a smoother pattern for nearest values than the Triweight kernel. However, as

TABLE 1: Results of normality test with Shapiro-Wilk method for each K -nearest neighborhood. DF represents degree of freedom and P value means significance probability.

	4-NN			6-NN			8-NN		
	W	DF	P value	W	DF	P value	W	DF	P value
Ep	0.808	19	0.0015	0.740	19	0.0002	0.766	19	0.0004
Qu	0.831	19	0.0033	0.768	19	0.0004	0.721	19	0.0001
Tw	0.827	19	0.0029	0.789	19	0.0008	0.745	19	0.0002
Tc	0.839	19	0.0045	0.764	19	0.0004	0.742	19	0.0002
Co	0.817	19	0.0020	0.742	19	0.0002	0.763	19	0.0003
Reg	0.876	19	0.0186	0.858	19	0.0089	0.883	19	0.0242

(Ep: Epanechnikov, Qu: Quartic, Tw: Triweight, Tc: Tricube, Co: Cosine, and Reg: regression).

the values move further away from the nearest values, it shows a steep trend. The Tricube kernel has the most sensitivity in terms of weighted distance due to the fact that it consists of a ninth-order equation, as shown in the following:

$$K(x) = \frac{70}{81} (1 - |x|^3)^3. \quad (4)$$

3.5. *Cosine.* The fifth kernel function used in this research was the Cosine kernel function. It is a widely applied kernel function in various fields because it has a constant curvature. Its shape is similar to the Epanechnikov kernel, even though it uses a cosine function as shown in the following:

$$K(x) = \frac{\pi}{4} \cos\left(\frac{\pi}{2}x\right). \quad (5)$$

3.6. *Calculation of the Missing Value.* After using a kernel function to calculate the weight of the missing data, estimation of the missing data is performed using the following:

$$M = \frac{1}{P} \sum_{i=1}^P x_i \cdot K(u_i),$$

$$u_i = \frac{N_i}{0.5P + 1}, \quad (6)$$

$$N_i = -\frac{P}{2}, \dots, \frac{P}{2},$$

where M is the missing value, P is the number of the nearest neighborhood, and u_i is the N th nearest values which correspond to x_i (positive means the right side and negative means the left side). The kernel function should have bilateral symmetry based on a value of zero. If using, for example, the four nearest neighborhoods for estimating the missing value, the neighborhood values used will be two from right side and another two from left side. The specific equation for this example is shown in the following and example calculation is described in Appendix B:

$$M = \frac{1}{4} \left\{ K\left(-\frac{2}{3}\right) \cdot x_1 + K\left(-\frac{1}{3}\right) \cdot x_2 + K\left(\frac{1}{3}\right) \cdot x_3 + K\left(\frac{2}{3}\right) \cdot x_4 \right\}. \quad (7)$$

3.7. *Statistic Tests.* A normality test is required to evaluate for infilling the methods for filling in interpolation data. The Shapiro-Wilk [36] normality test was used with nineteen samples to determine whether the average difference is normally distributed or not. The test statistic is as shown in the following:

$$W = \frac{(\sum_{i=1}^n a_i y_i)^2}{\sum_{i=1}^n (y_i - \bar{y})^2}, \quad (8)$$

where y_i is the i th order statistic, namely, the i th smallest value in the sample, \bar{y} is the mean of y_i , and a_i is a constant given by ordered data. The null hypothesis of the Shapiro-Wilk normality test is that sample is normally distributed, and if significance probability is less than 5%, the null hypothesis will be denied, meaning the sample does not satisfy normal distribution. Since the significance probability for the entire group (Table 1) is below 5%, the null hypothesis is denied. This study should, therefore, use a nonparametric test for normality analysis.

The Friedman test [37], which is a kind of k -sample test that can provide the difference between paired values, was selected as a nonparametric test. This method evaluates a small sample for differences by ranking a sequence list. The null hypothesis of the Friedman test is that there is no average difference in each group and if the significance probability is less than 5%, the null hypothesis will be denied, thus conducting that in each group exists an average difference. A brief description of Friedman test is in the following:

$$Q = \frac{SS_t}{SS_e}, \quad (9)$$

where SS_t and SS_e are the sum of the squared treatment and sum of the squared error, respectively.

The null hypothesis in this instance was denied because the significance probability was less than 5% for each and this study concluded that each interpolation method has an average difference, which is why each method is considered independent, even though this study used five different kernel methods. For example, the average rank for four reference points for k nn-regression, Tricube, Quartic, Cosine, Triweight, and Epanechnikov varies from a large average to a small average rank (Table 2). For six reference points,

TABLE 2: Chi-square (X^2) test with Friedman method for finding difference among six infilling methods. SD represents standard deviation. P value means significance probability.

(a) 4-NN								
	N	Mean	SD	Min.	Max. value	Mean rank	X^2	P value
Ep	19	-1.29	4.46	-15.50	5.76	2.53	55.602	0.0000
Qu	19	-1.42	5.03	-15.06	7.51	2.74		
Tw	19	-1.64	5.37	-14.90	8.13	2.58		
Tc	19	-1.18	5.06	-14.87	8.29	4.47		
Co	19	-1.40	4.69	-15.42	6.08	2.68		
Reg	19	2.76	5.42	-13.47	14.38	6.00		
(b) 6-NN								
	N	Mean	SD	Min.	Max. value	Mean rank	X^2	P value
Ep	19	-2.61	4.72	-16.68	1.58	1.53	66.519	0.0000
Qu	19	-2.27	4.71	-16.20	2.82	3.16		
Tw	19	-2.18	4.84	-15.89	4.06	3.79		
Tc	19	-2.15	4.63	-16.20	2.84	4.21		
Co	19	-2.54	4.69	-16.59	1.50	2.32		
Reg	19	0.06	4.97	-15.48	7.33	6.00		
(c) 8-NN								
	N	Mean	SD	Min.	Max. value	Mean rank	X^2	P value
Ep	19	-3.40	5.04	-17.33	1.94	1.32	75.812	0.0000
Qu	19	-3.10	4.75	-16.90	0.45	3.21		
Tw	19	-2.74	4.79	-16.59	1.29	4.58		
Tc	19	-2.93	4.77	-16.96	1.51	3.68		
Co	19	-3.28	4.93	-17.25	1.85	2.21		
Reg	19	-1.24	5.35	-16.49	8.08	6.00		

(Ep: Epanechnikov, Qu: Quartic, Tw: Triweight, Tc: Tricube, Co: Cosine, and Reg: regression).

the knn -regression, Tricube, Triweight, Quartic, Cosine, and Epanechnikov were ranked as shown in Table 2. In another example, eight reference points used knn -regression, Triweight, Quartic, Cosine, and Epanechnikov average rank (Table 2). As shown in Table 2, the knn -regression has the largest average rank and Epanechnikov has the smallest rank average for all of the reference point cases. This result proves the dissimilarity of these methods.

To determine which methods are dissimilar to the others, this study performed the Wilcoxon signed rank test [38]. The basic feature of the Wilcoxon signed rank test is that data samples that come from the same population are paired and it is detailed in the following:

$$W = \left| \sum_{i=1}^N [\text{sign}(y_{2,i} - y_{1,i}) R_i] \right|, \quad (10)$$

where N is the sample size, $y_{2,i}$ is i th value of the second data point, $y_{1,i}$ is i th value of the first data point, and R_i is the rank of $|y_{2,i} - y_{1,i}|$. If the W value is less than 5%, it means there is different mechanism used on the sample data or method. Table 3 shows that the W value for knn -regression is less than 5% for all cases. Accordingly, this signifies that knn -regression is completely dissimilar to the other methods. Although the five different kernel methods for

data interpolation exhibit similarity or dissimilarity to each other depending on the number of reference points, all of the kernel methods can be distinguished from knn -regression using the Wilcoxon signed rank test.

4. Results

Since Epanechnikov has the smallest average rank, which signifies a small difference between the observation value and the interpolated value for all reference points in Table 2, interpolation data obtained from the Epanechnikov method has the best result among the studied methods. Figure 2 shows that filling in data from knn -regression has a large difference at both four and six reference points. Interpolation data from the kernel methods are close to zero for both the average and median values at four reference points, meaning that the interpolation data are similar to the observation data. On the other hand, more than 75% of the interpolation data from knn -regression exhibits a difference than zero. When the interpolation data are evaluated at six reference points in Figure 2, the median value from the knn -regression is shown to be far away from zero. At eight reference points, knn -regression is close to zero for both average and median values; however, it is difficult to conclude that this is an ideal method

TABLE 3: Chi-square (X^2) test with Wilcoxon signed rank method between regression and five different kernel methods.

		(a) 4-NN				
		Ep	Qu	Tw	Tc	Co
Reg	X^2	-3.823	-3.823	-3.823	-3.823	-3.823
	P value	0.0001	0.0001	0.0001	0.0001	0.0001
		(b) 6-NN				
		Ep	Qu	Tw	Tc	Co
Reg	X^2	-3.823	-3.823	-3.823	-3.823	-3.823
	P value	0.0001	0.0001	0.0001	0.0001	0.0001
		(c) 8-NN				
		Ep	Qu	Tw	Tc	Co
Reg	X^2	-3.823	-3.823	-3.823	-3.823	-3.823
	P value	0.0001	0.0001	0.0001	0.0001	0.0001

(Ep: Epanechnikov, Qu: Quartic, Tw: Triweight, Tc: Tricube, Co: Cosine, and Reg: regression).

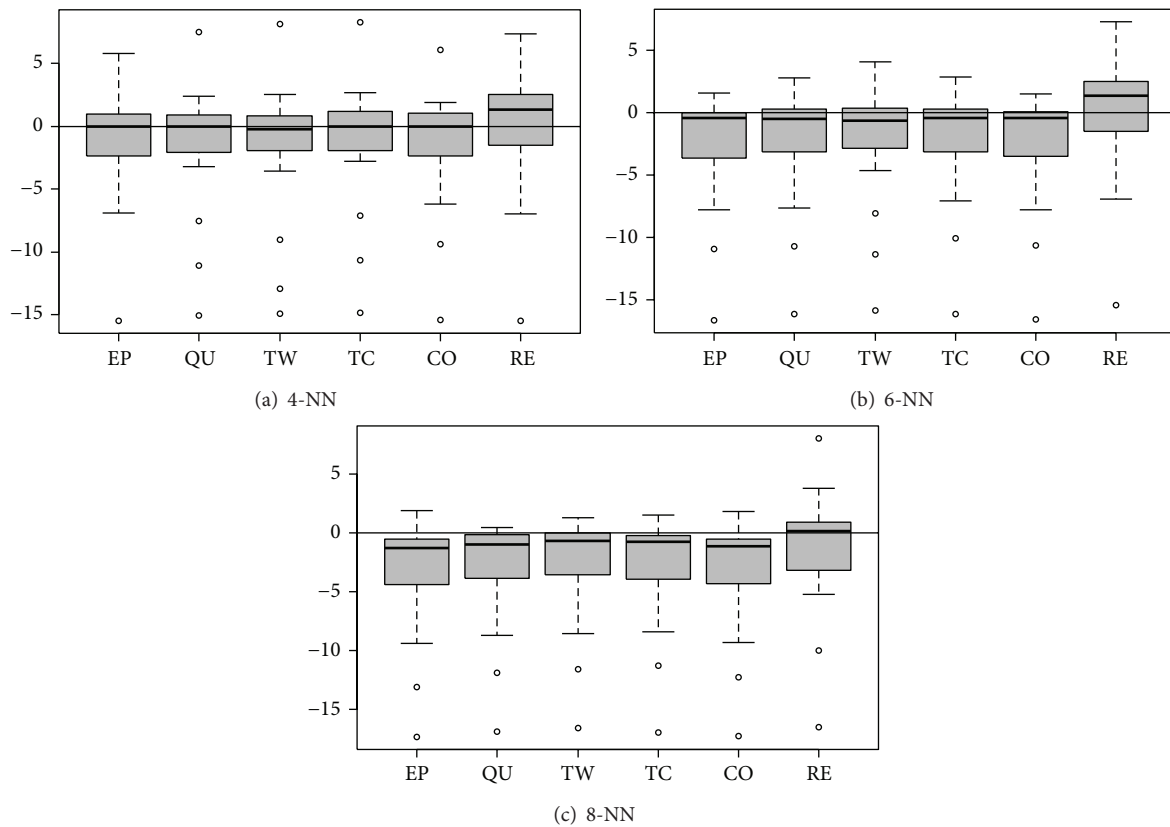


FIGURE 2: Box plots for difference between actual precipitation and interpolated precipitation. y -axis represents mm per day.

because outlying maximum values will affect the average and median value.

This study on precipitation data interpolation also evaluated the simulation of the interpolated data using the SWAT hydrologic model. In SWAT hydrologic modeling, the surface runoff is estimated by considering excess precipitation with abstractions and infiltration factor through Soil Conservation Service Curve Number (SCS-CN) method.

Green-Ampt (GA) infiltration method is another method to calculate the surface runoff in SWAT. A study shows that both methods give reasonable results, and there is no significant advantage observed in using one over the other. However, the GA method appears to have more limitations in modeling seasonal variability than the SCS-CN method does. Hence, the SCS-CN method is used for infiltration factor in this study. An SCS curve number based simulation needs

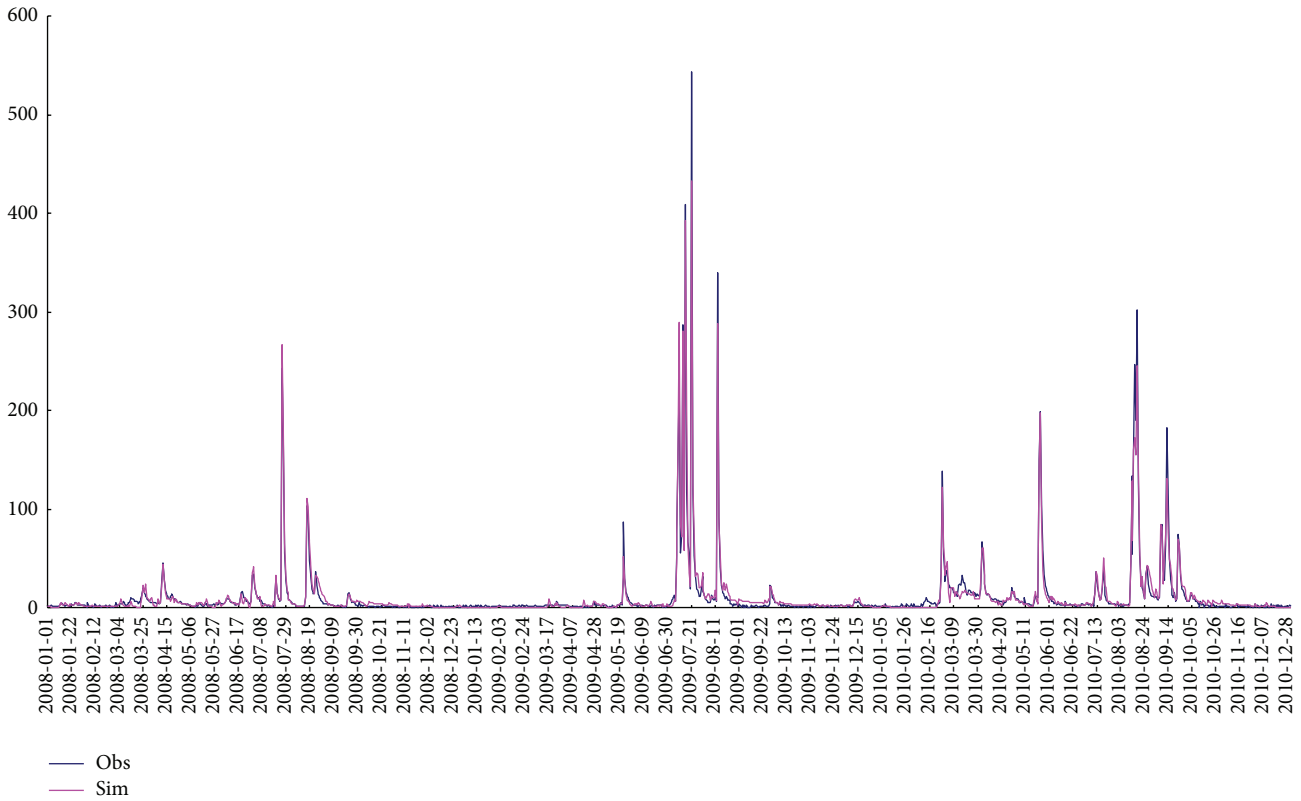


FIGURE 3: Calibrated model result using original precipitation input. *x*-axis represents time in days and *y*-axis represents flow in cubic meters per second.

TABLE 4: Details of SWAT parameters which are related to runoff mechanism for Imha watershed.

Parameter	Description	Selected value
ESCO	Soil evaporation compensation factor	0.9500
EPCO	Plant water uptake compensation factor	1.0000
EVLAI	Leaf area index at which no evaporation occurs from water surface [m ² /m ²]	3.0000
FFCB	Initial soil water storage expressed as a fraction of field capacity water content	0.0000
IEVENT	Rainfall/runoff code: 0 = daily rainfall/CN	0.0000
ICRK	Crack flow code: 1 = model crack flow in soil	0.0000
SURLAG	Surface runoff lag time [days]	4.0000
ADJ_PKR	Peak rate adjustment factor for sediment routing in the subbasin (tributary channels)	0.0000
PRF	Peak rate adjustment factor for sediment routing in the main channel	1.0000
SPCON	Linear parameter for calculating the maximum amount of sediment that can be reentrained during channel sediment	0.0001
SPEXP	Exponent parameter for calculating sediment reentrained in channel sediment routing	1.0000

time step updated information as soil water content changes. Excess rainfall equation in SCS-CN method was generated based on historical relationship between the curve number and the hydrologic mechanism for over 20 years. Throughout the surface runoff calculation, infiltration should be updated over time according to the soil type. Other abstractions such as evapotranspiration and soil and snow evaporation are calculated by Penman-Monteith method and

meteorological statistics. Finally, the kinematic storage model is used to compute groundwater storage and seepage. Flow resulting in SWAT modeling is routed HRUs to watershed outlet. Figure 3 shows the calibration of the model simulation as the initial step and the specific parameters are described in Table 4. After the calibration of the SWAT model, the six different interpolated precipitation datasets, with three different reference ranges for each (a total of twenty-four

TABLE 5: Details of simulation results with six different precipitation infilling methods in Imha watershed.

	4-NN			6-NN			8-NN		
	E_{NS}	R^2	RMSE	E_{NS}	R^2	RMSE	E_{NS}	R^2	RMSE
Ep	0.80	0.83	15.32	0.91	0.92	10.60	0.78	0.82	16.16
Qu	0.73	0.78	17.83	0.91	0.93	10.48	0.88	0.92	11.80
Tw	0.91	0.91	10.56	0.93	0.94	9.25	0.95	0.95	8.10
Tc	0.95	0.95	7.72	0.93	0.94	9.03	0.95	0.95	7.64
Co	0.93	0.94	8.83	0.95	0.95	7.72	0.91	0.93	10.44
Reg	0.69	0.80	19.14	0.21	0.65	30.71	0.71	0.73	21.48

interpolated precipitations data points), were used to assess the performance of interpolated precipitation data for hydrologic model simulation. Streamflow simulations were done for three years from 2008 to 2010. To evaluate the model performance considering the use of different interpolated precipitation datasets, this study used E_{NS} (Nash-Sutcliffe coefficient), R -square (coefficient of determination), and RMSE (root mean square error). Table 5 and Figure 4 show that the simulation results from knn -regression exhibit low SWAT simulation performance for streamflow estimations, with $0.54 E_{NS}$, $0.74 R$ -square, and $23.78 \text{ m}^3/\text{s}$ RMSE as an average. All of the kernel functions, on the other hand, exhibit good performance for hydrologic simulations with interpolated precipitation data (Table 5 and Figure 4), the average of E_{NS} , R -square, and RMSE (1) for Epanechnikov is 0.83 , 0.86 , and $14.03 \text{ m}^3/\text{s}$; (2) for Quartic is 0.84 , 0.88 , and $13.03 \text{ m}^3/\text{s}$; (3) for Triweight is 0.93 , 0.93 , and $9.30 \text{ m}^3/\text{s}$; (4) for Tricube is 0.94 , 0.95 , and $8.13 \text{ m}^3/\text{s}$; and (5) for Cosine is 0.93 , 0.94 , and $9.00 \text{ m}^3/\text{s}$, respectively.

5. Conclusions

Five different kernel functions were applied to the Imha watershed to evaluate the performance of each weighted method for estimating missing precipitation data and the use of interpolated data for hydrologic simulations was assessed. The following conclusions can be drawn from this research.

- (1) To estimate missing precipitation data points, exploratory procedures should consider the spatiotemporal variations of precipitation. Due to difficulty on accounting for these variations, statistical methods for estimating missing precipitation data are commonly used.
- (2) Although ANNs are an advanced approach for estimating missing data, mechanisms are unclear because the neuron system is ultimately a black-box model. Thus, regression methods are widely used for estimating missing data, even though there are limitations in that regression methods cannot follow normal distribution when the sample is small.
- (3) When using kernel functions as a weighted method, estimated missing data would satisfy normal distribution which is more statistically sound. Also, kernel methods can overcome weakness in knn -regression if

the data have outliers and/or a nonlinear trend around the missing data points in terms of mean value.

- (4) This study assessed the five kernel functions, Epanechnikov, Quartic, Triweight, Tricube, and Cosine, as a weight for predicting missing values. In comparison with the knn -regression method, this study demonstrates that the kernel approaches provide higher quality interpolated precipitation data than the knn -regression approach. In addition, the kernel function results better conform to statistical standards.
- (5) Furthermore, higher quality of interpolated precipitation data results in better performance for hydrologic simulations, as exemplified in this study. All of the statistical analyses of the streamflow simulations showed that the simulations using the interpolated precipitation data from the kernel functions provide better results than using knn -regression.
- (6) Use of kernel distribution is a more effective method than regression when the precipitation data have an upward or downward trend. However, if the precipitation data have a nonlinear trend, it is difficult to effectively reconstruct the missing values. For further research, a time series analysis or a random walk model using a stochastic process are possible methods by which to estimate missing data where there is a nonlinear trend.

Appendices

A. Kernel Functions

Kernel density estimation is an unsupervised learning procedure, which historically precedes kernel regression. It also leads naturally to a simple family of procedures for nonparametric classification.

A.1. Kernel Density Estimation. Suppose we have a random sample x_1, x_2, \dots, x_N draw from a probability density $f_x(x)$ and we wish to estimate f_x at a point x_0 . For simplicity we assume for now that $x \in R$ (*real value*). Arguing as before, a natural local estimate has the form

$$\hat{f}_x(x_0) = \frac{\#x_i \in N(x_0)}{N\lambda}, \quad (\text{A.1})$$

where $\#x_i$ means number of x_i which converges to $N(x_0)$ and $N(x_0)$ is a small metric neighborhood around x_0 of width λ .

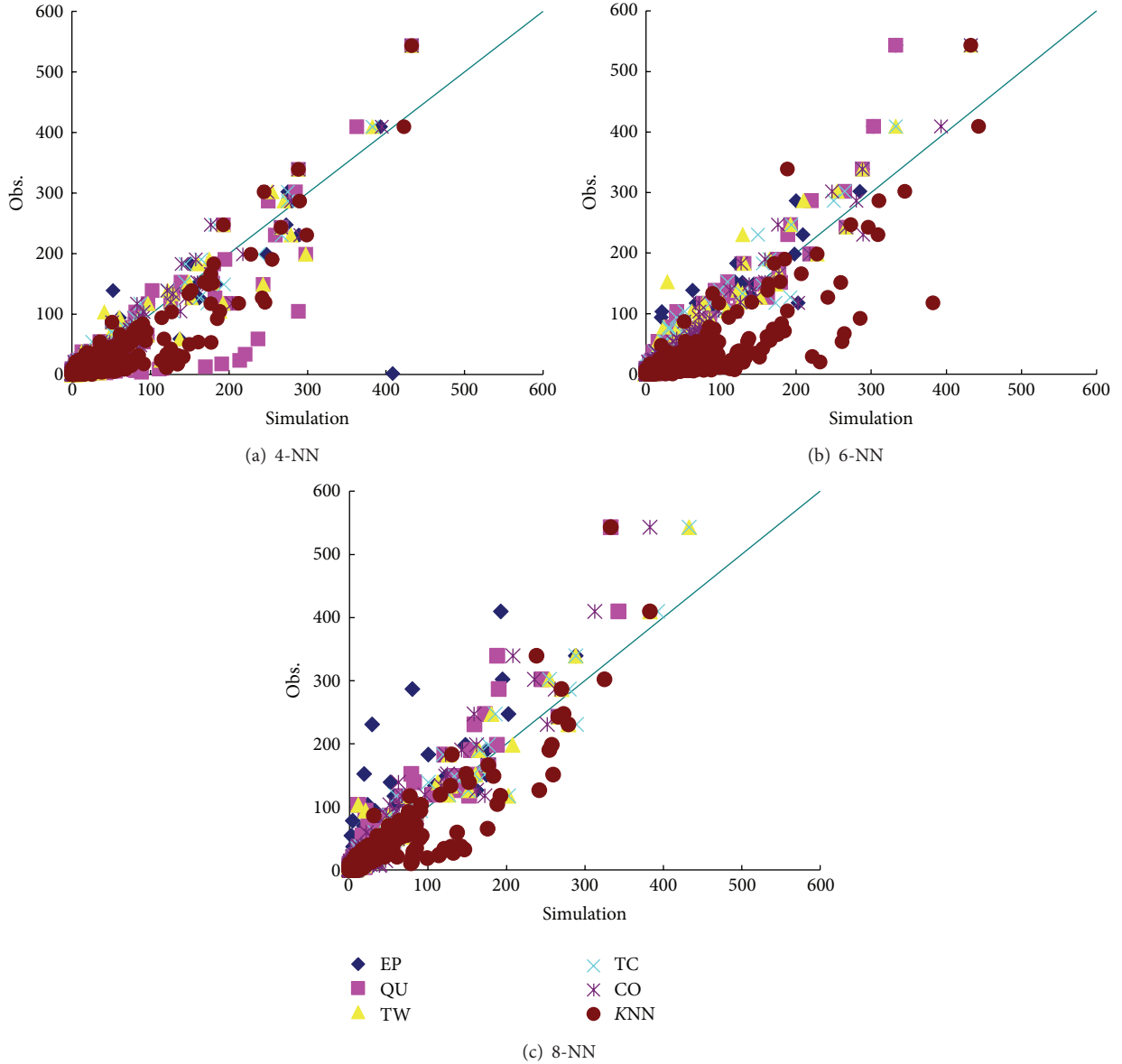


FIGURE 4: Scatter plots for SWAT simulation (EP, QU, TW, TC, CO, and KNN represents Epanechnikov, Quartic, Triweight, Tricube, Cosine, and KNN-regression, resp.).

This estimate is bumpy, and the smooth Parzen estimate is preferred,

$$\hat{f}_x(x_0) = \frac{1}{N\lambda} \sum_{i=1}^N K_\lambda(x_0, x_i), \quad (\text{A.2})$$

because it counts observations close to x_0 with weights that decrease with distance from x_0 . In this case a popular choice for K_λ is the Gaussian kernel $K_\lambda(x_0, x_i) = \phi(|x - x_0|/\lambda)$. Letting ϕ_λ denote the Gaussian density with mean zero and standard-deviation λ , then (A.2) has the form

$$\hat{f}_x(x_0) = \frac{1}{N} \sum_{i=1}^N \phi_\lambda(x - x_i) = (\hat{F} * \phi_\lambda)(x), \quad (\text{A.3})$$

the convolution of the sample empirical distribution \hat{F} with ϕ_λ . The distribution $\hat{F}(x)$ puts mass $1/N$ at each of the observed x_i and is jumpy; in $\hat{f}_x(x)$ we have smoothed \hat{F} by adding independent Gaussian noise to each observation x_i .

The Parzen density estimate is the equivalent of the local average, and improvements have been proposed along the lines of local regression (on the log scale for densities). We will not pursue these here. In R^p the natural generalization of the Gaussian density estimate amounts to using the Gaussian product kernel in (A.3),

$$\hat{f}_x(x_0) = \frac{1}{N(2\lambda^2\pi)^{p/2}} \sum_{i=1}^N e^{-(1/2)(\|x_i - x_0\|/\lambda)^2}. \quad (\text{A.4})$$

TABLE 6: Weighted values depending on day distance with each KNN.

	4-NN		6-NN			8-NN			
	1st	2nd	1st	2nd	3rd	1st	2nd	3rd	4th
Ep	0.667	0.417	0.703	0.563	0.328	0.720	0.630	0.480	0.270
Qu	0.741	0.289	0.824	0.527	0.179	0.864	0.662	0.384	0.122
Tw	0.768	0.188	0.901	0.461	0.092	0.968	0.648	0.287	0.051
Tc	0.772	0.301	0.824	0.579	0.167	0.844	0.709	0.416	0.100
Co	0.680	0.393	0.726	0.555	0.301	0.747	0.635	0.462	0.243

A.2. Kernel Density Classification. One can use nonparametric density estimates for classification in a straight-forward fashion using Bayes' theorem. Suppose for a J class problem we fit nonparametric density estimates $\hat{f}_j(X)$, $j = 1, \dots, J$ separately in each of the classes, and we also have estimates of the class priors $\hat{\pi}_j$ (usually the sample proportions). Then

$$\widehat{\Pr}(G = j | X = x_0) = \frac{\hat{\pi}_j \hat{f}_j(x_0)}{\sum_{k=1}^J \hat{\pi}_k \hat{f}_k(x_0)}. \quad (\text{A.5})$$

In this region the data are sparse for both classes, and since the Gaussian kernel density estimates use matrix kernels, the density estimates are low and of poor quality (high variance) in these regions. The local logistic regression method uses the tricube kernel with k -NN bandwidth; this effectively widens the kernel in this region and makes use of the local linear assumption to smooth out the estimate (on the logit scale).

If classification is the ultimate goal, then learning the separate class densities well may be unnecessary and can in fact be misleading. In learning the separate densities from data, one might decide to settle for a rougher, high-variance fit to capture these features, which are irrelevant for the purposes of estimating the posterior probabilities. In fact, if classification is the ultimate goal, then we need only to estimate the posterior well near the decision boundary (for two classes, this is the set $\{x | \Pr(G = 1 | X = x) = 1/2\}$).

B. Procedures of Missing Precipitation

This step shows example calculation for kernel functions for weighted mean. It is an example question about the weight of each situation. If the kernel functions are all symmetric, same values are used for weight based on day distance. Following Table 6 1st, 2nd, 3rd, and 4th day distance and weighted values are shown. For example, if we want to estimate missing precipitation for 2010-02-12 (actual value is 6), see following procedures (3 steps) with 4-NN Epanechnikov kernel (Table 7).

Step 1. Select the date for target interpolation data.

Step 2. Decide K th nearest days precipitation and each kernel weight.

Step 3. Calculate the weight average to estimate missing.

TABLE 7: Example calculation to interpolate for missing precipitation.

Step 1		Step 2		Step 3
Date	Prec.	Weight	Prec.·Weight	Estimation
2010-02-10	15	0.417	6.255	
2010-02-11	17.2	0.667	11.472	
2010-02-12	6	—	—	5.949
2010-02-13	9.1	0.667	6.070	
2010-02-14	0	0.417	0	

TABLE 8: Calculating missing precipitation for 2010-02-12 (actual value is 6) with six different methods.

Method	4NN	6NN	8NN
Ep	5.949	5.172	4.862
Qu	5.956	5.302	4.936
Tw	5.755	5.294	4.952
Tc	6.205	5.407	4.963
Co	5.945	5.197	4.876
Reg	10.325	8.967	8.813

(Ep: Epanechnikov, Qu: Quartic, Tw: Triweight, Tc: Tricube, Co: Cosine, and Reg: regression).

The rest of the kernel methods for estimating missing precipitation are described in Table 8.

C. Sample Calculations with Real Value

This section shows how to calculate missing precipitation with kernel mean weighed function by using certain number. This sample selected daily data from 2008 to 2010 with 0.02 possibilities to bivariate by random. After selected data, setting data location is operated. Zhang et al. [39] addressed that kernel based nonparametric multiple imputation has better performance than general linear regression when the sample data is small or limited.

Table 9 shows procedure of kernel weight in each function. We used data Feb. 10, 2012 from Feb. 14, 2014 to estimate Feb. 12, 2012 missing data. Epanechnikov kernel showed that longest data has highest estimation as 0.417; however, Triweight kernel showed that longest data has lowest estimation as 0.188. Highest weight in nearest value is Tricube kernel and lowest weight is Epanechnikov kernel. Generally,

TABLE 9: Sample calculation with certain number.

(a) Epanechnikov					
Date	2.10.	2.11.	2.12.	2.13.	2.14.
Prec.	15.0	17.2	6.0	9.1	0.0
Ep. weight	0.417	0.667	—	0.667	0.417
Prec.·weight	6.26	11.47	—	6.07	0.00
Estimation	5.95				
(b) Quartic					
Date	2.10.	2.11.	2.12.	2.13.	2.14.
Prec.	15.0	17.2	6.0	9.1	0.0
Qu. weight	0.289	0.741	—	0.741	0.289
Prec.·weight	4.34	12.75	—	6.74	0.00
Estimation	5.96				
(c) Triweight					
Date	2.10.	2.11.	2.12.	2.13.	2.14.
Prec.	15.0	17.2	6.0	9.1	0.0
Tw. weight	0.188	0.768	—	0.768	0.188
Prec.·weight	2.82	13.21	—	6.99	0.00
Estimation	5.75				
(d) Tricube					
Date	2.10.	2.11.	2.12.	2.13.	2.14.
Prec.	15.0	17.2	6.0	9.1	0.0
Tc. weight	0.301	0.772	—	0.772	0.301
Prec.·weight	4.52	13.28	—	7.03	0.00
Estimation	6.20				
(e) Cosine					
Date	2.10.	2.11.	2.12.	2.13.	2.14.
Prec.	15.0	17.2	6.0	9.1	0.0
Co. weight	0.393	0.680	—	0.680	0.393
Prec.·weight	5.90	11.70	—	6.19	0.00
Estimation	5.94				

Tricube, that is, high weight, shows the overestimation for missing precipitation.

Conflict of Interests

The authors declare that there is no conflict of interests regarding the publication of this paper.

References

- [1] K. Kang and V. Merwade, "Development and application of a storage-release based distributed hydrologic model using GIS," *Journal of Hydrology*, vol. 403, no. 1-2, pp. 1-13, 2011.
- [2] A. J. Abebe, D. P. Solomatine, and R. G. W. Venneker, "Application of adaptive fuzzy rule-based models for reconstruction of missing precipitation events," *Hydrological Sciences Journal*, vol. 45, no. 3, pp. 425-436, 2000.
- [3] P. Ramos-Calzado, J. Gómez-Camacho, F. Pérez-Bernal, and M. F. Pita-López, "A novel approach to precipitation series completion in climatological datasets: application to Andalusia," *International Journal of Climatology*, vol. 28, no. 11, pp. 1525-1534, 2008.
- [4] T. Schneider, "Analysis of incomplete climate data: estimation of mean values and covariance matrices and imputation of missing values," *Journal of Climate*, vol. 14, no. 5, pp. 853-871, 2001.
- [5] S. K. Regonda, D.-J. Seo, B. Lawrence, J. D. Brown, and J. Demargne, "Short-term ensemble stream forecasting using operationally-produced single-valued streamflow forecasts—a Hydrologic Model Output Statistics (HMOS) approach," *Journal of Hydrology*, vol. 497, pp. 80-96, 2013.
- [6] P. Coulibaly and N. D. Evora, "Comparison of neural network methods for infilling missing daily weather records," *Journal of Hydrology*, vol. 341, no. 1-2, pp. 27-41, 2007.
- [7] H. A. El Sharif and R. S. V. Teegavarapu, "Evaluation of spatial interpolation methods for missing precipitation data: preservation of spatial statistics," in *Proceedings of the World Environmental and Water Resources Congress*, pp. 3822-3832, May 2012.
- [8] A. Bárdossy and G. Pegram, "Infilling missing precipitation records—a comparison of a new copula-based method with other techniques," *Journal of Hydrology*, vol. 519, pp. 1162-1170, 2014.
- [9] K. Schamm, M. Ziese, A. Becker et al., "Global gridded precipitation over land: a description of the new GPCP first guess daily product," *Earth System Science Data*, vol. 6, no. 1, pp. 49-60, 2014.
- [10] R. S. V. Teegavarapu, "Statistical corrections of spatially interpolated missing precipitation data estimates," *Hydrological Processes*, vol. 28, no. 11, pp. 3789-3808, 2014.
- [11] Y. Da and G. Xiurun, "An improved PSO-based ANN with simulated annealing technique," *Neurocomputing*, vol. 63, pp. 527-533, 2005.
- [12] A. di Piazza, F. L. Conti, L. V. Noto, F. Viola, and G. La Loggia, "Comparative analysis of different techniques for spatial interpolation of rainfall data to create a serially complete monthly time series of precipitation for Sicily, Italy," *International Journal of Applied Earth Observation and Geoinformation*, vol. 13, no. 3, pp. 396-408, 2011.
- [13] E. Pisoni, F. Pastor, and M. Volta, "Artificial Neural Networks to reconstruct incomplete satellite data: application to the Mediterranean Sea Surface Temperature," *Nonlinear Processes in Geophysics*, vol. 15, no. 1, pp. 61-70, 2008.
- [14] V. Sharma, S. Rai, and A. Dev, "A comprehensive study of artificial neural networks," *International Journal of Advanced Research in Computer Science and Software Engineering*, vol. 2, no. 10, pp. 278-284, 2012.
- [15] ASCE Task Committee, "Artificial neural networks in hydrology. II: hydrologic applications," *Journal of Hydrological Engineering*, vol. 5, no. 2, pp. 124-137, 2000.
- [16] ASCE Task Committee, "Artificial neural networks in hydrology. I: preliminary concepts," *Journal of Hydrological Engineering*, vol. 5, no. 2, pp. 115-123, 2000.
- [17] D. E. Rumelhart, B. Widrow, and M. A. Lehr, "The basic ideas in neural networks," *Communications of the ACM*, vol. 37, no. 3, pp. 87-92, 1994.
- [18] J. Amorocho and W. E. Hart, "A critique of current methods in hydrologic systems investigation," *Transactions of the American Geophysical Union*, vol. 45, no. 2, pp. 307-321, 1964.

- [19] A. W. Minns and M. J. Hall, "Artificial neural networks as rainfall-runoff models," *Hydrological Sciences Journal*, vol. 41, no. 3, pp. 399–417, 1996.
- [20] K. Kang and V. Merwade, "The effect of spatially uniform and non-uniform precipitation bias correction methods on improving NEXRAD rainfall accuracy for distributed hydrologic modeling," *Hydrology Research*, vol. 45, no. 1, pp. 23–42, 2014.
- [21] C. Daly, W. P. Gibson, G. H. Taylor, G. L. Johnson, and P. Pasteris, "A knowledge-based approach to the statistical mapping of climate," *Climate Research*, vol. 22, no. 2, pp. 99–113, 2002.
- [22] J. D. Creutin, H. Andrieu, and D. Faure, "Use of a weather radar for the hydrology of a mountainous area. Part II: radar measurement validation," *Journal of Hydrology*, vol. 193, no. 1–4, pp. 26–44, 1997.
- [23] Y. L. Xia, P. Fabian, A. Stohl, and M. Winterhalter, "Forest climatology: estimation of missing values for Bavaria, Germany," *Agricultural and Forest Meteorology*, vol. 96, no. 1–3, pp. 131–144, 1999.
- [24] C. J. Willmott, S. M. Robeson, and J. J. Feddema, "Estimating continental and terrestrial precipitation averages from rain-gauge networks," *International Journal of Climatology*, vol. 14, no. 4, pp. 403–414, 1994.
- [25] R. S. V. Teegavarapu and V. Chandramouli, "Improved weighting methods, deterministic and stochastic data-driven models for estimation of missing precipitation records," *Journal of Hydrology*, vol. 312, no. 1–4, pp. 191–206, 2005.
- [26] J. A. Smith, "Precipitation," in *Handbook of Hydrology*, D. R. Maidment, Ed., vol. 3, chapter 3, McGraw Hill, New York, NY, USA, 1993.
- [27] J. R. Simanton and H. B. Osborn, "Reciprocal-distance estimate of point rainfall," *Journal of Hydraulic Engineering Division*, vol. 106, no. 7, pp. 1242–1246, 1980.
- [28] J. D.-J. Salas, "Analysis and modeling of hydrological time series," in *Handbook of Hydrology*, D. R. Maidment, Ed., vol. 19, chapter 19, pp. 19.1–19.72, McGraw-Hill, New York, NY, USA, 1993.
- [29] S. J. Jeffrey, J. O. Carter, K. B. Moodie, and A. R. Beswick, "Using spatial interpolation to construct a comprehensive archive of Australian climate data," *Environmental Modelling and Software*, vol. 16, no. 4, pp. 309–330, 2001.
- [30] M. Franklin, V. R. Kotamarthi, M. L. Stein, and D. R. Cook, "Generating data ensembles over a model grid from sparse climate point measurements," *Journal of Physics: Conference Series*, vol. 125, Article ID 012019, 2008.
- [31] K. C. Young, "A three-way model for interpolating for monthly precipitation values," *Monthly Weather Review*, vol. 120, no. 11, pp. 2561–2569, 1992.
- [32] F. Filippini, G. Galliani, and L. Pomi, "The estimation of missing meteorological data in a network of automatic stations," *Transactions on Ecology and the Environment*, vol. 4, pp. 283–291, 1994.
- [33] W. P. Lowry, *Compendium of Lecture Notes in Climatology for Class IV Meteorological Personnel*, Secretariat of the World Meteorological Organization, Geneva, Switzerland, 1972.
- [34] M. C. Acock and Y. A. Pachepsky, "Estimating missing weather data for agricultural simulations using group method of data handling," *Journal of Applied Meteorology*, vol. 39, no. 7, pp. 1176–1184, 2000.
- [35] S. L. Neitsch, J. G. Arnold, J. R. Kiniry, J. R. Williams, and K. W. King, *Soil and Water Assessment Tool—Theoretical Documentation (Version 2005)*, Texas Water Resource Institute, College Station, Tex, USA, 2005.
- [36] S. S. Shapiro and M. B. Wilk, "An analysis of variance test for normality: complete samples," *Biometrika*, vol. 52, no. 3–4, pp. 591–611, 1965.
- [37] M. Friedman, "The use of ranks to avoid the assumption of normality implicit in the analysis of variance," *Journal of the American Statistical Association*, vol. 32, no. 200, pp. 675–701, 1937.
- [38] F. Wilcoxon, "Individual Comparisons by Ranking Methods," *Biometrics Bulletin*, vol. 1, no. 6, pp. 80–83, 1945.
- [39] S. Zhang, Z. Jin, X. Zhu, and J. Zhang, "Missing data analysis: a kernel-based multi-imputation approach," in *Transactions on Computational Science III*, vol. 5300 of *Lecture Notes in Computer Science*, pp. 122–142, Springer, Berlin, Germany, 2009.

Research Article

Effects of Climate Change and Human Activities on Surface Runoff in the Luan River Basin

Sidong Zeng,¹ Chesheng Zhan,² Fubao Sun,² Hong Du,³ and Feiyu Wang²

¹Changjiang Institute of Survey, Planning, Design and Research, Changjiang Water Resources Commission, Wuhan 430010, China

²Key Laboratory of Water Cycle and Related Land Surface Processes, The Institute of Geographic Sciences and Natural Resources Research, CAS, Beijing 100101, China

³College of Chemistry and Materials, South-Central University for Nationalities, Wuhan 430074, China

Correspondence should be addressed to Chesheng Zhan; zhancs@igsrr.ac.cn

Received 28 November 2014; Accepted 4 February 2015

Academic Editor: Hiroyuki Hashiguchi

Copyright © 2015 Sidong Zeng et al. This is an open access article distributed under the Creative Commons Attribution License, which permits unrestricted use, distribution, and reproduction in any medium, provided the original work is properly cited.

Quantifying the effects of climate change and human activities on runoff changes is the focus of climate change and hydrological research. This paper presents an integrated method employing the Budyko-based Fu model, hydrological modeling, and climate elasticity approaches to separate the effects of the two driving factors on surface runoff in the Luan River basin, China. The Budyko-based Fu model and the double mass curve method are used to analyze runoff changes during the period 1958~2009. Then two types of hydrological models (the distributed Soil and Water Assessment Tool model and the lumped SIMHYD model) and seven climate elasticity methods (including a nonparametric method and six Budyko-based methods) are applied to estimate the contributions of climate change and human activities to runoff change. The results show that all quantification methods are effective, and the results obtained by the nine methods are generally consistent. During the study period, the effects of climate change on runoff change accounted for 28.3~46.8% while those of human activities contributed with 53.2~71.7%, indicating that both factors have significant effects on the runoff decline in the basin, and that the effects of human activities are relatively stronger than those of climate change.

1. Introduction

The water cycle is subjected to the dual influences of both climate change and human activities [1]. Climate change, especially the change of rainfall and temperature, will largely determine the future runoff of a basin [2]. Human activities such as land use and cover change (LUCC) [3] and water resources projects [4] will also affect the water resources. Hence, it is important to separate the effects of climate change and human activities on runoff changes in order to identify the leading factors and to develop sustainable water resources management strategies in a changing environment. To date, several studies have been attempted to separate the effects of climate change and human activities. For example, Wang et al. [2] analyzed the effects of climate change and human activities on runoff in two basins in northern China using a monthly water balance model and fixing-changing method and showed that the effects of human activities (accounting

for 65% and 69%, resp.) are stronger than those of climate change (accounting for 35% and 31%, resp.) in the two basins. Zhang et al. [5] concluded that the effects of climate change on annual runoff reduction accounted for about 43% according to the Budyko-based Fu model applied to the Hun-Tai River basin in China. Li et al. [6] found that the land use change effects contributed with about 31~40% to runoff decline when using both hydrological models and sensitivity-based approaches in three catchments in southeast Australia. These studies together show that the effects of climate change and human activities on runoff vary between different basins, and regional analysis of the local-scale effects needs to be considered, particularly for the basins with intensive human activities where more aspects related to hydrological cycle should be considered.

Present studies mainly follow the paradigm of “determining the abrupt change points and baseline period, and then quantifying the effects of climate change and human

activities.” Firstly, statistical methods (e.g., nonparametric tests and time series analysis) and graphical methods (e.g., double mass curve and flow duration curves) are often used to detect the change points of runoff changes [7]. Secondly, the hydrological modeling approach [8, 9] and climate elasticity approach [10, 11] are used to quantify the effects of climate change and human activities on runoff changes. Usually, the hydrological modeling approach is used to measure the effects using physically based distributed hydrological models or lumped conceptual models. The lumped conceptual models are often easier to calibrate and use fewer input datasets, while the distributed hydrological models are difficult to apply to large basins due to their requirement of more detailed inputs. However, the distributed hydrological models could provide more details of the hydrological cycle with respect to different spatial patterns. Compared to the hydrological modeling approach, the climate elasticity approach is another useful method using fewer hydroclimatic datasets; however, climate elasticity methods are usually based on annual means and so provide generalized relationships without considering the underlying surface of a basin [6]. Two common types of climate elasticity approaches are the statistical analysis-based nonparametric method [12] and the Budyko-based analytical derivation method [13, 14]. A comparison of the two types may help to improve and extend the climate elasticity methods. In general, integrating the hydrological modeling and climate elasticity approaches will be better for understanding the complex relationships between climate change, human activities, and the water cycle. Thus, this paper presents an integrated method based on the Budyko-based Fu model, hydrological modeling, and climate elasticity approaches to quantify the effects of climate change and human activities on surface runoff. Moreover, the two approaches (hydrological modeling and climate elasticity methods) are also discussed in terms of the uncertainties and the influencing factors of the quantitative results, whereas few previous studies have conducted these analyses.

The Luan River basin is one of the most vulnerable areas to intensive human activities and climate change in China [15]. It is also the main water source of some big cities in northern China. Fan et al. [16] found that reduced streamflow is mainly an impact of precipitation change. However, Wang and Liu [17] found that the reduced water resources are mainly due to the impacts of human activities, including irrigation and water diversion. The studies found different conclusions, yet quantitative research distinguishing the influences of climate change and human activities on the water cycle in this basin remains scarce. Therefore, we tried to conduct a systemic study on this topic in the basin using long-term datasets covering 1958–2009 and found an efficient and practical approach to separate the effects of climate change and human activities.

The objective of this study is to quantify the influence of climate change and human activities on runoff in the Luan River basin using an integrated method combining a climate elasticity approach (using one nonparametric method and six Budyko-based methods) with a hydrological modeling approach (the Soil and Water Assessment Tool (SWAT) distributed model and SIMHYD lumped model). In addition,

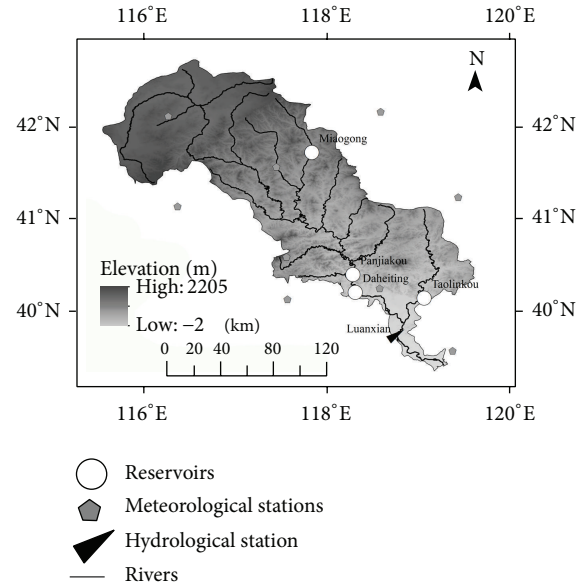


FIGURE 1: Location of the Luan River basin with meteorological and hydrological stations and reservoirs.

the two approaches used for the quantification are also discussed and analyzed. The paper is arranged as follows. Section 2 describes the characteristics of the study basin and data sources used. Section 3 describes the methodology including the Fu model for the abrupt change point detection, the structures of the SIMHYD and SWAT models, the hydrological model calibration and validation, details of the climate elasticity methods, and methodology for separating the effects of climate change and human activities. Results are provided and discussed in Section 4 and conclusions are summarized in Section 5.

2. Study Area and Data

The Luan River basin (LRB), shown in Figure 1, is located in the region 115.5°E~119.3°E, 39.2°N~42.5°N in North China, and covers an area of 44,750 km². The basin lies in the temperate continental monsoon zone with a hot and rainy summer, dry and rainless spring and autumn, and dry and cold winter. From 1958 to 2009 the average annual precipitation was 491 mm and the average annual temperature was 6.9°C. Since the 1980s, several large reservoirs including Miaogong Reservoir, Daheiting Reservoir, Panjiakou Reservoir, and Taolinkou Reservoir were built (Figure 1), and some water diversion projects were also constructed to supply water to Tianjin and Tangshan cities and for irrigation in the Luanxian Irrigation Area.

Data used in this study consist of daily precipitation, maximum and minimum temperature, and sunshine duration at nine meteorological stations from 1958 to 2009 supplied by the China Meteorological Data Sharing Service System. Monthly runoff data covering the same period were obtained for the Luanxian gauge station (Figure 1). The Luanxian gauge station is located in the lower reaches of the basin and

its hydrological characteristics represent the characteristics of the whole basin. Daily potential evapotranspiration data needed for hydrological modeling were calculated by the Hargreaves method [18], which has been validated in this region [19].

The digital geographic information data applied in the distributed hydrological modeling including digital elevation model (DEM) data at 500 m resolution are from the public domain of GTOPO 30 of the American Geological Survey, and the land use and soil type data are from the resources and environment data center of the Chinese Academy of Sciences at 1000 m resolution.

3. Methods

3.1. Detection of the Abrupt Change Point. According to the Budyko [20, 21] hypothesis, there exists a water-heat coupling balance relationship between the water and energy in a basin, for which Fu [22] developed the following equation:

$$\frac{E}{P} = 1 + \frac{E_0}{P} - \left[1 + \left(\frac{E_0}{P} \right)^w \right]^{1/w}, \quad (1)$$

where P , E , and E_0 represent the average annual precipitation, actual evapotranspiration, and potential evapotranspiration, respectively; w is the model parameter, which has little correlation with the area of a certain basin but has a close relationship with the properties of the underlying surface, including the soil infiltration capability, plant-soil relative water demand capability, mean slope of the basin [23], and the runoff coefficient [24]. Also w has a dependency on the climatic properties of the watershed and the interaction between the climate and the hydrological response in a basin [25]. Therefore the parameter w can be used to represent the characteristics of the water cycle in a basin.

This study uses the 5-year moving averages of precipitation and of actual and potential evapotranspiration as the input to (1). In addition, the 5-year average actual evapotranspiration is calculated by the water balance equation based on the presumption that soil water content remains stable within a 5-year period [26]. With the results of w based on (1), the abrupt change point due to the effects of human activities can be identified by the Mann-Kendall test [27, 28].

3.2. Framework of Separating the Effects of Climate Change and Human Activities. In this study, the human activities effects refer to the total influence of land use and cover change and water diversion for irrigation and industrial and domestic usage. The climate change effects refer to the total influence by the precipitation, temperature, or potential evapotranspiration changes. The total changes in mean annual runoff between two periods with different human activities and climate characteristics can be estimated by the following equation:

$$\Delta Q = \overline{Q_{\text{obs}}^{\text{test}}} - \overline{Q_{\text{obs}}^{\text{pre}}}, \quad (2)$$

where ΔQ is the difference in annual average runoff. $\overline{Q_{\text{obs}}^{\text{pre}}}$ and $\overline{Q_{\text{obs}}^{\text{test}}}$ are the mean annual measured runoff during the

pretreatment period and the testing period, respectively; the period is divided by the abrupt change point identified in Section 3.1. For a given catchment, the total runoff change between the two periods can also be described as follows, when considering climate change and human activities as independent variables at the basin scale [2]:

$$\Delta Q = \Delta Q_C + \Delta Q_H, \quad (3)$$

where ΔQ_C is the average runoff change due to the climate change and ΔQ_H is the runoff change due to human activities. Sections 3.3 and 3.4 provide the details for estimating ΔQ_C and ΔQ_H using the hydrological modeling approach and climate elasticity approach, respectively.

3.3. Hydrological Modeling Approach. In view of the uncertainties associated with the model structure, parameter calibration, and scale change, we select two kinds of hydrological models, the SIMHYD lumped model and the SWAT distributed model. The hydrological model is calibrated and validated in the pretreatment period and then used to simulate the hydrological processes in the testing period. The difference between simulated runoff and observed runoff in the testing period is used to quantify the impact of human activities as follows:

$$\Delta Q_H = \overline{Q_{\text{obs}}^{\text{test}}} - \overline{Q_{\text{sim}}^{\text{test}}}, \quad (4)$$

where $\overline{Q_{\text{sim}}^{\text{test}}}$ and $\overline{Q_{\text{obs}}^{\text{test}}}$ are the average simulated and observed annual runoff for the testing period, respectively. The impact of climate change can be quantified via (3).

The SIMHYD model is a lumped hydrological model developed by Chiew et al. [29], which is simple but useful and has been tested in China [30]. In SIMHYD, evapotranspiration is calculated based on the potential evapotranspiration constrained by available soil moisture. Runoff generation is estimated from three sources: infiltration excess runoff, interflow (saturation excess runoff), and base flow. The inputs of this model are the daily precipitation and potential evapotranspiration.

The SWAT model is a management model for large and medium-size basins developed by the American Agricultural Ministry [31]. In this study, the SWAT version 2005 is used. The SCS curve method is adopted to calculate runoff for the daily meteorological data available and the Penman-Monteith Equation is used to calculate the potential evapotranspiration. Similar studies have confirmed the applicability of the SWAT model in the Luan River basin [32]. The inputs to this model include both meteorological datasets and the digital geographic information datasets.

The Shuffled Complex Evolution Method (SCE-UA) [33] is used to calibrate the parameters by maximizing the Nash-Sutcliffe efficiency coefficient (NS) [34] for both models. The NS, relative error (RE), and correlation coefficient (r) are selected as the model performance indicators.

3.4. Climate Elasticity Approach. Schaake [35] firstly employed the climate elasticity method to analyze the sensitivity of runoff to climate change. The runoff elasticity is defined

TABLE 1: Six commonly used forms based on Budyko hypothesis.

	$F(\phi)$	$F'(\phi)$
Schreiber, 1904 [36]	$1 - e^{-\phi}$	$e^{-\phi}$
Oldekop, 1911 [37]	$\phi \tanh(1/\phi)$	$\tanh(1/\phi) - 4/\left[\phi(e^{-1/\phi} + e^{1/\phi})^2\right]$
Budyko, 1948 [20]	$[\phi \tanh(1/\phi)(1 - e^{-\phi})]^{0.5}$	$0.5[\phi \tanh(1/\phi)(1 - e^{-\phi})]^{-0.5} \times$ $[(\tanh(1/\phi) - \text{sech}^2(1/\phi)/\phi)(1 - e^{-\phi}) + \phi \tanh(1/\phi)e^{-\phi}]$
Pike, 1964 [38]	$(1 + \phi^{-2})^{-0.5}$	$1/\left[\phi^3(1 + (1/\phi)^2)^{1.5}\right]$
Fu, 1981 [22]	$1 + \phi - (1 + \phi^\alpha)^{1/\alpha}$	$1 - (1 + \phi^\alpha)^{1/\alpha-1} \phi^{\alpha-1}$
Zhang et al., 2001 [39]	$(1 + w\phi)/(1 + w\phi + 1/\phi)$	$(w + 2w/\phi - 1 + 1/\phi^2)/(1 + w\phi + 1/\phi)^2$

The parameters α and w in the Fu and Zhang method should be calibrated firstly.

as the ratio of the runoff variation rate to the variation rate of a certain climate factor as follows:

$$\varepsilon_X = \frac{\partial Q/Q}{\partial X/X}, \text{ namely: } \frac{\partial Q}{\partial X} = \varepsilon_X \frac{Q}{X}. \quad (5)$$

Based on the assumption that the response of runoff to the climate factors is mainly caused by precipitation and potential evapotranspiration, we can obtain the following equation [10]:

$$\Delta Q_C = \varepsilon_P \frac{Q}{P} \Delta P + \varepsilon_{E_0} \frac{Q}{E_0} \Delta E_0, \quad (6)$$

where ΔP and ΔE_0 are the variation of precipitation and potential evapotranspiration, and ε_P and ε_{E_0} are the runoff elasticity to precipitation and potential evapotranspiration, respectively. By calculating ΔQ_C , the effects of climate change and human activities can be separated. ε_P and ε_{E_0} need to be estimated firstly. Sections 3.4.1 and 3.4.2 describe the nonparametric method and Budyko-based methods to estimate the climate elasticity coefficients.

3.4.1. Nonparametric Method. Sankarasubramanian et al. [12] developed a nonparametric method to estimate ε_P , and the method has been validated in China [40]:

$$\varepsilon_P = \text{median} \left(\frac{(Q_i - \bar{Q})/\bar{Q}}{(P_i - \bar{P})/\bar{P}} \right), \quad (7)$$

where Q_i, P_i are the annual runoff and precipitation and \bar{Q}, \bar{P} are the average annual runoff and precipitation.

3.4.2. Budyko-Based Methods. Based on the water balance equation and the Budyko coupling balance theory, we can obtain the following equation [13, 41]:

$$\varepsilon_P = 1 + \frac{\phi F'(\phi)}{1 - F(\phi)}, \quad \varepsilon_P + \varepsilon_{E_0} = 1, \quad (8)$$

where the aridity index $\phi = E_0/P$ and six commonly used forms of the Budyko hypothesis [13, 42] adopted in this study are showed in Table 1.

4. Results

4.1. Abrupt Change Point Analysis. In this study, the Fu model based on the Budyko hypothesis and the Mann-Kendall (MK) test are used to detect the abrupt change point in the LRB using data covering 1958~2009. First, the values of w in the Fu model are calculated based on (1) using observed precipitation, calculated potential evapotranspiration by Hargreaves method, and actual evapotranspiration obtained from the water balance, as shown in Figure 2(a). The actual evapotranspiration, which is important for the application of (1), should be validated first. The average annual actual evapotranspiration is about 400 mm and shows a slight increasing trend from 1958 to 2009, which is similar to the results obtained by Xu and Yang [43]. Figure 2(a) shows that w varied markedly in the range 2.0 to 4.7 from 1958 to 2009 and then increased abruptly in the late 1990s. The MK test is employed to analyze the change point of the w series. Yue and Wang [44] found that the MK test result is distinct from the influence of time series autocorrelation when the significance level is greater than 95%. Therefore, we analyze the change point after excluding the series autocorrelation. The results show that the change point in w occurred in 1999 (Figure 2(b)). Furthermore, the double mass curve analysis (the curve of the relationship between accumulated annual observed runoff (RA) and precipitation (PA)), which is frequently used to detect hydrological changes caused by human activities [45], is also used to detect whether there is a change point of the water cycle, as shown in Figure 3. The predicted lines (I and II) show the slopes between RA and PA changed in 1999 from 0.194 before 1999 to 0.027 after 1999. Consistent with the results above, we can conclude that the inflection point occurred in 1999; that is, the pretreatment period is 1958–1998 and the testing period is 1999–2009.

In this work, time series analysis is also used to estimate the variation of annual runoff, precipitation, and potential evapotranspiration (PET), as shown in Figure 4. The results show a slight decreasing trend in PET (−0.51) and precipitation (−1.25) and a relatively stronger decreasing trend in runoff (−2.04). In addition, compared with the pretreatment period, the reductions were 62.61 mm, 15.06 mm, and 87.30 mm for precipitation, PET, and runoff, respectively, in the testing period. The corresponding changing ratios were −12.4%, −1.70%, and −84.5% (see Table 2). These values show

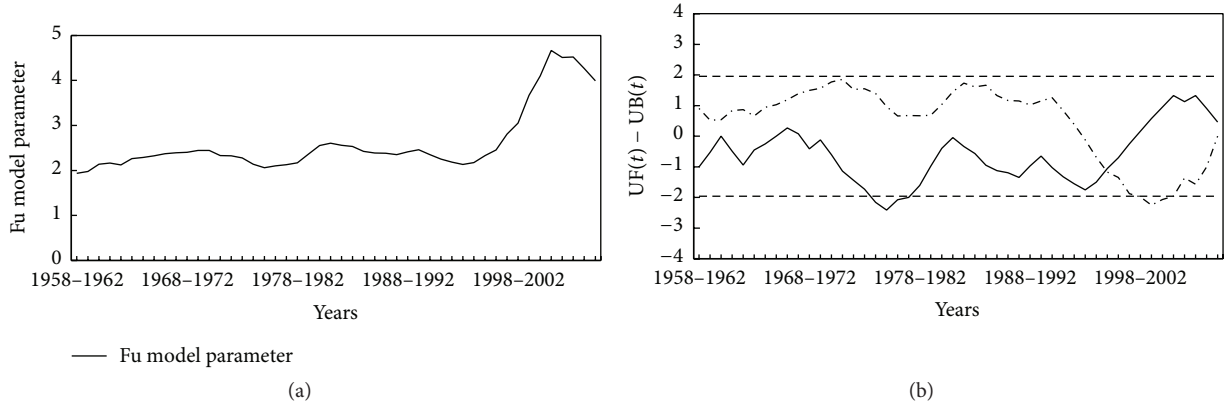


FIGURE 2: Variations of w from 1958 to 2009 (a) and the UF (forward trend-solid line), UB (backward trend-dash dotted line) curves by Mann-Kendall test for w and the 95% confidence level line (dashed horizontal line) (b).

TABLE 2: The Mann-Kendall test statics slope (Z_c) and changes of annual precipitation, potential evapotranspiration (PET), and observed runoff during the pretreatment period and testing period.

	Z_c	Pretreatment period (mm)	Testing period (mm)	Difference (mm)	Ratio (%)
Precipitation	-1.26	504.61	442.00	-62.61	-12.40
PET	-1.79	886.40	871.34	-15.06	-1.70
Observed runoff	-2.29	103.31	16.01	-87.30	-84.50

In a two-side test, when $-Z_{1-\alpha/2} \leq Z_c \leq Z_{1-\alpha/2}$ accepts a null hypothesis, or when $Z_c < -Z_{1-\alpha/2}$ indicates a decreasing trend, and when $Z_c > Z_{1-\alpha/2}$ indicates an increasing trend, α is the significance level. In this study, α is set to be 0.05 and the corresponding value of $Z_{1-\alpha/2}$ is 1.96 [27, 28].

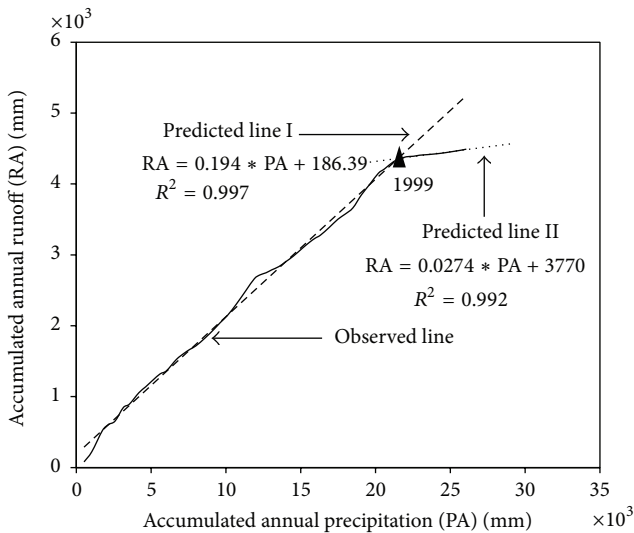


FIGURE 3: Double mass curve of accumulated annual runoff (RA) and accumulated annual precipitation (PA).

that the variation ratio of average annual runoff was much larger than that of precipitation and PET. Table 2 also provides the trend results of annual runoff, precipitation, and PET based on the MK test, which indicate that annual runoff decreased significantly ($\alpha = 0.05$, α is the significance level) with an MK statistics slope of -2.29 , while the annual precipitation and PET showed no significant decreasing trends ($\alpha = 0.05$). The results above suggest that the reduction of

runoff was not caused solely by the reduction in precipitation and PET, so human activities may also have had an important impact on the runoff decline.

4.2. Hydrological Modeling

4.2.1. Model Performance. The SWAT and SIMHYD models are applied to simulate the hydrological processes in the LRB. First, two-thirds of the observed data are used to calibrate the two models and the calibrated parameters are used to simulate the streamflow for the remaining one-third of the observed data in the pretreatment period for model validations. It should be noted that the two hydrological models do not simulate the reservoirs in the calibration and validation for the human activities is limited in this period.

Results of the model calibration and validation at monthly time steps for the two models are shown in Figure 5. In the scatter plots in Figure 5, the observed monthly streamflow is plotted along the x -axis and the simulated streamflow is plotted along the y -axis. Figure 5 shows that both models perform well in model calibration and validation with high Nash-Sutcliffe efficiency coefficient (NS), correlation coefficient (r) values, and low relative error (RE) values, as also shown in Table 3. The calibration NS values are 82% and 85% for the SWAT model and the SIMHYD model, respectively. The RE values are 0.05 and 0.07 for the two models, and the r values are 0.91 and 0.92 in the calibration period. In the validation period, the NS, RE, and r values are 92%, 0.003, and 0.95 for the SWAT model and 90%, 0.02, and 0.96 for the SIMHYD model, respectively.

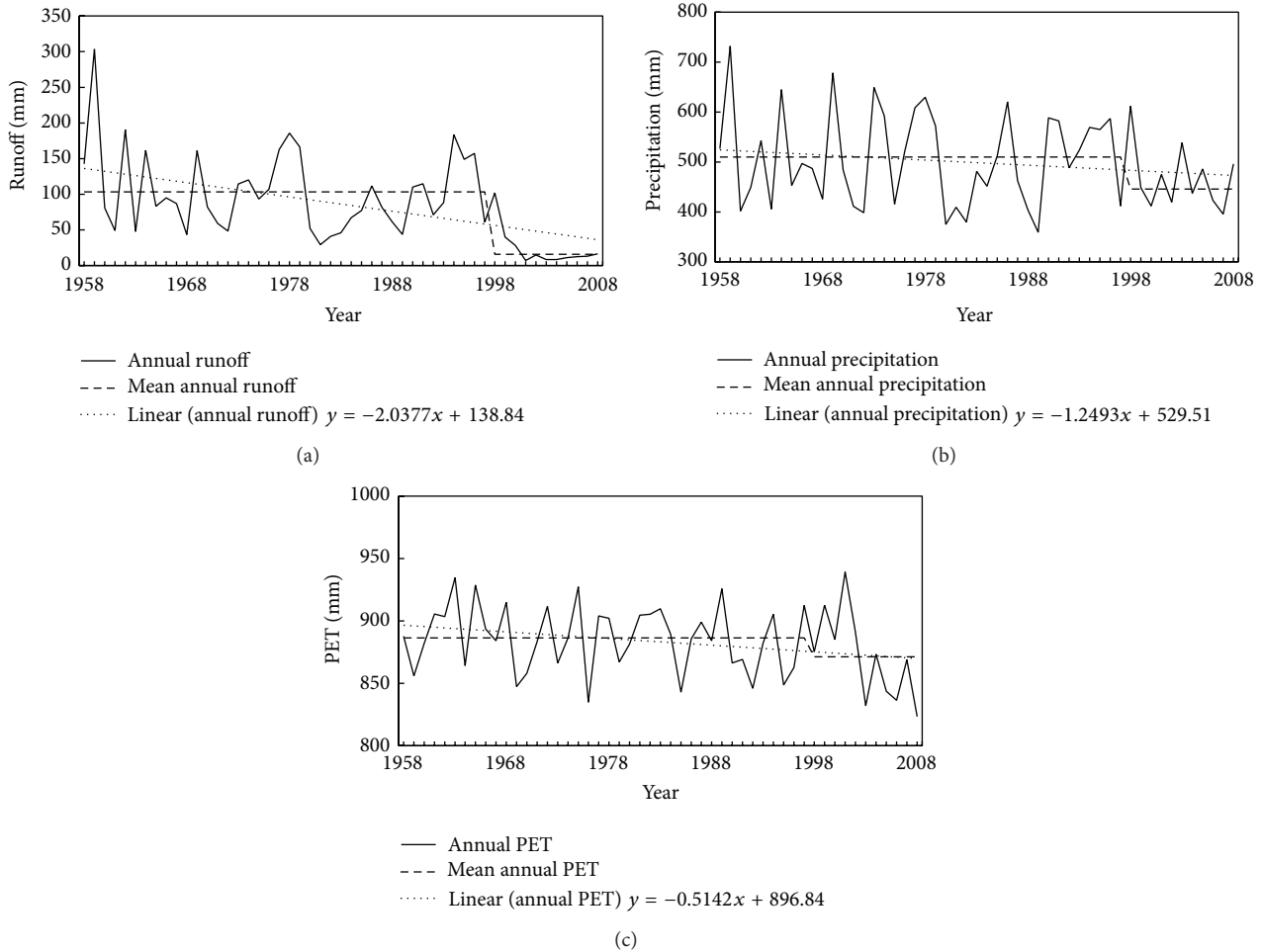


FIGURE 4: Variations of annual runoff (a), precipitation (b), and potential evapotranspiration (PET) (c) before and after inflection point (solid line), the average annual values (dashed line), and the linear trend (dotted line).

TABLE 3: The performance of SWAT model and SIMHYD model.

	Calibration (1958–1985)					Validation (1986–1998)				
	NS	RE	r	AWBE	AWED	NS	RE	r	AWBE	AWED
SWAT	0.82	0.05	0.91	0.05	0.14	0.92	0.003	0.95	0.03	0.02
SIMHYD	0.85	0.07	0.92	0.10	0.08	0.90	0.02	0.96	0.08	0.15

As discussed above, the difference between average annual simulated runoff and observed runoff in the testing period represents the impact of human activities. The water balance error between annual observed runoff and annual simulated runoff (AWBE) will impact the quantitative results. From the statistical results in Table 3, the values of AWBE are 0.05 and 0.10 in the calibration period and 0.03 and 0.08 in the validation period for the SWAT and SIMHYD models, respectively; that is, the errors are acceptable for the two models and they perform well for annual runoff simulation. From Figures 5 and 6, we can see that the simulated streamflow is much greater than the observed streamflow in the testing period. Therefore, it is necessary to examine the water balance error between annual observed runoff and simulated runoff in the dry periods (AWED)

in the pretreatment period. We select the dry years (at a guaranteed rate of 75%) to test the two models. As shown in Table 3, the AWED values are 0.14 and 0.08 in the calibration period and 0.02 and 0.15 in the validation period for the SWAT model and the SIMHYD model, respectively. These results indicate that the two models perform well and there are no systemic errors in the simulation of annual runoff in the dry periods, which can be regarded as a scientific basis for distinguishing the influences of climate change and human activities.

4.3. Quantifying the Effects of Climate Change and Human Activities. The SWAT and SIMHYD models are used to simulate the hydrological processes in the LRB during the testing period, based on the calibrated parameters in

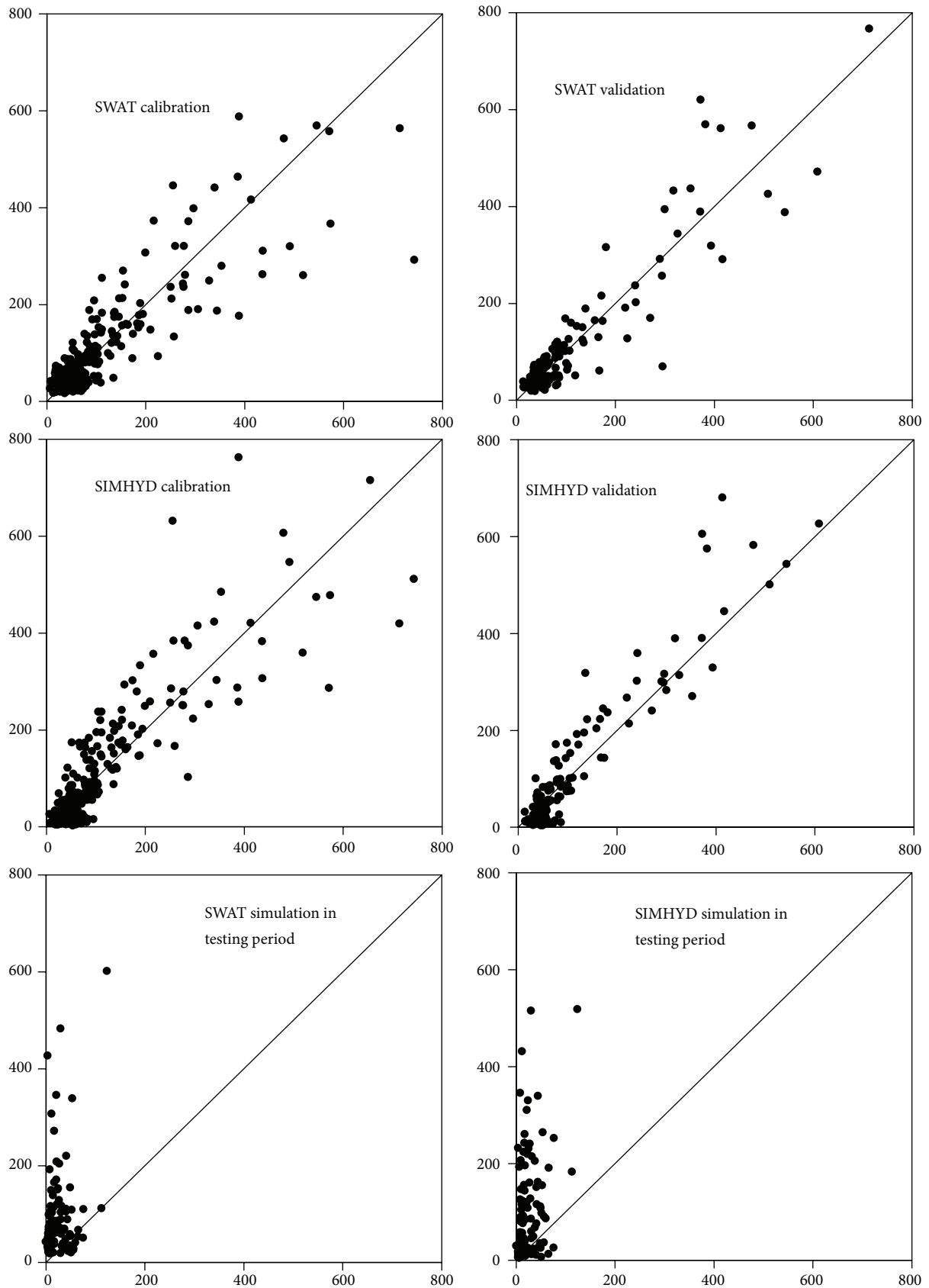


FIGURE 5: Comparison of observed and simulated monthly streamflow in calibration and validation periods and the testing period m^3/s .

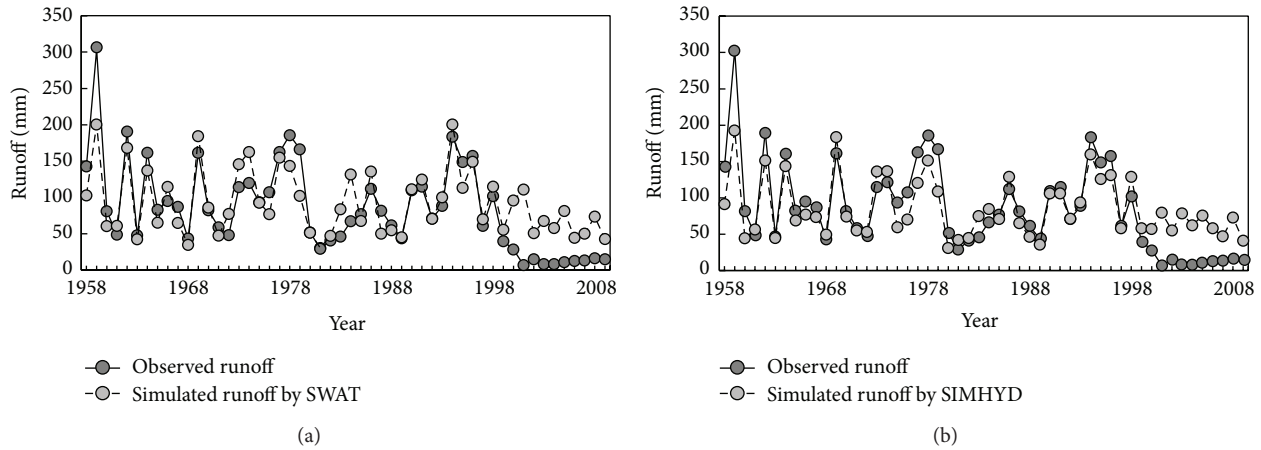


FIGURE 6: Comparison of observed annual runoff and simulated annual runoff by the SWAT (a) and SIMHYD (b) models.

TABLE 4: The average annual simulated and observed runoff during the pretreatment and testing periods (unit: mm).

Periods	Observed runoff	Simulated by SWAT	Simulated by SIMHYD
Pretreatment period	103.31	99.54	91.59
Testing period	16.01	66.57	62.45

the pretreatment periods. The scatter plots in Figure 5 (the third column) and Figure 6 show a great difference between observed streamflow and simulated streamflow at monthly and yearly time steps in the testing period. Table 4 provides the statistical values of observed and simulated runoff in the pretreatment and testing periods. We can see that the simulated annual runoff after the change point is much greater than the observed annual runoff.

As stated previously, the difference between the average observed and simulated runoff reflects the influence of human activities. Meanwhile, the difference in the observed runoff between the testing period and the pretreatment period represents the total influence of climate change and human activities. Therefore, the effects of climate change can be obtained by calculating the difference between total influence and human activities influence. Results presented in Table 5 show the total difference caused by climate change and human activities is 87.3 mm. The reduction runoff caused by human activities is 50.56 mm and 46.44 mm based on the SWAT and SIMHYD models, respectively. The runoff reduction caused by climate change was 36.74 mm and 40.86 mm based on the two models. The influence of human activities on the runoff accounted for 57.9% and the influence of climate change accounted for up to 42.1% according to the SWAT model. According to the SIMHYD model, human activities accounted for 53.2% of runoff decrease and the influence of climate change accounted for up to 46.8%.

4.4. Climate Elasticity Analysis. The Fu and Zhang methods should be calibrated with the average annual observed runoff

during the pretreatment period firstly. The parameter is 2.3 in the Fu method and 0.8 in the Zhang method. The simulated average annual runoff is 95.7 mm with the relative values of 7.33% by Fu method and 93.8 mm with the relative values of 9.25% by Zhang method during the pretreatment period, respectively. Then the climate elasticity of runoff to precipitation in the basin is calculated by the nonparametric method and six Budyko-based methods. From the results in Table 6, we can see that there are some differences among the seven methods for estimating the elasticity coefficients varying from 2.078 to 2.849.

Based on (5), the impacts of climate change on runoff are quantified as shown in Table 6. The results indicate that the influence of climate change accounted for 28.3~38.1% of the runoff reduction, equivalent to about 29.9 mm reduction in runoff, while the contribution of human activities was 61.9~71.7%.

5. Discussion

The compared results by the two approaches including nine methods in Figure 7 show that the runoff reduction caused by climate change was 28.3~46.8%, and the corresponding contribution due to human activities was 53.2~71.7%. The results indicate that the effect of human activities was stronger than that of climate change. This finding agrees with the previous studies [46]. As described earlier, runoff showed a remarkable decreasing trend even though precipitation and PET presented no significant trends, thereby indicating that human activities may be the driving factors for runoff decline. Water-related human activities including land use and cover change and water diversion for irrigation and industrial and domestic water use are considered to be responsible for the runoff decline.

Statistics shows that the forest cover has decreased by 8% in the LRB since the mid-1990s, and the reduction in forest cover usually results in an increase in runoff [47, 48]. However, the observed runoff in the LRB has shown a decreasing trend in the past years; this may be related

TABLE 5: Quantification of the impact of climate change (CC) and human activities (HA) on runoff based on hydrological modeling.

Model	Total difference (mm)	Runoff decline caused by CC (mm)	Runoff decline caused by HA (mm)	Percentage of influence of CC	Percentage of influence of HA
SWAT	87.30	36.74	50.56	42.1%	57.9%
SIMHYD		40.86	46.44	46.8%	53.2%

TABLE 6: Quantification of the impacts of climate change based on climate elasticity methods.

Climate change Impact	Nonparametric	Schreiber	Ol'dekop	Budyko	Pike	Fu	Zhang et al.
ϵ_p	2.849	2.797	2.780	2.804	2.637	2.158	2.078
Decline (mm)	-33.27	-32.70	-32.51	-32.78	-30.93	-25.64	-24.75
Percentage (%)	38.1	37.5	37.2	37.5	35.4	29.4	28.3

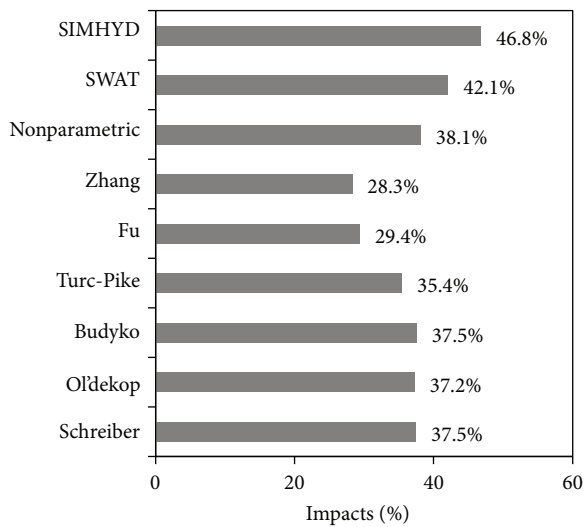


FIGURE 7: Comparison of impact results of change climate by the nine methods.

to the negative effects of the human activities like water diversion for irrigation and industrial and domestic water use within this basin. There are four large reservoirs in the catchment (Miaogong Reservoir (MR) in the upstream, Panjiakou Reservoir (PR) in the midstream, Daheiting Reservoir (DR) in the downstream, and Taolinkou Reservoir (TR) in the Qinglong River (a tributary of the Luan River)). Water diversion to Tianjin and Tangshan is used for industry and urban life from the PR and DR. Water is also diverted for the irrigation in the Luanxia Irrigation district from the PR, DR, and TR and in Miaogong Irrigation district from the MR following increases in the area of farmland. As a result of the economic development and the population increase, the water demand by industry, domestic usage, and irrigation has increased [49, 50], subsequently resulting in the decreases in streamflow in the basin. Meanwhile, the irrigation may trigger high evapotranspiration and farmers have to collect runoff to enhance crop yield, which will also reduce the runoff [46]. Furthermore, the Mann-Kendall test results of the outflow in the downstream of PR and TR show a change point around 1999. The corresponding reduction in

the average annual streamflow was $43.98 \text{ m}^3/\text{s}$ and $18.73 \text{ m}^3/\text{s}$ in the PR and TR, respectively. The reductions also indicate human activities have a dominated impact on the surface runoff compared with the climate change in the LRB.

In this study, two kinds of climate elasticity methods are used to separate the effects using only the observed annual hydroclimate data. The quantitative results mainly depend on the estimation of the runoff elasticity to precipitation. From these results, the nonparametric method overestimates the reduction caused by climate change when compared with the Budyko-based methods. A possible reason may be the relatively small sample size of the historical data which leads to a relatively large error in the nonparametric method [10]. Another reason may be the reduction in runoff influenced by human activities, which lead to an overestimation of the runoff elasticity to precipitation by nonparametric method as shown in Figure 8(a), where the runoff elasticity increases with the runoff decline. Among the six Budyko-based methods, the results of the Fu and Zhang methods indicate a lower impact of climate change than the other four methods, which is also caused by the underestimation of the runoff elasticity. Figure 8(b) shows the relationship between aridity index and runoff elasticity to precipitation. From the curves in Figure 8(b), we can see that when the aridity index is around 1.5 to 2.0 (the aridity index is 1.797 in the Luan River basin), the runoff elasticity to precipitation calculated by Zhang and Fu methods is smaller than that obtained by the other four methods.

The quantitative results of the two hydrological models reveal a slight difference between the models, which is mainly due to the model uncertainties. The uncertainties associated with parameter calibration are shown in Figure 9. Figure 9 shows the simulated annual runoff in the testing period, along with the 95% confidence range as obtained by the two models. We can see that the difference of simulated runoff and observed runoff ranges between 34.55 mm and 63.41 mm. In the SWAT model, the contribution of human activities to the reduction in runoff was 40~70% with a mean value 55%. With the SIMHYD model, the difference between simulated runoff and observed runoff varied from 23.80 mm to 65.60 mm. The contribution of human activities to the reduction in runoff was 30~75% with a mean value of 53%. From the uncertainty analysis, we can see that parameter calibration

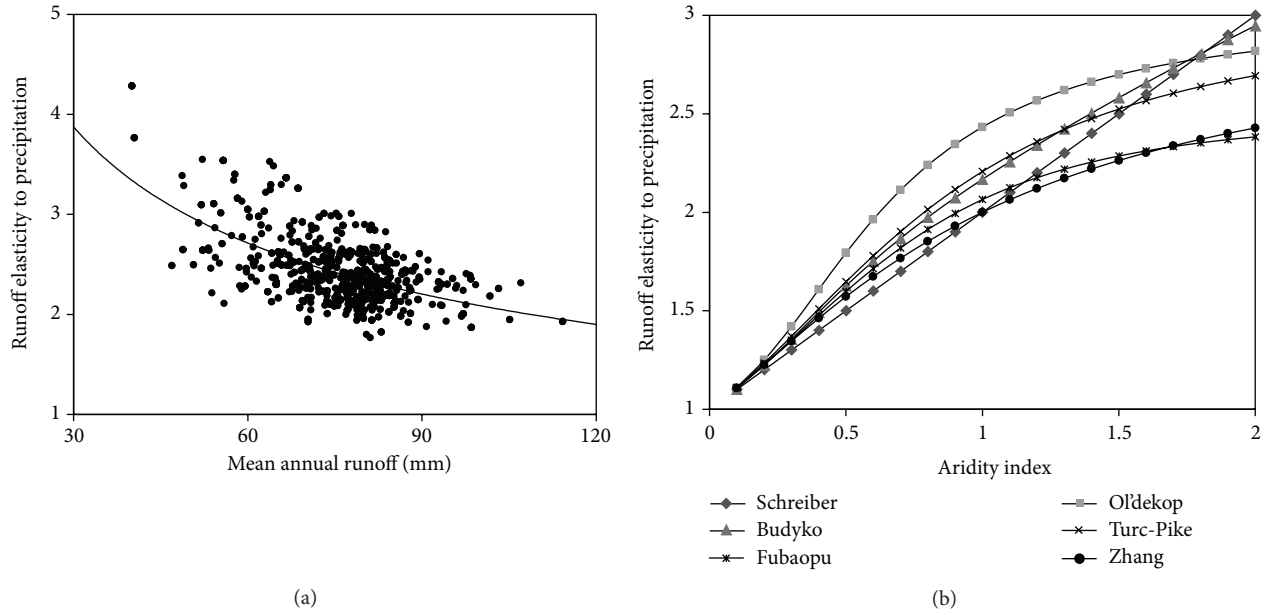


FIGURE 8: The relationship between mean annual runoff and the runoff elasticity to precipitation (a), the relationship between aridity index and the runoff elasticity to precipitation (b).

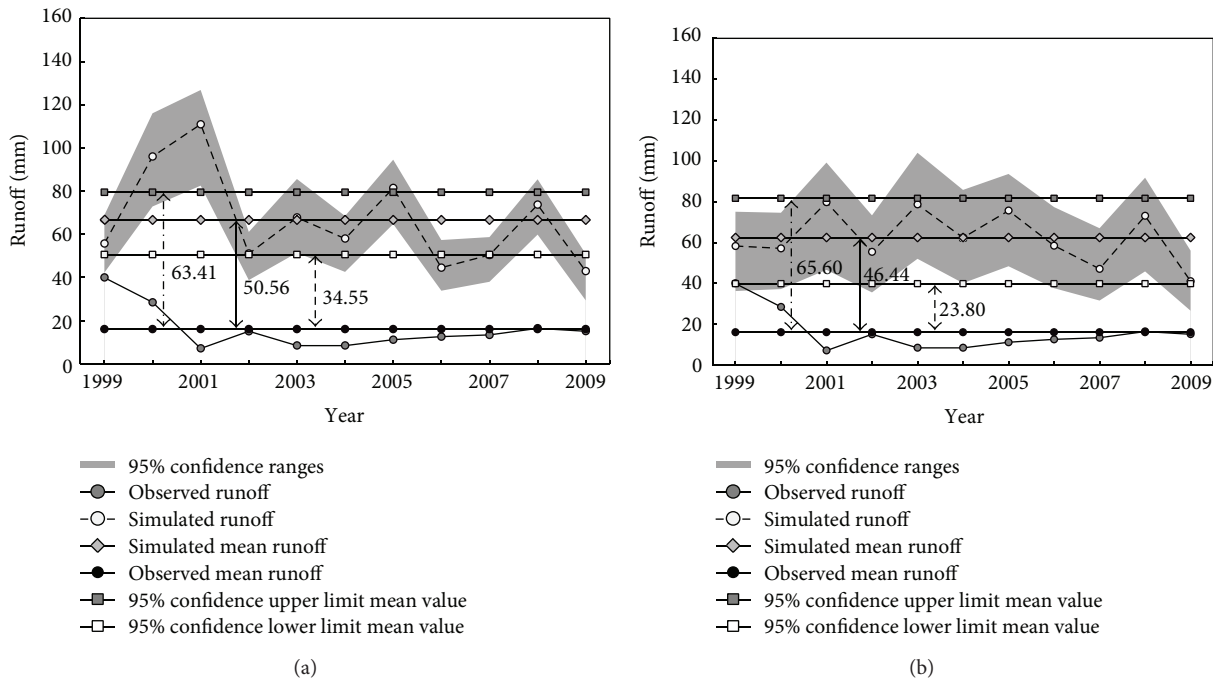


FIGURE 9: Uncertainties of the quantification results based on the SWAT (a) and SIMHYD (b) models.

may have an influence on the quantitative results. Meanwhile, we can see both the lumped SIMHYD model and the SWAT model provide useful means of quantifying the impacts, but the SIMHYD model uses fewer input datasets and is easier calibrated as described above. However, to reveal more details of the hydrological cycle, distributed hydrological models are required in the quantitative studies.

In general, both of the climate elasticity and hydrological modeling approaches have their own advantages.

The climate elasticity methods are comparatively simple with fewer inputs, while the hydrological models can simulate the water cycle with higher spatial and temporal resolution. However, there are still uncertainties associated with the results obtained by both approaches. The estimation of runoff elasticity is still a difficult problem for the climate elasticity methods, and the model uncertainties will affect the quantitative results produced by the hydrological modeling approach. Furthermore, the method used for separating the effects of

climate change and human activities as two independent variables will also introduce uncertainties because these two factors interact with each other. For example, human activities such as urbanization may affect the energy and water fluxes back to the atmosphere which could cause changes in climate variables such as temperature and precipitation and thus changes in runoff. Meanwhile, climate change would also influence human activities such as land use and therefore subsequently cause runoff changes.

6. Conclusions

Here, an integrated quantitative method is successfully applied in the Luan River basin using the Budyko-based Fu model, hydrological modeling, and climate elasticity approaches. Firstly, the Budyko-based Fu model is used to explore the underlying surface characteristics of the basin. The results indicate that the change point takes place in 1999. Secondly, the hydrological modeling and climate elasticity approaches are used to separate the effects of climate change and human activities. The effect of climate change on runoff changes is about 28.3~46.8% and that of human activities accounted for about 53.2~71.7%. The human activities including land use and cover change and water diversion for irrigation and industrial and domestic water use are considered to be responsible for the runoff decline in the basin. The results in this study could provide a scientific basis for the sustainable water resources planning and management under the influence of climate change and human activities.

In addition, the hydrological modeling approach and climate elasticity approach are compared. Climate elasticity methods are comparatively simplistic and based on fewer data, which is a good attribute for large-scale application, while the hydrological models can simulate the water cycle with higher spatial and temporal resolution. It has been proved that both approaches can effectively evaluate the influences of climate change and human activities on hydrological processes. Although the effects of climate change and human activities are successfully separated in this study, a more in-depth analysis of the effects of climate variables, land use and cover change, water diversion, and other water-related human activities is needed in further work.

Conflict of Interests

The authors declare that there is no conflict of interests regarding the publication of this paper.

Acknowledgments

This study is supported by the National Basic Research Program of China ("973" Program) (2015CB452701) and National Natural Science Foundation of China (41271003).

References

- [1] J. Xia, C. Z. Liu, and G. Y. Ren, "Opportunity and challenge of the climate change impact on the water resource of China," *Advances in Earth Science*, vol. 26, no. 1, pp. 1–12, 2011 (Chinese).
- [2] G. Wang, J. Xia, and J. Che, "Quantification of effects of climate variations and human activities on runoff by a monthly water balance model: a case study of the Chaobai River basin in northern China," *Water Resources Research*, vol. 45, no. 7, 2009.
- [3] Y. K. Zhang and K. E. Schilling, "Effects of land cover on water table, soil moisture, evapotranspiration, and groundwater recharge: a field observation and analysis," *Journal of Hydrology*, vol. 319, no. 1–4, pp. 328–338, 2006.
- [4] J. X. Xu and J. Sun, "Influence of precipitation and human activities on water fluxes from the Yellow River into the sea in the past 50 years," *Advances in Water Science*, vol. 14, no. 6, pp. 690–695, 2003 (Chinese).
- [5] Y. F. Zhang, D. X. Guan, C. J. Jin, A. Z. Wang, J. B. Wu, and F. H. Yuan, "Analysis of impacts of climate variability and human activity on streamflow for a river basin in Northeast China," *Journal of Hydrology*, vol. 410, no. 3–4, pp. 239–247, 2011.
- [6] H. Y. Li, Y. Q. Zhang, J. Vaze, and B. E. Wang, "Separating effects of vegetation change and climate variability using hydrological modelling and sensitivity-based approaches," *Journal of Hydrology*, vol. 420–421, pp. 403–418, 2012.
- [7] W. G. Wang, Q. X. Shao, T. Yang et al., "Quantitative assessment of the impact of climate variability and human activities on runoff changes: a case study in four catchments of the Haihe River basin, China," *Hydrological Processes*, vol. 27, no. 8, pp. 1158–1174, 2013.
- [8] N. K. Tuteja, J. Vaze, J. Teng, and M. Mutendeudzi, "Partitioning the effects of pine plantations and climate variability on runoff from a large catchment in southeastern Australia," *Water Resources Research*, vol. 43, no. 8, Article ID W08415, 2007.
- [9] Z. Bao, J. Zhang, G. Wang et al., "Attribution for decreasing streamflow of the Haihe River basin, Northern China: climate variability or human activities?" *Journal of Hydrology*, vol. 460–461, pp. 117–129, 2012.
- [10] H. X. Zheng, L. Zhang, R. Zhu, C. Liu, Y. Sato, and Y. Fukushima, "Responses of streamflow to climate and land surface change in the headwaters of the Yellow River Basin," *Water Resources Research*, vol. 45, no. 7, Article ID W00A19, 2009.
- [11] X. Liu, C. Liu, Y. Luo, M. Zhang, and J. Xia, "Dramatic decrease in streamflow from the headwater source in the central route of China's water diversion project: climatic variation or human influence?" *Journal of Geophysical Research D: Atmospheres*, vol. 117, no. 6, Article ID D06113, 2012.
- [12] A. Sankarasubramanian, R. M. Vogel, and J. F. Limbrunner, "Climate elasticity of streamflow in the United States," *Water Resources Research*, vol. 37, no. 6, pp. 1771–1781, 2001.
- [13] V. K. Arora, "The use of the aridity index to assess climate change effect on annual runoff," *Journal of Hydrology*, vol. 265, no. 1–4, pp. 164–177, 2002.
- [14] G. B. Fu, S. P. Charles, and F. H. S. Chiew, "A two-parameter climate elasticity of stream flow index to assess climate change effects on annual stream flow," *Water Resources Research*, vol. 43, Article ID W11419, 2007.
- [15] C. Z. Liu, Z. Y. Liu, and Z. H. Xie, "Study of trend in runoff for the Haihe River Basin in recent 50 years," *Quarterly Journal of Applied Meteorology*, vol. 15, pp. 385–393, 2004 (Chinese).
- [16] G. Z. Fan, S. H. Lü, and G. D. Cheng, "Simulation of influence of climate change on water resource over Luanhe River Valley using a hydrological model (I): introduction of precipitation-runoff modeling system (PRMS) and its replant over Luanhe River Valley," *Plateau Meteorology*, vol. 20, pp. 173–179, 2001 (Chinese).

- [17] Q. P. Wang and J. Y. Liu, "Analyzing the impact of climate change and human activity on the water resources change in the lower reach of Luan River," *China Water Resources*, no. 15, pp. 41–44, 2010 (Chinese).
- [18] G. H. Hargreaves and Z. A. Samani, "Estimating potential evapotranspiration," *Journal of the Irrigation & Drainage Division*, vol. 108, no. 3, pp. 223–230, 1982.
- [19] X. Y. Liu, Y. Z. Li, and Q. S. Wang, "Evaluation on several temperature-based methods for estimating reference crop evapotranspiration," *Transactions of the Chinese Society of Agricultural Engineering*, vol. 22, no. 6, pp. 12–18, 2006 (Chinese).
- [20] M. I. Budyko, *Evaporation under Natural Conditions*, Gidrometeorizdat, Leningrad, Russia, 1948.
- [21] M. I. Budyko, *Climate and Life*, Academic Press, Orlando, Fla, USA, 1974.
- [22] B. P. Fu, "On the calculation of the evaporation from land surface," *Chinese Journal of Atmospheric Sciences*, vol. 5, pp. 23–31, 1981 (Chinese).
- [23] F.-B. Sun, D.-W. Yang, Z.-Y. Liu, and Z.-T. Cong, "Study on coupled water-energy balance in Yellow River basin based on Budyko hypothesis," *Journal of Hydraulic Engineering*, vol. 38, no. 4, pp. 409–416, 2007 (Chinese).
- [24] B. P. Fu, "On the calculation of the evaporation from land surface in mountainous area," *Scientia Meteorologica Sinica*, vol. 16, pp. 328–335, 1996 (Chinese).
- [25] P. C. D. Milly, "Climate, soil water storage, and the average annual water balance," *Water Resources Research*, vol. 30, no. 7, pp. 2143–2156, 1994.
- [26] M. T. Hobbins, J. A. Ramírez, and T. C. Brown, "The complementary relationship in estimation of regional evapotranspiration: an enhanced advection-aridity model," *Water Resources Research*, vol. 37, no. 5, pp. 1389–1403, 2001.
- [27] H. B. Mann, "Nonparametric tests against trend," *Econometrica*, vol. 13, pp. 245–259, 1945.
- [28] M. G. Kendall, *Rank Correlation Methods*, Griffin, London, UK, 1975.
- [29] F. H. S. Chiew, M. C. Peel, and A. W. Western, "Application and testing of the simple rainfall-runoff model SIMHYD," in *Mathematical Models of Small Watershed Hydrology and Application*, V. P. Singh and D. Frevert, Eds., pp. 335–367, Water Resource Publications, Littleton, Colo, USA, 2002.
- [30] G. Q. Wang, J. Y. Zhang, R. M. He, N. Q. Jiang, and X. A. Jing, "Runoff reduction due to environmental changes in the Sanchuanhe river basin," *International Journal of Sediment Research*, vol. 23, no. 2, pp. 174–180, 2008.
- [31] P. W. Gassman, M. R. Reyes, C. H. Green, and J. G. Arnold, "The soil and water assessment tool: historical development, applications, and future research directions," *Transactions of the ASABE*, vol. 50, no. 4, pp. 1211–1250, 2007.
- [32] L. P. Zhang, S. D. Zeng, R. C. Wang, and J. Xia, "Impacts of climate change on the hydrological cycle in the Luan River Basin," *Resources Science*, vol. 33, no. 5, pp. 966–974, 2011.
- [33] Q. Y. Duan, S. Sorooshian, and V. Gupta, "Effective and efficient global optimization for conceptual rainfall-runoff models," *Water Resources Research*, vol. 28, no. 4, pp. 1015–1031, 1992.
- [34] J. E. Nash and J. V. Sutcliffe, "River flow forecasting through conceptual models, part I—a discussion of principles," *Journal of Hydrology*, vol. 10, no. 3, pp. 282–290, 1970.
- [35] J. C. Schaake, "From climate to flow," in *Climate Change and U.S. Water Resources*, P. E. Waggoner, Ed., chapter 8, pp. 177–206, John Wiley & Sons, New York, NY, USA, 1990.
- [36] P. Schreiber, "Über die Beziehungen zwischen dem Niederschlag und der Wasserführung der Flüsse in Mitteleuropa," *Zeitschrift für Meteorologie*, vol. 21, pp. 441–452, 1904.
- [37] E. M. Ol'dekop, "On evaporation from the surface of river basins," *Transactions on Meteorological Observations, University of Tartu*, vol. 4, p. 200, 1911.
- [38] J. G. Pike, "The estimation of annual run-off from meteorological data in a tropical climate," *Journal of Hydrology*, vol. 2, no. 2, pp. 116–123, 1964.
- [39] L. Zhang, W. R. Dawes, and G. R. Walker, "Response of mean annual evapotranspiration to vegetation changes at catchment scale," *Water Resources Research*, vol. 37, no. 3, pp. 701–708, 2001.
- [40] L. J. Li, L. Zhang, H. Wang et al., "Assessing the impact of climate variability and human activities on streamflow from the Wuding River basin in China," *Hydrological Processes*, vol. 21, no. 25, pp. 3485–3491, 2007.
- [41] J. C. I. Dooge, M. Bruen, and B. Parmentier, "A simple model for estimating the sensitivity of runoff to long-term changes in precipitation without a change in vegetation," *Advances in Water Resources*, vol. 23, no. 2, pp. 153–163, 1999.
- [42] H. Yang and D. Yang, "Derivation of climate elasticity of runoff to assess the effects of climate change on annual runoff," *Water Resources Research*, vol. 47, no. 7, Article ID W07526, 2011.
- [43] X. Xu and D. Yang, "Analysis of catchment evapotranspiration at different scales using bottom-up and top-down approaches," *Frontiers of Architecture and Civil Engineering in China*, vol. 4, no. 1, pp. 65–77, 2010.
- [44] S. Yue and C. Y. Wang, "Applicability of prewhitening to eliminate the influence of serial correlation on the Mann-Kendall test," *Water Resources Research*, vol. 38, Article ID W00A11, 2002.
- [45] S. R. Zhang and X. X. Lu, "Hydrological responses to precipitation variation and diverse human activities in a mountainous tributary of the lower Xijiang, China," *Catena*, vol. 77, no. 2, pp. 130–142, 2009.
- [46] Y. H. Yang and F. Tian, "Abrupt change of runoff and its major driving factors in Haihe River Catchment, China," *Journal of Hydrology*, vol. 374, no. 3–4, pp. 373–383, 2009.
- [47] E. D. Hetherington, "The importance of forests in the hydrological regime," in *Canadian Bulletin Fisheries and Aquatic Sciences*, M. D. Healy and R. R. Wallace, Eds., no. 215, p. 533, Department of Fisheries and Oceans, Ottawa, Canada, 1987.
- [48] J. D. Stednick, "Monitoring the effects of timber harvest on annual water yield," *Journal of Hydrology*, vol. 176, no. 1–4, pp. 79–95, 1996.
- [49] X. Zhu, W. Cao, and Y. Zhang, "Water resources analysis in Haihe river catchment," *Water Resources*, vol. 6, pp. 6–8, 2007 (Chinese).
- [50] B. Y. Yang, "Reason analysis of runoff reduction in Nanzhuang station of Hutuohe River Basin," *Shanxi Water Resources*, vol. 6, pp. 34–35, 2007 (Chinese).

Research Article

Web-Based Data Integration and Interoperability for a Massive Spatial-Temporal Dataset of the Heihe River Basin EScience Framework

Qingchun Guo,^{1,2,3} Yaonan Zhang,⁴ Zhenfang He,^{3,4} and Yufang Min⁴

¹State Key Laboratory of Loess and Quaternary Geology, Institute of Earth Environment, Chinese Academy of Sciences, Xi'an, Shaanxi 710061, China

²University of Chinese Academy of Sciences, Beijing 100049, China

³Liaocheng University, Liaocheng, Shandong 252059, China

⁴Cold and Arid Regions Environmental and Engineering Research Institute, Chinese Academy of Sciences, Lanzhou 730000, China

Correspondence should be addressed to Yaonan Zhang; yaonan@lzb.ac.cn

Received 7 October 2014; Revised 25 January 2015; Accepted 3 February 2015

Academic Editor: Yongqiang Zhang

Copyright © 2015 Qingchun Guo et al. This is an open access article distributed under the Creative Commons Attribution License, which permits unrestricted use, distribution, and reproduction in any medium, provided the original work is properly cited.

To solve the messy problem of data types and form a unified data-processing solution, data in the Heihe River Basin were first classified into five types to integrate them and achieve unified management of data and metadata, preventing the loss of metadata, in the data model of eScience framework. Considering many of the challenges that exist in the construction of the online spatial-temporal data integration and interoperability eScience platform, we used the open data interfaces and standards such as the Common DataModel (CDM) interface, common scientific data modelling (i.e., NetCDF, GRIB, and HDF), and Open Geospatial Consortium (OGC) standards. Through the eScience platform, we also provided online data processing tools by collecting free tools (e.g., NetCDF tool, quality control tool). This eScience platform enables researchers to make full use of scientific research information and results and facilitates collaboration, especially between the GIS community and other members of the earth science community, with the purpose of establishing an online platform of uniform spatial data from the Heihe River Basin via common scientific data modelling.

1. Introduction

Modern geoscience often requires massive datasets and a huge amount of computation for numerical simulation and data handling, and data needs increase daily [1–4]. In earth and environmental science, data management is becoming more challenging [5–7]. Volumes of geographic data have been collected with modern acquisition techniques such as global positioning systems (GPS), remote sensing, wireless sensor, and surveys [8–12]. The increase in data volume has led to more distributed archiving, and it is consequently more difficult to analyse data at a single location and store it locally [13, 14]. “Big Data” has become a ubiquitous new term for researchers. It concerns not only the amount of data but also timeliness (velocity), variety, and veracity. The eScience environment makes full use of people, data,

and computing resources. Software enables convenient data applications and saves manpower and resources [15]. In addition to researchers, governments and private industries also have enormous interest in both collecting spatial data and using massive dataset resources for various application needs, especially Web-based needs [16–19]. The eScience environment supports the combination environment mentioned above and provides online workflow including integration, access, analysis, visualization, and quality control for various data sources and formats [18, 20, 21]. Compared to traditional research methods, eScience applications enable researchers to make full use of scientific research and facilitate international collaboration [22, 23]. Chen et al. proposed a geoprocessing eScience workflow model to integrate logical and physical processes into a composite process chain for sensor observations [24]. A case study on e-Cadastres

was proposed to analyse the results of a survey to several European Cadastral Agencies and estimate the benefits of spatial data infrastructure [25]. The challenge of constructing a suitable data model for basin-scale research is real and requires improved data interoperability, developing better algorithms and good case studies.

Studies in the Heihe River Basin have examined the weather, ecology, hydrology, and water resources of cold and arid regions. With the development of remote sensing and wireless sensor network technologies, the amount of data that needs acquisition, storage, processing, and transmission has multiplied [26, 27]. Data have been and continue to be accumulated for the study of the Heihe River Basin, becoming the basis for forecasting and decision analysis [28]. As the data from the Heihe River Basin have become more diverse in time period and format, more complex, dynamic, and high-dimensional, and more metadata than ever before, it is more difficult to analyse and effectively visualize [29, 30]. Therefore, constructing an eScience context has been recognised as an urgent need for the unified management of data and metadata and unifying data formats from different disciplines. The eScience context provides the gamut of spatial data through Web services with both efficient data processing algorithms and effective visualization approaches for data applications via the THREDDS (Thematic Real-time Environmental Distributed Data Services) data server (TSD), OGC (Web Coverage Servers) WCS/WMS (Web Map Service), NcML-GML (NetCDF Markup Language-Geography Markup Language), and object-oriented components technology [9, 10, 12, 31, 32]. The internet-based platform provides a convenient way to achieve spatial-temporal data mining, integration, analysis, and distribution and can help researchers to make full use of existing data resources. Maximizing existing resources can reduce the duplication of work and charges for data acquisition and collection, which enhances collaboration, especially between the GIS community and the rest of the earth science community.

The research issues that need to be solved for online-integrated data management of the Heihe River Basin are as follows. First, when constructing an online data integration and interoperability platform, the data contributed by different users have different formats, unprecedentedly large size, unexpected metadata, high dimensionality, and heterogeneous data sources. These data include remote sensing data with the formats such as HDF5, JPGE, and TIFF, raster data, radar data that are collected and processed by special software, climate observations in GRIB, NetCDF, and ASCII formats, shapefiles, and free-text files (e.g., TXT, word, and CSV). Multiple service interfaces and algorithms for data integration and interoperability are needed by data in different formats, which increases the difficulty of data sharing and interoperability. The data's computational algorithms are directed at various time scales and research objectives, for example, using daily versus monthly averages for forecasts of short-term weather and large-scale climate changes. Second, seamless management is difficult because the data has been separated from the metadata. In addition, it is difficult to download data on a specified period from a dataset, to transmit data or share various fields and software systems.

Metadata must be effectively archived. There is an urgent need for the design of a user-friendly interface to facilitate interoperability, geocomputation, and geovisualisation. Third, unification of the heterogeneity of existing protocols and standards in service-oriented architecture is also needed, such as those applied to establish GIS standards. Finally, experts from different disciplines are familiar with their specific data format and processing software. They encounter problems in converting one format to another or losing information in converting the data formats.

To address these issues, spatial and temporal data from the basin in an eScience context was classified to five categories according to the data source. The data model is a key factor of data sharing. Selecting the data model to integrate spatial-temporal data is very important for the efficient and seamless management in basin eScience. The model determines whether we can efficiently describe the state or evolution of a geographical entity and effectively solve various problems related to time. Considering the compatibility of data, it is hard to achieve a single, completely uniform data model, so the goal may be a few data models. The Heihe River Basin eScience platform selected the Network Common Data Form (NetCDF) (<http://www.unidata.ucar.edu/software/netcdf/>), Hierarchical Data Format (HDF) (<http://www.hdfgroup.org/projects/>), and GRIB in Binary (GRIB) (<http://www.wmo.int/pages/prog/www/>) to integrate and interoperate the data according to requirements analysis. The platform integrates multisource and differently formatted data into a few data models. It can solve the contradiction between the high performance computing and the low efficiency of the processing software, creating management standards for massive spatial-temporal datasets and metadata. The new organization mode and collaborative environment can unite disciplines, regions, and time scales and achieve the complete value chain of the data integration, acquisition, transport, storage, processing, application, and service on this eScience platform via Web services [33]. The eScience environment framework is convenient for cooperation between experts in various fields and simplifies data postprocessing analysis and data retrieval. It can be accessed openly and freely by everyone. The primary focus is to improve data and application interoperability via data models, interfaces, standards, and Web services.

The emphasis of this paper is on the process and methods of unifying data from the Heihe River Basin in NetCDF and on introducing the modules of online data integration and interoperability.

2. Study Areas

The Heihe River is the second largest inland river in China. It is 821 km long and originates from Qilianshan Mountain. The Heihe River Basin is a typical large inland river basin that covers an area of approximately 130,000 km² in the arid zone of northwestern China. It is located in the middle section of the Hexi Corridor of Gansu Province, which is composed of upper, middle, and lower reaches. Its upper reaches originate in the Qilian Mountains, where the headwater streams form

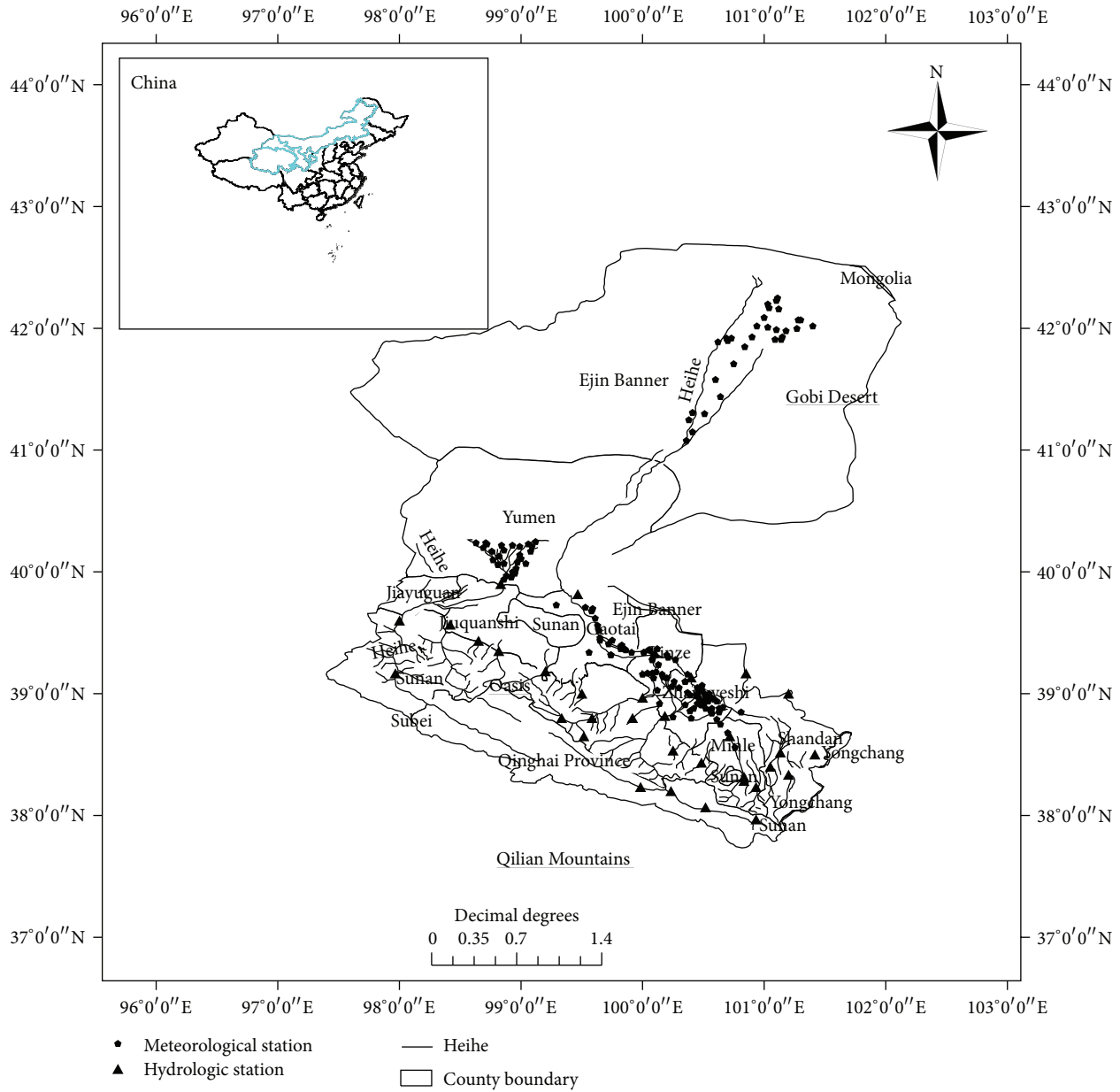


FIGURE 1: The study area map of Heihe River Basin.

strong drainages, and its lower reaches end in the desert Inner Mongolia. The middle reaches are primarily oases surrounded by the Gobi Desert, and the landscape includes heterogeneously distributed farmland, forest, and residential areas [34]. The study area is shown in Figure 1.

The Heihe River Basin, as a typical study area for earth science, has been the object of recent research on weather, climate and remote sensing, ecology, and hydrology, which frequently require analysing hundreds of thousands of variables. The data processing produces large numbers of results, explanations, and other information in various formats and files. In the Heihe River Basin, long-term monitoring, testing, and research are the main sources of data and the important

basis of earth system science research. Managing and processing the long-term monitoring data are some of the important tasks for basin research. Therefore, in the eScience context of the basin, issues such as the distribution, heterogeneity, and volume of data need to be addressed during the design and implementation of new data-oriented infrastructures, services, standards, and systems.

3. Methods

3.1. Common Data Model and Spatial-Temporal Data Model for EScience Context. The chosen spatial-temporal data model has to address platform compliance with model

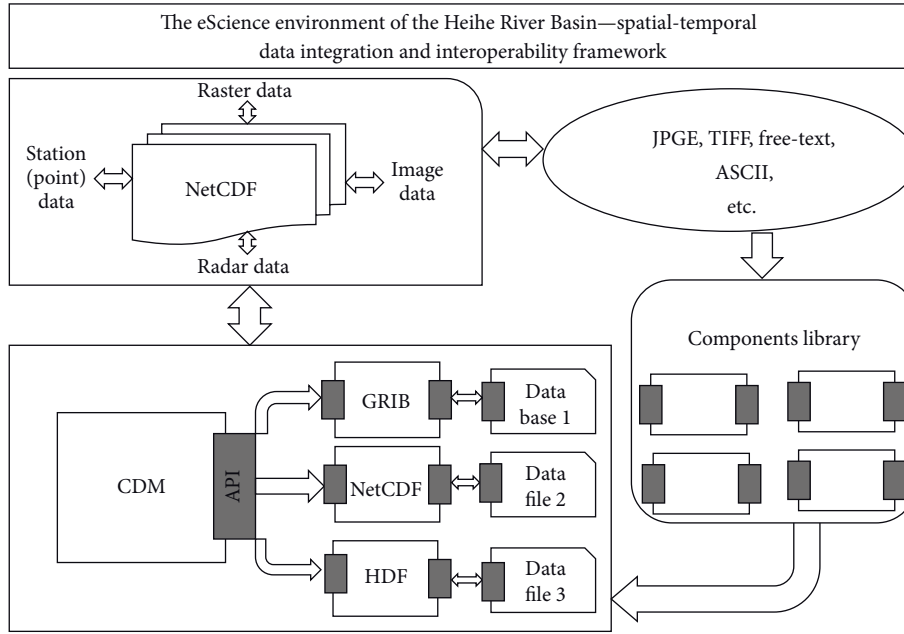


FIGURE 2: The data integration and interoperability interfaces of spatial-temporal data.

interfaces and several protocols. It must also fit the service-oriented architecture through open and free interfaces because the eScience context is a service-oriented distributed environment that allows scientist to share distributed data resources and data processing components. Unidata’s Common Data Model (CDM) has a unified interface to access NetCDF, HDF, and GRIB to build a bridge of interoperability for different data models. The CDM interface is applied to form the workflow of data integration, visualization, distribution, and analysis in the eScience framework. The data integration and interoperability interfaces of spatial-temporal data are shown in Figure 2.

3.2. Data Classification and Archive in the Heihe River Basin eScience Context. In the Heihe River Basin, to generate the NetCDF format from heterogeneous multisource data (e.g., geoTiff, ASCII, free-text, shapefile, and grid), it is important to classify and archive the Heihe River Basin data. According to the characteristics of the NetCDF and the data formats, these formats were classified into five types including station point, point, grid, image, and radial to address messy problems in data formats (Table 1). Station types describe the time series observation data that remain fixed in space and have an exact set of specified spatial coordinates (e.g., hydrologic station data and weather station data). Unlike station points, points can change their location and have no relationship with each other. They can record data in text formats. Grid includes structured and unstructured data. A number of traditional data files can be integrated and archived into a single NetCDF file (e.g., free-text data) via these types, as shown in Table 1. The NetCDF structure provides a powerful mechanism for dealing with complicated scientific workflows and resolves “messy” issues, such as traditional multiple files and heterogeneous data.

TABLE 1: Classification and archive of various data types.

Data type	Definition
Station point	Station observations/time series
Point	Unconnected point data
Grid	Structured grid and unstructured grid
Radial	Radar observation data
Image	Satellite observation data

3.3. The Design Flow and Function of Data Integration and Interoperability. Spatial-temporal data integration and interoperability platform were constructed based on the Web service of B/S architecture to enhance sharing and interoperability. The design flows of conversion and interoperability for data in the framework are shown in Figure 3. The CDM interface was used to access different scientific data including NetCDF, HDF, and GRIB. In addition to the CDM, we also used two other technologies (XML schemas and object-oriented components) to realize the data integration and interoperability framework. TSD data server, NCML-GML, and OGC WCS/WMS were achieved mainly through the XML schemas. The XML schemas resolve the problems in remote access to data and facilitate the interoperability of GIS and other data via Web services. Object-oriented component technology mainly addressed the issues that different domains develop different data processing algorithms in various computer languages (e.g., C, MATLAB, and Fortran). We needed to provide object-oriented components technology to construct components library via collecting data processing program. In addition, we can access these three data formats through the CDM interfaces via OPeNDAP or HTTP protocols. NcML-GML and the WCS/WMS achieved the Web service of GIS data encoded in NetCDF.

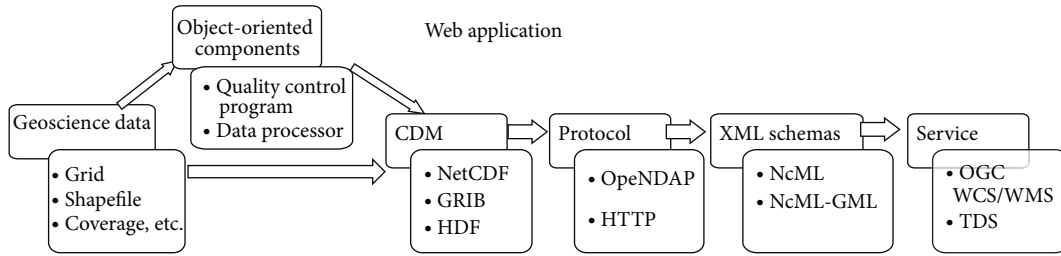


FIGURE 3: The design flow of data format conversion and interoperability in the framework.

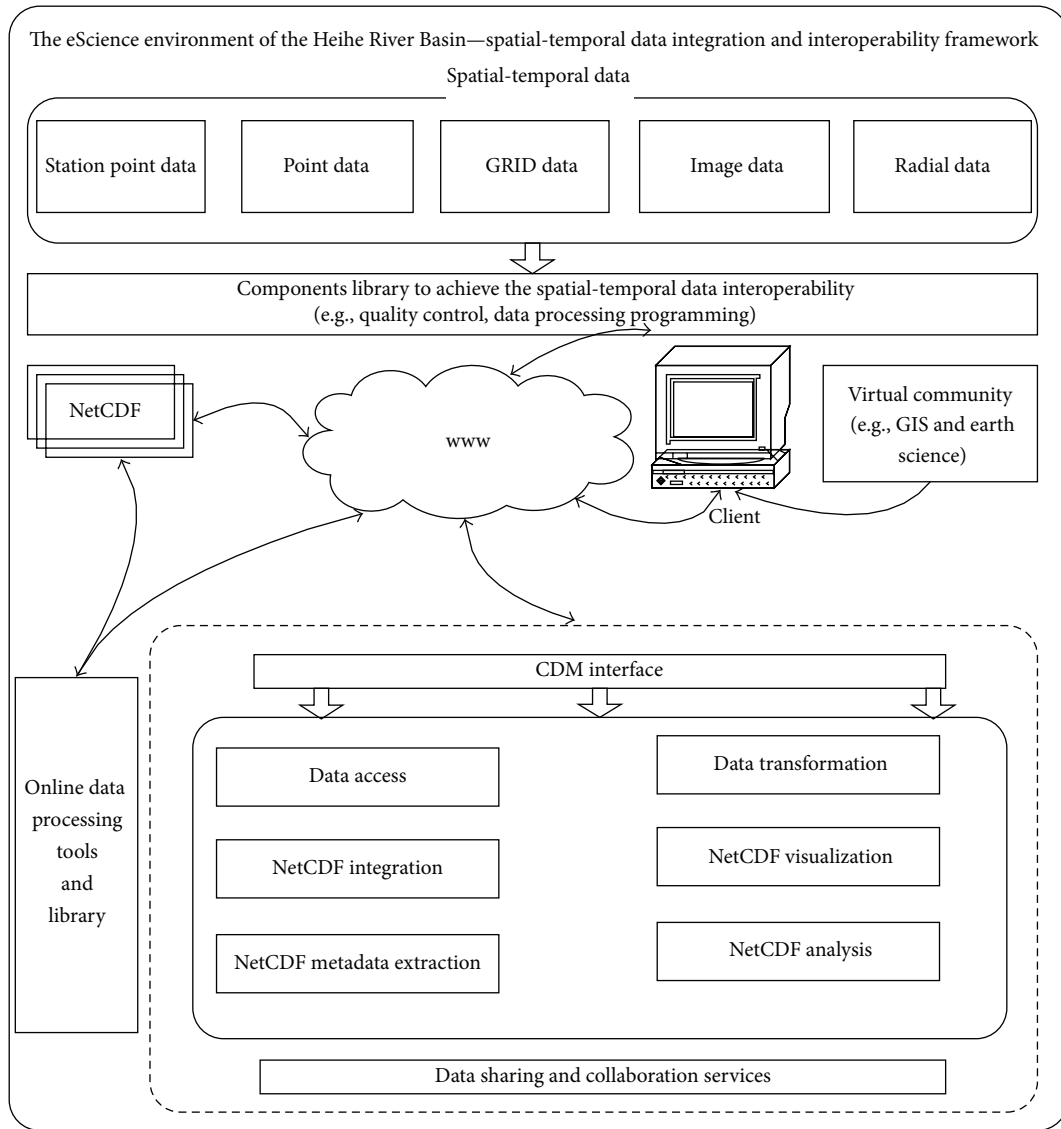


FIGURE 4: The primary functions of spatial-temporal data integration and interoperability in the eScience framework.

The framework is convenient for the standard management of large-scale spatial-temporal data and facilitates cooperative research across disciplines.

Figure 4 shows the main functions of the spatial-temporal data in the eScience platform. The platform provides the services including NetCDF metadata extraction, NetCDF

dataset operation, data format conversion, data visualization, and data access. If the CDM interface cannot achieve special data processing, appropriate components in component libraries were selected according to the requirements of the researchers. If a component does not exist, a new component can be designed and added to the component libraries.

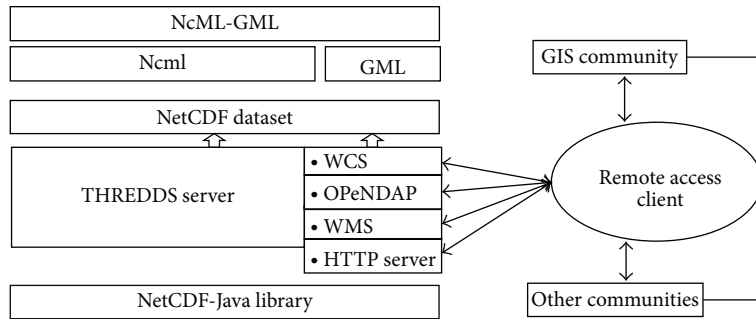


FIGURE 5: The key technology of the eScience interoperability platform of GIS community and other communities.

The metadata extraction services in NetCDF extract dataset attribute information including department, author, and coordinate system and attribute names. They also can be extracted via NcML. Dataset operation services include the basic operations such as appending spatial-temporal data, renaming, modifying and deleting attributes, variables, and dimensions. Data format conversion services convert the formats of point data, remote sensing data, radar data, and the grid data to NetCDF and convert NetCDF to raster and vector data format through third party software or an online tools library such as GIS software to promote the sharing and interoperability of data. The visualization services of NetCDF offer dynamic visualization of long series spatial-temporal data to achieve convenient comparisons and selection of the data in a study area via WCS/WMS or online tools. NetCDF access services acquire data online through THREDDS Data Server and existing protocols (e.g., OPeNDAP and ADDE). When the users are not interested in all the data, they can extract sections of data for certain variables at certain times or in certain regions from these datasets via the Web. Analysis of NetCDF realises arithmetic operations through the browser on the NetCDF datasets such as computing averages.

3.4. NetCDF Data Interoperability with TSD, OGC WCS/WFS, and NcML-GML Technology in EScience Framework. Web technology provides support for eScience development through innovative technologies and protocols, the message format and algorithms, and creative services such as Wikis, TSD, and WCS [35, 36]. The eScience framework is a service-oriented interoperability platform for large spatial-temporal datasets. The key technologies, THREDDS Data Server, OGC WCS/WFS, and NcML-GML, facilitate the interoperability of the scientists in different disciplinary areas, as shown in Figure 5. The THREDDS Data Server (TDS) is the Web server for scientific data and lists the datasets in a THREDDS catalogue, which is simply an XML file offering available datasets and services. Through the TDS, users can obtain the name and location of datasets from different institutions and then access the datasets through OPeNDAP, ADDE, or NetCDF/HTTP protocols [37]. TDS can serve any dataset that the NetCDF-Java library can read (e.g., NetCDF-3, NetCDF-4, HDF-4, HDF-5, HDF-EOS, GRIB-1, and GRIB-2). It can also provide data access (subset) services (e.g., OGC

WMS and WCS), data collection services (e.g., aggregation), and metadata services (e.g., NcML). Researchers can obtain select parts of these datasets via Web browser (e.g., certain variables at certain times or regions).

An NcML document is an XML document describing the content and structure of the data stored in a NetCDF file and represents a generic NetCDF dataset (<http://www.unidata.ucar.edu/software/netcdf/ncml/>) [38]. In our eScience context, it can be used as a “public interface” for spatial-temporal online data, conforming to the NetCDF data model. NcML describes the metadata of the NetCDF data and does not encode the data. The purpose of NcML is to define and redefine NetCDF file. The NcML has the function as follows:

- (i) Metadata to be added, deleted, and changed.
- (ii) Variables to be renamed, added, deleted, and restructured.
- (iii) Aggregated data from multiple CDM files (e.g., Union, JoinNew, and JoinExisting).

We take average monthly temperature NetCDF data of the Heihe River Basin as an example. The data are in a CF-complaint NetCDF format, and the visualisation is shown via online tools in Figure 6. The NcML of the data is seen in Appendix.

The aggregation function of the NcML is useful for time series data combinations. Multiple time series NetCDF data can be aggregated into a single, logical dataset with several types of aggregation including Union, JoinExisting, and JoinNew. To facilitate interdisciplinary work between earth sciences and the GIS communities, NcML-GML is developed to use NetCDF datasets in GIS software, providing them with all the necessary metadata in the form of GML (Geography Markup Language) extensions to NcML. GML is written in XML schema for the storage of geographic information with the GIS community semantics. NcML-GML supports referencing information of spatial-temporal data and realizing the function of the platform that describes the coverage data derived from NetCDF data file. NcML-GML and WCS/WMS can map the NetCDF model into the model of GIS and facilitate the interoperability between these two models and different scientists. Through the technology above, users can obtain metadata and the slices of data they require from remote NetCDF files on a Web server accessible directory.

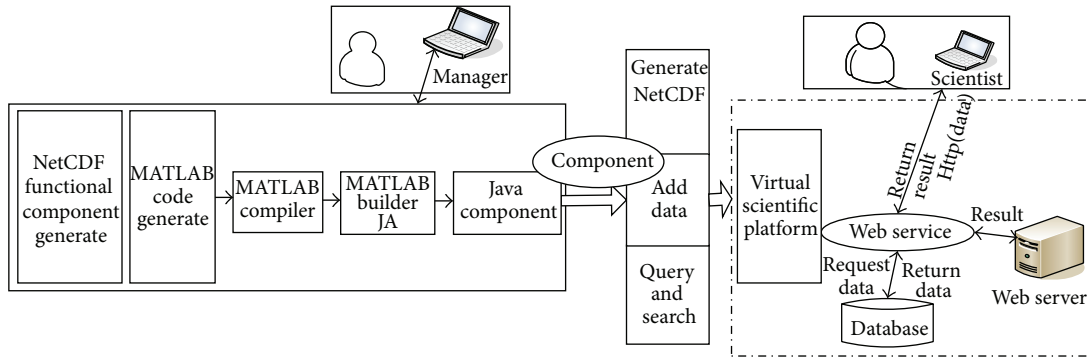


FIGURE 6: The key integrated NetCDF data technology based on Web via object-oriented method with MATLAB and Java mixed solution.

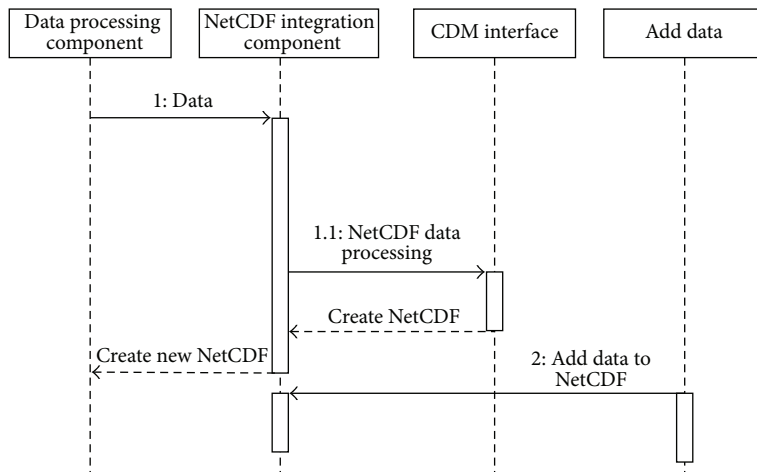


FIGURE 7: A simplified sequence diagram for the NetCDF integration.

3.5. *The Key Object-Oriented Component Technologies of Spatial-Temporal Online Data Integration and Interoperation.* To improve the calculation speed and convenient visualization of the data, we selected the mixed solution of MATLAB and Java to complete data integration based on the Web as one example of the object-oriented method to build components. Quality control components are also built by the object-oriented method. Figure 6 shows the technical framework.

The MATLAB and Java mixed solution is to complete the custom framework and interface via Java and Web technology for special data processing and computation through MATLAB with powerful matrix and numerical analysis capabilities. The mixed solution can solve the problems posed by MATLAB's poor interactivity and the fact that MATLAB programs cannot run outside the environment. In addition, the characteristics of Java language such as crossing platforms and exception handling, multithreading, and stable and fast operation could also be utilized.

Figure 6 shows the workflow of mixed solutions technology; first, the MATLAB code completes core algorithms of NetCDF integration and generates the m files. Second, the m files are then transformed into a component which will interact with server-side through the Java language without the MATLAB environment through MATLAB compiler and MATLAB builder JA. Finally, an encapsulation function

would be called to achieve the core calculation of MATLAB and online computing on the Web through the Java program with the MATLAB dynamic library.

Figure 7 depicts an example of the processes within a scientific workflow. The NetCDF integration process contains an integrated chain invoking first the data processing component and then the integration process. After creating new NetCDF, the add data component continues to increase the variable to NetCDF, extending time dimension or adding other variables. CDM is available as free software to process NetCDF and is actually called several times as part of different scientific workflows.

3.6. *Online Spatial-Temporal Data Quality Control Methods on ESscience Platform.* Spatial data quality has been recognised as an important issue in GIS. However, online spatial-temporal data quality control has received little attention from data processing. Irregularities cause unreliable results because any initial spatial data error can be propagated through the spatial data processing. Based on glaciers, permafrost, deserts, and atmospheric, ecological, environmental, hydrological, and other elements, monitoring systems established in Heihe River Basin realize automatic data transmission and connect with the basin eScience context. Before data integration and analysis, we achieve real-time

data detection and calibration to ensure data quality control on the eScience platform.

In this study, we mainly focus on the online data quality control of outliers in the spatial-temporal data before conversion to NetCDF. This is very important for data quality control, especially for data transmission in wireless sensor networks before data formats are converted to NetCDF files. We provided quality control components for Web services in the components library. In addition, we will continue to enrich our components library to facilitate data processing and data quality control.

According to the data request, the basin eScience platform provides online outlier detection methods, including extreme test method, 3δ test method, Dixon's test method, and Grubbs' test method. The platform will provide convenient detection of abnormal data points, which will help users to understand the data change rules over time and the intrinsic relationships among the data. Based on the physical characteristics and statistical experience of the various elements, the extreme test method gives the maxima and minima values of the real-time data. For the 3δ test method, according to the theory of error, the random error δ obeys a normal distribution. As the standard differential is generally unknown, S counted with a Bezier formula is typically used instead of δ . In formula (1), \bar{x} is the true value, and x_i is observation data. Consider

$$\bar{x} = \frac{1}{N} \sum_{i=1}^n x_i, \quad i = 1, 2, 3, \dots, n, \quad (1)$$

$$S = \sqrt{\frac{\sum_{i=1}^n v_i^2}{N-1}}, \quad i = 1, 2, 3, \dots, n. \quad (2)$$

For an observation data point x_i , if its residuals v_i meet $v_i = |x_i - \bar{x}| > 3S$, $i = 1, 2, 3, \dots, n$, x_i is marked as outlying data. For Dixon' test method, suppose the overall observation data are normally distributed. In the sample $x_1, x_2, x_3, \dots, x_n$, n is the number of the samples, and the observation data are arranged in order of size $x'_1, x'_2, x'_3, \dots, x'_n$. Depending on the number of samples, we select a different formula, such as formula (3). We marked $r_{10}, r'_{10}, r_{11}, r'_{11}, r_{21}, r'_{21}, r_{22}$, and r'_{22} as r_{ij} and r'_{ij} . To determine the significance level α , look up the threshold $D(\alpha, n)$ in the threshold table of the Dixon test. If $r_{ij} > r'_{ij}$, $r_{ij} > D(\alpha, n)$, then x'_n is judged as an abnormal value. If $r_{ij} < r'_{ij}$, $r_{ij} > D(\alpha, n)$, then x'_1 is judged as abnormal value. Otherwise, there are no abnormal values. Dixon's test method is suitable for real-time data quality control. Consider

$$r_{10} = \frac{x'_n - x'_{n-1}}{x'_n - x'_1}, \quad r'_{10} = \frac{x'_2 - x'_1}{x'_n - x'_1} \quad (3 \leq n \leq 7),$$

$$r_{11} = \frac{x'_n - x'_{n-1}}{x'_n - x'_2}, \quad r'_{11} = \frac{x'_2 - x'_1}{x'_{n-1} - x'_1} \quad (8 \leq n \leq 10),$$

$$r_{21} = \frac{x'_n - x'_{n-2}}{x'_n - x'_2}, \quad r'_{21} = \frac{x'_3 - x'_1}{x'_{n-1} - x'_1} \quad (11 \leq n \leq 13),$$

$$r_{22} = \frac{x'_n - x'_{n-2}}{x'_n - x'_3}, \quad r'_{22} = \frac{x'_3 - x'_1}{x'_{n-2} - x'_1} \quad (14 \leq n \leq 30). \quad (3)$$

For Grubbs' test method, we assumed normal independently measured samples $x_1, x_2, x_3, \dots, x_n$, where n is the number of the samples, the residual absolute value of the data is x_i , and \bar{x} is the maximum. \bar{x} is the average of the samples. Then, we constructed the statistic $(x_i - \bar{x})/S$, with the formula for S being given by formula (2). At the selected significance level α , we obtain the threshold $G(\alpha, n)$ by formula (4). α is usually a value of 0.05 or 0.01. Consider

$$P\left(\frac{x_i - \bar{x}}{S} \geq G(\alpha, n)\right) = \alpha. \quad (4)$$

If $|x_i - \bar{x}| \geq G(\alpha, n)S$, then x_i is abnormal value and $G(\alpha, n)$ can be given by the lookup table.

In the eScience platform, we also collect a range of open and free data processing tools and provide them online, such as visualization tools to facilitate collaboration like the NetCDF tools (<http://www.unidata.ucar.edu/downloads>).

4. Results

4.1. The Case Study of Spatial-Temporal Data Integration and Interoperability on EScience Platform. In this paper, observation data from the Mafengou subbasin wireless sensor transmission site in the Heihe River Basin is used as a case study for abnormal data quality control. The temperature data are transmitted every 30 minutes with a total of 73 records. Figures 8(a), 8(b), 8(c), and 8(d) compare the dataset before and after outlier quality control with four methods, the extreme test, 3δ test, Dixon's test, and Grubbs' test, respectively. Figure 8(a) shows that three outliers were found by the extreme test method. Figure 8(b) shows that the 3δ test method found the obvious abnormal data. Figure 8(c) shows that five outliers were found by Dixon's test method. Grubbs' test method is the best, finding seven outliers, as shown in Figure 8(d).

Figure 9 shows the NetCDF tools display of the grid map of the temperature for the Heihe River Basin. The NetCDF tools can also browse remote data model datasets (e.g., NetCDF, GRIB, and HDF) via the TSD data server. An online tools library facilitates data processing and the interoperability of the eScience context using tools with which researchers are familiar.

4.2. Raster Data Integration. To demonstrate the data integration, we took average monthly temperature raster data of the Heihe River Basin as an example and integration components of the component library via Web services as shown in Figure 10. The tool mainly achieved integration and aggregation of the data. First, it converted grid data to ASCII and then integrated the data online as NetCDF to complete the long series data integration. In this example, the grid size is 500 meters, the line number is 899, the column number is 1041, the coordinate x of the left bottom corner is 666083.7 meters, and coordinate y is 4008999.5 meters. These parameters and coordinate system were needed on the webpage. When generating the m function files, we choose grid size, rank number of the grid, and the left bottom corner coordinates as the function's parameters for NetCDF

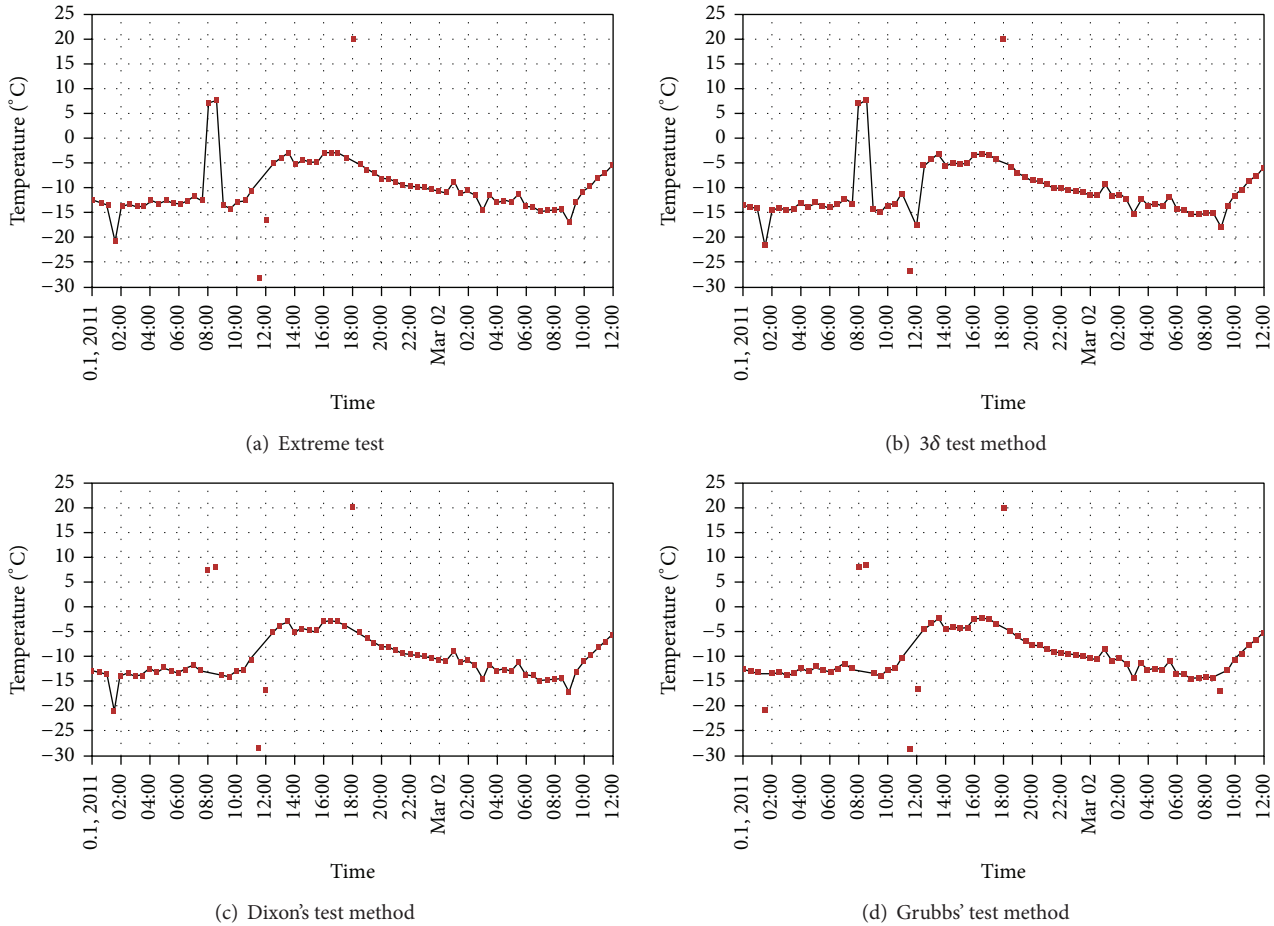


FIGURE 8: (a), (b), (c), and (d) compare a dataset before and after the outliers quality control with the methods extreme, 3δ , Dixon's, and Grubbs' tests, respectively.

data integration, time as an unlimited dimensional variable parameter, and the coordinate system as the metadata according to the CF. The components can also add variables to the NetCDF via aggregation. Figure 10 shows a visualization map of one-month data from the NetCDF datasets of the Heihe river upstream temperature data in November, 2005.

4.3. The Integration of Wireless Sensor Network Station Data.

Station point data from a wireless sensor transmission site in the Heihe River Basin was used as a case study for integrating point data. The data were transmitted every 15 minutes and examined via the quality control components mentioned in Section 4.4 before conversion to NetCDF. The soil humidity data of the observation data were defined in NetCDF. The integration of NetCDF is divided into two parts: the first describes the information of station number, latitude, longitude, and altitude, and the other describes the measurements such as meteorological and hydrological elements. The visualization map of the NetCDF dataset for soil humidity of the Mafengou subbasin wireless sensor station in October is shown in Figure 11. The lines named soil humidity1 and soil humidity2 were the data of NetCDF from different time, and the soil humidity10 lines were aggregations

of two NetCDF datasets with one of soil humidity1 NetCDF and soil humidity2 NetCDF.

For the time series data of the observation station, variables aggregated can integrate different time series NetCDF data into one NetCDF database via NcML files in order to add time series data. The following codes are a program example aggregating different time series soil humidity data, shown in Figure 8.

```
<NetCDF xmlns="http://www.unidata.ucar.edu/
namespaces/NetCDF/ncml-2.2">
  <aggregation dimName="time" type=
"joinExisting">
    <NetCDF location="humidity1.nc"/>
    <NetCDF location="humidity2.nc"/>
  </aggregation>
</NetCDF>
```

4.4. The Integration Examples of Image and Radial Data.

In integrating the array structure of image data into the NetCDF data model, we consider the following variables: line

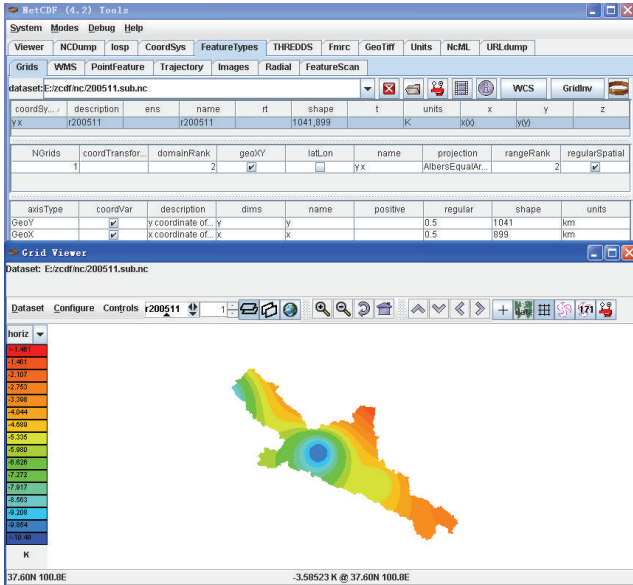


FIGURE 9: Example using freely available software (NetCDF (4.2) Tools) from the online library, which can process and visualize NetCDF and NcML files and remotely access NetCDF, GRIB, and HDF files via TSD.

(the number of satellites scan lines), elem (the element point per scan line number), and the band (the band number of observations). The geographical location is described by latitude and longitude, and the observation values of each band are defined as the main data variable of NetCDF.

In integrating the radial data (e.g., radar data), we mainly consider the radial data to be located by azimuth, elevation, angle, and orientation. A scan record is made up of a number of adjacent radial data records. The main variables of the NetCDF data model in the program include gate (the number of the pulse of a radial data record), radial (the number of radial data of recording a scan), scan (scan number), distance (the distance of pulse), time (the time of the data record), eleva (elevation angular), and azim (azimuth). In this paper, NetCDF is used as a case study of technology to implement the framework.

5. Conclusion

The eScience platform provides effective interfacing and interacting strategies for data processing, sharing scientific research and decision support with the general public. It is an important method to solve the common problem of information islands by offering public Web data access. Online integration of heterogeneous data sources provided a uniform interface for users to access, analyse, and seamlessly manage the data and give a standard format for data processing programs. The problem of messy data formats was resolved by the eScience platform. It improved the ability of the users to investigate complex phenomena such as climate change, hydrological change, and soil dynamics. Finally, the eScience environment will be gradually used to support decision-making in the Heihe River Basin.

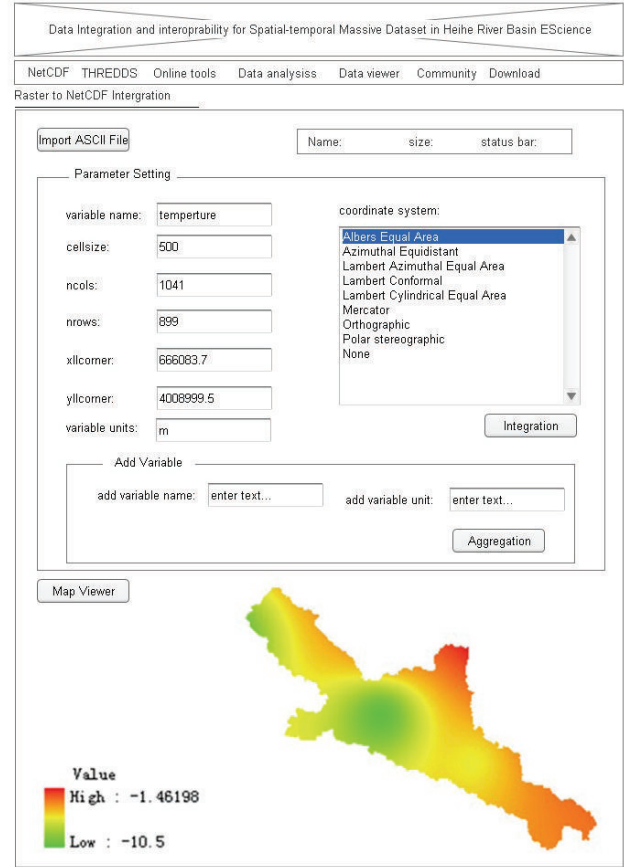


FIGURE 10: The raster data were integrated to NetCDF through the components library based on Web service.

In further research, we will examine HDF and GRIB data processing methods and gradually establish a single online spatial data process in the eScience context for the Heihe River Basin, developing a suite of efficient parallel algorithms and constructing a geoscience data-supporting library suitable for high performance parallel computation.

This study constructed the Heihe River Basin data integration and interoperability eScience context, which integrated the spatial-temporal data and different formats into NetCDF data models. The framework was constructed based on HDF, NetCDF, and GRIB for uniform management of the spatial-temporal data and metadata, which were long-term, massive, and multidimensional. In addition, we can access and analyse these data formats (e.g., HDF, NetCDF, and GRIB) through the CDM interface, which provided a convenient method for data mining, integration, and the analysis of spatial-temporal data. The framework can establish the eScience cooperative work environment and support the efficient application of the data via Web services. It is especially beneficial to the GIS and the earth science communities for cooperative communication via eScience platform.

The data integration and interoperability eScience platform of the combination of technological solutions can achieve the following goals: (i) the integration of real-time and historical data; (ii) solving the data application

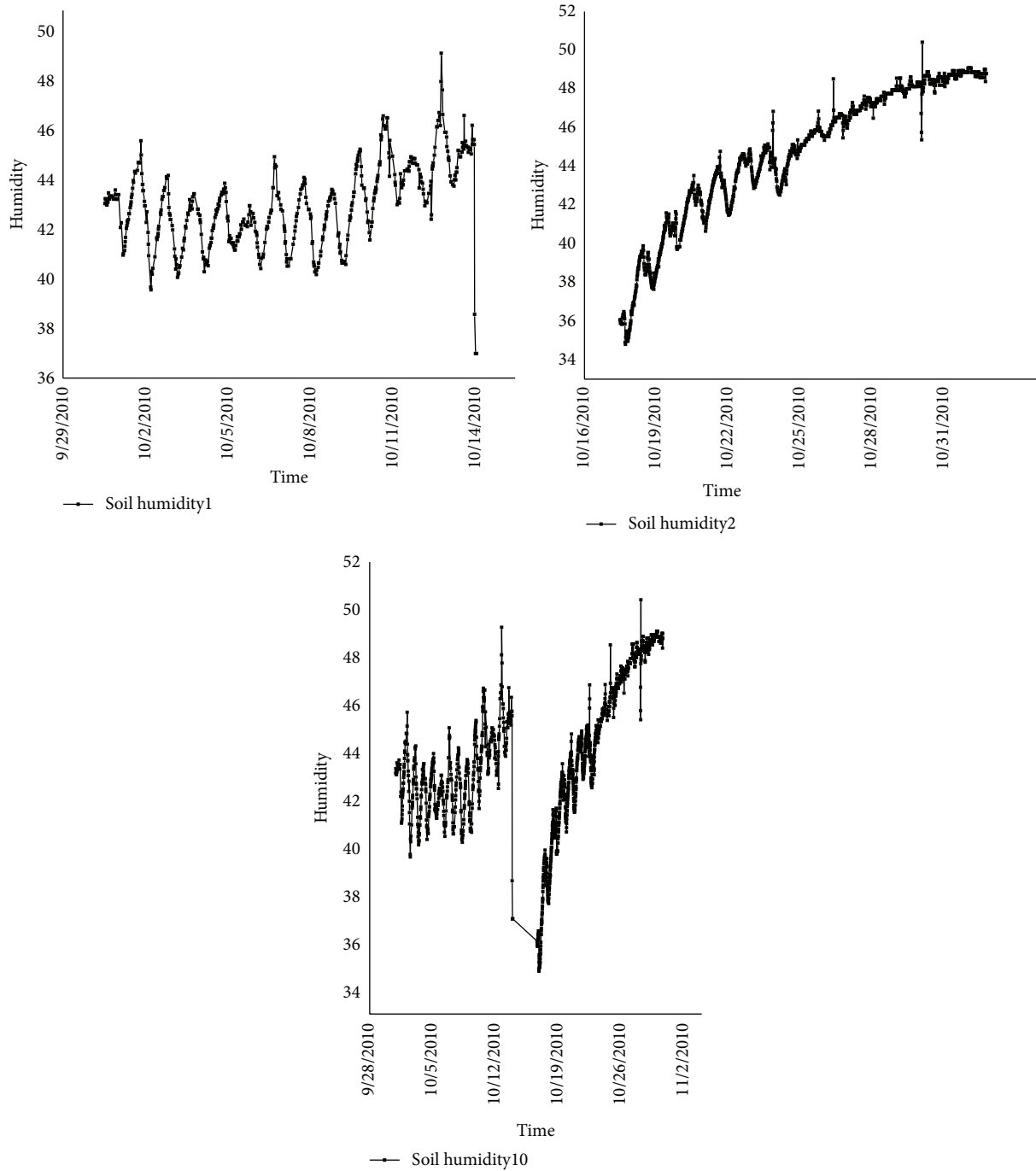


FIGURE 11: Aggregated different time series soil humidity data with one NetCDF.

problems cross fields, areas, and disciplines; (iii) conveniently accessing and analysing the data resources from different institutions; and (iv) addressing issues about heterogeneous existing standards and existing protocols of Web data access. The combination of solutions chosen could be interesting for achieving the goals, but one kind of technology cannot achieve them.

Through the platform, to generate the NetCDF format from heterogeneous multisource data (e.g., geoTiff, ASCII,

free-text, shapefile, and grid), it is different from other data share platforms and it is important to manage and share scientific data. And Heihe River Basin eScience platform is superior to other data share platforms in sophisticated analysis algorithm workflows, access to powerful computational resources, analysis, and interactive visualization interface. Our continuing work will provide scientists access to a wide range of datasets, algorithm applications, access to computational resources, services, and support.

Appendix

The NcML of the data is as follows:

```
<?Xml version="1.0" encoding="UTF-8"?>

<NetCDFxmlns=http://www.unidata.ucar.edu/
namespaces/NetCDF/ncml-2.2
location="E:/200511.nc">
<dimension name="y" length="1041"/>
<dimension name="x" length="899"/>
<attribute name="Conventions" value="CF-
1.0"/>
<attribute name="Source_Software" value=
"ESRI ArcGIS"/>
  <attribute name="History" value=
  "Translated to CF-1.0 Conventions by
  NetCDF-Java CDM (NetCDFCFWriter)"/>
<variable name="r200511" shape="y x" type=
"float">
  <attribute name="long_name" value=
  "r200511"/>
  <attribute name="esri_pe_string" value=
  "PROJCS"/>
  <attribute name="coordinates" value=
  "y x"/>
  <attribute name="grid_mapping" value=
  "albers_conical_equal_area"/>
  <attribute name="units" value="K"/>
  <attribute name="missing_value" type=
  "float" value="-3.4028235E38"/>
</variable>
<variable name="y" shape="y" type="double">
  <attribute name="units" value="km"/>
  <attribute name="long_name" value="y
coordinate of projection"/>
  <attribute name="standard_name" value=
  "projection_y_coordinate"/>
</variable>
<variable name="x" shape="x" type="double">
  <attribute name="units" value="km"/>
  <attribute name="long_name" value="x
coordinate of projection"/>
  <attribute name="standard_name" value=
  "projection_x_coordinate"/>
</variable>
<variable name="albers_conical_equal_area"
shape="" type="int">
  <attribute name="grid_mapping_name"
value="albers_conical_equal_area"/>
  <attribute name="longitude_of_central_
meridian" type="double" value="105.0"/>
  <attribute
name="latitude_of_projection_origin"
type="double" value="0.0"/>
```

```
<attribute name="false_easting" type=
"double" value="0.0"/>
<attribute name="false_northing" type=
"double" value="0.0"/>
<attribute name="standard_parallel" type=
"double" value="25.0 47.0"/>
<attribute
name="_CoordinateTransformType"
value="Projection"/>
<attribute name="_CoordinateAxisTypes"
value="GeoX GeoY"/>
</variable>
```

```
</NetCDF>
```

Conflict of Interests

The authors declare that there is no conflict of interests regarding the publication of this paper.

Acknowledgments

This work was supported by the National Natural Science Foundation of China (91125005/D011004), the National Natural Science Foundation of China (41290255), the Strategic Priority Research Program of the Chinese Academy of Sciences (XDB03020601), the CAS/SAFEA International Partnership Program for Creative Research Teams (KZZD-EW-TZ-03), and China Data Sharing Infrastructure of Earth System Science.

References

- [1] K. V. Knyazkov, S. V. Kovalchuk, T. N. Tchurov, S. V. Maryin, and A. V. Boukhanovsky, "CLAVIRE: e-Science infrastructure for data-driven computing," *Journal of Computational Science*, vol. 3, no. 6, pp. 504–510, 2012.
- [2] M. Lutz, J. Sprado, E. Klien, C. Schubert, and I. Christ, "Overcoming semantic heterogeneity in spatial data infrastructures," *Computers & Geosciences*, vol. 35, no. 4, pp. 739–752, 2009.
- [3] NRC, *Grand Challenges in Environmental Sciences*, National Academy of Sciences, Washington, DC, USA, 2001.
- [4] Y. L. Simmhan, B. Plale, and D. Gannon, "A survey of data provenance in e-science," *ACM SIGMOD Record*, vol. 34, no. 3, pp. 31–36, 2005.
- [5] J. L. Goodall, J. S. Horsburgh, T. L. Whiteaker, D. R. Maidment, and I. Zaslavsky, "A first approach to web services for the National Water Information System," *Environmental Modelling & Software*, vol. 23, no. 4, pp. 404–411, 2008.
- [6] J. S. Horsburgh, D. G. Tarboton, M. Piasecki et al., "An integrated system for publishing environmental observations data," *Environmental Modelling & Software*, vol. 24, no. 8, pp. 879–888, 2009.
- [7] S. Fiore and G. Aloisio, "Data management for eScience," *Future Generation Computer Systems*, vol. 27, no. 3, pp. 290–291, 2011.
- [8] M. F. Goodchild, "Citizens as sensors: the world of volunteered geography," *GeoJournal*, vol. 69, no. 4, pp. 211–221, 2007.
- [9] W. Li, C. Yang, D. Nebert et al., "Semantic-based web service discovery and chaining for building an Arctic spatial data

- infrastructure,” *Computers & Geosciences*, vol. 37, no. 11, pp. 1752–1762, 2011.
- [10] L. Li, J. Guardiola, and Y. Liu, “Qualitative spatial representation and reasoning for data integration of ocean observing systems,” *Computers, Environment and Urban Systems*, vol. 35, no. 6, pp. 474–484, 2011.
- [11] J. Mennis and D. S. Guo, “Spatial data mining and geographic knowledge discovery—an introduction,” *Computers, Environment and Urban Systems*, vol. 33, no. 6, pp. 403–408, 2009.
- [12] G. W. Johnson, A. G. Gaylord, J. C. Franco et al., “Development of the Arctic Research Mapping Application (ARMAP): interoperability challenges and solutions,” *Computers & Geosciences*, vol. 37, no. 11, pp. 1735–1742, 2011.
- [13] T. Foerster, L. Lehto, T. Sarjakoski, L. T. Sarjakoski, and J. Stoter, “Map generalization and schema transformation of geospatial data combined in a Web Service context,” *Computers, Environment and Urban Systems*, vol. 34, no. 1, pp. 79–88, 2010.
- [14] L. S. R. Froude, “Storm tracking with remote data and distributed computing,” *Computers & Geosciences*, vol. 34, no. 11, pp. 1621–1630, 2008.
- [15] K. V. Knyazkov, S. V. Kovalchuk, T. N. Tchurov, S. V. Maryin, and A. V. Boukhanovsky, “CLAVIRE: e-Science infrastructure for data-driven computing,” *Journal of Computational Science*, vol. 3, no. 6, pp. 504–510, 2012.
- [16] T. Blanke, M. Hedges, and S. Dunn, “Arts and humanities e-science—current practices and future challenges,” *Future Generation Computer Systems*, vol. 25, no. 4, pp. 474–480, 2009.
- [17] L. Díaz, C. Granell, M. Gould, and J. Huerta, “Managing user-generated information in geospatial cyberinfrastructures,” *Future Generation Computer Systems*, vol. 27, no. 3, pp. 304–314, 2011.
- [18] G. Giuliani, N. Ray, and A. Lehmann, “Grid-enabled Spatial Data Infrastructure for environmental sciences: challenges and opportunities,” *Future Generation Computer Systems*, vol. 27, no. 3, pp. 292–303, 2011.
- [19] M. G. Tait, “Implementing geoportals: applications of distributed GIS,” *Computers, Environment and Urban Systems*, vol. 29, no. 1, pp. 33–47, 2005.
- [20] E. Deelman, D. Gannon, M. Shields, and I. Taylor, “Workflows and e-Science: an overview of workflow system features and capabilities,” *Future Generation Computer Systems*, vol. 25, no. 5, pp. 528–540, 2009.
- [21] G. Folino, A. Forestiero, G. Papuzzo, and G. Spezzano, “A grid portal for solving geoscience problems using distributed knowledge discovery services,” *Future Generation Computer Systems*, vol. 26, no. 1, pp. 87–96, 2010.
- [22] D. D. Pennington, “Collaborative, cross-disciplinary learning and co-emergent innovation in eScience teams,” *Earth Science Informatics*, vol. 4, no. 2, pp. 55–68, 2011.
- [23] J. Rowley, “E-Government stakeholders—who are they and what do they want?” *International Journal of Information Management*, vol. 31, no. 1, pp. 53–62, 2011.
- [24] N. C. Chen, C. L. Hu, Y. Chen, C. Wang, and J. Y. Gong, “Using SensorML to construct a geoprocessing e-Science workflow model under a sensor web environment,” *Computers and Geosciences*, vol. 47, pp. 119–129, 2012.
- [25] M. T. Borzacchiello and M. Craglia, “Estimating benefits of spatial data infrastructures: a case study on e-Cadastris,” *Computers, Environment and Urban Systems*, vol. 41, pp. 276–288, 2013.
- [26] J. Wu, “The effect of ecological management in the upper reaches of Heihe River,” *Acta Ecologica Sinica*, vol. 31, no. 1, pp. 1–7, 2011.
- [27] J. R. Millan-Almaraz, I. Torres-Pacheco, C. Duarte-Galvan et al., “FPGA-based wireless smart sensor for real-time photosynthesis monitoring,” *Computers and Electronics in Agriculture*, vol. 95, pp. 58–69, 2013.
- [28] Q. Dahe, “China’s meteorological science data sharing process and prospect,” *Scientific Chinese*, vol. 9, pp. 18–20, 2004.
- [29] B. Plale, D. A. Gannon, J. Alameda et al., “Active management of scientific data,” *IEEE Internet Computing*, vol. 9, no. 1, pp. 27–34, 2005.
- [30] D. P. Lanter, “A lineage metadata approach to removing redundancy and propagating updates in a GIS database,” *Cartography and Geographic Information Science*, vol. 21, no. 2, pp. 91–98, 1994.
- [31] R. B. Jerard and O. Ryou, “NCML: a data exchange format for internet-based machining,” *International Journal of Computer Applications in Technology*, vol. 26, no. 1-2, pp. 75–82, 2006.
- [32] K. Stock, T. Stojanovic, F. Reitsma et al., “To ontologise or not to ontologise: an information model for a geospatial knowledge infrastructure,” *Computers & Geosciences*, vol. 45, pp. 98–108, 2012.
- [33] A. M. Castronova, J. L. Goodall, and M. M. Elag, “Models as web services using the Open Geospatial Consortium (OGC) Web Processing Service (WPS) standard,” *Environmental Modelling & Software*, vol. 41, pp. 72–83, 2013.
- [34] X. Li, L. Lua, W. Yang, and G. Chenga, “Estimation of evapotranspiration in an arid region by remote sensing—a case study in the middle reaches of the Heihe River Basin,” *International Journal of Applied Earth Observation and Geoinformation*, vol. 17, no. 1, pp. 85–93, 2012.
- [35] G. Fox and M. Pierce, “Grids challenged by a web 2.0 and multicore sandwich,” *Concurrency and Computation: Practice and Experience*, vol. 21, no. 3, pp. 265–280, 2009.
- [36] L. D. Stein, “Towards a cyberinfrastructure for the biological sciences: progress, visions and challenges,” *Nature Reviews Genetics*, vol. 9, no. 9, pp. 678–688, 2008.
- [37] R. P. Signell, S. Carniel, J. Chiggiato, I. Janekovic, J. Pullen, and C. R. Sherwood, “Collaboration tools and techniques for large model datasets,” *Journal of Marine Systems*, vol. 69, no. 1-2, pp. 154–161, 2008.
- [38] Y. B. Li, A. J. Brimicombe, and M. P. Ralphs, “Spatial data quality and sensitivity analysis in GIS and environmental modelling: the case of coastal oil spills,” *Computers, Environment and Urban Systems*, vol. 24, no. 2, pp. 95–108, 2000.

Research Article

An Evaluation of River Health for the Weihe River in Shaanxi Province, China

Jinxi Song,^{1,2} Dandong Cheng,² Qi Li,² Xingjun He,³ Yongqing Long,² and Bo Zhang²

¹State Key Laboratory of Soil Erosion and Dryland Farming on the Loess Plateau, Institute of Soil and Water Conservation, CAS & MWR, Yangling 712100, China

²College of Urban and Environmental Sciences, Northwest University, Xi'an 710027, China

³Shenzhen Green Island Environmental Water Technology Co., Ltd, Shenzhen 518108, China

Correspondence should be addressed to Jinxi Song; jinxisong@nwu.edu.cn

Received 15 December 2014; Accepted 3 February 2015

Academic Editor: Yongqiang Zhang

Copyright © 2015 Jinxi Song et al. This is an open access article distributed under the Creative Commons Attribution License, which permits unrestricted use, distribution, and reproduction in any medium, provided the original work is properly cited.

Excessive socioeconomic activities in the Weihe River region have caused severe ecosystem degradation, and the call for the recovery and maintenance of the river health has drawn great attention. Based on the connotation of river health, previous research findings, and status quo of the Weihe River ecosystem, in this study, we developed a novel health evaluation index system to quantitatively determine the health of the Weihe River in Shaanxi Province. The river in the study area was divided into five reaches based on the five hydrological gauging stations, and appropriate evaluation indices for each river section were selected according to the ecological environmental functions of that section. A hybrid approach integrating analytic hierarchy process (AHP) and a fuzzy synthetic evaluation method was applied to measure the river health. The results show that Linjancun-Weijiabao reach and Weijiabao-Xianyang reach are in the “moderate” level of health and Lintong-Huaxian reach and downstream of Huaxian reach are in the “poor” health rating, whereas Xianyang-Lintong reach is in the “sick” rating. Moreover, the most sensitive factors were determined, respectively, for each reach from upper stream to lower stream in the study area.

1. Introduction

From an economic point of view, water resources are composite assets that provide a variety of goods and services for consumptive and productive activities of human being [1, 2]. Water is an essential resource for the existence of both human and other species on the earth [3]. In recent years, the concept of environmental flow (E-flow) has received increasing awareness; common understanding has come to recognize the importance of preserving some amount of water in a river to maintain the health of a river ecosystem [4–7].

However, the problems of water scarcity and deteriorating water quality, due to rapid socioeconomic development [1, 8] and climate change [9], have become more serious around the world, resulting in an increase in water demand for socioeconomic sectors and reduction in E-flow [7]. The survey results of the United Nations Environment Programme (UNEP) on

25 rivers reveal that water quality of the major rivers in the world is poor and deteriorated, and water quantity in the rivers is decreasing [10]. It is estimated that, in 2025, 5 billion out of the world's 7.9 billion people will be living in areas where it will be difficult or even impossible to meet basic water demand for drinking, cooking, and sanitation [3, 11].

Catchment and riparian degradation has caused declining ecosystem health of streams worldwide [12]. Many studies on river health evaluation have been conducted in order to prevent river ecosystem from further deterioration [13–18]. For example, the declines and improvements in river health related to land use have been studied by using macroinvertebrates sampled from sites along a dry-land river in northwestern Zimbabwe to assess biotic responses to land use changes along the course of the river [19]. Water quality index, biotic index, and physical habitat quality index have been used to assess river health conditions using 25 sampling sites in the Liao River in China [20]. Biological monitoring,

using coliform bacteria and macroinvertebrate populations and diversity, was carried out monthly to determine the ecological health of the Usuthu and Mbuluzi rivers in Swaziland [21]. Sheldon et al. [12] identified the spatial scale of land use that most strongly influenced overall river ecosystem health score in Southeast Queensland, Australia, in which the five component indicators (fish, macroinvertebrates, water quality, nutrients, and ecosystem processes) make up the score. Pinto et al. [22] used six water quality parameters, namely, temperature, chlorophyll-a, dissolved oxygen, oxides of nitrogen, suspended solids, and reactive silicates at weekly intervals along the Hawkesbury-Nepean River (HNR) system in South-Eastern Australia to evaluate the human and natural influences on the river system health in a periurban landscape.

China possesses total water resources of 2812.4 billion m^3 ranking the 6th in the world, while its per capita water resource only accounts for a quarter of world average in terms of per capita water resources [1, 3]. The rapid development results in increasing water requirements and overwhelming amounts of waste discharge, which degrades the water ecosystem. The Weihe River in China is the largest tributary of the Yellow River and plays an important role in developing West China and the maintenance of ecosystem health of the Yellow River [23]. Since the late 1990s, many parts of the river have lost ecosystem functionality and such problems have disturbed the sustainable development of the region [23], which has become a widespread concern in China [24]. Many researchers have conducted studies on ecological environment of the river with significant results [25–27]. For the Weihe River, Shi [28] established healthy controlling indicator system of the Weihe River based on the riverbed, aquatic environment, and socioeconomic functions of the river, while this system lacks specific evaluation and analysis of the results. Feng [29] established the evaluation index system applied to assess the Weihe River health based on the status of environmental issues of the river. However, this evaluation only focuses on flood control and river sediment transport capacity. More recently, Wei et al. [7] developed a complex system dynamics model (SD) to assess socioeconomic impacts of different levels of E-flow allocation in the Weihe River Basin of China, which aims to find an optimal growth pattern considering both socioeconomic growth and E-flow requirements. Li et al. [24] determined the changes in major factors of stream flow, water quality, channel morphology, and riparian vegetation affecting its ecosystem health of the Weihe River. Wu et al. [30] assessed the ecological health of the Weihe River using an index of water and habitat quality (IWHQ) based on environmental variables and habitat quality (QHEI). The study proposed a strategy for sustainable development at a river basin scale, in which water resources should be allocated efficiently, equally, and fairly for socioeconomic development and a healthy river system. However, this study does not analyze and evaluate the current ecosystem health situations of the Weihe River.

This study developed an evaluation index system for the health of the Weihe River in Shaanxi Province, where the Weihe River (Shaanxi section) was divided into five sections based on water function zoning method and then the river

health was evaluated section by section. This study improves the indicator evaluation system for river health; the methods and results concerned will provide theoretic and practical support for river health assessment, river development, utilization, and management, and river ecological restoration of the Weihe River.

2. Study Area Description

The Weihe River, originating from north of Niaoshu Mountain with an altitude of 3485 m above sea level, is the largest tributary of the Yellow River. It runs across 818 km through the provinces of Gansu and Shaanxi and joins the Yellow River from the right bank in the city of Tongguan, from where the Yellow River turns to the east (Figure 1). The drainage area, annual flow flux, and annual sediment discharge of the Weihe River account for 17.9%, 16.5%, and 2.5% of the total amount of the Yellow River Basin, respectively. The channel length in the confluence area is about 13.1 km [31].

The Weihe River flows across about 502.4 km with a drainage area of 67,100 km^2 in Shaanxi Province where the well-known Guanzhong Plain in Northwest China is located. The river basin plays a great role in social, ecological, and economical development of Shaanxi Province (Figure 1). About 64% of the population, 56% of the farmland, 72% of the irrigation area, and 82% of gross industrial output value of Shaanxi Province are distributed in this area. And about 81% of gross domestic product (GDP) of the Shaanxi Province derived from the Weihe River Basin [32]. Xi'an, the capital of Shaanxi Province, is one of the birthplaces of the ancient Chinese civilization in the Yellow River Basin and the starting point of Silk Road. The total population of the municipality is up to 8.5 million. Known as the leading city of China's Western Development Drive Program since 1990s, Xi'an is an important economic, cultural, industrial, and educational center in central-northwest region [33].

The most important topographic feature of the Weihe River Basin is the Loess Plateau in the north, which is the main source of sediments in the river [34, 35]. The Jinghe River, the Beiluo River, and the Shichuan River flow into the Weihe River from the Loess Plateau with hyperconcentrated sediments. The topographic feature for the southern part of the Weihe River Basin is the Qinling Mountains, and the precipitation there is the main water supply resource for the river flow. Tributaries of the river from the Qinling Mountains are with less sediment [36].

The climate of the Weihe River Basin in Shaanxi Province is continental, warm, and semihumid controlled by the East Asian monsoon climate [33]. The annual average temperature is about 13.3°C and the annual rainfall is in the range of 558–750 mm with a general increasing trend from north to south. The mean annual precipitation of this basin area is 31.16 billion m^3 , accounting for 22.4% of the total precipitation of Shaanxi Province [24]. About 78% of the rainfall concentrates during May to October, among which the rainfall from July to September accounts for 47% of the annual total. The mean annual runoff of the basin area is 10.37 billion m^3 , and

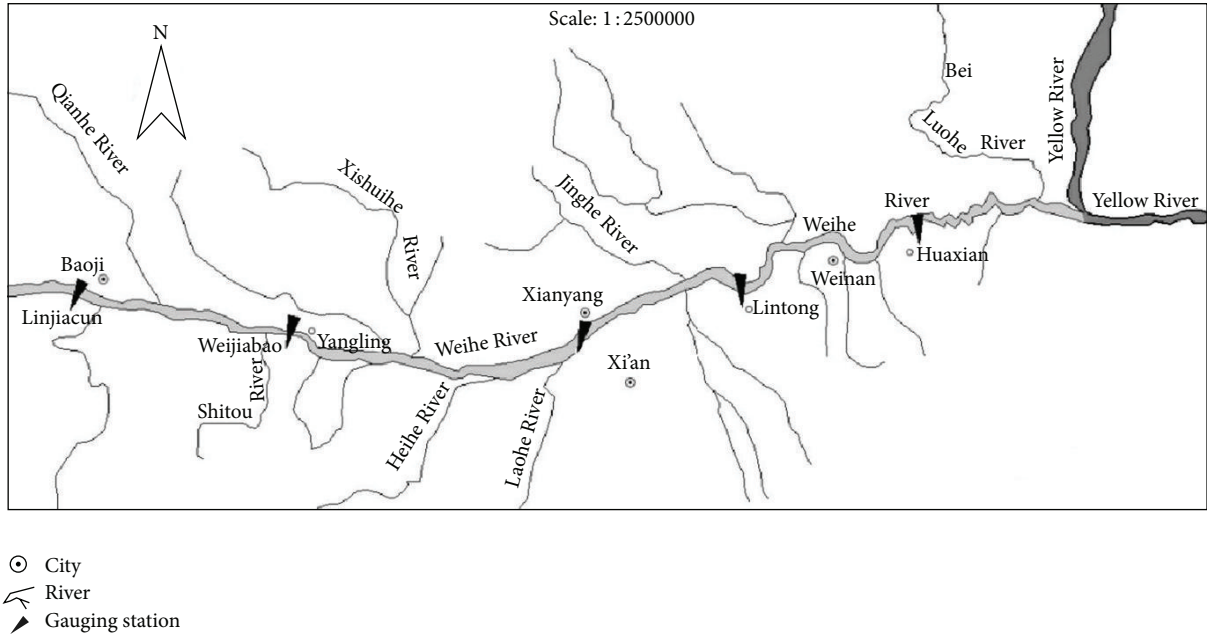


FIGURE 1: Study area showing hydrological gauging stations.

the mean annual variation coefficient of runoff is about 0.30–0.35. The runoff discharge patterns are dominated by runoff from July to September, which accounts for about 60–70% of annual discharge [6].

A large number of groundwater pumping wells were constructed near the river, which potentially reduces the infiltration of river water into the adjacent aquifers of the Weihe River. Agricultural irrigation is the largest water consumer, representing 60% of the total amount of water consumption, which is withdrawn from the river and aquifers. Even in the low flow period, 80% of water in the stream is impounded by dams for agriculture irrigation in the Baoji district [24]. The ratio of water utilization volume for domestic, industry, and agriculture makes up 47.9% to the total volume of water resources in the Weihe River Basin. Meanwhile, the Weihe River Basin has been one of the most serious soil loss areas in the Yellow River Basin. The area suffering from serious soil loss has reached 360,000 km², taking up 65% of total land area in the Weihe River Basin, which has not only aggravated the deterioration of ecosystem but also resulted in serious sediment deposition in the lower reach of the Weihe River [31, 37]. The cumulative yield of sediment deposition was 1.30 billion m³ in 2001, while the maximum amount was 1.32 billion m³ in 1997 (Figure 2). The capacity of the levees to prevent flood in the lower Weihe River decreased from 50-year to 20-year frequency of flooding and further to 10-year flood frequency [31]. The Weihe River streambed was, however, elevated downstream near Tongguan due to accumulation of silt and clay, leading to water logging and increased risk of flooding in this region [38].

In addition, the Weihe River is the major sewage discharge channel in the Guanzhong Region. Large amount of untreated industrial wastewater and domestic sewage is directly discharged into the Weihe River. Also, the nonpoint

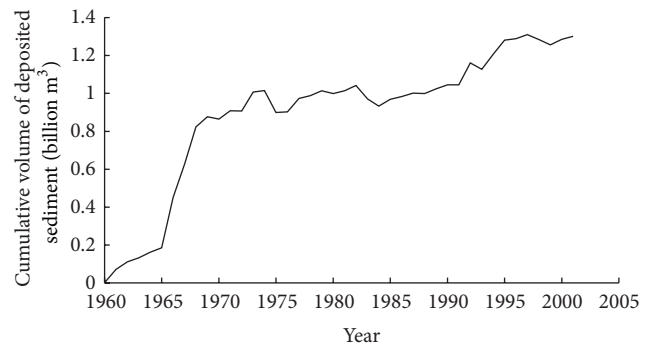


FIGURE 2: Cumulative volume of deposited sediment in the channel of the lower Weihe River.

source of contaminated stormwater washing off parking lots, roads and highways, and lawns (containing fertilizers and pesticides) is drained into the river. According to the survey data from Shaanxi Provincial Environmental Protection Bureau, a total number of 245 sewage discharge ports are distributed on both sides of the Weihe River, and more than 700 million tons of sewage is discharged into the river annually, which has resulted in serious water pollution [24].

There are five hydrological gauging stations (Linjiacun, Weijabao, Xianyang, Lintong, and Huaxian) along the Weihe River in Shaanxi Province (Figure 1). Stream gradient becomes gentle from Linjiacun to the mouth of the lower reaches of the Weihe River. The average stream gradients for the reaches of Linjiacun-Xianyang and downstream from Xianyang are 1.24 m/km and 0.28 m/km, respectively [39]. On the basis of data related to ecology, society, economy, hydraulics, and hydrology measured in 2007, a typical hydrological year, the river health for five reaches is estimated,

including Linjiacun-Weijiabao (LW), Weijiabao-Xianyang (WX), Xianyang-Lintong (XL), Lintong-Huaxian (LH), and the downstream of Huaxian (DH).

3. Methods

3.1. Fuzzy Synthetic Evaluation Method. Fuzzy synthetic evaluation method applies fuzzy mathematical principles to evaluate things and phenomenon affected by variety of factors [40, 41]. Fuzzy-based techniques are helpful in addressing deficiencies inherent in binary logic and propagating uncertainties through models. Contrary to binary logic, fuzzy-based techniques provide an intensity of exceeding regulated thresholds with the help of memberships to various health levels [42]. The fuzzy synthetic evaluation method regards evaluation objectives as a fuzzy set (named the factor set U) composed of variety of factors with different assessment levels selected. Another fuzzy set named the evaluation set V is employed to calculate the membership degree of each individual factor in the evaluation set to establish a fuzzy matrix. The quantitative evaluation value of each factor is finally determined by calculating the weight distribution of each factor in evaluation goal. It applies the fuzzy transformation theory and maximum membership degree law and makes a comprehensive evaluation on various factors [43, 44]. Specific steps are as follows.

Firstly, evaluation factors are defined. In order to obtain accurate assessment results for river health conservation and protection, the factors reflecting the river health are determined based on the following rules. (1) Naturality: The factors reflect the essential attribute of the ecosystem functions of each section for the river [45]. (2) Representativeness: The most significant factor is identified to represent the same categorical ones. (3) Stability and variability: The domain factors can be determined within a certain time even though they change for a larger temporal scale [46]. (4) Quantification: The factors can be valued by the measured data and used to calculate the evaluation of river health. (5) Operability: The quality or function of these factors can be improved through treatment measures by related government agency.

Based on these rules, the main ecosystem function of the Weihe River and the water environmental function zoning of Shaanxi Province was enacted by provincial government in 2004. Factor set of evaluation object is determined, which is expressed by $U = \{u_1, u_2, \dots, u_m\}$. It is a set composed of m evaluation indicators, which are defined as follows. (1) Water quality: the major pollutant in the Weihe River is organic pollution including chemical oxygen demand (COD) and ammonia-nitrogen ($\text{NH}_3\text{-N}$), which are the national pollution indicators classified by environmental quality standards for surface water (GB 3838-2002) defined by the environment protection law of the People's Republic of China. (2) Guaranteed rate of discharge in dry flow season: it is the ratio of average flow volume in the dry flow season to the annual mean flow volume. (3) The ratio of wetland area: it is the percentage of the wetland area to the whole basin area. (4) Recreational value index: it is the ratio of measured in-stream flow to desired flow for supplying recreational

activities, such as landscape appreciation, riverine travel. (5) Riparian vegetation coverage ratio: it is the ratio of riparian vegetation (grass, forestland, orchard, shrub, and riparian zone) area to the total riparian land area. (6) Capacity of flood discharge: it is the ratio of actual flood drainage flow to the desired flood drainage flow. (7) Requirement rate of bankfull discharge: it is the ratio of bankfull discharge to critical flow under the conditions without erosion or deposition. (8) Variation rate of streambed gradient: it is the ratio of stream gradient during measured period to the previous gradient before Sanmenxia Reservoir operation. (9) Proportion of fish species: it is the ratio of current fish species amount to amount in the 1980s.

Secondly, remarkable grades of evaluation factors are determined: the rationality of the evaluation criteria directly affects the accuracy of evaluation results. Considering field investigation, expert advice, and literature review, the five remarkable grades including excellent, good, moderate, poor, and sick for the significance of the evaluation factors are defined, which is expressed by set, $V = \{v_1, v_2, v_3, v_4, v_5\}$.

Thirdly, the factor weights are determined. The accuracy determination of the factor weight is of great importance to the evaluation of estimation results. Many methods have been developed to calculate factor weight, which can be roughly divided into subjective method and objective method according to the different sources of the original data. Subjective method, such as Delphi method and analytic hierarchy process (AHP), depends on the expert's experience and judgment, and so on. In contrast, objective method, such as principal component analysis method, standard variance method, and maximizing deviation method, is based on measured data and thus has less subjective errors caused by human judgment. Objective ways cannot reflect the subjective requirements of decision-makers though they avoid human interference. This study used AHP, one commonly used method, to evaluate the health of the Weihe River in Shaanxi Province. A formal questionnaire for evaluation factor weights is proposed, the values of which are suggested by researches and governors. Then, the weight for each evaluation factor is determined, which is expressed by $W = \{w_1, w_2, w_3, \dots, w_m\}$, a set composed of m weight values.

Fourthly, the fuzzy membership function is estimated. There are some commonly used forms of functions to calculate membership degree, such as normal type, partial large-scale, partial small, triangular fuzzy numbers, lower semitrapezoidal, trapezoidal, and ridge [47]. The conclusions for the final analyses are consistent though the forms of these membership functions vary; which membership to select does not affect the study results [48]. In this paper, the triangular fuzzy number membership function was selected to determine the membership degree value of the evaluation factors. Different evaluation degree U_{ij} is measured by the standard value V_{ijk} of each evaluation factor. The membership functions are defined as follows [47, 49].

For the first grade ($K = 1$)

$$g(x) = \begin{cases} 1, & x \leq v_k, \\ \cos^2 \left[\left(\frac{x - v_k}{v_{k+1} - v_k} \right) \times \frac{\pi}{2} \right], & v_k \leq x \leq v_{k+1}, \\ 0, & x \geq v_{k+1}. \end{cases} \quad (1)$$

For the second, third, and fourth grade ($K = 2, 3, 4$)

$$g(x) = \begin{cases} 0, & x \leq v_{k-1}, \\ \sin^2 \left[\left(\frac{x - v_{k-1}}{v_k - v_{k-1}} \right) \times \frac{\pi}{2} \right], & v_{k-1} \leq x \leq v_k, \\ \cos^2 \left[\left(\frac{x - v_k}{v_{k+1} - v_k} \right) \times \frac{\pi}{2} \right], & v_k \leq x \leq v_{k+1}, \\ 0, & x \geq v_{k+1}. \end{cases} \quad (2)$$

For the fifth grade ($K = 5$)

$$g(x) = \begin{cases} 0, & x \leq v_{k-1}, \\ \sin^2 \left[\left(\frac{x - v_{k-1}}{v_k - v_{k-1}} \right) \right], & v_{k-1} \leq x \leq v_k, \\ 1, & x \geq v_k. \end{cases} \quad (3)$$

Formulas (1)–(3) are suitable for a factor with less value indicating better quality. But for a factor with greater value indicating better quality, the symbol “<” should be changed to “>” and “>” to “<”.

Finally, the hierarchical fuzzy evaluation is calculated. The fuzzy relation matrix R_i of each evaluation factor u_i for remarkable grade v_j can be expressed as follows:

$$R_i = \begin{bmatrix} r_{i11} & r_{i12} & r_{i13} & r_{i14} & r_{i15} \\ r_{i21} & r_{i22} & r_{i23} & r_{i24} & r_{i25} \\ \vdots & \vdots & \vdots & \vdots & \vdots \\ r_{ij1} & r_{ij2} & r_{ij3} & r_{ij4} & r_{ij5} \\ \vdots & \vdots & \vdots & \vdots & \vdots \end{bmatrix}, \quad (4)$$

where r_{ijk} is the judge result of evaluation factor u_i to remarkable grade v_j .

The first-grade fuzzy comprehensive evaluation set B_i for the evaluation factor u_i to remark j is calculated as follows:

$$B_i = W_i \circ R_i$$

$$= (W_{i1}, W_{i2}, \dots, W_{ij}, \dots) \circ \begin{bmatrix} r_{i11} & r_{i12} & r_{i13} & r_{i14} & r_{i15} \\ r_{i21} & r_{i22} & r_{i23} & r_{i24} & r_{i25} \\ \vdots & \vdots & \vdots & \vdots & \vdots \\ r_{ij1} & r_{ij2} & r_{ij3} & r_{ij4} & r_{ij5} \\ \vdots & \vdots & \vdots & \vdots & \vdots \end{bmatrix} \quad (5)$$

$$= (B_{i1}, B_{i2}, B_{i3}, B_{i4}, B_{i5}),$$

where W_{ij} stands for weights of the evaluation factor u_i to remark j and “ \circ ” is the matrix composite operator. In this paper, considering the effect of input single data on the evaluation results, one of general matrix algorithm performed as $M(\cdot, +)$ operator is used. This can clearly reflect the differences in the membership functions of each evaluation factor for each remarkable grade.

Based on formula (4), the judge decision-making matrix of m evaluation factors is provided as follows:

$$R = \begin{bmatrix} B_1 \\ B_2 \\ \vdots \\ B_m \end{bmatrix} = \begin{bmatrix} W_1 \circ R_1 \\ W_2 \circ R_2 \\ \vdots \\ W_m \circ R_m \end{bmatrix}, \quad (6)$$

where R is the fuzzy connection of U to V .

Then, the second-grade fuzzy synthetic evaluation set B is determined as

$$B = W \circ R = (b_1, b_2, b_3, b_4, b_5). \quad (7)$$

According to the principle of maximum membership degree, the greatest value in the set B indicates river health conditions of the study area.

3.2. Sensitivity Analysis. Sensitivity analysis is a useful method to determine which factors are the key drivers to river health [50]. In general, the methods based on mathematical programming are complex and opaque, which has the disadvantage of providing reference for identification of factor’s sensibility. The simplest and most common approach is one-factor-at-a-time (OFAT or OAT), where. To see which parameters are the most sensitive factors to affect this produces on the output [51]. OAT is a measurement process to take out one parameter at a time while keeping the other parameters constant. In comparison with the deviations for the value from the whole parameter, the most sensitive factors are determined [52].

4. Results and Analysis

4.1. Definition of River Health Indicators. The reasonability of determining the evaluation indicator will directly affect the evaluation results of river health. Up to now, there has been no cohesive standard to assess the river health in China [20]. Generally speaking, an improper evaluation method will lead to unfair consequences, and the main cause of which is that every district, basin, or river has its distinctive characteristics and uniqueness. Thus, there is no mandatory and probable method to unify the evaluation standard to determine river health [53]. The main objectives of river health evaluation are to explore the main problems of the river health by assessing the current situation of the river and hence to investigate measures for amendment. To achieve these objectives, the evaluation indicators with weight for river health evaluation are determined by hierarchical structure including target layer, criterion layer, and index layer (Table 1).

TABLE 1: Evaluation indicators, weight, and current values for five reaches of the Weihe River in Shaanxi Province.

Reach	Criterion layer (weight)	Indicator layer	Evaluation criterion					Current value
			Excellent	Good	Moderate	Poor	Sick	
LW	Water quality (0.25)	COD (mg/L)	15.00	20.00	30.00	40.00	50.00	19.16
		NH ₃ -N (mg/L)	0.15	0.50	1.00	1.50	2.00	0.69
	Ecological function (0.59)	Ratio of wetland area (%)	5.00	4.00	3.00	2.00	1.00	1.24
		Riparian vegetation coverage ratio (%)	90.00	70.00	50.00	30.00	10.00	59.89
Recreation function (0.16)	Guaranteed rate of discharge in dry flow season (%)	Recreation value index	80.00	60.00	40.00	20.00	0.00	44.00
			90.00	70.00	50.00	30.00	10.00	40.00
WX	Water quality (0.32)	COD (mg/L)	15.00	20.00	30.00	40.00	50.00	53.77
		NH ₃ -N (mg/L)	0.15	0.50	1.00	1.50	2.00	8.57
	Ecological function (0.34)	Riparian vegetation coverage ratio (%)	90.00	70.00	50.00	30.00	10.00	60.97
		Proportion of fish species (%)	0.80	0.60	0.40	0.20	0.00	0.35
Recreation function (0.34)	Guaranteed rate of discharge in dry flow season (%)	Recreation value index	80.00	60.00	40.00	20.00	0.00	40.00
			90.00	70.00	50.00	30.00	10.00	36.00
XL	Water quality (0.34)	COD (mg/L)	15.00	20.00	30.00	40.00	50.00	49.60
		NH ₃ -N (mg/L)	0.15	0.50	1.00	1.50	2.00	7.25
	Ecological function (0.14)	Ratio of wetland area (%)	5.00	4.00	3.00	2.00	1.00	8.90
		Riparian vegetation coverage ratio (%)	90.00	70.00	50.00	30.00	10.00	60.43
Flood control (0.52)	Guaranteed rate of discharge in dry flow season (%)	Variation rate of streambed gradient (%)	90.00	70.00	50.00	30.00	10.00	51.85
		Capacity of flood discharge (%)	100.00	90.00	80.00	60.00	40.00	87.00
LH	Water quality (0.20)	COD (mg/L)	15.00	20.00	30.00	40.00	50.00	41.46
		NH ₃ -N (mg/L)	0.15	0.50	1.00	1.50	2.00	6.01
	Ecological function (0.37)	Riparian vegetation coverage ratio (%)	90.00	70.00	50.00	30.00	10.00	65.08
		Guaranteed rate of discharge in dry flow season (%)	90.00	70.00	50.00	30.00	10.00	61.00
Flood control (0.43)	Requirement rate of bankfull discharge (%)	Variation rate of streambed gradient (%)	100.00	90.00	80.00	60.00	40.00	44.00
			100.00	80.00	60.00	40.00	20.00	39.00
DH	Water quality (0.16)	COD (mg/L)	15.00	20.00	30.00	40.00	50.00	37.26
		NH ₃ -N (mg/L)	0.15	0.50	1.00	1.50	2.00	5.46
	Ecological function (0.30)	Ratio of wetland area (%)	5.00	4.00	3.00	2.00	1.00	1.64
		Guaranteed rate of discharge in dry flow season (%)	80.00	60.00	40.00	20.00	0.00	37.50
Flood control (0.54)	Requirement rate of bankfull discharge (%)	Variation rate of streambed gradient (%)	100.00	90.00	80.00	70.00	60.00	71.00
			100.00	80.00	60.00	40.00	20.00	62.50

TABLE 2: The evaluation results for the criterion layer of Weihe River in Shaanxi Province.

Section	Criterion layer	Excellent	Good	Moderate	Poor	Sick
LW	Water quality	0.04	0.81	0.16	0.00	0.00
	Ecological function	0.00	0.20	0.47	0.05	0.28
	Recreation function	0.00	0.00	0.50	0.50	0.00
WX	Water quality	0.00	0.00	0.00	0.00	1.00
	Ecological function	0.00	0.19	0.76	0.05	0.00
	Recreation function	0.00	0.00	0.21	0.79	0.00
XL	Water quality	0.00	0.00	0.00	0.00	1.00
	Ecological function	0.33	0.18	0.49	0.00	0.00
	Flood control	0.00	0.40	0.11	0.42	0.09
LH	Water quality	0.00	0.00	0.00	0.48	0.53
	Ecological function	0.00	0.72	0.28	0.00	0.00
	Flood control	0.00	0.00	0.00	0.55	0.46
DH	Water quality	0.00	0.00	0.09	0.42	0.50
	Ecological function	0.00	0.00	0.48	0.38	0.15
	Flood control	0.00	0.02	0.49	0.49	0.00

4.2. *Evaluation Results from Criterion Layer.* According to the principle of maximum membership degree and the estimated value from the criterion layer (Table 2), result revealed that that water quality was good in the upstream reach of LW. However, water pollution became very serious in the reaches of WX and XL but got better in the reach below the Lintong gauging station. For the ecological function of the river, the reach of LH maintained good state while the other four reaches were in a moderate grade. The recreation function for the reaches of LW and WX was poor and the flood controlling capacity for the lower reaches was also in a poor condition. The status of river health for segmented reaches is demonstrated as follows.

(1) *Reach of LW.* In general, water quality is good (Table 3), which indicates that the executive measures implemented to control pollutants discharged from industrial and domestic wastewater in recent years were significantly effective. However, the results show that water ecological and recreation functions in the reach were not good. In particular, the ecological function has sick grade, and this mainly resulted from the larger shortage of environmental flow. Due to reduction of precipitation and increase of water use for agriculture irrigation, industry production, and domestic life, the water flow reserved in the stream for maintaining ecological functions has been decreased. Agricultural irrigation is the largest water consumer, accounting for 60% of the total amount of water consumption. The ratio of water use volume for domestic, industry, and agriculture to the total volume of water resources in the Weihe River Basin runs up to 47.9%. Even in the low flow period, about 80% of the river flow is impounded by dams for agriculture irrigation in Baoji district (Table 4). Therefore, the guaranteed rate of discharge in dry flow season is very low. Meanwhile, the shortage of incoming water induces a larger area of exposed sediments in river channel, which has been cultivated as farmlands by farmers. The aesthetic value and ecological functions of

stream landscape have been deteriorated due to destruction of the connectivity between river and wetland.

(2) *Reach of WX.* Water pollution is very serious in this river section (Table 3). The concentrations of typical pollutants like chemical oxygen demand (COD) and ammonia-nitrogen ($\text{NH}_3\text{-N}$) are greater than the upper threshold values in the environmental quality standard based on the surface water function zoning of Shaanxi Province in 2004. A large numbers of lands in Baoji area are cultivated with crops and irrigated by dam water. Water pollutants from nonpoint source of agriculture are the main factors causing serious pollution of the river [24]. This reach is in the moderate level and poor level, respectively, in terms of ecological function and recreation function (Table 3). The coverage ratio of riparian vegetation is high. However, fish species has significantly decreased compared with that of 1980s, which is caused by heavy pollution and great shortage of environmental flow [24]. Moreover, the recreational value has decreased due to loss of aquatic biological diversity and damage of river landscape.

(3) *Reach of XL.* The pollution of water is also very serious in this reach (Table 3). Most reach pollutants are discharged from industrial wastewater and domestic sewage, especially in Xi'an. The concentration of water pollution is greater than that of aquatic environmental capacity. The ecological functions are in good condition, which are mainly attributed to the large areas of wetland. Meanwhile, the satisfaction degree of water flow for ecological function requirements is high. However, the capacity of flood discharge is low. From the Xianyang hydrological gauging station, channel sedimentation becomes a serious problem, which decreases sediment transport capacity and increases the risks of flood.

(4) *Reach of LH.* Water quality is poor in this reach (Table 3), especially the most serious pollution of the ammonia-nitrogen ($\text{NH}_3\text{-N}$) whose concentration is greater than the

TABLE 3: The estimated values of membership degree for evaluation indicator of the Weihe River in Shaanxi Province.

Reach	Criterion layer	Indicator layer	Value of membership degree				
			Excellent	Good	Moderate	Poor	Sick
LW	Water quality	COD (mg/L)	0.07	0.93	0.00	0.00	0.00
		NH ₃ -N (mg/L)	0.00	0.68	0.32	0.00	0.00
	Ecological function	Ratio of wetland area (%)	0.00	0.00	0.00	0.14	0.86
		Riparian vegetation coverage ratio (%)	0.00	0.49	0.51	0.00	0.00
Recreation function	Guaranteed rate of discharge in dry flow season (%)	0.00	0.10	0.90	0.00	0.00	
	Recreation value index	0.00	0.00	0.50	0.50	0.00	
WX	Water quality	COD (mg/L)	0.00	0.00	0.00	0.00	1.00
		NH ₃ -N (mg/L)	0.00	0.00	0.00	0.00	1.00
	Ecological function	Riparian vegetation coverage ratio (%)	0.00	0.58	0.42	0.00	0.00
		Proportion of fish species (%)	0.00	0.00	0.85	0.15	0.00
Recreation function	Guaranteed rate of discharge in dry flow season (%)	0.00	0.00	1.00	0.00	0.00	
	Recreation value index	0.00	0.00	0.21	0.79	0.00	
XL	Water quality	COD (mg/L)	0.00	0.00	0.00	0.00	1.00
		NH ₃ -N (mg/L)	0.00	0.00	0.00	0.00	1.00
	Ecological function	Ratio of wetland area (%)	1.00	0.00	0.00	0.00	0.00
		Riparian vegetation coverage ratio (%)	0.00	0.53	0.47	0.00	0.00
Flood control	Guaranteed rate of discharge in dry flow season (%)	0.00	0.02	0.98	0.00	0.00	
	Variation rate of streambed gradient (%)	0.00	0.79	0.21	0.00	0.00	
LH	Water quality	Capacity of flood discharge (%)	0.00	0.00	0.00	0.83	0.17
		COD (mg/L)	0.00	0.00	0.00	0.95	0.05
	Ecological function	NH ₃ -N (mg/L)	0.00	0.00	0.00	0.00	1.00
		Riparian vegetation coverage ratio (%)	0.00	0.86	0.14	0.00	0.00
Flood control	Guaranteed rate of discharge in dry flow season (%)	0.00	0.58	0.42	0.00	0.00	
	Variation rate of streambed gradient (%)	0.00	0.00	0.00	0.10	0.90	
DH	Water quality	Requirement rate of bankfull discharge (%)	0.00	0.00	0.00	0.99	0.01
		COD (mg/L)	0.00	0.00	0.17	0.83	0.00
	Ecological function	NH ₃ -N (mg/L)	0.00	0.00	0.00	0.00	1.00
		Ratio of wetland area (%)	0.00	0.00	0.00	0.71	0.29
Flood control	Guaranteed rate of discharge in dry flow season (%)	0.00	0.00	0.96	0.04	0.00	
	Variation rate of streambed gradient (%)	0.00	0.00	0.02	0.98	0.00	
Flood control	Requirement rate of bankfull discharge (%)	0.00	0.04	0.96	0.00	0.00	

TABLE 4: Comparison of impounding water by dams and the runoff in Baoji area [23].

Month	Jan.	Feb.	Mar.	Apr.	May	Jun.	Jul.	Aug.	Sep.	Oct.	Nov.	Dec.
Impounding water (10^6 m^3)	38.0	34.5	38.8	34.0	31.0	46.2	55.3	81.6	65.9	71.0	47.2	40.1
Runoff (10^6 m^3)	44.7	40.7	60.6	63.6	88.2	99.3	166.8	181.5	165.2	184.3	76.7	48.5
Ratio of impounding water to runoff	0.85	0.85	0.64	0.53	0.35	0.47	0.33	0.45	0.40	0.39	0.62	0.83

TABLE 5: Health evaluation results of the Weihe River in Shaanxi Province.

	Reaches	Excellent	Good	Moderate	Poor	Sick
River health index (RHI)	LW	0.01	0.32	0.40	0.11	0.17
	WX	0.00	0.06	0.33	0.29	0.32
	XL	0.05	0.23	0.13	0.22	0.39
	LH	0.00	0.27	0.10	0.33	0.30
	DH	0.00	0.01	0.42	0.45	0.13

upper threshold value of heavy pollution grade V in Environmental Quality Standards for Surface Water (GB 3838-2002) defined by the Environment Protection Law of the People's Republic of China. Industrial wastewater and agricultural nonpoint source pollutants are the main sources inducing such heavy water pollution [24]. Both the guaranteed rate of discharge in dry flow season and riparian vegetation coverage ratio are good (Table 3), which maintain well ecological function. However, due to the operation of Sanmenxia Reservoir, the gradual channel sedimentation has resulted in a decrease of stream gradient as well as capacity of bankfull discharge (Table 3).

(5) *Reach of DH.* Water quality is still bad in this river section though progresses on the treatment of some pollutants have been made. Water quality in terms of chemical oxygen demand (COD) is better in this reach than the above three reaches (Table 3), while concentration of ammonia-nitrogen ($\text{NH}_3\text{-N}$) is still inferior to the water quality of grade V in environmental quality standards for surface water (GB 3838-2002). Due to increase of construction and agricultural lands, and shrinking of wetland caused by the decrease of river runoff, ecological function has degraded to the moderate grade (Table 3). The habitat of aquatic organisms has deteriorated and is in danger of becoming extinct, and wetland ecosystems have been severely damaged. Improper operation of the Sanmenxia Reservoir has reduced the stream gradient of the upper river, which is the direct reason resulting in river channel deposition. Thus reducing elevation and enhancing flood control capacity are the difficulty but also the focus for management and governance of this reach.

4.3. *Evaluation Results from Fuzzy Relation Matrix.* Membership matrix and the corresponding weights in the evaluation criteria layer of each reach were used to calculate the health situation of the Weihe River in Shaanxi Province (Table 5). According to the principle of maximum membership degree, the maximum level of membership in the healthy level was taken as the river health status of each reach. The maximum degree of membership is in morbid level in the XL reach, indicating that the river health in this reach is in the "sick"

rating. The maximum degree of membership in LH reach is in the "poor" health rating, which suggests that river health in this reach is in poor health status level. The health situation in DH section is in poor level because the maximum membership degree in this reach is in poor rating. There is no membership degree locating in excellent and good health grading, which reveals that water health in this reach is less than "moderate" health level. In summary, health status of the Weihe River downstream demonstrated a deteriorating trend along its flowing way, although health situation in the river estuary is improved. In general, the river health of downstream is in a poor rating, which suggests an urgent calling for the protection of the health of the Weihe River.

4.4. *Sensitive Indicators for the River Health Evaluation.* In this study, the sensitive degree of an indicator to the river health was determined by comparing the difference of measurement values between keeping the whole indicators and taking out of the indicator. Based on the result variation of each indicator before and after being removed, the influence degree, that is, sensitivity degree of the indicator to the health evaluation results of the Weihe River, was determined.

For the reach of LW, the guaranteed rate of discharge in the dry flow season is the most sensitive factor, and the second sensitive factor is the ratio of wetland area (Table 6). This result indicates that the guaranteed rate of discharge in the dry flow season is the most important factor influencing river health of this reach. It suggests that insufficient in-stream flow is the key issue in river health protection in this reach; meanwhile wetland protection should not be neglected.

For the reach of WX, the riparian vegetation coverage ratio, the proportion of fish species, and the guaranteed rate of discharge in the dry flow season had an impact on the results of the river health evaluation in this river section (Table 6). The sensitivity analysis results confirm that the guaranteed rate of discharge in the dry flow season and the proportion of fish species are two factors which could cause the largest variations of the comprehensive evaluation results. However, from the results of a comprehensive evaluation of river health, it is seen that membership in sick levels caused by water quality still remained constant. Thus improving

TABLE 6: Sensitive analysis results for the health evaluation of the Weihe River in Shaanxi Province.

Reach	Removed indicators	Value of membership degree				
		Excellent	Good	Moderate	Poor	Sick
LW	Non	0.01	0.32	0.40	0.11	0.17
	COD (mg/L)	0.01	0.32	0.40	0.11	0.17
	NH ₃ -N (mg/L)	0.00	0.29	0.44	0.11	0.17
	Ratio of wetland area (%)	0.02	0.35	0.36	0.11	0.17
	Riparian vegetation coverage ratio (%)	0.01	0.38	0.54	0.08	0.00
	Guaranteed rate of discharge in dry flow season (%)	0.01	0.23	0.39	0.12	0.25
	Non	0.00	0.06	0.33	0.29	0.32
	COD (mg/L)	0.00	0.06	0.33	0.29	0.32
	NH ₃ -N (mg/L)	0.00	0.06	0.33	0.29	0.32
	Riparian vegetation coverage ratio (%)	0.00	0.00	0.39	0.29	0.32
WX	Proportion of fish species (%)	0.00	0.10	0.31	0.27	0.32
	Guaranteed rate of discharge in dry flow season (%)	0.00	0.10	0.29	0.29	0.32
	Non	0.05	0.23	0.13	0.22	0.39
	COD (mg/L)	0.05	0.23	0.13	0.22	0.39
	NH ₃ -N (mg/L)	0.05	0.23	0.13	0.22	0.39
	Ratio of wetland area (%)	0.00	0.24	0.16	0.22	0.38
	Riparian vegetation coverage ratio (%)	0.07	0.21	0.12	0.22	0.38
	Guaranteed rate of discharge in dry flow season (%)	0.07	0.24	0.09	0.22	0.38
	Variation rate of streambed gradient (%)	0.05	0.03	0.07	0.43	0.42
	Capacity of flood discharge (%)	0.05	0.44	0.18	0.00	0.34
LH	Non	0.00	0.27	0.10	0.33	0.30
	COD (mg/L)	0.00	0.27	0.10	0.24	0.40
	NH ₃ -N (mg/L)	0.00	0.27	0.10	0.43	0.21
	Riparian vegetation coverage ratio (%)	0.00	0.21	0.16	0.33	0.30
	Guaranteed rate of discharge in dry flow season (%)	0.00	0.32	0.05	0.33	0.30
	Variation rate of streambed gradient (%)	0.00	0.27	0.10	0.52	0.11
	Requirement rate of bankfull discharge (%)	0.00	0.27	0.10	0.14	0.49
	Non	0.00	0.01	0.42	0.45	0.13
	COD (mg/L)	0.00	0.01	0.41	0.38	0.21
	NH ₃ -N (mg/L)	0.00	0.01	0.44	0.51	0.05
DH	Ratio of wetland area (%)	0.00	0.01	0.44	0.51	0.05
	Guaranteed rate of discharge in dry flow season (%)	0.00	0.01	0.57	0.34	0.08
	Variation rate of streambed gradient (%)	0.00	0.01	0.28	0.54	0.17
	Requirement rate of bankfull discharge (%)	0.00	0.02	0.68	0.18	0.13
	Non	0.00	0.00	0.17	0.71	0.13

of water quality will definitely lead to the changes of the comprehensive evaluation results of the river health. These analysis results suggest that, in addition to the guaranteed rate in the dry flow season, the impact of the river water quality is the most important factor for river health of this reach; thereby improving water quality is the most important task for the governance of this river section.

For the reach of XL, the indicators that had greater impacts on the comprehensive evaluation results included the riparian vegetation coverage ratio, variation rate of streambed gradient, and capacity of flood discharge (Table 6). The indicator that will affect the evaluation result to the largest extent is capacity of flood discharge, and this is mainly because the Jinhe River with large amounts of sediment transport joins the Weihe River in the reach and the sediments are settled due to reduction of flow velocity here. A large quantity of settled sediments block the channel, which causes flooding, and thus improving flood control capacity including nonstructural measures and engineering measures is the focus for the protection of this reach.

For the reach of LX, pollutant of COD and the requirement rate of bankfull discharge are the most influential factors affecting health evaluation results. In general, the requirement rate of bankfull discharge was slightly more sensitive than COD to the river health (Table 6). The reach is located in the downstream of Xi'an city, the capital of Shaanxi Province, and its water quality is very poor due to large amounts of sewage and waste discharged from Xi'an, and many organic pollutants from soil erosion of irrigated agriculture on both sides of the Weihe River. Water pollution control in Xi'an city is the key issue for water quality improvement in this reach. Reduction of riverbed gradient has resulted in sedimentation settlement, which is the most important reason that led to insufficient requirement rate of bankfull discharge. Another reason for river channel recession is that low peak flows in recent years have not effectively scoured the river channel. These analyses suggest that the river water quality management and river regulation are the most fundamental concerns for river protection and exploitation in the reach.

For the reach of DH, each indicator directly impacts the results of comprehensive health assessment to some extent (Table 6), which suggests that each of these indicators has a certain sensitivity degree to the river health evaluation results in this reach. The sensitive indices in Table 6 display that COD, the ratio of wetland area, and the variation rate of the streambed gradient have large impacts on the comprehensive evaluation results of river health in this reach, among which the variation rate of the stream gradient has the largest impacts. The sediment deposition in the lower Weihe River has been cumulating over 1.3 billion m³ since the Sanmenxia Reservoir was operated in 1960s [24]. Riverbed sedimentation, river channel shrink, and raising of Tongguan elevation every year have gradually reduced the variation rate of the riverbed gradient from 1/5000 before the construction of the reservoir to 1/6000. Difficult sediment transport, pollutant discharge, and exacerbating flood and related wetland losses are the major problems that this reach is facing, which are

all caused by the reduction of variation rate of the stream gradient.

5. Conclusions

River health is an indicator of the harmony between human and water resources; therefore river health assessment is an important tool for human to develop, utilize, and manage the river in a sustainable way. This study applied a hybrid approach combining AHP and fuzzy comprehensive evaluation to calculate the river health of the Weihe River in China. The results reveal that the reaches of LW and WX were in the "moderate" level of health, and the reaches of LH and DH were in the "poor" health rating, whereas the reach of XL was in the "sick" rating. The key factors which influence the river health are the guaranteed rate of discharge in the dry flow season, water quality, capacity of flood discharge, requirement rate of bankfull discharge, and variation rate of streambed gradient, respectively, for each reach from upper stream to lower stream in the study area.

Many factors in the evaluation process affect the results of river health assessment in varying degrees, such as indicator chosen, index weight determination, basis of reference, and evaluation methods. There are various factors affecting river health, which mainly include natural factors and human disturbance. Natural factors mainly include precipitation decrease, significant reduction in vegetation, and severe soil erosion in the Guanzhong area, which have increased the pressure on flood control in the downstream. As for human disturbance, great increasing of water demand due to rapid development of industry and agriculture and population growth in recent years has greatly aggravated the situation of insufficient river baseflow and even caused river blanking in parts of reaches, which has reduced stream's self-purification capacity and exacerbated water pollution. In general, river health is more intensely affected by human activities, and thus more attention should be paid in aspects of planning water use, water saving, water protection, and promoting harmony between human and water.

The health of the Weihe River is closely related to the benefits of local people in the river basin, and thus the aspects of a healthy river that supplies their basic living needs should be fully investigated and incorporated in the evaluation system. Their concepts and choice of a healthy river are affected by the socioeconomic development situation and their education and awareness. The expectation of river health from local people according to their living needs and so on requires more comprehensive social and economic studies; therefore, it is not included in this study.

Conflict of Interests

The authors declare that there is no conflict of interests regarding the publication of this paper.

Acknowledgments

This study is jointly supported by National Natural Science Foundation of China (Grant no. 51379175), Specialized

Research Fund for the Doctoral Program of Higher Education (Grant no. 20136101110001), Program for Key Science and Technology Innovation Team in Shaanxi Province (Grant no. 2014KCT-27), and Program for New Century Excellent Talents in University (Grant no. NCET-11-1045).

References

- [1] S. Wei, H. Yang, K. Abbaspour, J. Mousavi, and A. Gnauck, "Game theory based models to analyze water conflicts in the Middle Route of the South-to-North Water Transfer Project in China," *Water Research*, vol. 44, no. 8, pp. 2499–2516, 2010.
- [2] D. Zuo, Z. Xu, W. Wu, J. Zhao, and F. Zhao, "Identification of streamflow response to climate change and human activities in the Wei River Basin, China," *Water Resources Management*, vol. 38, no. 3, pp. 833–851, 2014.
- [3] S. Wei and A. Gnauck, "Simulating water conflicts using game theoretical models for water resources management," in *Ecosystems and Sustainable Development VI*, E. Tiezzi, J. C. Marques, C. A. Brebbia, and S. E. Jørgensen, Eds., pp. 3–12, WIT Press, Southampton, UK, 2007.
- [4] R. E. Tharme and J. M. King, *Development of the Building Block Methodology for Instream Flow Assessments, and Supporting Research on the Effects of Different Magnitude Flows on Riverine Ecosystems*, Water Research Commission, 1998.
- [5] V. Smakhtin, C. Revenga, and P. Döll, "Taking into account environmental water requirements in global-scale water resources assessments," Comprehensive Assessment Research Report 2, Comprehensive Assessment Secretariat, Colombo, Sri Lanka, 2004.
- [6] J. X. Song, Z. X. Xu, C. M. Liu, and H. E. Li, "Ecological and environmental instream flow requirements for the Wei River—the largest tributary of the Yellow River," *Hydrological Processes*, vol. 21, no. 8, pp. 1066–1073, 2007.
- [7] S. Wei, H. Yang, J. Song, K. C. Abbaspour, and Z. Xu, "System dynamics simulation model for assessing socio-economic impacts of different levels of environmental flow allocation in the Weihe River Basin, China," *European Journal of Operational Research*, vol. 221, no. 1, pp. 248–262, 2012.
- [8] K. Vairavamoorthy, S. D. Gorantiwar, and A. Pathirana, "Managing urban water supplies in developing countries—climate change and water scarcity scenarios," *Physics and Chemistry of the Earth*, vol. 33, no. 5, pp. 330–339, 2008.
- [9] J. J. Kashaigili, K. Rajabu, and P. Masolwa, "Freshwater management and climate change adaptation: experiences from the great Ruaha River catchment in Tanzania," *Climate and Development*, vol. 1, no. 3, pp. 220–228, 2009.
- [10] J. R. Karr and E. W. Chu, "Sustaining living rivers," *Hydrobiologia*, vol. 422–423, pp. 1–14, 2000.
- [11] R. Leete, F. Donnay, S. Kersemaekers, M. Schoch, and M. Shah, *Global Population and Water*, UNFPA Report on Population and Development Strategies Series, 2003.
- [12] F. Sheldon, E. E. Peterson, E. L. Boone, S. Sippel, S. E. Bunn, and B. D. Harch, "Identifying the spatial scale of land use that most strongly influences overall river ecosystem health score," *Ecological Applications*, vol. 22, no. 8, pp. 2188–2203, 2012.
- [13] A. J. Boulton, "An overview of river health assessment: philosophies, practice, problems and prognosis," *Freshwater Biology*, vol. 41, no. 2, pp. 469–479, 1999.
- [14] R. H. Norris and M. C. Thoms, "What is river health?" *Freshwater Biology*, vol. 41, no. 2, pp. 197–209, 1999.
- [15] J. R. Karr, "Defining and measuring river health," *Freshwater Biology*, vol. 41, no. 2, pp. 221–234, 1999.
- [16] T. Oberdorff, D. Pont, B. Hugué, and J.-P. Porcher, "Development and validation of a fish-based index for the assessment of 'river health' in France," *Freshwater Biology*, vol. 47, no. 9, pp. 1720–1734, 2002.
- [17] R. A. A. Noble, I. G. Cowx, D. Goffaux, and P. Kestemont, "Assessing the health of European rivers using functional ecological guilds of fish communities: standardising species classification and approaches to metric selection," *Fisheries Management and Ecology*, vol. 14, no. 6, pp. 381–392, 2007.
- [18] D. Pont, B. Hugué, and C. Rogers, "Development of a fish-based index for the assessment of river health in Europe: the European Fish Index," *Fisheries Management and Ecology*, vol. 14, no. 6, pp. 427–439, 2007.
- [19] A. Chakona, C. Phiri, T. Chinamaringa, and N. Muller, "Changes in biota along a dry-land river in northwestern Zimbabwe: declines and improvements in river health related to land use," *Aquatic Ecology*, vol. 43, no. 4, pp. 1095–1106, 2009.
- [20] W. Meng, N. Zhang, Y. Zhang, and B. Zheng, "Integrated assessment of river health based on water quality, aquatic life and physical habitat," *Journal of Environmental Sciences*, vol. 21, no. 8, pp. 1017–1027, 2009.
- [21] C. N. Magagula, A. B. Mansuetus, and J. O. Tetteh, "Ecological health of the Usuthu and Mbuluzi rivers in Swaziland based on selected biological indicators," *African Journal of Aquatic Science*, vol. 35, no. 3, pp. 283–289, 2010.
- [22] U. Pinto, B. L. Maheshwari, and R. L. Ollerton, "Analysis of long-term water quality for effective river health monitoring in peri-urban landscapes—a case study of the Hawkesbury-Nepean river system in NSW, Australia," *Environmental Monitoring and Assessment*, vol. 185, no. 6, pp. 4551–4569, 2013.
- [23] S. Wei, J. X. Song, and N. I. Khan, "Simulating and predicting river discharge time series using a wavelet-neural network hybrid modelling approach," *Hydrological Processes*, vol. 26, no. 2, pp. 281–296, 2012.
- [24] Q. Li, J. X. Song, A. Wei, and B. Zhang, "Changes in major factors affecting the ecosystem health of the Weihe River in Shaanxi Province, China," *Frontiers of Environmental Science and Engineering*, vol. 7, no. 6, pp. 875–885, 2013.
- [25] G. Y. Li, "Keeping the yellow river healthy," in *Proceedings of the 9th International Symposium on River Sedimentation*, pp. 18–21, Yichang, China, 2004.
- [26] C. M. Liu and X. Y. Liu, "Healthy river and its indication, criteria and standards," *Journal of Geographical Sciences*, vol. 19, no. 1, pp. 3–11, 2009.
- [27] Y. W. Zhao and Z. F. Yang, "Integrative fuzzy hierarchical model for river health assessment: a case study of Yong River in Ningbo City, China," *Communications in Nonlinear Science and Numerical Simulation*, vol. 14, no. 4, pp. 1729–1736, 2009.
- [28] C. W. Shi, "Healthy controlling indicator system of the Weihe River," *Yellow River*, vol. 33, no. 1, pp. 12–14, 2011 (Chinese).
- [29] P. L. Feng, "Assessment indicator for the river health of the Weihe River," *Yellow River*, vol. 27, no. 8, pp. 3–6, 2005 (Chinese).
- [30] W. Wu, Z. Z. Xu, X. W. Yin, and D. P. Zuo, "Assessment of ecosystem health based on fish assemblages in the Wei River basin, China," *Environmental Monitoring and Assessment*, vol. 186, no. 6, pp. 3701–3716, 2014.
- [31] J.-Y. Li, C.-W. Shi, X.-B. Xu, and Z.-J. Fu, "Mechanism and effect of channel evolution at estuary of Weihe River to Huanghe River," *Chinese Geographical Science*, vol. 16, no. 2, pp. 122–126, 2006.

- [32] Y. Tong, L. X. Fan, and L. H. Cao, "Identification of water environment in Wei River basin," *China Resources Comprehensive Utilization*, vol. 30, no. 7, pp. 43–45, 2012 (Chinese).
- [33] D. P. Zuo, Z. Z. Xu, D. Z. Peng et al., "Simulating spatiotemporal variability of blue and green water resources availability with uncertainty analysis," *Hydrological Processes*, 2014.
- [34] H. Wang and Z. H. Zhang, "Regulation on runoff and sediment discharge of main branches located in Wei River valley and benefits of runoff and sediment decrease under control measures of soil and water conservation," *Bulletin of Soil and Water Conversation*, vol. 15, no. 4, pp. 55–59, 1995 (Chinese).
- [35] F. Z. Chen, M. Y. Dai, and Q. Q. Wu, "Analysis on variation and characteristic of water and sediment in the Wei River," *Yellow River*, vol. 21, no. 8, pp. 16–18, 1999 (Chinese).
- [36] J. X. Song, Z. X. Xu, Y. H. Hui, H. E. Li, and Q. Li, "Instream flow requirements for sediment transport in the lower Weihe River," *Hydrological Processes*, vol. 24, no. 24, pp. 3547–3557, 2010.
- [37] G. E. Wang, L. Ji, and Y. J. Li, "Effect of water and sediment variation on erosion and deposition of the Weihe River bed," *Journal of Sediment Research*, vol. 4, pp. 49–52, 2001 (Chinese).
- [38] X. H. Chen, H. C. Mi, H. M. He et al., "Hydraulic conductivity variation within and between layers of a high floodplain profile," *Journal of Hydrology*, vol. 515, no. 16, pp. 147–155, 2014.
- [39] X. Z. Lin, N. Q. Jiang, Z. Y. Liang, and D. J. Yue, *Study on Instream Flow Requirement for Transportation of Sediment in the Lower Wei River*, The Yellow River Press, 2005, (Chinese).
- [40] R. Sadiq, T. Husain, B. Veitch, and N. Bose, "Risk-based decision-making for drilling waste discharges using a fuzzy synthetic evaluation technique," *Ocean Engineering*, vol. 31, no. 16, pp. 1929–1953, 2004.
- [41] F. Li, W. Wang, Y. Shi, and C. Jin, "Fuzzy synthetic evaluation model based on the knowledge system," *International Journal of Innovative Computing, Information and Control*, vol. 9, no. 10, pp. 4073–4084, 2013.
- [42] R. Sadiq and M. J. Rodriguez, "Fuzzy synthetic evaluation of disinfection by-products—a risk-based indexing system," *Journal of Environmental Management*, vol. 73, no. 1, pp. 1–13, 2004.
- [43] Y. Zhang, *Methodology and Application of Fuzzy Mathematics*, Coal Industry Press, Beijing, China, 1992, (Chinese).
- [44] N.-B. Chang, H. W. Chen, and S. K. Ning, "Identification of river water quality using the fuzzy synthetic evaluation approach," *Journal of Environmental Management*, vol. 63, no. 3, pp. 293–305, 2001.
- [45] M. J. Feio, T. Alves, M. Boavida, A. Medeiros, and M. A. S. Graça, "Functional indicators of stream health: a river-basin approach," *Freshwater Biology*, vol. 55, no. 5, pp. 1050–1065, 2010.
- [46] J. X. Song and H. E. Li, *Ecological and Environmental Water Requirements for the Wei River*, China Water Conservancy and Electronic Power, Beijing, China, 2004 (Chinese).
- [47] X. H. Xue and X. G. Yang, "Seismic liquefaction potential assessed by fuzzy comprehensive evaluation method," *Natural Hazards*, vol. 71, no. 3, pp. 2101–2112, 2014.
- [48] Y. Wang, W. Yang, M. Li, and X. Liu, "Risk assessment of floor water inrush in coal mines based on secondary fuzzy comprehensive evaluation," *International Journal of Rock Mechanics and Mining Sciences*, vol. 52, pp. 50–55, 2012.
- [49] F. Xie and D. S. Tang, "The application of AHP and fuzzy comprehensive evaluation in harmonious level measurement between human and water in city," *Journal of Computational Information Systems*, vol. 6, no. 14, pp. 4647–4656, 2010.
- [50] D. G. Cacuci, M. Ionescu-Bujor, and I. M. Navon, *Sensitivity and Uncertainty Analysis, Volume II: Applications to Large-Scale Systems*, CRC Press, Boca Raton, Fla, USA, 2005.
- [51] J. M. Murphy, D. M. H. Sexton, D. N. Barnett et al., "Quantification of modelling uncertainties in a large ensemble of climate change simulations," *Nature*, vol. 430, no. 7001, pp. 768–772, 2004.
- [52] A. Saltelli and P. Annoni, "How to avoid a perfunctory sensitivity analysis," *Environmental Modelling and Software*, vol. 25, no. 12, pp. 1508–1517, 2010.
- [53] Y. Feng, B. Kang, and L. Yang, "Feasibility analysis of widely accepted indicators as key ones in river health assessment," *Journal of Geographical Sciences*, vol. 22, no. 1, pp. 46–56, 2012.

Research Article

Identifying Vegetation Dynamics and Sensitivities in Response to Water Resources Management in the Heihe River Basin in China

Dongqin Yin,¹ Xiang Li,² Yuefei Huang,¹ Yuan Si,¹ and Rui Bai¹

¹State Key Laboratory of Hydro-Science & Engineering, Tsinghua University, Beijing 100084, China

²State Key Laboratory of Simulation and Regulation of Water Cycle in River Basin, China Institute of Water Resources and Hydropower Research, Beijing 100038, China

Correspondence should be addressed to Yuefei Huang; yuefeihuang@tsinghua.edu.cn

Received 27 November 2014; Revised 18 January 2015; Accepted 20 January 2015

Academic Editor: Yongqiang Zhang

Copyright © 2015 Dongqin Yin et al. This is an open access article distributed under the Creative Commons Attribution License, which permits unrestricted use, distribution, and reproduction in any medium, provided the original work is properly cited.

The Heihe River Basin, the second largest inland river basin in China, plays a vital role in the ecological sustainability of the Hexi Corridor. However, the requirements for regional economic development and ecological balance cannot be fully met due to water resource shortage and overexploitation induced by an extremely dry climate and population growth, especially in the middle and lower basins. Thus, environmental conservation projects that reallocate water resources have been planned and implemented step by step since 2001. The aim of this study is to evaluate ecosystem restoration benefits by identifying vegetation dynamics and sensitivities. The MODIS Normalized Difference Vegetation Index (NDVI) and its derivative indices, coupled with Geographic Information System (GIS), are introduced to explore ecosystem evolution at the pixel level, based on the hydrological and meteorological data in the whole region at varying temporal and spatial scales. Results indicate there are slight vegetation restoration trends in the upper, middle, and lower basin; the results of correlation analyses between vegetation and runoff into the lower basin suggest that the impact of a water supplement lasts at most three years, and engineering or nonengineering measures should be maintained for permanent ecosystem recovery.

1. Introduction

The Heihe River Basin (HRB, see Figure 1), the second largest inland river basin in China, plays a vital role in sustaining ecological balance in the Hexi Corridor. However, in recent decades, the HRB has suffered serious ecosystem degradation and desertification due to its extreme dry climate and population growth, particularly in the middle and lower basins [1–3]. The water resource situation of the HRB can be summarized in two major points. (1) Water resource shortage: the continental climate of the whole basin affects the water resource availability. The mean annual precipitation drops from 140 mm in the southwest to 47 mm in the northeast, whereas the mean annual evaporation increases from 1410 mm to 2250 mm. Most areas in the HRB, approximately

93% of the total basin, hardly yield runoff in the middle and lower basins. (2) Water resource overexploitation: with the rapid social and economic development, the sharp increase in water consumption in the middle basin for living and production uses (from 1.5 billion m³ in the early 1950s to 2.45 billion m³ in the late 1990s) has resulted in a continuous decrease in runoff into the lower basin (from 1.16 billion m³ to 0.77 billion m³). Water usage waste and inefficiency are rather serious, resulting from unmanaged and unsupervised water resources in the whole basin. Thus, ecological problems of varying extents appear; specifically, natural forest and grassland degradation and biodiversity loss occur in the upper basin; soil salinization and desertification occur in the middle basin; and a series of prominent problems such as zero-flow rivers, dried-up lakes (the East and West Juyan

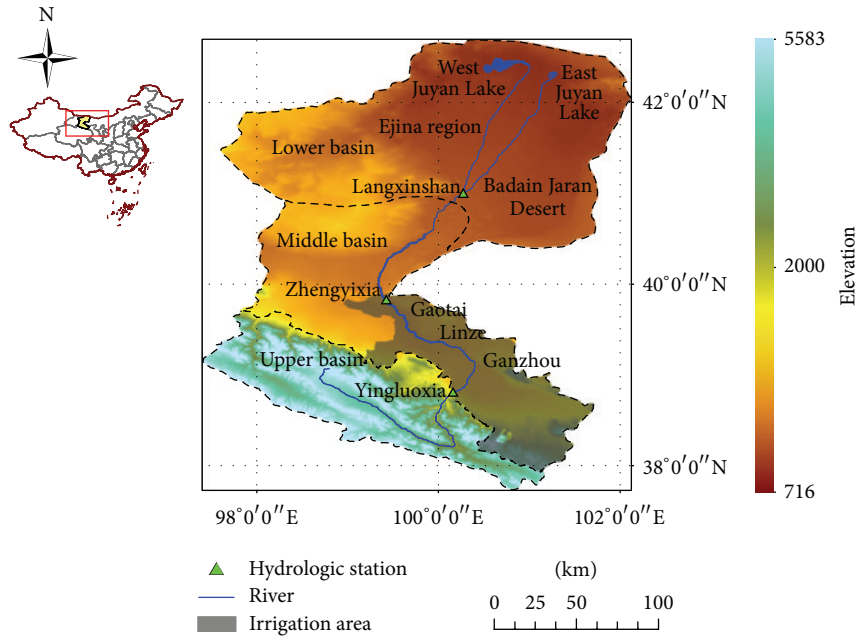


FIGURE 1: Map of study area.

Lakes), declining water tables, and a sharp reduction in natural forest and grassland areas occur in the lower basin, aggravating desertification and sandstorms.

Because of ecological problems resulting from water resource shortage and overexploitation, the near-term environmental conservation program (NTECP) has been planned and implemented for the HRB since 2001 by the Ministry of Water Resources (MWR) in China [4]. The objective of the NTECP is to reallocate water resources between ecological system maintenance and social-economic development. Moreover, the allowable water resource amounts have also been reallocated among upper, middle, and downstream river basin. In the upper basin, ecological restoration projects were implemented including forest and grassland conservation and artificial afforestation. Water-saving projects, especially for the irrigation regions, were undertaken in the middle river basin to ensure enough water releasing into the lower basin. The projects, such as water diversion canal construction, river regulation, irrigation system improvement, and grazing control, have been implemented in the lower basin for ensuring sufficient water reaching the most downstream region, where ecological system is significantly vulnerable.

Vegetation has a significant impact on interactions between terrestrial ecosystems and atmospheric processes [5, 6]. Identifying the response mechanisms of vegetation dynamics and sensitivities to water resource availability at varying temporal and spatial scales makes it possible to evaluate the ecosystem restoration benefits. For a long time, the response of vegetation variability to air, water, and soil has been an active study subject because of various natural and cultural statuses in the context of changing climate and frequent human activities [7–9]. Water resource availability dominates the temporal-spatial distributions and dynamics of vegetation, which maintains a regional ecosystem [10, 11].

Past studies indicate that climate change affects water resource availability in the long term, and human activities have recently become more dominant in the short term, particularly in arid and semiarid regions with high population density but limited water resources [12, 13]. In general, rainfall and runoff are the two major direct water sources for nourishing regional vegetation. However, in an arid/semiarid region, the rainfall is so scarce that it plays little role in supplying water, making runoff the major water source [14, 15]. It is necessary to study the underlying correlations between vegetation and hydrometeorological impact factors to better manage limited water resources for ecosystem conservation or restoration in arid and semiarid regions.

Because there is little field survey data, remote sensing-based vegetation indices have been widely used to study land uses and cover changes, including the Normalized Difference Vegetation Index (NDVI) [16], the perpendicular vegetation index (PVI) [17], soil-adjusted vegetation index (SAVI) [18], and green index (GI) [19]. The NDVI is the normalized difference between the near-infrared reflectance and visible red waveband [16, 20]. It reflects the vigor and greenness of the vegetation canopy by measuring the chlorophyll content changes using visible red radiation absorption and by measuring spongy mesophyll changes using near-infrared radiation reflection [21]. The NDVI and its derivative indices such as coefficient of variation (CV) [22] and vegetation condition index (VCI) [23] have been proved effective for vegetation dynamics identification [24, 25]. The NDVI has also been successfully applied in many other fields, including land cover classification [26], plant phenology [27], drought assessment [28], and evapotranspiration estimation [29].

In this paper, ecosystem restoration benefits are evaluated by identifying vegetation dynamics and sensitivities since the environmental conservation projects in the HRB were

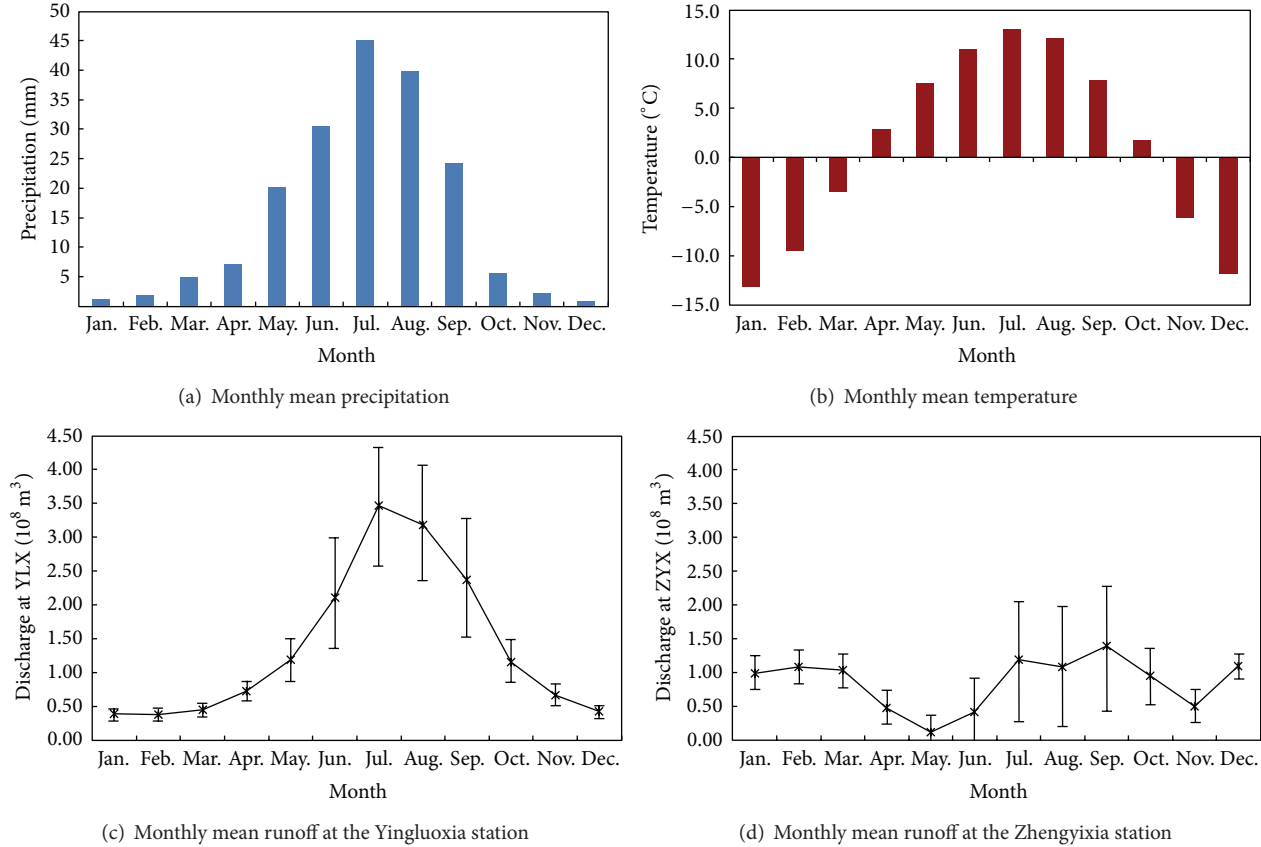


FIGURE 2: Meteorological and hydrological conditions in the Heihe River Basin (1957–2010). *Bars indicate standard deviation of monthly runoff during 1957–2010.

planned and implemented in 2001. This paper differs from previous efforts [2, 30–32] through investigating vegetation dynamics in the upper, middle, and lower HRB after implementation of the NTECP. Additionally, vegetation sensitivities and the corresponding time lags of vegetation change to water reallocation in the lower basin are quantitatively identified at the pixel level, rather than qualitatively at the regional scale. The paper is organized as follows: Section 2 describes the study area; Section 3 introduces the data acquisition and processing, along with the Normalized Difference Vegetation Index (NDVI), based on the MODIS images, along with its derivative indices, coupled with Geographic Information System (GIS); Section 4 explores the vegetation dynamics and sensitivities in response to the NTECP, using historical data from the entire region; and Section 5 presents conclusions and suggestions.

2. Study Area

The Heihe River Basin (HRB) is located in northwestern China, covering an area of approximately $14.29 \times 10^4 \text{ km}^2$ (between $37^\circ 43' - 42^\circ 41' \text{ N}$ and $97^\circ 23' - 102^\circ 72' \text{ E}$), as shown in Figure 1. The Heihe River originates from the north of the Qilian Mountains in Qinghai Province, flows through the middle Hexi Corridor in Gansu Province, and reaches the Ejina basin in the Inner Mongolia Autonomous Region. The annual

mean runoff generated from the Qilian Mountains (the Yingluoxia station) is approximately $16 \times 10^8 \text{ m}^3$ from both rainfall and melt water from glacier/snow in the mountain region. As shown in Figure 2(a), approximately 80% of precipitation occurs during the period of May to October. At this period the melt water from glacier/snow also significantly increases due to temperature rising (Figure 2(b)). Both of them result in runoff increase at the mountainous region (the Yingluoxia station, Figure 2(c)). However, irrigation in the middle Hexi Corridor consumes large amount of water, leading to little surface water recharge to the lower Ejina basin (the Zhengyixia station, Figure 2(d)). Therefore, the HRB can be characterized with its extreme dry climate with low precipitation, high potential evaporation, and low runoff.

The HRB is divided into the upper, middle, and lower reaches by the Yingluoxia (YLX) and Zhengyixia (ZYX) hydrologic stations, with lengths of 303 km, 185 km, and 333 km, respectively. The upper basin is characterized by a wet and cold climate and serves as the major runoff yield region, with annual precipitation of approximately 350 mm/yr. The elevation in this region is 2000–5000 m, with steep topography, and the vegetation cover in the upper basin is diversified and complex. The mountainous zone in this region is covered with relatively dense vegetation (consisting of forest, shrub, and grassland), and the plain terrain contains oasis and gobi/desert. The middle basin is located in a dry

environment with low annual precipitation (60–160 mm) and high annual potential evaporation (1000–2000 mm). The elevation in the middle basin is 1300–1700 m, with relatively flat topography. Most of the areas in this region are artificial oases supported by highly developed irrigation systems with a history of more than 2000 years, with the fastest expansion of agricultural development occurring in the last 50 years. The lower basin is in an extremely arid environment with little annual precipitation (less than 100 mm) and high annual potential evaporation (more than 3500 mm). The elevation in the lower basin is 910–1450 m, with very flat topography. The lower basin is covered mainly by Gobi and desert, except for regions close to the river. The Heihe River is separated into two branches at the Langxinshan station, that is, the East River and the West River, which end in the East and West Juyan Lake, respectively. Water usage in the middle and lower basins is primarily dependent on the runoff from the upper basin. The middle basin serves as the major water usage region for human beings (the population in the middle basin occupies approximately 94% of the whole river basin) and has an extensive irrigation system.

There are 10 cities/counties belonging to three provinces in the HRB, and the total population is approximately 1.4 million, as of 2009. The upper HRB is dominated by shrub- and grassland-based animal husbandry, with a small amount of farming. Most areas in the middle HRB are covered by artificial oases (3533 km²) which consume large amounts of irrigation water. Part of the lower HRB, mainly the Ejina oasis, is composed of grassland-based animal husbandry. According to previous studies, the population in the HRB increased by more than 100,000 from 1999 to 2009, with the most dramatic increase occurring in the middle HRB (approximately 80% of the total increase). The irrigation area in the HRB increased by approximately 200 km² from 1999 to 2009, with the most obvious increase also occurring in the middle HRB. Overall, the HRB can be summarized as a region with a shortage of water resources and a consistent increase in population and water consumption, which stress the water resources.

3. Materials and Methods

The geographic data, including the basin boundary, rivers and lakes, and the locations of hydrologic stations, were downloaded from the Cold and Arid Regions Science Data Center at Lanzhou (<http://westdc.westgis.ac.cn/>). The hydrological and meteorological data, including the historical runoff at hydrologic control stations (i.e., the Yingluoxia, the Zhengyixia, and the Langxinshan hydrologic stations) and precipitation, were collected from the Heihe River Bureau of the Yellow River Conservancy Commission and the CRU TS3.21 database [33], respectively.

The Normalized Difference Vegetation Index (NDVI) is acquired from the Terra-MODIS Vegetation Indices MOD13A1 products from the Earth Observing System of the National Aeronautics and Space Administration (NASA) [34]. These products provide the vegetation conditions with

a 500-meter spatial resolution and a 16-day temporal resolution. For analysis, the time series of NDVI data from 2001 to 2010 are smoothed using the Savitzky-Golay filter to reduce noise [35], and only NDVI data for the vegetation growing season (from April to October) are selected to avoid distorted or low values [36, 37]. Note that a higher NDVI value of a pixel represents more vegetation coverage, and a lower NDVI value represents less or no vegetation coverage.

To identify the vegetation dynamics at the pixel level, derivative indices based on NDVI data are introduced, including (1) annual mean of NDVI (referred to as the mean NDVI hereafter): this is the mean NDVI value from April to October of each year and represents the average overall state of vegetation coverage; (2) annual variation trend of NDVI: this depicts the linear regression of NDVI data through the year; the slope of the linear regression (referred to as the NDVI slope hereafter) can represent restoration when the value is positive and degradation otherwise and can therefore assist in qualitative and quantitative analyses of vegetation change direction and magnitude; (3) interannual coefficient of variation (CV) of NDVI: this is the dispersion of NDVI data over multiple years to its mean value; the value can indicate the variation amplitude at the pixel level, with a higher value representing a greater variation [22].

The impact of upstream runoff, that is, runoff at the Langxinshan (LXS) station, on vegetation in the Ejina region is expected to show a one-year lag due to agricultural activities and groundwater recharge [9]. To quantify the detailed distribution of time scales at the pixel level, we investigated the relation between anomalies of LXS runoff and NDVI at different time lags (0–4 years) by shifting runoff anomalies by one year at a time. In the correlation analyses, only the positive time lags are considered because the water supply generally leads the growth of vegetation. Additionally, the specific time lags between anomalies of NDVI and LXS runoff in these derived pixels are identified. The Pearson correlation analysis is used to analyze the relationship between runoff and vegetation to identify the vegetation sensitivities. Significant pixels are selected to produce a statistically valid value using the two-tailed *t*-test (where $P \leq 0.05$ means statistical significance).

4. Results and Discussion

4.1. Overall Vegetation Dynamics. The overall vegetation dynamics of the HRB are analyzed with the abovementioned indices. The mean NDVI, NDVI slope, and interannual CV from 2001 to 2010 are shown in Figures 3(a)–3(d). As shown in Figure 3(a), there is a high vegetation coverage in the upper basin but relatively low coverage in the middle basin (mostly distributed among the irrigation regions) and lower basin (mostly distributed among the riverside regions). Figures 3(b) and 3(c) show that the vegetation evolutions exhibit obvious distribution differences: vegetation restoration trends are distributed throughout most regions (depicted in green), but vegetation degradation trends still exist in a small portion of regions (depicted in red), mostly in the upper portion of the upper basin, the central irrigation region in the middle

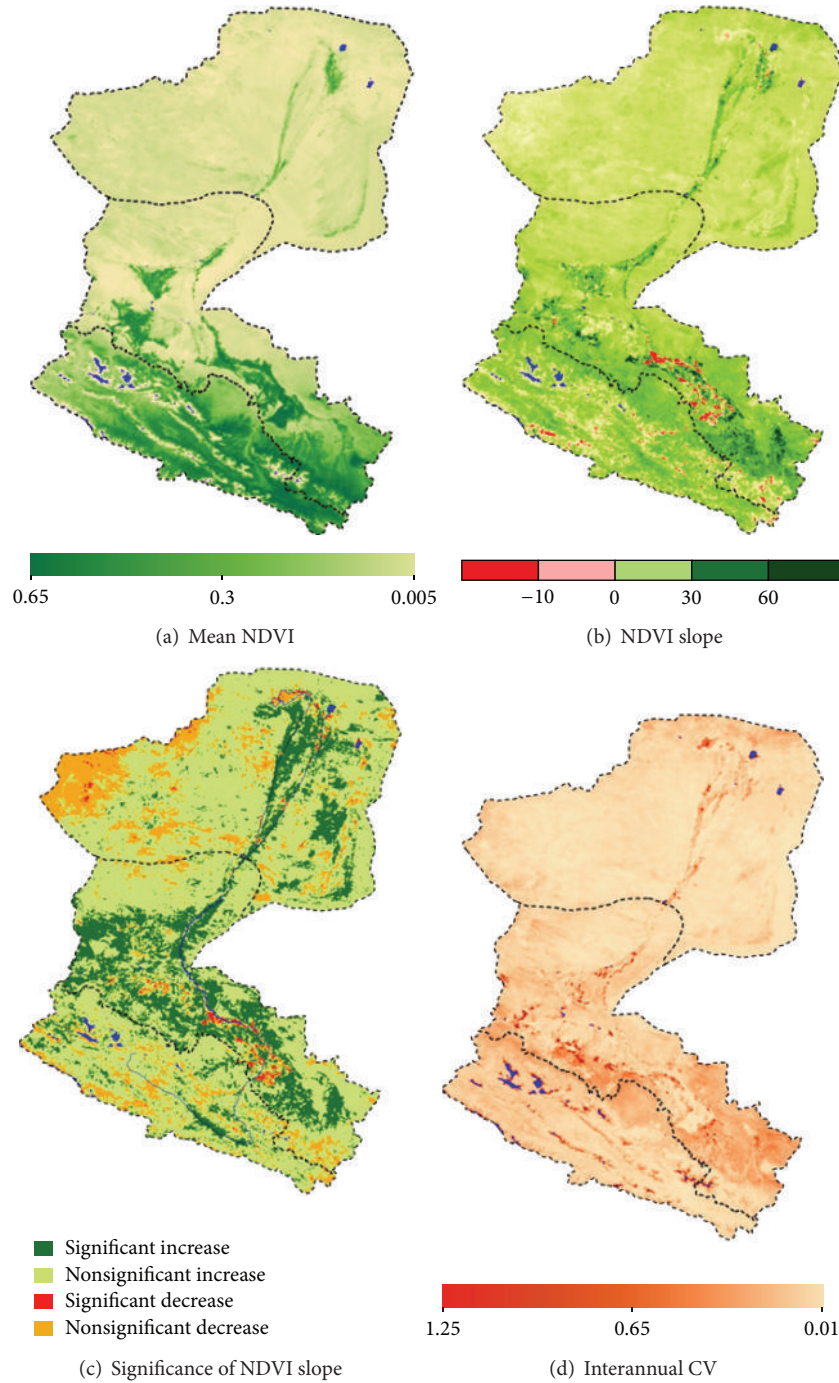


FIGURE 3: Vegetation dynamics in the Heihe River Basin.

basin, and the West Juyan Lake in the lower basin. As shown in Figure 3(c), the significant increase of vegetation mostly occurred in the middle and lower basins, rather than in the upper basin. Moreover, vegetation increase mostly occurred along the Heihe River in the upper and lower basins. In the middle basin, a large proportion of areas show significant improvement and a small region along the river in the Linze and Ganzhou County shows a significant decrease due to anthropogenic activities. The intensive restoration

or degradation of vegetation in the irrigation region in the middle basin is probably due to the adjustment of irrigation areas since the implementation of environmental conservation projects in 2001. On average, vegetation has recovered at the whole basin scale since 2001; the overall vegetation restoration rates of the upper and middle basins are similar to each other and faster than in the lower basin, as the slopes of their linear regressions are similar to each other and larger than that of the lower basin (see Figure 4).

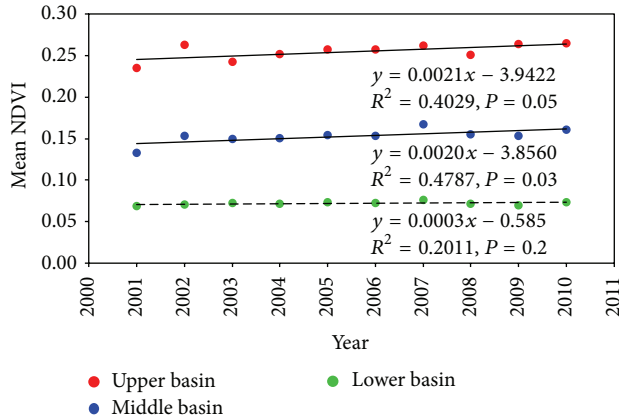


FIGURE 4: Vegetation evolutions of the upper, middle, and lower basins. *Regression that is significant ($P \leq 0.05$) or nonsignificant ($P > 0.05$) is presented with solid line or dashed line, respectively.

The vegetation variation is very small in the mean interannual CV at the whole basin scale, as shown in Figure 3(d). The high interannual CV values are distributed either in regions of the upper and middle basins where vegetation coverages are relatively low or in regions close to the rivers or water bodies. This is likely because the regions with low vegetation coverage are very unstable and sensitive to rainfall and runoff variations in the upper and middle basins; the variation in surface water level leads to the frequent transition between high vegetation coverage and swamp near the rivers or water bodies. The low interannual CV values are distributed in the regions with no vegetation coverage because these regions are significantly affected by desertification and in regions with high and stable vegetation coverage but which are far away from rivers or water bodies.

With the continuously increasing water discharge from the middle basin to the lower basin, the ecological situation of oases in the lower basin has significantly improved. For this study, several years of data from the oases in the lower basin are extracted from the NDVI data and shown in Figure 5. Because the water resources' management was implemented in 2001, the area of East Juyan Lake (depicted in black dotted lines) has increased significantly, at an average rate of approximately 4 km^2 per year. The maximum area of the East Juyan Lake has reached 46.8 km^2 in 2010. The ecological impact of water resource reallocation is positive for the regions close to the East Juyan Lake. However, it is worth noting that water resource reallocation has not prevented the West Juyan Lake (depicted in red dotted lines) from shrinking; the vegetation in the regions close to the West Juyan Lake also shows a slight decreasing trend. The results indicate that the water resource reallocation only brought about benefits to the East Juyan Lake.

Though the vegetation has slight restoration trends in some regions, the vegetation coverage has not changed that much over the whole HRB. This may be because the ecosystem conservation projects have not been completely implemented in the upper basin; the improvement in water usage efficiency in the middle river basin, while not

decreasing runoff to the lower regions, has limited impact on vegetation recovery in the middle basin.

4.2. Vegetation Transformation Characteristics. To identify the transformation speed quantitatively at the pixel level, the frequency distribution of the NDVI slope with mean NDVI for the upper, middle, and lower basins is shown in Figure 6, where the domain of the mean NDVI is divided into seven intervals (i.e., 0–0.1; 0.1–0.2; 0.2–0.3; 0.3–0.4; 0.4–0.5; 0.5–0.6; and 0.6–0.7). The domain of the NDVI slope is divided into five grades (i.e., <0 ; 0–20; 20–40; 40–60; and >60) and defined as “degradation,” “slow restoration,” “medium restoration,” “fast restoration,” and “extremely fast restoration” for conducting subsequent analysis equidistantly based on the distribution of the NDVI slope. In the upper basin, the vegetated area (as represented by NDVI values more than 0.1) accounted for approximately 90% of the total area, and 38% of these areas were covered by relatively dense vegetation (with NDVI values more than 0.3). Approximately 84% of the total area in the upper basin showed vegetation restoration trends, leaving only 16% of the total area in vegetation degradation trends. Among the five intervals of the NDVI slope, “slow restoration” occupied most of the total area (approximately 40%), followed by 30% for “medium restoration” and 12% for “fast restoration.” In the middle basin, the vegetated area accounted for approximately 44% of the total area, and only 16% of these areas were relatively densely vegetated. Approximately 92% of the total vegetation in the middle basin showed restoration trends, with only 8% in degradation trends. Among these restoration areas, 56% of them were “slow restoration” and 20% were “fast restoration” and “extremely fast restoration.” In the lower basin, 96% of the areas were covered by Gobi/desert (with NDVI values less than 0.1), leaving only 4% of the areas vegetated. 77% of the areas in the lower basin showed “slow restoration” and 18% showed “degradation,” with these two parts explaining 95% of the vegetation change trends in the lower basin. Overall, there was a vegetation restoration trend over the whole basin, and the fastest vegetation recovery occurred in regions where mean NDVI values were between 0.1 and 0.5. The regions with nearly no vegetation (mean NDVI values between 0 and 0.1) occupied most of the basin and the restoration speed in these regions was slow; this might be because they are far away from the river (e.g., most desert regions in the lower basin).

To identify the transformation dispersion at the pixel level, the correlation between interannual CV and mean NDVI for the upper, middle, and lower basins is shown in Figure 7. The overall trends of interannual CVs in the whole basin showed a decrease with the increase in mean NDVI values, indicating that the regions with high vegetation cover were more stable than areas with low vegetation cover. The pattern is clearly shown in the upper basin in Figure 7(a); the regions with NDVI values less than 0.05 were highly unstable, and the corresponding CVs were between 0.1 and 1.2. CVs decreased to 0–0.2 when NDVI values were between 0.05 and 0.1. Finally, CVs were small when NDVI values were more than 0.1, which indicates a relatively stable status. Similar patterns also appear in the middle and lower basins, and the

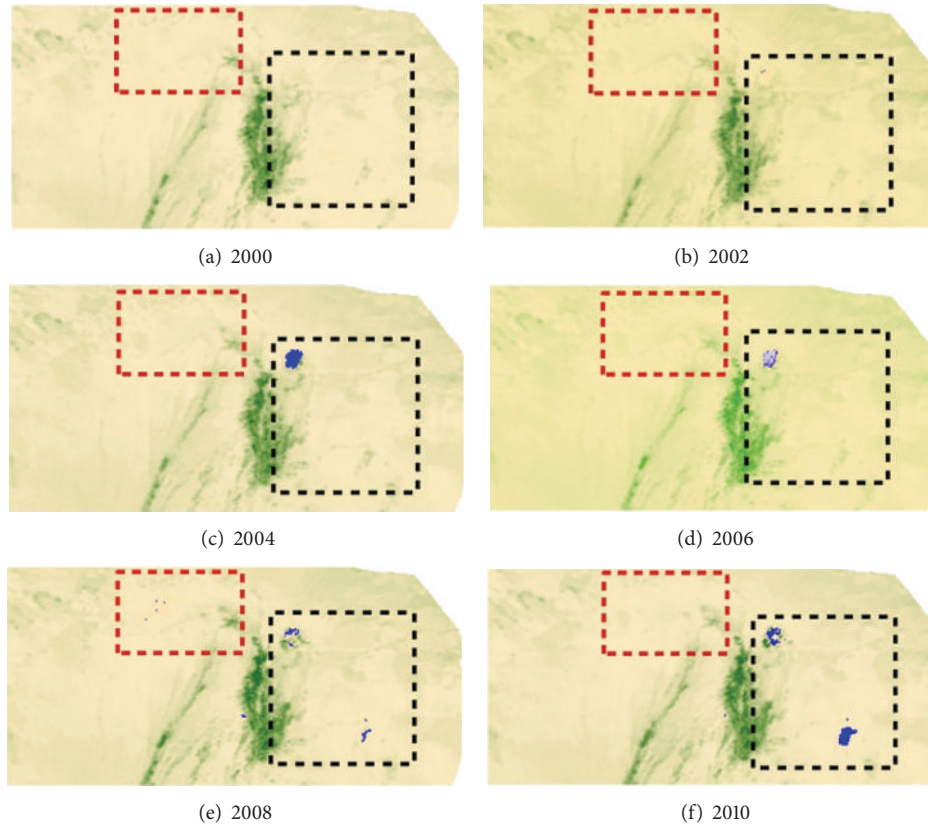


FIGURE 5: Variations in water bodies in both East and West Juyan Lakes. *The black and red dotted lines encompass the regions of the East and West Juyan Lakes, respectively.

correlations of CVs and mean NDVI were separated into two zones by a mean NDVI of approximately 0.05. Thus, the mean NDVI of approximately 0.05 distinguished the stable regions from the unstable ones for the whole basin.

4.3. Vegetation Sensitivity in the Lower Basin. Water supply from the middle basin is the essential factor that dominates ecosystem restoration in the lower basin. As seen in Figure 8(a), the runoff changes at the ZYX, LXS, LXS West, and LXS East stations located in the downstream of the Heihe River show increasing trend after the implementation of water reallocation projects since 2001. Similarly, in Figure 8(b), ratios of runoffs (i.e., ratio of runoff at the downstream stations to runoff at upstream YLX station) at the LXS and LXS stations also present increasing trends since 2001. That means an increase of water supply to the lower basin since the 2000s. On the other hand, the oases, which protect wildlife habitat and prevent fast desertification, are largely located in the lower basin. Thus, it is necessary to identify the temporal and spatial response of vegetation in the lower basin to the release from the middle basin. The correlations between NDVI data and releases of several past periods are studied, with significant and positive correlation points ($P \leq 0.05$) picked out and shown in Figure 9. Note that the historical release at the Langxinshan (LXS) hydrologic station is used for the correlations, and the “ n year(s) before”

denotes the correlation between NDVI data of a period and water releases into this region n year(s) before; for instance, in this case, “Two years before” means the correlation between NDVI data from 2001 to 2010 and water releases from 1999 to 2008, and “Current year” represents the relation between NDVI and water release in the same year.

From the perspectives of temporal and spatial responses, water release from the middle basin has a remarkable impact on vegetation in the lower basin. The affected vegetation (80% of the total area of the lower basin) is distributed in the regions within 50–100 km along the Heihe River and the East Juyan Lake. The vegetation affected by upstream water release with one-year time lag is distributed in the regions close to the Heihe River and the Badain Jaran Desert (40% of the total area of the lower basin). The regions with time lag more than two years are located near the Heihe River (20%, 5%, and nearly 0% of total area of the lower basin, with two, three, and four years’ time lags, resp.). The correlation analysis results indicate that water release from the middle basin will generate accumulative efforts to vegetation in the lower basin within at most three years. Ecosystem restoration can only be achieved through continuous efforts in water supply increasing into the lower basin.

Figure 10 shows the distribution of specific time lags between anomalies of NDVI and runoff at the LXS station

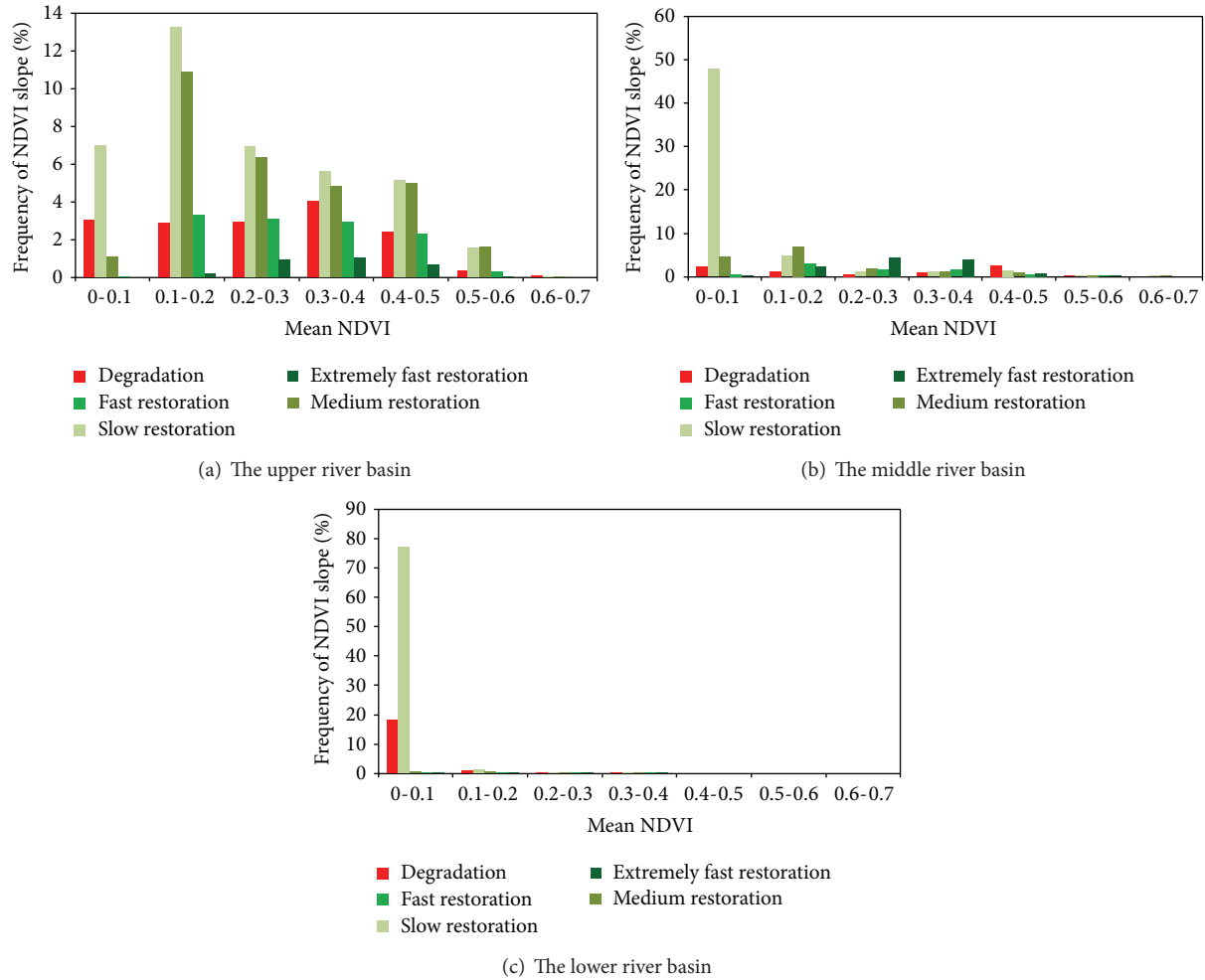


FIGURE 6: Frequency distribution of NDVI slope with mean NDVI.

in the derived pixels in Figure 9. Compared with Figure 9, vegetation along the Heihe River is influenced by runoff at the LXS station with time lag less than three years. Most of these regions are affected by runoff at the LXS station one year before. Additionally, regions along the West River are prominently impacted by the runoff one to two years before, while only small fractions at both the beginning and end of the East River have significant correlations with runoff anomalies. Except for regions along the river, a small area located at the west side of the West River also shows an obvious relation to runoff with one-year time lag.

5. Conclusions

In this study, the ecosystem restoration benefits in the upper, middle, and lower HRB are evaluated by identifying the vegetation dynamics and sensitivities in response to the near-term environmental conservation program in progress since 2001. Surface water area has significantly increased

in the East Juyan Lake in the lower basin, but there is no obvious increase in the water body of the West Juyan Lake. Most regions in the basin have vegetation restoration trends, with the fastest increase in vegetation occurring in parts of the irrigation area in the middle basin and along the Heihe River in the lower basin. Parts of regions still show vegetation degradation trends, mainly located in the less vegetated area of the upper basin, some in the irrigation area in the middle basin and near the West Juyan Lake in the lower basin. In terms of the vegetation variation represented by the interannual CV values, the high variations are distributed in regions either close to the rivers and water bodies or with low vegetation coverage, which is caused by variation in the surface water level and the instability of less vegetated regions, respectively. The NDVI slope indicates that the fastest vegetation recovery occurs in regions with medium mean NDVI values (between 0.1 and 0.5) instead of the extremely sparsely (less than 0.1) and highly (more than 0.5) vegetated regions. The vegetation variations (CVs) of the upper, middle, and lower basins are separated into two zones by an annual average NDVI value of approximately 0.05;

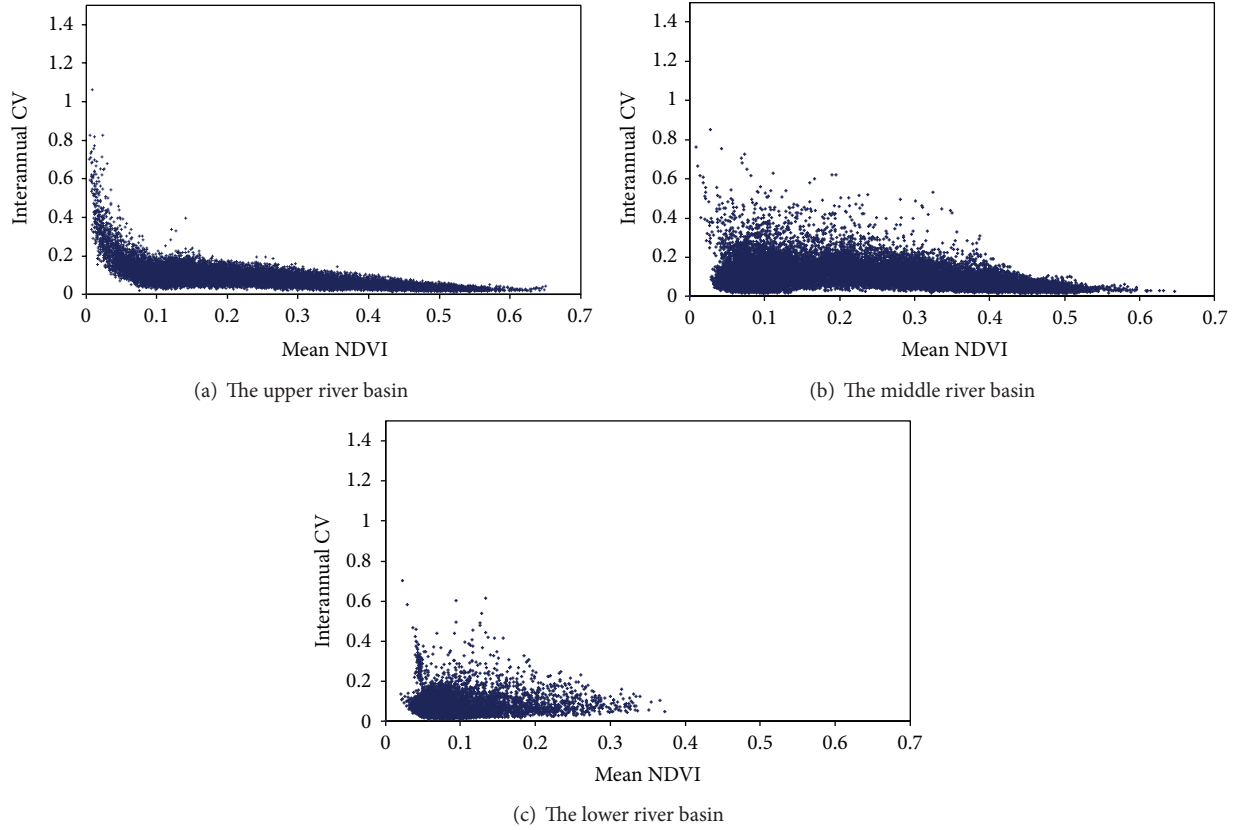


FIGURE 7: Relations between interannual CV and mean NDVI.

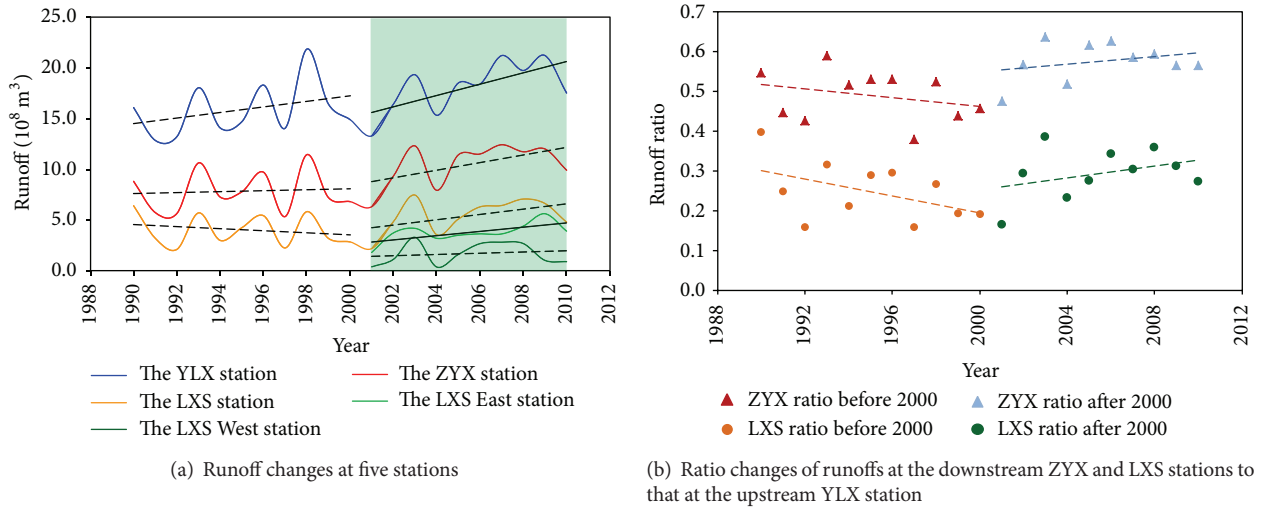


FIGURE 8: Runoff variation in the Heihe River Basin before and after NTECP. *Regression that is significant ($P \leq 0.05$) or nonsignificant ($P > 0.05$) is presented with solid line or dashed line, respectively.

regions with mean NDVI values more than 0.05 and less than 0.05 show stable and unstable status, respectively. Finally, the correlation between vegetation and water release into the lower basin suggests that there is a prominent impact from the water supply (mainly the previous year's runoff) on

the vegetation in the lower basin, particularly along the river. The significant impact of water supplement could last at most three years, and engineering or nonengineering measures should be maintained continuously for at least three years for permanent ecosystem recovery.

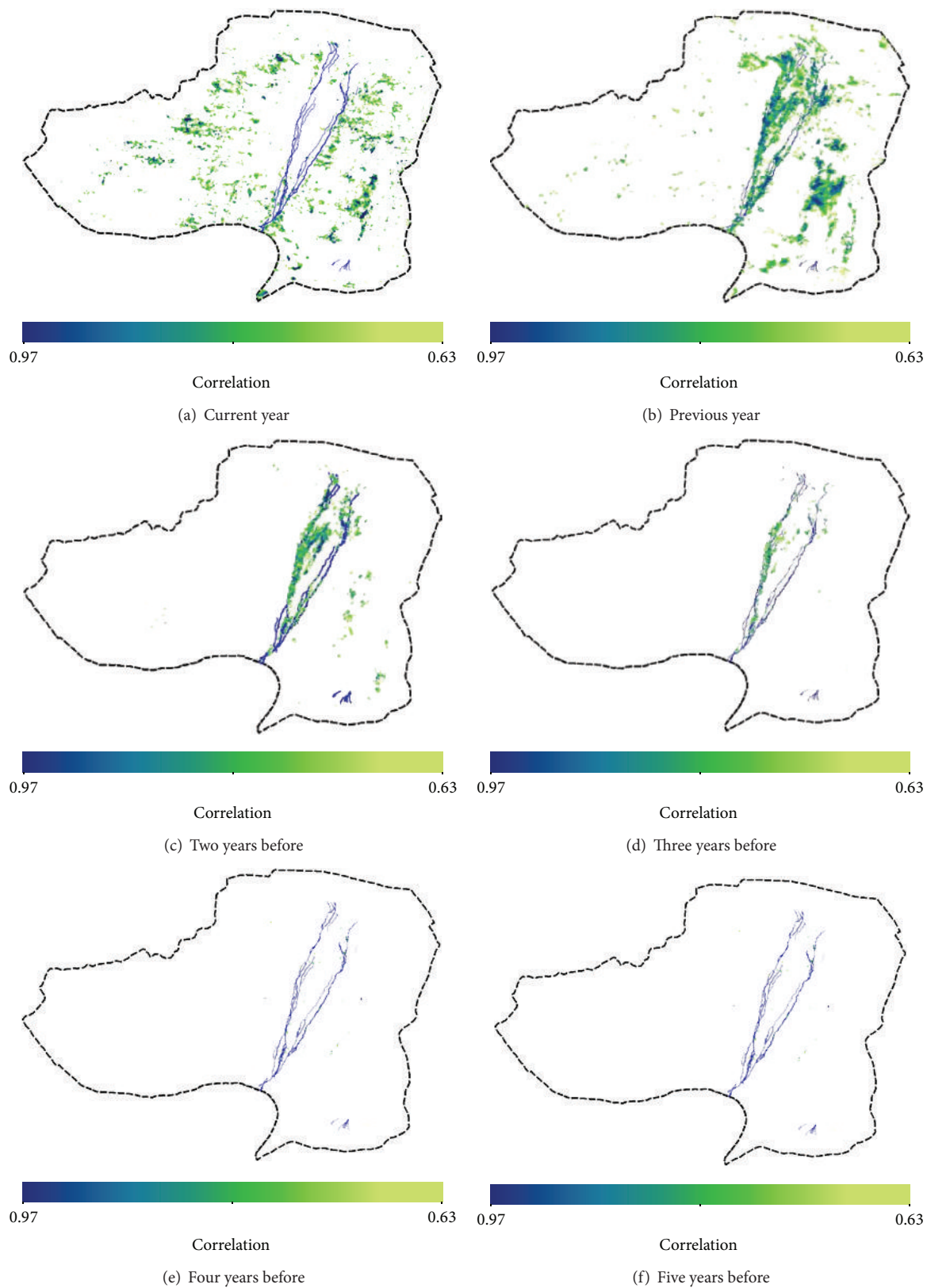


FIGURE 9: Vegetation sensitivities to runoff in the lower Heihe River Basin.

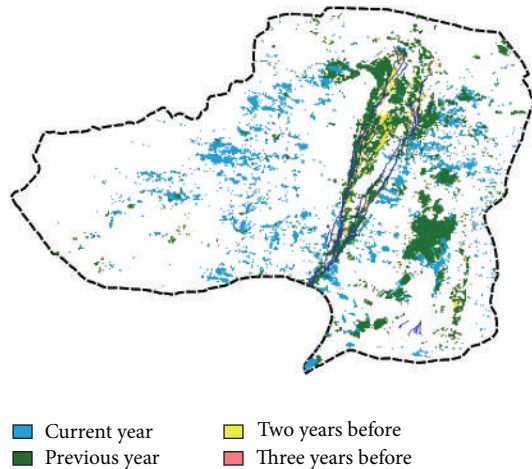


FIGURE 10: Time lag distribution between anomalies of NDVI and runoff at the Langxinshan station at the pixel level.

Conflict of Interests

The authors declare that there is no conflict of interests regarding the publication of this paper.

Acknowledgments

This paper is financially supported by the National Natural Science Foundation of China (91125018), the National Key Science and Technology Project Fund from the Ministry of Science and Technology (MOST) during the Twelfth Five-Year Project (2013BAB05B03), and the Research and Development Special Fund for Public Welfare Industry of the Ministry of Water Research in China (201301081).

References

- [1] L. Jia, H. Shang, G. Hu, and M. Menenti, "Phenological response of vegetation to upstream river flow in the Heihe River basin by time series analysis of MODIS data," *Hydrology and Earth System Sciences*, vol. 15, no. 3, pp. 1047–1064, 2011.
- [2] Y.-C. Zhang, J.-J. Yu, M.-Y. Qiao, and H.-W. Yang, "Effects of eco-water transfer on changes of vegetation in the lower Heihe River basin," *Journal of Hydraulic Engineering*, vol. 42, no. 7, pp. 757–765, 2011.
- [3] P. Wang, J. Yu, Y. Zhang, and C. Liu, "Groundwater recharge and hydrogeochemical evolution in the Ejina Basin, northwest China," *Journal of Hydrology*, vol. 476, pp. 72–86, 2013.
- [4] Ministry of Water Resources (MWR), *Recent Management Planning for Heihe River Basin (China)*, China Water Power Press, Beijing, China, 2001.
- [5] R. A. Pielke Sr., R. Avissar, M. Raupach, A. J. Dolman, X. Zeng, and A. S. Denning, "Interactions between the atmosphere and terrestrial ecosystems: influence on weather and climate," *Global Change Biology*, vol. 4, no. 5, pp. 461–475, 1998.
- [6] L. Bounoua, F. G. Hall, P. J. Sellers et al., "Quantifying the negative feedback of vegetation to greenhouse warming: a modeling approach," *Geophysical Research Letters*, vol. 37, no. 23, 2010.
- [7] R. B. Myneni, C. D. Keeling, C. J. Tucker, G. Asrar, and R. R. Nemani, "Increased plant growth in the northern high latitudes from 1981 to 1991," *Nature*, vol. 386, no. 6626, pp. 698–702, 1997.
- [8] R. J. Donohue, M. L. Roderick, T. R. McVicar, and G. D. Farquhar, "Impact of CO₂ fertilization on maximum foliage cover across the globe's warm, arid environments," *Geophysical Research Letters*, vol. 40, no. 12, pp. 3031–3035, 2013.
- [9] Y. Wang, M. L. Roderick, Y. Shen, and F. Sun, "Attribution of satellite-observed vegetation trends in a hyper-arid region of the Heihe River basin, Western China," *Hydrology and Earth System Sciences*, vol. 18, no. 9, pp. 3499–3509, 2014.
- [10] D. A. Devitt, A. Sala, K. A. Mace, and S. D. Smith, "The effect of applied water on the water use of saltcedar in a desert riparian environment," *Journal of Hydrology*, vol. 192, no. 1, pp. 233–246, 1997.
- [11] D. Gries, F. Zeng, A. Foetzki et al., "Growth and water relations of *Tamarix ramosissima* and *Populus euphratica* on Taklamakan desert dunes in relation to depth to a permanent water table," *Plant, Cell and Environment*, vol. 26, no. 5, pp. 725–736, 2003.
- [12] G. Wang, J. Q. Liu, J. Kubota, and L. Chen, "Effects of land-use changes on hydrological processes in the middle basin of the Heihe River, northwest China," *Hydrological Processes*, vol. 21, no. 10, pp. 1370–1382, 2007.
- [13] M. Ryner, K. Holmgren, and D. Taylor, "A record of vegetation dynamics and lake level changes from Lake Emakat, northern Tanzania, during the last c. 1200 years," *Journal of Paleolimnology*, vol. 40, no. 2, pp. 583–601, 2008.
- [14] A. J. Elmore, S. J. Manning, J. F. Mustard, and J. M. Craine, "Decline in alkali meadow vegetation cover in California: the effects of groundwater extraction and drought," *Journal of Applied Ecology*, vol. 43, no. 4, pp. 770–779, 2006.
- [15] P. Wang, Y. Zhang, J. Yu, G. Fu, and F. Ao, "Vegetation dynamics induced by groundwater fluctuations in the lower Heihe River Basin, northwestern China," *Journal of Plant Ecology*, vol. 4, no. 1-2, pp. 77–90, 2011.
- [16] C. J. Tucker, "Red and photographic infrared linear combinations for monitoring vegetation," *Remote Sensing of Environment*, vol. 8, no. 2, pp. 127–150, 1979.
- [17] M. Schlerf, C. Atzberger, and J. Hill, "Remote sensing of forest biophysical variables using HyMap imaging spectrometer data," *Remote Sensing of Environment*, vol. 95, no. 2, pp. 177–194, 2005.
- [18] A. R. Huete, "A soil-adjusted vegetation index (SAVI)," *Remote Sensing of Environment*, vol. 25, no. 3, pp. 295–309, 1988.
- [19] A. A. Gitelson, F. Kogan, E. Zakarin, L. Spivak, and L. Lebed, "Using AVHRR data for quantitative estimation of vegetation conditions: calibration and validation," in *Synergistic Use of Multisensor Data for Land Processes*, B. J. Choudhury, S. Tanaka, A. Kondo, M. Menenti, and F. Becker, Eds., pp. 673–676, 1998.
- [20] A. Huete, K. Didan, T. Miura, E. P. Rodriguez, X. Gao, and L. G. Ferreira, "Overview of the radiometric and biophysical performance of the MODIS vegetation indices," *Remote Sensing of Environment*, vol. 83, no. 1-2, pp. 195–213, 2002.
- [21] D. Y. Chen and W. Brutsaert, "Satellite-sensed distribution and spatial patterns of vegetation parameters over a tallgrass prairie," *Journal of the Atmospheric Sciences*, vol. 55, no. 7, pp. 1225–1238, 1998.
- [22] E. Weiss, S. E. Marsh, and E. S. Pfirman, "Application of NOAA-AVHRR NDVI time-series data to assess changes in Saudi Arabia's rangelands," *International Journal of Remote Sensing*, vol. 22, no. 6, pp. 1005–1027, 2001.

- [23] R. Amri, M. Zribi, Z. Lili-Chabaane, B. Duchemin, C. Gruhier, and A. Chehbouni, "Analysis of vegetation behavior in a North African semi-arid region, using SPOT-VEGETATION NDVI data," *Remote Sensing*, vol. 3, no. 12, pp. 2568–2590, 2011.
- [24] E. O. Box, B. N. Holben, and V. Kalb, "Accuracy of the AVHRR vegetation index as a predictor of biomass, primary productivity and net CO₂ flux," *Vegetatio*, vol. 80, no. 2, pp. 71–89, 1989.
- [25] R. Fensholt, K. Rasmussen, P. Kaspersen, S. Huber, S. Horion, and E. Swinnen, "Assessing land degradation/recovery in the african sahel from long-term earth observation based primary productivity and precipitation relationships," *Remote Sensing*, vol. 5, no. 2, pp. 664–686, 2013.
- [26] C. J. Tucker, J. R. G. Townshend, and T. E. Goff, "African land-cover classification using satellite data," *Science*, vol. 227, no. 4685, pp. 369–375, 1985.
- [27] S. Moulin, L. Kergoat, N. Viovy, and G. Dedieu, "Global-scale assessment of vegetation phenology using NOAA/AVHRR satellite measurements," *Journal of Climate*, vol. 10, no. 6, pp. 1154–1170, 1997.
- [28] Y. Gu, J. F. Brown, J. P. Verdin, and B. Wardlow, "A five-year analysis of MODIS NDVI and NDWI for grassland drought assessment over the central Great Plains of the United States," *Geophysical Research Letters*, vol. 34, no. 6, Article ID L06407, 2007.
- [29] P. L. Nagler, J. Cleverly, E. Glenn, D. Lampkin, A. Huete, and Z. Wan, "Predicting riparian evapotranspiration from MODIS vegetation indices and meteorological data," *Remote Sensing of Environment*, vol. 94, no. 1, pp. 17–30, 2005.
- [30] X. Jin, M. Schaepman, J. Clevers, Z. Su, and G. Hu, "Correlation between annual runoff in the Heihe River to the vegetation cover in the Ejina Oasis (China)," *Arid Land Research and Management*, vol. 24, no. 1, pp. 31–41, 2010.
- [31] W. Yaobin, F. Qi, S. Jianhua, S. Yonghong, C. Zongqiang, and X. Haiyang, "The changes of vegetation cover in Ejina Oasis based on water resources redistribution in Heihe River," *Environmental Earth Sciences*, vol. 64, no. 7, pp. 1965–1973, 2011.
- [32] Y. Zhang, J. Yu, P. Wang, and G. Fu, "Vegetation responses to integrated water management in the Ejina basin, northwest China," *Hydrological Processes*, vol. 25, no. 22, pp. 3448–3461, 2011.
- [33] I. Harris, P. D. Jones, T. J. Osborn, and D. H. Lister, "Updated high-resolution grids of monthly climatic observations—the CRU TS3.10 Dataset," *International Journal of Climatology*, vol. 34, no. 3, pp. 623–642, 2014.
- [34] NASA, "National Aeronautics and Space Administration Earth Observing System Data and Information System," <http://reverb.echo.nasa.gov/>.
- [35] J. Chen, P. Jönsson, M. Tamura, Z. Gu, B. Matsushita, and L. Eklundh, "A simple method for reconstructing a high-quality NDVI time-series data set based on the Savitzky-Golay filter," *Remote Sensing of Environment*, vol. 91, no. 3–4, pp. 332–344, 2004.
- [36] C. J. Tucker, D. A. Slayback, J. E. Pinzon, S. O. Los, R. B. Myneni, and M. G. Taylor, "Higher northern latitude normalized difference vegetation index and growing season trends from 1982 to 1999," *International Journal of Biometeorology*, vol. 45, no. 4, pp. 184–190, 2001.
- [37] S. R. Karlson, A. Tolvanen, E. Kubin et al., "MODIS-NDVI-based mapping of the length of the growing season in northern Fennoscandia," *International Journal of Applied Earth Observation and Geoinformation*, vol. 10, no. 3, pp. 253–266, 2008.

Research Article

Research on Nonpoint Source Pollution Assessment Method in Data Sparse Regions: A Case Study of Xichong River Basin, China

Xing Liu,¹ Donglong Li,² Hongbo Zhang,³ Shixiang Cai,¹ Xiaodong Li,¹ and Tianqi Ao¹

¹Department of Hydrology and Water Resources, State Key Laboratory of Hydraulics and Mountain River Engineering, College of Water Resource & Hydropower, Sichuan University, Chengdu, Sichuan 610065, China

²Sichuan Electric Power Design & Consulting Co., Ltd., Chengdu, Sichuan 610016, China

³Department of Hydraulic Engineering, Electric Power College, Kunming University of Science and Technology, Kunming, Yunnan 650500, China

Correspondence should be addressed to Xiaodong Li; lxdsu@163.com

Received 13 October 2014; Accepted 30 December 2014

Academic Editor: Yongqiang Zhang

Copyright © 2015 Xing Liu et al. This is an open access article distributed under the Creative Commons Attribution License, which permits unrestricted use, distribution, and reproduction in any medium, provided the original work is properly cited.

The NPS pollution is difficult to manage and control due to its complicated generation and formation mechanism, especially in the data sparse area. Thus the ECM and BTOPMC were, respectively, adopted to develop an easy and practical assessment method, and a comparison between the outputs of them is then conducted in this paper. The literature survey and field data were acquired to confirm the export coefficients of the ECM, and the loads of TN and TP were statistically analyzed in the study area. Based on hydrological similarity, runoff data from nearby gauged sites were pooled to compensate for the lack of at-site data and the water quality submodel of BTOPMC was then applied to simulate the monthly pollutant fluxes in the two sections from 2010 to 2012. The results showed agricultural fertilizer, rural sewage, and livestock and poultry sewage were the main pollution sources, and under the consideration of self-purification capacity of river, the outputs of the two models were almost identical. The proposed method with a main thought of combining and comparing an empirical model and a mechanistic model can assess the water quality conditions in the study area scientifically, which indicated it has a good potential for popularization in other regions.

1. Introduction

The nonpoint source (NPS) pollution refers to the pollution that does not come from a specific, easily identifiable source and generally results from the scouring effect of rainfall or snowmelt, and the dissolved contaminant solids entered into the receiving water bodies (including rivers, lakes, reservoirs, and bays) through the process of runoff. NPS pollution, which can cause the eutrophication of water bodies or other forms of pollution [1], is generated from land use activities associated with agricultural development, rural areas, or uncontrolled urban runoff from development activities. The rural excessive and unreasonable use of pesticides and fertilizers, small-scale livestock manure, untreated waste in agricultural production, and rural garbage are the direct factors causing the NPS pollution. According to the reports

by the United States and Japan, even though the point source pollution is fully controlled, the compliance rates of water, lake, and marine are only 56%, 42%, and 78%, respectively [2]. At present, NPS pollution becomes the leading cause of surface water impairment in many countries, such as UK, USA, and China [3]. China has already been the largest fertilizer consumer and is also the largest producing and using country of pesticides in the world [4], and NPS pollution, especially agricultural NPS, has already become a major contributing factor to water pollution and one of the important reasons for the deteriorating ecological environment in China [5, 6]. Therefore, the research of NPS pollution is of great importance for the restoration of water quality.

Nowadays, developing a model to assess NPS pollution and taking appropriate preventive measures have attracted increasing attentions in the environmental research. NPS

pollution assessment models can be generally divided into two types: mechanistic models and empirical models [2]. Combined with hydrological process, soil erosion process, and pollutants migration process, mechanistic model can simulate hydrodynamic and water quality transformation processes within the rivers. Most frequently used mechanistic models, such as QUAL2K [7], WASP6 [8], MIKE11 [9], SWAT [10], and AnnAGNPS [11], require time series of hydrometeorological data. Meanwhile, all sorts of data, such as land use, soil, population, livestock breeding, pesticide, and fertilizer use, should be collected and prepared for modeling [12]. In fact, it shows difficulties on practical applications especially in the watershed in most parts of China because the reliable related data are scarce and only very limited monitoring data for spatial and temporal variations of pollution sources and water quality are available. Besides, there are some complications. Taking the SWAT, a very promising and popular mechanistic model for modelling NPS pollution on the catchment scale for more than 20 years, as an example, it has hundreds of parameters with tremendous uncertainties to model outputs [13, 14], and how to detect the key parameters for calibration is one of the most difficult problems that restricted the use of SWAT. Compared with complex mechanistic model, the simple empirical model has the advantages of requiring less data and having fewer parameters. Based on the establishment of empirical relationship between the natural physical characteristics of the watershed and the output of pollutants, empirical model, such as export coefficient model (ECM) [3, 15] and source strength coefficient method [16], can easily calculate the NPS pollution loads in the outlet of the basin under the low requirement of inputting data and parameters setting. Although it can neither describe the hydrological pathways in determining nutrient delivery to surface waters and the mechanism of contaminant migration, furthermore, nor predict them in real time, it is still an ideal tool with strong practical and wide application in regions with sparse data.

NPS pollution shows some characteristics, such as randomness, hysteresis, and uncertainty. Obviously, the selection of model should be based on the study purpose and data accessibility. An empirical model can easily give some necessary and useful assessment results and is less data demanding and a distributed simulation model can well characterize the NPS pollution process and provide more precise results to reflect the variety of quantitative pollution mechanism of pollutants and spatial-temporal distribution in detail as long as the space of the study area is discretized for better analysis, so to combine and compare an empirical model and a distributed simulation model is very attractive.

The goal of this study was to establish a simple and practical NPS pollution assessment method for the data sparse regions. A basin in Xichong county, China, was taken as a case study in this study. Two widely used models including an empirical model and a physically based distributed hydrological model, ECM and BTOPMC, are adopted to build an easy and practical assessment method on NPS pollution. By integrating the advantages and comparing the results of the two models, a more objective assessment conclusion was obtained. The principles of this method were as follows: (1) it is to quantitatively assess the total nitrogen (TN) and total

phosphorus (TP) which are the main pollutants in Xichong River basin by using the ECM and (2) based on hydrological similarity, the BTOPMC was adopted to solve the problem in regions with sparse hydrological data by using the parameter transferring method, trying to generate discrete grids in the space of study area, and quantitatively reflected the pollution mechanism of TN and TP by applying a simple submodel of water quality.

2. Materials and Methods

2.1. Study Area and Available Data. Xichong County, of which the latitude and longitude are $30^{\circ}52'N\sim 31^{\circ}15'N$ and $104^{\circ}4'E\sim 105^{\circ}36'E$, is situated in the north part of Sichuan Province, China. It is in the back zone of Jialing River and Fujiang River and its altitude varies from 282 m to 569 m, lying northwest high and southeast low. The region is characterized by a subtropical monsoon humid climate and has an average precipitation of about 1000 mm per year, most of which occurs between July and September. Xichong River, which is the largest river in the Xichong County and flows through 23 villages and towns, includes two branches, the Hongxi River and Longtan River (Figure 1). The Hongxi River has a total length of 42.5 km and the basin area is 289.87 km², and the Longtan River has a total length of 39.8 km and the basin area is 189.73 km². After the main stream flows out of the Xichong County, the river flows through Jialing district and Shunqing district in Nanchong city in the direction of southeast before importing the Jialing River.

Xichong River is regarded as the mother river in Xichong County. Not only is it an important regional water source for the basin along the river, but it also plays an important role in local environment protection and national economy development. Unfortunately, it has been seriously polluted since the 1980s. According to China's water quality classification criteria, the monitoring results on the two sections (Yanjiaxiang section and Xiyangsi section, see Figure 1) from 2010 to 2012 showed that the monthly concentrations of TN and TP were worse than that of the V class of water quality.

The sources of the data used in this study include the following: (i) the terrain data was obtained from Computer Network Information Center, Chinese Academy of Sciences Data Center (<http://www.gscloud.cn/>) which can provide 90 m × 90 m resolution digital elevation model (DEM) data; (ii) land use/vegetation cover type data was obtained from the Standard International Geosphere Biosphere Programme (IGBP) 1 km × 1 km resolution data which were provided by the US Geological Survey; (iii) the soil information was obtained from the Food and Agriculture Organization of the United Nations (FAO) which can provide 1 km × 1 km resolution data; (iv) daily observed precipitation data from 2010 to 2012 in study area were provided by the Xichong meteorological station. The hydrometeorological data from 1985 to 1987 in hydrological reference basin were collected from the Hydrological Yearbook, Ministry of Water Resource, China; (v) in the study area, there are two water quality monitoring sites, Yanjiaxiang section in the Longtan River and Xiyangsi section in the Hongxi River. The two water

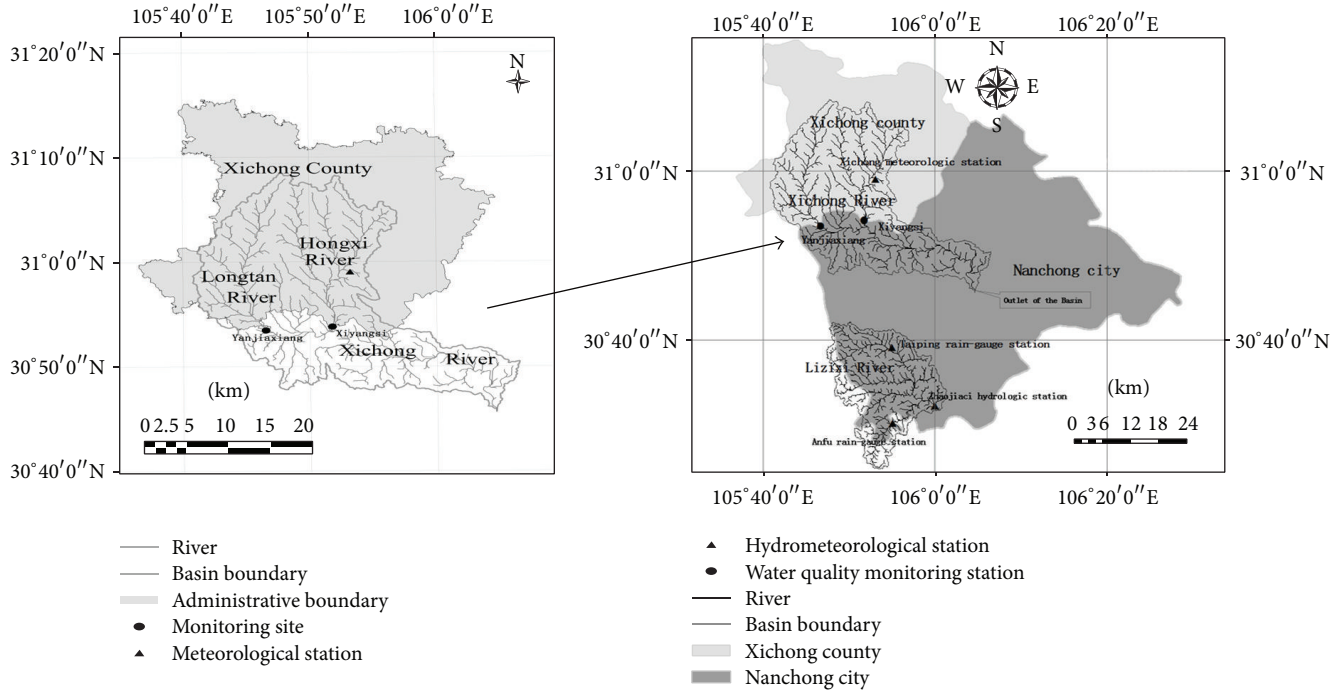


FIGURE 1: Stream network, division of influence regions, and the distribution of stations.

quality monitoring sites have a total amount of water quality monitoring data for 20 months from September 2010 to April 2012 and all the data were provided by the local environmental monitoring department; (vi) the number of agricultural and nonagricultural populations, livestock, and poultry of each town was mainly provided by corresponding local government sectors, as well as the field survey for the local committees of the village, farmers, and scientific and technical personnel. All above the satellite data should be standardized to 300 m × 300 m in order to match the resolution of the BTOPMC calculation with ArcGIS software.

2.2. ECM Description

2.2.1. Method. The ECM was first presented by Johnes and O’Sullivan in 1989 [17] and then modified by Johnes in 1990 [18]. The modified model takes some new nutrient export factors into account: inputs of nitrogen to the catchment through nitrogen fixation by each agricultural crop, areas of seminatural vegetation and woodland, whether human settlements were connected to a main sewage system or used a septic tank system, and notable land management practices known as the cause of the increases in nutrient export, such as the direct grazing of fodder crops on the fields by livestock and the cultivation of oilseed rape. The ECM has been recognized as an applicable and acceptable model for NPS pollution assessment; however, the ECM still has some limitations; for example, the ECM does not take the terrain and the uneven temporal-spatial distribution of precipitation into account, which are supposed to be the key

factors affecting NPS pollution [19]. The modified model is formulated as follows:

$$L = \sum_{i=1}^n E_i [A_i (I_i)] + p, \quad (1)$$

where L is the loss of nutrients, E_i is the export coefficient for the nutrient source i , A_i is the area of the land use type i , or the number of the livestock and poultry type i , or the population in the catchment, I_i is the input of the nutrients to source i , and p is the input of the nutrients from atmospheric deposition.

2.2.2. Export Coefficients. The main nutrient sources can be identified into five categories: agricultural fertilizer pollution related to six kinds of land use types (such as natural woodland, wasteland, dry land, paddy fields, fruit woodland, urban land, and livestock), poultry pollution related to four kinds of types (such as cattle, pigs, sheep, and poultry), and rural and urban residential pollution. The determination of the ECM parameters (export coefficients) exerting greatest control over model output is usually summed up in three ways: the literature survey, field experiment, and the hydrological statistics, which can determine the export rate of nutrients (TN and TP) from each identifiable nutrient source to the surface stream network. These three methods have their respective advantages and disadvantages: (1) the literature survey is relatively easier and cheaper than the latter two methods, but with a lower accuracy; (2) the field experiment has the highest accuracy but needs more investment and is time consuming; (3) and the third method reflects the hydrological mechanism

TABLE 1: The classification and value of export coefficient in study area.

Type	Land use/t·km ⁻² ·yr ⁻¹					Livestock and poultry/t·(10 ⁴ ca·yr) ⁻¹					
	Dry land	Paddy field	Fruit wood land	Natural woodland	Waste land	Urban	Cattle	Pig	Sheep	Poultry	Rural population/t·(10 ⁴ ca·yr) ⁻¹
TN	0.115	0.075	0.040	0.119	0.745	0.550	3.660	0.695	0.700	0.030	18.700
TP	0.006	0.006	0.003	0.009	0.031	0.014	0.186	0.085	0.027	0.003	2.140

with higher accuracy [20] but requires a large amount of hydrological data and water quality data which is lacking in most medium and small basins of developing countries. Due to the shortage of the monitoring data, this study mainly adopted the literature survey [21–26] which makes sure the export coefficients are adjusted only within the range of data published for basins in upper reaches of Yangtze River combined with the field data, such as land use, the agricultural and nonagricultural population of each town, the dosage of the chemical fertilizer, and the number of the livestock and poultry to determine the export coefficients. The export coefficients in this study were determined in Table 1.

2.3. BTOPMC Description. BTOPMC is a physically based distributed hydrological model, in which runoff and nutrient are transported grid by grid along stream networks, and it consists of some submodels for topographical analysis, TOPMODEL based runoff generation, and Muskingum-Cunge flow routing [27–30]. A submodel of water quality was originally developed by Zhang [31] which has the ability to simulate pollutants migration in slope surface and pollutants migration and transformation in channel. The model can not only effectively show the spatial-temporal heterogeneity of topography, soil, land use, and pollution load but also reflect the response of the quantity and quality of water caused by natural variations and human activities. The mechanism of pollutants (including TN and TP) transformation on channel is based on the SWAT concept [32] and the process of pollutants migration on channel and slope surface is based on mass balance of pollutants within the grid established. It is outlined as follows [31]:

$$\begin{aligned}
 \Delta TN &= \sum TN_{\text{self.in}} + \sum TN_{\text{direct.in}} \\
 &\quad + \sum C_{\text{TN.in}} V_{\text{in}} - C_{\text{TN.out}} V_{\text{out}}, \\
 V_{\text{in}} &= \frac{q_{\text{ini.in}} + q_{\text{end.in}}}{2} \Delta t, \\
 V_{\text{out}} &= \frac{q_{\text{ini.out}} + q_{\text{end.out}}}{2} \Delta t,
 \end{aligned} \tag{2}$$

where ΔTN is the mass change of water pollutants in the grid within the period, $\sum TN_{\text{self.in}}$ is the self-generated or reduction amount of pollutants in the grid within the period, $\sum TN_{\text{direct.in}}$ is the direct human-activity-caused amount of pollutants in the grid within the period, V_{in} is the inflow of water body in the grid within the period, V_{out} is the outflow of water body in the grid within the period, $q_{\text{ini.in}}$ is the initial inflow, $q_{\text{ini.out}}$ is the initial outflow, $q_{\text{end.in}}$ is the final inflow, $q_{\text{end.out}}$ is the final outflow, $C_{\text{TN.in}}$ is the input of

pollutant concentration in the grid, and $C_{\text{TN.out}}$ is the output of pollutant concentration in the grid.

The parameters related to runoff generating and flow routing in BTOPMC have physical meaning and can reflect the physical characteristics of underlying surface in the basin. Due to the characteristics of parsimonious calibrated parameters, relatively low requirement on inputs, being simple to operate and able to take advantage of satellite remote-sensing data, and so forth, BTOPMC can be applied to ungauged basins for hydrological simulation [33]. The main structure of BTOPMC is shown in Figure 2.

3. Results and Discussion

3.1. Calculation of TN and TP Based on ECM. The loads of all kinds of pollution sources (TN and TP) in study area in 2012 can be calculated by the ECM general expression after the export coefficient and data source information are determined. And they were summed to obtain the total area loads as shown in Table 2. According to Table 2, the polluted loads of TN and TP in this area are 868.50 t·yr⁻¹ and 65.08 t·yr⁻¹, respectively.

The estimated average TN and TP load intensities are 1.811 ton·km⁻²·yr⁻¹ and 0.136 t·km⁻²·yr⁻¹, respectively. The results of source apportionment are shown in Figure 3 and it shows that the agricultural fertilizer and sewage from rural residents contribute the most to TN and TP which is because the sewage from residents and livestock is often simply processed through septic tanks and digesters due to the lack of proper sewage pipe network and sewage treatment facilities in the study area. Thus, the generated biogas can be directly used as energy resource and a large amount of chemical fertilizers can be used in agricultural production with low utilization rates, which causes serious NPS pollution. The major sources of TN are agricultural fertilizer, which accounted for 53.42% of the total, followed by rural sewage (23.37%) and livestock and poultry sewage (11.18%). Besides, urban sewage is also a major polluted source. Among those six land use types, dry land, paddy field, and natural woodland which have been fertilized contribute the most (52.73%). Rice, wheat, and corn are the dominant crops in agricultural land. To improve the economic yield from these crops, large doses of fertilizer have been used, which in turn raised environmental contamination level. Furthermore, crop residues, which are not systematically managed, are an N-rich pollution source [34]. The major sources of TP ranked differently from those of TN, with rural sewage (42.82%), followed by agricultural fertilizer (23.76%), urban sewage (16.81%), and livestock and poultry sewage (15.61%). Taking

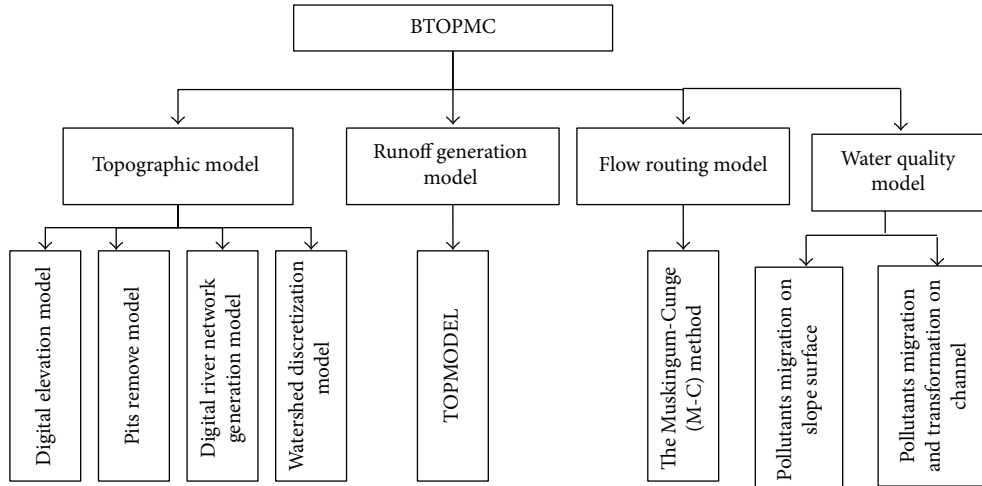


FIGURE 2: The main structure of BTOPMC.

TABLE 2: TN and TP loads calculation of all kinds of pollution sources in 2012 (unit: ton·yr⁻¹).

Types	Types of pollution source	TN	Proportion/%	TP	Proportion/%
<i>Land use</i>					
Dry land		340.84	39.24	9.47	14.55
Paddy field		97.28	11.20	4.24	6.52
Orchard	Fertilizer	2.36	0.27	0.10	0.15
Natural woodland		19.85	2.29	1.50	2.30
Waste land		3.63	0.42	0.15	0.23
Subtotal		463.96	53.42	15.46	23.76
Urban land	Urban runoff	24.77	2.85	0.65	1.00
<i>Livestock and poultry</i>					
Cattle		10.05	1.16	0.51	0.78
Pig	Livestock and poultry	70.85	8.16	8.70	13.37
Sheep		11.09	1.28	0.43	0.66
Poultry		5.15	0.59	0.51	0.78
Subtotal		97.13	11.18	10.16	15.61
<i>Population</i>					
Rural population	Rural sewage	202.96	23.37	27.87	42.82
Urban population	Urban Sewage	79.67	9.17	10.94	16.81
Total		868.5	100.00	65.08	100.00

into account the synthetic factors for loads TN and TP, therefore agricultural fertilizer, rural sewage, and livestock and poultry sewage are the main pollution sources influencing loads of nonpoint source nitrogen and phosphorus in the study area. Obviously, these sources should be controlled first.

One limitation of this ECM is that calibration of export coefficients is not based on hydrological and water quality data and may affect the accuracy of the calculation. But available field data are reliable, and the ECM can identify to some extent the main pollution sources and reflect NPS pollution status in study area. Furthermore, compared with output of BTOPMC, the calculation of the ECM can be assessed scientifically.

3.2. Simulation by BTOPMC

3.2.1. Runoff Simulation. Runoff data in control sections are required to simulate the water quality, but there is no measured runoff data in Xichong River basin. Therefore, the BTOPMC was adopted to simulate the daily average runoff in 2010 and 2011 by the transplantation of hydrological parameters derived from Lizixi River. Lizixi River basin (Figure 1) is about 40 km away from the Xichong River basin. They share the same climate zone and show similarities about the basin area, annual rainfall, temperature, soil, and the land use.

The daily runoff data from 1985 to 1986 at Zhaojiaci station in Lizixi River basin were applied to calibrate the

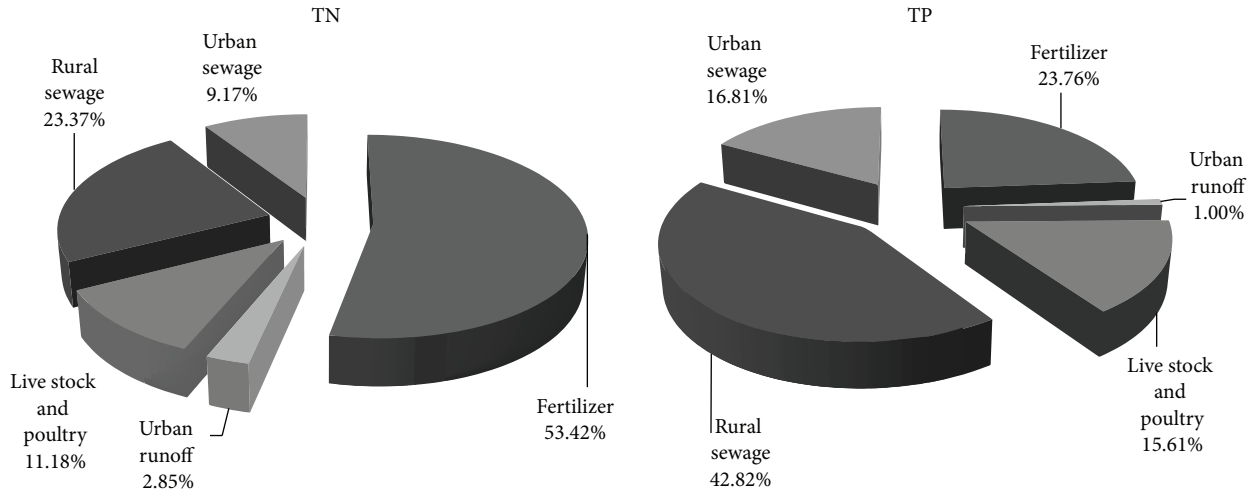


FIGURE 3: TN and TP load of all kinds of pollution source distribution figure.

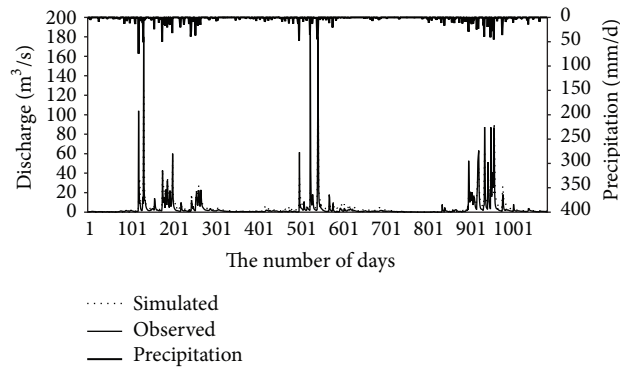


FIGURE 4: Calibration and validation results in Lizixi River basin: observed and simulated daily hydrographs.

parameters and the daily runoff data in 1987 were used for validation. Figure 4 shows the simulated and observed hydrographs of the flood and the long-term case (including calibration and validation periods). It can be seen that most of the simulated hydrograph agrees well with observed, except the low flow. The simulated discharges during dry season of calibration period were notably higher than those observed. This discrepancy might have been caused by the influences of water use systems or limited by the resolution of the soil and land cover map. The Nash efficiency coefficients [35] of calibration and validation periods were determined to be 67.9% and 76.30%, respectively.

Parameter transferring from Lizixi River basin to the Xichong River basin was needed before the daily runoff processes of Xiyangsi section and Yanjiaxiang section in Xichong River basin were simulated by BTOPMC (Figure 5). The simulated results show that the yearly average flows of Xiyangsi section and Yanjiaxiang section in 2010 and 2011 are 2.47 m³/s and 1.89 m³/s, respectively, and the maximum yearly flows are 68.47 m³/s and 53.00 m³/s, respectively, which both appear in the 506th day. From Figure 5, it can be seen that there is an obvious corresponding relationship between the process of daily runoff and rainfall sequences.

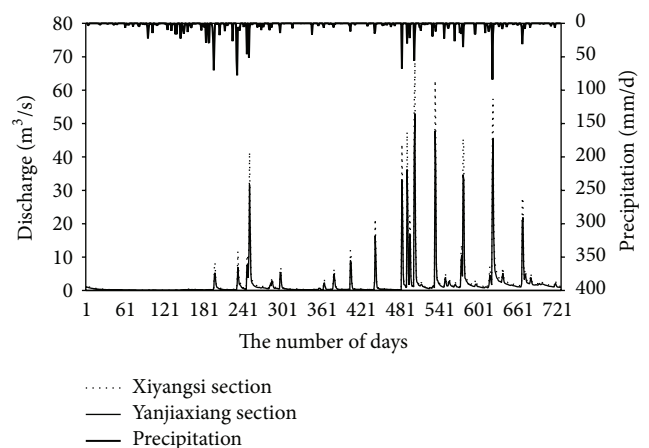


FIGURE 5: Precipitation and simulated daily hydrographs at water quality monitoring stations.

Meanwhile, the runoff coefficient is 0.36 which fits the range of runoff coefficient in Jialing River basin (the runoff coefficients in Beibei station and Shanxi station are 0.37 and

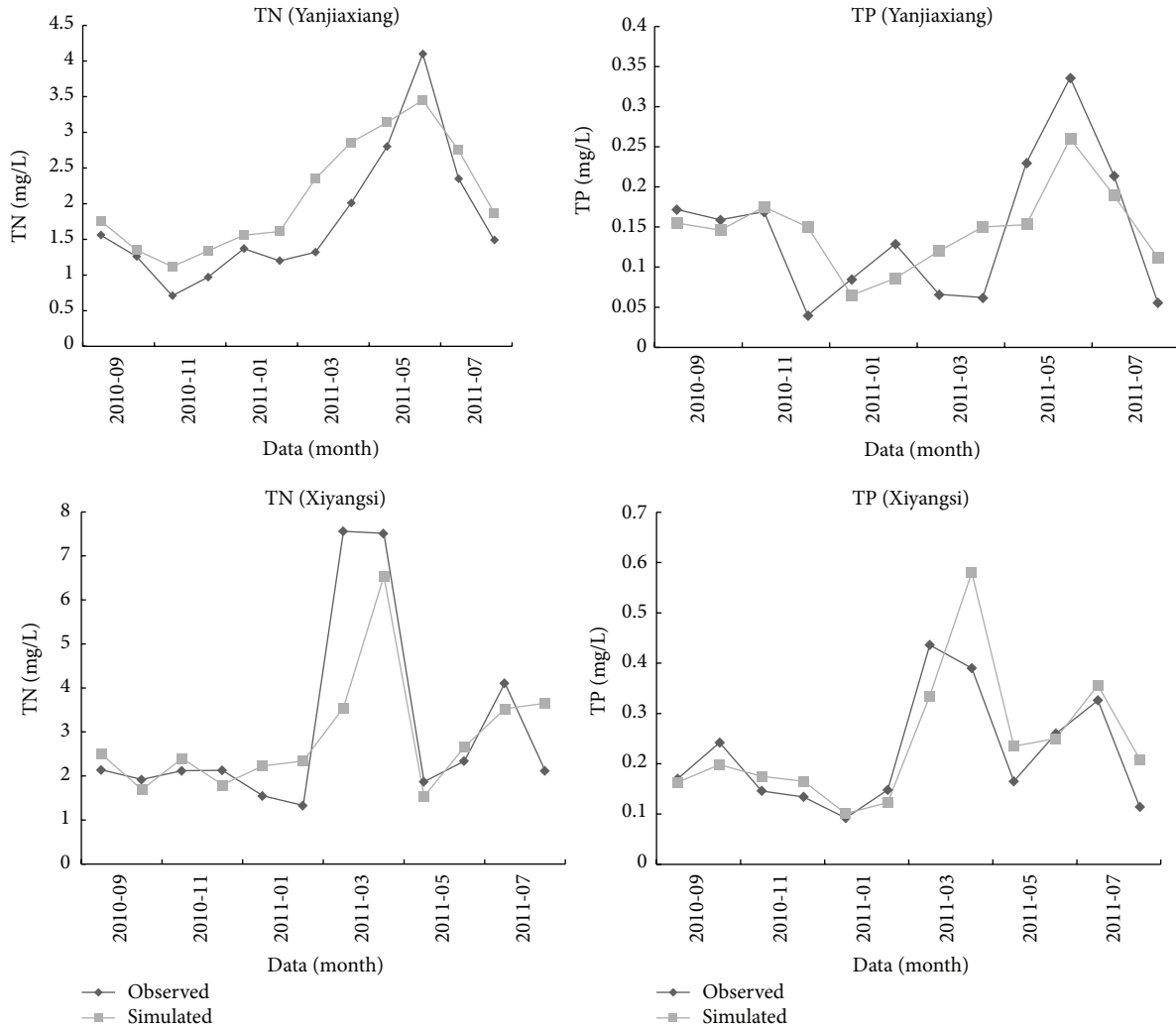


FIGURE 6: Observed and simulated TN and TP at Yanjiaxiang or Xiyangsi (monthly calibration period).

0.28, resp.). From the analysis above, the simulated results related to the runoff are reasonable.

3.2.2. *Water Quality Simulation.* The model parameters related to the TN and TP are calibrated and validated by using the data measured in Xiyangsi section and Yanjiaxiang section. The data for calibration are monthly measured from September 2010 to August 2011 and the data for validation are monthly measured data from September 2011 to April 2012. The calibration and validation results show that all Nash efficiency coefficients are above 50%, of which the Nash efficiency coefficient in Yanjiaxiang section is 67.24% (Table 3). By comparing the simulated and measured curve, it is obvious that this model can offer reasonable simulations of actual water quality, but it shows some gaps in the peak value in the curve between the simulated and measured data due to the relatively low accuracy of simulation at some node points (Figures 6 and 7). Overall, the calibrated model is comparatively efficient for simulating the process of nonpoint resources pollution.

TABLE 3: The evaluation of calibration and validation of the model.

Period	Section	Pollutants	The efficiency of Nash (%)
Calibration	Yanjiaxiang	TN	67.24
		TP	52.31
	Xiyangsi	TN	59.05
		TP	53.12
Validation	Yanjiaxiang	TN	55.64
		TP	53.07
	Xiyangsi	TN	57.3
		TP	54.2

The NPS pollutions in the Longtan River and Hongxi River were simulated from 2010 to 2012 by using calibrated model. The simulated annual fluxes of these two sections are shown in Table 4, which indicates a growing trend about the TN and TP from 2010 to 2012. In 2012, the total flux of TN in two sections is 642.55 t, of which the flux of TN amounts to 362.58 t in Hongxi River section and 279.98 t in Longtan

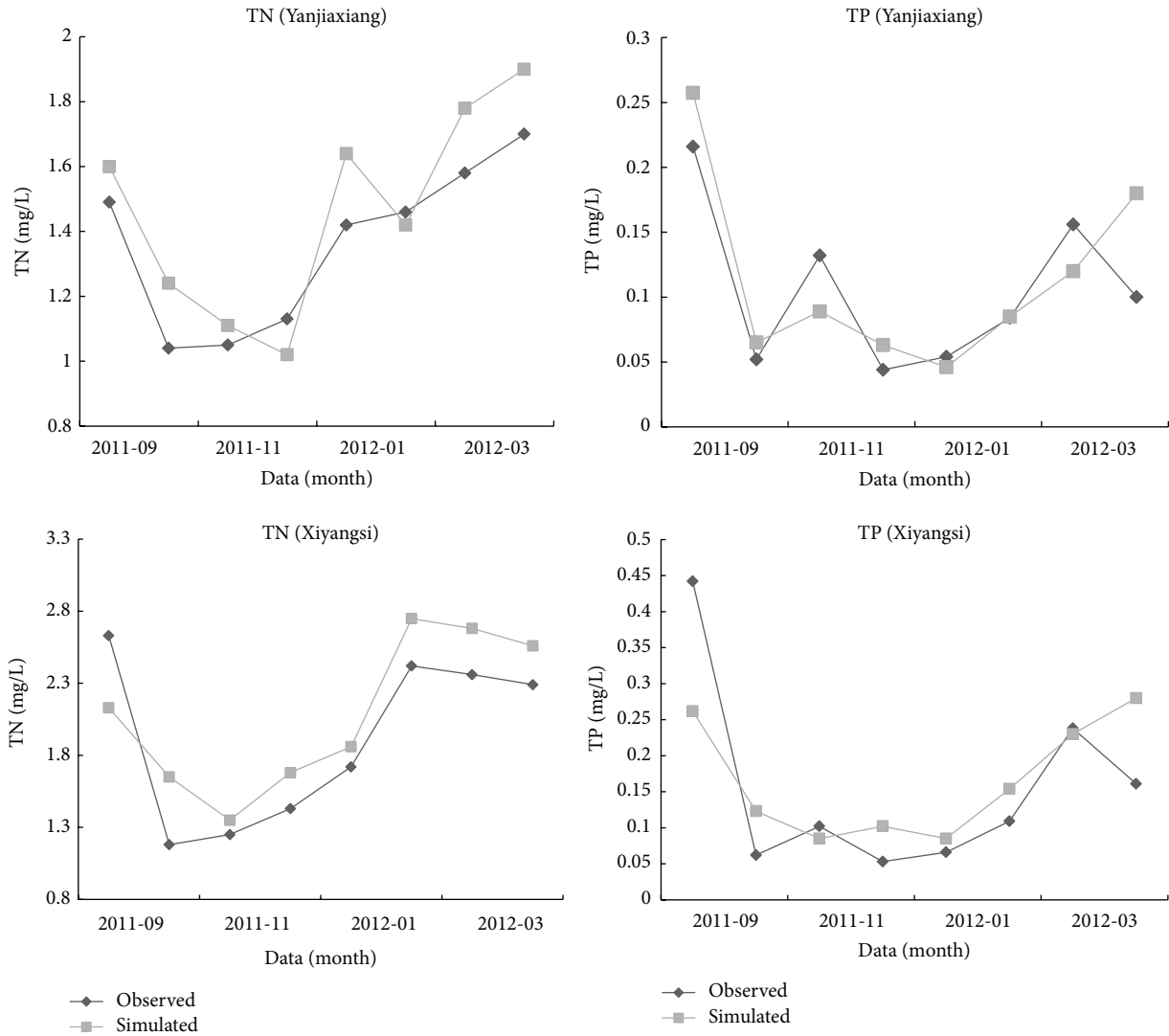


FIGURE 7: Observed and simulated TN and TP at Yanjiaxiang or Xiyangsi (monthly validation period).

TABLE 4: The simulated results of pollutant loads in TN and TP.

Year	Index	2010	2011	2012
Longtan River	Average flow (unit: m^3/s)	0.7	3.08	4.94
	TN (unit: ton)	79.13	199.21	279.98
	TP (unit: ton)	7.73	16.69	17.08
Hongxi River	Average flow (Unit: m^3/s)	0.96	3.98	6.32
	TN (unit: ton)	146.24	269.2	362.58
	TP (unit: ton)	11.05	26.13	33.62
Total	TN (unit: ton)	225.37	468.41	642.55
	TP (unit: ton)	18.78	42.82	50.7

River section. And the fluxes of TP in two sections amount to 50.7 t, of which the flux of TP in Hongxi River section and Longtan River section is 33.62 t and 17.08 t, respectively. It indicates that the flux of pollution in Hongxi River is more than that in Longtan River and this phenomenon is highly related to the area of basin, population distribution, industrial

structure, and other factors. The area of Hongxi River basin and Longtan River basin is $289.86 km^2$ and $189.73 km^2$.

The ECM and BTOPMC were, respectively, adopted to calculate pollutant loads in Xichong River in 2012. The comparisons of results of the two models are listed in Table 5. The statistical results by the ECM are the yearly input amount

TABLE 5: The comparison of loads in TP and TN between the ECM and BTOPMC model (unit: ton).

Pollutants	Data source	Hongxi River	Longtan River
TN	ECM	530.31	338.19
	BTOPMC	362.58	279.98
	Difference	167.73	58.21
TP	ECM	40.49	24.59
	BTOPMC	33.62	17.08
	Difference	6.87	7.51

Note: the statistical results by ECM are expressed as the amount of pollutants which are input to the river in 2012. The results by BTOPMC are expressed as the yearly fluxes of pollutants in sections in 2012. The amount of difference between these two results reflects the environmental capacity and self-purification capacity of rivers.

of pollutants and the simulated results by BTOPMC are the fluxes of pollutants in two sections. The differences between the outputs of the two models can reflect the self-purification capacity of the river. The simulated results indicate that the differences of TN and TP in Hongxi River sections are 167.73 t and 6.87 t, respectively, while those in Longtan River are 58.21 t and 7.51 t, respectively, which reflect that the self-purification capacity of the Hongxi River is higher than that of Longtan River. According to the runoff data, the yearly average runoff in Hongxi River and Longtan River is 6.32 m³/s and 4.94 m³/s, respectively. The yearly average runoff in Hongxi River is larger than that in Longtan River which also reflects that the self-purification capacity of the Hongxi River is higher than that of Longtan River. In summary, considering self-purification capacity of rivers and a reliable calibration of the BTOPMC against the observed TN and TP concentrations in the two water quality monitoring sites, results of statistical analysis and mechanistic model simulation are mostly identical and reasonable.

4. Conclusions

Due to easy acquisition of initial input data, an easy and practical assessment method on NPS pollution can be built by combining the ECM with the BTOPMC. The main conclusions are as follows: (1) based on the literature survey in the study area, the field data was adopted to confirm the export coefficients of the ECM, the loads of TN and TP were statistically analyzed, and the main pollutant sources were identified in 2012. The quantity of TN and TP estimated by the ECM was 868.5 t and 65.08 t; (2) based on hydrological similarity, runoff data from nearby gauged sites were pooled to compensate for the lack of at-site data; thus, the water quality submodel of distributed hydrological model can be developed to simulate the monthly fluxes of TN and TP in the two sections (Yanjiaxiang section and Xiyangsi section) from 2010 to 2012, and the quantity of TN and TP in 2012 simulated by the BTOPMC was 642.56 t and 50.70 t, respectively. Under the consideration of self-purification capacity of river, the results of these two models in 2012 were both reasonable and mostly identical; (3) based on an overall analysis of conditions counting in all factors, agricultural fertilizer, rural sewage,

and livestock and poultry sewage are the main pollution sources influencing loads of TN and TP in study area and should be controlled first; (4) considering the data shortage in developing countries, the method adopted in this paper can require minimal input data and is especially effective for NPS pollution loads estimation and pollution sources identification in the small-scale and data-sparse watersheds or regions.

Conflict of Interests

The authors declare that there is no conflict of interests regarding the publication of this paper.

Acknowledgments

This study was supported by the National Natural Science Foundation of China (Project no. 50979062), the International S&T Cooperation Projects, the Ministry of Science and Technology of P. R. China (no. 2012DFG21780), the S&T Project of Sichuan Environmental Protection (no. 11HBT-01), the National Basic Search Fund Project of Sichuan University (no. 2010SCU22005), the Development Project of Sichuan Province's Flash Flood Real-Time Prediction System, and the Development and Application Project of the Integrated Storm-Flood Simulation and Prediction System of Flood Disaster Mountain Basin in Sichuan Province.

References

- [1] V. Novotny, *Water Quality: Diffuse Pollution and Watershed Management*, John Wiley & Sons, New York, NY, USA, 2nd edition, 2003.
- [2] F.-H. Hao, H.-G. Cheng, and S.-T. Yang, *Theoretical Methods and Application of Non-Point Source Pollution*, Environmental Science Press of China, Beijing, China, 1st edition, 2006.
- [3] X. W. Ding, Z. Y. Shen, R. M. Liu, L. Chen, and M. Lin, "Effects of ecological factors and human activities on nonpoint source pollution in the upper reach of the Yangtze River and its management strategies," *Hydrology and Earth System Sciences Discussions*, vol. 11, no. 1, pp. 691–721, 2014.
- [4] Z. L. Zhu, D. Norse, and B. Sun, *Policy for Reducing Non-Point Pollution from Crop Production in China*, Environmental Science Press of China, Beijing, China, 1st edition, 2006.
- [5] X. Wang, "Management of agricultural nonpoint source pollution in China: current status and challenges," *Water Science and Technology*, vol. 53, no. 2, pp. 1–9, 2006.
- [6] E. D. Ongley, Z. Xiaolan, and Y. Tao, "Current status of agricultural and rural non-point source pollution assessment in China," *Environmental Pollution*, vol. 158, no. 5, pp. 1159–1168, 2010.
- [7] G. J. Pelletier, S. C. Chapra, and H. Tao, "QUAL2Kw—a framework for modeling water quality in streams and rivers using a genetic algorithm for calibration," *Environmental Modelling & Software*, vol. 21, no. 3, pp. 419–425, 2006.
- [8] T. A. Wool, R. B. Ambrose, J. L. Martin, E. A. Comer, and T. Tech, *Water Quality Analysis Simulation Program (WASP). User's Manual Version 6*, 2006.
- [9] DHIWater & Environment, "A modelling system for rivers and channels," Mike11, version 2007, Reference Manual, DHIWater & Environment, Hørsholm, Denmark, 2007.

- [10] Z. Shen, J. Qiu, Q. Hong, and L. Chen, "Simulation of spatial and temporal distributions of non-point source pollution load in the Three Gorges Reservoir Region," *Science of The Total Environment*, vol. 493, pp. 138–146, 2014.
- [11] Y. Chahor, J. Casali, R. Giménez, R. L. Bingner, M. A. Campo, and M. Goñi, "Evaluation of the AnnAGNPS model for predicting runoff and sediment yield in a small Mediterranean agricultural watershed in Navarre (Spain)," *Agricultural Water Management*, vol. 134, pp. 24–37, 2014.
- [12] USEPA, *National Management Measures for the Control of Nonpoint Pollution from Agriculture*, USEPA, Washington, DC, USA, 2000.
- [13] M. Talebizadeh, S. Morid, S. A. Ayyoubzadeh, and M. Ghasemzadeh, "Uncertainty analysis in sediment load modeling using ANN and SWAT model," *Water Resources Management*, vol. 24, no. 9, pp. 1747–1761, 2010.
- [14] A. M. Sexton, A. Shirmohammadi, A. M. Sadeghi, and H. J. Montas, "Impact of parameter uncertainty on critical SWAT output simulations," *Transactions of the ASABE*, vol. 54, no. 2, pp. 461–471, 2011.
- [15] P. J. Johnes and A. L. Heathwaite, "Modelling the impact of land use change on water quality in agricultural catchments," *Hydrological Processes*, vol. 11, no. 3, pp. 269–286, 1997.
- [16] Chinese Academy for Environmental Planning (CAEP), *National Water Environmental Capacity Validation Manual*, Chinese Academy for Environmental Planning (CAEP), Beijing, China, 2003.
- [17] P. J. Johnes and P. E. O'Sullivan, "The natural history of Slapton Ley Nature Reserve XVIII. Nitrogen and phosphorus losses from the catchment—an export coefficient approach," *Field Studies*, vol. 7, no. 2, pp. 285–309, 1989.
- [18] P. J. Johnes, *An investigation of the effects of land use upon water quality in the Windrush catchment [Ph.D. dissertation]*, University of Oxford, 1990.
- [19] X. Ma, Y. Li, M. Zhang, F. Zheng, and S. Du, "Assessment and analysis of non-point source nitrogen and phosphorus loads in the Three Gorges Reservoir Area of Hubei Province, China," *Science of the Total Environment*, vol. 412–413, pp. 154–161, 2011.
- [20] L.-L. Ying, X.-Y. Hou, X. Lu, and M.-M. Zhu, "Discussion on the export coefficient model in NPS pollution studies in China," *Journal of Water Resources & Water Engineering*, vol. 21, no. 6, pp. 90–95, 2010.
- [21] G.-J. Zhao, P. Tian, X.-M. Mu, J.-F. Gao, H.-P. Li, and Z.-X. Zhang, "Estimation of nitrogen and phosphorus loads in the Xitiaoxi catchment using PCRaster software," *Advances in Water Science*, vol. 23, no. 1, pp. 80–86, 2012.
- [22] X.-W. Ding, R.-M. Liu, and Z.-Y. Shen, "Method for obtaining parameters of export coefficient model using hydrology and water quality data and its application," *Journal of Beijing Normal University (Natural Science)*, vol. 42, no. 5, pp. 534–538, 2006.
- [23] D. Xiao-wen, S. Zhen-yao, and L. Rui-min, "Temporal-spatial changes of non-point source nitrogen in upper reach of Yangtze River Basin," *Journal of Agro-Environment Science*, vol. 26, no. 3, pp. 836–844, 2007.
- [24] X.-W. Ding and Z.-Y. Shen, "Spatial distribution and pollution source identification of agricultural non-point source pollution in Fujiang watershed," *Environmental Science*, vol. 33, no. 11, pp. 4025–4032, 2012.
- [25] R.-M. Liu, Z.-Y. Shen, X.-W. Ding, X. Wu, and F. Liu, "Application of export coefficient model in simulating pollution load of non-point source in upper reach of Yangze River Basin," *Journal of Agro-Environment Science*, vol. 27, no. 2, pp. 667–682, 2008.
- [26] G.-W. Ma, Y.-Y. Wang, B. Xiang et al., "Diversity and effect of diffuse source pollution load caused by land use change in the upper reach of Yangtze River Basin, China," *Journal of Agro-Environment Science*, vol. 31, no. 4, pp. 791–797, 2012.
- [27] T. Ao, H. Ishidaira, and Akeuchi, K., "Study of distributed runoff simulation model based on block type Topmodel and Muskingum—Cunge method," *Annual Journal of Hydraulic Engineering*, vol. 43, pp. 7–12, 1999 (Japanese).
- [28] T. Ao, H. Ishidaira, K. Takeuchi et al., "Relating BTOPMC model parameters to physical features of MOPEX basins," *Journal of Hydrology*, vol. 320, no. 1–2, pp. 84–102, 2006.
- [29] Y.-A. Wan, F. Yin, Z.-Z. Liu, W.-C. Cui, and T.-Q. Ao, "Study on the effect of DEM spatial resolution and sampling algorithms on runoff simulation by BTOPMC," in *Proceedings of the 2nd International Symposium on Hydrological Modelling and Integrated Water Resources Management in Ungauged Mountainous Watersheds for IAHS-PUB*, pp. 130–136, IAHS Press, Chengdu, China, November 2008.
- [30] X. Liu, X. Wen, X. Li, Y. Ma, Y. Dong, and T. Ao, "Influence of time scale of precipitation on parameters of BTOPMC model and simulation results of flood," *Water Resource of Power*, vol. 30, no. 6, pp. 49–52, 2012.
- [31] H.-B. Zhang, *Basic study on the assessment methods of rural non-point source pollution in basin scale and their application [Ph.D. dissertation]*, Sichuan University, 2014.
- [32] J. G. Arnold, R. Srinivasan, R. S. Muttiah, and J. R. Williams, "Large area hydrologic modeling and assessment part I: model development," *Journal of the American Water Resources Association*, vol. 34, no. 1, pp. 73–89, 1998.
- [33] T. Ao, *Development of a distributed hydrological model for large river basins and its application to Southeast Asian rivers [Ph.D. dissertation]*, University of Yamanashi, Kofu, Japan, 2001.
- [34] H. Chen, Y. Teng, and J. Wang, "Load estimation and source apportionment of nonpoint source nitrogen and phosphorus based on integrated application of SLURP model, ECM, and RUSLE: a case study in the Jinjiang River, China," *Environmental Monitoring and Assessment*, vol. 185, no. 2, pp. 2009–2021, 2013.
- [35] M. Garrick, C. Cunnane, and J. E. Nash, "A criterion of efficiency for rainfall-runoff models," *Journal of Hydrology*, vol. 36, no. 3–4, pp. 375–381, 1978.

Research Article

Analysis of Changes in Precipitation and Drought in Aksu River Basin, Northwest China

Yuhu Zhang,¹ Wanyuan Cai,¹ Qiuhua Chen,² Yunjun Yao,³ and Kaili Liu²

¹College of Resources Environment & Tourism, Capital Normal University, Beijing 100048, China

²School of Mathematical Sciences, Capital Normal University, Beijing 100048, China

³State Key Laboratory of Remote Sensing Science, College of Global Change and Earth System Science, Beijing Normal University, Beijing 100875, China

Correspondence should be addressed to Wanyuan Cai; 743483324@qq.com

Received 23 October 2014; Revised 15 January 2015; Accepted 11 February 2015

Academic Editor: Ming Pan

Copyright © 2015 Yuhu Zhang et al. This is an open access article distributed under the Creative Commons Attribution License, which permits unrestricted use, distribution, and reproduction in any medium, provided the original work is properly cited.

The analysis of the spatiotemporal trends of precipitation and drought is relevant for the future development and sustainable management of water resources in a given region. In this study, precipitation and Standardized Precipitation Index (SPI) trends were analyzed through applying linear regression, Mann–Kendall, and Spearman's Rho tests at the 5% significance level. For this goal, meteorological data from 9 meteorological stations in and around Aksu Basin during the period 1960–2010 was used, and two main annual drought periods were detected (1978–1979 and 1983–1986), while the extremely dry years were recorded in 1975 and 1985 at almost all of the stations. The monthly analysis of precipitation series indicates that all stations had increasing trend in July, October, and December, while both increasing and decreasing trends were found in other months. For the seasonal scale, precipitation series had increasing trends in summer and winter. 33% of the stations had the decreasing trend on precipitation in the spring series, and it was 11% in the autumn. At the same time, the SPI-12 values of all stations had the increasing trend. The significant trends were detected at Aheqi, Baicheng, Keping, and Kuche stations.

1. Introduction

Drought is the result of insufficient or lack of rainfall for an extended period, which causes a substantial hydrological (water) imbalance. Numerous indices have been applied to determine different drought characteristics depending on the study purpose. Precipitation-based drought indices with prearranged thresholds are valid since the main reason of drought is rainfall deficit [1, 2].

In the past decade, many scientists have analyzed the spatial variability of drought using drought indices and precipitation characteristics [2–8]. There were a lot of studies on drought [8–13] and various indices have been applied to measure different drought characteristics depending on research goals. The study related to precipitation is a prerequisite for other research studies. Analysis of precipitation data outputs helpful conclusion, which will be applied to plan and manage water resources system. For arid and semiarid regions, precipitation is a particularly important factor for

water resources planning and drought risk management. Moreover, arid areas propose a challenge due to large contradistinction between dry and wet conditions within a temporal cycle.

The arid region of northwest China is one of the most sensitive areas in the world in terms of responding to global climate change [14, 15]. The Aksu River Basin is located in the western part of the middle southern slope of the Tianshan Mountains and at the northwestern edge of the Tarim Basin in Xinjiang Uygur Autonomous Region of northwestern China. Research on drought for this area can contribute to early warning and water resource plan. Therefore, it is important to research the spatiotemporal trend of precipitation and drought in the past several decades in the Aksu River Basin.

Many scholars have studied the characteristics of precipitation changes in different regions in China over the past 50 years [16–20]. The major results indicated that precipitation in summer in eastern China shifted southward in the late 1970s [21, 22], national average precipitation increased with

the increasing precipitation in spring but slightly decreasing in autumn in the last decades [23] and the frequency of heavy precipitation events increased in China [24]. Mechanisms have also been proposed to explain precipitation changes [25–27]. Affected by decadal changes of the global climate system, precipitation in China is characterized with significant decadal changes, especially since the 1990s, and the increased global warming plus the reenhanced East Asian monsoon are bound to influence the regional precipitation distribution and its changing trend. Precipitation changes might greatly affect regional climate stability, hydrological processes, and water availability.

Furthermore, there have been a number of drought and precipitation studies for different periods in Aksu River Basin. Related studies [28–35] have indicated that there is a change about precipitation and drought indices. For example, Chen et al. [36] summarized that the streamflow from the headwaters of the Tarim River shows significant increase and is sensitive to precipitation, but the streamflow along the mainstream of the river has decreased. Chen et al. [37, 38] analyzed the fifty-year climate change and its effect on annual runoff at Aksu River Basin. The streamflow showed a significant increasing monotonic trend. The annual runoff in the Aksu River had increased by 10.9% since 1990. They also detected the long-term trends of the hydrological time series using both parametric and nonparametric techniques based on temperature and precipitation data from the past 50 years. The temperature, the precipitation, and the streamflow from the headwater of the Tarim River exhibited a significant increase during the last 20 years. Lee and Zhang [39] further developed the relationship between NAO and drought disasters in northwestern China. Statistical results show that NAO and drought disaster were negatively correlated, as positive modes of NAO caused northward-displaced, stronger-than-average midlatitude Westerlies with an enhanced latitudinal water vapor gradient into the central Asian drylands, resulting in reduced drought frequency and intensity in northwestern China. Ling et al. [40] investigated intra-annual runoff trends and periods in the headstream areas of the Tarim River Basin by nonparametric tests and wavelet analysis. The results showed that the runoff, air temperature, and precipitation of the headstreams increased remarkably during both high-flow and low-flow periods.

However, most of the previous work on a comprehensive analysis of trends and variability using statistical test and drought indices in precipitation series over Aksu River Basin is still lacking. Thus, it is necessary to analyze the trend of precipitation and characteristics of drought to explore the causes and the formation mechanism of Aksu River Basin drought, which is vital for drought forecast, defense, and mitigation. The analysis of drought variability can improve water resources management in the area.

The main goals of the study were to study variability of precipitation on monthly, seasonal, and annual time scale through applying the linear regression, Mann–Kendall, and Spearman's Rho methods to assess precipitation prediction for the Aksu River Basin in China and to analyze the impact of serial correlation in detecting trends and to investigate the drought in study area from 1960 to 2010.

2. Materials and Methods

2.1. Study Area and Database. The Aksu River Basin (75°35'–82°00'E; 40°17'–42°27'N) is located in the western part of the middle southern slope of the Tianshan Mountains and at the northwestern edge of the Tarim Basin. The total area is $5.14 \times 10^4 \text{ km}^2$, of which the area of the region in China is $3.1 \times 10^4 \text{ km}^2$. The basin is in the interior of the Eurasian continent. Vast territory, diverse topography, complex terrain, and typical regional climate variations made up the characteristics of the northwest mountain climate. It has lower temperatures, plentiful precipitation, and aged snow in the high mountain zone, while the middle mountain zone brings about changes in temperature clearly and is the largest precipitation distribution area. The low mountain zone suffers from drought, large temperature changes, and is fairly well in heat conditions. Due to the Taklimakan Desert in the south and the Tianshan Mountains in the north, the cool air and vapor derived from Central Asia, Siberia, and Arctic Ocean do not straightly enter into the southeastern plain region, which causes typical temperate continental dry climate regional characteristics such as minimal precipitation, intense evaporation, adequate sunshine, and extreme heat [41].

Daily precipitation, saturation vapor pressure, net radiation, soil heat flux density, temperature, average 24 h wind speed at 2 m height, and vapor pressure data were collected from 9 meteorological stations distributed in study area (shown in Figure 1) for the period 1961–2010 and were obtained from meteorological data shared in service system of China (<http://data.cma.gov.cn/>). Seasons were defined as follows: winter = December, January, and February; spring = March, April, and May; summer = June, July, and August, and autumn = September, October, and November. The geographical location of the selected meteorological stations is presented in Table 1.

The precipitation datasets were investigated for homogeneity and absence of trends. The autocorrelation analysis was applied to the monthly precipitation time series of each station. The precipitation data were quality controlled (QC) from [42].

2.2. Rainfall Variability Index (RVI). RVI (δ) is calculated as follows:

$$\delta_i = \frac{(P_i - \mu)}{\sigma}, \quad (1)$$

where δ_i = Rainfall Variability Index for year i , P_i = annual rainfall for year i , and μ and σ are the mean annual rainfall and standard deviation for the period of the year 1961–2010. A drought year occurs if the δ is negative.

According to WMO [43], rainfall time series can be classified into different climatic regimes:

$$\begin{aligned} \text{extreme dry: } & P < \mu - 2 \cdot \sigma, \\ \text{dry: } & \mu - 2 \cdot \sigma < P < \mu - \sigma, \\ \text{normal: } & \mu - \sigma < P < \mu + \sigma, \\ \text{wet: } & P > \mu + \sigma. \end{aligned} \quad (2)$$

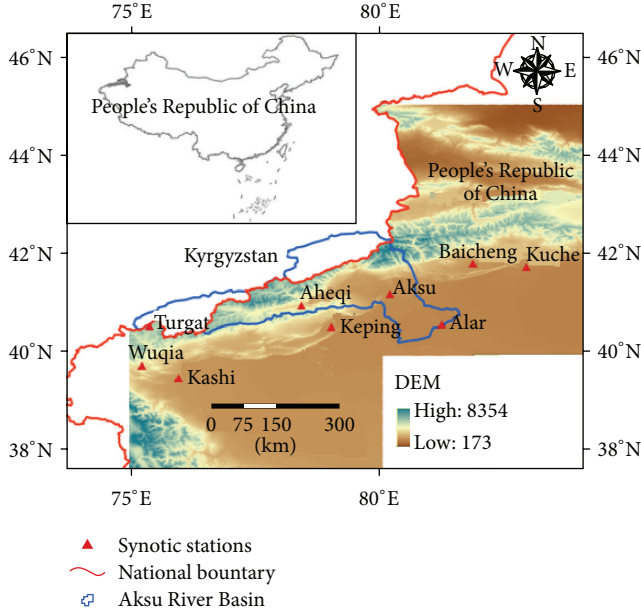


FIGURE 1: Location map of the 9 synoptic stations in Aksu River Basin of China.

TABLE 1: Location of the stations.

Site name	Code	Lat. (N)	Long (E)	Elev. (m)
Aksu	51628	41.10	80.14	1105
Aheqi	51711	40.93	78.45	1986
Alar	51730	40.55	81.27	1012
Baichen	51633	41.79	81.9	1229
Keping	51720	40.5	79.05	1162
Kuche	51644	41.72	82.97	1082
Turgat	51701	40.31	75.24	3507
Wuqia	51705	39.72	75.25	2176
Kashi	51709	39.28	75.59	1291

2.3. *Aridity Index (AI)*. In this study, we employed Aridity Index [44] to quantify the drought occurrence as a numerical indicator of the degree of dryness of the climate at each study location. According to the ratio of precipitation (P) to potential evapotranspiration (PET), regions were classified from extremely arid to humid. PET was calculated using the FAO Penman-Monteith method widely [45]. It can be calculated as [46]

$$PET = \frac{0.408 \cdot \Delta \cdot (R_n - G) + \gamma \cdot (900 / (T + 273)) U_2 \cdot VPD}{\Delta + \gamma \cdot (1 + 0.34 \cdot U_2)}, \quad (3)$$

where PET = potential evapotranspiration (mm day^{-1}); Δ = slope of the saturation vapor pressure function ($\text{kPa}^\circ\text{C}^{-1}$); R_n = net radiation ($\text{MJ m}^{-2} \text{day}^{-1}$); G = soil heat flux density ($\text{MJ m}^{-2} \text{day}^{-1}$); γ = psychrometric constant ($\text{kPa}^\circ\text{C}^{-1}$); T =

mean air temperature ($^\circ\text{C}$); U_2 = average 24-h wind speed at 2 m height (ms^{-1}); and VPD = vapor pressure deficit (kPa).

The locations were then classified as extremely arid ($P/PET \leq 0.05$), arid ($0.05 < P/PET \leq 0.2$), semiarid ($0.2 < P/PET \leq 0.5$), subhumid ($0.5 < P/PET \leq 0.65$), or humid ($P/PET > 0.65$) [2, 47].

2.4. *Drought Indices*. Drought indices are the most indispensable elements for drought analysis and monitoring since they enable identification and quantification of droughts. There have been numerous drought indices such as Standardized Precipitation Index (SPI), the Palmer Hydrological Drought Index (PHDI), Standardized Precipitation Evapotranspiration Index (SPEI), the Surface Water Supply Index (SWSI), Palmer Drought Severity Index (PDSI), and the Standardized Anomaly Index (SAI). The establishment of unique and universally accepted drought indices does not exist, although a number of drought indices have been proposed [13, 48, 49].

In this study, the SPI was applied, because of its good characteristics in drought identification and prediction of drought class transitions [8–10]. During the first decade of the 21st century, the Standardized Precipitation Index (SPI) was widely used. And it is simple and considers only precipitation data, which can be found nearly everywhere.

2.4.1. *Standardized Precipitation Index*. The Standardized Precipitation Index (SPI) was proposed by McKee et al. [50, 51] to indicate the precipitation deficit at different time scales (i.e., accumulated over given time spans). The SPI is a probability index that involves only precipitation. The probabilities are standardized so that an index of zero indicates the mean precipitation amount. The relative simplicity of the SPI is one solid advantage of the index [52]. The main criticism to the SPI is that its calculation is based solely on precipitation data, not considering other variables that determine drought conditions such as temperature, evapotranspiration, wind speed, or the soil water holding capacity.

Calculating the SPI for a certain time period at any places requires completed monthly data for the quantity of precipitation, at least 30-annual sequence [53, 54].

SPI is mathematically based on the cumulative probability of some precipitation recorded at the observation post. Research has shown that precipitation is subject to the law of gamma distribution [55–57]. One whole period of observation at one meteorological station is used to determine the parameters of scaling and the forms of precipitation probability density function:

$$g(x) = \frac{1}{\beta^\alpha \cdot \Gamma(\alpha)} x^{\alpha-1} \cdot e^{-x/\beta}, \quad x > 0, \quad (4)$$

where α = form parameter; β = scale parameter; x = precipitation quantity; $\Gamma(\alpha)$ = gamma function defined by the following statement:

$$\Gamma(\alpha) = \int_0^\infty y^{\alpha-1} e^{-y} dy. \quad (5)$$

Parameters α and β are determined by the method of maximum probability for a multiyear data sequence; that is,

$$\alpha_{\text{pro}} = \frac{1}{4A} \left(1 + \sqrt{1 + \frac{4A}{3}} \right),$$

$$A = \ln(x_{\text{sr}}) - \frac{\sum_{i=1}^n \ln(x_i)}{n}, \quad (6)$$

$$\beta_{\text{pro}} = \frac{x_{\text{sr}}}{\alpha_{\text{pro}}},$$

where x_{sr} is the mean value of precipitation quantity; n is the precipitation measurement number; x_i is the quantity of precipitation in a sequence of data.

The acquired parameters are further applied to the determination of a cumulative probability of certain precipitation for a specific time period in a time scale of all the recorded precipitation. The cumulative probability can be presented as

$$G(x) = \int_0^x g(x) dx = \frac{1}{\beta_{\text{pro}}^{\alpha_{\text{pro}}} \Gamma(\alpha_{\text{pro}})} \int_0^x x^{\alpha_{\text{pro}}-1} e^{-x/\beta_{\text{pro}}} dx. \quad (7)$$

Because the gamma function has not been defined for $x = 0$ and the precipitation may be up to zero, the cumulative probability becomes

$$H(x) = q + (1 - q)G(x), \quad (8)$$

where q is the probability that the quantity of precipitation equals zero, which is calculated using the following equation:

$$q = \frac{m}{n}, \quad (9)$$

where m is the number which represented how many times the precipitation was zero in a temporal sequence of data and n is the precipitation observation number in a sequence of data.

The calculation of the SPI is presented on the basis of the following equation [58–60]:

$$\text{SPI} = \begin{cases} - \left(t - \frac{c_0 + c_1 t + c_2 t^2}{1 + d_1 t + d_2 t^2 + d_3 t^3} \right), & 0 < H(x) \leq 0.5, \\ + \left(t - \frac{c_0 + c_1 t + c_2 t^2}{1 + d_1 t + d_2 t^2 + d_3 t^3} \right), & 0.5 < H(x) \leq 1.0, \end{cases} \quad (10)$$

where t is determined as

$$t = \begin{cases} \sqrt{\frac{\ln \frac{1}{(H(x))^2}}}, & 0 < H(x) \leq 0.5, \\ \sqrt{\frac{\ln \frac{1}{(1-H(x))^2}}}, & 0.5 < H(x) \leq 1.0. \end{cases} \quad (11)$$

And $c_0, c_1, c_2, d_1, d_2,$ and d_3 are coefficients whose values are [58–60]

$$\begin{aligned} c_0 &= 2.515517, & c_1 &= 0.802853, & c_2 &= 0.010328, \\ d_1 &= 1.432788, & d_2 &= 0.189269, & d_3 &= 0.001308. \end{aligned} \quad (12)$$

TABLE 2: Drought classification of SPI.

Drought class	SPI value
Nondrought	SPI ≥ 0
Near normal	$-1 < \text{SPI} < 0$
Moderate	$-1.5 < \text{SPI} \leq -1$
Severe/extreme	SPI ≤ -1.5

The drought classification of SPI is presented in Table 2 that grouped the severe and extremely severe drought classes for modeling aims since transitions referring to the extremely severe droughts are much less frequent than those for other classes [9]. The SPI on shorter time scales (e.g., 3 and 6 months) describes drought events affecting agricultural practices. In this study, the SPI at 12-month time scale was selected and analyzed because it is more suitable for water resources management purposes in a certain region and more appropriate for identifying the persistence of dry periods [8, 10, 13, 61, 62].

According to the criteria of McKee et al. [50, 51], severe and extreme droughts corresponding to the categories, respectively, are as shown in Table 2.

2.5. Statistical Methods. Many statistical techniques (parametric or nonparametric) have been developed to detect trends within time series such as linear regression, Spearman's Rho test, Mann–Kendall test, Sen's slope estimator, and Bayesian procedure [63–68]. In this study, the Mann–Kendall and Spearman's Rho tests were used to analyze the precipitation trends, while the linear regression was used to calculate magnitude of trends.

2.5.1. Mann–Kendall Trend Test. The Mann–Kendall test statistic S [69, 70] is calculated as

$$S = \sum_{i=1}^{n-1} \sum_{j=i+1}^n \text{sgn}(x_j - x_i), \quad (13)$$

where n is the number of data points, x_i and x_j are the data values in time series i and j ($j > i$), respectively, and $\text{sgn}(x_j - x_i)$ is the sign function determined as

$$\text{sgn}(x_j - x_i) = \begin{cases} +1, & \text{if } x_j - x_i > 0, \\ 0, & \text{if } x_j - x_i = 0, \\ -1, & \text{if } x_j - x_i < 0. \end{cases} \quad (14)$$

In cases where the sample size $n > 10$, the mean and variance are given by

$$\begin{aligned} \mu(S) &= 0, \\ \sigma^2(S) &= \frac{n(n-1)(2n+5) - \sum_{i=1}^m t_i(t_i-1)(2t_i+5)}{18}, \end{aligned} \quad (15)$$

where m is the number of tied groups and t_i denotes the number of ties of extent i . A tied group is a set of sample data having the same value.

In the absence of ties between the observations, the variance is computed as

$$\sigma^2(S) = \frac{n(n-1)(2n+5)}{18}. \quad (16)$$

The standard normal test statistic Z_S is computed as

$$Z_S = \begin{cases} \frac{S-1}{\sqrt{\sigma^2(S)}}, & \text{if } S > 0, \\ 0, & \text{if } S = 0, \\ \frac{S+1}{\sqrt{\sigma^2(S)}}, & \text{if } S < 0. \end{cases} \quad (17)$$

Positive values of Z_S indicate increasing trends while the negative Z_S shows decreasing trends.

Testing of trends is done at a specific α significance level. In this study, the significance level of $\alpha = 0.05$ was used. At the 5% significance level, the null hypothesis of no trend is rejected if $|Z_S| > 1.96$.

2.5.2. Spearman's Rho Test. Spearman's Rho test is nonparametric method commonly used to verify the absence of trends. Its statistic D and the standardized test statistic Z_D are expressed as follows [71, 72]:

$$D = 1 - \frac{6 \sum_{i=1}^n (R(X_i) - i)^2}{n(n^2 - 1)}, \quad (18)$$

$$Z_D = D \sqrt{\frac{n-2}{1-D^2}},$$

where $R(X_i)$ is the rank of i th observation X_j in the time series and n is the length of the time series.

Positive values of Z_D indicate increasing trends while negative Z_D show decreasing trends. At the 5% significance level, the null hypothesis of no trend is rejected if $|Z_D| > 2.08$.

2.5.3. Serial Autocorrelation Test. To remove serial correlation from the series, von Storch and Navarra [73] suggested to prewhiten the series before applying the Mann-Kendall and Spearman's Rho tests. The lag-1 serial correlation coefficient of sample data x_i (designated by r_1) is computed as [74, 75]

$$r_1 = \frac{(1/(n-1)) \sum_{i=1}^{n-1} (x_i - \mu(x_i)) \cdot (x_{i+1} - \mu(x_{i+1}))}{(1/n) \sum_{i=1}^n (x_i - \mu(x_i))^2}, \quad (19)$$

$$\mu(x_i) = \frac{1}{n} \sum_{i=1}^n x_i,$$

where $\mu(x_i)$ is the mean of sample data and n is the sample size.

For the two-sided test, Unkašević and Tošić [68] recommended that the 0.05 significance level for r_1 can be computed by

$$r_1(0.05) = \frac{-1 \pm 1.96 \sqrt{n-2}}{n-1}, \quad (20)$$

where n is the sample size.

3. Results and Discussion

3.1. Summary of Statistical Parameters. Statistical parameters of monthly precipitation time series at 9 synoptic stations during the period 1960–2010 are summarized in Table 3. The minimal monthly precipitation is 0 mm for all stations. The mean monthly precipitation is ranged from 4.076 mm to 20.554 mm. Moreover, it is obvious that 3 mountainous synoptic stations in the northwest (Aheqi, Turgat, and Wuqia) had the highest mean monthly precipitation.

The highest kurtosis of the precipitation values was observed at Aksu station with 16.699, while the lowest kurtosis of 2.682 was found at Turgat. This phenomenon indicated that the monthly precipitation in Turgat is relatively homogeneous. But it is converse in Aksu.

Time series of annual precipitation at the 9 synoptic stations are shown in Figure 2. The results indicated that the annual precipitation had a certain degree of variance during the observed period. In Aksu, Alar, Kuche, and Kashi, the annual precipitation is relatively low and basic by about 50 mm. However, the annual precipitation in Aheqi, Wuqia, and Turgat, is above 200 mm. In addition, the annual precipitation in Baicheng, Kuche, and Keping has obvious upward trend during the observed period. These results show that the precipitation in upstream of Aksu basin is larger than that in downstream.

3.2. Aridity Index. The estimated UNEP Aridity Index for the 9 synoptic stations is given in Table 4. The FAO-56 Penman-Monteith equation as a part of the model based on service-oriented paradigm [76, 77] is used for estimating PET. The results indicated that the Aridity Index ranged from 0.048 at the Alar station to 0.397 at the Turgat station. The Alar station is extremely arid and the Aheqi station and the Turgat station are semiarid, while all other stations are arid. The upper limit for extremely arid climate is 0.05, but Alar had a slightly lower value. The Alar station is extremely arid because of the highest PET, minimum of the annual precipitation, and the highest value of the temperature difference.

3.3. Rainfall Variability. Annual rainfall variability indices for the observed synoptic stations are shown in Figure 3, while the percentage distribution of dry, normal, and wet years during the period 1960–2010 is given in Figure 4. It is obvious that there was no extremely dry year for all stations. Although, considering both time series of precipitation and annual rainfall variability indices for the 9 synoptic stations, there were two main periods which were characterized by long and severe droughts, namely, 1978–1979 and 1983–1986.

During the first period, the drought years were approximately 55% of the total years. The second period is characterized by approximately 47% of the drought years. In addition, it should be noticed that there were 4 dry years, 1961, 1975, 1985, and 2007. These four years were characterized by approximately 89% negative values of the annual rainfall variability index.

3.4. Analysis of Precipitation. The serial correlation coefficient can improve the verification of the independence of

TABLE 3: Statistical parameters of monthly precipitation time series at 9 synoptic stations during the period 1960–2010.

Station name	Min (mm)	Max (mm)	Mean (mm)	Standard deviation (mm)	CV (%)	Skewness	Kurtosis
Aksu	0	92.2	6.162	10.148	164.672	3.343	16.699
Aheqi	0	145.2	17.920	23.597	131.676	1.983	4.520
Alar	0	50.9	4.076	7.546	185.139	2.737	8.473
Baicheng	0	76.8	9.920	12.367	124.664	2.115	5.874
Keping	0	81.2	8.029	13.348	166.253	2.553	7.537
Kuche	0	65.3	5.818	8.832	151.812	2.499	7.620
Turgat	0	122.1	20.554	21.380	104.015	1.615	2.682
Wuqia	0	121.6	15.009	18.471	123.071	1.878	4.080
Kashi	0	78.5	5.615	9.561	170.283	3.099	12.861

Note: cv-coefficient of variation.

TABLE 4: Aridity Index, annual precipitation, and reference evapotranspiration estimated using FAO-56 Penman–Monteith equation.

Station name	Precipitation (mm/year)	PET (mm/year)	Aridity index	Climate
Aksu	73.947	972.22	0.076	Arid
Aheqi	215.045	985.51	0.218	Semiarid
Alar	48.910	1023.91	0.048	Extreme arid
Baicheng	119.041	832.52	0.143	Arid
Keping	96.343	1102.73	0.087	Arid
Kuche	69.812	1164.73	0.060	Arid
Turgat	246.653	621.34	0.397	Semiarid
Wuqia	180.106	1082.91	0.166	Arid
Kashi	67.380	1125.91	0.060	Arid

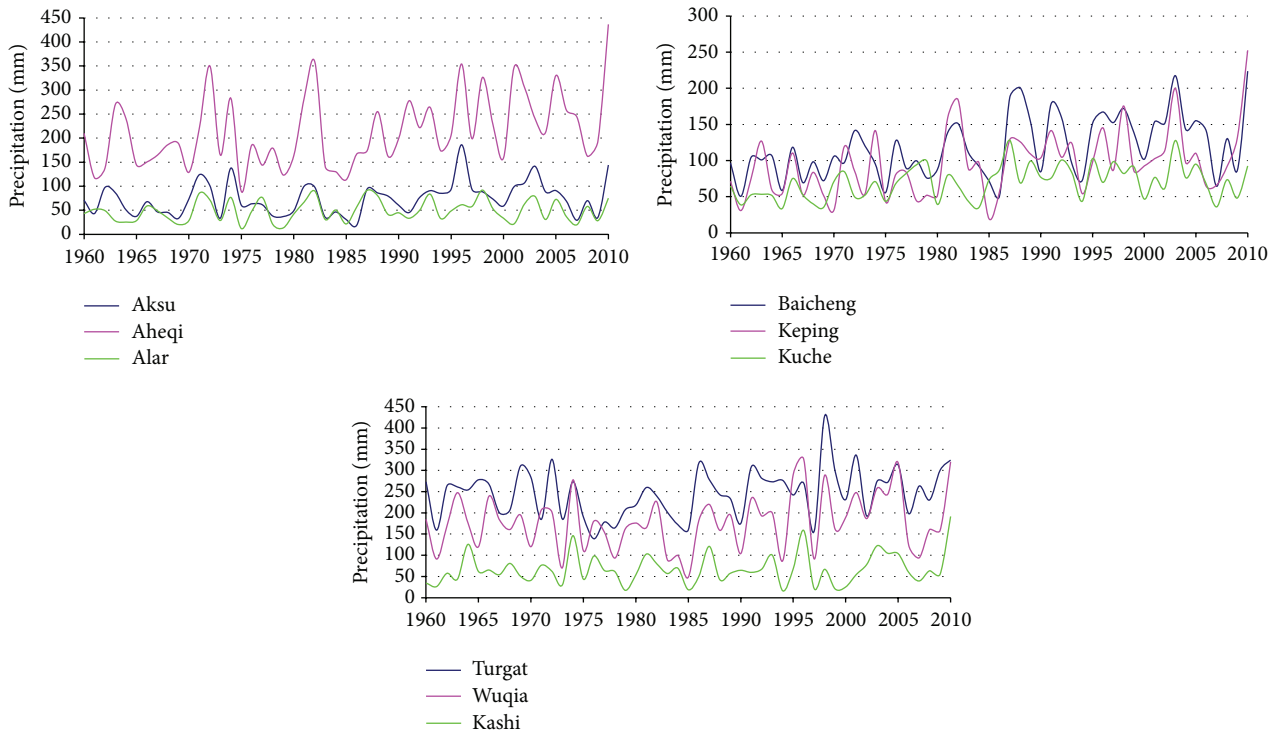


FIGURE 2: Annual precipitation time series at the 9 synoptic stations.

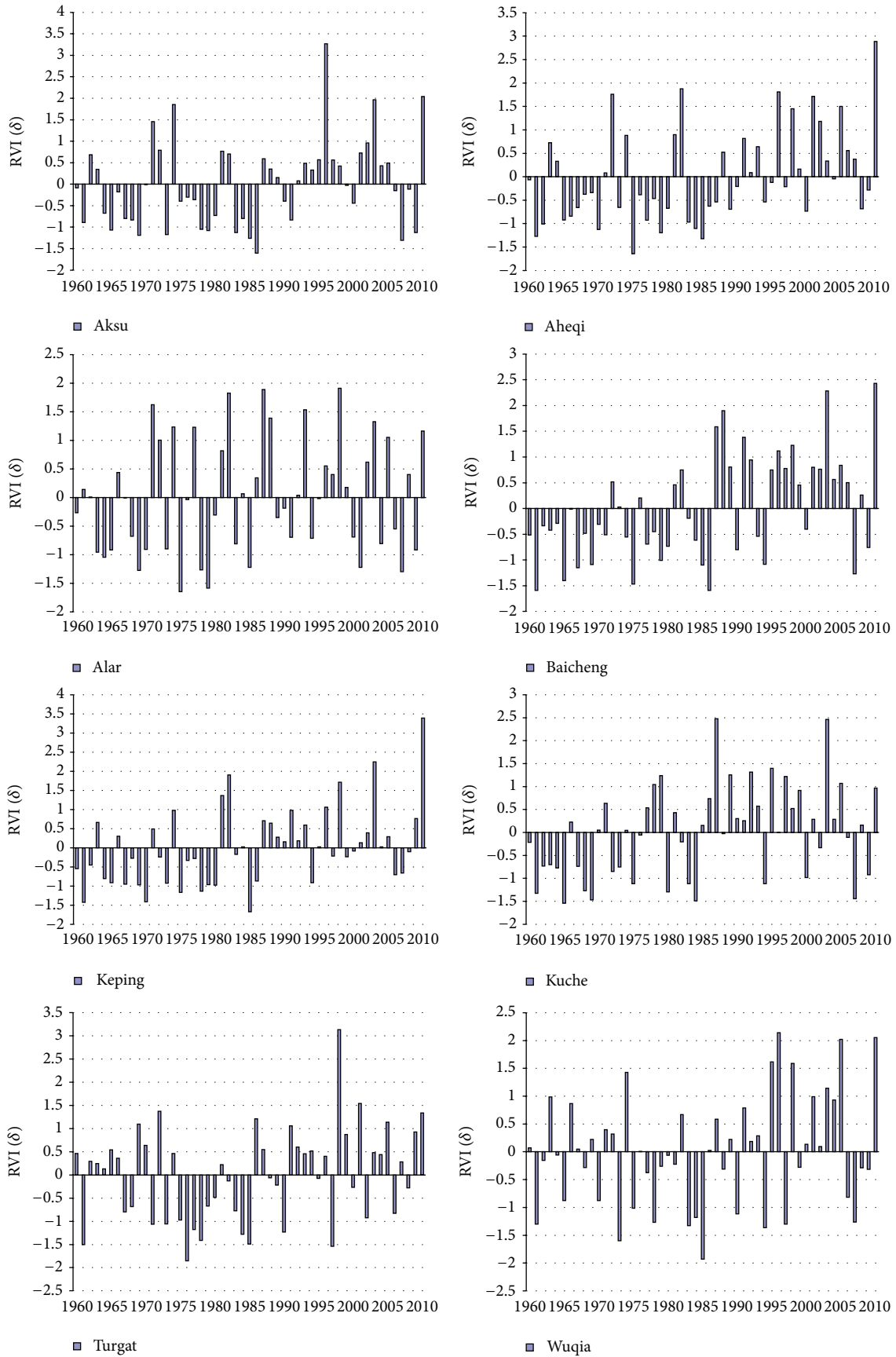


FIGURE 3: Continued.

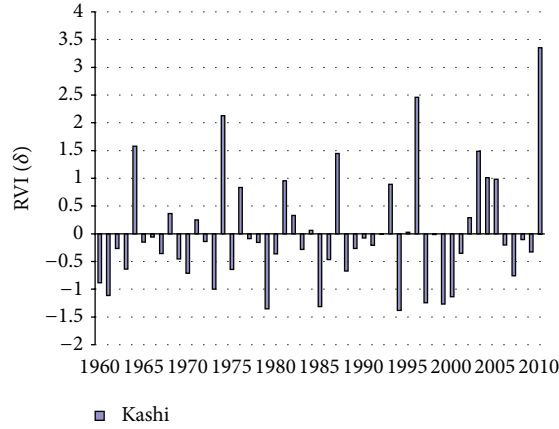


FIGURE 3: Annual rainfall variability indices for the 9 synoptic stations.

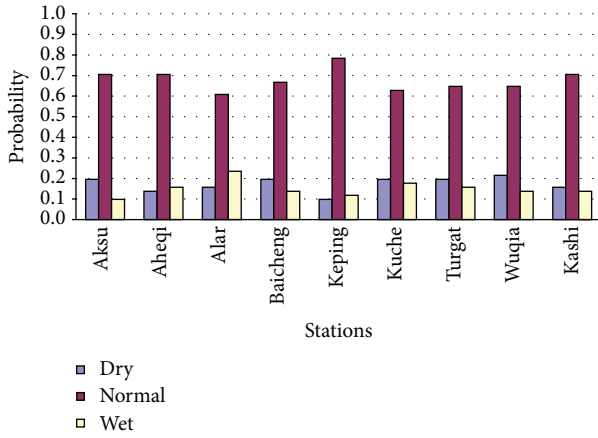


FIGURE 4: Distribution in percentage of dry, normal, and wet years for the 9 synoptic stations during the period 1960–2010.

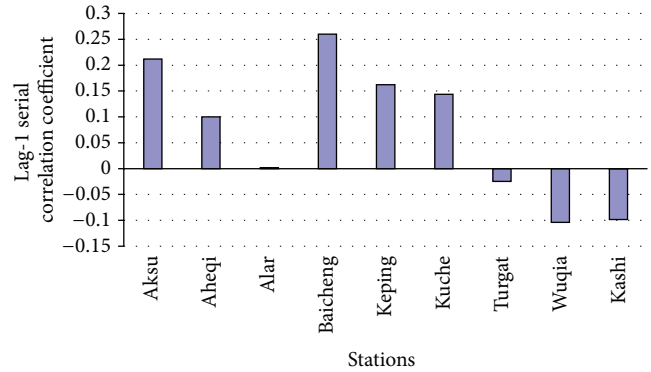


FIGURE 5: Lag-1 serial correlation coefficient for the precipitation at the synoptic stations.

precipitation time series. If the time series are completely random, the autocorrelation function will be zero for all lags other than zero. In this study, to accept the hypothesis $H_0: r_1 = 0$ (that there is no correlation between two consecutive observations and there is no persistence in the time series), the value of r_1 should fall between -0.2544 and 0.2544 .

Autocorrelation plot for the annual precipitation at the 9 synoptic stations is presented in Figure 5. As shown, the precipitation had both positive and negative serial correlations. The highest and at the same time the significant serial correlation of 0.260 was obtained at the Baicheng station, while the lowest serial correlation of -0.104 was detected at the Wuqia station.

Lag-1 serial correlation coefficients for seasonal precipitation data at the observed stations during the period 1960–2010 are presented in Table 5. As shown, a positive serial correlation was found in the spring, summer, autumn, and winter series at 77.8%, 88.9%, 66.7%, and 77.8% of the stations, respectively. The significant serial correlation was detected in the autumn at Aheqi station. Trends of precipitation are considered statistically at the 5% significance level using the

TABLE 5: Lag-1 serial correlation coefficients for seasonal precipitation data.

Station name	Spring	Summer	Autumn	Winter
Aksu	0.102	0.105	-0.042	0.181
Aheqi	0.199	0.009	0.395	0.102
Alar	-0.006	0.147	-0.108	-0.078
Baicheng	0.192	0.160	0.140	0.187
Keping	0.059	0.167	0.014	0.113
Kuche	0.106	0.035	-0.077	0.077
Turgat	0.028	0.019	0.090	0.163
Wuqia	-0.020	0.100	0.131	-0.068
Kashi	0.054	-0.050	0.090	0.019

Mann–Kendall test and the Spearman’s Rho test. When a significant trend is identified by two statistical methods, the trend is presented in bold character in Table 6.

The results of the statistical tests for the monthly precipitation series during the period 1960–2010 are summarized in Table 6. As shown, the precipitation in Baicheng station had the significant increasing trend in June and September. The significant increasing trend was also detected at the

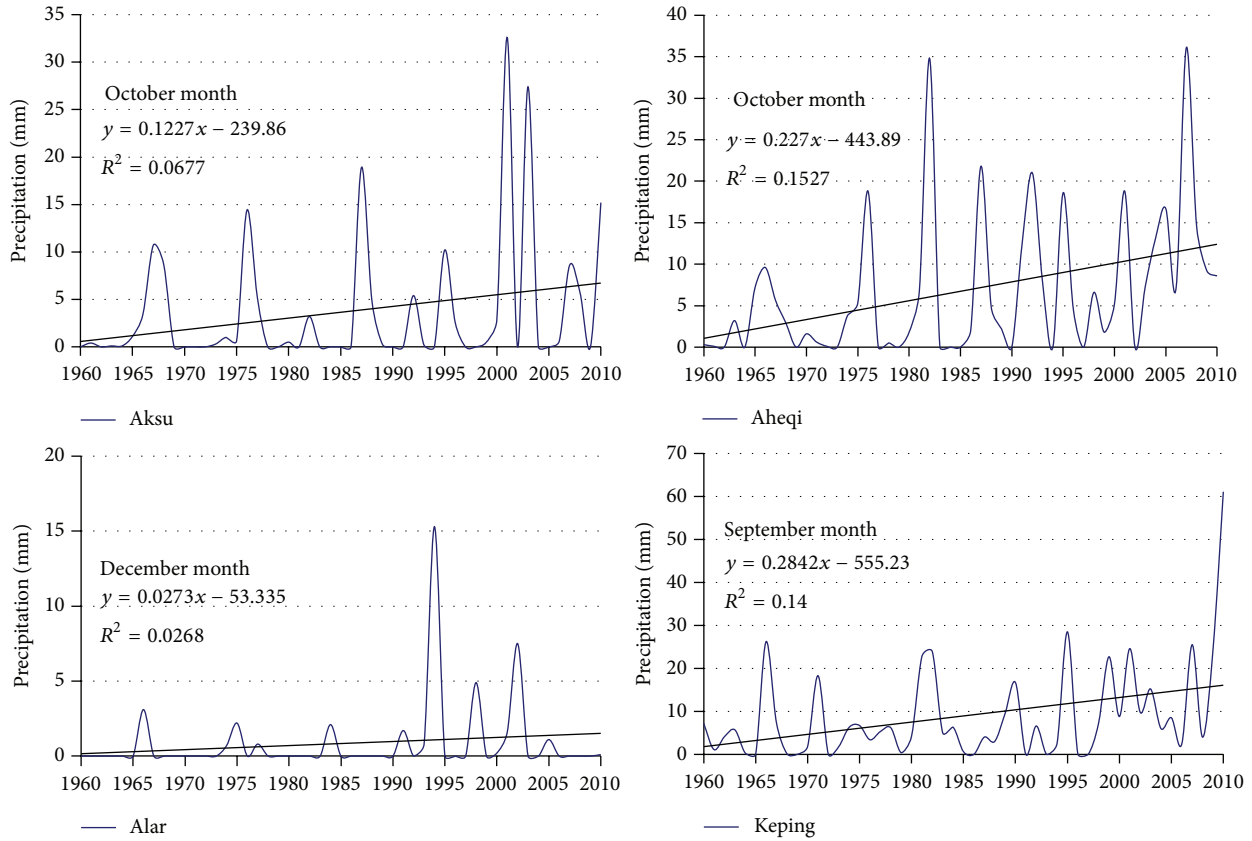


FIGURE 6: Variations of monthly precipitation in stations with the significant trends during the study period.

Kuche station in January, June, and December. There was no decreasing trend. Besides, A statistically significant trend $Z_S = 2.380$ was detected in September at the Aheqi station before eliminating the effect of serial correlation. After removing lag-1 serial correlation effect, an insignificant trend of $Z_S = 1.673$ was obtained. Furthermore, an insignificant trend $Z_D = 1.633$ was detected in January at the Kuche station before eliminating the effect of serial correlation. After removing lag-1 serial correlation effect a significant trend of $Z_S = 2.893$ was obtained.

Seasonal and annual trends of precipitation obtained by statistical methods are given in Table 7. According to these results, the increasing trends in annual precipitation series were detected at Aheqi, Baicheng, Keping, and Kuche, while there is no significant trend for other stations which is consistent with our analysis in Section 3.1. On annual level, precipitation quantities are increasing, with the highest increase in winter.

For the seasonal scale, there were increasing trends in summer and winter precipitation series. The decreasing precipitation trend was found in the spring and autumn series at 33% and 11% of the stations, respectively. Besides, the significant increasing trends were found at Aheqi and Kashi in autumn and at Alar and Kuche in winter. Furthermore, the significant increasing trends were detected at Baicheng in summer, autumn, and winter. The precipitation of Keping also had increasing trends in summer and autumn.

3.5. Analysis of SPI-12. Time series of SPI-12 at the 9 synoptic stations during the period 1960–2010 are shown in Figure 7. Characteristics of drought at 12-month time scale are shown in Table 8. It should be observed that the most severe drought of Aheqi and Alar was 1975, while that of Keping and Wuqia occurred in 1985. Besides, the most severe drought year was 1976 at Bacheng station and 1986 at Aksu station. The Wuqia station had the lowest SPI-12 with -2.5986 in 1985. The number of drought years during the observed period at the stations is presented in Table 8. According to the results, the total drought years ranged between 14 (at Wuqia and Kashi station) and 19 (at Alar station). Almost 32.2% of the observed years were drought years at all the 9 stations.

Lag-1 serial correlation coefficient for the SPI-12 at the observed synoptic stations is illustrated in Figure 8. The highest and at the same time the significant positive serial correlation coefficient of 0.2676 was detected at the Aksu station. On the other hand, negative values were observed at the Turgat, Wuqia, and Kashi stations.

The results of the Mann–Kendall and Spearman’s Rho tests for the SPI-12 series are presented in Figure 9. It can be noted that all stations have the increasing trend. The significant trends were detected at Aheqi, Baicheng, Keping, and Kuche stations.

Although a significantly increasing trend was detected in the SPI-12 series of all the observed stations, it can be determined that the western regions of Aksu River Basin have

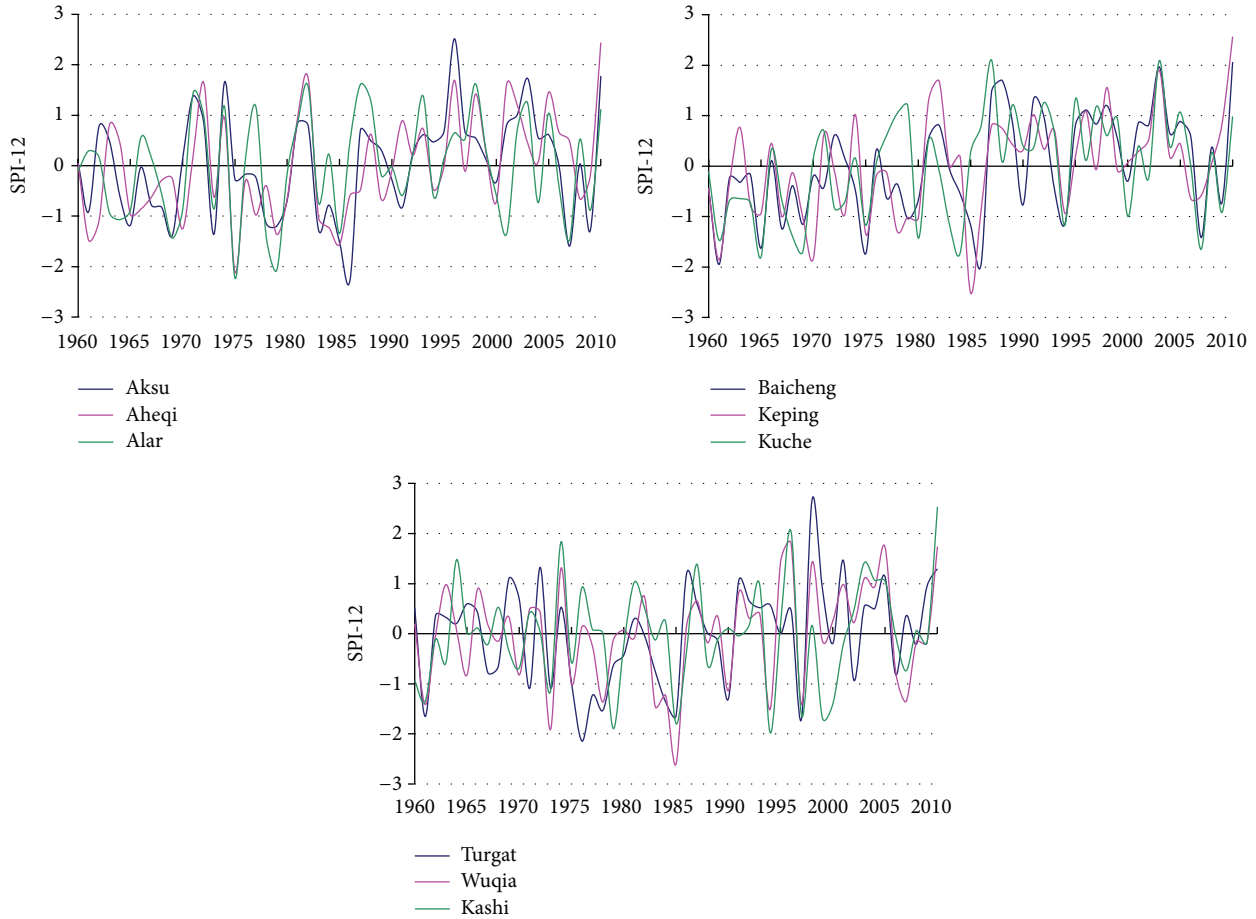


FIGURE 7: Time series of SPI-12 at the 9 synoptic stations.

become much drier than the other parts during the period 1960–2010. This had significant impact on agriculture and water supply.

4. Conclusions

Based on the analysis of the variation of precipitation and drought indices and correlation in the multisites in this study area during 1960–2010, the following conclusions can be drawn from this study.

Precipitation trends and drought behavior at monthly, seasonal, and annual time scale in Aksu River Basin between 1960 and 2010 were investigated, respectively. In order to achieve this, monthly, seasonal, and annual precipitation data from 9 Serbian synoptic stations were analyzed using the Mann–Kendall test and the Spearman’s Rho test after eliminating the effect of significant lag-1 serial correlation from the time series. Besides, aridity and annual rainfall variability indices were estimated.

According to these results, two main annual drought periods were detected (1978–1979 and 1983–1986), while the dry year was 1975 and 1985 at almost all of the stations. The monthly analysis of precipitation series suggests that all stations had increasing trend in July, October, and December,

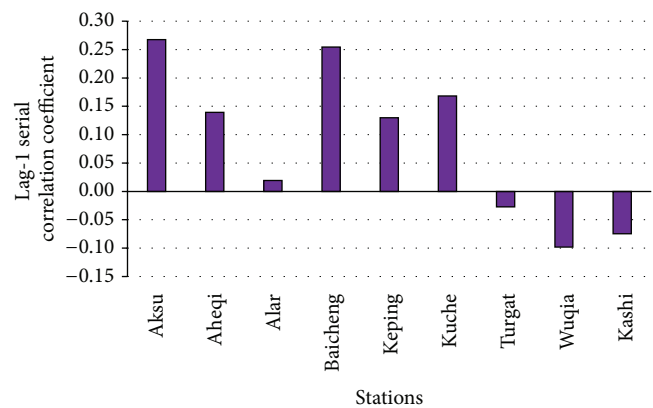


FIGURE 8: Lag-1 serial correlation coefficient for the SPI-12 at the 9 synoptic stations.

while both increasing and decreasing trends were found in other months. At the seasonal scale, there were increasing trends in summer and winter precipitation series. The decreasing precipitation trend was found in the spring and autumn series at 33% and 11% of the stations, respectively.

TABLE 6: Results of the statistical tests for the monthly precipitation during the period 1960–2010.

Station	Test	Month											
		January	February	March	April	May	June	July	August	September	October	November	December
Aksu	Z_S	0.233	0.760	0.411	-0.579	0.276	1.755	0.796	-0.926	1.365	0.976	0.000	1.588
	Z_D	0.410	0.884	0.586	-0.279	0.232	2.014	0.793	-0.890	1.318	1.203	0.789	2.060
	b	0.023	0.060	0.058	0.016	0.011	0.184	0.036	-0.075	0.138	0.122	-0.008	0.038
Aheqi	Z_S	0.139	0.383	0.789	0.545	0.016	-0.244	1.576	0.390	1.673	2.795*	0.798	1.088
	Z_D	0.159	0.319	0.816	0.615	0.026	-0.146	1.766	0.524	1.729	3.249*	1.020	1.250
	b	0.014	0.019	0.129	0.019	0.058	-0.054	0.513	0.236	0.877	0.227	-0.001	0.024
Alar	Z_S	1.454	1.175	-0.102	-0.171	0.073	1.276	1.186	-0.016	-0.552	0.026	0.603	1.523
	Z_D	1.964	2.166*	0.658	0.494	-0.025	1.439	1.309	0.021	-0.399	0.521	2.088*	2.747*
	b	0.025	0.028	0.023	-0.014	-0.050	0.078	0.106	0.069	-0.067	0.013	-0.003	0.027
Baicheng	Z_S	1.206	1.007	0.253	0.262	1.089	2.193*	1.901	1.324	2.161*	1.322	0.886	1.605
	Z_D	1.394	0.786	0.247	0.339	1.155	2.477*	1.926	1.175	2.207*	1.339	1.313	1.783
	b	0.042	0.083	0.037	-0.025	0.077	0.268	0.234	0.122	0.228	0.231	0.089	0.042
Keping	Z_S	0.311	1.171	1.308	-0.198	-0.073	0.918	1.706	1.405	2.278*	1.363	-0.249	0.937
	Z_D	0.525	1.064	1.665	-0.185	-0.026	0.999	1.849	1.485	2.447*	1.726	1.112	1.482
	b	0.045	0.037	0.102	0.009	-0.014	0.112	0.273	0.367	0.284	0.079	-0.012	0.031
Kuche	Z_S	2.633*	0.919	-0.694	0.679	0.699	2.437*	0.999	1.357	0.553	0.513	1.896	2.533*
	Z_D	2.893*	1.024	-0.541	0.773	0.808	2.747*	1.057	1.279	0.476	0.651	2.626*	3.113*
	b	0.048	0.052	-0.036	0.023	0.106	0.207	0.061	0.063	0.019	0.013	-0.010	0.039
Turgat	Z_S	0.033	-0.455	0.723	0.227	-0.382	1.527	0.796	0.398	-0.106	2.713*	0.122	2.211*
	Z_D	-0.046	-0.428	0.619	0.254	-0.387	1.498	0.794	0.392	-0.066	2.810*	0.190	2.307*
	b	-0.003	-0.018	0.019	0.091	-0.058	0.285	0.164	0.130	0.023	0.253	-0.006	0.093
Wuqia	Z_S	0.708	-1.122	-0.228	-0.041	0.195	1.600	1.787	-0.024	0.699	2.847*	-0.016	1.027
	Z_D	0.699	-1.394	-0.375	-0.097	0.007	1.822	2.194*	-0.008	0.677	2.983*	-0.151	1.176
	b	0.032	-0.039	-0.048	0.011	-0.092	0.465	0.407	-0.076	0.141	0.239	-0.015	0.029
Kashi	Z_S	0.507	-0.638	1.455	-0.156	0.602	0.999	1.406	0.268	1.223	3.249*	0.365	1.035
	Z_D	0.685	-0.387	1.758	-0.164	0.401	1.146	1.327	0.199	1.294	3.908*	1.071	1.430
	b	0.048	-0.015	0.106	-0.058	-0.115	0.096	0.111	-0.025	0.104	0.170	0.024	0.020

Z_S : Mann–Kendall test, Z_D : Spearman’s Rho test, and b : slope of linear regression.

Bold characters represent trends identified by 2 statistical methods together.

*Statistically significant trends at the 5% significance level.

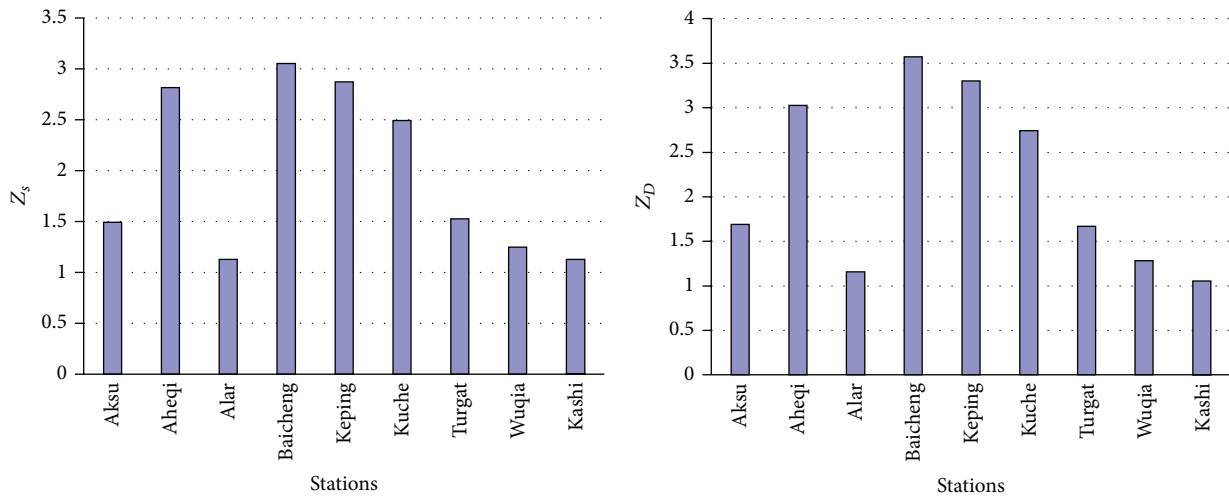


FIGURE 9: Mann–Kendall test (Z_S) and Spearman’s Rho test (Z_D) for the SPI-12 series.

TABLE 7: Results of the statistical tests for seasonal and annual precipitation during the period 1960–2010.

Station	Test	Season					Annual
		Spring	Summer	Autumn	Winter		
Aksu	Z_S	0.341	0.780	1.673	1.154	1.495	
	Z_D	0.295	0.952	1.696	1.264	1.690	
	b	0.084	0.145	0.253	0.125	0.603	
Aheqi	Z_S	0.309	1.056	2.209*	0.739	2.819*	
	Z_D	0.434	1.106	2.338*	0.529	3.026*	
	b	0.206	0.695	1.103	0.055	2.062	
Alar	Z_S	-0.520	1.592	-0.390	1.947	1.129	
	Z_D	-0.567	1.793	-0.325	2.152*	1.159	
	b	-0.041	0.253	-0.057	0.083	0.235	
Baicheng	Z_S	0.390	2.713*	2.266*	2.112*	2.193*	
	Z_D	0.392	3.029*	2.444*	2.214*	2.620*	
	b	0.089	0.624	0.548	0.166	1.427	
Keping	Z_S	0.244	2.372*	2.429*	1.357	2.875*	
	Z_D	0.404	2.567*	2.552*	1.483	3.300*	
	b	0.097	0.752	0.351	0.113	1.313	
Kuche	Z_S	0.430	1.852	0.423	2.145*	2.494*	
	Z_D	0.416	2.050*	0.263	2.274*	2.743*	
	b	0.093	0.331	0.023	0.141	0.585	
Turgat	Z_S	0.195	1.503	1.194	1.803	1.527	
	Z_D	0.283	1.379	1.225	1.874	1.667	
	b	0.052	0.579	0.270	0.099	0.973	
Wuqia	Z_S	-0.260	1.462	1.698	0.065	1.251	
	Z_D	-0.342	1.599	1.579	0.062	1.281	
	b	-0.129	0.796	0.365	0.014	1.054	
Kashi	Z_S	-0.195	1.121	2.527*	0.390	1.129	
	Z_D	-0.223	1.150	2.547*	0.499	1.055	
	b	-0.067	0.182	0.297	0.041	0.466	

Z_S : Mann–Kendall test, Z_D : Spearman's Rho test, and b : slope of linear regression.

Bold characters represent trends identified by 2 statistical methods together.

*Statistically significant trends at the 5% significance level.

TABLE 8: Characteristics of droughts at 12-month time scale.

Station	The most severe drought		Number of drought years during the observed period			
	SPI	Year	Near normal	Moderate	Severe/extreme	Total
Aksu	-2.2748	1986	7	7	3	17
Aheqi	-2.1138	1975	10	6	2	18
Alar	-2.2262	1975	11	6	2	19
Keping	-2.5112	1985	8	5	3	16
Baicheng	-1.9470	1961	5	6	4	15
Kuche	-1.8056	1965	8	6	4	18
Turgat	-2.1432	1976	7	5	5	17
Wuqia	-2.5986	1985	3	8	3	14
Kashi	-1.9757	1994	6	3	5	14

For the SPI-12, all stations have the increasing trend. The significant trends were detected at Aheqi, Baicheng, Keping, and Kuche stations (As shown in Figure 6). Based on the analysis of trends of precipitation and drought behavior, precipitation in Aksu River Basin had an increasing trend.

And drought condition, including drought severity and drought duration, became better. The analyzed results of precipitation and SPI-12 series can be helpful for basin-scale water resources management, agricultural production. Further research in analyzing the spatial variation of

precipitation trends and the relationship with the climate change projection is recommended. Moreover, the future work will be oriented into developing an information system for monitoring and early drought warning.

Conflict of Interests

The authors declare that there is no conflict of interests.

Authors' Contribution

Yuhu Zhang and Wanyuan Cai prepared the paper. Yuhu Zhang, Qiuhua Chen, and Kaili Liu made the data processing. Yunjun Yao contributed to the discussion.

Acknowledgments

The financial support of this work has been provided by the National Science and Technology Support Plan during the 12th Five-Year Plan Period of China projects (Grants nos. 2013BAC10B01 and 2012BAC19B03) and State Key Laboratory of Desert and Oasis Ecology, Xinjiang Institute of Ecology and Geography, Chinese Academy of Sciences downscaling correction model for satellite precipitation in mountainous area of Xinjiang. It is also realized as a part of the Project "Statistical Analysis and Information Extraction of High-Dimensional Complicate Data" jointly funded by Scientific Research Project of Beijing Educational Committee (no. KZ201410028030). The authors also would like to thank the editors and the anonymous reviewers for their crucial comments, which will improve the quality of this paper.

References

- [1] H. Hisdal, K. Stahl, L. M. Tallaksen, and S. Demuth, "Have streamflow droughts in Europe become more severe or frequent?" *International Journal of Climatology*, vol. 21, no. 3, pp. 317–333, 2001.
- [2] M. Gocic and S. Trajkovic, "Analysis of precipitation and drought data in Serbia over the period 1980–2010," *Journal of Hydrology*, vol. 494, pp. 32–42, 2013.
- [3] M. Gemmer, S. Becker, and T. Jiang, "Observed monthly precipitation trends in China 1951–2002," *Theoretical and Applied Climatology*, vol. 77, no. 1–2, pp. 39–45, 2004.
- [4] T. Partal and E. Kahya, "Trend analysis in Turkish precipitation data," *Hydrological Processes*, vol. 20, no. 9, pp. 2011–2026, 2006.
- [5] Q. Liu, Z. Yang, and B. Cui, "Spatial and temporal variability of annual precipitation during 1961–2006 in Yellow River Basin, China," *Journal of Hydrology*, vol. 361, no. 3–4, pp. 330–338, 2008.
- [6] P. G. Oguntunde, B. J. Abiodun, and G. Lischeid, "Rainfall trends in Nigeria, 1901–2000," *Journal of Hydrology*, vol. 411, no. 3–4, pp. 207–218, 2011.
- [7] H. Tabari and P. H. Talaei, "Temporal variability of precipitation over Iran: 1966–2005," *Journal of Hydrology*, vol. 396, no. 3–4, pp. 313–320, 2011.
- [8] H. Tabari, H. Abghari, and P. Hosseinzadeh Talaei, "Temporal trends and spatial characteristics of drought and rainfall in arid and semiarid regions of Iran," *Hydrological Processes*, vol. 26, no. 22, pp. 3351–3361, 2012.
- [9] E. E. Moreira, C. A. Coelho, A. A. Paulo, L. S. Pereira, and J. T. Mexia, "SPI-based drought category prediction using loglinear models," *Journal of Hydrology*, vol. 354, no. 1–4, pp. 116–130, 2008.
- [10] A. A. Paulo and L. S. Pereira, "Stochastic prediction of drought class transitions," *Water Resources Management*, vol. 22, no. 9, pp. 1277–1296, 2008.
- [11] S. Shahid, "Spatial and temporal characteristics of droughts in the western part of Bangladesh," *Hydrological Processes*, vol. 22, no. 13, pp. 2235–2247, 2008.
- [12] D. Khalili, T. Farnoud, H. Jamshidi, A. A. Kamgar-Haghighi, and S. Zand-Parsa, "Comparability analyses of the SPI and RDI meteorological drought indices in different climatic zones," *Water Resources Management*, vol. 25, no. 6, pp. 1737–1757, 2011.
- [13] A. K. Mishra and V. P. Singh, "A review of drought concepts," *Journal of Hydrology*, vol. 391, no. 1–2, pp. 202–216, 2010.
- [14] Y. H. Ding, G. Y. Ren, Z. C. Zhao et al., "Detection, causes and projection of climate change over China: an overview of recent progress," *Advances in Atmospheric Sciences*, vol. 24, no. 6, pp. 954–971, 2007.
- [15] Y. Shi, Y. Shen, E. Kang et al., "Recent and future climate change in northwest China," *Climatic Change*, vol. 80, no. 3–4, pp. 379–393, 2007.
- [16] H. Weng, K.-M. Lau, and Y. Xue, "Multi-scale summer rainfall variability over China and its long-term link to global sea surface temperature variability," *Journal of the Meteorological Society of Japan*, vol. 77, no. 4, pp. 845–857, 1999.
- [17] C.-P. Chang, Y. Zhang, and T. Li, "Interannual and interdecadal variations of the East Asian summer monsoon and tropical pacific SSTs. Part I: Roles of the subtropical ridge," *Journal of Climate*, vol. 13, no. 24, pp. 4310–4325, 2000.
- [18] G. Ren, H. Wu, and Z. Chen, "Spatial patterns of change trend in rainfall of China," *Quarterly Journal of Applied Meteorology*, vol. 11, pp. 322–330, 2000.
- [19] Y. Ding, Z. Wang, and Y. Sun, "Inter-decadal variation of the summer precipitation in east China and its association with decreasing Asian summer monsoon. Part I: observed evidences," *International Journal of Climatology*, vol. 28, no. 9, pp. 1139–1161, 2008.
- [20] Y. Lei, B. Hoskins, and J. Slingo, "Exploring the interplay between natural decadal variability and anthropogenic climate change in summer rainfall over China. Part I: observational evidence," *Journal of Climate*, vol. 24, no. 17, pp. 4584–4599, 2011.
- [21] R. H. Zhang, B. Y. Wu, P. Zhao, and J. Han, "The decadal shift of the summer climate in the late 1980s over East China and its possible causes," *Acta Meteorological Sinica*, vol. 66, pp. 697–706, 2008.
- [22] P. Zhao, Y. Song, and R. C. Yu, "Long-term changes in rainfall over Eastern China and large-scale atmospheric circulation associated with recent global warming," *Journal of Climate*, vol. 23, no. 6, pp. 1544–1562, 2010.
- [23] D. Yihui, R. Guoyu, S. Guangyu et al., "China's national assessment report on climate change (I): climate change in China and the future trend," *Advances in Climate Change Research*, vol. 3, supplement, pp. 1–5, 2007.
- [24] K. E. Trenberth and P. D. Jones, "Observations: surface and atmospheric climate change," in *Climate Change 2007: The Physical Science Basis*, S. Solomon, D. Qin, M. Manning et al., Eds., chapter 3, pp. 235–336, Cambridge University Press, Cambridge, UK, 2007.

- [25] H. Ye and R. Lu, "Subseasonal variation in ENSO-related east asian rainfall anomalies during summer and its role in weakening the relationship between the ENSO and summer rainfall in eastern china since the late 1970s," *Journal of Climate*, vol. 24, no. 9, pp. 2271–2284, 2011.
- [26] A. Duan, M. Wang, Y. Lei, and Y. Cui, "Trends in summer rainfall over china associated with the Tibetan Plateau sensible heat source during 1980–2008," *Journal of Climate*, vol. 26, no. 1, pp. 261–275, 2013.
- [27] Z. Zhu, T. Li, and J. He, "Out-of-phase relationship between Boreal spring and summer decadal rainfall changes in Southern China," *Journal of Climate*, vol. 27, no. 3, pp. 1083–1099, 2014.
- [28] Y. N. Chen and Z. X. Xu, "Plausible impact of global climate change on water resources in the Tarim River Basin," *Science in China, Series D: Earth Sciences*, vol. 48, no. 1, pp. 65–73, 2005.
- [29] H. Li, Z. Jiang, and Q. Yang, "Association of north atlantic oscillations with aksu river runoff in China," *Journal of Geographical Sciences*, vol. 19, no. 1, pp. 12–24, 2009.
- [30] S. Zhang, S. Liu, X. Mo, C. Shu, Y. Sun, and C. Zhang, "Assessing the impact of climate change on reference evapotranspiration in Aksu River Basin," *Acta Geographica Sinica*, vol. 65, no. 11, pp. 1363–1370, 2010.
- [31] S. Zhang, S. Liu, X. Mo, C. Shu, Y. Sun, and C. Zhang, "Assessing the impact of climate change on potential evapotranspiration in Aksu River Basin," *Journal of Geographical Sciences*, vol. 21, no. 4, pp. 609–620, 2011.
- [32] B. Li, Y. Chen, X. Shi, Z. Chen, and W. Li, "Temperature and precipitation changes in different environments in the arid region of northwest China," *Theoretical and Applied Climatology*, vol. 112, no. 3-4, pp. 589–596, 2013.
- [33] H. Wang, Y. Chen, S. Xun, D. Lai, Y. Fan, and Z. Li, "Changes in daily climate extremes in the arid area of northwestern China," *Theoretical and Applied Climatology*, vol. 112, no. 1-2, pp. 15–28, 2013.
- [34] S. Han and H. Hu, "Spatial variations and temporal changes in potential evaporation in the Tarim Basin, Northwest China (1960–2006): influenced by irrigation?" *Hydrological Processes*, vol. 26, no. 20, pp. 3041–3051, 2012.
- [35] Q. Zhang, J. Li, V. P. Singh, and Y. Bai, "SPI-based evaluation of drought events in Xinjiang, China," *Natural Hazards*, vol. 64, no. 1, pp. 481–492, 2012.
- [36] Y. N. Chen, K. Takeuchi, C. Xu, Y. P. Chen, and Z. X. Xu, "Regional climate change and its effects on river runoff in the Tarim Basin, China," *Hydrological Processes*, vol. 20, no. 10, pp. 2207–2216, 2006.
- [37] Y.-N. Chen, W.-H. Li, C.-C. Xu, and X.-M. Hao, "Effects of climate change on water resources in Tarim River Basin, Northwest China," *Journal of Environmental Sciences*, vol. 19, no. 4, pp. 488–493, 2007.
- [38] C. Yaning, X. Changchun, H. Xingming et al., "Fifty-year climate change and its effect on annual runoff in the Tarim River Basin, China," *Quaternary International*, vol. 208, no. 1-2, pp. 53–61, 2009.
- [39] H. F. Lee and D. D. Zhang, "Relationship between NAO and drought disasters in northwestern China in the last millennium," *Journal of Arid Environments*, vol. 75, no. 11, pp. 1114–1120, 2011.
- [40] H. Ling, H. Xu, and J. Fu, "Changes in intra-annual runoff and its response to climate change and human activities in the headstream areas of the Tarim River Basin, China," *Quaternary International*, vol. 336, no. 26, pp. 158–170, 2014.
- [41] R. Ouyang, W. Cheng, W. Wang, Y. Jiang, Y. Zhang, and Y. Wang, "Research on runoff forecast approaches to the Aksu River basin," *Science in China, Series D: Earth Sciences*, vol. 50, no. 1, supplement, pp. 16–25, 2007.
- [42] X. L. Wang, "Comment on 'detection of undocumented change point: a revision of the two-phase regression model,'" *Journal of Climate*, vol. 16, no. 20, pp. 3383–3385, 2003.
- [43] World Meteorological Organization (WMO), *Drought and Agriculture*, WMO/TN 138, World Meteorological Organization (WMO), Geneva, Switzerland, 1975.
- [44] United Nations Environmental Programme (UNEP), *World Atlas of Desertification*, United Nations Environmental Programme (UNEP), 1992.
- [45] R. G. Allen, M. E. Jensen, J. L. Wright, and R. D. Burman, "Operational estimates of reference evapotranspiration," *Agronomy Journal*, vol. 81, no. 4, pp. 650–662, 1989.
- [46] R. G. Allen, L. S. Pereira, D. Raes, and M. Smith, "Crop evapotranspiration. Guidelines for computing crop water requirements," FAO Irrigation and Drainage Paper 56, Food and Agriculture Organization of the United Nation, Rome, Italy, 1998.
- [47] M. Bannayan, S. Sanjani, A. Alizadeh, S. S. Lotfabadi, and A. Mohamadian, "Association between climate indices, aridity index, and rainfed crop yield in Northeast of Iran," *Field Crops Research*, vol. 118, no. 2, pp. 105–114, 2010.
- [48] R. R. Heim Jr., "A review of twentieth-century drought indices used in the United States," *Bulletin of the American Meteorological Society*, vol. 83, no. 8, pp. 1149–1165, 2002.
- [49] M. V. K. Sivakumar, R. P. Motha, D. A. Wilhite, and D. A. Wood, *Agricultural Drought Indices: Proceedings of an Expert Meeting, 2–4 June 2010, Murcia, Spain*, World Meteorological Organization, Geneva, Switzerland, 2010.
- [50] T. B. McKee, N. J. Doesken, and J. Kleist, "The relationship of drought frequency and duration to time scales," in *Proceedings of the 8th Conference on Applied Climatology*, pp. 179–184, Anaheim, Calif, USA, January 1993.
- [51] T. B. McKee, N. J. Doesken, and J. Kleist, "Drought monitoring with multiple time scales," in *Proceedings of the 9th Conference on Applied Climatology*, pp. 233–236, American Meteorological Society, Boston, Mass, USA, January 1995.
- [52] K. E. Logan, N. A. Brunsell, A. R. Jones, and J. J. Feddema, "Assessing spatiotemporal variability of drought in the U.S. central plains," *Journal of Arid Environments*, vol. 74, no. 2, pp. 247–255, 2010.
- [53] M. J. Hayes, M. D. Svoboda, D. A. Wilhite, and O. V. Vanyarkho, "Monitoring the 1996 drought using the standardized precipitation index," *Bulletin of the American Meteorological Society*, vol. 80, no. 3, pp. 429–438, 1999.
- [54] R. A. Seiler, M. Hayes, and L. Bressan, "Using the standardized precipitation index for flood risk monitoring," *International Journal of Climatology*, vol. 22, no. 11, pp. 1365–1376, 2002.
- [55] H. C. S. Thom, "A note on the gamma distribution," *Monthly Weather Review*, vol. 86, no. 4, pp. 117–122, 1958.
- [56] H. C. S. Thom, "Some methods of climatological analysis," WMO Technical Note 81, Secretariat of the World Meteorological Organization, Geneva, Switzerland, 1966.
- [57] D. C. Edwards and T. B. McKee, "Characteristics of 20th century drought in the United States at multiple scales," *Atmospheric Science Paper* 634, 1997.
- [58] M. Abramowitz and I. A. Stegun, *Handbook of Mathematical Functions*, Dover Publications, New York, NY, USA, 1965.

- [59] I. Bordi, S. Frigio, P. Parenti, A. Speranza, and A. Sutera, "The analysis of the Standardized Precipitation Index in the Mediterranean area: large-scale patterns," *Annals of Geophysics*, vol. 44, no. 5-6, pp. 965-978, 2001.
- [60] B. Lloyd-Hughes and M. A. Saunders, "A drought climatology for Europe," *International Journal of Climatology*, vol. 22, no. 13, pp. 1571-1592, 2002.
- [61] B. Bonaccorso, I. Bordi, A. Cancelliere, G. Rossi, and A. Sutera, "Spatial variability of drought: an analysis of the SPI in Sicily," *Water Resources Management*, vol. 17, no. 4, pp. 273-296, 2003.
- [62] T. Raziei, B. Saghafian, A. A. Paulo, L. S. Pereira, and I. Bordi, "Spatial patterns and temporal variability of drought in Western Iran," *Water Resources Management*, vol. 23, no. 3, pp. 439-455, 2009.
- [63] M. Gocic and S. Trajkovic, "Analysis of changes in meteorological variables using Mann-Kendall and Sen's slope estimator statistical tests in Serbia," *Global and Planetary Change*, vol. 100, pp. 172-182, 2013.
- [64] M. A. Kohler, "Double-mass analysis for testing the consistency of records and for making adjustments," *Bulletin of the American Meteorological Society*, vol. 30, pp. 188-189, 1949.
- [65] T. Niedźwiedź, R. Twardosz, and A. Walanus, "Long-term variability of precipitation series in east central Europe in relation to circulation patterns," *Theoretical and Applied Climatology*, vol. 98, no. 3-4, pp. 337-350, 2009.
- [66] A. A. Paulo, R. D. Rosa, and L. S. Pereira, "Climate trends and behaviour of drought indices based on precipitation and evapotranspiration in Portugal," *Natural Hazards and Earth System Science*, vol. 12, no. 5, pp. 1481-1491, 2012.
- [67] J. D. Ruiz Sinoga, R. Garcia Marin, J. F. Martinez Murillo, and M. A. Gabarron Galeote, "Precipitation dynamics in southern Spain: trends and cycles," *International Journal of Climatology*, vol. 31, no. 15, pp. 2281-2289, 2011.
- [68] M. Unkašević and I. Tošić, "A statistical analysis of the daily precipitation over Serbia: trends and indices," *Theoretical and Applied Climatology*, vol. 106, no. 1-2, pp. 69-78, 2011.
- [69] H. B. Mann, "Nonparametric tests against trend," *Econometrica*, vol. 13, pp. 245-259, 1945.
- [70] M. G. Kendall, *Rank Correlation Methods*, Griffin, London, UK, 1975.
- [71] E. L. Lehmann, *Nonparametrics: Statistical Methods Based on Ranks*, HoldenDay, San Francisco, Calif, USA, 1975.
- [72] R. Sneyers, "On the statistical analysis of series of observations," Technical Note no. 143, World Meteorological Organization, Geneva, Switzerland, 1990.
- [73] H. von Storch and A. Navarra, *Analysis of Climate Variability—Applications of Statistical Techniques*, Springer, New York, NY, USA, 1995.
- [74] J. D. Salas, J. W. Delleur, V. M. Yevjevich, and W. L. Lane, *Applied Modeling of Hydrologic Time Series*, Water Resources Publications, Littleton, Colo, USA, 1980.
- [75] M. G. Kendall and A. Stuart, *The Advanced Theory of Statistics: Design and Analysis, and Time-Series*, vol. 3, Charles Griffin & Company Limited, London, UK, 1968.
- [76] M. Gocic and S. Trajkovic, "Software for estimating reference evapotranspiration using limited weather data," *Computers and Electronics in Agriculture*, vol. 71, no. 2, pp. 158-162, 2010.
- [77] M. Gocic and S. Trajkovic, "Service-oriented approach for modeling and estimating reference evapotranspiration," *Computers and Electronics in Agriculture*, vol. 79, no. 2, pp. 153-158, 2011.